Electric Field Assisted Chemical Vapour Deposition Processes on Titanium Dioxide Thin Films for Photocatalysis

Luz Romero

Thesis Submitted in Partial Fulfilment for Requirements of Doctor of Philosophy

Declaration

I, Luz Maria Romero-Nunez, confirm that the research included within this thesis is my own work or that where it has been carried out in collaboration with, or supported by others, that this is duly acknowledged below and my contribution indicated. Previously published material is also acknowledged below.

I attest that I have exercised reasonable care to ensure that the work is original, and does not to the best of my knowledge break any UK law, infringe any third party's copyright or other Intellectual Property Right, or contain any confidential material.

I accept that the College has the right to use plagiarism detection software to check the electronic version of the thesis.

I confirm that this thesis has not been previously submitted for the award of a degree by this or any other university.

Signature:

Date: 05/12/2014

Details of collaboration and publications:

L. Romero, C. Piccirillo, P.M.L. Castro, C. Bowman, M.E.A. Warwick and R. Binions (2014). *Chem. Vap. Dep.* in press.
L. Romero, A.B. Jorge, P.F. McMillan and R. Binions (2014). *J. Solid State Sci. Technol.*, 3, N107-N113.
M.E.A. Warwick, L.M. Romero-Nunez, A.J.T. Naik and R. Binions (2014). Electric Field-Assisted Chemical Vapour Deposition for Nanostructured Thin Films. Comprehensive Materials Processing, Elsevier.
L. Romero and R. Binions (2013). *Surface and Coatings Technology*, 230**,** 196-201.
L. Romero and R. Binions (2013). *Langmuir*, 29**,** 13542-13550.

Abstract

This work investigates the use of the novel electric field assisted chemical vapour deposition (EACVD) process in the production of titanium dioxide thin films for photocatalytic applications on glass substrate. This work looks into the interaction of applied electric fields with the precursor species during the aerosol assisted chemical vapour deposition (AACVD) and atmospheric pressure chemical vapour deposition (APCVD) reaction of Titanium isopropoxide (TTIP) and Titanium (IV) Chloride ($TiCl_4$) with different solvents. The electric field was generated by applying a potential difference between two fluorine-doped tin oxide glass sheets. The electric field was varied between 0 – 3000 Vm^{-1}. The deposited films were analysed and characterized using scanning electron microscopy, X-ray diffraction, Raman spectroscopy, atomic force microscopy, UV-vis spectroscopy, water-contact angles and resazurin photcatalytic testing. It was observed that the application of electric fields produced changes in the morphology, particle size, growth rate, crystal orientation and crystal phases. Generally, films produced under the influence of the electric fields showed higher photo-activity than films produced in absence of electric fields. The deposited films produced from the electric field assisted aerosol chemical vapour deposition (EAACVD) showed higher photo-activity with applied AC electric fields than with applied DC electric fields. Likewise, they showed higher photo-activity than the deposited films produced from the electric field assisted atmospheric pressure chemical vapour deposition (EAAPCVD) with applied AC electric fields. The results obtained were explained by the interaction mechanisms between the electric fields and the precursor species, which differ depending on the CVD technique used. Although titanium dioxide photo-activity is comprised by a combination of factors, it was observed that an optimum can be obtained by varying both experimental conditions and field strength. In particular, optimum results were obtained for deposited films which showed long-shaped particles, reduced particle size and high preferential orientation in the anatase (004) plane.

Electric field assisted chemical vapour deposition (EACVD) shows a great potential for the improvement of commercial products available in the market such as self-cleaning and antibacterial surfaces.

Acknowledgements

First and foremost I would like to thank my supervisor Dr. Russell Binions for having trusted in me to do this project and also for all his support and guidance throughout my research. I would also like to thank my colleagues and friends, Louise Andersson and Shuqun Chen who have been a great support inside and outside the lab.

My thanks to Dr. Michael Warwick who kindly helped me, especially when I first started my PhD. Thanks to Dr. Joe Briscoe for sharing your knowledge and for being such a good friend. I would also like to mention my colleagues and friends from the PhD hub; Nimra, Pelin, Adam, Mike and Stefania. My special thanks to my good friend Dave, who not only made my days at work more fun but also supported me by giving me good pieces of advice. That bay would have not been the same without you. I would also like to mention my friends outside university; Gemma, Maria and Miguel, who always succeeded in amusing me and putting a smile in my face in my stressful times.

I would also like to thank my family to have supported my decisions and to have been there for me even in the distance.

My final thanks to Joe, who has been so important to make this happen. Your love and positivity made all this loads easier, especially when it felt like there was no end in sight. Thanks for your support and just for being there.

Table of Contents

List of Figures

Chapter 1

Chapter 2

Chapter 3

Chapter 4

Chapter 5

Chapter 6

List of Tables

Chapter 2

Chapter 3

Chapter 5

Chapter 6

List of Equations

Chapter 1

Chapter 3

Chapter 4

List of Abbreviations

+ve: Positive bias on substrate.

-ve: Negative bias on substrate

AC: Alternating Current.

AFM: Atomic Force Microscopy.

ALD: Atomic Layer Deposition.

CB: Conduction band.

CVD: Chemical Vapour Deposition.

DBG: Direct band gap.

DC: Direct Current.

DC +: Direct Current (positive bias on substrate).

DC -: Direct Current (negative bias on substrate).

DLI-MO: Direct liquid injection metal organic.

EAACVD: Electric Field Assisted Aerosol Chemical Vapour Deposition.

EACVD: Electric Field Assisted Chemical Vapour Deposition.

EAAPCVD: Electric Field Assisted Atmospheric Pressure Chemical Vapour Deposition.

FTO: Fluorine-doped Tin Oxide.

GFR: Gas flow rate.

LPCVD: Low-Pressure Chemical Vapour Deposition.

PVD: Physical Vapour Deposition.

Rf: Resofurin.

Rz: Resazurin.

RMS: Root Mean Square.

SEM: Scanning Electron Microscopy.

VB: Valence band.

XRD: X-Ray Diffraction.

Chapter 1:

Introduction

1.1. Research question

This research intends to address three main questions in regards to the effect of the electric fields on the chemical vapour deposition growth of titanium dioxide (TiO_2) and the photocatalytic properties of the material. The main questions are:

1. What are the possible interaction mechanisms of electric fields during the chemical vapour deposition of TiO_2 and how this influences the microstructure of the material?
2. How the induced changes on the microstructure influence the photocatalytic performance of the material?
3. What are the experimental conditions that lead to optimum photocatalytic performance of the material? This includes the type of CVD rig, type of precursor and oxygen source, type of electric field (AC or DC) and other experimental conditions such as substrate temperature and gas flow rate.

1.2. Titanium dioxide thin films in the modern world

Titanium dioxide (TiO_2) is one of the most widely used benchmark standard photocatalysts for environmental applications. The discovery of the photolysis of water on TiO_2 surface in 1972 [1] led to decades of intensive research into the chemical – physical processes involved. The continuing interest of TiO_2 as a coating material resides in its chemical and biological inertness, photo-activity, inexpensiveness, ease of preparation [2] and other advantageous properties. Due to its high refractive index, it is used as anti-reflection coating in silicon solar cells and other optical devices [3]. Such intrinsic properties has made TiO_2 a widely used material in different process such as water splitting for hydrogen generation [4–6],

protective and antireflective coatings [7], as well as photocatalytic processes for self-cleaning surfaces [8,9], purification [10] and sterilization processes [11,12]. The search for improvements in self-cleaning glazing has led to the investigation of new compounds with photocatalytic properties. The combination of hetero-nanostructures such as AgCl/BiOCl [13] and ZnO/In_2O_3 [14] by chemical co-precipitation methods have been reported to show high photocatalytic performance in the visible. Bismuth germinate compounds ($Bi_{12}GeO_{20}$) [15] and other compounds such as $BaM_{1/3}N_{2/3}O_3$ (M=Ni, N=Nb, Ta) [16] have reported to give good photocatalytic performance but the potential for self-cleaning glazing is limited as they have been only studied in powder form. Many metal oxides and sulphides such as WO_3, ZnO and CdS along with polyoxometallates have been also investigated over the years but none of these have showed better photocatalytic results than titania (TiO_2) using light alone [17].

However, TiO_2 has a wide band gap (larger than 3 eV) equivalent to the UV region which only consists of 3% of the solar spectrum [18]. In addition, the high recombination of photo-generated charge carriers has detrimental effects on the photocatalytic performance. The rate of recombination can be corrected by modifying the surface properties of titanium dioxide by fluorination or sulfanation or by the addition of suitable electron acceptors besides molecular oxygen in the reaction medium [19]. Other studies have aimed to modify the electronic band structure of titanium dioxide to increase the photo-response in the visible by modifying their surface structure, properties and composition [18] such as N-doped TiO_2 thin films by atmospheric pressure CVD [20] or Ag-doped titania thin films prepared by direct liquid injection metal organic (DLI-MO) CVD [21]. Another methodology which has been gaining interest is the application of electric fields on thin films. Thus, recent studies [22–24] have shown that the application of electric fields on CVD thin films induce changes in the microstructure, increasing the growth rate as well as the surface area improving this way the properties of materials.

1.3. Titanium dioxide structure

1.3.1. Band theory

Electronic states

The electronic states of TiO_2 are depicted in Figure 1.1. The upper valence bands can be decomposed in 3 regions: σ bonding in the lower region mainly due to O pσ bonding, the π bonding in the middle of the energy region and O pπ states in the higher energy region due to O pπ non-bonding states at the top of the valence bands where the hybridization with d states is almost negligible [18].

Conduction bands decomposed into: Ti eg (>5eV), and t_{2g} bands (<5 eV). The d_{xy} states are dominantly at the bottom of conduction bands. The rest of t_{2g} are antibonding with p states. The main peak of the t_{2g} band is identified to be mostly d_{yz} and d_{zx} states.

Band edges positions

The photocatalytic performance of TiO_2 is directly related to its band edge positions and redox potential of adsorbates. Titanium dioxide typically occurs naturally in three polymorphic forms: anatase, brookite and rutile. Nevertheless, as it will be explained in following sections, only anatase and rutile have interest for photocatalytic applications. Anatase and rutile differ in their band gaps and band edges positions (Figure 1.2). Thus, the band gap of anatase (3.2 eV) is slightly larger than that of rutile (3.0 eV). This is important because the potential level of donor (oxidation potential) needs to be above the valence band whereas the potential level of acceptor (reduction potential) needs to be more negative than the conduction band.

Due to these band edge positions, the solid – solid interface between the two phases has been reported to facilitate charge separation and thus, supress recombination [19]. Two main models explain the interfacial charge transfer pathways between anatase and rutile. The first model, proposed by Bickley *et al.* [25] , suggest that rutile serves as a passive sink due to the relative position of its conduction band (0.2 eV below the conduction band of anatase) which thermodynamically favours the electron transfer from the anatase conduction band (CB), impeding recombination (Figure 1.3 a). The second model, proposed by Hurum *et al.* [26],

suggest that the electron transfer is produced from the rutile CB edge to electron trapping sites of anatase which is 0.8 eV lower in energy than anatase CB. Recent investigations based on photoemission techniques [27] support that the electron transfer is produced from the rutile CB to anatase. However, this has been attributed to the work function of rutile to be 0.2 eV lower than that of anatase which places the anatase CB 0.2 eV below that of rutile (Figure 1.3 b).

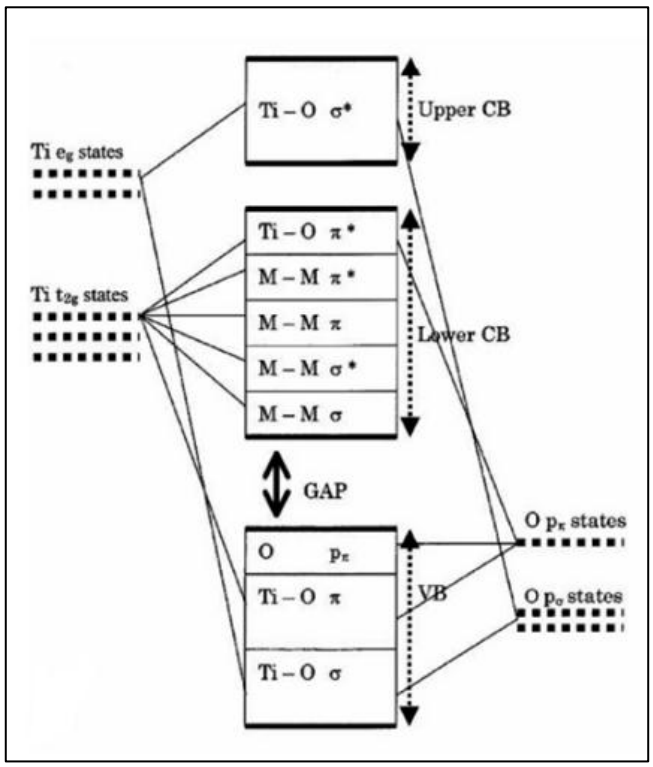

Figure 1.1: Schematic of TiO_2 band structure (adapted from [18]).

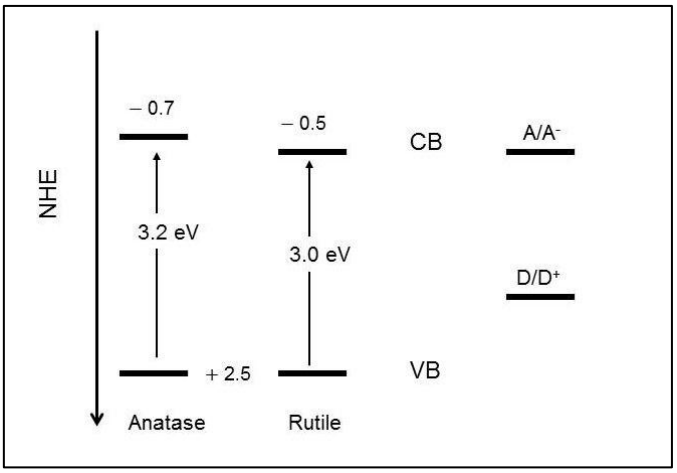

Figure 1.2: Schematic of anatase and rutile band gaps and band edge positions (adapted from [28]).

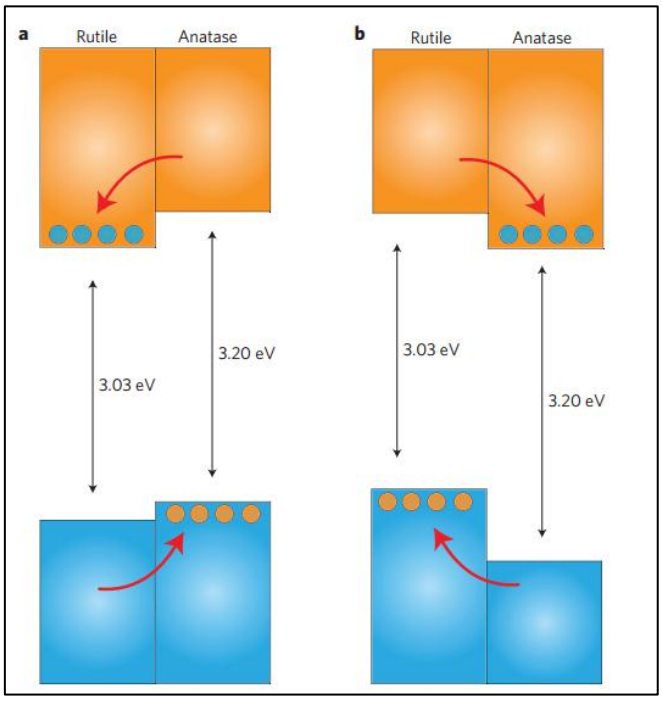

Figure 1.3:Schematic of anatase and rutile interfacial charge transfer models (a) rutile as an electron sink (b) electron transfer from rutile to anatase (adapted from [27]).

1.3.2. Lattice structure

The structure of titania is composed of chains of TiO_6^{2-} octahedra where each Ti^{4+} ion is surrounded by an octahedron of six O^{2-} ions. For the purpose of this study, the most important cell structures of titania are rutile and anatase which differ in the distortion of each octahedron and the assembly pattern of the octahedra chains [18].

TiO_2 crystals are formed by two types of linkages, edge-sharing and corner-sharing. In rutile crystal phase (Figure 1.4 a) two opposite edges of each octahedron are edge-shared forming a linear chain and the chains are linked together via corner oxygen atoms [29]. Anatase has four edges shared per octahedron (Figure 1.4 b) which is significantly distorted so its symmetry is lower than orthorhombic.

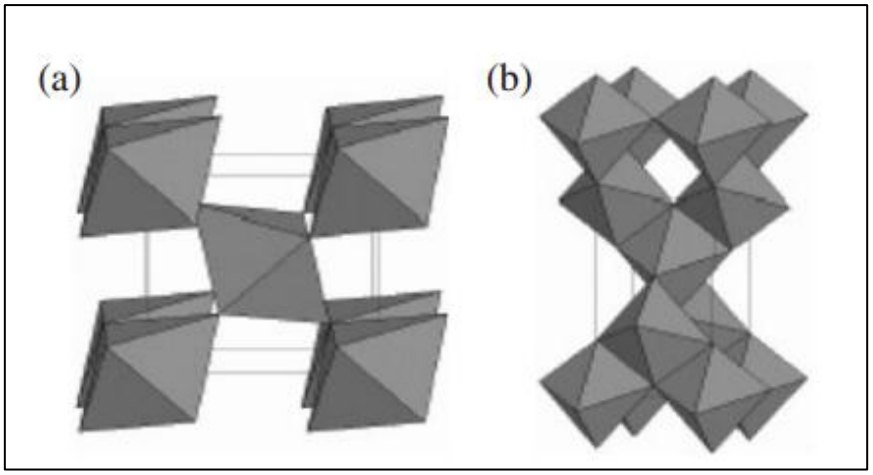

Figure 1.4:Schematic of TiO_2 crystal structure for (a) rutile and (b) anatase crystal phase [30].

Furthermore, the Ti –Ti distances in anatase are greater (3.79 and 3.04 Å in anatase vs 3.57 and 2.96 Å in rutile) and the Ti –O distances are shorter than in rutile (1.93 and 1.98 Å in anatase vs 1.94 and 1.98 Å in rutile) [31] (Figure 1.5).

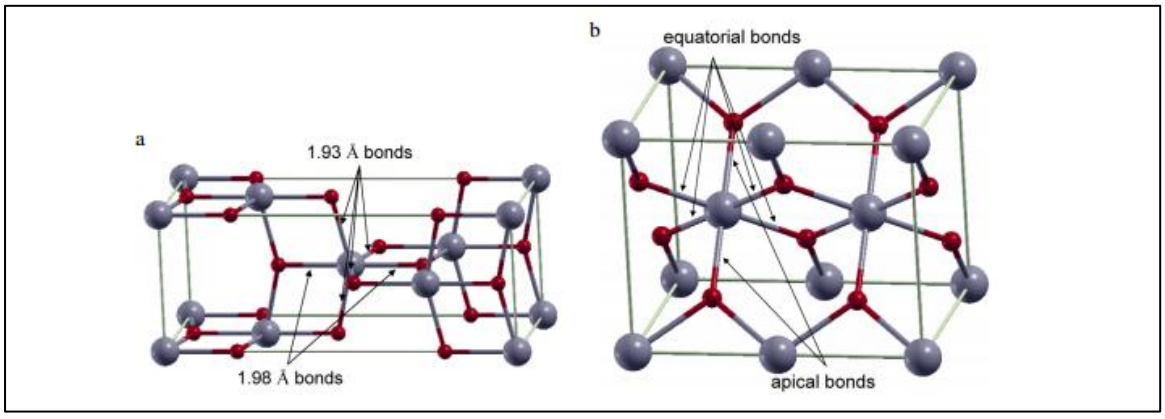

Figure 1.5: Schematic of anatase (a) and rutile (b) cell structure showing distances of Ti –O bonds (adapted from [32]).

1.3.3. Transformation of titania crystal phases

Pure bulk anatase is widely considered to begin to transform into rutile in air above 600 °C. However, the temperature at which the transformation from anatase to rutile occurs has not been universally agreed upon as it depends on the method and synthesis parameters [33]. TiO_2 thin films produced on Si (100) from APCVD have been reported to be constituted of a

mixture of anatase and rutile in the temperature range of 450 – 700 °C and mainly rutile in temperatures greater than 700 °C [34]. The change of crystal phase from anatase to rutile (or anatase-rutile mixed phase) is in part due to oxygen vacancies originated during the particle growth which in turn depends on the temperature [35]. Surface defects act as nucleation sites and thus, an increase of these defects enhances the rutile transformation [3]. Other factors, such as particle size and shape as well as surface area which are influenced by temperature and time, also play an important role in the anatase to rutile transformation [33]. Furthermore, it has been reported that the transformation of anatase to rutile responded an interface and surface nucleation when producing titania by hydrothermal methods at 600 – 700 ºC. According to this argument, rutile crystals are initialized at the interface of small sized anatase nanoparticles that also serve as nucleation sites for rutile growth. Anatase has a greater transformation rate for smaller particles. However, the stability crossover in the transformation depends on a critical size mechanism which Zhang *et al*. [36] identified at 14 nm. The proposed explanation was that the smaller crystals showed larger fractions and therefore, the surface energy was favourable for anatase crystal phase. Hence, according to this study when the particle decreased below 14 nm in diameter, anatase became more stable than rutile. Furthermore, the agglomeration state has been reported to influence the anatase to rutile transformation. As anatase has four edges shared per octahedron the collision among molecules favours the formation of this crystal phase as more edges are available to form a bond [37].

In addition, factors such as the precursor, substrate and method used for titania thin film growth, makes a substantial difference in the crystalline phase produced. For example, Evans *et al* .[38] found that deposited films from the APCVD reaction of $TiCl_4$ in ethyl acetate showed the rutile phase at deposition temperatures between 550 – 650 °C whereas only anatase peaks were found in deposited films from titanium isopropoxide. However, stainless steel was used as a substrate which had an important influence in the crystal phase as under similar conditions only anatase crystal phase was found using $TiCl_4$ as a precursor on glass substrate [39]. In other cases, polymorphs of anatase and rutile have been reported at lower temperatures (500 °C) [40]. Edusi *et al.* [41] also investigated the effect of substrate in the morphology and properties of TiO_2 thin films from TTIP using both APCVD and AACVD. The study revealed at temperatures from 400 – 550 °C AACVD tended to produce rutile whereas APCVD leaned towards anatase. It was also observed that the deposition was highly

depending on the substrate, showing rutile on metal substrate and a combination of anatase and rutile on glass substrate depending on the temperature and time of deposition.

1.4. Functional properties

1.4.1. Photocatalysis

Semiconductors act as a photocatalyst for the light-induced photochemical reactions due to its electronic structure consisting of a filled valence band (VB) and an empty conduction band (CB). The energy gap between the populated valence band and a vacant conduction band is a forbidden energy state, and the difference in energy is called the band gap. Efficient photocatalysts have the redox potential for the evolution of hydrogen and oxygen from water and the formation of reactive species (hydrogen peroxide, hydroxyl and superoxide radicals) within their band gap. The photocatalytic reaction is produced through intermediate energy states in such a way that the initial state of the photocatalyst is regained once the reaction is complete. This requires chemi-absorbed reagents that remain at the surface long enough for the adsorbates to undergo transformation. Furthermore, the binding energy of the reaction products must be low so the reactant desorbs from the photocatalyst surface, and the photocatalyst can return to its original state.

Photons with energy greater than the band gap energy generate a pair of electron (e^-) -hole (h^+) in the bulk of the semiconductor (Figure 1.6 a, Equation 1.1). The energy of the incident photon promotes the electron from the valence band to the conduction band. Photogenerated electrons and holes can recombine (Equation 1.2) either in the bulk (Figure 1.6 e) or at the surface (Figure 1.6 d). Photoexcited carriers that do not undergo recombination can migrate to the surface causing oxidation (holes) or reduction (electrons) of adsorbed species. Thus, photogenerated electrons and holes in titania can migrate and react with adsorbed species which can result in the formation of reactive species such as $OH^\bullet$ radicals and superoxide ions ($O_2^{\bullet-}$). Carriers at the surface can be trapped by intrinsic subsurface energy traps (equations 1.3 and 1.4), or by extrinsic surface traps via interfacial electron transfer with adsorbed acceptors (A) and donor molecules (D) (Equations 1.5 and 1.6) [18].

$$SC + h\nu \rightarrow e^{-}_{CB} + h^{+}_{VB}$$ (Equation 1.1)

$$e^{-}_{CB} + h^{+}_{VB} \rightarrow SC + h\nu + (heat)$$ (Equation 1.2)

$$Ti^{IV} - O^{2-} - Ti^{IV} + h^{+}_{VB} \rightarrow Ti^{IV} - O^{\bullet -} - Ti^{IV}$$ (Equation 1.3)

$$Ti^{IV} + e_{CB} \rightarrow Ti^{III}$$ (Equation 1.4)

$$h^{+}_{VB} + D \rightarrow D^{+}$$ (Equation 1.5)

$$e^{-}_{CB} + A_{(ads)} \rightarrow A^{-}$$ (Equation 1.6)

Surface absorbed oxygen can act as an electron trap, producing oxygen radicals, preventing recombination **(**Equation 1.7). Conversely, absorbed water and hydroxide and can act as hole traps leading to the formation of hydroxyl radicals (Equation 1.8. and 1.9) [18]. These hydroxyl radicals have been found to mineralise or degrade organic pollutants, and can participate photocatalytic reactions [42].

$$e^{-}_{CB} + O_{2(abs)} \rightarrow O_2^{-}$$ (Equation 1.7)

$$h^{+}_{VB} + H_2O_{(ads)} \Leftrightarrow H^{+}_{(ads)} + OH^{\bullet}{}_{(ads)}$$ (Equation 1.8)

$$h^{+}_{VB} + OH^{-}_{(ads)} \Leftrightarrow OH^{\bullet}_{(ads)}$$ (Equation 1.9)

In Figure 1.6 the letters correspond to:

(a) Generation of an electron (negative) – hole (positive).
(b) Oxidation of adsorbed donor species.
(c) Reduction of adsorbed acceptor species.
(d) Recombination at the surface.
(e) Recombination in the bulk.

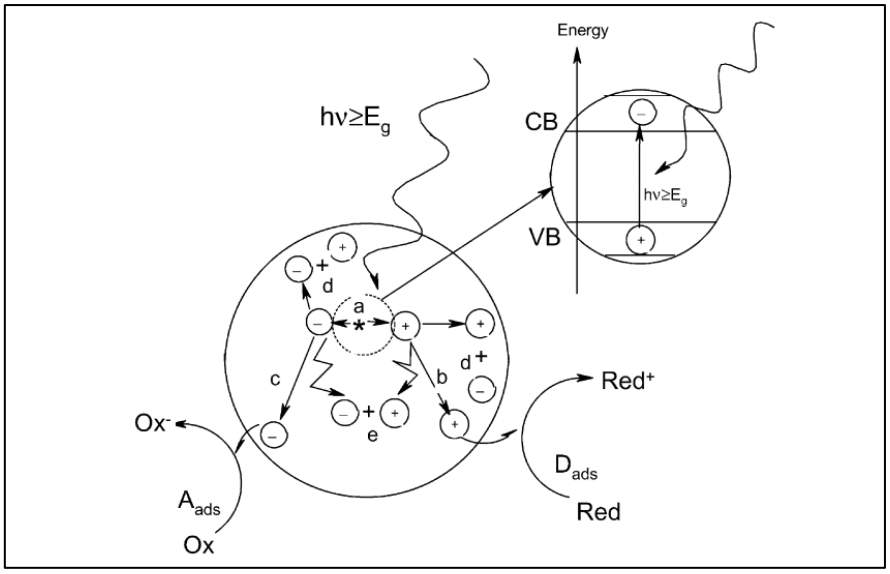

Figure 1.6: Schematic of photoexcitation in a semiconductor [3].

1.4.1.1. Factors influencing titania photocatalysis

TiO_2 photo-activity is not determined by any isolated factor but by a combination of factors such as the particle size and shape, crystal orientation, crystal phase and defects, among others.

1.4.1.1.1. Particle size and morphology

The particle size and morphology significantly influences the specific surface area which has been reported to be determinant in TiO_2 photo-activity [43]. As particle size decreases, the surface area to volume ratio increases which generally favours increased photo-activity by increasing the number of active sites.

The particle size also influences the rate of recombination. Increasing the particle size also increases the number of defects which reduces photo-activity [36]. As particles get smaller, surface recombination, migration and reduction of adsorbed species dominate over bulk recombination. At nano-scale, most of the electron – hole pairs are generated sufficiently close to the surface hindering the recombination in the bulk. Nevertheless, charge carriers reaching the surface might undergo surface recombination due to abundant surface trapping sites and the lack of driving force for electron hole separation [44].

Particle morphology also plays an important role in titania photo-activity by impeding recombination. Thus, long – shaped crystals consist of isolectronic materials that allow the easy transfer of electrons across the long direction. Likewise, the elongated shape decrease the number of contact barriers between crystals and therefore, grain boundaries which act as electron traps [43].

Finally, the reactivity and physico-chemical properties of the materials are highly dependent of the morphology of single crystals because it determines the crystal facet exposed [45].

1.4.1.1.2. Crystal orientation

The importance of crystal orientation in the generation of reactive sites for photocatalysis has been previously reported [46–48]. Thus, it is believed that crystal facets influence the photocatalytic activity of TiO_2 by assisting in the electron-hole separation which could be achieved by the control of the surface arrangement [47]. Under equilibrium, single crystals grow in the facets which minimise the total surface free energy. In anatase, the most stable and frequently observed crystal orientation is in the (101) plane [49]. However, the anatase (101) plane has been reported to be less reactive than the (001) plane [50]. In particular, studies on the effect of preferred orientation of sputtered films on the photo-oxidation of acetaldehyde showed that the alignment of crystallites when the (004) planes lie orthogonal to the film surface facilitates higher reactivity rates [46]. The higher reactivity of anatase (001) has been attributed to the high surface underco-ordinated Ti atoms and to the strained configuration of the surface atoms [51]. In other words, the bond Ti – O –Ti angles at the surface are larger (Figure 1.7.a) and therefore oxygen atoms are destabilised and very reactive [50]. As Figure 1.17 b shows, the dissociative adsorption of water leads to a shorter Ti-O_{2c} and a cleavage of Ti_{5c} and O_{2c} bonds with the formation of Ti – OH bonds in such a way that ever water molecule can stabilise two Ti_{5c} atoms [45].

1.4.1.1.3. Film thickness

Thin films thickness has been also reported to be an important factor in TiO_2 photo-reactivity. High thickness values have been reported to hinder the effective diffusion of photo-generated

carriers to the surface [52]. In semiconductor-liquid junctions (Figure 1.8), the built-in potential (V_d) is a result of Schottky barriers preventing the recombination of photo-excitons and assisting holes in moving towards the film surface. When the film thickness is less than the depletion layer width (x_d), the electron transfer is insufficient and recombination is inevitable [53].

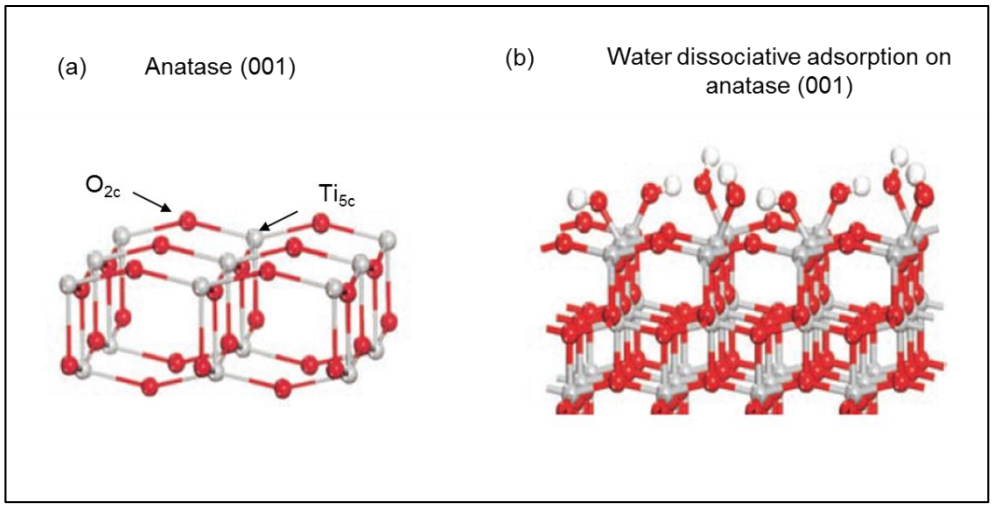

Figure 1.7: Atomic structure of anatase and water dissociative behavior a) -reactive (001) surface showing strained Ti-O-Ti bond angles. O_{2c} and Ti_{5c} denote surface two-fold coordinated O and fivefold coordinated Ti atoms, respectively; b) water dissociative absorption on TiO_2 (001) surface. Adapted from [50].

However, optimum film thickness for photocatalytic processes would rely on the combination with other factors as well as on experimental conditions. Wu *et al.* [54] found an optimum thickness of 93 nm when producing titania thin films from sol-gel methods with thickness in the range of 38 –214 nm. Hyett *et al.* [55] found an optimum film thickness of 200 nm for TiO_2 thin films produced from the APCVD on titanium metal substrate. However, no correlation between film thickness and photo-activity was found for titania thin films produced on glass substrates.

1.4.1.1.4. Crystal phase

The difference in the unit cell structure of anatase and rutile is believed to play an important role in titania properties as anatase presents higher photocatalytic potential than rutile.

Although rutile is traditionally assigned to possess a smaller band gap (3.03 *vs.* 3.20 eV), anatase is the preferred crystal phase for photocatalytic applications. This has been attributed to a higher density of localised states and therefore higher surface-absorbed hydroxyl radicals [33] as well as differences in carrier lifetimes [56]. However, the photo-activity of rutile has been found to be superior [57–59] which has attributed to favourable modifications in the microstructure leading to suppression of recombination centres [59] and to an increase of surface area and agglomerate state [57]. Rutile is produced at higher temperatures and thus, particles are normally larger. This favours band bending and subsequently, photo-degradation processes [59].

In recent years, the combined photo-activity of anatase and rutile has been investigated. Studies carried out on titania powders have revealed that there is a synergistic effect between anatase and rutile on the photocatalytic reaction [60–62]. As explained in section 1.3.1, this synergy is related to the band alignment of rutile and anatase that increases the separation of photoexcited charge carriers by successfully transferring holes from anatase to the rutile valence band. Nevertheless, this synergistic effect on titania thin films has been controversial. Kafizas *et al.* [63] carried out a study using combinatorial APCVD to deposit titania thin films with composition and thickness gradients. They found that increasing the amount of rutile caused a dramatic fall in photocatalytic activity and that no synergy occurred between anatase–rutile composites with $29 \leq \text{rutile\%} \leq 83$. This was attributed to trapping electrons within the bulk of dense films. Other studies on ALD titania thin films observed this synergistic effect but at film thickness in the range of 15 – 65 nm [64] which would avoid such trapping effects. However, a synergistic effect has been found in deposited films with a thickness of up to 1 micron with an optimum rutile to anatase ratio of approximately 1:1 [65]. Likewise, Edusi *et al.* [41] observed that TiO_2 thin films with an equal mix of both polymorphs showed a faster de-coloration on Resazurin photocatalytic testing compared to those that contained only anatase.

1.4.1.1.5. Defects

Defects in the structure provide trapping sites for electrons and holes and can lead to recombination, reducing the photocatalytic activity. Oxygen vacancies in the structure will affect the absorption

of water and disassociation to hydroxyl ions and protons, thus affecting the photocatalysis. In addition, non-stoichiometry can affect the amount of surface hydroxylation [66].

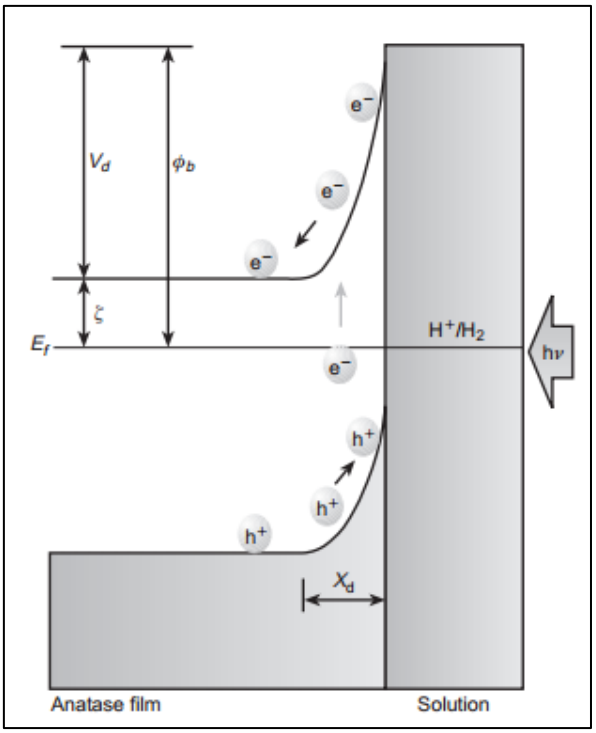

Figure 1.8: Schottky-barrier formed in solid-liquid interface [53].

1.4.1.2. Modifications of titania photocatalytic activity

Some methods to enhance titania photocatalytic activity include phase separated semiconductors, metal and non – metal doping and induced changes in the microstructure by electric fields.

1.4.1.2.1. Phase Separated Semiconductors

The photo-activity of TiO_2 can be improved through integration with other photoactive materials to form phase separated semiconductors as incorporated nanoparticles or as a separate layer forming hetero-nanostructures. In both cases, the enhancement of photocatalysis is produced by a compatible coupling of band gaps which favours the effective separation of charged carriers at the interfaces of coupling phases and an increase of the

photo-response in the visible light [67]. Metal nanoparticles can be incorporated into TiO_2 assisting photo-catalysis by separating charge carriers. Excited electrons are transferred from the conduction band of the semiconductor to the metal preventing recombination. Electrons accumulated on the metal particle surface can reduce adsorbed species and thus increase photocatalytic rate. At the interface, electrons and holes migrate between phases depending on the relative energies of their conduction and valence bands.[17] Incorporation of silver [68] and gold nanoparticles [69] to *mesoporous* titania coatings via sol-gel processes have reported to increase the photocatalytic rate by increasing the photo-response of TiO_2 in visible light. The exposure of nanoparticles to the medium may result in undesirable corrosion or dissolution of metals during repeating photocatalytic reactions which can be avoided by incorporating the metal into titania as core-shell nanocomposite.[70]

Hetero-nanostructures formed by coupling titania with visible light absorbing semiconductors such as bismuth based semiconductors are another possibility to induce photocatalysis and super-hydrophilicity. Hierarchical flake-like Bi_2MoO_6 on TiO_2 nanoparticle film substrate produced by the solvothermal process showed an important improvement of the photocatalytic performance by enhancing the visible light absorption.[71] This was attributed to a combination of controlled factors such as surface morphology and adequate coupling of both semiconductors band-gap. Bismuth based heteronanostructures have been reported as excellent photosensitizers due to their narrow band gap (~1.4 eV) which allows light harvesting in the visible range [72]. In addition, the conduction band energy is approximately 0.26 eV higher than that of TiO_2[73] which allows for fast injection of photo-generated electrons from the bismuth based semiconductor into the TiO_2 conduction band [71]. Hetero-nanostructures of other compatible materials in determined structures such as Cu_2O-TiO_2-ZnO have been also reported to enhance photocatalytic properties by inducing interfacial states and energy band differentials which favour electron transitions and inhibit photo-generated electron-hole recombination[74]. In this study, it was observed that the photocatalytic performance of the hetero-nanostructure Cu_2O-TiO_2 remarkably increased with the incorporation of ZnO nanoparticles on the surface which as attributed to an increase of surface area and active sites for photochemical reactions [74].

1.4.1.2.2. Doping

Doping interferes with the photocatalytic performance by introducing discrete energy states into the band gap. Energy levels near the conduction band allow a wider range of wavelengths that can be absorbed. Metals such as cadmium [75], silver [76] and platinum [77] have been investigated for TiO_2 thin films doping. The redox energy states of many transition metals ions lie within the band gap states of TiO_2. Therefore, the substitution of metal ions into TiO_2 produces an intraband close to the CB or the VB edge, inducing visible light absorption at sub-band gap energies [19].

Non-metal doping using nitrogen (N) or sulphur (S) has been the most used method to reduce the titanium dioxide band gap in order to increase the photocatalytic activity under UV irradiation. However, doping has been found to be limited due to poor absorbance under UV irradiation and an increase of recombination rates resulting in lower photo-activity than pure TiO_2 [78,79]. N-F co-doping have been reported to produce better photocatalytic performance than pure TiO_2, N-doped and F-doped TiO_2 [80]. This has been attributed to a synergy effect between the increase in absorption in the visible by N-atoms and the formation of new active sites by F-atoms [81]. Transparent C-F-N co-doped titanium dioxide thin films produced by the sol-gel method have been reported to show strong visible-light absorption and high photocatalytic performance. In addition, the increase in surface roughness produced by the co-doping induced superhydrophilicity even under dark conditions [80].

1.4.2. Self-cleaning

In the last decade, TiO_2 has been extensively investigated for self-cleaning surfaces for external envelopes of building. Self-cleaning glazing is mainly divided into two categories; hydrophilic and hydrophobic. In both cases, the self-cleaning effect is produced through the action of water by forming water sheets (hydrophilic) or by forming rolling droplets (hydrophobic) that carries away dirt. The hydrophilicity or hydrophobicity of surfaces can be determined by water contact angle measurements.

1.4.2.1. Water contact angles

The contact angle of a surface is strongly dependent on the surface topography and chemical structure. The most widely known models to explain the relationship between surface roughness and the contact angle of the surface are the Wenzel and the Cassie –Baxter models. The Wenzel model explains the surface contact angle as an effect of the surface roughness (difference between the actual and geometric surface areas) [82]. The Cassie – Baxter is an extension of the Wenzel model which also considers the chemical and physical heterogeneity of the surface [83]. In the Cassie and Baxter model the contact angle is determined by the surface free energies of solid-liquid, solid-gas and liquid-gas boundaries. For heterogeneous surfaces, the droplet is not entirely in contact with the rough surface and some air bubbles will be trapped at the interface (Fig. 1.9 a). The Wenzel model is effective when the water droplet sinks into the surface structure and has greater surface contact (Figure 1.9 b).

1.4.2.2. Hydrophobic self-cleaning

Hydrophobic surfaces for self-cleaning applications have also been extensively investigated [84 - 85] . However, these materials have not beaten the advantageous properties of titania thin film hydrophilic surfaces in terms of life expectancy and performance. Whereas hydrophilic surfaces can be used for at least 25 years, hydrophobic surfaces have a much shorter life expectancy of 3-4 years which has been attributed to the mechanical strain resulted from necessary maintenance work and to the degradation nature of pollutants. Moreover, contradictorily to hydrophilic surfaces, hydrophobic coatings show lower self-cleaning performance when comparing to untreated float glass [86].

Following the Cassie – Baxter model, the self-cleaning mechanism arises from the poor contact area of particles (or dirt) on the rough surfaces resulting in low adhesion forces. Dirt would be easily trapped by droplets placed on the surface since capillary forces would prevail over adhesion forces of the particle and the surface and, as a result, the dirt is wash away [87].

Neinhuis and Barthlott [88] accomplished the first comprehensive experimental study on the self-cleaning action of hydrophobic coatings by investigating different plants and contaminants. They described the hydrophobic self-cleaning process as the Lotus-Effect from the observations of the lotus leaves. Almost perfect spherical droplets of water form on the

surface trapping the dirt that will be carried away before the water evaporates. It was observed that in smooth surfaces, with high contact angles water droplets tended to disperse contaminants, whereas in rough surfaces with high contact angles, water droplets could trap contaminants and remove them from the surface.

If additional liquid is added to a drop, the contact line advances. When the motion ceases, the drop shows an advancing contact angle (θ_a) (Figure 1.9 c). If liquid is removed from the drop, the contact angle decreases to a receding value (θ_r) before the contact angle retreats (Figure 1.9 d) [89]. The difference between advancing and receding angles is known as hysteresis and ideally should be as close as possible to zero. In other words, low hysteresis angles mean that drops would roll easily along the surface at low surface inclination angles. Generally, it is considered that the requirements for a self-cleaning hydrophobic or superhydrophobic surface is a static contact angle > 160° and a very low roll-off angle (<10°), i.e. the minimum inclination angle necessary for a droplet to roll off the surface [90].

Nanocomposites of TiO_2 nanoparticles in silicon- based polymers produced by sol-gel processes have been reported to show excellent self-cleaning properties and good mechanical properties [91,92] which make them highly suitable for outdoor applications. Similarly, nanocomposites produced from titanium and silicon alkoxides in the presence of oxalic acid have been reported to show excellent photocatalytic properties on stone with potential commercial applications as protective coatings of building materials [93]. Further investigations have integrated antireflective, water-repelling and self-cleaning properties from methyl modified SiO_2 and TiO_2 bilayer highly suitable for photovoltaic cells [94].

1.4.2.3. Hydrophilic self-cleaning

Hydrophilic self-cleaning windows are coated with a thin transparent layer of titanium dioxide. The self-cleaning mechanism arises from the combination of two properties; photocatalysis and hydrophilicity. Thus, photocatalysis causes the chemical break down of the organic matter absorbed on the surface while hydrophobicity causes water to form sheets which washes away dirt. The hydrophilicity or superhydrophilicity mechanism of titania can be explained by the photo-generated charge carriers. Mills et al. [95] argue that one of the possible mechanisms for this is that photo-generated holes get trapped in the titania lattice thereby weakening the bond between titanium and oxygen (Equation 1.10). As a

consequence, an oxygen vacancy is produced and thus the dissociative adsorption of water at the site makes it more hydroxylated. The resulted surface is unstable and, with time, when placed in the dark, the newly-formed hydroxyl groups desorb to form hydrogen peroxide or water and oxygen- leaving an oxygen vacancy. Thus, the photo-induced superhydrophilic titania returns to its hydrophilic state when stored for a long time in the dark.

$$\equiv Ti - O - Ti \equiv + H_2O \overset{h\nu > E_{BG}}{\Longleftrightarrow} \equiv Ti - OH\ HO - Ti \equiv \qquad \text{(Equation 1.10)}$$

Current investigations aim to further develop integrated self-cleaning coatings with other materials mostly related to building energy cost saving. UV-light cut and low emissivity self-cleaning glazing can be achieved by integrating CeO_2 and TiN with TiO_2 via sol gel processing [96]. The benefits of integrating antireflective properties with self-cleaning coatings using typically sol-gel processing and sputtering processes have been reported [97-98]. It is well known that in photovoltaic cells glass transparency is strictly linked with efficiency which is believed to drop by 33% per 1 g/m^2 of dust accumulation on the surface [99]. Other studies on the combination of renewable power generation and destruction of air pollutants in urban environments reported a gain of 2.65 % after measurements under standard test conditions with antireflective glass [100].

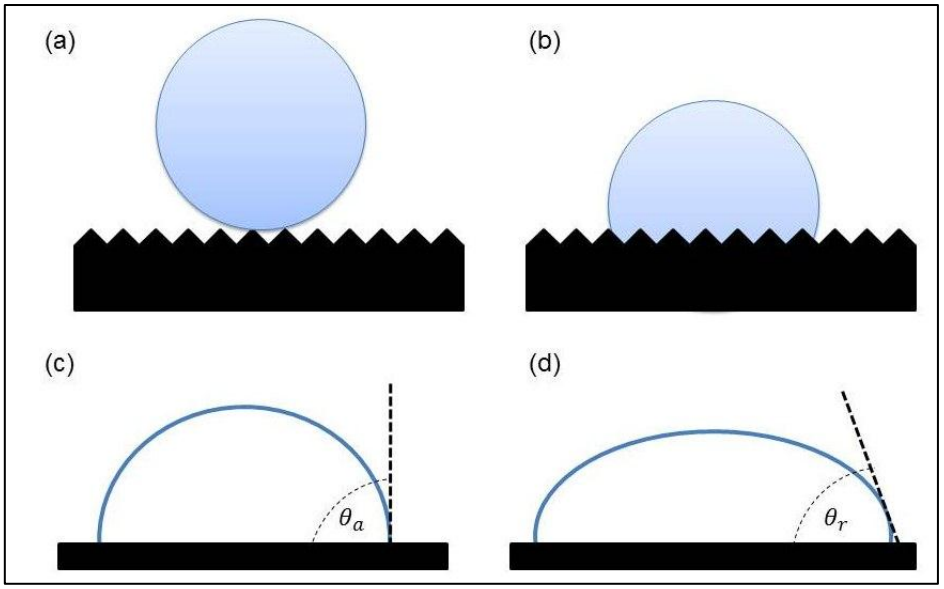

Figure 1.9: Droplet over a patterned heterogenous surface, (b) definition of advancing (θ_a) and (d) receding (θ_r) contact angles for a moving droplet (hysteresis).

1.4.3. Other functional properties

The above mentioned photo-activity properties of TiO_2 makes the material suitable for other related applications such as water splitting for hydrogen generation [4,5,101], depuration [10] and sterilization processes [11,12].

Titania nanoparticles have a wide spectrum of activity against microorganisms such as Gram-negative and positive bacteria and funghi [102]. Antimicrobial nanocomposites based on TiO_2 has been extensively investigated, including doping with nanoparticles such as copper [103,104], silver [104,105] and nickel [106,107]. As titania photocatalytic activity is only effective under light irradiation, metal doping is advantageous to reduce microbial activity even under dark conditions. However, metal ions can be realised from TiO_2 surfaces causing undesirable environmental problems [108]. For this reason, further investigations have been conducted on TiO_2 / polymer based nanocomposites, especially for medical applications [102,109]. Polymer based nanocomposites are particularly interesting when controlled drug release of organic molecules or inorganic antimicrobial compounds is predicted. However, the antibacterial effectiveness is limited by the loading and kinetics of the drugs in the matrix [109].

Promising studies have been conducted to increase titania microbial activity without the use of metals or polymer compounds. The application of electric fields during the CVD growth of titania thin films has shown to produce modifications in the material microstructure, favouring the antimicrobial activity [110]. In the study, titania thin films in the anatase form were deposited using aerosol assisted chemical vapour deposition, with and without the application of an electric field. Results showed that the electric field lead to substantial positive changes in the surface morphology and crystallographic orientation. As a consequence, functional properties such as photocatalytic and antibacterial activity were improved. In particular, coatings deposited at low field strength (1 – 10 Vm^{-1}) showed significant enhanced photocatalytic behaviour, with a reduction of the dye half-life from 39 minutes to 15 minutes. As for the antibacterial behaviour, higher field strength (20 Vm^{-1}) showed the best performance, with an inactivation of *E. coli* strain of 12 % after two hours.

1.5. Thin films production

1.5.1. Chemical vapour deposition

Chemical vapour deposition (CVD) is a well-known technology which entails the delivery of volatile compounds to decompose on a heated substrate to produce a film. Broadly speaking, the CVD system comprises three components: the precursor supply unit, the reactor and the exhaust gas handling. The precursor supply unit is responsible for the production and delivery of the vapour compounds which relies on the temperature and pressure of the source as well as the carrier gas flow rate [111].

The reactor is a cylindrical chamber in which the chemical reaction takes place. This shape allows flow symmetry and safety for vacuum conditions [112]. The design of the reactor depends on the type of CVD method, but generally they are classified as either hot-wall and cold-wall reactors. The main difference is that in hot wall reactors the whole chamber works as a furnace heating the substrate indirectly, whereas in cold wall reactors only the substrate is heated either inductively or resistively [111].

The process begins when the precursors are evaporated and transported to the main gas flow region into the reactor. Figure 1.10 illustrates the basic reactions routes inside the CVD reaction chamber. Once the precursor is delivered into the reaction chamber the following routes might occur [111].

1) Gaseous reactants undergo gas phase reactions forming intermediate species:
    a) When the heated substrate is below the intermediate species dissociation temperature, intermediate species undergo diffusion or convection processes across the boundary layer to reach the substrate. The intermediate species subsequently undergo steps 2 – 5.
    b) When the reactor temperature is above the intermediate species dissociation temperature, homogeneous gas phase reactions might occur. Thus, intermediate species undergo chemical reactions forming powders and volatile by-products in the gas phase that are transported in the exhaust (5). The resulting powder might also remain in the reaction chamber, acting as crystallisation nuclei if falling on

the substrate. This might produce films with poor adhesion to the substrate or pin-hole defects.

2) Gaseous reactants adsorbs onto the heated substrate leading to heterogeneous reactions (gas-solid interface) resulting in the deposits and by-products species.
3) Deposits undergo diffusion processes along the heated substrate to a crystallisation centre resulting in the production of a thin film.
4) Gaseous by-products are removed from the boundary layer through diffusion or convection mechanisms.
5) Unreacted gaseous precursors and by products are removed from the reaction chamber through the exhaust.

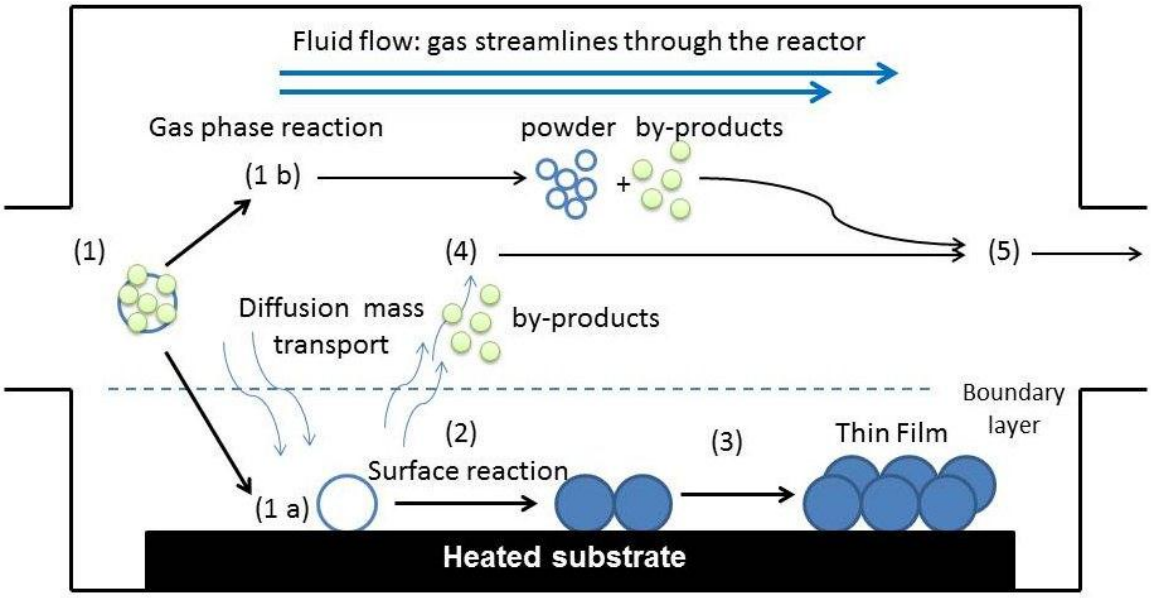

Figure 1.10: Schematic illustration of the reaction routes in the CVD reactor [111].

1.5.1.1. Thin film structure and morphology

Thin films are deposited following three types of film growth: the island growth (Volmer – Weber), the layer by layer growth (Frank – van der Merwe) and the mixed growth (Stranski-Krastanov) (Figure 1.11). The predominance of one type of growth over another is explained by the bonding strength. In the island growth (Figure 1.11 a), film atoms are more strongly bound to each other than to the substrate and there is a slow diffusion of atoms. In the layer

by layer growth (Figure 1.11 b), film atoms are more stongly bound to the substate than to each other and there is a fast difussion of atoms. In the mixed type (Figure 1.11 c), the growth is initially produced layer by layer but then the film grows forming three dimensional islands.

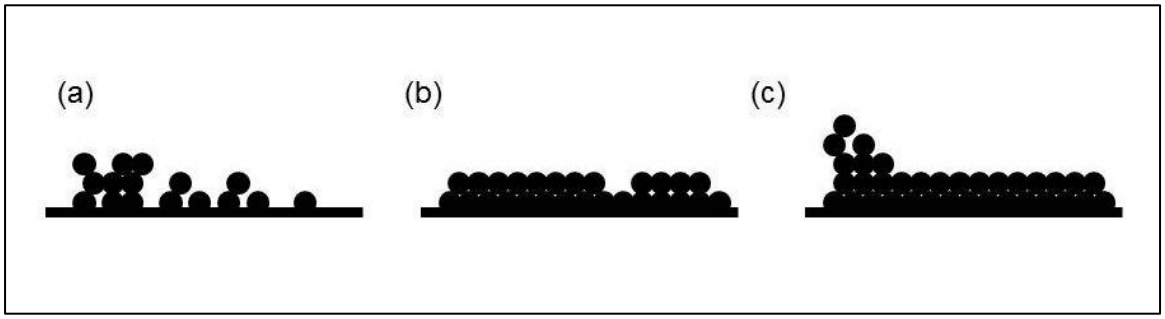

Figure 1.11: Film growth types (a) island growth, (b) layer by layer and (c) mixed growth.

Films produced from CVD processes produce three main types of structure (Figure 1.12); (a) columnar grains with domed tops, (b) columnar grains with angular facets, (c) fine agglomerations [113]. The predominance of one structure over another is governed by the thermodynamics and kinetics of the system, which are controlled by the deposition conditions. At high temperatures, deposits tend to be columnar (Figure 1.12 a - b) as a result of continuous grain growth toward the reactant source. The grain size and the columnar grain size structure will increase with film thickness. Fine-grained structures (Figure 1.12 c) are produced at low pressures and/or temperatures, conditions in which the diffusion of reactants through the boundary layer is limited.

Figure 1.13 shows the morphological changes in columnar growth. The changes in morphology depend on the sintering rate, which depend on the temperature and particle size [114]. When the substrate temperature is not high enough or the initial particle size is too large, the sintering time for particles is much longer than the travel time of a particle. Subsequently, the particles on the substrate are only partially sintered, forming a randomly oriented granular structure. When the substrate temperature is high enough particles nucleate rapidly and films grow with a 1 D orientation.

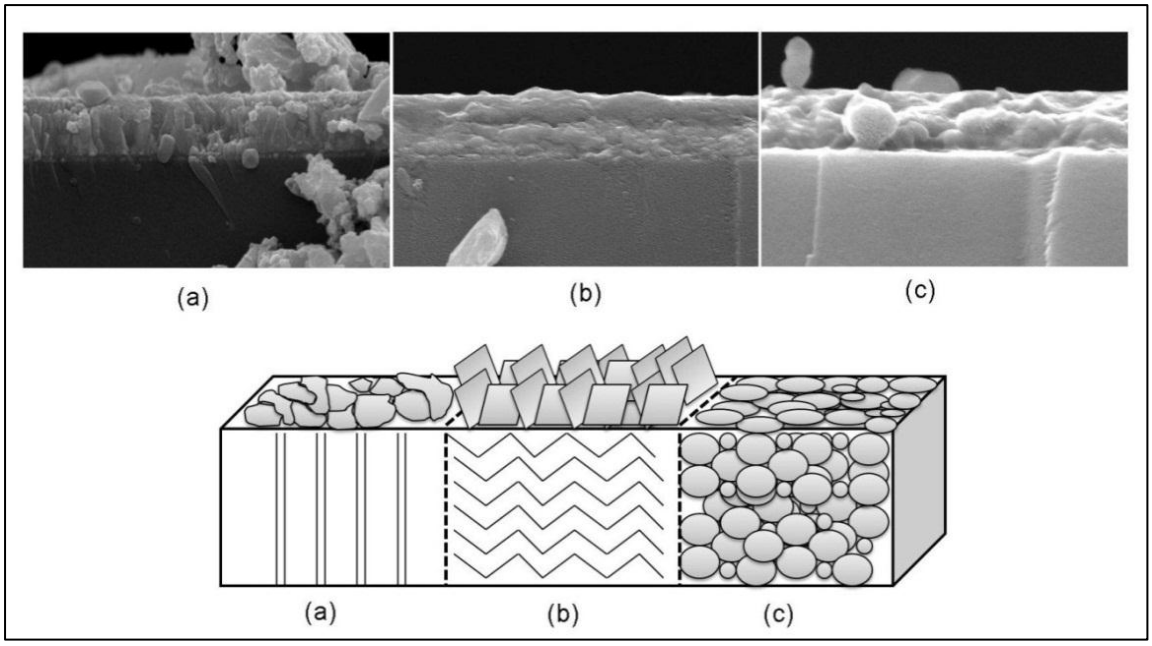

Figure 1.12: Schematic of the typical structure obtained in CVD processes (a) columnar grains with domed tops, (b) faceted columnar grains, (c) equiaxed fine grains.

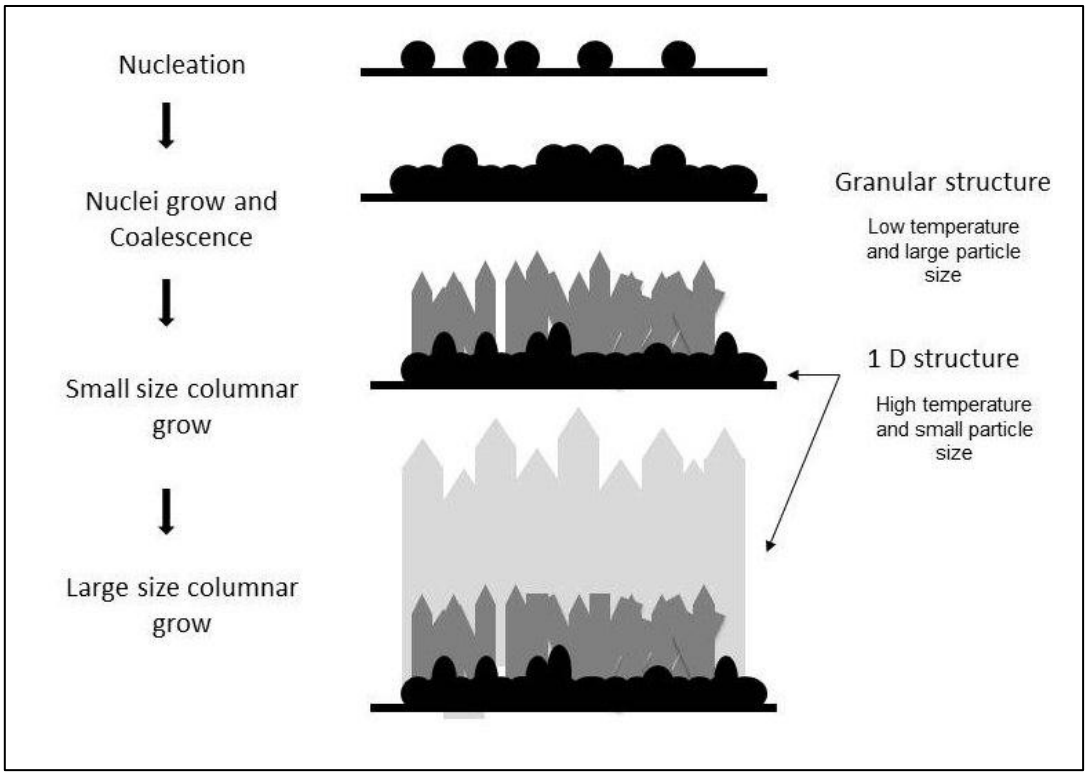

Figure 1.13: Morphological changes in columnar growth (adapted from [115]).

1.5.1.2. Thin film growth

The film is initiated with the collision of atoms to produce small clusters that are thermodynamically unstable. Thus, they can dissolve before reaching a critical radius or overcome a critical free energy barrier to become thermodynamically stable. The nucleation process can be explained in terms of the Gibbs free energy (Equation 1.11) [116].

$$\Delta G_r = \Delta G_s + \Delta G_b \quad \text{(Equation 1.11)}$$

Where: ΔG_r:Excess free energy.

ΔG_s: Changes in the surface free energy (positive as increases the number of unused surface bonds).

ΔG_b : Changes in the bulk free energy (negative as it minimises free bonds).

The excess free energy (ΔG_r) reaches the maximum when clusters grow to the critical size (r*) and it is called critical excess free energy ($\Delta G*$) (Figure 1.14). If the radius is smaller than the critical value, the system lowers its free energy by dissolving clusters and creating new ones by spontaneous collision.

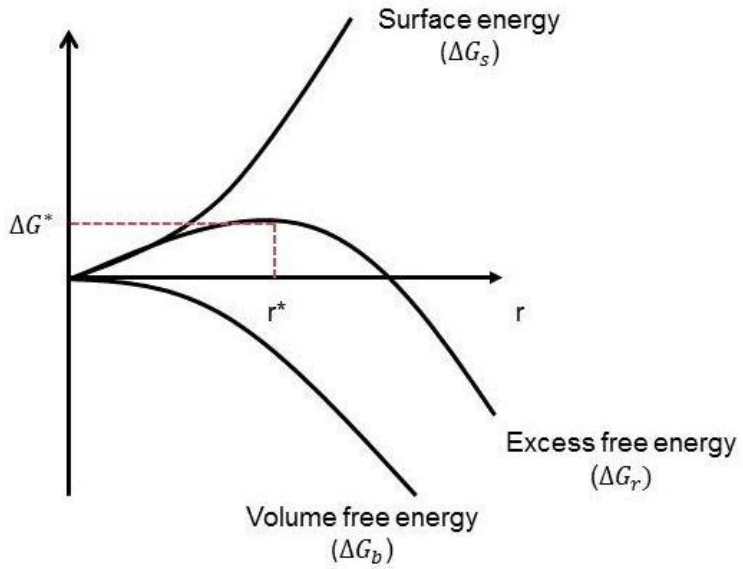

Figure 1.14: Gibbs free energy components for cluster growth.

The growth rate of a CVD reaction can be defined as shown in equation 1.12.

$$V = \frac{1}{N}\left(\frac{k_s\, h_g}{k_s + h_g}\right) C_g \qquad \text{(Equation 1.12)}$$

Where: V = Growth rate.

N = Number of atoms per unit of volume of film.

k_s = Surface reaction rate constant.

h_g = Gas phase mass transport coefficient.

C_g = Concentration of the precursor.

In a traditional CVD system the film growth is determined mainly by the substrate temperature, the operating pressure of the reactor as well as the composition and chemical chemistry of the gas-phase [117]. Figure 1.15 illustrates the dependant relationship between substrate temperature and growth rate.

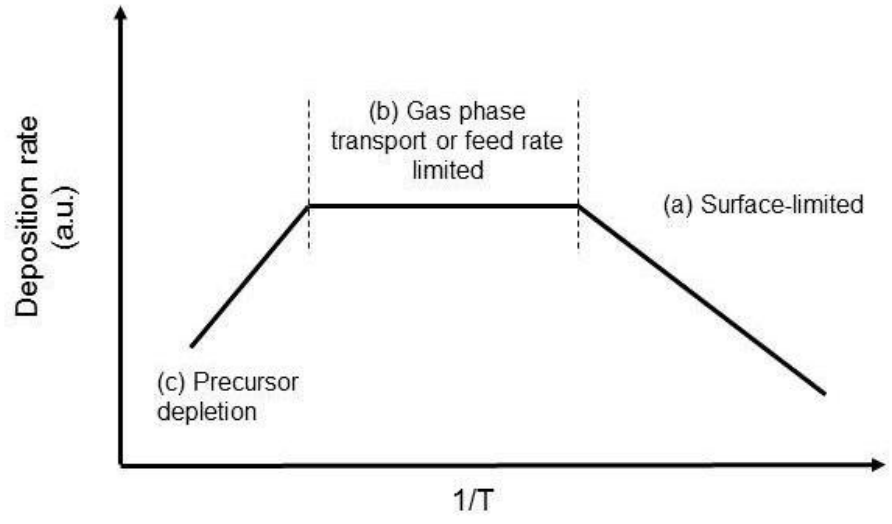

Figure 1.15: Schematic illustration of the deposition rate vs substrate temperature for a typical CVD system.

a) Surface limited growth: at lower temperatures the growth is controlled by the kinetics of the chemical reactions either in the gas phase or on the substrate surface (Figure 1.15 a). In case, from Equation 1.12, $h_g \gg k_s$ and thus the growth rate would be given by equation 1.13.

$$V = \frac{1}{N} \; k_s \, C_g \qquad \text{(Equation 1.13)}$$

Thus, in this region the deposition rate increases exponentially with the substrate temperature according to the Arrhenius equation (Equation 1.14). As the growth rate in this region is controlled by the chemical kinetics, uniform thickness can be achieved by controlling temperature variations.

$$\text{Growth rate} = A \, exp \, (-E_a/RT) \qquad .. \qquad \text{(Equation 1.14)}$$

Where: E_a = Apparent activation energy.

R = Universal gas constant.

T = Temperature.

A = Pre-exponential factor.

b) Mass transport or diffusion-controlled growth: at higher temperatures the deposition rate is practically independent of the temperature and the film growth is controlled by the mass transport of the reactants through the boundary layer to the substrate surface (Figure 1.15 b). In this case, from Equation 1.12, $k_s \gg h_g$ and thus the growth rate would be given by equation 1.15.

$$V = \frac{1}{N} \; h_g \, C_g \qquad \text{(Equation 1.15)}$$

c) Precursor depletion: at even higher temperatures the deposition rate tends to decrease due to an increase of desorption of precursors off the film and/or depletion of reactants on the reactor walls due to gas-phase side reactions.

Increasing the reactant concentration encourages the deposition rate. Nevertheless, at high reactant concentrations gas phase nucleation might occur and thus, a decrease in deposition [118] (Figure 1.16).

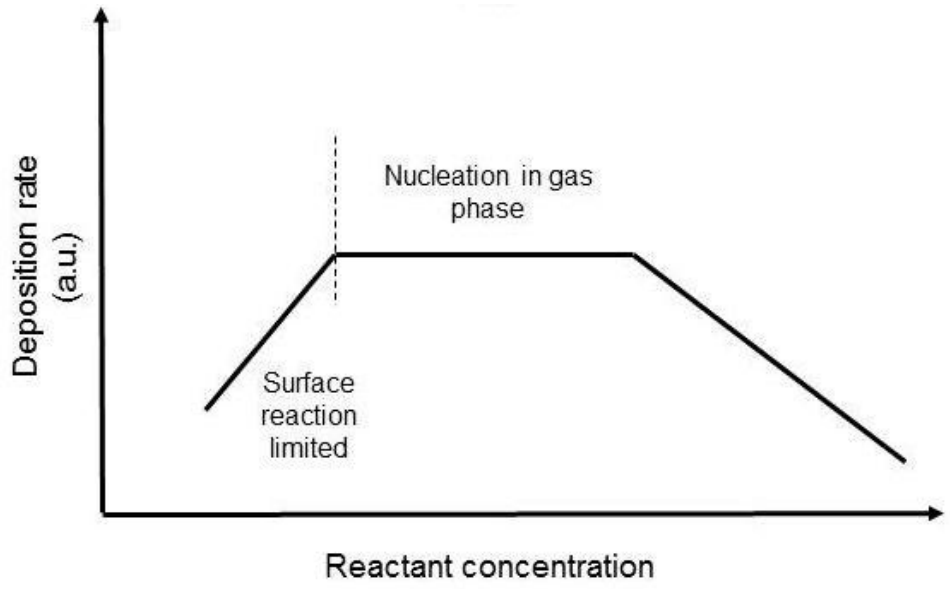

Figure 1.16: Schematic illustrating the dependent relationship between the deposition rate and reactant concentration (adapted from [118]).

1.5.1.3. Kinetics

The precursors are transported through the boundary layer to the substrate principally by convection and diffusion mechanisms. Certainly, diffusion is the dominant transport mechanism near the substrate of a solid surface [119] but convective currents may also occur due to the heated walls of the reactor. Thus, in cold-wall reactors convective forces perpendicular to the gas flow are produced as a consequence of the heated substrate. The result is a geometric variation of the film thickness which relies on the temperature of the chamber [120]. The precursor motion highly determines the deposition rate, which is mainly governed by the regime flow and the thickness of the boundary layer.

1.5.1.3.1. Flow regime

The motion of precursor in the reactor can be calculated from the flux (Equation 1.16), i.e. the motion of a volume of precursor across an area in a set time [119].

$$Flux = Density\ x\ Velocity \quad \text{(Equation 1.16)}$$

More accurately, the motion of the precursor in the CVD can be determined by the type of flow (turbulent or laminar) which is given by Reynolds number (Re):

$$\mathrm{Re} = \frac{\rho\ U\ L}{\mu} \quad \text{(Equation 1.17)}$$

Where: ρ = Mass density.

U = Gas flow velocity.

L = Length of the chamber.

μ = Fluid viscosity.

Thus, the Reynolds number gives information about the diffusion momentum in relation to the size of the system. At high Re values (Re >2000) the momentum diffuses ineffectively resulting in a turbulent flow. At low Re values (Re < 20) the momentum diffuses rapidly resulting in a laminar flow which is usually the appropriate flow regime in CVD processes as it allows conformal coating [117].

1.5.1.3.2. Gas molecules free mean path

Another factor to be considered in the precursor kinetics is the number of molecules that actually strike the surface in a given time. This can be calculated by the Knudsen equation (Equation 1.18) which is the ratio of gas mean free path (or the distance a molecule travels without colliding) to the reactor width [119].

$$k_n = \frac{w}{x} \quad \text{(Equation 1.18)}$$

Where: k_n = Knudsen number.

w = Reactor width.

x = Mean free path of gas phase molecule.

CVD reactors generally work under either molecular flow regime or a continuum flow regime. In the molecular flow regime (k_n<<1), the free mean path length of the gas molecule is large before collision with another gas molecule. This is normally the regime in which LPCVD reactors run. In the continuum flow regime (k_n>>1), the free mean path is short and thus, the collision among gas molecules is higher. This is normally the regime in which APCVD reactors run.

1.5.1.3.3. Boundary layer thickness

The boundary layer formation is the result of diffusion of momentum from the wall into the stream [119]. The boundary layer thickness has special importance when the system is mass transport limited and it is determined by factors such as gas velocity of the precursor, concentration of the precursor and temperature of the reactor. The thickness of the boundary layer is inversely proportional to the square root of the Reynolds number as Equation 1.19 shows [113].

$$\Delta = \sqrt{\frac{x}{Re}} \qquad \text{(Equation 1.19)}$$

Where: Δ= Thickness of the boundary layer

x = Distance from inlet in flow direction

Re = Reynolds number.

Thus, the thickness of the boundary layer increases with lower gas flow velocity and with increase distance from the tube inlet.

As most of CVD reactors operate in a laminar flow, the velocity of the gas precursor at the deposition surface (the inner wall of the tube) is close to zero. The boundary layer is the

region in which the flow velocity changes from zero at the wall until the flow becomes stabilized. Figure 1.17 shows the formation of a velocity boundary layer profile in a hot wall reactor.

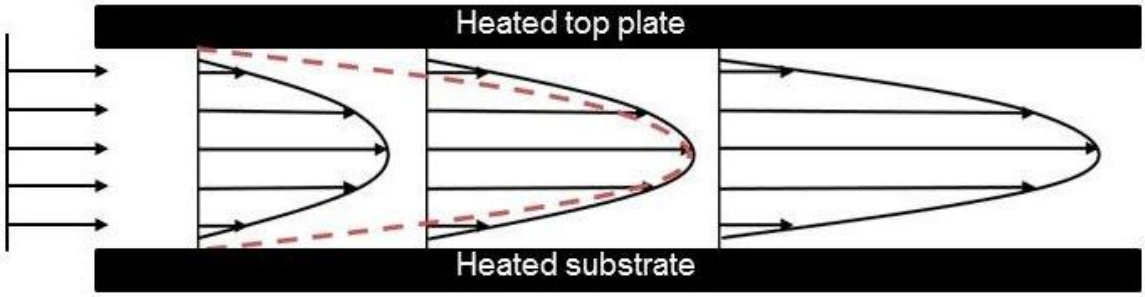

Figure 1.17: Formation and development of velocity boundary layer with velocity proportional to arrow length. Dashed line shows the temperature boundary layer.

The boundary layer thickness is also dependent on the concentration of the precursor. As Figure 1.18 shows, the precursor is consumed as it flows along the reaction chamber resulting in a concentration profile.

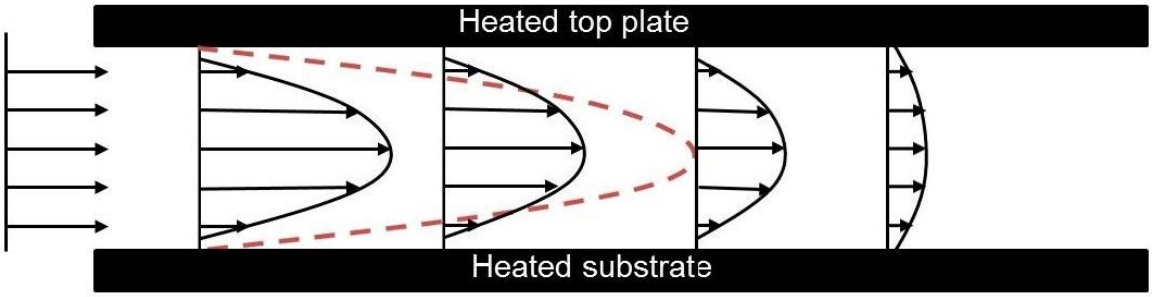

Figure 1.18: Formation and development of gas precursor concentration boundary layer with concentration proportional to arrow length. Dashed line shows the concentration boundary layer.

The temperature boundary layer is similar to the velocity layer (Figure 1.19). This is produced because the flowing gases heat rapidly as they come in contact with the hot surface of the tube resulting in a steep temperature gradient.

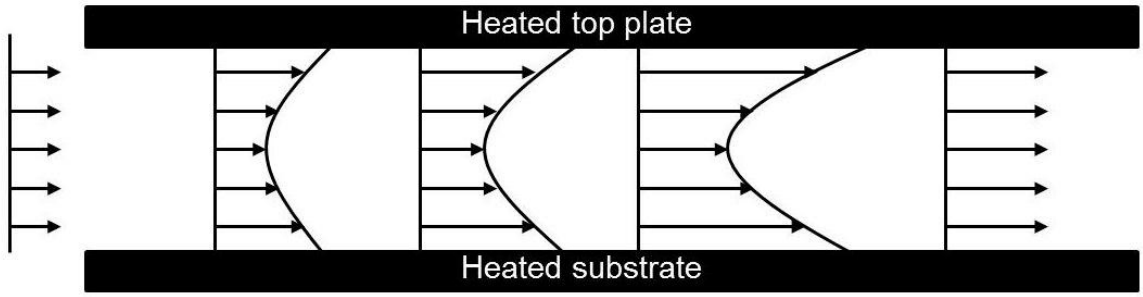

Figure 1.19: Precursor temperature profile in a hot reactor with temperature proportional to arrow length.

1.5.2. Aerosol Assisted Chemical Vapour Deposition

Aerosol assisted chemical vapour deposition (AACVD) is liquid-phase variation of the conventional CVD process. The dissolved precursor is placed in an unheated ultrasonic actuator which releases a steady torrent of micron and sub-micron droplets off the liquid surface. Aerosol particles are then driven to the CVD reactor by the carrier gas flow (Figure 1.20). The advantage of aerosol-assisted CVD is that the problem of differential evaporation is minimized and it facilitates a stable operation in an equally short time [112]. The main advantage of AACVD over conventional CVD is that the delivery of the precursor does not rely on its volatility so a wider range of precursors can be utilised.

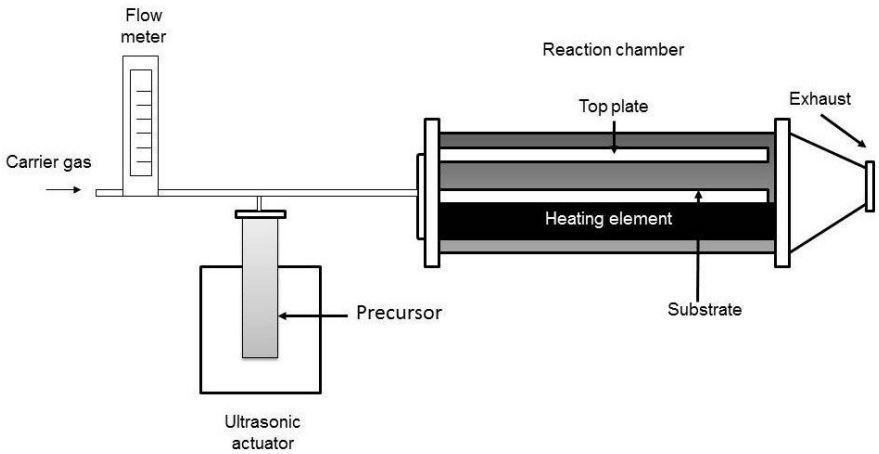

Figure 1.20: Schematic of AACVD rig.

The general CVD reaction routes have been already detailed in section 1.4.1. Specifically, in AACVD aerosols entering the reaction chamber can undergo four different processes depending on the substrate temperature [111] (Figure 1.21).

1. Precursor aerosols are sprayed directly onto a heated substrate followed by the removal of the solvent through evaporation and the decomposition of the precursor to give the final film.
2. The solvent is evaporated before reaching the substrate and the precursor precipitate deposits onto the heated substrate leading to subsequent decomposition and chemical reactions to yield the desired material.
3. The solvent is evaporated while approaching the substrate surface and the precursor precipitate undergoes volatilisation near the surface and adsorption of the vapour onto the heated substrate surface with the subsequent decomposition and/or chemical reactions to yield the desired material. This is the equivalent of the CVD heterogeneous reaction described in section 1.5.1.
4. At high deposition temperature the decomposition or chemical reactions occur in the gas-phase leading to the homogenous reactions described in section 1.5.1. The ultrafine particles formed are sintered on the heated surface leading to the formation of porous films with poor adhesion.

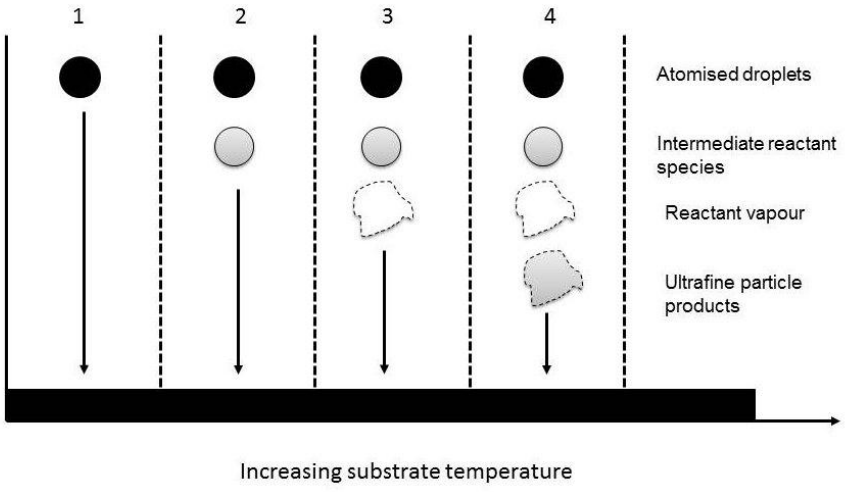

Figure 1.21: Schematic of AACVD process in terms of deposition temperature (Adapted from [111]).

TiO_2 thin films have been extensively produced by Aerosol Assisted Chemical Vapour Deposition (AACVD) [41,121,122] using mainly titanium tetraisopropoxide (TTIP) as a precursor [123,124, 41].

Thin films with the desired microstructure can be achieved from AACVD by tailoring experimental conditions such as type of precursor and solvent, substrate temperature or deposition time. Differences in morphology for different precursors have been attributed to the variation of the donor-functional moieties of the respective alcohol used in the formation of the aerosol [125]. Conde-Gallardo *et al* [126] found substantial differences in deposited films thickness and crystallinity using Titanium-n-butoxide and Titanium-isopropoxide. This was attributed to differences in the precursor activation energy values, which influenced the gas diffusion and surface reaction. The morphology of the films has been also reported to change depending on temperature and type of solvent. Duminica *et al*. [127] observed an increase of film thickness and porosity with increasing temperatures for films deposited from the AACVD reaction of TTIP in acetylacetone and pure TTIP (Figure 1.22). However, the morphology of deposited films drastically changed depending on the solution as pure TTIP gave more defined columnar structures. It was observed that increasing the TTIP concentration slightly decreased the deposition rate. This was attributed to a decrease of the aerosol flow rate as a result of an increase of the viscosity.

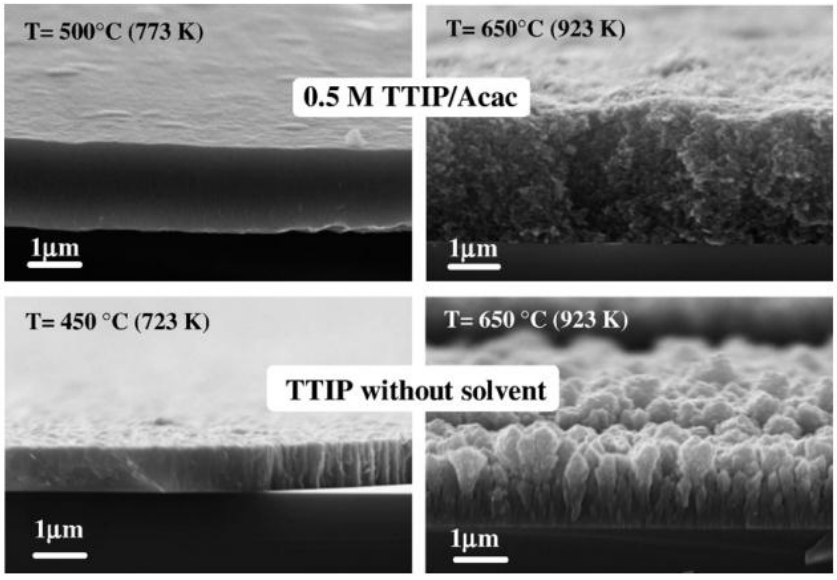

Figure 1.22: SEM images of TiO_2 deposited films from two different solutions, (TTIP/Acac) and pure TTIP, at different substrate temperatures [127].

Furthermore, films morphology is governed by the growth pattern, which highly depends on the deposition time. For instance, branch-tree morphologies are produced from the sintering process of columnar structures [114]. With time, the surface temperature of the TiO_2 structure decreases in the axial direction because of a decrease in the thermal conduction, resulting in this kind of morphology (Figure 1.23).

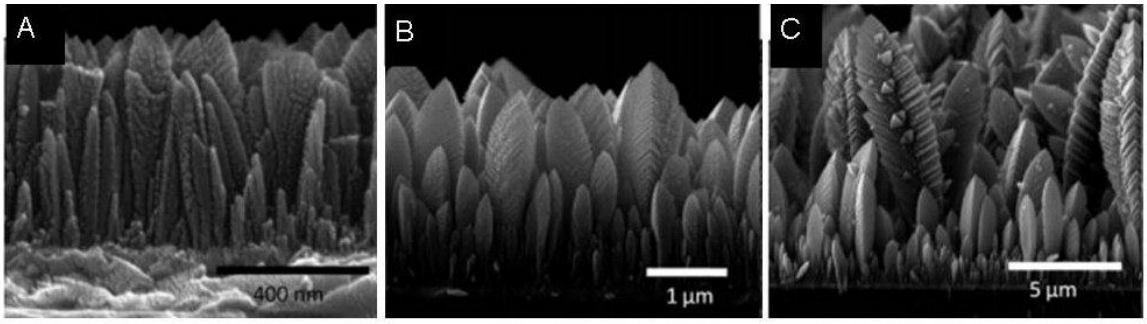

Figure 1.23: SEM images of TiO_2 deposited from TTIP at different deposition times. A) 15 minutes, B) 60 min, C) 75 min (adapted from[114]).

1.5.3. Atmospheric Pressure Chemical Vapour Deposition

In Atmospheric Pressure Chemical Vapour Deposition (APCVD) the carrier gas supply system consists of independent gas lines connected to a pre-heating unit. The carrier gas lines then pass through the different bubbler units driving this way the precursors to the reactor. Figure 1.24 shows a diagram of the atmospheric pressure CVD system. APCVD is widely used in industrial coating manufacturing as it allows a large area uniformity which can be achieved through the control of temperature and gas flow. Furthermore, the source gas generation is physically separated from the reaction chamber, which simplifies the process control. However, the gas density and residence times are higher in APCVD systems, which make them susceptible to oxidation.

TiO_2 thin films have been extensively produced by Atmospheric Pressure Chemical Vapour Deposition (APCVD) [40,128–130]. Studies on the APCVD growth of titania from $TiCl_4$.[131] have reported hazy and three dimensional nanoparticles at substrate temperatures above 140 °C as well as an increase of the growth rate with temperature until reaching a maximum. Evans *et al.* [38] carried out a study to investigate the effect of tin oxide on the photocatalytic properties

of TiO_2. Titania thin films were grown on two different substrates (stainless steel and silica) using APCVD and both TTIP and $TiCl_4$ as precursors. The study revealed similar morphologies on the same substrate (Figure 1.25) Nevertheless, TTIP films were more densely nucleated and showed smaller particle size than $TiCl_4$ films. In addition, TTIP film showed higher photocatalytic activity than $TiCl_4$ on stainless steel substrate. This was explained by the generation of recombination centres result of the chemical reactions between $TiCl_4$ and the stainless substrate. Cross *et al*. [132] took this research further by depositing TiO_2 thin films on steel substrate from the decomposition reaction of $TiCl_4$ and ethylacetate at temperatures below 550 °C. They observed that decreasing the mass flow rate of both titanium precursor and oxygen source significantly increased the particle size (Figure 1.26). Likewise, they observed an important decrease of film thickness when decreasing the mass flow rate. These changes in the microstructure led to changes in polymorphs content, which significantly influenced the photo-activity of the material.

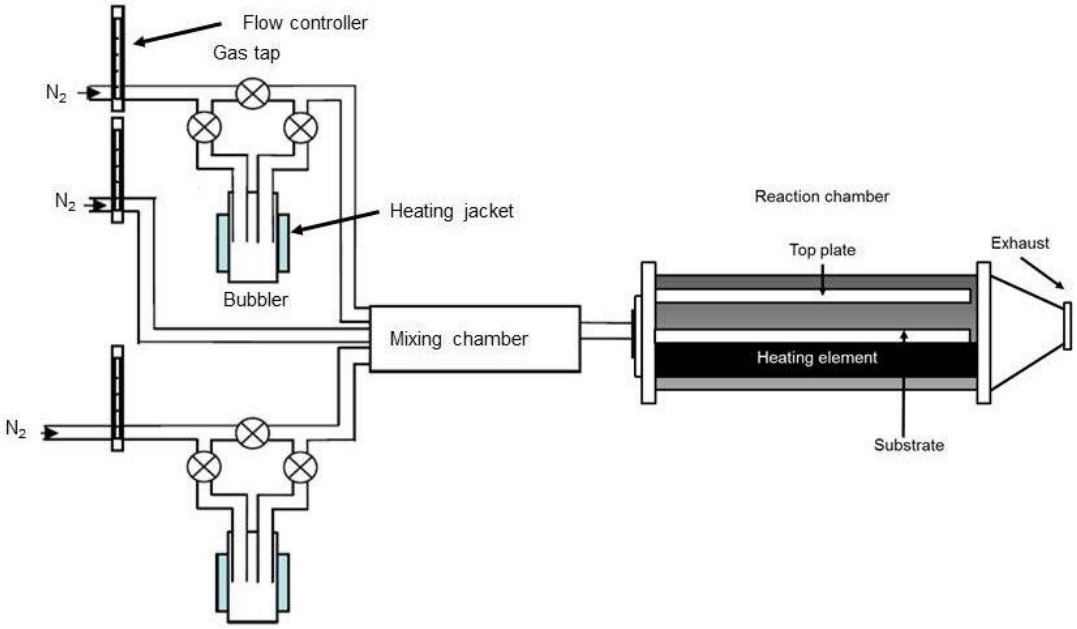

Figure 1.24: Schematic of APCVD rig.

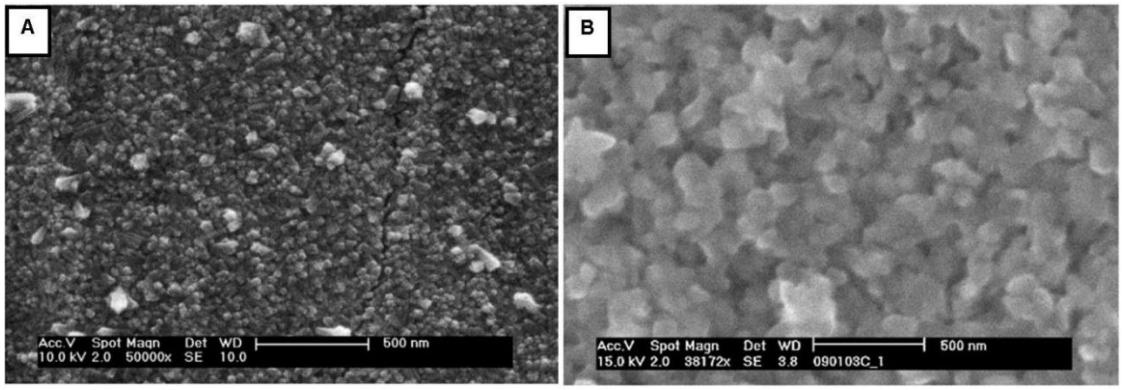

Figure 1.25: SEM images of TiO_2 deposited on silica substrate from A)TTIP and B)$TiCl_4$ (adapted from[38]).

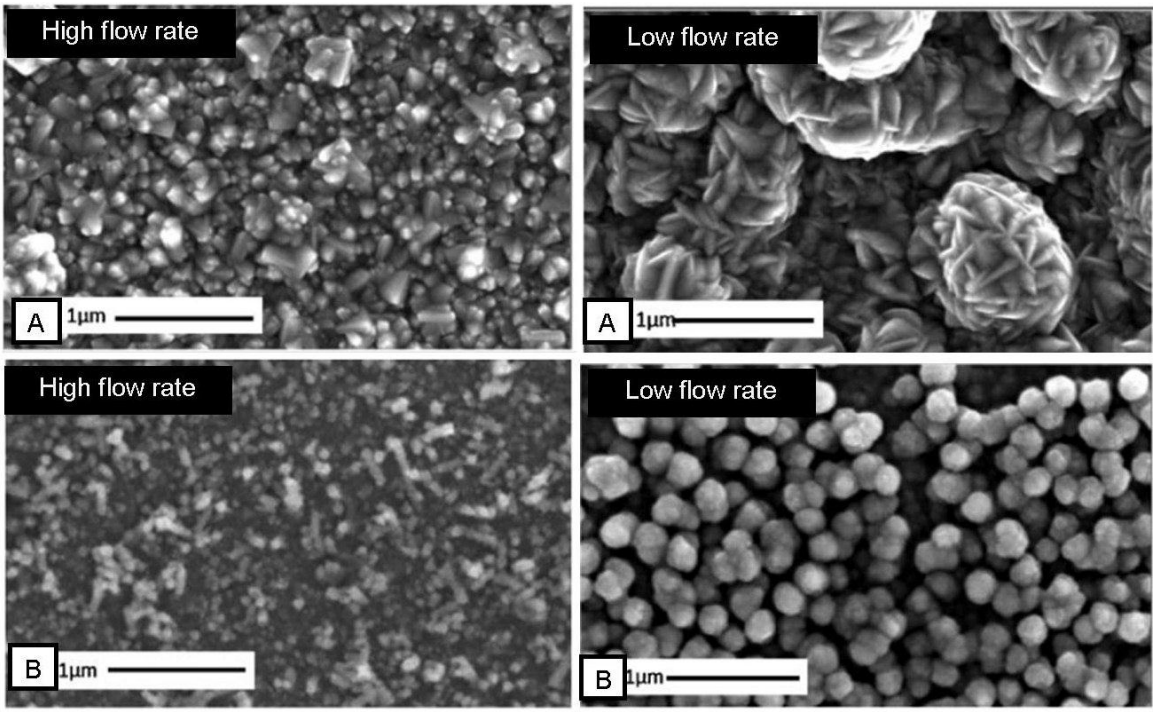

Figure 1.26: SEM images of different morphologies of TiO_2 deposited on two different steel substrates (A and B) at high and low flow rates (adapted from[132]).

1.5.4. Effects of electric fields on CVD

Although the literature available on the effect of electric fields on CVD processes is not large, the results obtained have been promising to continue this thread of investigation. Previous works have shown that the application of electric fields during chemical vapour deposition processes can induce changes in the crystal orientation, growth rate and the surface area of deposited thin films improving gas sensing properties of different materials [24,133]. It has been

also reported that the application of electric fields during the deposition of vanadium or tungsten oxides cause significant changes in the microstructure of the deposited material [133,23], including a significant reduction in crystallite size [22,134]. Naik *et al.* [133] have proposed different possible ways in which electric fields might interfere in metal oxides CVD deposition (Figure 1.27). Applied electric fields might interfere with a permanent or induced dipole in the gas phase (Figure 1.27 A). With time, precursor molecules would be oriented and accelerated towards the surface in the event of dielectrophoresis or asymmetry in the field strength. The permittivity of precursor species changes as a result of a density gradient. This is likely to happen due to a gradient temperature in the wall reactor. Electric fields may also activate precursors bonds by extending the molecular bond along the axis of the dipole, making the precursor more reactive as a result of a decrease in the activation energy (Figure 1.27 B). Electric fields might interfere with the permanent or induced dipole on the substrate, increasing the localised field strength (Figure 1.27 C). Subsequently, the attraction of electrically charged gaseous species would produce a localised growth.

As mentioned, the photocatalytic performance of titania significantly depend on the microstructure. Therefore, induced changes on the microstructure by the effect of electric fields should affect the photocatalytic performance.

1.5.5. Other deposition techniques

Numerous technologies have been used to produce titania thin films elsewhere, which include such as sol-gel methods [135–137], atomic layer deposition (ALD) [138 - 136] and physical vapour deposition (PVD) [141,142]. Solution based methods from the hydrolysis of titanium alkoxides have been widely used as they are easy to implement. Photoactive titanium dioxide thin films have been successfully deposited from sol-gel method coupled with solvothermal using tetraisopropyl orthotitanate (TIOT) as a precursor [143]. In this study, an increase of crystallinity and a subsequent enhance of the material photo-activity was observed when the water content was close to the stoichiometry needed to hydrolyze the precursor molecule. Further investigations reported a shift band gap of 3.27 eV and an increase of photo-activity for a molar ratio of water to TIOT of 3.5 [144].

ALD is a vapour phase technique which consists of sequential alternating pulses of gaseous precursors that react with the substrate. This technique offers exceptional conformallity on high-aspect ratio structure, thickness control at Angstrom level and tuneable film composition at lower deposition temperatures [145] . Although films might reveal amorphous structure at low temperatures, the crystallinity can be improve by increasing the number of cycles [138].

In PVD films are formed from the gas phase but without a chemical transition from precursor to product. The vapourisation is produced either by thermal, electron beam vapourisation or sputtering. Studies on DC sputtering TiO_2 layers deposition have reported high photo-activity despite low crystallinity. This was obtained by nitrogen and carbon doping which produced a red-shift in the energy band gap and improved the mechanical properties [146]. Similar findings were obtained by Tavares *et al*. [147] when producing nitrogen doped titania films. They observed a critical limit of nitrogen (set on 1.19 at.%), improved film crystallinity and showed a band gap reduction to 3.18 eV.

1.6. Summary

Titanium dioxide has been extensively investigated due to its suitable properties for photocatalytic applications. Investigations over the past years have been focused on the modification of titania properties, mostly by increasing the photo-response in the visible. The photocatalytic performance of titania thin films can be influenced by a number of factors such as the particle size and morphology, crystal orientation, crystal phase, thickness and defects. CVD is a well-known technology used for the production of thin films at industrial scale. Among them, aerosol assisted and atmospheric pressure CVD has been of particular interest in the last decade. Inducing electric fields during the CVD reaction is a novel method which has shown important improvements on materials properties.

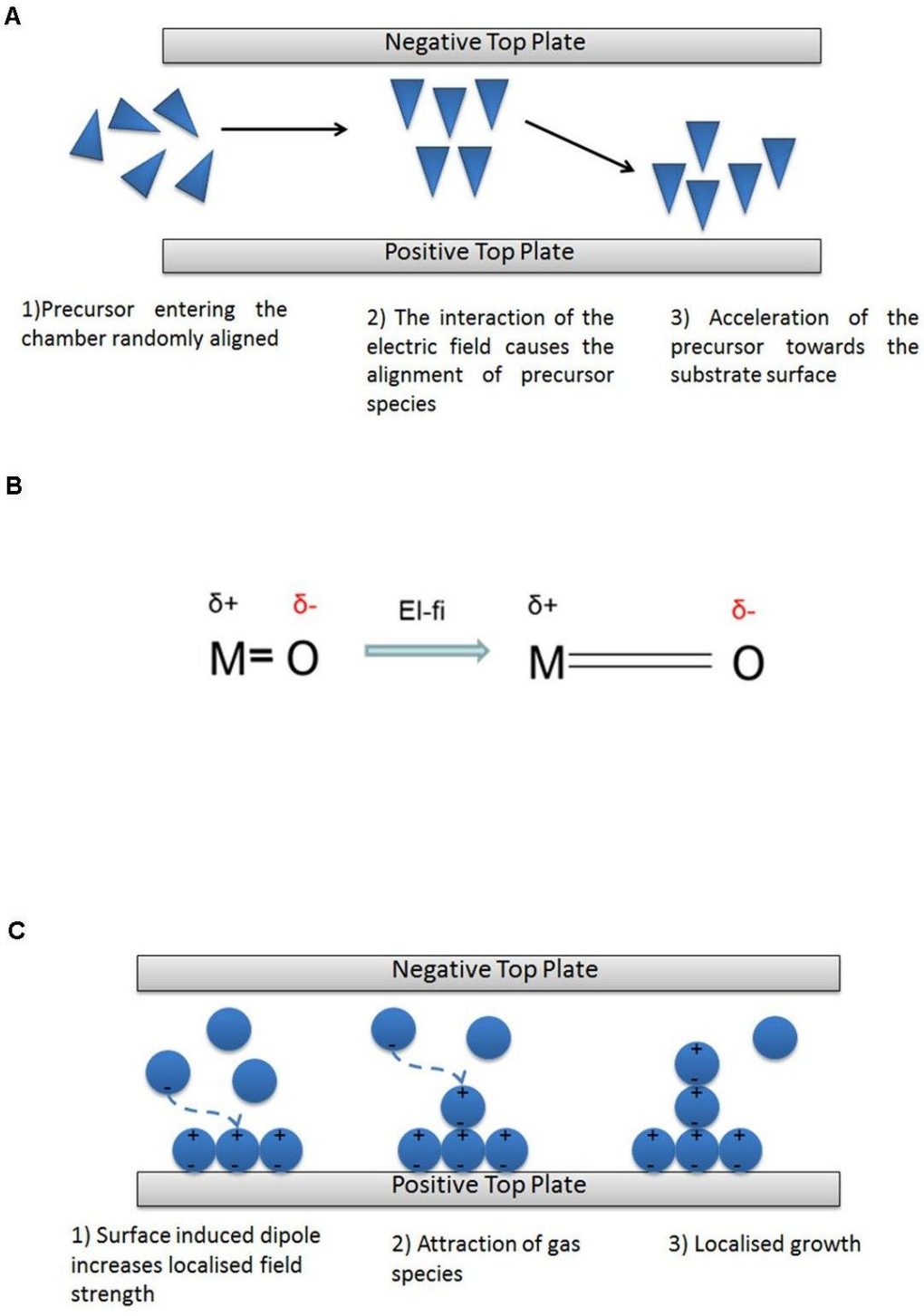

Figure 1.27: Schematic of possible effects in electric field assisted CVD. A) Gas phase alignment and acceleration towards the substrate, B) bond activation (M stands for metal and O for oxygen), C) surface induced dipoles leading to preferred orientation (adapted from [133]).

Chapter 2:

Method, Experimental Conditions, Characterisation and Functional Properties

2.1. Introduction

This chapter describes the method and experimental conditions used for the results shown in chapters 3 – 6. Likewise, the equipment and methods used for characterisation and assessing functional properties are also presented.

2.2. Electric field Assisted Chemical Vapour Deposition

Electric field assisted CVD is a variation of a standard CVD system. The technique involves the application of field strengths between a top plate and the substrate during the deposition. The field strength was applied using two metal electrodes which were placed so that one electrode presses up against the top plate and the other one down on the substrate (Figure 2.1). The silicone discs showed in Figure 2.1 were designed to avoid the contact between the electrodes and the metallic reaction chamber, which would result in short circuiting. The electrodes are connected to a variable voltage unit to produce an electric field. All depositions of films discussed in Chapters 3 to 6 were conducted on glass sheets (90 mm x 45 mm x 4 mm) coated by a fluorine doped tin oxide layer (FTO, NSG Tec 15). FTO glass substrates were used so that the electric field would be present along the entire length of the reaction chamber. The FTO top plate and substrate were placed into the reaction chamber with a separation gap of 1 cm. All substrates were carefully cleaned in deionised water, acetone and isopropanol, using an ultrasonic bath. Then the substrates were dried using nitrogen. AC and DC electric fields were generated using a variable voltage unit in a range from 0 to 30 V. All depositions were conducted at least twice to ensure reproducibility.

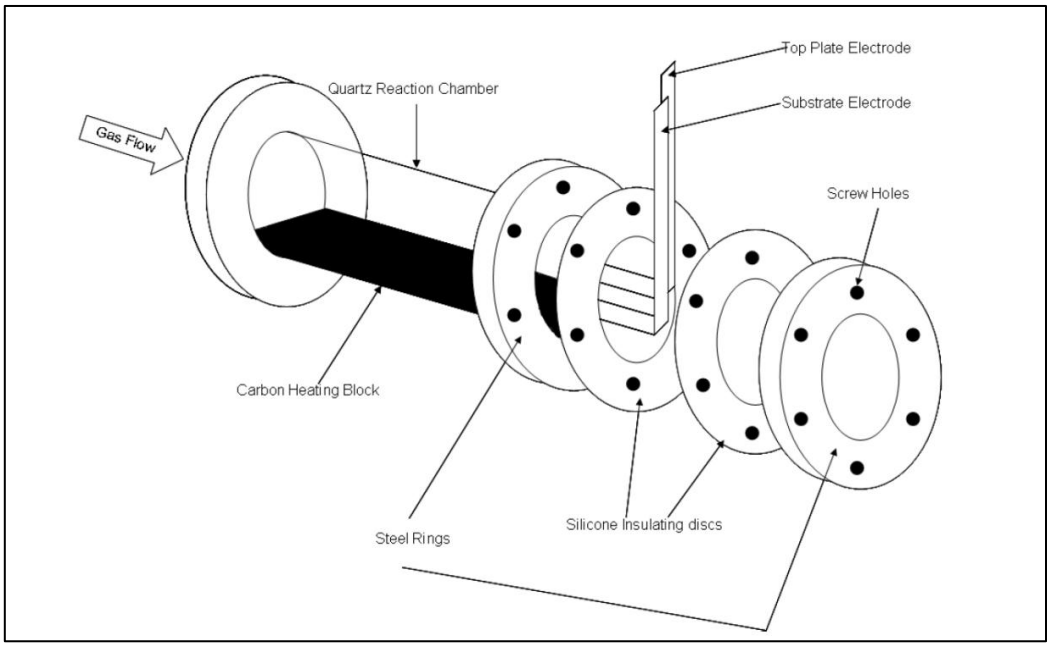

Figure 2.1:Diagram of an electric field assisted CVD reactor showing how electrodes are placed into the system [148].

2.2.1. Electric field Aerosol Assisted Chemical Vapour Deposition (EACVD)

This section describes the apparatus and experimental conditions outlined for the results shown in Chapter 3 and 4. The apparatus in a standard AACVD as described in chapter 1, section 1.5.2, in which the electrodes are placed as described above. Figure 2.2 shows a schematic of a typical EACVD rig.

The precursor solution was introduced into a flask which was placed in an ultrasonic humidifier to form the aerosol at room temperature. The humidifier used for results shown in chapter 3 was a Vicks ultrasonic humidifier (20 kHz) and, for the results in chapter 4, a Mini-fog & Multi-LED Mystery Wonder (Maplin Electronics) humidifier (240 V, 50 Hz). Once the mist was produced, the precursor in form of aerosol was directed to the reaction chamber using nitrogen gas as a carrier gas (BOC 99.9%) which was controlled by a gas flow meter. The temperature of the reactor was set by heating a graphite block containing a Whatman heating cartridge, which was controlled by a Pt-Rh thermocouple.

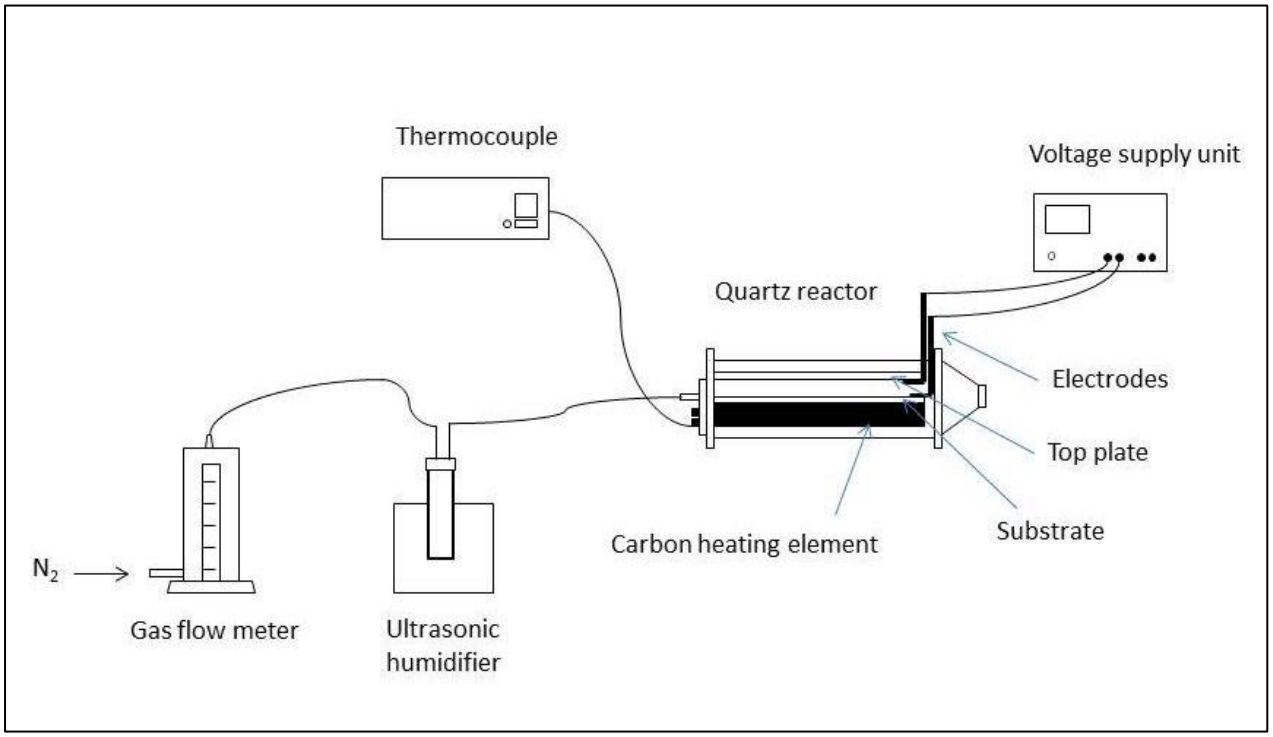

Figure 2.2: Schematic of an EACVD rig.

2.2.1.1. EACVD reaction of titanium isopropoxide (TTIP) in toluene

This section describes the experimental conditions used for results shown in chapter 3.

Fixed conditions

The titanium precursor used was titanium isopropoxide (TTIP, 99.99% trace metals, Aldrich) and the solvent used was toluene (Aldrich). For the precursor 0.5 mL of TTIP was mixed in 10 mL toluene to obtain a 0.17 M solution. The precursor was delivered to the reaction chamber at a gas flow rate (G.F.R) of 2 $L.min^{-1}$. The substrate was set at a temperature of 450 °C (Tsubs). The reaction was conducted until precursor depletion which happened at different deposition time (Dep.time) (Table 2.1). All deposited films showed good coverage on the substrate and birefringence deposition, indicating variations in thickness.

Table 2.1: Experimental conditions for films deposited from the EACVD reaction of 0.17 M TTIP in toluene.

Sample	Applied Voltage (V)	Field Strength (Vm^{-1})	Substrate bias	Tsubs (°C)	G.F.R ($L.min^{-1}$)	Dep. time (min)	Deposition/appearance
A	0	0	--	450	2	18.8	Transparent, birefringence
B	1	100	--	450	2	18.2	Light brown, birefringence
C	5	500	--	450	2	16	Transparent, birefringence
D	10	1000	--	450	2	16	Light brown, birefringence
E	15	1500	--	450	2	17	Transparent, birefringence
F	20	2000	--	450	2	17.75	Transparent, birefringence
G	30	3000	--	450	2	18.8	Transparent, birefringence
H	1	100	Positive	450	2	17.2	Light brown, birefringence
I	5	500	Positive	450	2	17.8	Light brown, birefringence
J	10	1000	Positive	450	2	20	Light brown, birefringence
K	15	1500	Positive	450	2	22	Light brown, birefringence
L	20	2000	Positive	450	2	18	Light brown, birefringence
M	30	3000	Positive	450	2	17.5	Light brown, birefringence
N	1	100	Negative	450	2	16.5	Light brown, birefringence
O	5	500	Negative	450	2	15	Light brown, birefringence
P	10	1000	Negative	450	2	16	Transparent, birefringence
Q	15	1500	Negative	450	2	17	Transparent, birefringence
R	20	2000	Negative	450	2	16.5	Light brown, birefringence
S	30	3000	Negative	450	2	17	Transparent, birefringence

Variable conditions

In order to identify the experimental conditions that gave films with optimum photocatalytic performance, experimental variables were changed taking as a reference two samples produced in previous sections (Sample E and J). Sample E was taken as a reference as it gave the best photocatalytic performance of all AC deposited samples. As samples produced from DC electric fields gave similar photocatalytic results, sample J was selected to do an in-depth study of the most influential aspects for a detrimental effect on the photo-activity. The experimental conditions which were changed were the precursor concentration (0.08 –0.34 M), substrate temperature (300 – 400 °C), gas flow rate (0.5 –3 $L.min^{-1}$) and deposition time (5 –15 min). A total of 12 samples were obtained at different conditions for each reference sample. Thus, samples 1 – 12 were produced at 15 x 10^2 Vm^{-1} and samples 13 –24 were produced at positive bias 10 x 10^2 Vm^{-1}. The experimental variables are listed in Table 2.2. All films showed transparent deposition with birefringence except for samples 4-6, 11-12, 17-18, and 22-23. Due to the high incorporation of carbon, those films showed an opaque appearance.

2.2.1.1. EACVD reaction of titanium tetrachloride ($TiCl_4$) in toluene

The titanium precursor was titanium (IV) chloride (1 M solution in toluene, Aldrich). TiO_2 deposition was obtained despite of the absence of oxygen in the solvent used. This was attributed to the presence of impurities in the system. The reaction was conducted with 5 ml of 1M solution until the depletion of the precursor. Parameters such as substrate temperature (T_{subs}) and gas flow rate (G.F.R) were varied to obtain as much deposition as possible and avoid thermophoresis effects. The aim was to obtain deposition at all field strengths applied. Table 2.2 lists the trial experimental conditions conducted and the appearance of deposited films. No deposition was observed with substrate temperatures in the range from 350 °C to 450 °C; G.F.R in the range of 0.5 to 3 $L.min^{-1}$ and high field strength ($20 \times 10^2 – 30 \times 10^2$ Vm^{-1}) (experiments 1 – 5). When the experiment was conducted with substrate temperatures of 450 °C and gas flow rate of 1 $L.min^{-1}$ (experiments 6 – 12), it was observed that the deposition only occurred either with no electric fields or when applying higher field strengths (greater than 15×10^2 Vm^{-1}). In this case, the film deposition seems to be limited by the mass transport. The thermal decomposition of the reactants rapidly occurs in the gas phase and the kinetics applied by the lower field strength (1×10^2 -10×10^2 Vm^{-1}) are not enough to direct the resulted intermediate species towards the surface. However, when conducting the experiments at the same substrate temperature (450 °C) but higher G.F.R (2 $L.min^{-1}$) the opposite effect was observed (experiments 13 - 18). Birefringence deposition indicating different thickness was obtained for the films produced in absence of electric fields. As the field strength was applied and increased deposited films showed incorporation of carbon (1×10^2 Vm^{-1}) and a deposited cover of opaque white material (5×10^2 Vm^{-1}) which indicates that the reaction happened partially in the gas phase. No deposition was observed at 10×10^2 Vm^{-1} and higher field strength (20×10^2 - 30×10^2 Vm^{-1}).

Depositions were obtained for all films deposited at a substrate temperature of 600 °C and gas flow rate of 5 $L.min^{-1}$. This approach was intended to increase the reaction rate by decreasing the height of the boundary and therefore facilitating the diffusion of reactants to the substrate. Although deposition was obtained at all field strengths tested, in all cases samples presented a deposited cover of opaque white material likely a result of the reaction in the gas phase. Table 2.4 lists the experimental conditions for the films deposited under those conditions. In order to improve the crystallinity of the films, further annealing was carried out

in a Carbolite type 301 programmable furnace in air atmosphere at 600 °C for 2 h and at ramp rate 15 °C min^{-1}.

2.2.2. Electric field Aerosol Assisted Atmospheric Pressure Chemical Vapour Deposition (EAAPCVD)

This section describes the apparatus and experimental conditions outlined for the results shown in Chapter 5 and 6. The apparatus in a standard APCVD as described in chapter 1, section 1.5.3, in which the electrodes are placed as previously described. Figure 2.3 shows a schematic of a typical EACVD rig. The titanium precursor and the oxygen source were placed in independent bubblers. Gases were pre-heated before they were delivered to a mixing chamber by independent tubing lines. The carrier gas was nitrogen (BOC, 99.9%) which was controlled by independent gas flow meters. The temperature of the reactor was set by heating a graphite block containing a Whatman heating cartridge, which was controlled by a Pt-Rh thermocouple. The temperature of the bubblers and all pre-heated lines was also controlled by a Pt-Rh thermocouples and Eurotherm heat controllers.

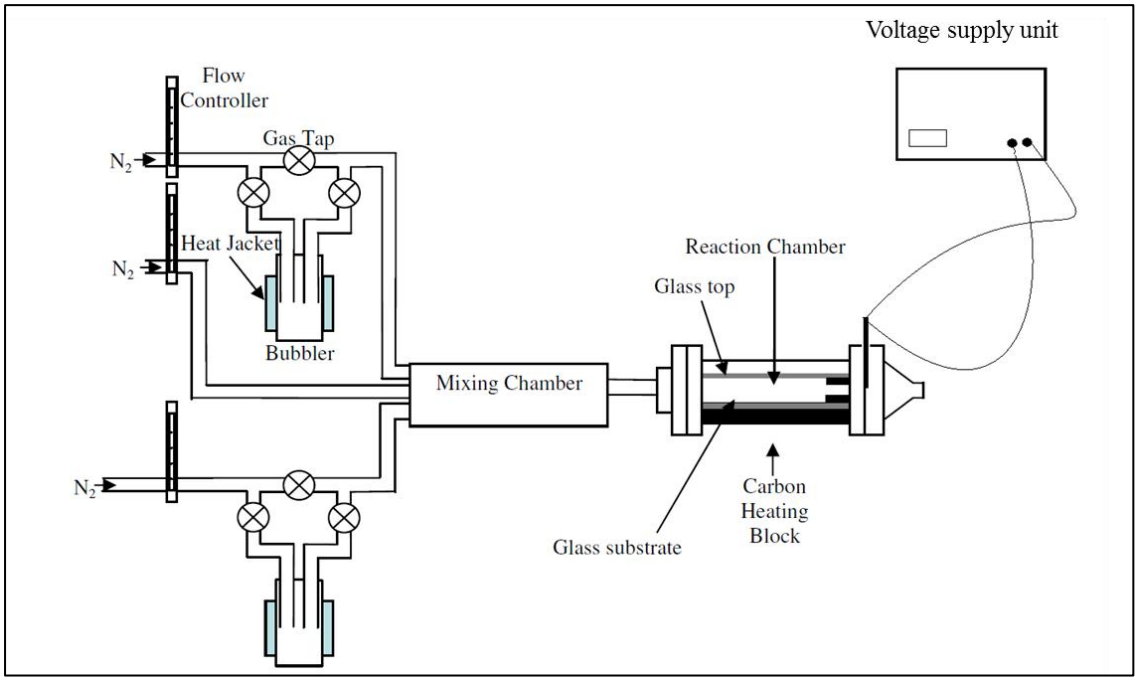

Figure 2.3: Schematic of an EAAPCVD rig.

Table 2.2: Experimental conditions for films deposited from the EACVD reaction of TTIP in toluene at different conditions.

Condition	Field Strength (Vm^{-1})	TTIP Volume (mL)	Molarity (M)	Tsubs (°C)	G.F.R ($L.min^{-1}$)	Dep. time (min)	Thin Film Appearance
1	15×10^2	0.5	0.17	450	2	5	Transparent, birefringence
2	15×10^2	0.5	0.17	450	2	10	Transparent, birefringence
3	15×10^2	0.5	0.17	450	2	15	Transparent, birefringence
4	15×10^2	0.25	0.08	450	2	19.8	Opaque
5	15×10^2	0.75	0.25	450	2	19.8	Opaque
6	15×10^2	1	0.34	450	2	22.3	Opaque
7	15×10^2	0.5	0.17	300	2	16	Transparent, birefringence
8	15×10^2	0.5	0.17	350	2	16.5	Transparent, birefringence
9	15×10^2	0.5	0.17	400	2	16	Transparent, birefringence
10	15×10^2	0.5	0.17	450	0.5	25.2	Transparent, birefringence
11	15×10^2	0.5	0.17	450	1	25.9	Opaque
12	15×10^2	0.5	0.17	450	3	14.9	Opaque
13	$+ 10 \times 10^2$	0.5	0.17	450	2	5	Transparent, birefringence
14	$+ 10 \times 10^2$	0.5	0.17	450	2	10	Transparent, birefringence
15	$+ 10 \times 10^2$	0.5	0.17	450	2	15	Transparent, birefringence
16	$+ 10 \times 10^2$	0.25	0.08	450	2	19.9	Transparent, birefringence
17	$+ 10 \times 10^2$	0.75	0.25	450	2	16.3	Opaque
18	$+ 10 \times 10^2$	1	0.34	450	2	16.6	Opaque
19	$+ 10 \times 10^2$	0.5	0.17	300	2	22.6	Transparent, birefringence
20	$+ 10 \times 10^2$	0.5	0.17	350	2	12.6	Transparent, birefringence
21	$+ 10 \times 10^2$	0.5	0.17	400	2	15.2	Transparent, birefringence
22	$+ 10 \times 10^2$	0.5	0.17	400	2	19.9	Opaque
23	$+ 10 \times 10^2$	0.5		400	2	14.1	Opaque
24	$+ 10 \times 10^2$	0.5		400	2	16.5	Transparent, birefringence

2.2.2.1. EAAPCVD reaction of TTIP and ethanol.

This section describes the experimental conditions for the results shown in chapter 5. The precursor, titanium isopropoxide (TTIP, trace metals 99.9%, Aldrich), and oxygen source (ethanol) were pre-heated at 150 °C and 65 °C, respectively. Gases were independently conducted through the pipelines at a gas flow rate of 1 $L.min^{-1}$ and were delivered to the mixing chamber at a gas flow rate of 2 $L.min^{-1}$. The reactor chamber temperature was set at 550 °C. All the reactions were conducted for 60 seconds. Table 2.5 shows the experimental conditions for the films deposited from the EAAPCVD reaction of TTIP and ethanol.

Table 2.3: Trial experimental conditions for films deposited from EACVD reaction of $TiCl_4$ in toluene.

Sample	Field Strength (Vm^{-1})	AC/DC	Tsubs (°C)	G.F.R ($L.min^{-1}$)	Deposition/appearance
1	2000	AC	350	1	Poor deposition coverage
2	3000	AC	350	3	Poor deposition coverage
3	3000	AC	400	1	Poor deposition coverage
4	3000	AC	400	2	No deposition
5	3000	AC	450	0.5	No deposition
6	0	--	450	1	Transparent/ birefringence
7	100	AC	450	1	No deposition
8	500	AC	450	1	No deposition
9	1000	AC	450	1	Poor deposition coverage
10	1500	AC	450	1	Transparent/ birefringence
11	2000	AC	450	1	Transparent/ birefringence
12	3000	AC	450	1	Birefringence/incorporation of carbon
13	0	--	450	2	Transparent/ birefringence
14	100	AC	450	2	Birefringence/incorporation of carbon
15	500	AC	450	2	Birefringence/white appearance
16	1000	AC	450	2	No deposition
17	1500	AC	450	2	Birefringence
17	2000	AC	450	2	No deposition
18	3000	AC	450	2	No deposition
19	3000	AC	450	4	No deposition
20	0	--	600	5	Birefringence /white appearance
21	100	AC	600	5	Birefringence /white appearance
22	500	AC	600	5	Birefringence /white appearance
23	1000	AC	600	5	Birefringence /white appearance
24	1500	AC	600	5	Birefringence /white appearance
25	2000	AC	600	5	Birefringence /white appearance
26	3000	AC	600	5	Birefringence /white appearance

2.2.2.2. EAAPCVD reaction of $TiCl_4$ and ethyl acetate.

This section describes the experimental conditions for the results shown in chapter 6.

Fixed conditions

The precursor, titanium tetrachloride ($TiCl_4$, Aldrich), and oxygen source (ethyl acetate) were pre-heated at 150 °C and 65 °C, respectively. Gases were independently conducted through the pipelines at a gas flow rate of 0.8 $L.min^{-1}$ and were delivered to the mixing chamber at a gas flow rate of 5 $L.min^{-1}$. The reactor chamber temperature was set at 460 °C. All the

reactions were conducted for 60 seconds. Table 2.6 shows the experimental conditions for the films deposited from the EAAPCVD reaction of $TiCl_4$ and ethyl acetate.

Variable conditions

In order to identify the experimental conditions for the optimum photocatalytic performance, experimental variables were changed. A total of 18 conditions were tested with an applied AC field strength of 1 x 10^2 Vm^{-1} and negative bias 5 x 10^2 Vm^{-1}. Furthermore, a sample in absence of electric fields was produced for every condition tested. The experimental conditions that were changed were substrate temperature (350 – 500 °C), $TiCl_4$ pre-heating temperature (50 –85 °C), ethyl acetate temperature (30 –60 °C), plain flow rate (2 –4 $L.min^{-1}$), bubbler gas flow rate (1 –2 $L.min^{-1}$) and deposition time (15 – 45 seconds). Table 2.7 – 2.8, show the experimental conditions for the films deposited from the EAAPCVD reaction of $TiCl_4$ and ethyl acetate at variable conditions.

Table 2.4: Experimental conditions for films deposited from the EACVD reaction of 1 M $TiCl_4$ in toluene.

Sample	Applied Voltage (V)	Field Strength (Vm^{-1})	Substrate bias	Tsubs (°C)	G.F.R ($L.min^{-1}$)	Dep. time (min)	Deposition/appearance
A	0	0	--	600	5	8	Birefringence /white appearance
B	1	100	--	600	5	7	Birefringence /white appearance
C	5	500	--	600	5	7.5	Birefringence /white appearance
D	10	1000	--	600	5	11	Birefringence /white appearance
E	15	1500	--	600	5	7	Birefringence /white appearance
F	20	2000	--	600	5	9	Birefringence /white appearance
G	30	3000	--	600	5	9.5	Birefringence /white appearance
H	1	100	Positive	600	5	7	Birefringence /white appearance
I	5	500	Positive	600	5	7.5	Birefringence /white appearance
J	10	1000	Positive	600	5	8.4	Birefringence /white appearance
K	15	1500	Positive	600	5	7.3	Birefringence /white appearance
L	20	2000	Positive	600	5	8	Birefringence /white appearance
M	30	3000	Positive	600	5	6	Birefringence /white appearance
N	1	100	Negative	600	5	7	Birefringence /white appearance
O	5	500	Negative	600	5	8	Birefringence /white appearance
P	10	1000	Negative	600	5	8	Birefringence /white appearance
Q	15	1500	Negative	600	5	8	Birefringence /white appearance
R	20	2000	Negative	600	5	6	Birefringence /white appearance
S	30	3000	Negative	600	5	7	Birefringence /white appearance

2.3. Characterisation

2.3.1. Scanning Electron Microscope (SEM)

Scanning electron microscopy (SEM) was completed using a FEI Inspect F Scanning Electron Microscope. Images were collected at 30,000; 40,000 and 60,000 x magnification using 10 mm working distance, 10 kV acceleration voltage, beam spot size of 3.5 µm and objective aperture of 6 µm.

SEM was used to obtain thickness values from the cross-section of all deposited films. A cross section of 2 cm x 1.1 cm was effectuated in the central part of the substrate for all deposited films. Then, SEM images of at least ten points along the sample were captured and measured.

2.3.2. X-ray Diffraction (XRD)

X-ray diffraction (XRD) analysis was conducted using Siemens D5000 (Karlsruhe, Germany) and Panalytical X'Pert Pro (Almelo, The Netherlands) with $Cu_{k\alpha 1}$X-ray source in grazing incidence mode. Siemens D5000 was used for films produced from the EACVD reaction of TTIP in toluene (Chapter 3) and unannealed films produced from the EACVD reaction of TiCl4 in toluene (Chapter 4). Panalytical X'Pert Pro was used for the rest. Patterns were obtained from 10 - 70° in order to obtain all major peaks.

2.3.3. Raman Spectroscopy

Raman spectroscopy was carried out using a Renishaw (UK) Raman system 1000 with a helium neon laser of wavelength 514.5 nm. For experiments of section 2.2.2.2, Raman spectroscopy was carried out using a Renishaw (UK) Raman system G41226 with a helium neon laser of wavelength 633 nm.

Quantifiable values of the content of anatase and rutile in deposited films (Chapter 4, Chapter 5 and Chapter 6) were obtained by deconvoluting the overlapping rutile A_{1g} (612 cm^{-1}) and anatase E_g (639 cm^{-1}) contributions and inserting the % area of contribution of rutile

component (x) into a predetermined equation derived from powder standards as previously reported [63].

2.3.4. Atomic Force Microscopy (AFM)

Atomic force microscopy (AFM) analysis was completed using NT-MDT NTEGRA (Zelenograd, Moscow). Semi-contact mode imaging was performed under ambient conditions in air using silicon tips (Acta-20-Appnano ACT tapping mode with aluminium reflex coating, Nanoscience instruments) with Resonant Frequency of 300 KHz and Spring constant of 40 N/m. Scan resolution of 256 samples per line were used. Images were processed and analysed by the offline software Nova 1.0.26.1443.

2.3.5. UV-Vis Spectroscopy

Transmission values were measured using a Perkin Elmer Lambda 950 UV/VIS spectrometer between 200 – 900 nm with 5 nm increments.

2.4. Functional Properties

2.4.1. Photocatalytic testing

Photocatalytic behaviour was monitored using an intelligent ink based on the dye Resazurin (Rz) [149,150]. The ink was made up of 40 mL of deionized water, 3 g of a 1.5 wt. % aqueous solution of hydroxyethyl cellulose (HEC) polymer (Aldrich), 0.3 g of glycerol (Aldrich) and 4 mg of Rz (Aldrich). The titania thin films formed on glass were cut in dimensions of 2 cm x 1.5 cm and repeatedly washed in deionised water, acetone and isopropanol and dried with nitrogen gas. Then, the samples were placed under UV irradiation (365 nm) for at least 2 h to ensure the photoactivation. Subsequently, the samples were stored in the dark at least for 24 h prior the photocatalytic testing. For the photocatalytic testing, the samples were sprayed with the ink solution using an aerosol spray gun (Figure 2.4 A) and subsequently irradiated with a 365 nm lamp (Figure 2.4 B).

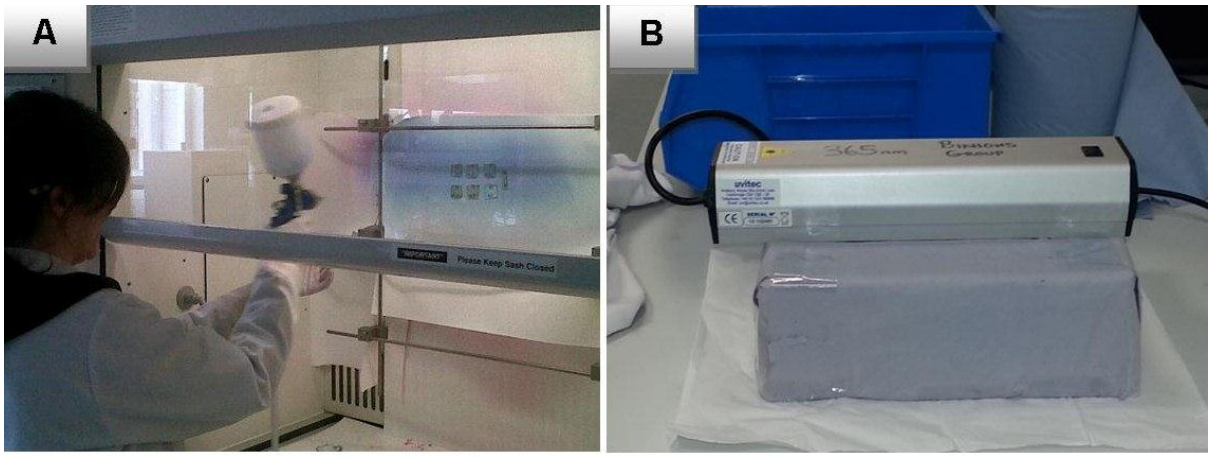

Figure 2.4: Images showing photocatalytic testing set up. A) Spraying samples with Rz aqueous solution, B) UV lamp 365 nm used to irradiate samples.

Resazurin photocatalytic testing is based on a simple redox reaction (Figure 2.5). Upon excitation of an indicator ink coated semiconductor photocatalyst thin film, the photogenerated electrons and holes migrate to the surface. Subsequently, an irreversible reaction between the sacrificial electron donor and holes are produced, hindering the recombination. The photogenerated electrons produce the reduction reaction of the ink. Resazurin ink was chosen because its reduced form cannot be re-oxidised by oxygen [149,150].

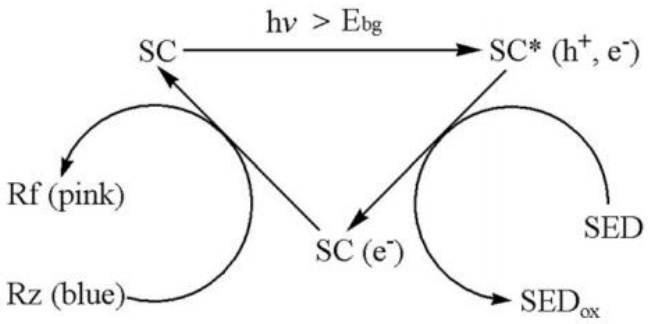

Figure 2.5: Proposed reaction scheme of the indicator ink on an underlying semiconductor photocatalyst (SC), where SED/SED_{ox} represent the reduced/oxidised forms of the sacrificial electron donor (glycerol) and Rz/Rs the oxidised/reduced form of the dye (resazurin/resofurin) [150].

The dye coated films changed colour from blue (photoreduction of Rz) to pink (Rezofurin). Further photodegradation of the dye produces a colourless state indicating the total reduction of rezofurin (Figures2.6).

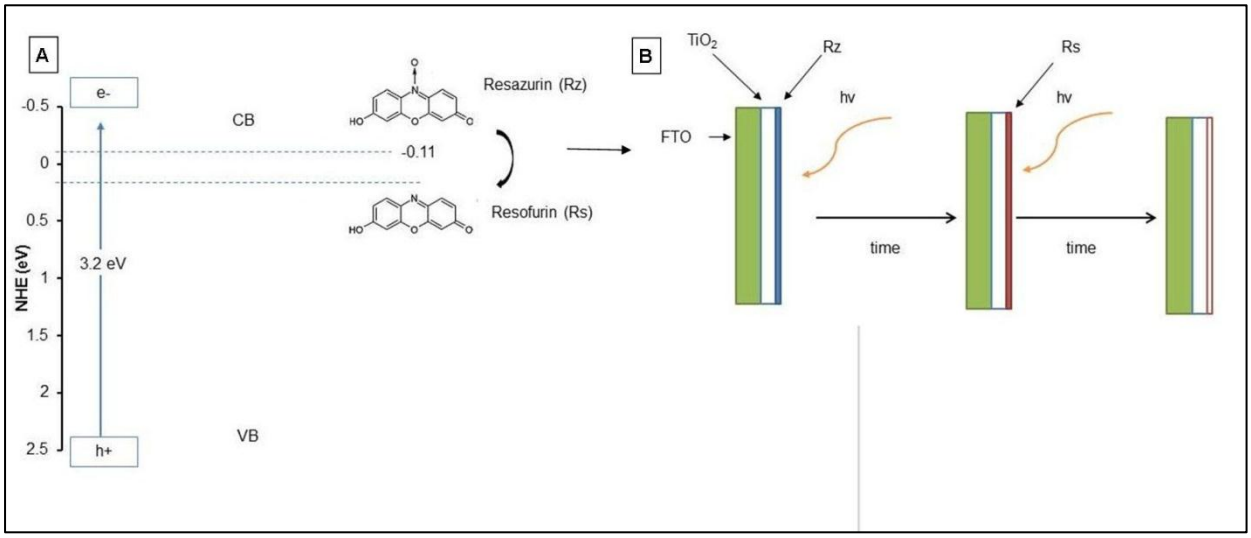

Figure 2.6: Scheme showing indicator ink redox process with anatase TiO2 as an underlying SC (A) Decoloration process from blue (Rz) to pink (Rs) to colourless (total photodegradation) (B).

Thus, the photodegradation process can be observed with the naked eye differing to other photocatalytic tests such as stearic acid. Figure 2.7 shows the de-coloration process of electric field assisted deposited TiO_2 thin films coated with Rz ink.

Kafizas *et al*. [149] that changes in the red-green-blue components of digital colour images were inversely proportional to the changes at corresponding wavelengths via UV-vis spectroscopy. Thus, in the photo-reduction of Rz ink, the red component of digital colour (~630 nm) was produced, reaching a maximum when Rz was completely converted into Rs. In order to conduct a quantitative analysis of the photo-activity of deposited films, the reduction of the dye absorption peak in the wavelength range between 500 –700 nm was monitored using a Perkin Elmer Lambda 25 UV/Vis spectrometer, before and after 60 min (in intervals of 5 – 10 min) of 365 nm UV irradiation. Figure 2.7 shows the UV-vis spectra of the reduction of absorption of Rz on a representative electric field deposited TiO_2 thin film. Resazurin absorption spectra normally shows two peaks, one located at about 560 nm (green region) and another one located at around 630 nm (red region). In order to conduct a quantitative

analysis of the photocatalytic activity of deposited films, absorption values of the second peak was selected, as normally appeared stronger. Then, the absorption values at 630 nm were normalised subtracting the absorption values of the blank samples, clean plain FTO glass and ink coated plain FTO glass. The normalised curves at 630 nm were plotted such that the half-life values could be calculated. The half-life value gives information about the time needed by the sample to degrade the initial concentration of the ink in 50%.

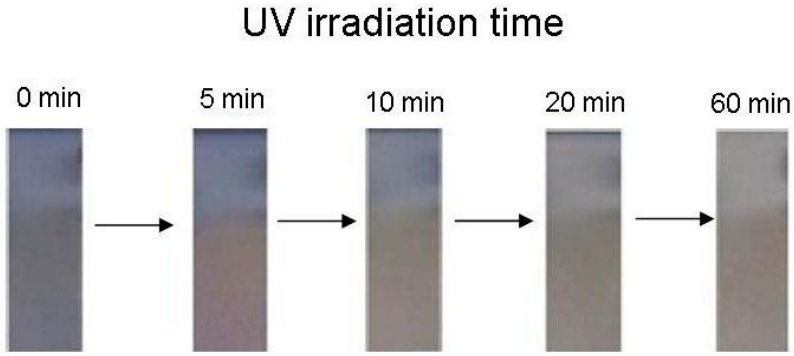

Figure 2.7: Scheme showing de-colouration process of electric field assisted deposited TiO2 thin films coated with Rz ink.

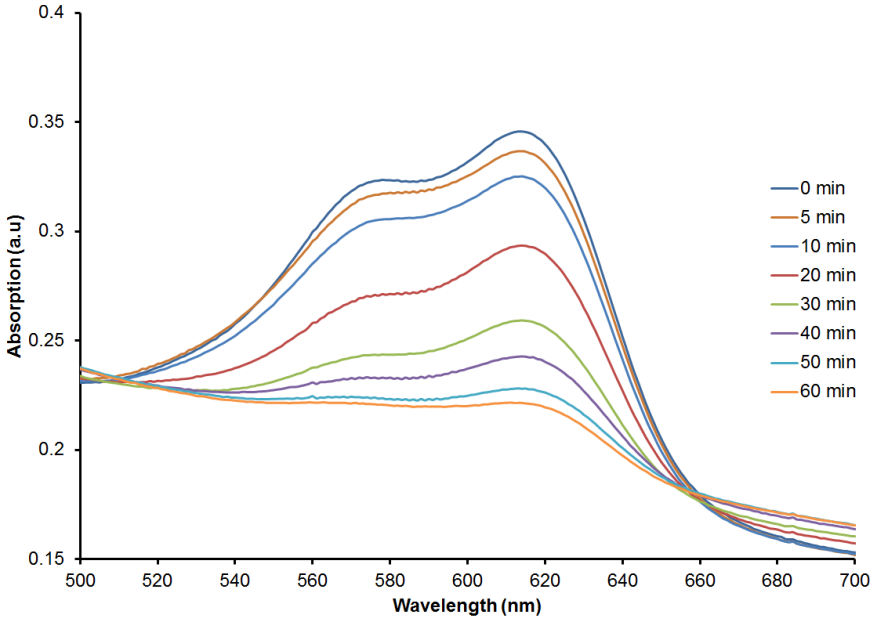

Figure 2.8: UV-vis spectra of the reduction of absorption of Rz on a representative electric field deposited TiO_2 thin film.

2.4.2. Water contact-angles

In order to study the wetting characteristics of the deposited films, water contact angle measurements before and after 30 minutes of irradiation with 254 nm light were carried out using a Goniometer Kruss DSA100 drop shape analyser. The water contact angles calculated using sessile drop fitting.

Table 2.5: Experimental conditions for films deposited from the EAAPCVD reaction of TTIP and ethanol.

Sample	Applied Voltage (V)	Field Strength (Vm^{-1})	Substrate bias	T_{TTIP} (°C)	T_{etOH} (°C)	Tsubs (°C)	G.F.R ($L.min^{-1}$)	Dep. Time (min)	Deposition/appearance
A	0	0	--	148	66	550	2	1	Brownish/ birefringence
B	1	100	--	149	67	550	2	1	Brownish/ birefringence
C	5	500	--	151	65	550	2	1	Brownish, birefringence
D	10	1000	--	150	66	550	2	1	Brownish, birefringence
E	15	1500	--	149	67	550	2	1	Transparent/ birefringence
F	20	2000	--	148	67	550	2	1	Transparent/ birefringence
G	30	3000		152	67	550		1	Transparent/ birefringence
H	1	100	Positive	150	66	550	2	1	Brownish/ birefringence
I	5	500	Positive	149	65	550	2	1	Transparent/ birefringence
J	10	1000	Positive	150	64	550	2	1	Transparent/ birefringence
K	15	1500	Positive	151	65	550	2	1	Transparent/ birefringence
L	30	3000	Positive	148	66	550	2	1	Brownish, birefringence
M	1	100	Negative	149	64	550	2	1	Transparent/ birefringence
N	5	500	Negative	149	67	550	2	1	Transparent/ birefringence
O	10	1000	Negative	150	66	550	2	1	Transparent/ birefringence
P	15	1500	Negative	151	65	550	2	1	Transparent/ birefringence
Q	30	3000	Negative	150	65	550	2	1	Transparent/ birefringence

Table 2.6: Experimental conditions for films deposited from the EAAPCVD reaction of $TiCl_4$ and ethyl acetate at fixed conditions.

Sample	Applied Voltage (V)	Field Strength (Vm^{-1})	Substrate bias	Deposition Temperature (°C)	$TiCl_4$ Temp (°C)	EtoAc Temp (°C)	Plain GRF ($L.min^{-1}$)	Bubblers GFR ($L.min^{-1}$)	Dep time (min)	Thin Film Appearance
A	0	0	--	459	70	44	5	0.8	1	Birefringence, white deposition
B	1	100	--	455	77	43	5	0.8	1	Birefringence, Transparent
C	5	500	--	459	70	38	5	0.8	1	Birefringence, Carbon
D	10	1000	--	458	69	43	5	0.8	1	Birefringence, white deposition
E	15	1500	--	458	71	45	5	0.8	1	Birefringence, white deposition, carbon
F	20	2000	--	460	71	46	5	0.8	1	Birefringence, white deposition, carbon
G	30	3000	--	459	77	42	5	0.8	1	Birefringence, Transparent
H	1	100	+ve	458	76	45	5	0.8	1	Birefringence, Transparent
I	5	500	+ve	462	78	43	5	0.8	1	Birefringence, Transparent
J	10	1000	+ve	460	78	44	5	0.8	1	Birefringence, white deposition, carbon
K	15	1500	+ve	461	75	43	5	0.8	1	Birefringence, Transparent
L	20	2000	+ve	459	67	40	5	0.8	1	Birefringence, carbon
M	30	3000	+ve	458	72	41	5	0.8	1	Birefringence, white deposition
N	1	100	-ve	455	70	38	5	0.8	1	Birefringence, white deposition, carbon
O	5	500	-ve	460	71	38	5	0.8	1	Birefringence, Transparent
P	10	1000	-ve	460	76	43	5	0.8	1	Birefringence, white deposition
Q	15	1500	-ve	460	70	48	5	0.8	1	Birefringence, Transparent
R	20	2000	-ve	462	67	43	5	0.8	1	Birefringence, carbon
S	30	3000	-ve	460	72	45	5	0.8	1	Birefringence, carbon

Table 2.7: Experimental conditions for films deposited from the EAAPCVD reaction of $TiCl_4$ and ethyl acetate at variable conditions.

Condition (C)	Sample	Field Strength (Vm^{-1})	Substrate bias	Deposition Temperature (°C)	$TiCl_4$ Temp (°C)	Ethyl acetate Temp (°C)	Plain GRF ($L.min^{-1}$)	Bubblers GFR ($L.min^{-1}$)	Dep. time (secs)	Appearance
1	0	0	--	352	68	38	5	0.8	60	Birefringence, Transparent
	1 V AC	100	--	350	71	43	5	0.8	60	Birefringence, Transparent
	5 –ve DC	500	Negative	358	72	38	5	0.8	60	Birefringence, Transparent
2	0	0	--	408	66	41	5	0.8	60	Birefringence, carbon
	1 V AC	100	--	408	72	45	5	0.8	60	Birefringence, high carbon
	5 –ve DC	500	Negative	399	72	45	5	0.8	60	Birefringence, high carbon
3	0	0	--	497	70	46	5	0.8	60	Birefringence, poor coverage
	1 V AC	100	--	507	72	44	5	0.8	60	Birefringence, Transparent
	5 –ve DC	500	Negative	507	68	41	5	0.8	60	Thin deposition, no birefringence
4	0	0	--	462	55	42	5	0.8	60	Birefringence, white deposition, carbon
	1 V AC	100	--	463	46	39	5	0.8	60	Birefringence, carbon
	5 –ve DC	500	Negative	464	51	39	5	0.8	60	Birefringence, carbon
5	0	0	--	454	57	41	5	0.8	60	Birefringence, white deposition
	1 V AC	100	--	455	58	40	5	0.8	60	Birefringence, Transparent
	5 –ve DC	500	Negative	463	65	40	5	0.8	60	Birefringence, white deposition
6	0	0	--	455	87	38	5	0.8	60	Thin deposition, no birefringence
	1 V AC	100	--	464	86	44	5	0.8	60	Birefringence, Transparent
	5 –ve DC	500	Negative	457	84	37	5	0.8	60	Birefringence, Transparent
7	0	0	--	462	71	35	5	0.8	60	Birefringence, carbon
	1 V AC	100	--	464	69	32	5	0.8	60	Birefringence, Transparent
	5 –ve DC	500	Negative	464	68	29	5	0.8	60	Birefringence, Transparent
8	0	0	--	461	70	54	5	0.8	60	Thin deposition, no birefringence
	1 V AC	100	--	463	73	52	5	0.8	60	Birefringence, carbon
	5 –ve DC	500	Negative	457	69	52	5	0.8	60	Birefringence, white deposition
9	0	0	--	463	69	62	5	0.8	60	Birefringence, Transparent
	1 V AC	100	--	465	75	63	5	0.8	60	Birefringence, Transparent
	5 –ve DC	500	Negative	463	67	59	5	0.8	60	Birefringence, Transparent
10	0	0	--	465	70	41	4	0.8	60	Birefringence, carbon
	1 V AC	100	--	466	68	44	4	0.8	60	Birefringence, white deposition, carbon
	5 –ve DC	500	Negative	464	74	41	4	0.8	60	Birefringence, Transparent
11	0	0	--	455	65	38	3	0.8	60	Birefringence, Transparent
	1 V AC	100	--	464	470	46	3	0.8	60	Birefringence, white deposition, carbon
	5 –ve DC	500	Negative	465	68	41	3	0.8	60	Birefringence, Transparent
12	0	0	--	466	66	45	2	0.8	60	Birefringence, carbon
	1 V AC	100	--	459	67	43	2	0.8	60	Birefringence, carbon
	5 –ve DC	500	Negative	460	69	45	2	0.8	60	Birefringence, white deposition

Table 2.8: Experimental conditions for films deposited from the EAAPCVD reaction of $TiCl_4$ and ethyl acetate at variable conditions.

Condition (C)	Sample	Field Strength (Vm^{-1})	Substrate bias	Deposition Temperature (°C)	$TiCl_4$ Temp (°C)	Ethyl acetate Temp (°C)	Plain GRF ($L.min^{-1}$)	Bubblers GFR ($L.min^{-1}$)	Dep. time (min)	Appearance
13	0	0	--	466	69	45	5	1	60	Birefringence, Transparent
	1 V AC	100	--	457	74	40	5	1	60	Birefringence, Transparent
	5 –ve DC	500	Negative	460	75	44	5	1	60	Birefringence, white deposition
14	0	0	--	460	75	47	5	1.5	60	Birefringence, carbon
	1 V AC	100	--	462	67	41	5	1.5	60	Birefringence, carbon
	5 –ve DC	500	Negative	464	68	44	5	1.5	60	Birefringence, high white deposition (very opaque)
15	0	0	--	466	74	45	5	2	60	Birefringence, carbon
	1 V AC	100	--	463	72	45	5	2	60	Thin deposition, no birefringence
	5 –ve DC	500	Negative	456	67	46	5	2	60	Thin deposition, no birefringence
16	0	0	--	465	77	45	5	0.8	15	Thin deposition, no birefringence
	1 V AC	100	--	464	65	42	5	0.8	15	Thin deposition, no birefringence
	5 –ve DC	500	Negative	460	70	44	5	0.8	15	Thin deposition, no birefringence
17	0	0	--	465	69	44	5	0.8	30	Birefringence, Transparent
	1 V AC	100	--	457	70	41	5	0.8	30	Birefringence, white deposition
	5 –ve DC	500	Negative	465	69	39	5	0.8	30	Birefringence, Transparent
18	0	0	--	455	71	47	5	0.8	45	Birefringence, carbon
	1 V AC	100	--	454	67	37	5	0.8	45	Birefringence, Transparent
	5 –ve DC	500	Negative	465	69	39	5	0.8	45	Birefringence, Transparent

Chapter 3:

Titanium Dioxide Thin Films Produced from the Electric Field Assisted Aerosol Chemical Vapour Deposition of Titanium (IV) Isopropoxide in Toluene

3.1. Introduction

Titanium dioxide has been extensively produced from the aerosol assisted chemical vapour deposition (AACVD) reaction of Titanium Tetraisopropoxide (TTIP) with different solvents and at different experimental conditions. This chapter presents the results on the experimental study of the TiO_2 thin films growth from Electric Field Assisted AACVD using 0.17 M TTIP solution in toluene.

3.2. Results

3.2.1. Film synthesis and characterisation of AC deposited films

The AACVD and EACVD reaction of TTIP in toluene onto glass substrate at 450 °C produced thin films with good adherence to the substrate, the films passed the Scotch tape test and could not be wiped off with a piece of towelling. XRD and Raman spectroscopy confirmed the presence of the anatase crystal phase across the substrate (Table 3.1).

Table 3.1: Experimental conditions of deposited films from the EAACVD reaction of 0.17 M TTIP solution in toluene at 450 °C and gas flow rate of 2 L.min-1 with an applied AC electric field.

Sample	Applied Voltage (V)	Field Strength (Vm^{-1})	Material Phase (XRD /Raman)
A	0	0	Anatase TiO_2
B	1	1×10^2	Anatase TiO_2
C	5	5×10^2	Anatase TiO_2
D	10	10×10^2	Anatase TiO_2
E	15	15×10^2	Anatase TiO_2
F	20	20×10^2	Anatase TiO_2
G	30	30×10^2	Anatase TiO_2

Scanning electron microscopy

Scanning electron microscopy images of the titanium dioxide depositions are shown in Figure 3.1. Deposition carried out in absence of an electric field (Figure 3.1 A) revealed a thin film comprised of agglomerated acicular nanoparticles of 200 ± 12 nm length with a film thickness of 120 ± 10 nm. The introduction of an electric field (1×10^2 Vm^{-1} to 5×10^2 Vm^{-1}, Figures 3.1 B – C) across the electrodes of the glass substrate during the deposition produced a change in the morphology to spherical nanoparticles of the same size (200 ± 31 nm). It was observed that when introducing the electric field the film thickness significantly dropped to 10 ± 5 nm (sample B). However, when the field strength was increased to 5×10^2 Vm^{-1} the film thickness dramatically increased to 450 ± 8 nm (sample C). As the electric field strength was further increased (10×10^2 Vm^{-1} to 15×10^2 Vm^{-1}) the shape of the particles changed from spherical to elongated particles 200 ± 10 – 140 ± 12 nm in length (Figures 3.1 D – E). The film thickness in this range was 250 ± 9 – 650 ± 13 nm. When the field strength was increased to 20×10^3 Vm^{-1} and 3×10^3 Vm^{-1} (samples F and G) the shape changed back to a spherical microstructure with a diameter of 120 ± 10 – 215 ± 17 nm (Figure 3.1 F – 2G). The film thickness in this range was found to be 300 ± 20 – 550 ± 12 nm. Agglomerate size and film thickness values can be seen listed in Table 3.2.

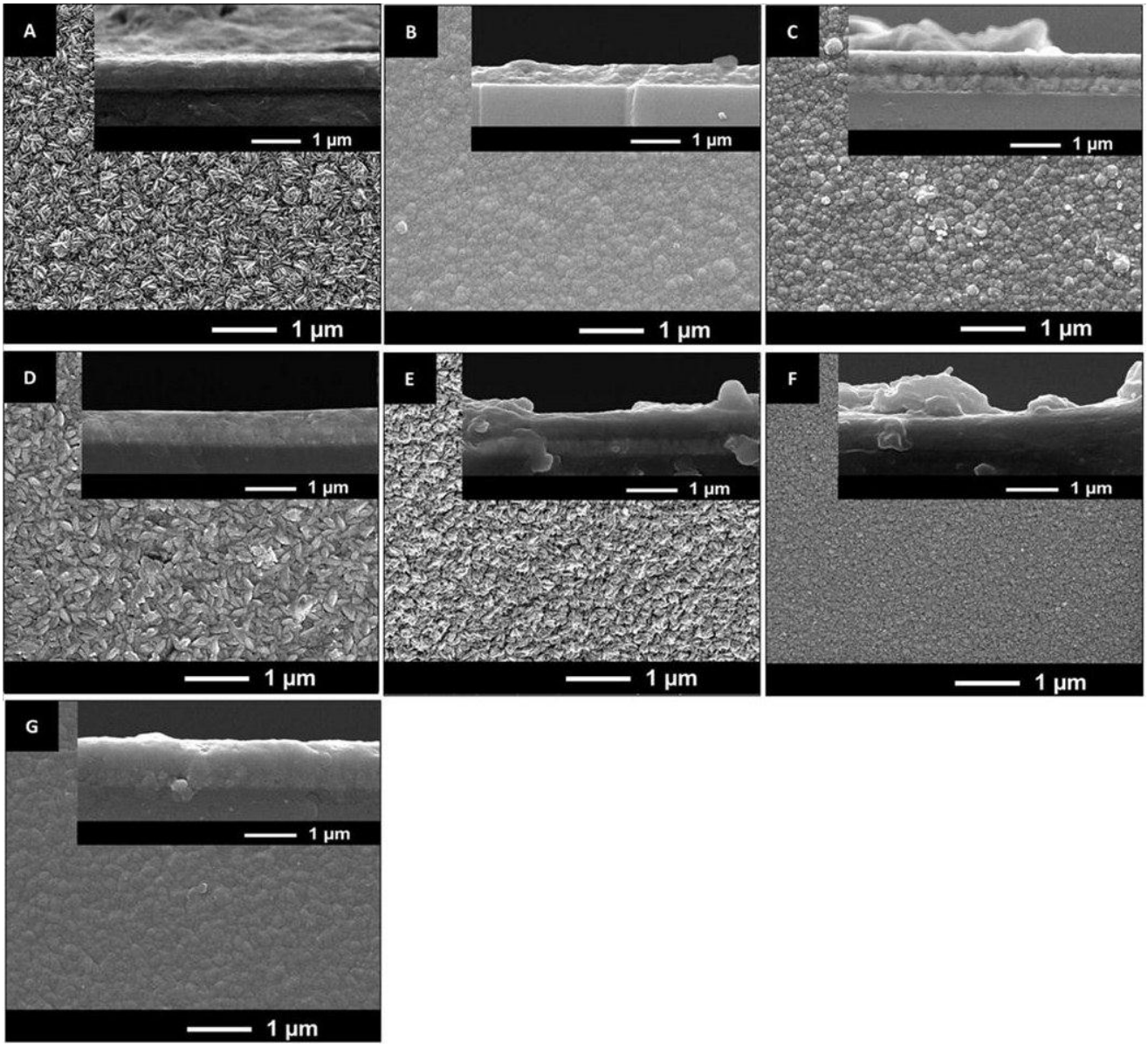

Figure 3.1: Scanning Electron Microscope images of samples prepared without electric field (Sample A) and from the AC EAACVD reaction (B to G) of 0.17 M TTIP solution in toluene. The images above correspond to A) 0 Vm^{-1}, B) 1 x 10^2 Vm^{-1}, C) 5 x 10^2 Vm^{-1}, D) 10 x 10^2 Vm^{-1}, E) 15 x 10^2 Vm^{-1}, F) 20 x 10^2 Vm^{-1}, G) 30 x 10^2 Vm^{-1}. Side-on images were captured at x 30,000 magnification and cross-section images at x 40, 000.

Table 3.2: Agglomerate size (nm), film thickness (nm) with standard error (SE) obtained from SEM and mean crystallite size (nm) obtained from the Scherrer equation, for deposited films from AC EAACVD reaction of 0.17 M TTIP solution in toluene at 450 °C and 2 $L.min^{-1}$.

Sample	Applied Voltage (V)	Field strength (Vm^{-1})	Agglomerate size (nm)	Thickness (nm)	Mean crystallite size (nm)
A	0	0	200±12	120±10	24±2
B	1	1 x 10^2	200±18	10±5	19±1
C	5	5 x 10^2	200±31	450±8	20±3
D	10	10 x 10^2	200±10	250±9	22±2
E	15	15 x 10^2	140±12	650±13	23±1
F	20	20 x 10^2	120±10	300±20	15±1
G	30	30 x 10^2	215±17	550±12	19±2

X-ray diffraction

X-ray diffraction was conducted and compared to the JCPDS database (JCPDS file number: 00-021-1272) to investigate the materials phase (Figure 3.2). All deposited films showed anatase TiO_2. Casserite SnO_2 from the underlying FTO coated glass substrate was also observed for the films deposited with field strength from 1 x 10^2 Vm^{-1} to 15 x 10^2 Vm^{-1} (Samples B – E). At the highest applied electric field strength, peaks due to cassiterite are not observed (Figure 3.2 F, 3.2 G) indicating an increase in crystallinity. The relative intensity of the Bragg peaks associated with TiO_2 changed with the field strength revealing a preferred orientation. The XRD patterns indicated higher diffraction intensity of the (101) plane for the sample grown with no electric field and, as the field strength is introduced, a higher diffraction intensity of the (004) plane is observed (Fig. 3.2 B). The increase of the applied field strength produces changes in the diffraction intensity peaks from the (004) to the (101) (Fig. 3.2 D - F) until the last sample which showed a diffraction peak from the (211) plane.

The preferred growth orientation of polycrystalline thin films can be quantified from the Texture Coefficient ($TC_{(hkl)}$) for all planes [151,152]. Table 3.3 shows that deposited films in absence of electric fields (Sample A) and films produced in the range from 1 x 10^2 to 15 x 10^2 Vm^{-1} (Sample B – E) showed high texture coefficient in the (004) plane. In particular, the

highest value of texture coefficient was found for Sample B with a texture coefficient of 3.19. Films deposited at higher field strength (Sample F and G) showed values of texture coefficient in the (211) plane of 1.73 – 2.49 confirming the preferential orientation in that plane.

The crystallite size of the deposited films was calculated from the full width at half maximum (FWHM) of different peaks using the Scherrer equation (Table 3.2). For samples A – E, characteristic peaks of 2θ = 25.28° (101), 2θ = 37.8° (004), 2θ = 48.05° (200) were used and for samples F and G, peaks 2θ = 25.28° (101), 2θ = 48.05° (200), 2θ = 55.06° (211) were selected. Likewise, shape factor of 0.9 [153] was chosen. The application of electric fields produced a decrease in the mean crystallite size from 24 to 19 nm (Sample B). As the electric field is increased the crystallite size also increases until reaching a maximum (23 nm) for sample E. Then, the crystallite size decreases to 15 and 19 nm with films deposited at higher field strengths (F and G).

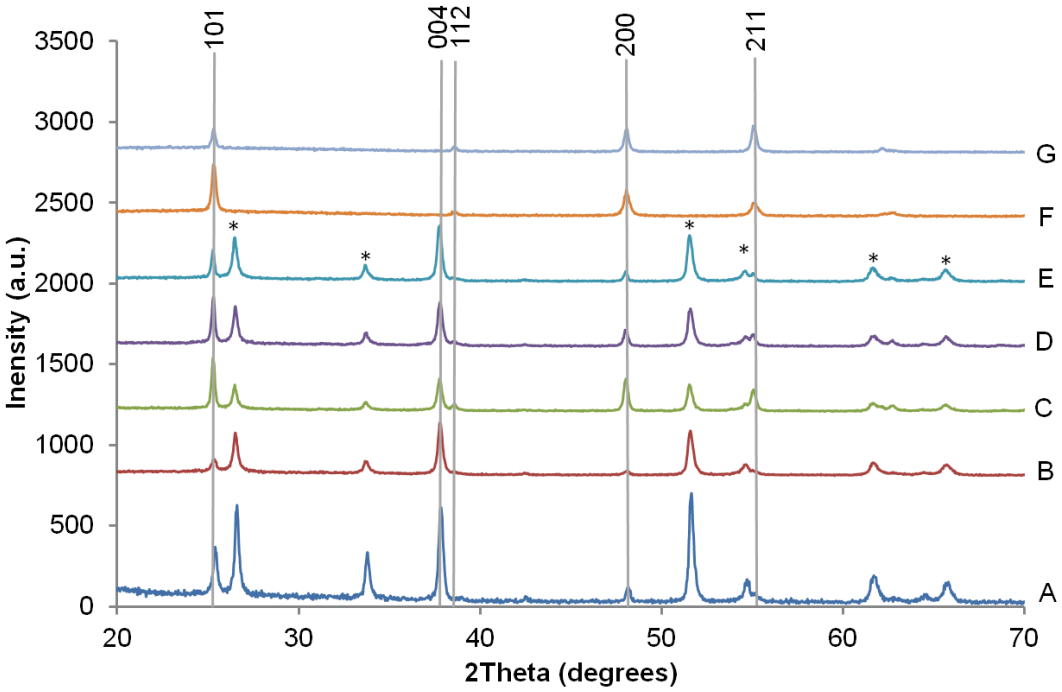

Figure 3.2: XRD patterns for samples prepared without an applied electric field (A) and from the EAACVD (B to G) reaction of 0.17M TTIP solution in toluene at 450 °C and a gas flow rate of 2 L.min^{-1}. All peaks correspond to anatase crystal phase. The peaks marked with dots denote the cassiterite peaks specific of SnO_2 crystalline phase, material used for the glass substrate coating.

Raman spectroscopy

Raman spectroscopy was carried out in order to complement XRD analysis for phase identification. Figure 3.3 shows Raman spectra for all the deposited films. Generally, samples gave strong Raman peaks centred at 147 cm^{-1} and 642 cm^{-1} and weaker peaks centred at 198 cm^{-1}, 395 cm^{-1}, 513 cm^{-1}, revealing characterizing bands of anatase TiO_2 [134]. The application of electric fields (Sample B) seemed to reduce crystallinity which was accentuated at 5 x 10^2 Vm^{-1} (Sample C). However, at higher field strength strong Raman peaks for anatase were observed. Bands characterising as rutile TiO_2 which can be expected at 143 cm^{-1}, 447 cm^{-1}, 612 cm^{-1}, 826 cm^{-1} [24] were not identified.

Table 3.3: Texture Coefficient of TiO_2 thin films produced from the AC EAACVD reaction of 0.17 M TTIP in toluene.

Sample	Field Strength (Vm^{-1})	Texture Coefficient ($TC_{(hkl)}$)			
		(101)	(004)	(200)	(211)
A	0	0.35	2.94	0.32	0.42
B	1 x 10^2	0.21	3.19	0.24	0.37
C	5 x 10^2	0.51	1.58	0.88	1.17
D	10 x 10^2	0.51	2.29	0.52	0.77
E	15 x 10^2	0.33	2.84	0.33	0.55
F	20 x 10^2	0.9	0.36	1.4	1.73
G	30 x 10^2	0.4	0.24	1.11	2.49

Atomic force microscopy

AFM was performed scanning over a 2 µm x 2 µm region in order to obtain Root Mean Square (RMS) roughness values as a proxy of surface roughness (Figure 3.4). As it can be observed, the application of AC electric fields slightly decreased the surface roughness from 26 ± 9 nm to 20 ± 10 nm (Sample A and B). The increase of field strength produced a gradual decrease in surface roughness to 15 – 12 ± 10 nm (Sample C – D). Sample E showed an increase of surface roughness to 16 ± 2 and Sample F an important decrease of the RMS

value to 4 ± 2 nm. At 30 x 10^2 Vm^{-1} (Sample G) the surface roughness increased to 27± 6 nm. RMS values are listed in Table 3.4.

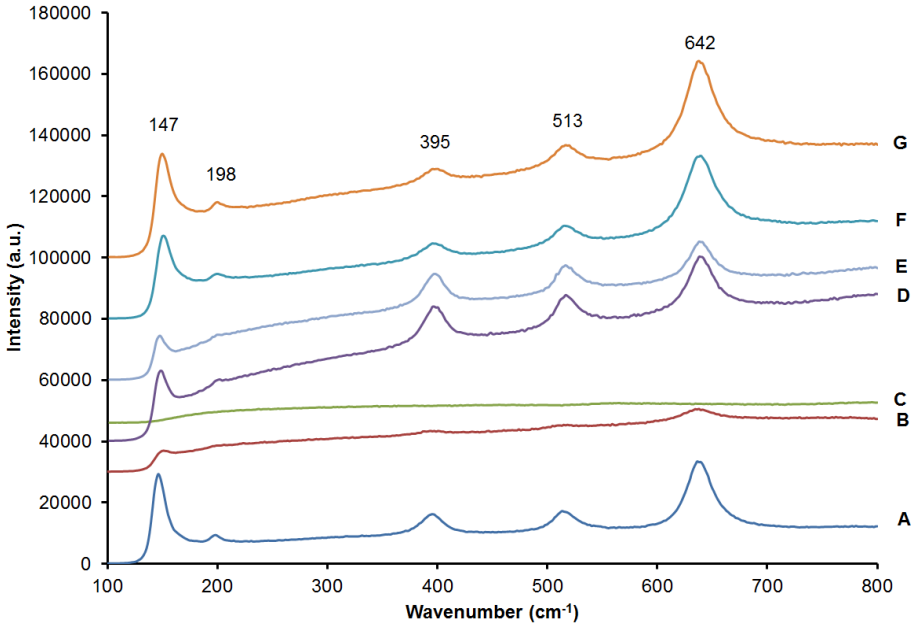

Figure 3.3: Raman spectra for samples prepared without an applied electric field (A) and from the AC EAACVD (B to G) reaction of 0.17M TTIP solution in toluene at 450 °C and a gas flow rate of 2 $L.min^{-1}$.

UV-vis spectroscopy

UV/VIS spectroscopy revealed that the application of field strength during the EACVD deposition had a detrimental effect on the maximum transmission in the visible of the thin films (Figure 3.5). Hence, maximum transmission values in the visible gradually decreased when applying and increasing the field strength. Sample A showed the highest maximum transmission values in the visible (79 %). As the field strength was applied and increased up to 1 x 10^2 Vm^{-1} the transmission in the visible gradually decreased to 56 %. At higher field strength (Samples E – F) transmission values in the visible were greater (74 – 70 %) but still lower than Sample A.

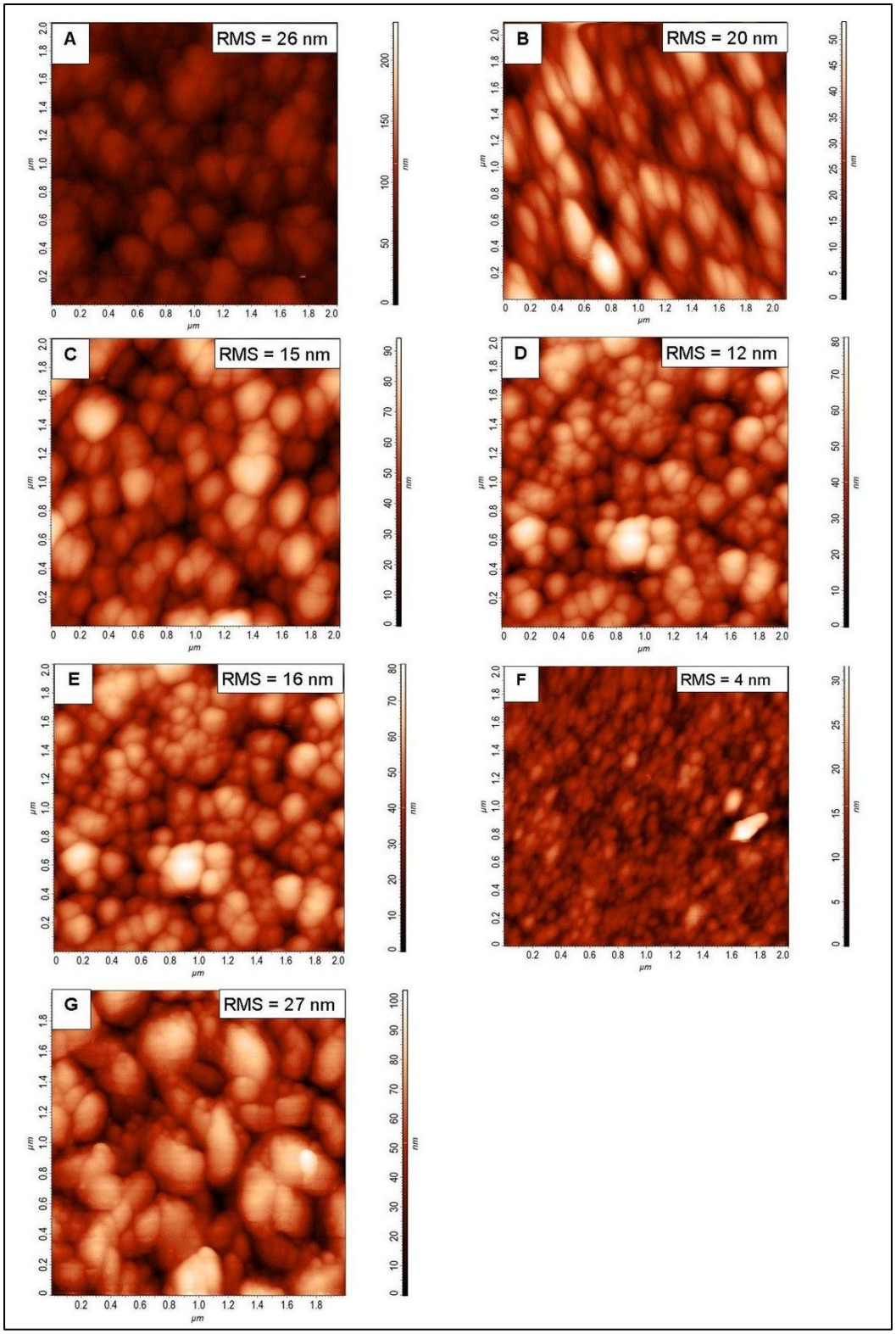

Figure 3.4: AFM images with corresponding Root Mean Square (RMS) values (nm) for films deposited from the AC EAACVD reaction of 0.7 M TTIP solution in toluene at 450 °C and 2 L.min^{-1}.

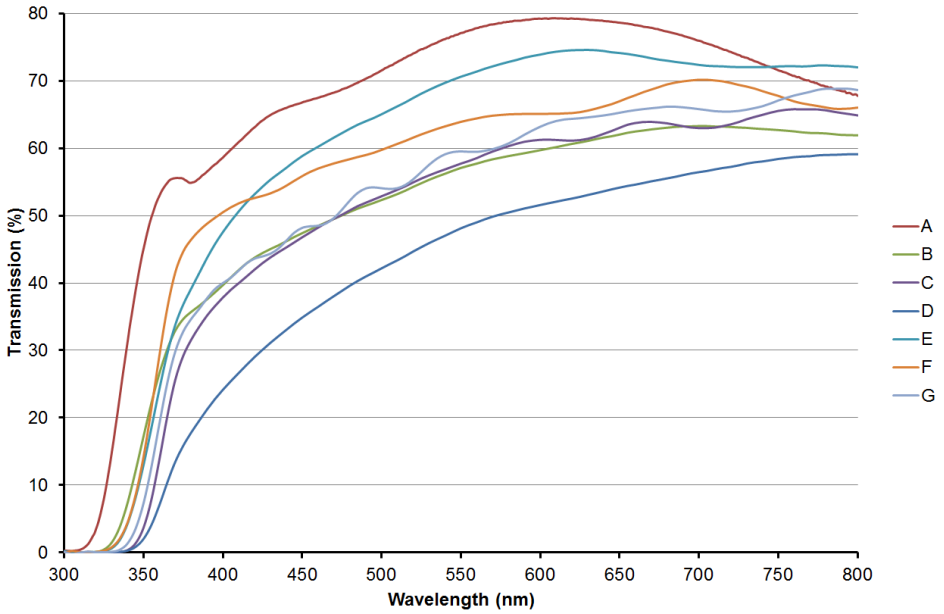

Figure 3.5: UV-vis spectroscopy for samples prepared without an applied electric field (A) and from the AC EAACVD (B to G) reaction of 0.17 M TTIP in toluene at 450 °C and 2 L.min^{-1}.

Direct band gap (DBG) values were calculated using the Tauc method [154]. The applied field strength appeared to have a minimal influence on the band gap of deposited films. All deposited films showed typical direct band gap values for anatase (3.3 – 3.2 eV). Lower values of 3.15 eV were found for the samples D.

3.2.2. Functional properties of deposited films from AC electric fields

3.2.2.1. Photo-activity of TiO_2 thin films

UV/Vis investigation of the films photocatalytic abilities (Figure 3.5), indicated that all the films grown with applied electric fields (Figure 3.6 B – G) showed higher photocatalytic activity than the film produced with no electric field (Figure 3.5 A). The time required for the concentration to decline by 50% ($t_{1/2}$) is shown in Table 3.5. It can be observed that sample E was the most active ($t_{1/2}$ = 4 minutes) closely followed by Samples F and D ($t_{1/2}$ = 6 minutes). The highest $t_{1/2}$ value was obtained for the film grown with no electric field (Sample A, $t_{1/2}$ = 24.5 minutes).

Table 3.4: Root Mean Square (RMS) values (nm) from AFM, maximum transmission in the visible (T%) from UV-vis spectroscopy and Direct Band Gap (D.B.G) values (e.V) calculated from the Tauc method for films produced from the AC EAACVD reaction of 0.7 M TTIP solution in toluene.

Sample	Applied Voltage (V)	Field Strength (Vm^{-1})	RMS (nm)	T%	B.G (eV)
A	0	0	26±9	79	3.2
B	1	1×10^2	20±10	63	3.3
C	5	5×10^2	15±10	64	3.2
D	10	10×10^2	12±5	56	3.15
E	15	15×10^2	16±3	74	3.3
F	20	20×10^2	4±2	70	3.3
G	30	30×10^2	27±6	66	3.25

3.2.2.2. Water-contact angles

Mean water-contact angles measurements were carried out to study the wettability of surfaces (Figure 3.7). The film produced with no electric field delivered the most hydrophilic surface with a mean water-contact angle of 17° (Table 3.5). It can be observed that as the introduction of an electric field influences the water contact angles of deposited films increasing the water contact-angle. Thus, when the electric field is applied and increased the water contact angle increased to 66° - 68° (Sample B and C). As the field strength was increased to 20×10^2 Vm^{-1} the water contact angle slightly decreased in the range of 56° – 29°. The highest water contact angle was found for Sample G (70°). After 30 minutes of 254 nm UV irradiation, all electric fields deposited films showed hydrophilicity with contact-angles between 56°-10°. The film deposited in absence of electric fields showed super-hydrophilicity with a water-contact angle of 4°.

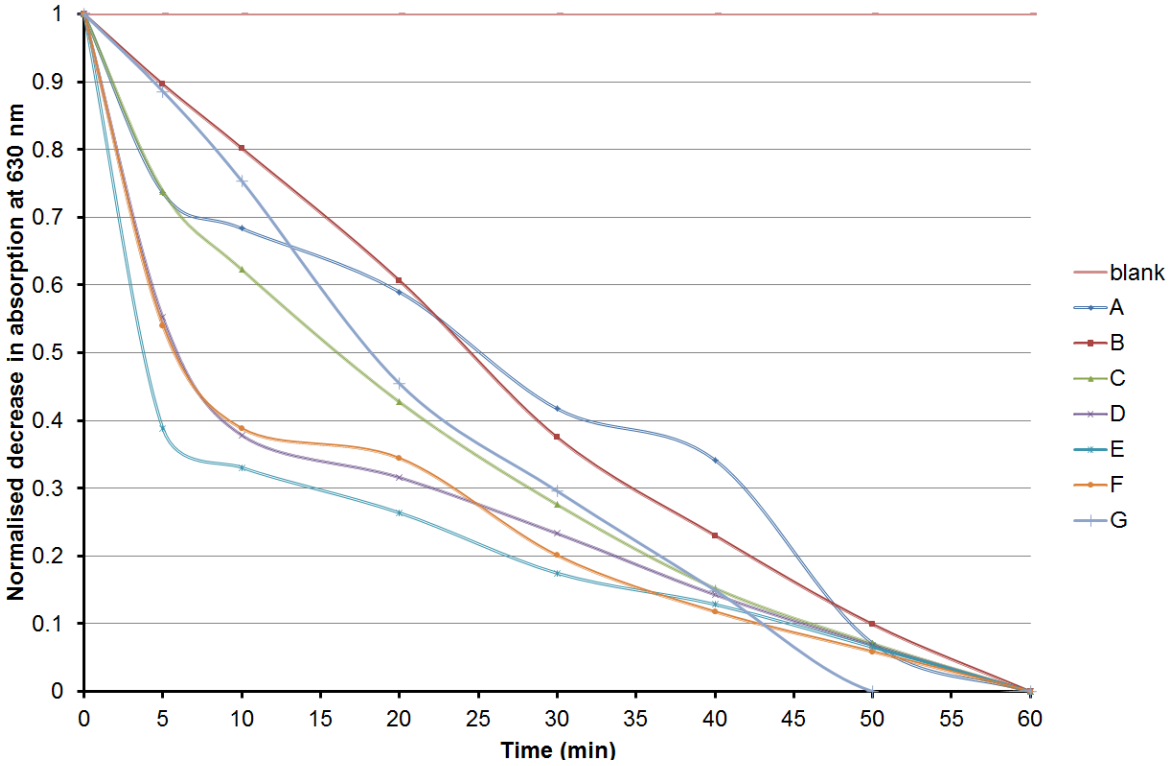

Figure 3.6: Normalised decrease in absorption of Resazurin intelligent ink at 630 nm with UVA irradiation (365 nm) against time (min) for deposited films from the AC AACVD reaction of 0.17 M TTIP in toluene at 450 °C and 2 L.min^{-1}.

Table 3.5: Mean water-contact angles of deposited TiO_2 thin films on glass substrate (before and after 30 min UV irradiation 30 min) and half-life values, $t_{1/2}$ (min), for films deposited from the AC EAACVD reaction of 0.17 M TTIP solution in toluene at 450 °C and 2 L.min^{-1}.

Sample	Field Strength (Vm^{-1})	Mean Contact Angle (degrees) ± SE		Half-life
		0 min	30 min	$t_{1/2}$ (min)
A	0	17 ± 1	4 ± 1	24.5
B	1 x 10^2	66 ± 1	56 ± 3	24.2
C	5 x 10^2	68 ± 1	48 ± 1	16
D	10 x 10^2	56 ± 4	41 ± 2	6
E	15 x 10^2	29 ± 2	10 ± 1	3.9
F	20 x 10^2	56 ± 5	49 ± 5	6
G	30 x 10^2	70 ± 6	55 ± 4	18.1

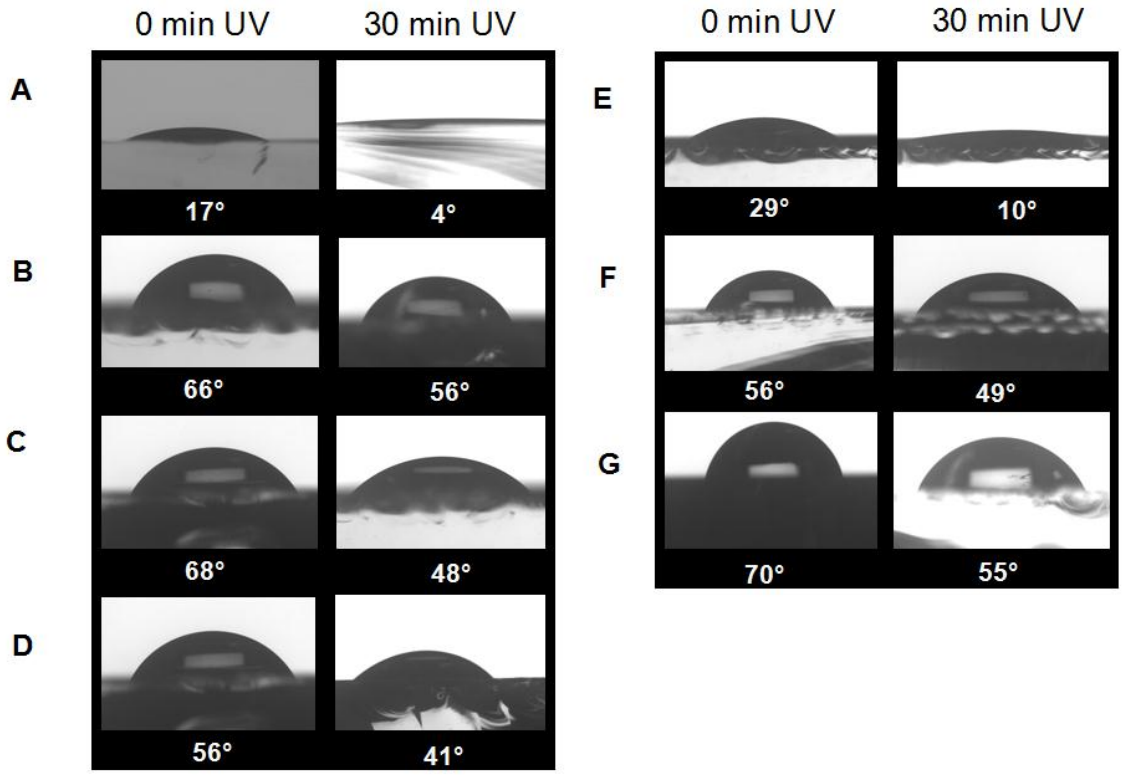

Figure 3.7: Mean water contact angle images for deposited films from the AC EAACVD reaction of 0.17 M in toluene at 450 °C and 2 L.min^{-1} before and after 30 min UVA irradiation 254 nm.

3.2.3. Film synthesis and characterisation of DC deposited films

The electric field assisted chemical vapour deposition (EACVD) from the reaction of titanium tetraisopropoxide (TTIP) in toluene at 450 °C under the influence of DC electric fields produced anatase TiO_2 thin films as confirmed by XRD and Raman spectroscopy (Table 3.6). Deposited films presented good adherence to the substrate passing the Scotch tape test and a scratch test using a piece of towel. See Table 2.1 for the experimental conditions and films appearance.

Scanning electron microscopy

Scanning electron microscopy (SEM) images of the deposited titanium dioxide films are shown in Figures 3.8 (DC +ve bias) and 3.9 (DC –ve bias). Deposition carried out in absence of an electric field (Figure 3.8 A) revealed a thin film comprised of agglomerated acicular nanoparticles of 200 ± 12 nm length with a film thickness of 120 ± 10 nm. The introduction and increase of a positive biased potential difference

across the electrodes of the glass substrate during the AACVD deposition produced a change of morphology and a reduction of particle size as well as variations in the thickness of the deposited films. Thus, at low field strength ($1 \times 10^2 - 5 \times 10^2$ Vm^{-1}) the morphology of deposited films changed to elongated microstructure of 200 ± 13 – 330 ± 24 nm length (Figures 3.8 H, 3.8 I) and 100 nm ± 5 width (no tabulated) with secondary growth of spherical nanoparticles of 340 ± 9 nm (Sample H) and 160 nm ± 11 (Sample I). In this range of field strength an increase in thickness is produced to 300 ± 18 – 500 ± 43 nm. When the field strength was increased (10×10^2 Vm^{-1} – 15×10^2 Vm^{-1}) the secondary spherical microstructure disappears and instead a rice-like microstructure remained with 360 ± 20 – 320 ± 18 nm length (Figures 3.8 J- K) and 130 – 100 ± 10 nm width. The thickness in the in range of field strength was 1050 ± 46 – 800 ± 20 nm. As the field strength was increased to 2×10^3 Vm^{-1} the size of the elongated growths decreased to 100 ± 9 nm length and 50 ± 5 nm width; forming spherical agglomerations of 150 ± 9 nm length (Figure 3.8 L). Likewise, films deposited at 30×10^2 Vm^{-1} showed elongated growths of 280 ± 17 nm in length and 100 ± 9 nm in width forming a spherical agglomerations of 300 ± 17 nm in diameter (Figure 3.8 M). The film thickness in this range remained in 850 ± 32 – 800 ± 9 nm.

Changing the film bias to a negative bias (Figure 3.9) led to further microstructural and thickness changes. The introduction of biased electric fields (1×10^2 Vm^{-1}) led to a slight increase of particle size to 250 ± 8 nm length (Figure 3.9 N) and 100 nm ± 8 width (not tabulated) and film thickness to 180 ± 32 nm. As the field strength was further increased continuous changes occurred to the deposited films. Thus, at 5×10^2 Vm^{-1} (Figure 3.9 O) the deposited thin films showed spherical growths of 130 ± 14 nm in diameter and a marked increase in film thickness to 640 ± 11 nm. A further increase in field strength (10×10^2 Vm^{-1}) produced a change in growth to elongated nanoparticles 250 ± 13 nm in length and ~90 ± 5 nm in width (Figure 3.9 P) as well as an increase of film thickness to 720 ± 20 nm. The increase of field strength (15×10^2 Vm^{-1}) produced not only changes in shape of microstructure to rice-like but also an increase in particle size (320 ± 9 x 160 ± 13 nm) (Figure 3.9 Q) and a decrease in film thickness to 560 ± 17 nm. At 2×10^3 Vm^{-1}, the shape of nanoparticles changed back to spherical with a reduction in particle size to 200 ± 18 nm (Figure 3.9 R) and the film thickness continued to decrease to 300 ± 46 nm. Finally, at 3×10^3 Vm^{-1} deposited films revealed a particular morphology pattern identifying elongated microstructures of reduced particle size (140 ± 10 x 50 ± 6 nm) forming spherical agglomerations

(Figure 3.9 S). This film also registered the lowest thickness (30 ± 21 nm). Agglomerate and film thickness values are listed in Table 3.7

Different trends in film thickness were observed for different substrate bias. As Figure 3.10 shows, an increase in film thickness with field strength was observed for positive bias deposited films whereas a decrease trend was shown for negatively bias deposited films.

Table 3.6: Experimental conditions of deposited films from the AACVD reaction of 0.17 M TTIP in toluene at 450 °C and 2 $L.min^{-1}$ with an applied DC electric field.

Sample	Applied Voltage (V)	Field Strength (Vm^{-1})	Substrate bias	Material Phase (XRD/Raman)
A	0	0	---	Anatase TiO_2
B	1	1×10^2	Positive	Anatase TiO_2
C	5	5×10^2	Positive	Anatase TiO_2
D	10	10×10^2	Positive	Anatase TiO_2
E	15	15×10^2	Positive	Anatase TiO_2
F	20	20×10^2	Positive	Anatase TiO_2
G	30	30×10^2	Positive	Anatase TiO_2
H	1	1×10^2	Negative	Anatase TiO_2
I	5	5×10^2	Negative	Anatase TiO_2
J	10	10×10^2	Negative	Anatase TiO_2
K	15	15×10^2	Negative	Anatase TiO_2
L	20	20×10^2	Negative	Anatase TiO_2
M	30	30×10^2	Negative	Anatase TiO_2

X-ray diffraction

X-ray diffraction (XRD) analysis was carried out and compared to previous investigations (JCPDS database file (021-1272)) to study the materials phase. All deposited films under the influence of electric fields showed anatase TiO_2 crystalline phase and also cassiterite SnO_2 from the FTO glass substrate. The relative intensity of the Bragg peaks associated with TiO_2 changed depending on the substrate bias applied, suggesting a preferred orientation. Thus, deposited films prepared with no electric field and films prepared with positive biased electric field showed an apparent crystallographic preferential orientation in the (101) (Figure 3.11). However, as

negative biased electric field is introduced an apparent change in the crystal orientation is produced in the (004) plane.

Texture coefficient calculations were carried out to confirm the preferred crystal orientation found in XRD analysis [152]. The results (shown in Table 3.8) revealed that the film produced with no electric field was strongly oriented in the (004). Contradictory to the XRD results, thin films produced with positive biased electric fields showed crystal preferred orientation in the (211) plane (Sample B) and in the (004) plane (Sample I to M). The films produced with negative biased electric fields showed preferred crystal orientation in the (004) plane (Sample N to S). However, as Table 3.7 reveals, thin films produced from negative biased electric fields showed higher texture coefficients in the (004) plane than thin films produced from positive biased electric fields.

Furthermore, XRD analysis of full width at half maximum (FWHM) was carried out using the Scherrer equation in order to investigate the crystallite size of deposited films. Characteristic peaks of 2 Theta = 25.28° (101), 2 Theta = 37.8° (004), 2 Theta = 48.05° (200) were selected and the generally used shape factor of 0.9 [153] was chosen. As Table 3.6 shows, the application of DC electric fields produced changes in the mean crystallite size. The application of positive bias electric fields produced a decrease in the mean crystallite size (17 ± 1 nm). The mean crystallite size gradually increased with the field strength to get the maximum value for Sample L (33 ± 3 nm). The application of negative bias electric fields had the opposite effect and an increase of the mean crystallite size was produced (29 ± 1 nm). The increase of the field strength produced lower values of the mean crystallite size but still higher than the film deposited in absence of electric fields. Although broadly speaking the crystallite size was similar for both positive and negative biased thin films, a smaller crystallite size for Sample H (17 ± 1 nm) was found.

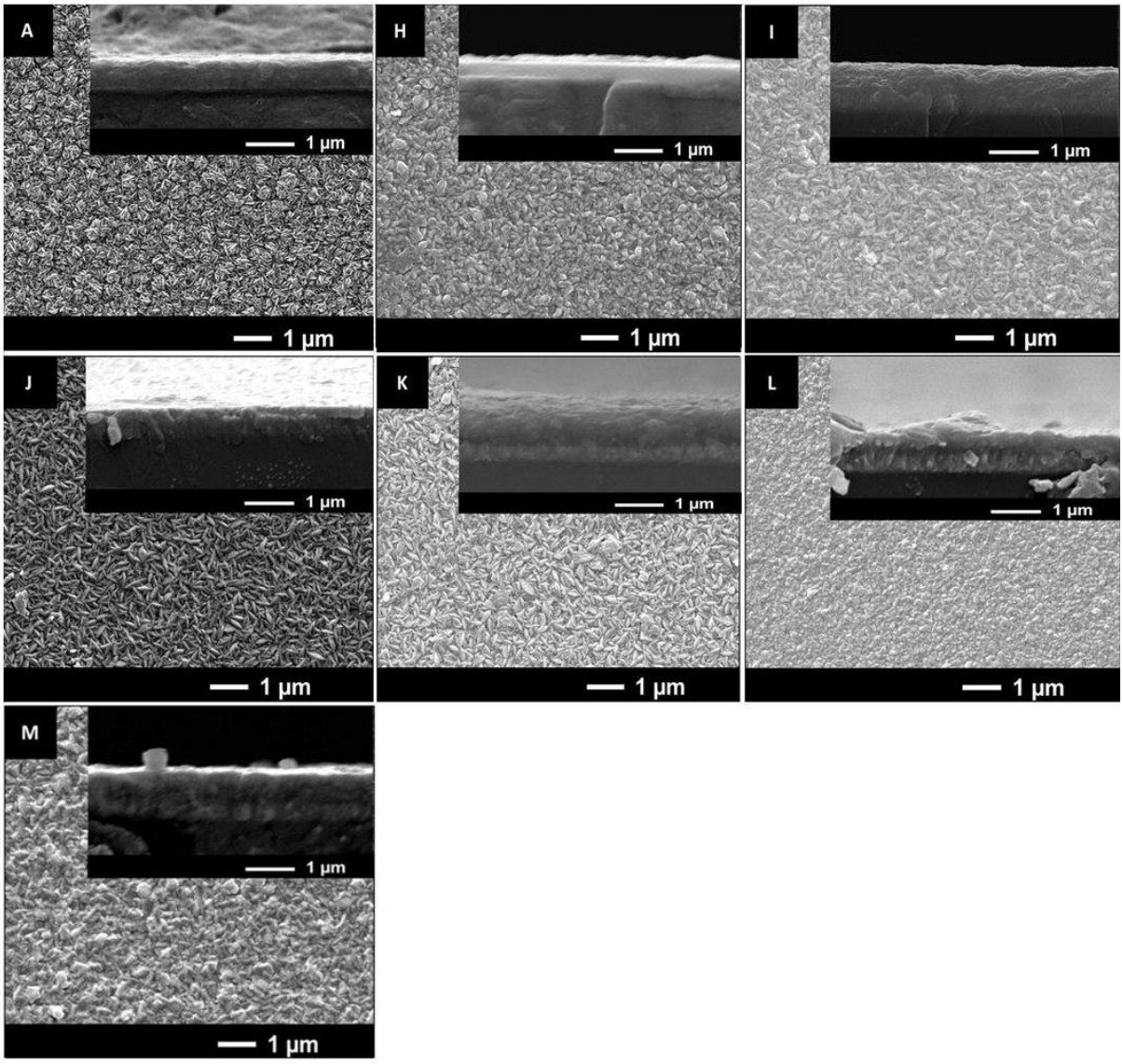

Figure 3.8: Scanning Electron Microscope images of samples prepared without electric field (A) and from the positive biased DC EAACVD reaction (H to M) of 0.7 M TTIP solution in toluene at 450 °C and 2 L.min^{-1}. The images above correspond to A) 0 Vm^{-1}, M) 1 x 10^{2} Vm^{-1}, N) 5 x 10^{2} Vm^{-1}, O) 10 x 10^{2} Vm^{-1}, P) 15 x 10^{2} Vm^{-1}, Q) 20 x 10^{2} Vm^{-1}, R) 30 x 10^{2} Vm^{-1}. Side-on images were captured at x 30,000 magnification and cross-section images at x 40, 000.

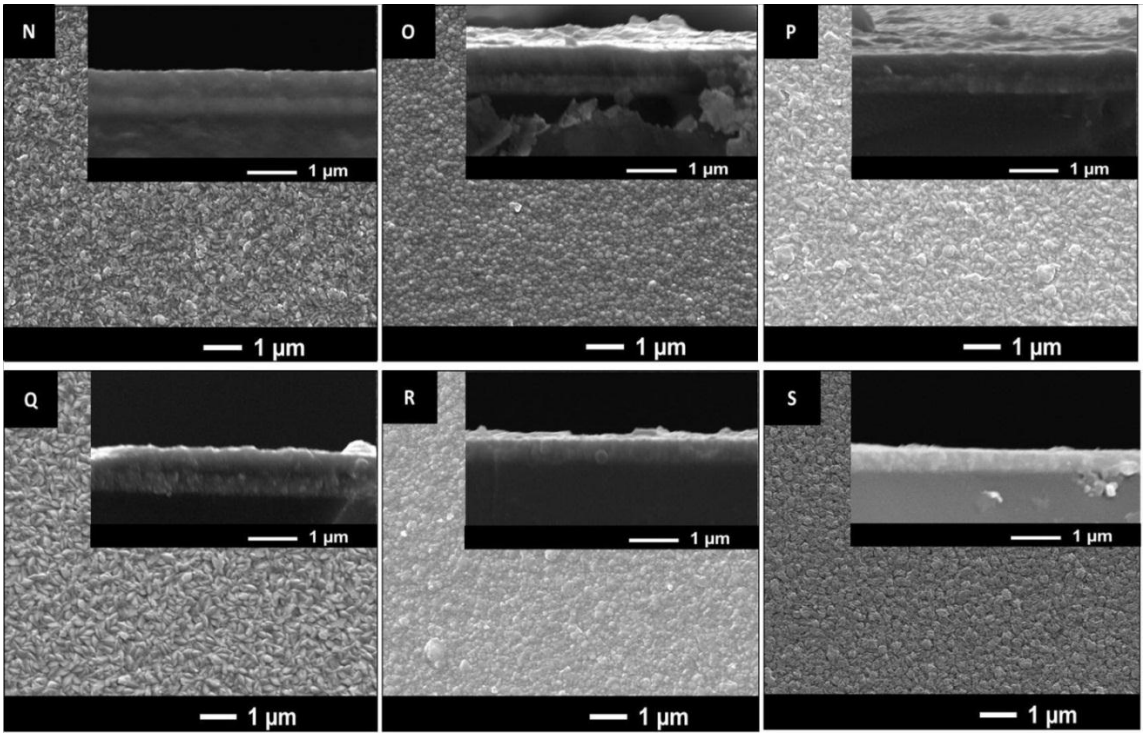

Figure 3.9: Scanning Electron Microscope images of samples prepared from the negative biased DC EACVD reaction of 0.17 M TTIP solution in toluene at 450 °C and 2 L.min^{-1}. N) 1 x 10^{2} Vm^{-1}, O) 5 x 10^{2} Vm^{-1}, P) 10 x 10^{2} Vm^{-1}, Q) 15 x 10^{2} Vm^{-1}, R) 20 x 10^{2} Vm^{-1}, S) 30 x 10^{2} Vm^{-1}. Side-on images were captured at x 30,000 magnification and cross-section images at x 40, 000.

Table 3.8: Texture Coefficient of TiO_2 thin films produced from the positive bias (H – M) and negative bias (N – S) DC EAACVD reaction of 0.7 M TTIP in toluene at 450 °C and 2 L.min^{-1}.

	Texture Coefficient (TC_{hkl})			
Sample	(101)	(004)	(200)	(211)
A	0.35	2.94	0.32	0.42
H	0.48	1.27	0.93	1.32
I	0.49	1.47	0.79	1.23
J	0.44	1.56	0.81	1.17
K	0.63	1.67	0.84	0.85
L	0.58	2.22	0.6	0.58
M	0.45	1.34	0.78	1.42
N	0.38	2.36	0.55	0.71
O	0.17	2.21	0.32	1.29
P	0.24	1.84	0.54	1.36
Q	0.24	2.38	0.45	0.92
R	0.34	2.8	0.32	0.52
S	0.28	2.94	0.3	0.47

Table 3.7: Agglomerate size (nm) from SEM with standard error (SE), film thickness (nm) from SEM cross section with SE and mean crystallite size (nm) obtained from the Scherrer equation for films deposited from the DC AACVD reaction of 0.17 M TTIP solution in toluene at 450 °C and 2 L.min^{-1}.

Sample	Field Strength (Vm^{-1})	Substrate bias	Agglomerate size (nm)	Film Thickness (nm)	Mean crystallite size (nm)
A	0	--	200 ± 12	120 ± 10	24±2
H	1 x 10^2	Positive	200 ± 13	300 ± 18	17±1
I	5 x 10^2	Positive	330 ± 24	500 ± 43	23±3
J	10 x 10^2	Positive	360 ± 20	1050 ± 46	27±2
K	15 x 10^2	Positive	320 ± 18	800 ± 20	28±2
L	20 x 10^2	Positive	100 ± 9	850 ± 32	33±3
M	30 x 10^2	Positive	280 ± 17	800 ± 9	28±2
N	1 x 10^2	Negative	250 ± 8	180 ± 32	29±1
O	5 x 10^2	Negative	130 ± 14	640 ± 11	23±1
P	10 x 10^2	Negative	250 ± 13	720 ± 20	28±2
Q	15 x 10^2	Negative	320 ± 9	560 ± 17	28±3
R	20 x 10^2	Negative	200 ± 18	300 ± 46	23±3
S	30 x 10^2	Negative	140 ± 10	30 ± 21	25±2

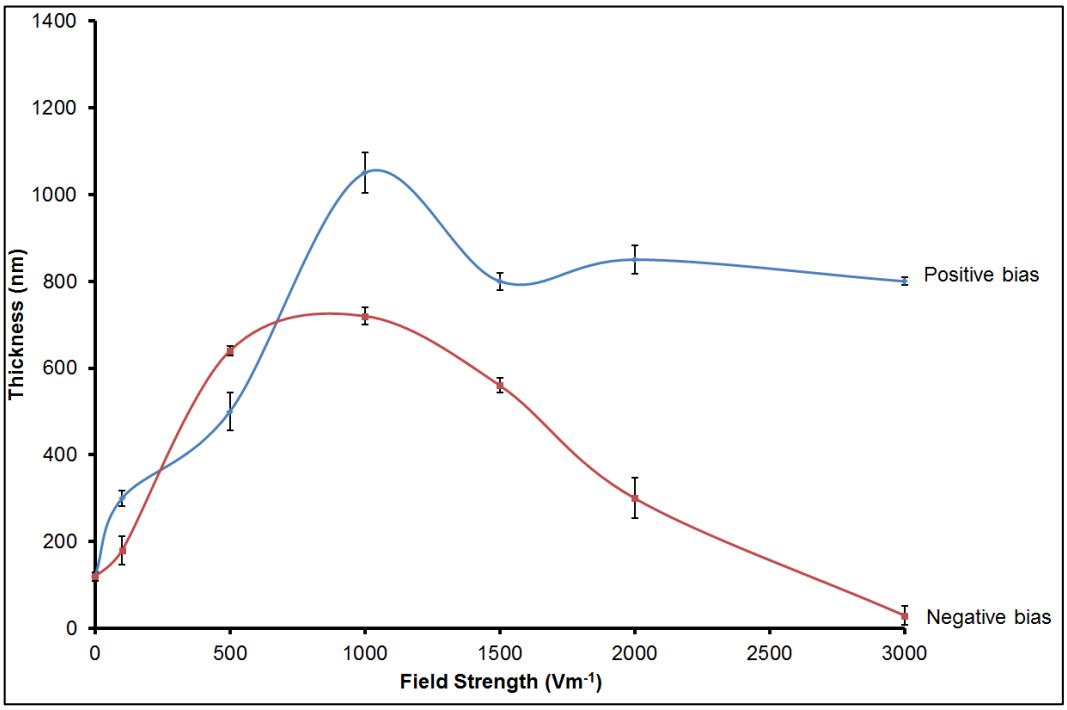

Figure 3.10: Film thickness trend with SE for positive and negative bias deposited films from the DC EAACVD reaction of 0.7 M TTIP solution in toluene at 450 °C and 2 L.min^{-1}.

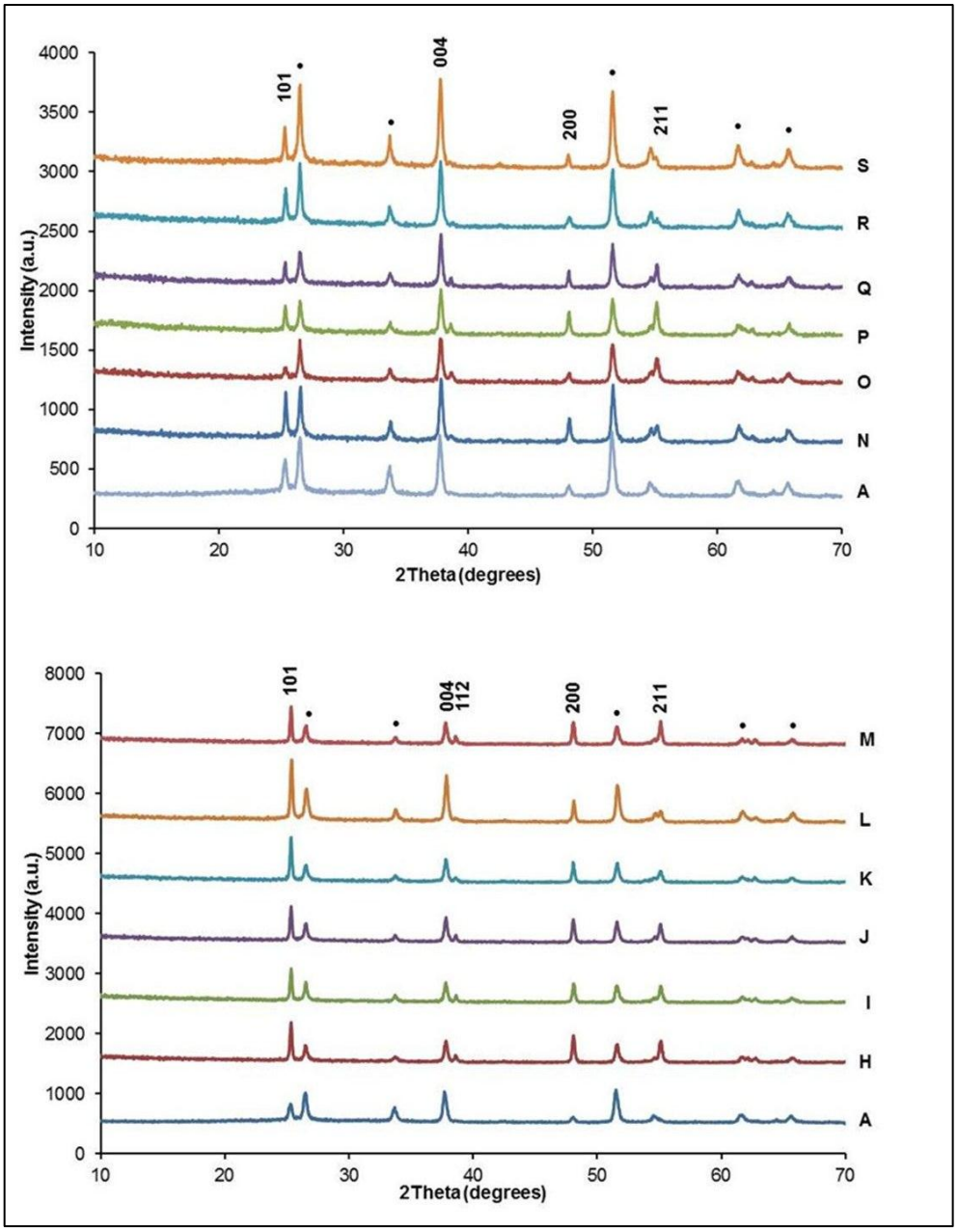

Figure 3.11: XRD pattern for samples prepared from the DC EAACVD reaction of 0.17 M TTIP solution in toluene at 450 °C and 2 $L.min^{-1}$, films deposited in absence of electric fields (A), positive biased (H-M) and negative biased electric fields (N-S). The peaks marked with asterisks denote the cassiterite peaks specific of SnO_2 crystalline phase, material used for the glass substrate coating.

Raman spectroscopy

Raman spectroscopy was carried out in order to complement XRD analysis for phase identification. Figure 3.12 shows Raman spectra for all the deposited films. The samples gave Raman centred at 147 cm^{-1}, 198 cm^{-1}, 395 cm^{-1}, 513 cm^{-1}, 642 cm^{-1}

which correspond to anatase crystal phase [134]. However, in some cases the Raman peaks were weaker. This was the case for Samples L and R.

Atomic force microscopy

Deposited films surfaces were scanned using AFM over a 2 μm x 2 μm region in order to obtain Root Mean Square (RMS) roughness values as a proxy of surface roughness (Figure 3.13). As observed for AC electric fields, the application of positive bias DC electric fields produced a decrease in surface roughness from 26 to 20 nm (Sample H). As the field strength was increased the surface roughness varied from 16 to 11 nm. Additionally, the application of negative bias produced similar surface roughness (Figure 3.14). As the field strength was increased the surface roughness varied from 14 to 8 nm. Generally, positive bias deposited films showed higher surface roughness than negative bias deposited films. RMS values are listed in Table 3.8.

UV-vis spectroscopy

UV/VIS spectroscopy showed that both field strength and substrate bias, had an influence on the maximum transmission values over the visible region. The application of positive and negative bias electric fields decreased the maximum transmission in the visible (Figure 3.15). The same increasing pattern in transmission was found for positive and negative biased at lower field strength (0 - 15 x 10^2 Vm^{-1}). In both cases at field strength values greater than 15 x 10^2 Vm^{-1}, the maximum transmission values decreased but it was more significant for positive bias deposited films. In general, lower maximum transmission values were found for positive bias deposited films (47 – 77 %) which can be attributed to the incorporation of carbon into the films. The highest maximum transmission values are found for the thin films prepared at -ve 15 x 10^2 (Sample Q) and at -ve 30 x 10^2 Vm^{-1} (Sample S) (81 % and 80 %, respectively). Direct band gap (DBG) analysis was performed using the Tauc method [154]. Field strength seems to have certain influence in the direct band gap of deposited films. Thus, standard anatase band gap values between 3.2 to 3.3 eV were found for positive and negative biased deposited films. Nevertheless, at higher field

strength lower direct band gaps values were found (3.05 eV at -ve 3 x 10^3 Vm^{-1} and 3.1 eV at +ve 20 x10^2 Vm^{-1}). Maximum transmission in the visible and direct band gap values are listed in Table 3.9.

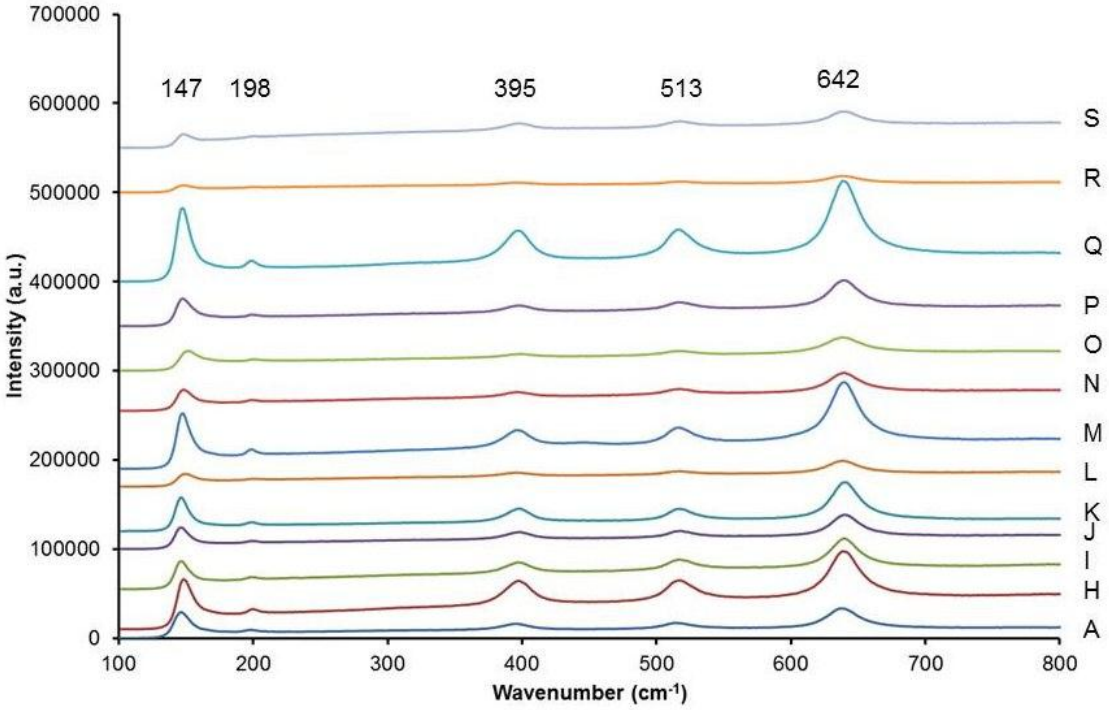

Figure 3.12: Raman spectra for films deposited in absence of electric fields (A) and from positive (H-M) and negative biased field strength (N-S) DC EAACVD reaction of 0.17 M TTIP at 450 °C and 2 $L.min^{-1}$. All peaks correspond to anatase crystal phase.

3.2.4. Functional properties of DC deposited films

3.2.4.1. Photo-activity of TiO_2 thin films

The photocatalytic activity of the titania thin films deposited from EACVD was investigated from the UV/Vis absorption of Resazurin intelligent ink under UV irradiation (365 nm). It was observed that most of titania thin films produced under the influence of DC electric fields showed lower decrease in absorption than the sample produced without electric fields (Figure 3.16). The time required for the initial dye concentration to decline by half ($t_{1/2}$) was calculated for all deposited films (Table 3.9). It was found that values for $t_{1/2}$ did not decrease remarkably when DC electric

fields were applied and were similar among the different field strengths. The most photoactive thin films were Sample K (20.9 min), Sample M (20.5 min) and Samples N and S (20.6 min). Thus, it was observed that the application of DC electric fields significantly reduced the photocatalytic activity of titania thin films comparing to AC electric fields.

3.2.4.2. Water contact angles

The films produced from DC electric fields showed hydrophilicity with water contact angles in the range of 19 – 64° (Table 3.10). The film produced in absence of electric fields showed a lower water contact angle (17°). Positive bias deposited films (Figure 3.17) showed lower water contact angles (14 – 35°) than negative bias deposited films (Figure 3.18) (19 – 64°). After 30 minutes UV irradiation (254 nm) all films hydrophilicity and in some cases superhydrophilicity with water contact angles lower than 5° (Sample M). Negative bias deposited films showed higher water contact angles after UV irradiation (7 – 46°). In particular, Sample R showed the highest water contact angle after UV irradiation (46°).

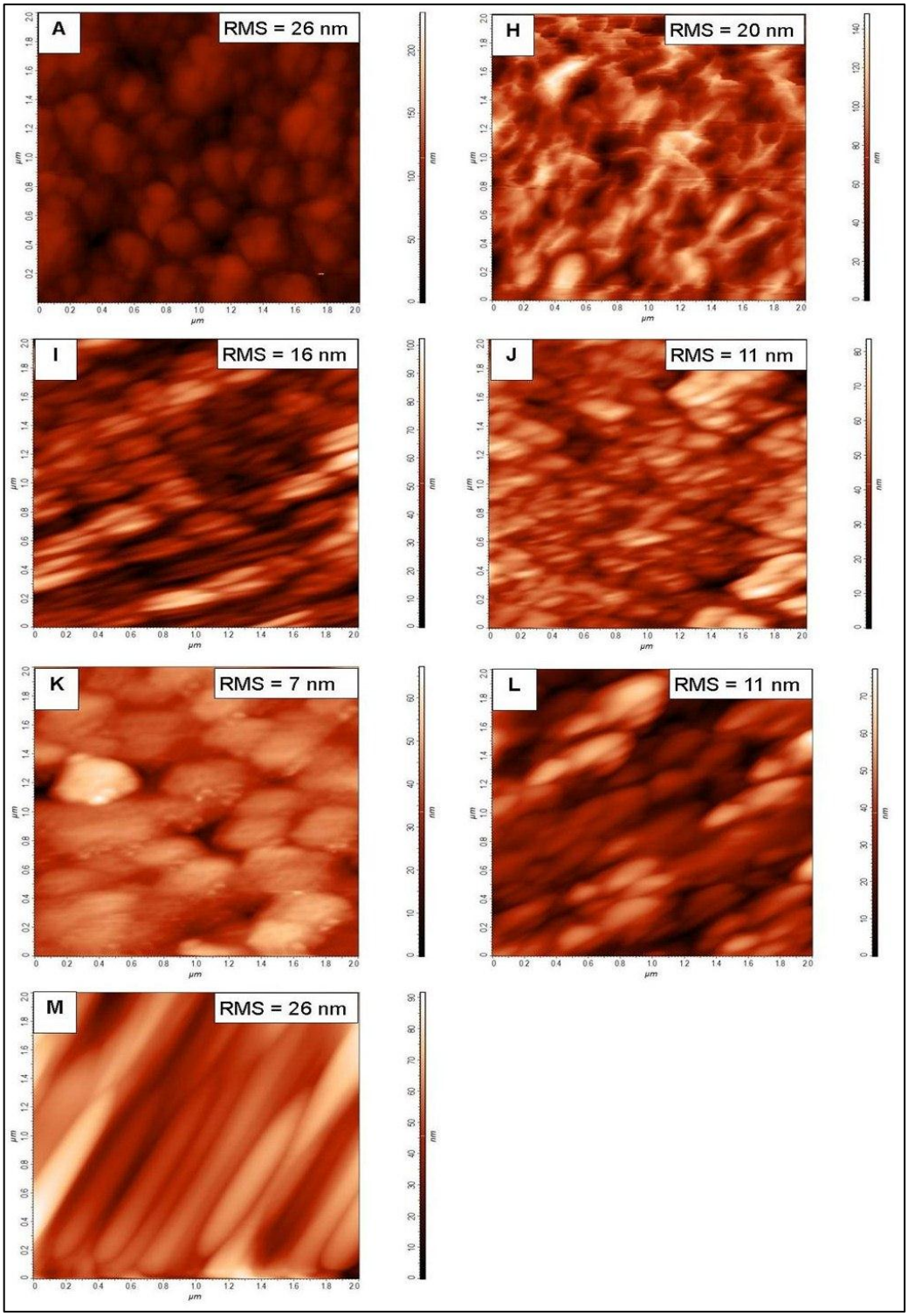

Figure 3.13: AFM images with corresponding Root Mean Square (RMS) values (nm) for films deposited in absence of electric fields (A) and positive bias DC electric fields (H- M) from the DC EAACVD reaction of 0.17 M TTIP solution in toluene at 450 °C and 2 L.min^{-1}.

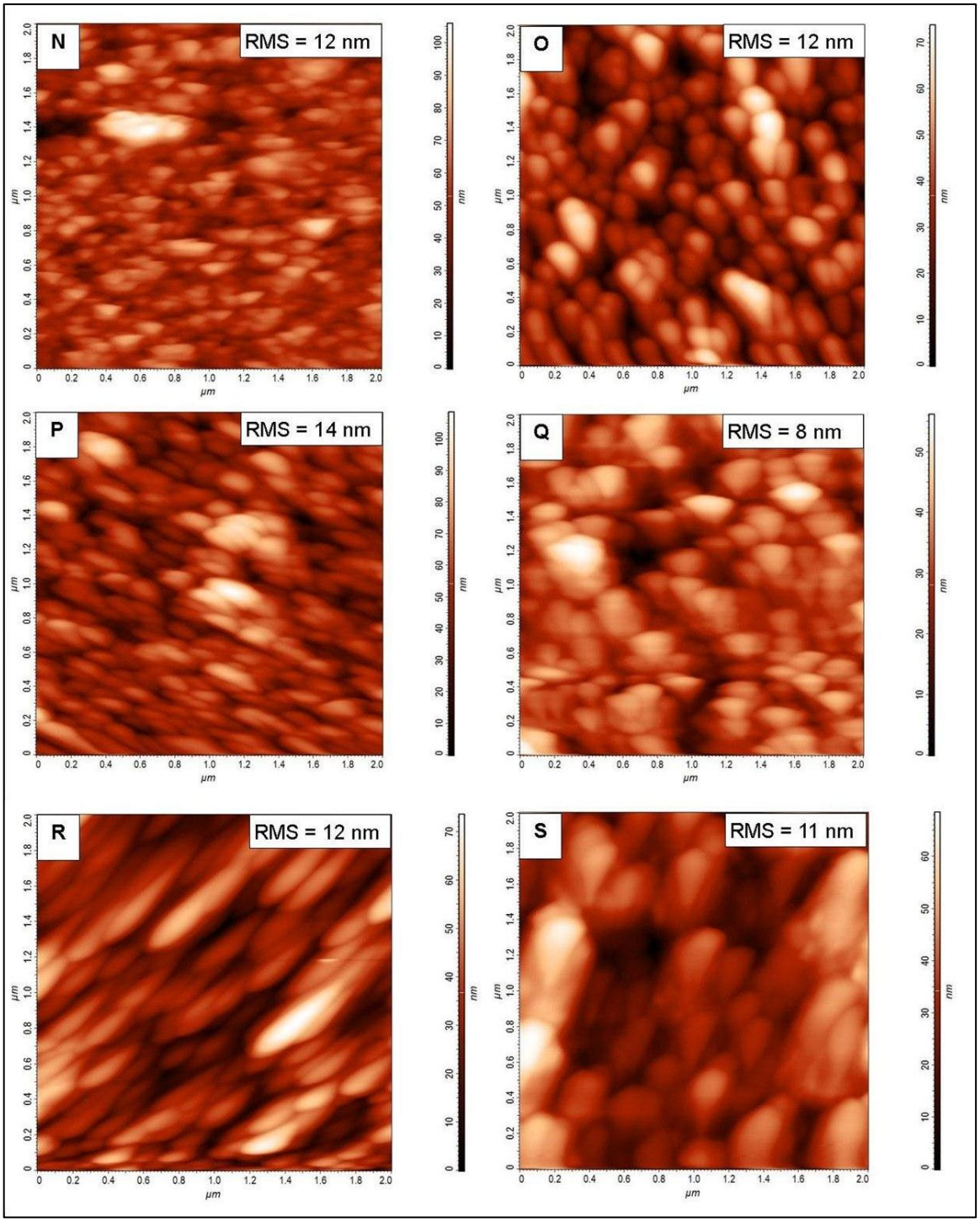

Figure 3.14: AFM images with corresponding Root Mean Square (RMS) values (nm) for films deposited from the negative bias DC electric fields (N –S) the DC EAACVD reaction of 0.17 M TTIP solution in toluene at 450 °C and 2 $L.min^{-1}$.

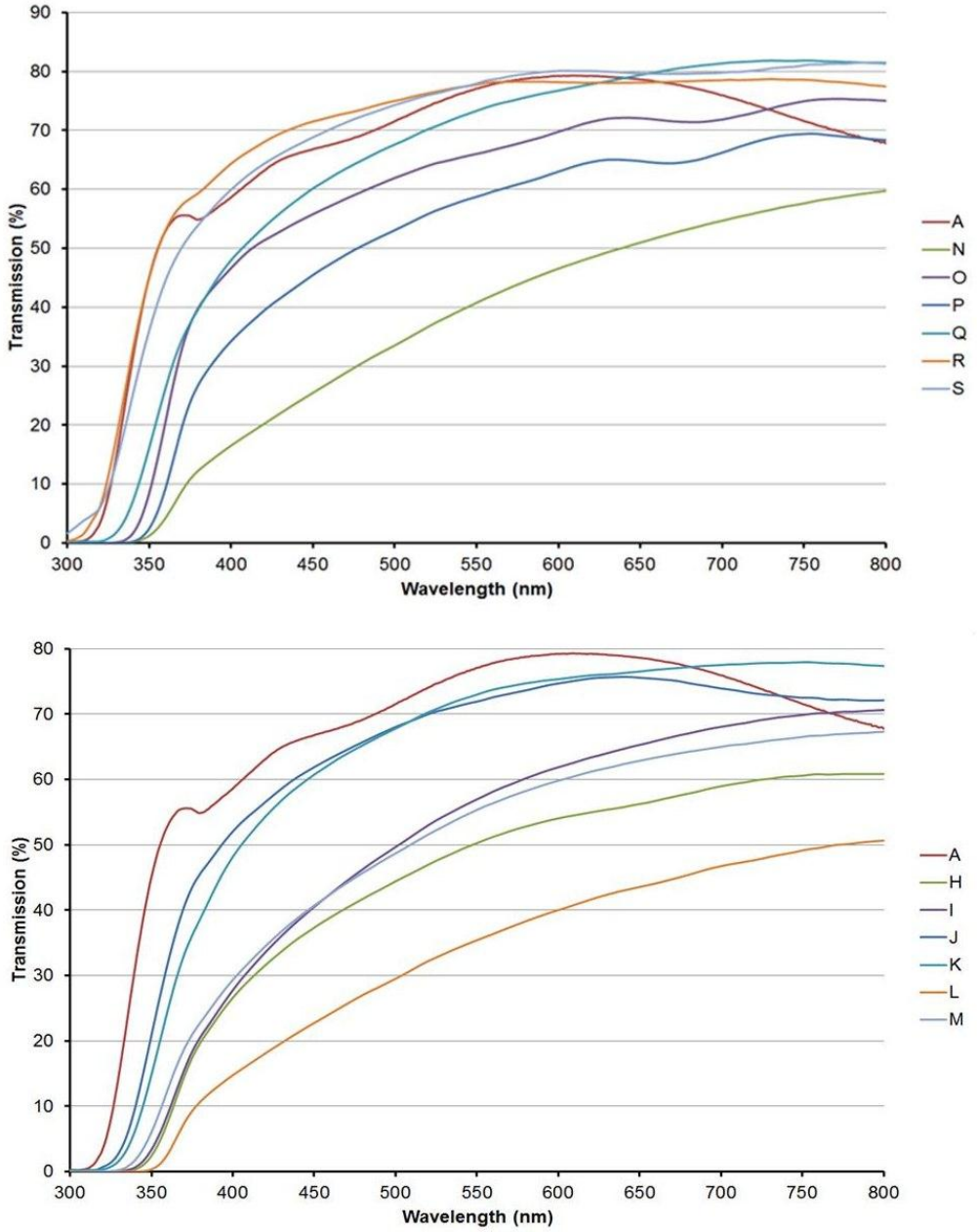

Figure 3.15: UV-vis spectroscopy for samples prepared without an applied electric field (A) and from the positive bias electric field (H to M) and the negative bias electric field (N to S) DC EAACVD reaction of 0.17 M TTIP in toluene at 450 °C and 2 $L.min^{-1}$.

Table 3.9: Root Mean Square (RMS) values (nm) from AFM, maximum transmission in the visible values (%) from UV-vis spectroscopy and Direct Band Gap (D.B.G) values (e.V) calculated from the Tauc method, for films deposited from the DC EAACVD reaction of 0.17 M TTIP solution in toluene at 450 °C and 2 $L.min^{-1}$.

Sample	Applied Voltage (V)	Field Strength (Vm^{-1})	Substrate bias	RMS (nm)	T%	D.B.G (eV)
A	0	0	--	26±9	79	3.2
H	1	1×10^2	Positive	20±11	59	3.2
I	5	5×10^2	Positive	16±5	68	3.2
J	10	10×10^2	Positive	11±5	76	3.3
K	15	15×10^2	Positive	7±3	77	3.2
L	20	20×10^2	Positive	11±5	47	3.1
M	30	30×10^2	Positive	11±7	65	3.2
N	1	1×10^2	Negative	12±8	55	3.1
O	5	5×10^2	Negative	12±6	72	3.3
P	10	10×10^2	Negative	14±7	67	3.3
Q	15	15×10^2	Negative	8±2	81	3.2
R	20	20×10^2	Negative	12±8	78	3.25
S	30	30×10^2	Negative	11±6	80	3.05

3.2.5. Film synthesis and characterisation at different conditions

For the experimental conditions and films appearance, the reader is referred to Table 2.2 (Chapter 2). The films produced at different conditions were compared to the films produced at the field strength of 15×10^2 Vm^{-1} (labelled in previous sections as Sample E) and at positive bias 10×10^2 Vm^{-1} (labelled in previous sections as Sample J). Sample E and J, which were produced at 450 °C and 2 $L.min^{-1}$ are set as reference samples and will be labelled in this section as Ref (E) and Ref (J), respectively. In all cases deposited films presented good adherence to the substrate passing the Scotch tape test. Furthermore, XRD and Raman analysis confirmed anatase crystal phase in all deposited films.

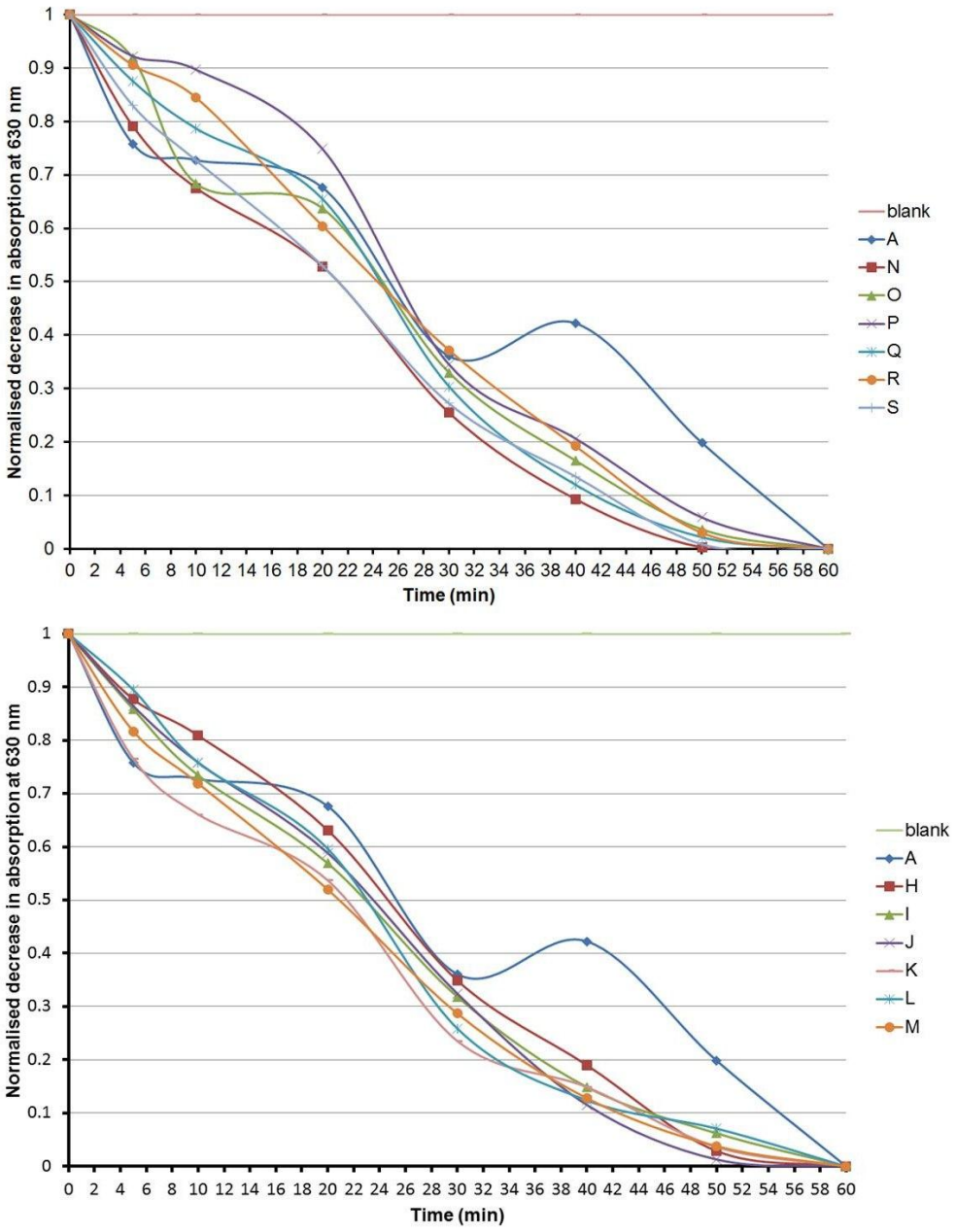

Figure 3.16 Normalised decrease in absorption of Resazurin intelligent ink at 630 nm with UVA irradiation (365 nm) against time (min) for film deposited from the DC EAACVD reaction of 0.17 M TTIP solution in toluene at 450 °C and 2 $L.min^{-1}$.

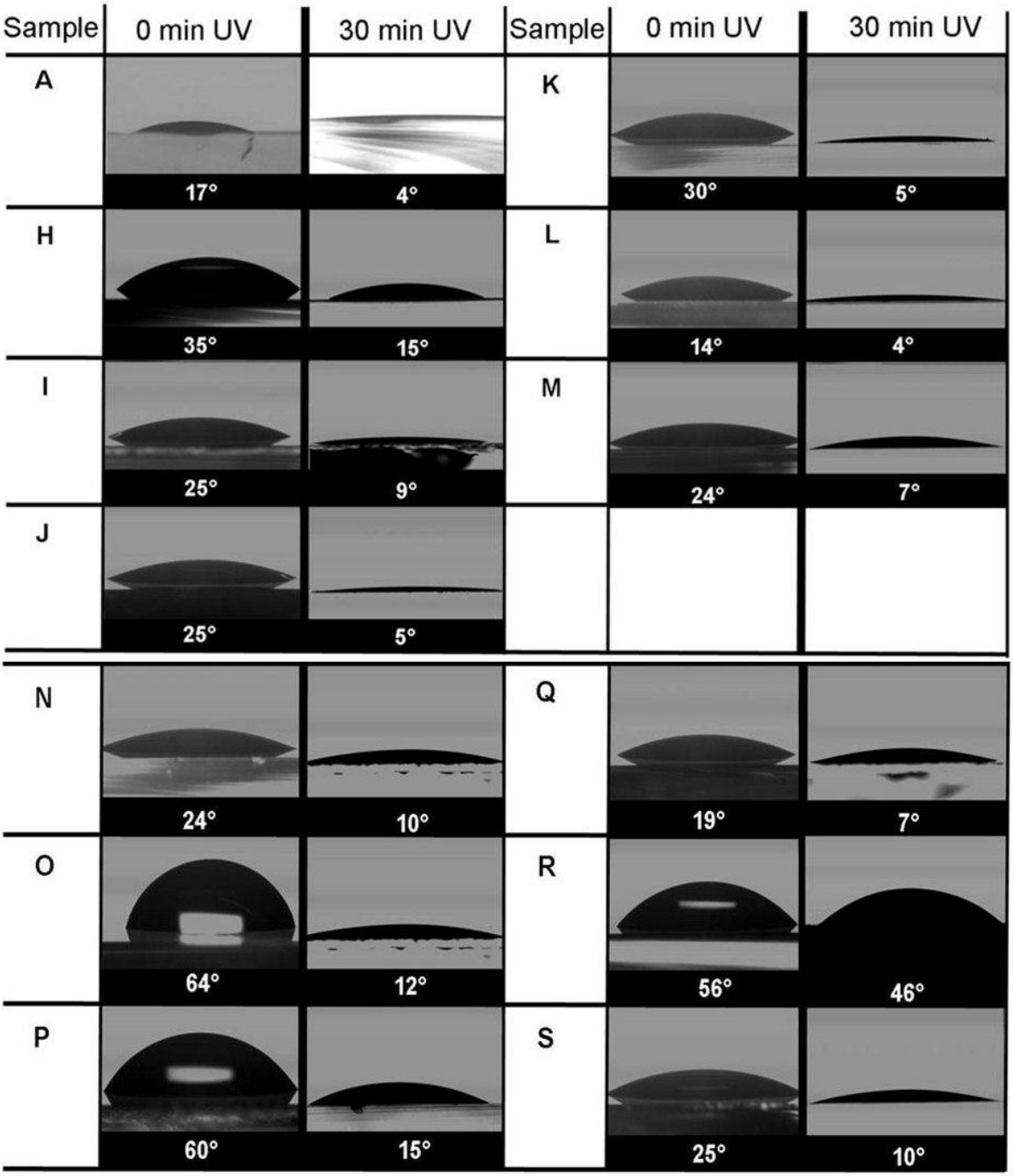

Figure 3.17: Mean water contact angle images for deposited films from the positive (H – M) and negative bias (N – S) DC EAACVD reaction of 0.17 M TTIP solution in toluene at 450 °C and 2 $L.min^{-1}$ before and after 30 min UVA irradiation 254 nm.

Scanning electron microscopy

Scanning electron microscopy (SEM) images of the deposited titanium dioxide films at different conditions are shown in Figures 3.18 –3.19 (for films deposited at 15 x 10^2 Vm^{-1}) and 3.20 – 3.21 (for films deposited at positive bias 10 x 10^2 Vm^{-1}). Agglomerate size and film thickness are tabulated in Table 3.11. The film produced at 15 x 10^2 Vm^{-1} (Ref E) showed elongated particles of 140 ± 12 nm in length and film thickness of 650 ± 13 nm (Figure 3.18, Ref E). The reduction of deposition time to 5 minutes (condition 1) produced an increase in particle size to 270 ± 15 nm in length and 115 ± 10 nm in width (Figure 3.18, 1) but an important reduction in film thickness (8 ± 5 nm). When increasing the deposition time to 10 minutes (condition 2) the particle size also increased with a length of 340 ± 12 nm and a width of 125 ± 12 nm (Figure 3.18, 2). The film thickness was found to be 3 ± 2 nm. Condition 3 (deposition time 15 min) showed smaller particle size (200 ± 13 x 60 ± 10 nm) (Figure 3.18, 3). For conditions 4 – 6 the experimental variable was TTIP volume. Condition 4 (0.25 mL) showed elongated particles of 315 ± 23 nm in length and 150 ± 20 nm in width and film thickness of 6 ± 2 nm (Figure 3.18, 4). Increasing the TTIP volume to 0.75 mL (condition 5) decreased the particle size (250 ± 18 x 130 ± 10 nm) but significantly increased the film thickness to 600 ± 16 nm (Figure 3.19, 5). For condition 6 (TTIP volume of 1 mL) dramatically increased the particle size showing elongated particles of 530 ± 46 nm in length and 125 ± 8 nm in width with spherical nanoparticles of 50 ± 5 nm diameter on the top (Figure 3.19, 6). The film thickness for this condition was found to be 75 ± 10 nm. For conditions 7 – 9 the experimental variable was substrate temperature. Condition 7 (300 °C) was the only sample which showed spherical and not elongated particles in the microstructure (Figure 3.19, 7). This sample showed the smallest particle size (150 ± 14 nm diameter) and film thickness (2 ± 0.5 nm). Increasing substrate temperature at 350 °C (condition 8) produced elongated particles of 220 ± 14 x 100 ± 10 nm and film thickness of 100 ± 20 nm (Figure 3.19, 8). Condition 9 (400°C) same particle size as condition 8 but higher film thickness (225 ± 54 nm) (figure 3.19, 9). For conditions 10 – 12 the experimental variable was the gas flow rate. At a gas flow rate of 0.5 $L.min^{-1}$ (condition 10), films showed elongated nanoparticles of reduced size (150 ± 12 x 40 ± 4 nm) and film thickness (110 ± 16 nm) (Figure 3.19, 10). Increasing the G.F.R to 1 $L.min^{-1}$ (condition 11) slightly increased the particle size (180 ± 13 x 40 ± 2 nm) and

decreased film thickness (72 ± 30 nm) (Figure 3.19, condition 11). The highest G.F.R tested (3 $L.min^{-1}$, condition 12) gave elongated nanoparticles of 140 ± 8 x 200 ± 25 nm and film thickness of 15 ± 6 nm (Figure 3.19, 12).

Table 3.10: Mean water-contact angles before and after UV irradiation (30 min) and half-life values, $t_{1/2}$ (min), for films deposited from the DC EAACVD reaction of 0.17 M TTIP solution in toluene at 450 °C and 2 $L.min^{-1}$.

Sample	Field Strength (Vm^{-1})	Substrate bias	Contact Angle (degrees) ± SE		Half-life
			0 min	30 min	$t_{1/2}$ (min)
A	0	--	17 ± 1	4 ± 1	22.1
H	1 x 10^2	Positive	35 ± 6	15 ± 8	24.4
I	5 x 10^2	Positive	25 ± 10	9 ± 6	22.5
J	10 x 10^2	Positive	25 ± 12	5 ± 4	23.5
K	15 x 10^2	Positive	30 ± 8	5 ± 3	20.9
L	20 x 10^2	Positive	14 ± 9	4 ± 4	22.6
M	30 x 10^2	Positive	24 ± 3	7 ± 3	20.5
N	1 x 10^2	Negative	24 ± 2	10 ± 2	26
O	5 x 10^2	Negative	64 ± 10	12 ± 5	24.4
P	10 x 10^2	Negative	60 ± 8	15 ± 4	24.8
Q	15 x 10^2	Negative	19 ± 5	7 ± 3	24.3
R	20 x 10^2	Negative	56 ± 6	46 ± 4	24.1
S	30 x 10^2	Negative	25 ± 6	10 ± 4	20.6

Films produced at positive bias 10 x 10^2 Vm^{-1} (Ref J) showed elongated particles of 360 ± 20 x 130 ± 10 nm and film thickness 1056 ± 46 nm (Figure 3.20, Ref J). The reduction of the deposition time to 5 min (Figure 3.20, 13) decreased the particle size of elongated nanoparticles to 140 ± 10 nm, forming spherical clusters of 290 ± 25 nm in diameter (not tabulated). The film thickness significantly decreased to 125 ± 37 nm. Increasing the deposition time to 10 minutes (condition 14) produced spherical

agglomerations of 200 ± 25 nm in diameter and a film thickness of 110 ± 16 nm (Figure 3.20, 14). At a deposition time of 15 minutes (condition 15), films showed elongated nanoparticles of 190 ± 10 nm in length forming spherical clusters of 30 ± 5 nm in diameter (Figure 3.20, 15). The film thickness at this condition was 560 ± 47 nm. When the TTIP volume was reduced to 0.25 mL (condition 16), films presented spherical nanoparticles of 270 ± 10 nm in diameter and an important reduction in film thickness to 25 ± 10 nm (Figure 3.20, 16). Increasing the TTIP volume to 0.75 mL (condition 17) produced a change to elongated nanoparticles of 200 ± 17 nm in length and 77 ± 8 nm in width (Figure 3.20, 17). The film showed an important increase in thickness to 1020 ± 56 nm. Further increase in TTIP volume to 1 mL (condition 18) produced a decrease in particle size to 160 ± 7 nm in length x 33 ± 4 nm in width, as well as a decrease in film thickness to 726 ± 27 nm (Figure 3.21, 18).

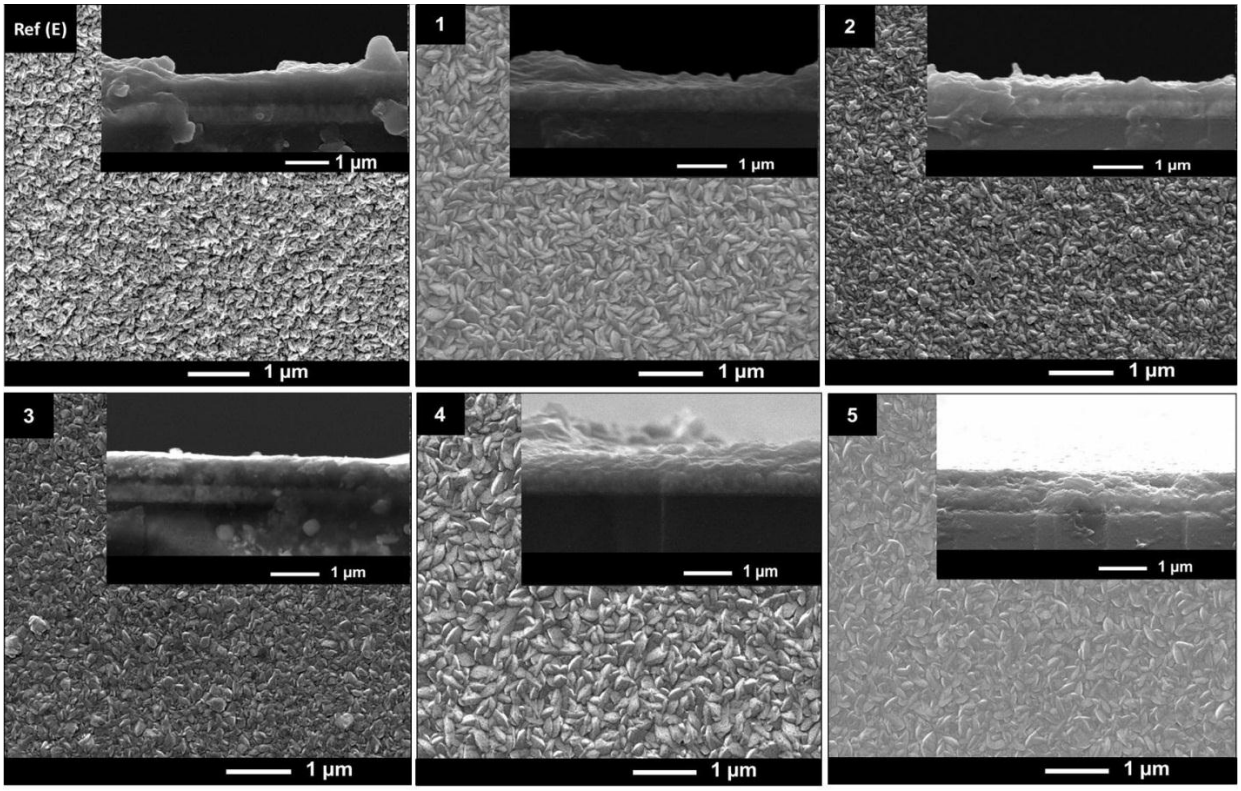

Figure 3.18: Scanning Electron Microscope images for films deposited from the EAACVD reaction of TTIP in toluene under experimental conditions 1 – 5 and reference sample produced at 15 x 10^2 Vm^{-1} (Ref E) produced at fixed conditions.

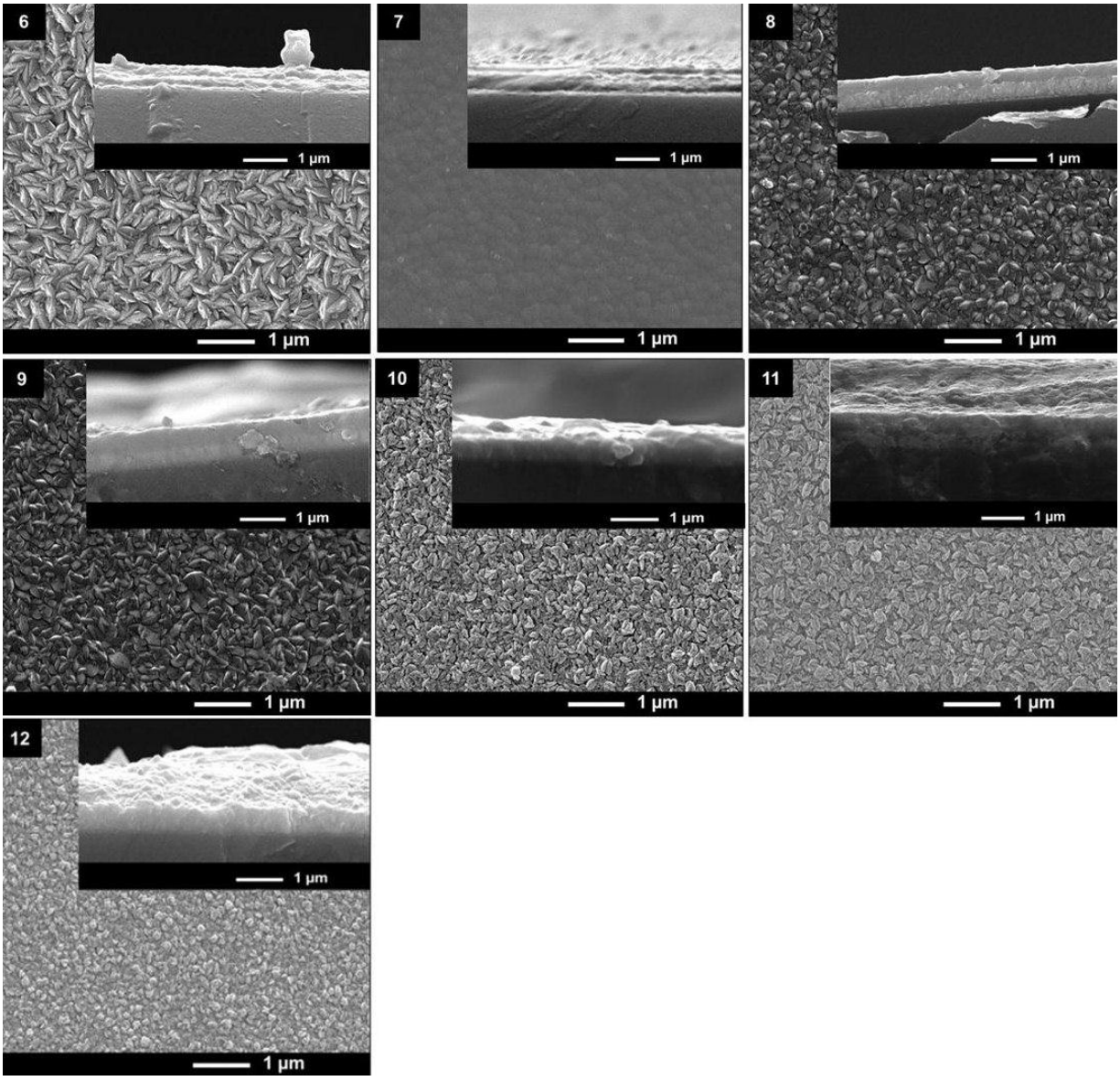

Figure 3.19: Scanning Electron Microscope images for films deposited from the EAACVD reaction of TTIP in toluene under experimental conditions 6 – 12.

Decreasing the substrate temperature to 300 °C (condition 19) had an important impact on the morphology of the microstructure, showing spherical nanoparticles of 210 ± 10 nm diameter (Figure 3.21, 19). In addition, the film thickness was very thin (2± 1 nm).

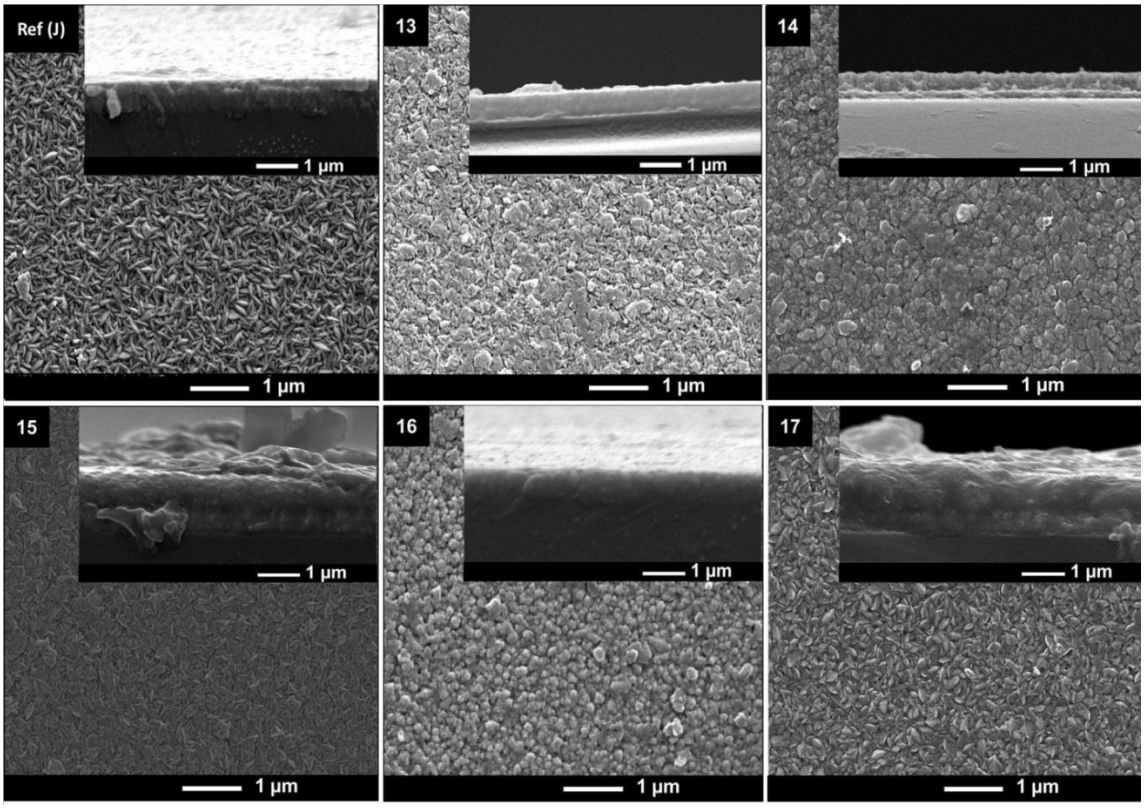

Figure 3.20: Scanning Electron Microscope images for films deposited from the EAACVD reaction of TTIP in toluene under experimental conditions 13 – 17 and reference sample (Ref J).produced at positive bias 10 x 10^2 Vm^{-1} at fixed conditions.

Increasing the substrate temperature to 350 °C (condition 20) produced a decrease in size of the spherical nanoparticles (140 ± 8 nm diameter) and an increase in film thickness to 119 ± 10 nm (Figure 3.21, 20). Further increase of the substrate temperature to 400 °C (condition 21) produced elongated nanoparticles of 190 ± 10 nm length x 48 ± 5 nm width as well as an increase of film thickness to 185 ± 10 nm (Figure 3.21, 21). Different gas flow rate values also induced changes in the microstructure. Decreasing the gas flow rate to 0.5 $L.min^{-1}$ (condition 22) produced films with elongated nanoparticles of 200 ± 15 nm length x 36 ± 4 nm width and film thickness of 65 ± 12 nm (Figure 3.21, 22). At a gas flow rate of 1 $L.min^{-1}$ (condition 23), an increase in nanoparticles size to 420±18 length x 54±7 nm width was produced (Figure 3.21, 23). Likewise, an increase in film thickness 370 ± 15 nm was produced. Further increase of the gas flow rate to 3 $L.min^{-1}$ (condition 24), produced a decrease of elongated nanoparticles size to 230 ± 12 nm length x 40 ± 7 nm and an increase of film thickness to 390 ± 15 nm (Figure 3.21, 24)

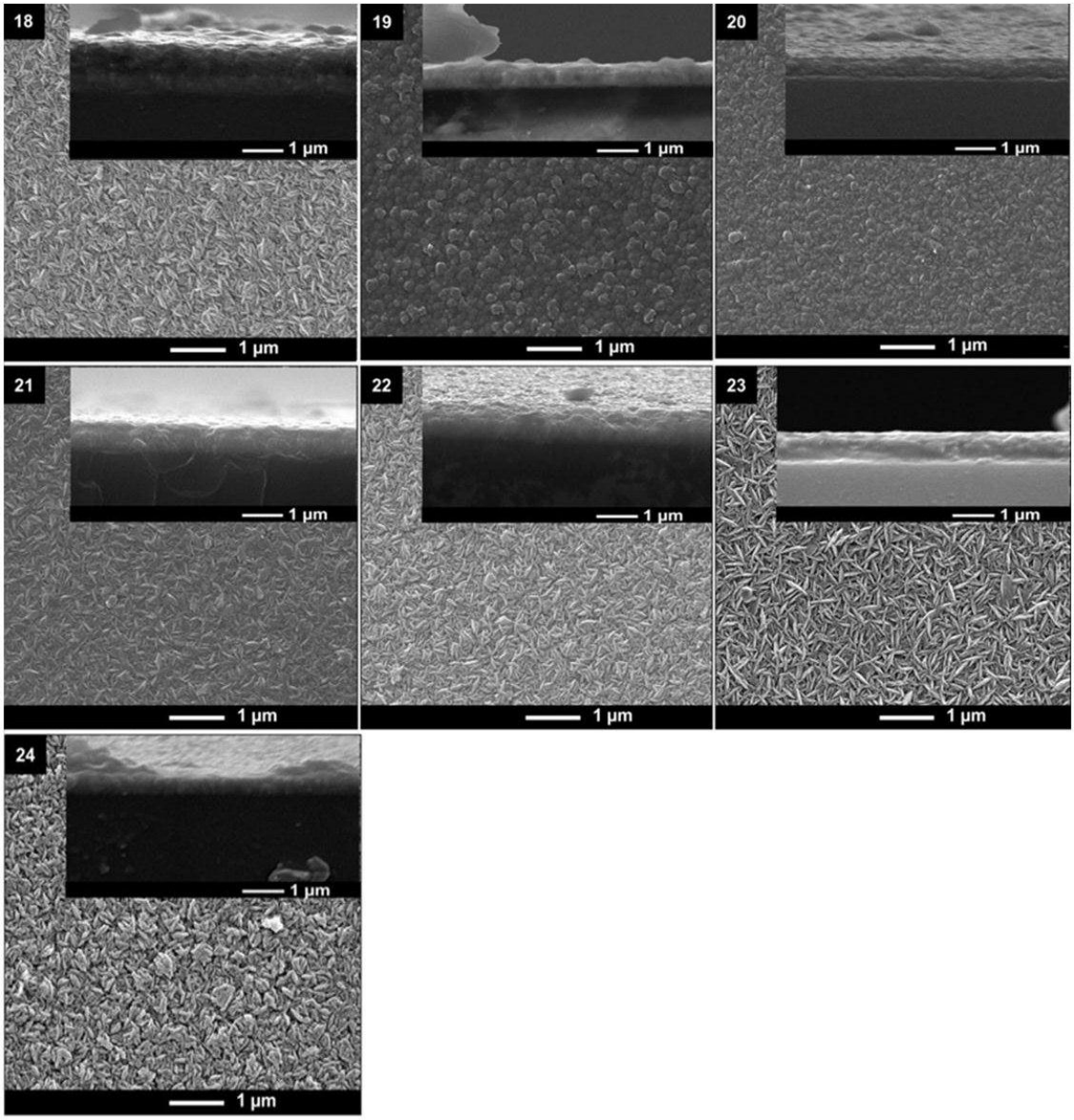

Figure 3.21: Scanning Electron Microscope images for films deposited from the EAACVD reaction of TTIP in toluene under experimental conditions 18 – 24.

X-ray diffraction

X-ray diffraction (XRD) analysis was carried out and compared to previous investigations (JCPDS database file (021-1272)) to study the materials phase. All deposited films under the influence of electric fields showed anatase TiO_2 crystalline phase and also cassiterite SnO_2 from the FTO glass substrate. The relative intensity of the Bragg peaks associated with TiO_2 changed depending on the experimental conditions. Ref (E) showed higher intensity peak in the anatase (101) plane (Figure

3.22). As the experimental conditions were varied the relative intensity peaks changed from the (101) to the (004) plane (conditions 2, 3, 5, 10 and 12) and even to the (211) plane (condition 6). However, conditions 7 and 11 only showed peaks from the substrate which impeded the identification of the crystal phase. Ref (J) showed higher intensity peak in the anatase (101) plane (Figure 3.22). As the experimental conditions were varied the relative intensity peaks changed from the (101) to the (004) plane (conditions 14 – 16, 18). Condition 19 only showed peaks from the substrate which impeded the identification of the crystal phase.

Texture Coefficient ($TC_{(hkl)}$) analysis was conducted to investigate the preferred growth orientation of polycrystalline thin films. The different conditions investigated did not seem to have a significant influence in the crystal preferred orientation in comparison to the reference samples. In any event, no texture coefficient values could have been obtained from conditions 7, 11 and 19 as their XRD patterns only showed peaks from the substrate. Samples produced at 15 x 10^2 Vm^{-1} showed high texture coefficient in the (004) as it was observed for the reference sample (Table 3.12). The highest texture coefficient in the (004) plane were found for conditions 2, 3, 5 (3.13 – 3.25). However, condition 6 showed crystal preferred orientation in the (211) plane. This sample, in which the variable was TTIP volume (1 mL), also showed (112) anatase peak. ven considering this plane for the texture coefficient calculations the crystal preferred orientation was in the (211) plane.

Likewise, the different experimental conditions investigated on samples produced at DC+ 10 x 10^2 Vm^{-1} had a neglecting effect on the preferred crystal orientation (Table 3.12). All samples showed crystal preferred orientation in the (004) plane except for condition 13 which showed crystal preferred orientation in the (211). In condition 13, the experimental variable was the deposition time (5 minutes) which seems to have influenced the crystal orientation. The rest of the conditions at 10 x 10^2 Vm^{-1} gave crystal preferred orientation in the (004) with the highest values for conditions 14-16 and 22 (3.25 – 3.39).

Table 3.11: Agglomerate size (nm) from SEM, film thickness (nm) from SEM cross section and mean crystallite size (nm) obtained from the Scherrer equation, for films deposited from the EAACVD reaction of TTIP in toluene at different conditions. Standard error was applied to all values.

Sample	Field Strength (Vm^{-1})	Substrate bias	Agglomerate size (nm)	Film Thickness (nm)	Mean crystallite size (nm)
Ref (E)	15×10^2	--	140±12	650 ± 13	23±
1	15×10^2	--	270±15	135 ± 12	27±2
2	15×10^2	--	340±12	325 ± 32	18±1
3	15×10^2	--	200±13	660 ± 24	28±2
4	15×10^2	--	315±23	90 ± 25	28±1
5	15×10^2	--	250±18	600 ± 16	17±3
6	15×10^2	--	530±46	75 ± 10	28±2
7	15×10^2	--	150±14	2 ± 0.5	--
8	15×10^2	--	220±14	100 ± 20	28±2
9	15×10^2	--	220±17	225 ± 54	28±1
10	15×10^2	--	150±12	110 ± 16	28±2
11	15×10^2	--	180±13	72 ± 30	--
12	15×10^2	--	140±8	15 ± 6	--
Ref (J)	10×10^2	Positive	360±20	1050 ± 46	27±3
13	10×10^2	Positive	140±10	125 ± 37	28±2
14	10×10^2	Positive	200±10	110 ± 16	29±1
15	10×10^2	Positive	190±10	560 ± 47	--
16	10×10^2	Positive	270±10	25 ± 10	26±2
17	10×10^2	Positive	200 ± 17	1020±56	25±2
18	10×10^2	Positive	160 ± 7	726±27	25±1
19	10×10^2	Positive	210 ± 10	2±1	--
20	10×10^2	Positive	140 ± 8	119±10	27±1
21	10×10^2	Positive	190 ± 10	185±10	23±1
22	10×10^2	Positive	200 ± 15	65±12	24±1
23	10×10^2	Positive	420 ± 18	370±15	27±2
24	10×10^2	Positive	230 ± 18	390±15	30±2

Mean crystallite size was calculated from the Scheerer equation [155] (Table 3.11) . XRD patter for Sample 12 showed weak peaks at 2 theta = 25.2 and 48.1 corresponding to anatase. Nevertheless, those peaks were not enough to carry out the mean crystallite size calculations. Generally, the different conditions applied produced an increase in the mean crystallite size. For films produced at 15 x 10^2 Vm^{-1}, conditions 1, 3 –4, 6 and 8 –10 produced an increase in mean crystallite size in the range of 27 –28 nm. Likewise, for films produced at positive bias 10 x 10^2 Vm^{-1}, conditions 13, 14, 16, 20 , 23 and 24 produced an increase in the mean crystallite size in the range of 27 –30 nm.

Raman spectroscopy

Raman spectroscopy was carried out in order to complement the XRD analysis for phase identification. Figure 3.23 shows Raman spectra for different conditions at 15 x 10^2 Vm^{-1} and at positive bias 10 x 10^2 Vm^{-1}. Most of the conditions tested gave Raman centred at 147 cm^{-1}, 198 cm^{-1}, 395 cm^{-1}, 513 cm^{-1}, 642 cm^{-1} which correspond to anatase crystal phase [134]. In some cases the Raman peaks were weaker and did not reveal the Raman shift centred at 198 cm^{-1} (condition 3, 10, 12, 14, 15, 18, 22 and reference sample at 15 x 10^2 Vm^{-1}). Conditions 7, 11 and 19 showed amorphous spectra which as observed in XRD impeded the identification of the crystal phase.

Atomic force microscopy

Deposited films surfaces were scanned using AFM over a 2 µm x 2 µm region in order to obtain Root Mean Square (RMS) roughness values as a proxy of surface roughness. Figures 3.24 – 3.27 show AFM images with corresponding RMS values for all experimental conditions. All RMS values can be seen listed in Table 3.13. Ref E showed a surface roughness of 16 nm (Figure 3.24, Ref E). For deposition time of 5 minutes (condition 1) and 10 minutes (condition 2) the surface roughness was very low with RMS values of 2 – 4 nm (± 0.5 – 2 nm) (Figure 3.24, 1-2). As deposition time was increased to 15 minutes (condition 3) the surface roughness increased to 10 ± 1 nm (Figure 3.24, 3). Decreasing the TTIP volume to 0.25 mL (condition 4) produced films with a surface roughness of 15 ± 2 nm (Figure 3.24, 4). As the TTIP

volume was increased to 0.75 mL (condition 5) and 1 mL (condition 6), the RMS values decreased to 9 ± 1 nm and 11 ± 0.8 nm, respectively (Figure 3.24, 5-6). When the substrate temperature was set to 300 °C (condition 7), films showed a surface roughness of 11 ± 2 nm (Figure 3.24, 7). The increase of substrate temperature to 350 °C produced an increase of the surface roughness to 15 ± 0.6 nm (Figure 3.25, 8). At 400 °C substrate temperature (condition 9), an important decrease of surface roughness to 5 ± 1 nm was observed (Figure 3.25, 9). Films produced at a gas flow rate of 0.5 $L.min^{-1}$ (condition 10) showed RMS values of 14 ± 2 nm (Figure 3.25, 10). The increase of the gas flow rate to 1 $L.min^{-1}$ (condition 11) produced higher surface roughness with RMS values of 16 ± 1 nm (Figure 3.25, 11). Further increase of the gas flow rate to 3 $L.min^{-1}$ (condition 12) produced a decrease in RMS values to 13 ± 1nm (Figure 3.25, 12).

Ref J showed a surface roughness of 10 ± 1 nm (Figure 3.26, Ref J). The different experimental conditions tested at this field strength produced thin films with varied surface roughness. Decreasing the deposition time to 5 minutes (condition 13) produced a reduction of surface roughness to 7 ± 3 nm (Figure 3.26, 13). At a deposition time of 10 minutes (condition 14), the surface roughness decreased to 3 ± 1 nm (Figure 3.26, 14). When the deposition time was set at 15 minutes (condition 15), an increase of the surface roughness to 8 ± 2 nm was observed (Figure 3.26, 15). Decreasing the TTIP volume to 0.25 mL (condition 16) produced films with a surface roughness of 10 ± 1 nm (Figure 3.26, 16). The increase of the TTIP volume to 0.75 mL (condition 17) produced an important increase in the surface roughness to 24 ± 1 nm (Figure 3.26, 17). However, further increase of the TTIP volume to 1 mL (condition 18) produced a reduction of RMS values to 13 ± 2 nm (Figure 3.26, 18). When the substrate temperature was set to 300 °C (condition 19), films showed a surface roughness of 19 ± 7 nm (Figure 3.26, 19). The increase of substrate temperature to 350 °C produced a decrease of the surface roughness to 6 ± 4 nm (Figure 3.27, 20). At 400 °C substrate temperature (condition 21), films showed a surface roughness of 10 ± 0.6 nm (Figure 3.27, 21). Films produced at a gas flow rate of 0.5 – 1 $L.min^{-1}$ (condition 22) showed RMS values of 10 ± 1 nm (Figure 3.27, 22 – 23). Further increase of the gas flow rate to 3 $L.min^{-1}$ (condition 24) produced an important decrease in RMS values to 2 ± 1 nm (Figure 3.27, 24).

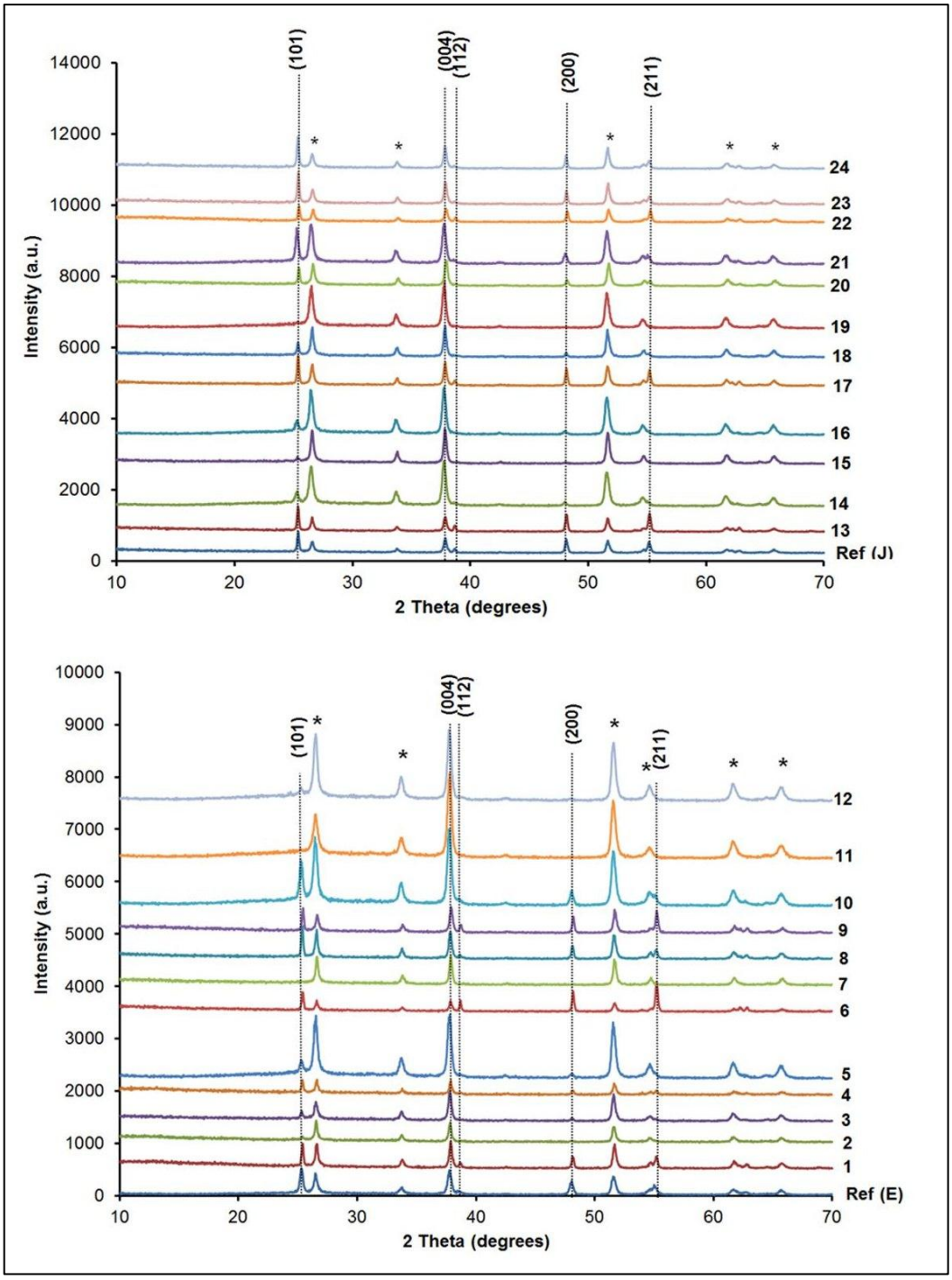

Figure 3.22: XRD pattern for TiO_2 thin films produced from the EAACVD reaction of TTIP in toluene at different conditions (1 to 24) and reference sample produced at 15 x 10^2 Vm^{-1}(Ref E) and at +ve 10 x 10^2 Vm^{-1} (Ref J) produced at fixed conditions.

Table 3.12: Texture Coefficient of TiO_2 thin films produced from the EAACVD reaction TTIP in toluene at different conditions (condition 1 to 24) and reference samples (Ref E and J) produced at fixed conditions.

	Texture Coefficient (TC_{hkl})			
Sample	(101)	(004)	(200)	(211)
Ref (E)	0.33	2.84	0.33	0.55
1	0.38	2.08	0.55	0.97
2	0.21	3.13	0.21	0.44
3	0.23	3.19	0.22	0.36
4	0.46	2.22	0.47	0.84
5	0.2	3.25	0.19	0.35
6	0.28	0.77	0.83	2.12
7	--	--	--	--
8	0.51	2.05	0.63	0.79
9	0.32	1.66	0.61	1.41
10	0.36	2.93	0.28	0.42
11	--	--	--	--
12	0.14	3.43	0.12	0.3
Ref (J)	0.44	1.56	0.81	1.17
13	0.42	1.24	0.82	1.51
14	0.22	3.25	0.17	0.35
15	0.15	3.39	0.13	0.33
16	0.21	3.29	0.2	0.3
17	0.43	1.68	0.72	1.16
18	0.29	3.03	0.3	0.36
19	--	--	--	--
20	0.38	2.64	0.4	0.58
21	0.45	2.48	0.41	0.65
22	0.19	3.33	0.16	0.32
23	0.36	1.51	0.74	1.38
24	0.57	1.96	0.7	0.76

UV-vis spectroscopy

Generally, the application of different experimental conditions increased the maximum transmission in the visible of Ref E (74 %) and Ref J (76 %) (Table 3.13). Experimental conditions at 15 x 10^2 Vm^{-1} (1 – 12) showed maximum transmission values in the visible in the range of 62 – 81 % (Figure 3.28). The condition which showed the highest transmission in the visible was condition 2 and 12. Experimental conditions at positive bias 10 x 10^2 Vm^{-1} (13 – 24) showed maximum transmission values in the visible in the range of 42 – 82 % (Figure 3.29). The conditions that showed the highest transmission in the visible were condition 3 and 15 – 16. The lowest transmission in the visible was found for condition 11 (62 %), condition 18 (52 %) and condition 22 (42%), probably due to the high incorporation of carbon into the

films. The high content of carbon had a significant effect on the direct band gap as values of 3 – 2.95 were found for conditions 11, 18 and 22 respectively (Table 3.13). For the rest of the conditions tested normal band gap values for anatase TiO_2 were found (3.2 – 3.3).

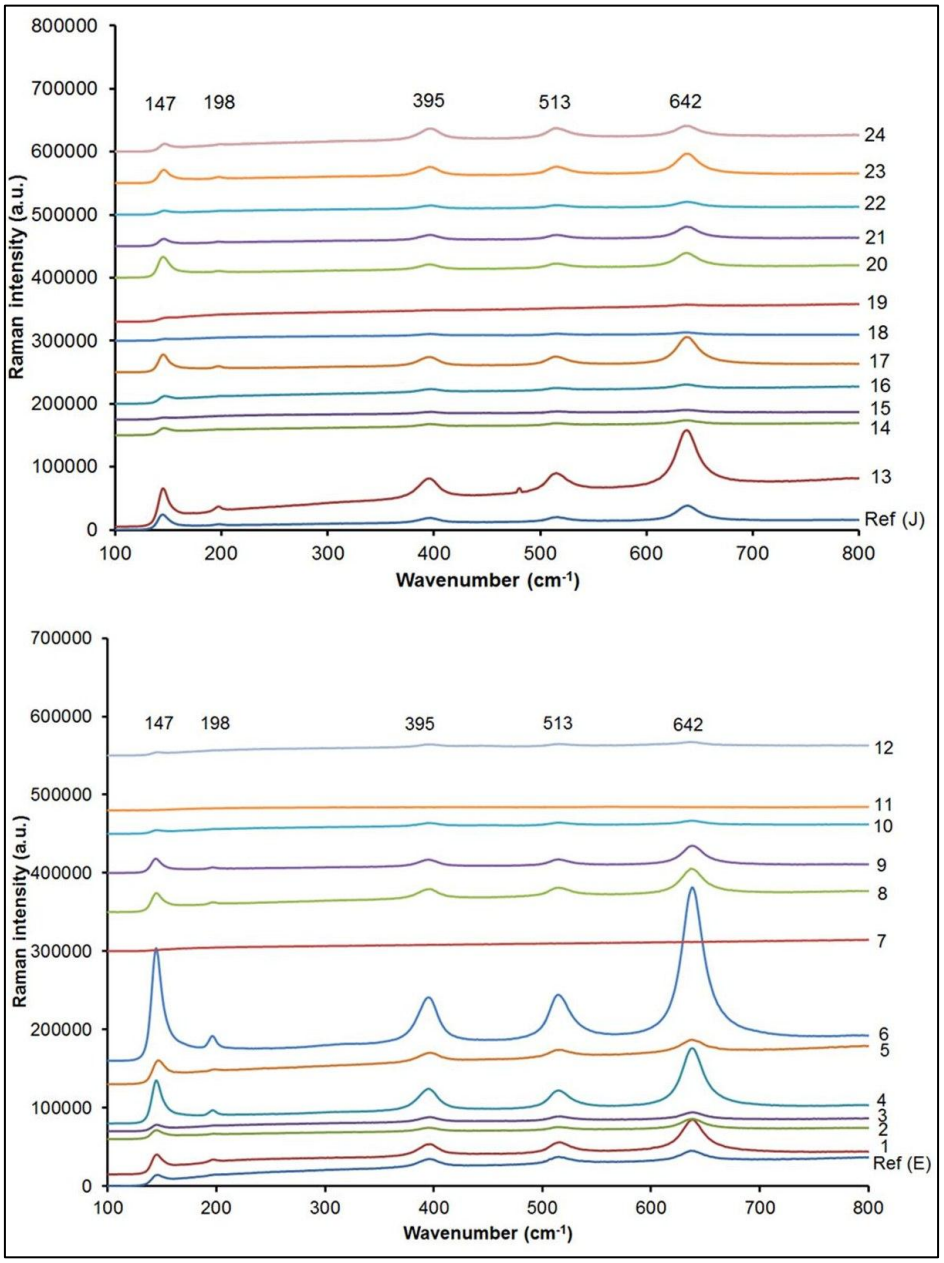

Figure 3.23: Raman spectra for TiO_2 thin films produced from the EAACVD reaction of TTIP in toluene at different conditions (1 to 24) and reference sample produced at 15 x 10^2 Vm^{-1}(Ref E) and at +ve 10 x 10^2 Vm^{-1} (Ref J) produced at fixed conditions. All peaks correspond to anatase crystal phase.

Table 3.13: Root Mean Square (RMS) values (nm) from AFM with standard error values, maximum transmission in the visible values (T%) from UV-vis spectroscopy and Direct Band Gap (D.B.G) values (e.V) calculated from the Tauc method, for films produced from the EAACVD reaction of TTIP at different conditions.

Sample	Applied Voltage (V)	Field Strength (Vm^{-1})	Substrate bias	RMS (nm)	T%	D.B.G (eV)
Ref (E)	15	15×10^2	--	16±3	74	3.3
1	15	15×10^2	--	2±1	76	3.2
2	15	15×10^2	--	4±2	81	3.2
3	15	15×10^2	--	10±4	78	3.3
4	15	15×10^2	--	15±8	75	3.1
5	15	15×10^2	--	9±1	78	3.2
6	15	15×10^2	--	11±1	71	3.2
7	15	15×10^2	--	11±2	78	3.3
8	15	15×10^2	--	15±1	74	3.25
9	15	15×10^2	--	5±2	80	3.15
10	15	15×10^2	--	14±2	74	3.2
11	15	15×10^2	--	16±4	62	3.05
12	15	15×10^2	--	13±2	81	3.15
Ref (J)	10	10×10^2	Positive	11±5	76	3.3
13	10	10×10^2	Positive	7±5	82	3.3
14	10	10×10^2	Positive	3±1	77	3.15
15	10	10×10^2	Positive	8±2	82	3.2
16	10	10×10^2	Positive	10±4	82	3.2
17	10	10×10^2	Positive	24±8	77	3.25
18	10	10×10^2	Positive	13±6	52	2.95
19	10	10×10^2	Positive	19±3	78	3.3
20	10	10×10^2	Positive	6±4	79	3.2
21	10	10×10^2	Positive	10±2	77	3.25
22	10	10×10^2	Positive	9±1	42	3
23	10	10×10^2	Positive	10±3	76	3.2
24	10	10×10^2	Positive	2±1	76	3.3

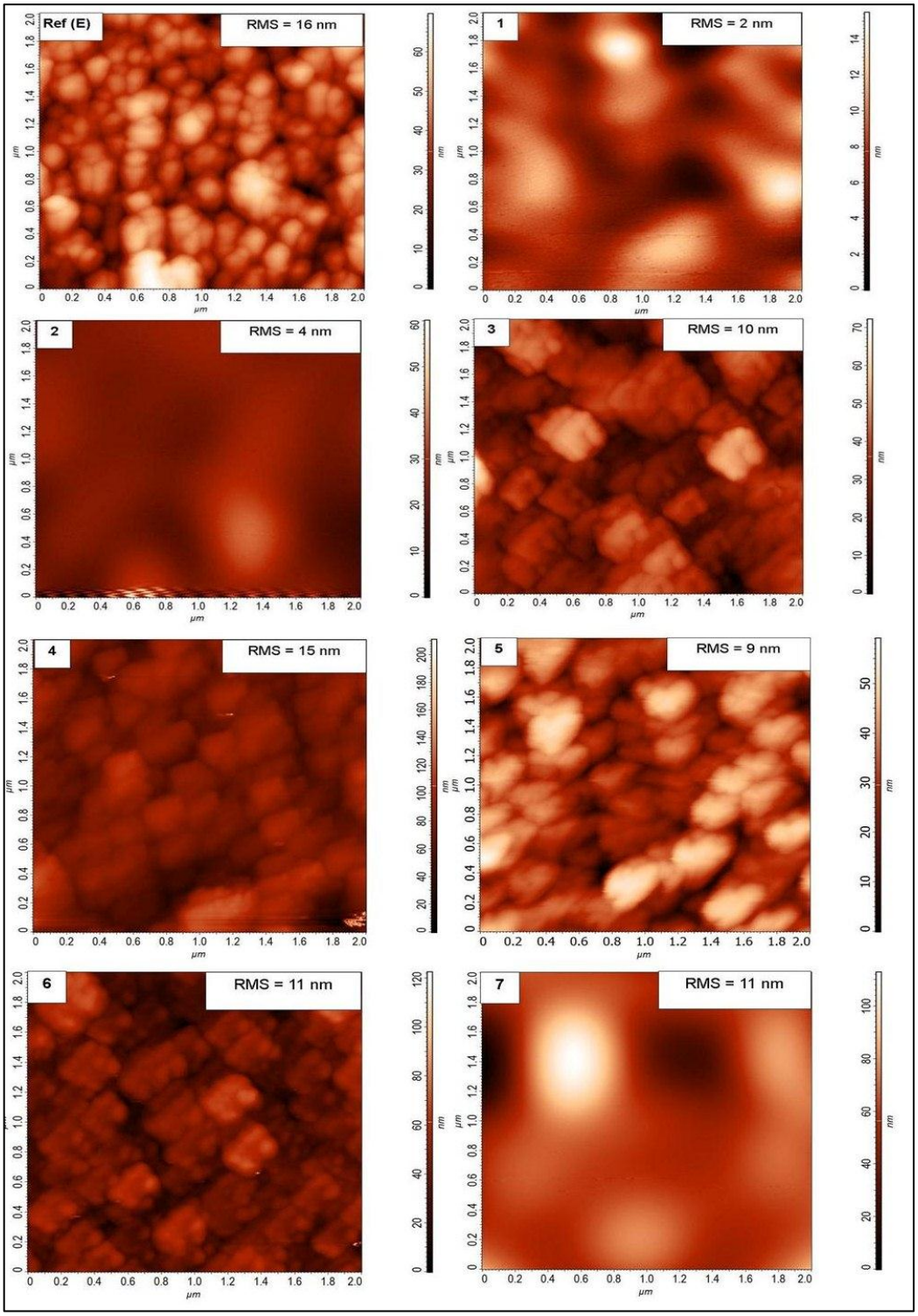

Figure 3.24: AFM images with corresponding Root Mean Square (RMS) values (nm) for films produced from the EAACVD reaction of TTIP in toluene under conditions 1 to 7 with reference sample deposited at 15 x 10^2 Vm^{-1} (Ref E).

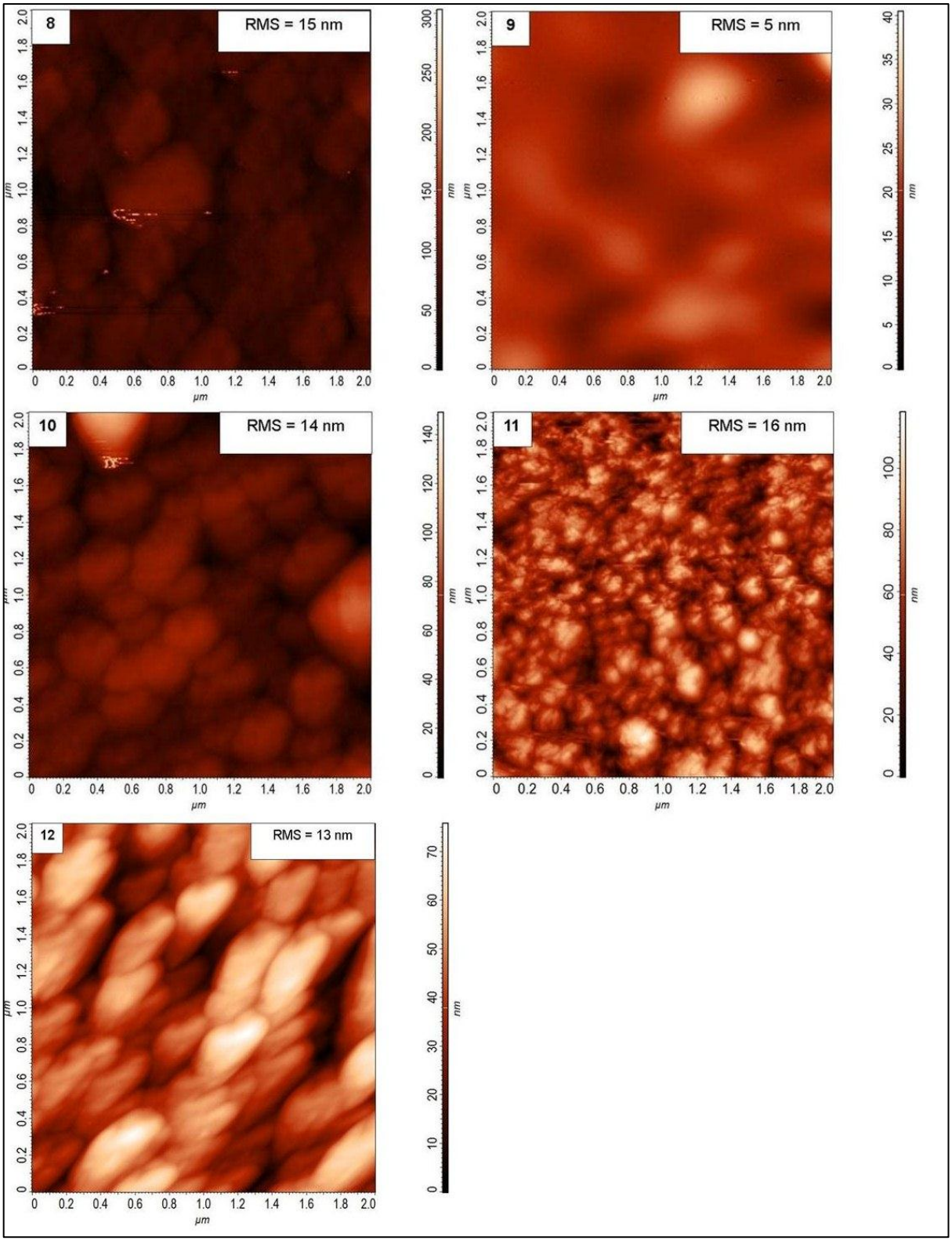

Figure 3.25: AFM images with corresponding Root Mean Square (RMS) values (nm) for films produced from the EAACVD reaction of TTIP in toluene under conditions 8 to 12.

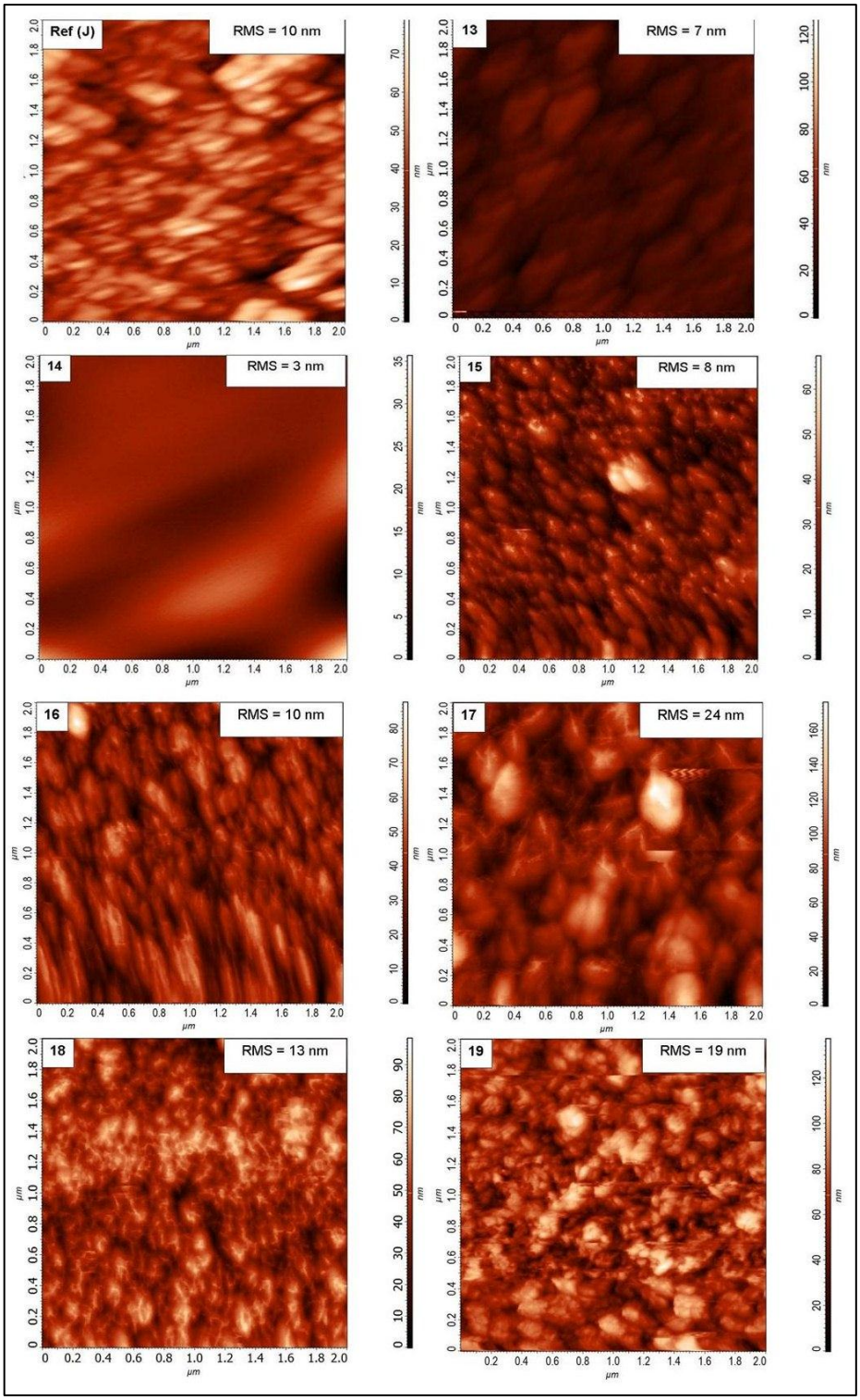

Figure 3.26: AFM images with corresponding Root Mean Square (RMS) values (nm) for films produced from the EAACVD reaction of TTIP in toluene under conditions 13 to 19 with reference sample deposited at +ve 10 x 10^2 Vm^{-1} (Ref J).

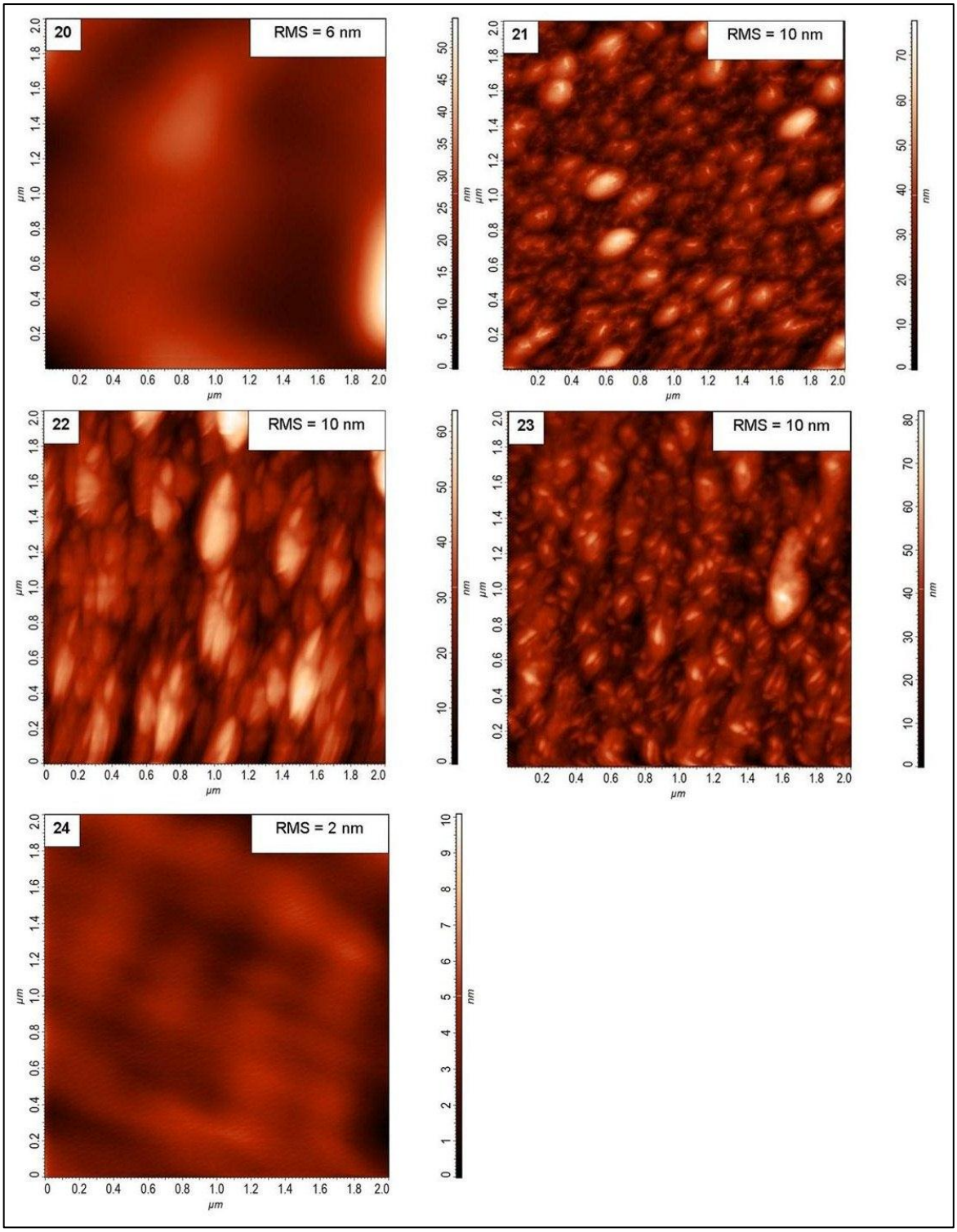

Figure 3.27: AFM images with corresponding Root Mean Square (RMS) values (nm) for films produced from the EAACVD reaction of TTIP in toluene under conditions 20 to 24.

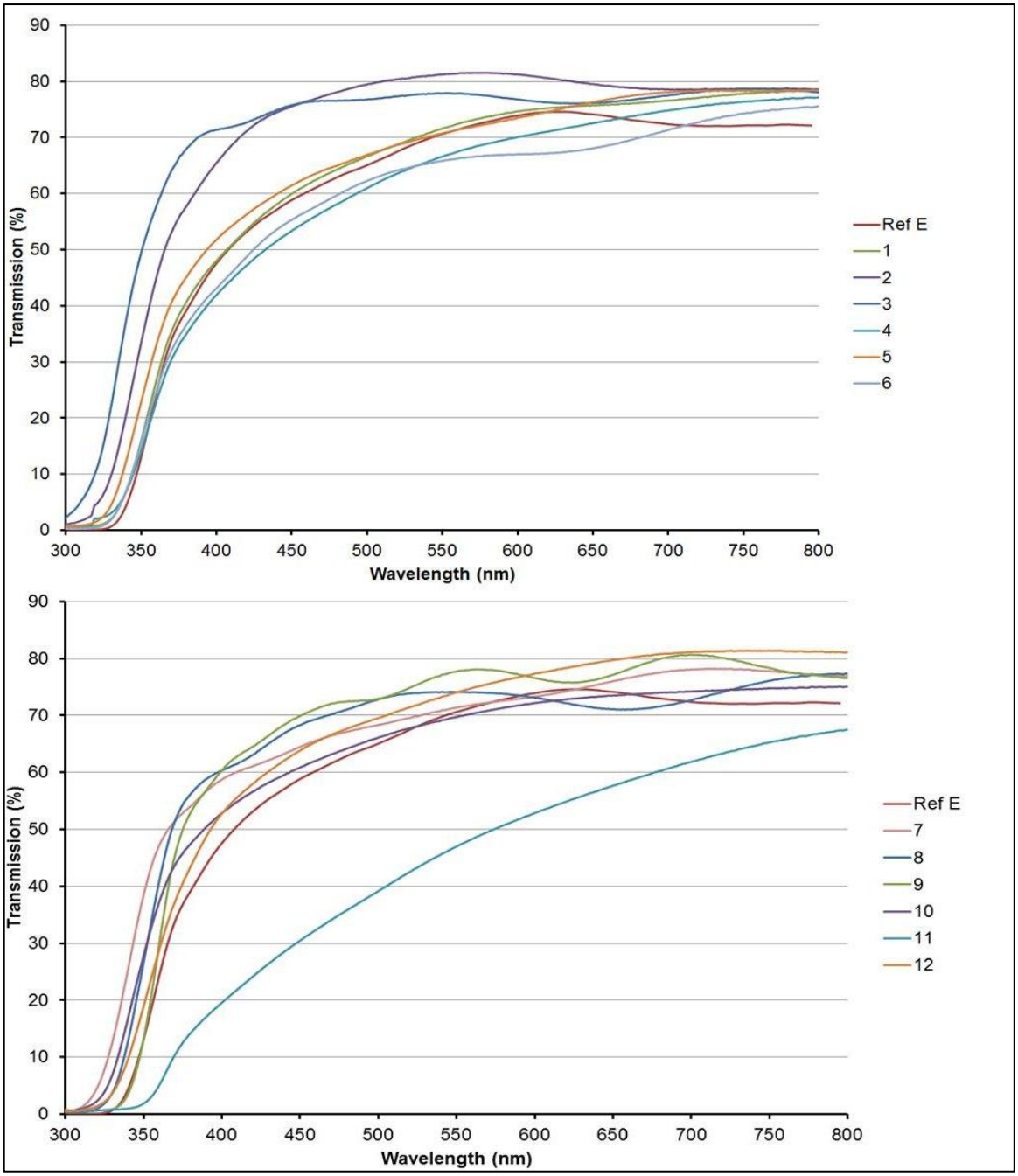

Figure 3.28: UV-vis spectroscopy for Ref (E) and conditions 1 – 12.

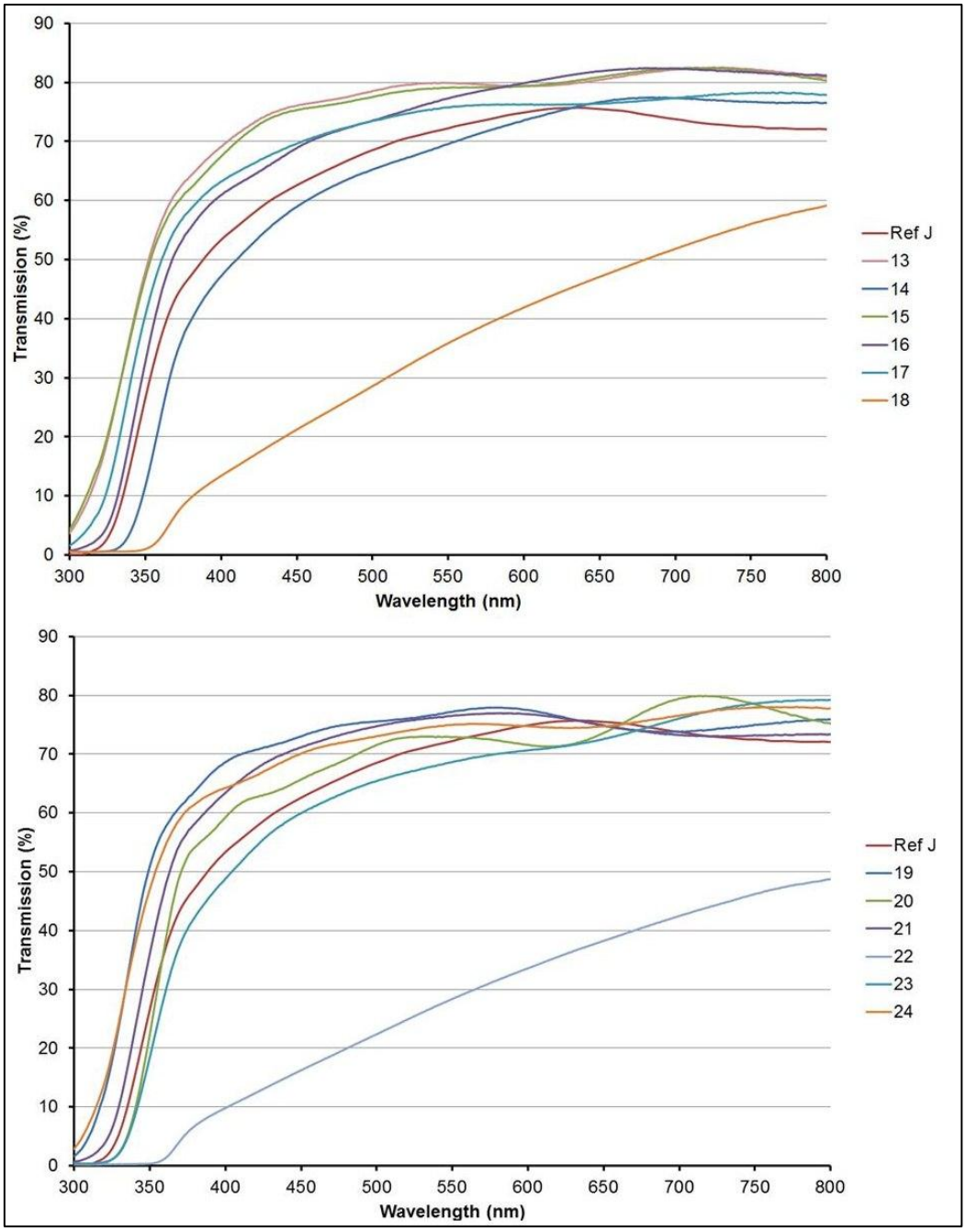

Figure 3.29: UV-vis spectroscopy for Ref (J) and conditions 13 – 24.

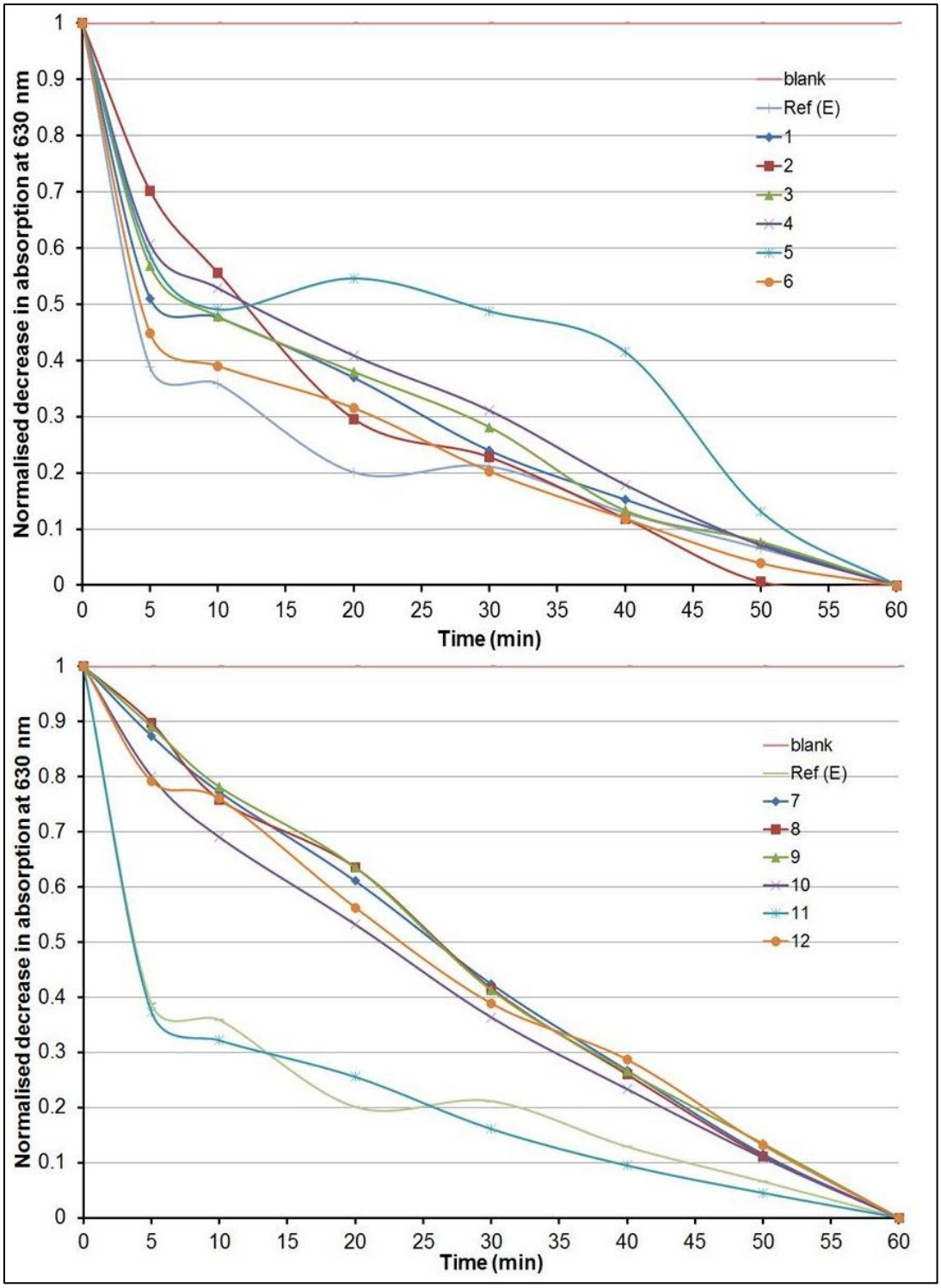

Figure 3.30: Normalised decrease in absorption of Resazurin intelligent ink at 630 nm with UVA irradiation (365 nm) against time (min) for experimental conditions 1-12 with reference sample (Ref E).

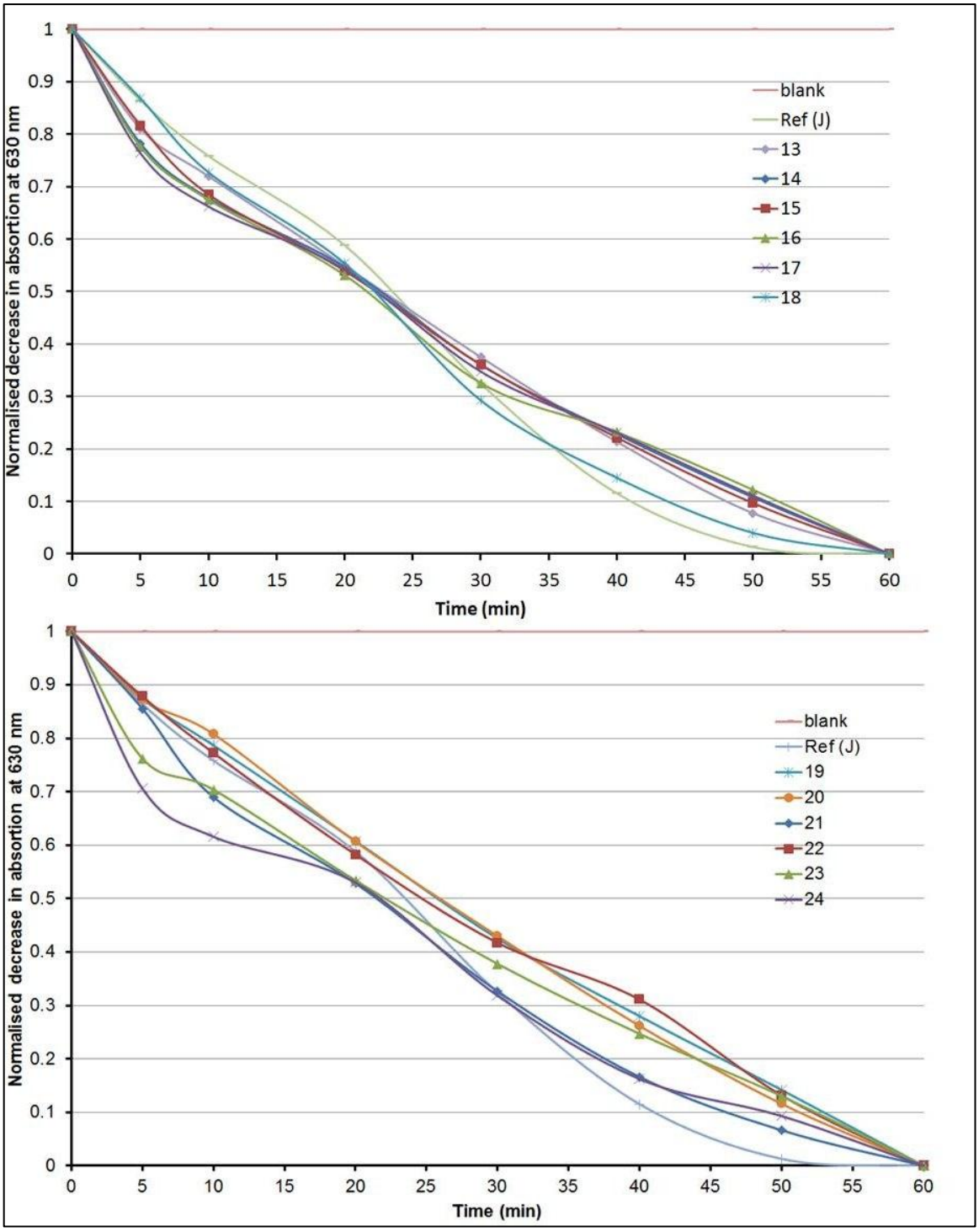

Figure 3.31: Normalised decrease in absorption of Resazurin intelligent ink at 630 nm with UVA irradiation (365 nm) against time (min) for experimental conditions 13-24 with reference sample (Ref J).

3.2.6. Functional properties of TiO_2 thin films at different conditions

3.2.6.1. Photo-activity of TiO_2 thin films at different conditions

Figure 3.30 shows the normalised decrease in absorption at 630 nm against UV irradiation time (min) for experimental conditions 1-12 with reference sample produced at 15 x 10^2 Vm^{-1} (Ref E). It was observed that, except for condition 11 (half-life value of 3.8 min), all experimental conditions showed higher half-life values than the reference sample (Ref E, 3.9 min) (Table 3.14). After condition 11, the conditions which gave the higher photo-activity were conditions 6 (4.5 min), 1 (5.2 min), 3 (7.9 min). Furthermore, conditions 7 -10 and 12 showed a detrimental effect on titania thin films photo-activity with half-life values in the range of 23.2 – 26.1 min. Figure 3.31 shows the normalised decrease in absorption at 630 nm against UV irradiation time (min) for experimental conditions 13 – 24 with reference sample produced at positive bias 10 x 10^2 Vm^{-1} (Ref J). The different experimental conditions applied could not significantly reduce the half-life value of the reference sample (Ref J) which was found to be 23.5 min (Table 3.13). Experimental conditions 13 – 18, 16, 21and 23 – 24 slightly improved titania thin films photo-activity with half-life values in the range of 21.6 – 23 min. The rest of experimental conditions showed a detrimental effect on titania photo-activity with half-life values in the range of 24.6 –26 min.

3.2.6.2. Water contact angles

Figure 3.32 shows the mean water-contact angle for films produced under experimental conditions 1 – 12 with reference sample produce at 15 x 10^2 Vm^{-1} (Ref E). The application of different experimental conditions reduced the water contact angle of the reference sample (Ref E) (29°) in some cases (conditions 2, 4, 6, 10, 12) and increased it in some others (conditions 1, 3, 5, 7 – 9, 11). In all cases, films showed hydrophilicity with water contact angles (15 – 51°). The highest mean water-contact angle was found for condition 5 (51°) and 7 (78°). After 30 minutes UV irradiation (254 nm) all films showed hydrophilicity with water contact angles of 10 – 66°. Figure 3.33 shows the mean water-contact angle for films produced under experimental conditions 13 – 24 with reference sample produced at positive bias 10 x

10^2 Vm^{-1} (Ref J). The application of different experimental conditions reduced in some cases (conditions 14, 15, 16 – 18) and increased in some others (conditions 13, 19 – 24) the water contact angle comparing to the reference sample (Ref J) (25°). In all cases, films (conditions 13 – 24) showed hydrophilicity with water contact angles (10 – 83°) except for condition 24 (100°). After 30 minutes UV irradiation (254 nm) all films showed hydrophilicity with water contact angles of 6 – 60°. Mean water-contact angles can be seen in Table 3.14.

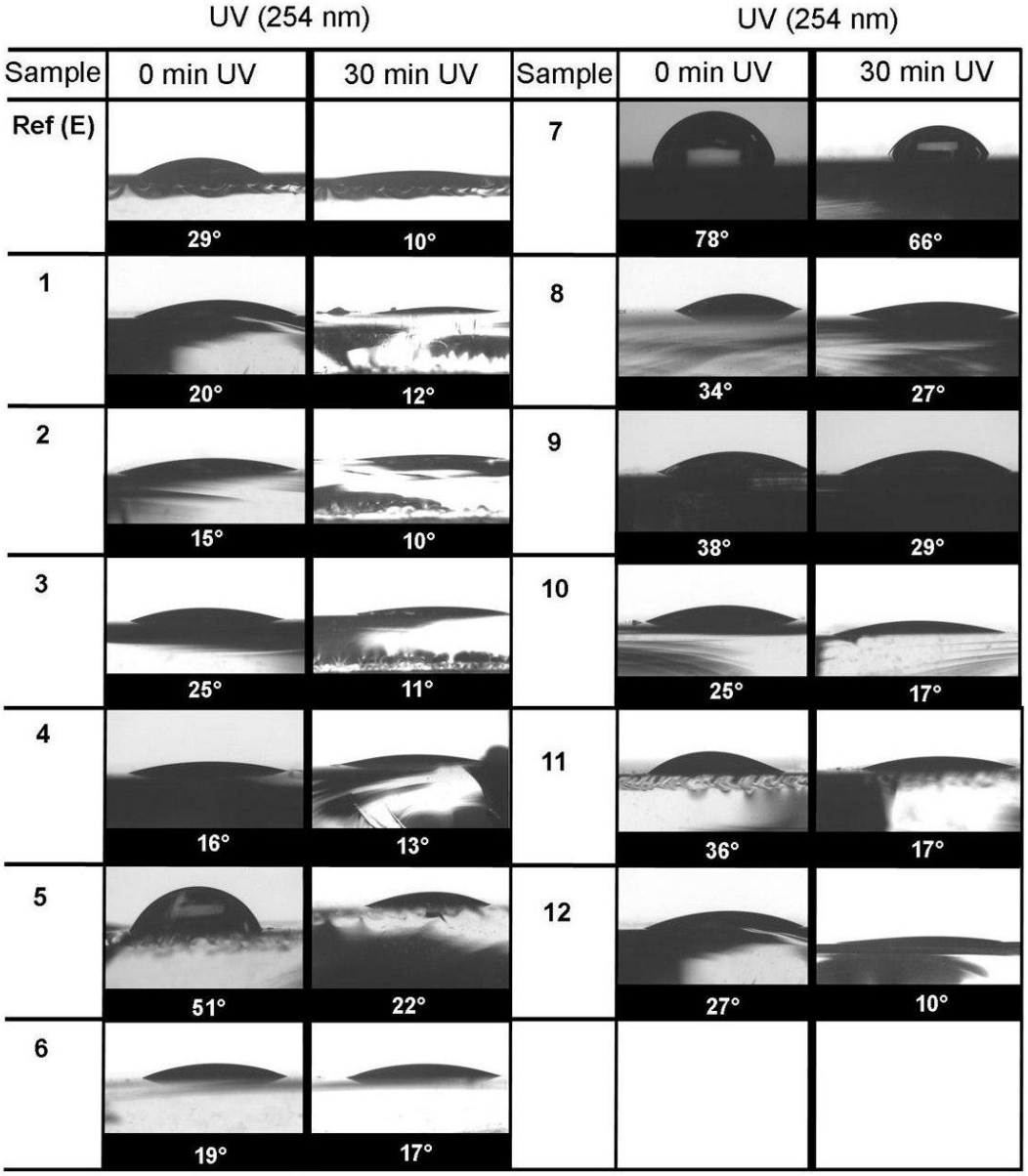

Figure 3.32: Mean water contact angles for Ref (E) and conditions 1 – 12 before and after 30 minutes UV irradiation (254 nm).

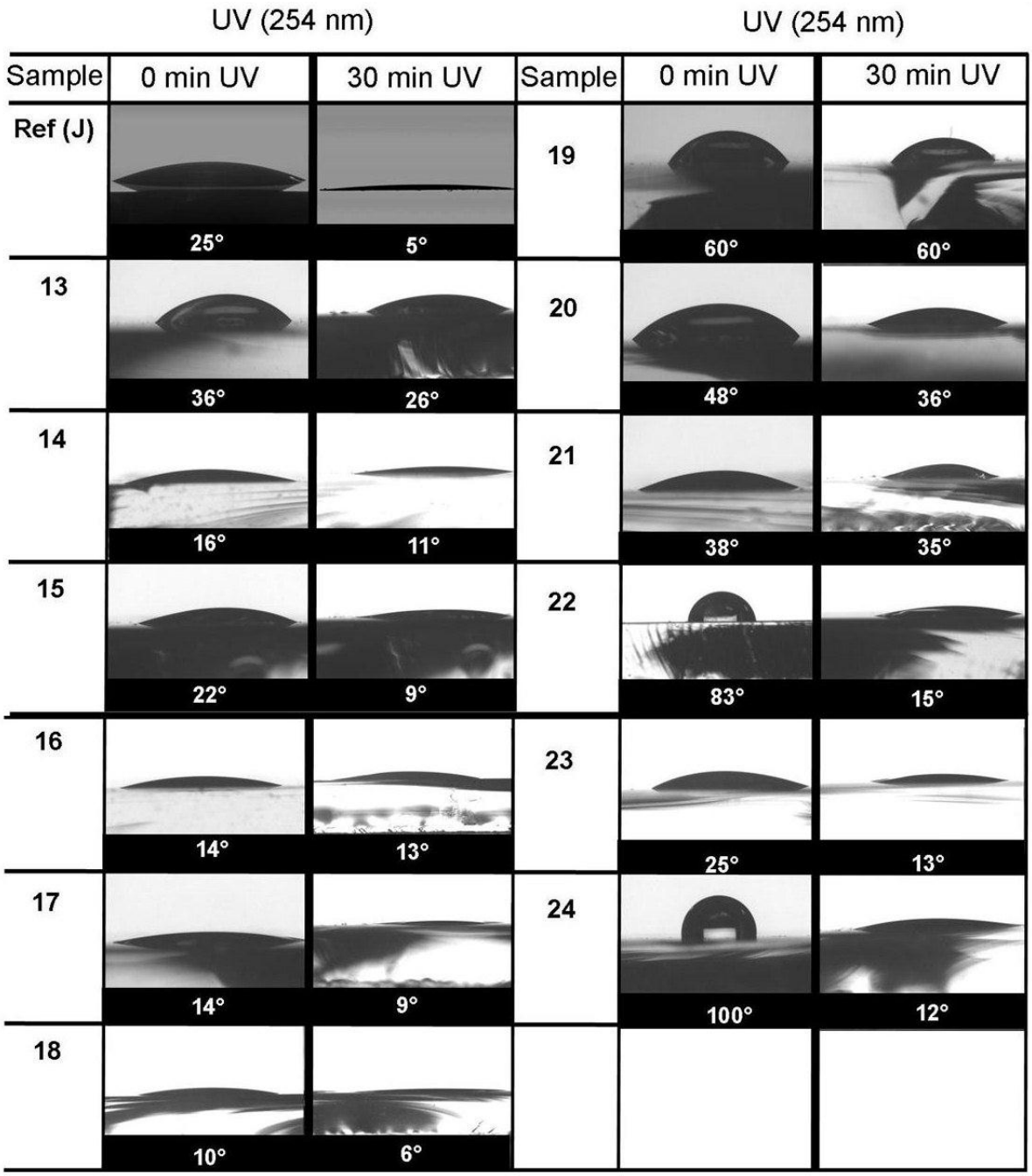

Figure 3.33: Mean water contact angles for Ref (E) and conditions 13 – 24 before and after 30 minutes UV irradiation (254 nm)

Table 3.14: Mean water-contact angle before and after UV irradiation (30 min) with SE; half-life photocatalytic testing or time needed to degrade 50% of the ink initial concentration, $t_{1/2}$ (min) for conditions 1- 12 and at reference sample deposited at 15×10^2 Vm^{-1} (Ref E).

Sample	Field Strength (Vm^{-1})	Substrate bias	Contact Angle (degrees) ± SE		Half-life
			0 min	30 min	$t_{1/2}$ (min)
Ref (E)	15×10^2	--	29 ± 2	10 ± 1	3.9
1	15×10^2	--	20 ± 3	12 ± 1	5.2
2	15×10^2	--	15 ± 3	10 ± 2	12
3	15×10^2	--	25 ± 7	11 ± 2	7.9
4	15×10^2	--	16 ± 1	13 ± 1	12.2
5	15×10^2	--	51 ± 10	22 ± 4	8.2
6	15×10^2	--	19 ± 2	17 ± 3	4.5
7	15×10^2	--	78 ± 3	66 ± 2	25.9
8	15×10^2	--	34 ± 9	27 ± 6	26.1
9	15×10^2	--	38 ± 8	29 ± 11	26
10	15×10^2	--	25 ± 10	17 ± 3	22
11	15×10^2	--	36 ± 3	17 ± 4	3.8
12	15×10^2	--	27 ± 5	10 ± 2	23.2
Ref (J)	10×10^2	Positive	25 ± 12	5 ± 4	23.5
13	10×10^2	Positive	36 ± 5	26 ± 1	23
14	10×10^2	Positive	16 ± 1	11 ± 4	22.9
15	10×10^2	Positive	22 ± 1	9 ± 2	22.5
16	10×10^2	Positive	14 ± 4	13 ± 1	21.8
17	10×10^2	Positive	14 ± 3	9 ± 2	22.2
18	10×10^2	Positive	10 ± 1	6 ± 1	22.1
19	10×10^2	Positive	60 ± 5	60 ± 5	25.7
20	10×10^2	Positive	48 ± 3	36 ± 8	26
21	10×10^2	Positive	38 ± 13	35 ± 11	21.3
22	10×10^2	Positive	83 ± 6	15 ± 3	24.6
23	10×10^2	Positive	25 ± 3	13 ± 1	22.1
24	10×10^2	Positive	100 ± 1	12 ± 2	21.6

3.3. Discussion

3.3.1. Modifications in microstructure at fixed conditions

The EACVD growth of TiO_2 from the reaction of 0.17 M TTIP in toluene under the influence of AC electric fields influenced the morphology and particle size of deposited films. Elongated nanoparticles were observed at lower field strengths and spherical nanoparticles at higher field strengths. Morphological changes induced by AC electric fields on the AACVD reaction of TTIP in toluene has been reported elsewhere [24]. Likewise, the application of DC electric fields had a significant influence in titania thin films microstructure. The application of DC electric fields during the EACVD growth of other materials has been proven to affect the morphology and size of nanoparticles [156] observing significant changes at higher field strengths. In this work, such changes in the microstructure were also observed with a clear tendency for elongated nanoparticles for positive bias deposited films and spherical nanoparticles for negative bias deposited films. This may support the argument which believes that the way TTIP precursor assembly under the influence of electric fields responds to a substrate effect rather than an interaction between the precursor and the electric field [133]. Previous research on the production of tungsten oxide from EACVD for gas sensing purposes [23] showed an increase of deposited material using both AC and DC electric fields. This was attributed to a polarisation of aerosol particles whose time of flight would be affected by the field strength. However, as it has been already reported TTIP is an electrically symmetrical precursor [133].

In contrast to AC electric fields, in direct current the field is always exerted in one constant direction. Thus, DC electric fields would encourage the acceleration towards and nucleation of appropriately charged species on the substrate, which may explain the increase in thickness of deposited materials. In particular, negative biased deposited films showed an increasing trend until 10×10^2 Vm^{-1} where the thickness gradually decreased. Positively biased EACVD produced thicker titania thin films formed of larger agglomerates which indicated that surfaces were more reactive or that the charged species attracted to this surface were more reactive.

The surface effect can be explained in terms of the thermal decomposition mechanism of the TTIP molecule (Ti $(OC_3H_7)_4$) on the substrate. Previous studies suggested that the thermal decomposition of the molecule was produced from the breakdown of Ti-O bonds giving isopropoxy ligand radicals $(OC_3H_7)^*$ at temperatures from 120-350 K [157].

$2Ti\text{-}OC_3H_7^* \rightarrow 2Ti^+ + HOC_3H_7\uparrow + OC_3H_6\uparrow$ (at 615 ºC) (Equation 3.1)

$Ti\text{-}OC_3H_7^* \rightarrow Ti\text{-}OH^- + C_3H_6\uparrow$ (at 657 ºC) (Equation 3.2)

At 890 K the breakdown of the TTIP molecule gave titanium cations as well as isopropanol and acetone products, which were volatised (Equation 3.1). At 930 K (Equation 3.2), the thermal decomposition of TTIP led to the production of titanium hydroxyl groups and propylene.

The higher observed thickness of the films deposited with a positively biased surface suggests that equation 3.2 is much more likely to be occurring. Thus, the titanium hydroxyl radicals would be attracted to the positively biased surface increasing the thickness of the deposited titania thin films. The negatively biased surfaces grow more slowly as is evidenced in Figure 3.9. This would also explain why all the samples produced with a positive substrate contained carbon contamination; the C_3H_6 with high electron density in the double bond would likely be attracted to the positively biased substrate and caught up in the growing film. The films produced with a strong electric field and negative substrate bias would effectively deflect any radicals, negatively charged species or centres of negative charge away from the substrate surface, accounting for why no carbon is found in the deposited films. The titanium species would still be able to diffuse to the surface, as they would be less affected by the electric field being heavier than the C_3H_6 species. In AC deposited fields, the application of weaker electric fields (samples B to D) led to the incorporation in carbon in the deposited films, whereas films produced with larger applied electric field strengths (samples E to G) appeared to be free of carbon contamination. This is most likely because the electric field adds some additional energy into the reaction whether through precursor acceleration or surface organization. It is therefore more likely to reduce the energy barrier for competing precursor decomposition pathways,

although may not provide enough energy for desorption of the newly formed by-products resulting in carbon becoming incorporated into the film. As the field strength is further increased the energy for desorption is supplied and subsequently in these cases carbon does not become incorporated in the growing film.

The interaction of electric fields during the thermal decomposition of the precursor would also explain the changes in morphology observed in AC and DC electric fields. Positive bias electric fields showed a predominance of long-shaped nanoparticles whereas negative bias deposited films showed a predominance of spherical nanoparticles. As Figure 3.34 A shows, as the field strength is increased the attracting forces toward the surface also increase. As a result, the intermediate species undergo a stretching effect either in the gas phase or during the nucleation on the substrate. Higher field strength (Sample M) would induce a higher acceleration to the intermediate species giving as a result the pyramidal morphology. Likewise, negative bias field strength would repel intermediate species out of the substrate which would be accentuated as the field strength is increased (Figure 3.34 B). The repelling forces at negative bias $10 - 15 \times 10^2$ Vm^{-1} produced a stretching effect in the intermediate species giving as a result elongated nanoparticles in the microstructure (Samples P and Q). However, as the field strength was increased, the repelling forces also increased. Hence, intermediate species may have bounced off the substrate as suggested by the spherical morphology and low thickness.

In AC deposited films, higher field strengths (Samples F and G) would have induced enough acceleration to repel the precursor out of the substrate but less than DC electric fields, which are continuously exerted on that direction. As a consequence, higher AC field strengths would have favoured spherical nanoparticles and similar thickness to positive bias deposited films at higher field strength (Sample M).

The effect of AC electric fields on the microstructure is subjected to the switching nature of it. Knowing the frequency, the time between field switches can be calculated using equation 3.3.

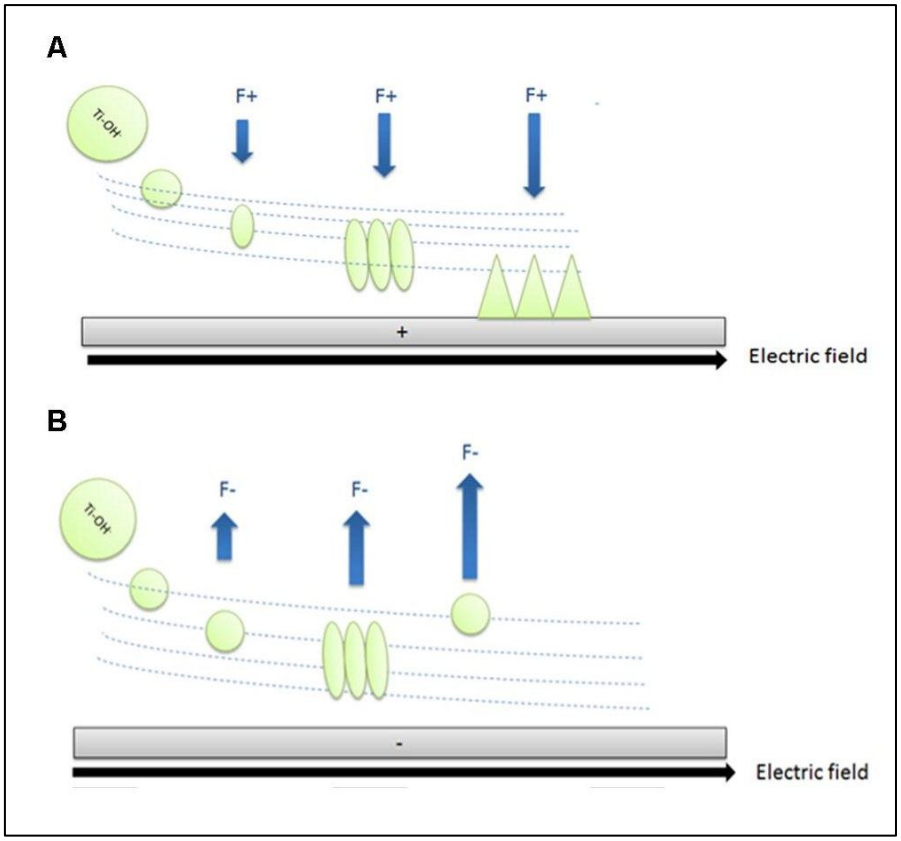

Figure 3.34: Sketch explaining how the interaction of electric fields with the intermediate species predominately produced elongated nanoparticles for positive bias (A) and spherical nanoparticles for negative bias (B).

$$t_{switch} = \frac{1}{f_q} \qquad \text{(Equation 3.3)}$$

Where: t_{switch} = Time between field switches (s)

f_q = Frequency of AC electric field (Hz)

Knowing that the frequency at which the electric field oscillates is 50 Hz, it is found that the time between switches is 0.02 s. As all reactions were conducted for several minutes, the precursor can interact with different fields before or during nucleation. This highly depend on the residence time of the precursor in the reaction chamber, which is given by equation 3.4 [119].

$$t_{res} = \frac{V}{F} \qquad \text{(Equation 3.4)}$$

Where: t_{res} = Residence time (s).

V = Volume of the reaction chamber (cm^3).

F = Volumetric flow ($cm^3\ s^{-1}$).

This expression gives information about the average time that the molecule gas spends in the chamber, ignoring any deposition or other reactions. For the ease of the study, it will be assumed that the precursor only flows in one direction at a constant speed. When the top plate and substrate glass are placed into the reactor, this has dimensions of 1 cm x 4.5 cm x 15 cm. [148].

$V = h\ x\ l\ x\ w = 1\ x\ 4.5\ x\ 15 = 67.5\ cm^3$

Where: h = Height of the reaction chamber.

l = Length of the reaction chamber.

w = Width of the reaction chamber.

The gas flow rate used at fixed conditions was 2 $L.min^{-1}$. Thus, converting into $cm^3\ s^{-1}$:

$F = 2\ L\ min^{-1} = 2000\ cm^3\ min^{-1} = 33.3\ cm^3\ s^{-1}$

Substituting these values into equation 3.4;

$t_{res} = \frac{67.5}{33.3} = 2.03$ s

Knowing the residence time of the precursor and the frequency of the electric field, it is possible to know the number of changes in bias (equation 3.5).

$N_{bias} = t_{res} \times f_q$ ..... (Equation 3.5)

Where: t_{res} = Residence time (s).

f_q = Frequency of AC electric field (Hz)

Thus,

$N_{bias} = 2.03 \times 50 = 101.5 \approx 102$.

In other words, during a residence time of 2.03 s the precursor can be influenced by a maximum of 102 changes throughout deposition. This would have produced a reduction in particle size and film thickness of AC deposited films comparing to DC deposited films.

The interaction of electric fields with the intermediate species was also revealed by the changes in preferred crystallographic orientation. As it was observed in the morphology and film thickness, the induction of AC electric fields produced a retarding effect of the intermediate species which also influenced the crystal orientation by increasing the texture coefficient in the (004) plane (Sample B) (Figure 3.35). As the field strength was increased the acceleration of the intermediate species towards the surface also increased which produced fluctuations in the texture coefficient values (Samples C to D). At higher field strength ($20 – 30 \times 10^2$ Vm^{-1}) the preferred crystal orientation changed from the (004) to the (211) plane. It seemed that the acceleration induced to the intermediate species by the field strength was high enough to make them rotate either in the gas phase or during nucleation. This effect was accentuated with the field strength as the increase in the texture coefficient in the (211) plane revealed (Sample G).

A similar behaviour was observed in DC deposited films. The induction of positive bias electric fields produced a change in the crystal orientation from the (004) to the (211) plane (Sample H). However, the texture coefficient values in the (004) and (211) planes did not differ in a great magnitude. As the positive bias field strength was increased the texture coefficient in the (211) plane gradually decreased to show preferred orientation in the (004) plane (Sample I to L). At higher field strength the preferred orientation changed from (004) to (211) (Sample M). The application and increase of negative biased electric fields caused higher preferred orientation in the (004) plane than positive biased deposited films. Thus, it seems that surface effect is favoured with negative biased field strength, which suggests a surface dipole directed growth. The films grown with positively biased surfaces were less textured than in the samples grown with the reverse bias. This has been previously attributed to crystallographic orientation effects as the result of surface dipole direction [133]. The reduced textured films deposited on the positively biased surfaces give support to this argument. The reactions occurring at the positively biased surface are likely to be quicker (as the implied growth rate is faster), this would mean that any surface dipole

effects would be expected to be less prevalent and the subsequently deposited film less textured.

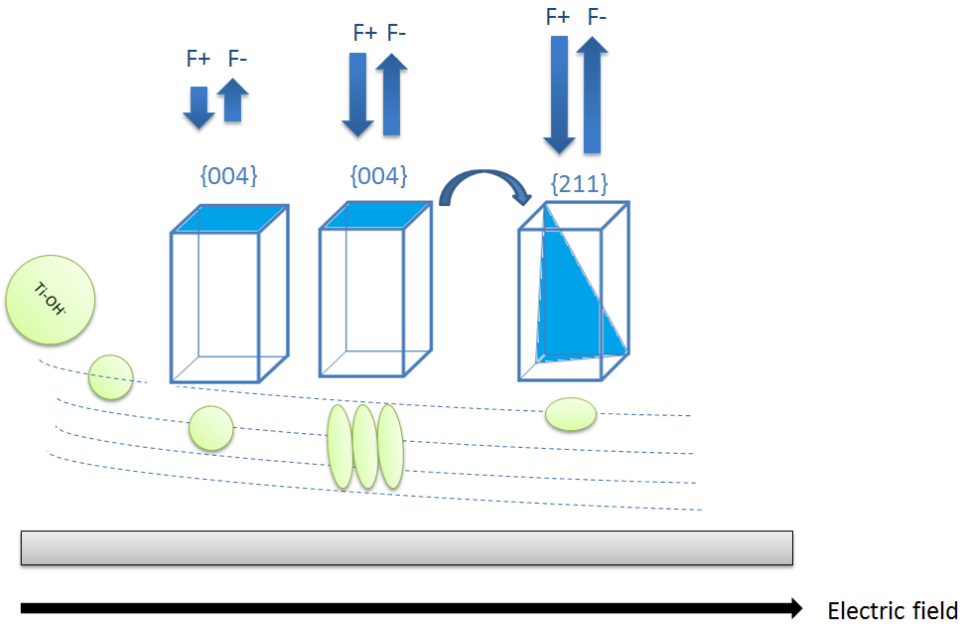

Figure 3.35: Sketch explaining how the interaction of electric fields with the intermediate species induced changes in the preferred crystal orientation of AC deposited films.

Generally, AC electric fields influenced surface roughness by varying deposited film thickness. Thus, higher surface roughness was found for thicker films. However, surfaces were found to bevery heterogenic and no direct relationship was found between the field strength applied and the surface roughness. Likewise, surface roughness seemed to have had little effect on the water-contact angles as all surfaces showed hydrophilicty for different RMS values.

3.3.2. Photocatalytic properties at fixed conditions

All films deposited at fixed conditions under the influence of AC electric fields showed higher photo-activity than the films produced in absence of electric fields. In particular, sample E showed the highest photocatalytic activity with half-life values of

3.9 minutes. As Table 3.3 showed, sample E was strongly oriented along the (004) plane, which has been reported to favour reactivity due to surface atoms configuration [45]. Samples D and F showed the second best photo-activity with half-life values of 6 minutes. Sample D showed the highest texture coefficient value in the (004) but sample F showed a slightly higher texture coefficient in the (211) plane. Bearing in mind the low surface energy of the (211) plane, the photo-activity was high. Nevertheless, this sample had a particularly small particle and crystallite size (Table 3.2), which are also believed to play an important role in titania photocatalytic activity [158,159]. As particle size decreases, the surface area to volume ratio increases which generally favours the photo-activity by increasing active sites. The shape of particles is also known to be an important factor in determining photocatalytic activity[42]. As stated in section 1.4.1.1.3, long – shaped crystals allow the easy transfer of electrons along the long direction, hindering recombination. Thus, the elongated shape found for samples D and E would have enhanced the photocatalytic activity, most likely due to an effective separation of electron-hole pairs in the (004) plane.

Sample B presented a small crystallite size and particle size as well as a preferred orientation in the favoured (004) plane. However, the photocatalytic activity obtained from this sample was poor (half-life = 24.2 min). Sample B showed spherical agglomerations which would have favoured the creation of grain boundaries. Furthermore, it was observed that this sample was poorly wetting even after exposure with UV light (Table 3.5). This is likely to inhibit the formation of hydroxyl radicals on the film surface, reducing the photocatalytic performance; indeed it will also reduce the absorption of the dye onto the surface. Sample B also showed close RMS values (20 nm) to the other two samples which showed poor photo-activity (sample B and G). Generally, the increase of surface roughness favours the photo-activity of deposited films by increasing the surface area [160]. However, titania photocatalytic activity is determined from an optimum balance between film thickness, grain size and surface area [159].

Generally, the application of DC electric fields had a detrimental effect on the photo-activity of deposited films. Only three samples showed better photo-activity than sample A (sample K, M and S). This can be attributed to a bigger agglomerate and crystallite size as well as higher thickness. As stated in section 1.4.1.1.4, high thickness can impede the effective charge carrier transfer to the surface.

3.3.3. Modifications in microstructure at different conditions

As expected, increasing deposition time (5 – 10 minutes) produced a gradual increase of films thickness (conditions 1 – 3 and 13 – 15). Condition 3 (deposition time = 15 minutes) showed similar thickness to the reference sample (Ref E) as the deposition time for this last sample was 17 minutes. However, condition 15 showed lower thickness than the reference sample (Ref J) as the deposition time for this last sample was 20 minutes. At 15 x 10^2 Vm^{-1} the agglomerate size is bigger after 10 minutes (condition 2) than after 15 minutes deposition time (condition 3). Furthermore, it was observed a progressive change in the morphology of the long-shaped nanoparticles to form clusters. However, DC deposited films showed similar agglomerate size and morphology (conditions 14 and 15). This gives further evidence that alternate currents influence the coarsening of particles through fluctuating interactions with the precursor in the gas phase or during nucleation over time.

Previous studies have revealed that titania thin films morphology can be influenced by the substrate temperature and TTIP mole fraction [34]. Increasing the concentration, and thus the precursor feed rate, results in more molecules in the gas phase and a shorter collision time, which favours the materials growth rate and the agglomerate size [161] Increasing TTIP concentration favoured film thickness growth regardless the voltage applied (conditions 4 – 5 and 16 – 17). However, the interaction of AC and DC electric fields produced a reduction in the particle size (conditions 5 and 17). Thus, electric fields might have interacted in the coarsening during nucleation reducing the particle size as observed in previous work [24,133,156].

Further increase in the precursor concentration (0.25 M) produced an important decrease in film thickness (conditions 6 and 18), which could be attributed to the difficulty to form aerosol at higher concentration and therefore, higher viscosity [127]. However, the SEM images of sample 6 evidence an increase of the nucleation in the gas phase as explained in previous sections (Figure 1.16). It was expected that an increase of the precursor concentration would lead to bigger agglomerate size as a result of an increase of the feed rate. However, this was only shown for AC deposited films (condition 6). The interaction of DC electric fields with the increasing concentration (conditions 16 – 18) produced not only a gradual change of morphology

but also a continuing decrease in particle size, which gave evidence of more reactive surfaces.

As illustrated in Figure 1.15, deposition rate is favoured with increasing temperatures. This was shown for conditions 7 – 9 and 19 – 21. T emperatures below 350 °C (conditions 7 and 19) did not favour the activation energy for the reaction to occur. This was evidenced by a low thickness and absence of crystallinity in Raman spectroscopy and XRD. Increasing the substrate temperature produced a gradual enhancement of the crystallinity and favoured the nucleation of elongated nanoparticles as a result of the interaction with the field strength.

Increasing gas flow rate produced different behaviour for AC and DC electric fields (conditions 10 – 12 and 22 – 24). As stated in section 1.5.1.4, decreasing the gas velocity produces an increase of the boundary layer thickness which hinders the diffusion of reactants to the substrate. As a result, low flow rates produce a decrease in film thickness as observed for conditions 22 –24. However, a different behaviour was observed in AC deposited films. The combination of the increase of the boundary layer and the retarding effect induced by the AC field strength produced a gradual decrease of film thickness with the gas velocity. This was also evidenced by the changes in particle morphology. In AC deposited films, the retarding effect induced by the electric fields with the increase of the gas velocity produced spherical nanoparticles as a result of a low interaction with the charged surface. A similar explanation can be applied to the changes in particle size observed in DC deposited films. Thus, the increase of the gas velocity gradually decreased the boundary layer thickness which with the kinetic energy induced to the precursor favoured a quick nucleation on the surface and a decrease in the particle size.

The different conditions tested also influenced the preferred crystal orientation. All deposited films showed a preferred crystal orientation in the (004) plane except for conditions 6 and 13 which showed preferred crystal orientation in the (211) plane. The texture coefficient for condition 13 in the (211) plane was similar to that of the (004) plane which denoted a low preferential orientation. However, condition 6 revealed a high texture coefficient in the (211) plane, which can be attributed to a decrease of the growth rate as a result of an increase of gas phase reaction [115].

AFM results did not show a relevant connection between the experimental conditions and the surface roughness. As an exception AC deposited films showed rougher surfaces with deposition time as a result of an increase of the growth rate. A decrease of the surface roughness was observed with increasing temperatures for AC and DC electric fields, which can be attributed to an enhancement of crystals assembly. Likewise, surface roughness decreased with the gas velocity which was more accentuated in DC deposited films.

In any case, the surface roughness seemed to have little effect on the water-contact angles of surfaces as all deposited films showed hydrophilicity independently of their RMS values.

3.3.4. Photocatalytic properties at different conditions

The photo-activity of TiO_2 thin films significantly depended on the optimum experimental conditions.

Deposition time

In AC deposited films, the most photoactive film was the reference sample (Ref E, 3.9 min). Thus, it was observed that the optimum deposition time was that for the depletion of the precursor (18 min). For DC deposited films, the most photoactive film was produced at a deposition time of 15 min (condition 15) with a half-life value of 22.5 min. Although the difference with the reference sample was not significant (Ref J, 23.5 min), reducing the deposition time also reduced the film thickness, which could have slightly enhanced the photo-activity.

Precursor concentration

Different trends were observed for films deposited from AC and positive bias DC electric fields. For AC deposited films, the increase in TTIP concentration favoured the photocatalytic performance (from 12.2 min to 4.5 min). However, the optimum performance was found for the reference sample with a precursor concentration of 0.17 M (Ref E). DC deposited films showed lower photo-activity with increasing concentration (21.8 min to 22.1 min), but in all cases the photo-activity was greater

than that of the reference sample (Ref J). In any case, AC deposited films showed significantly higher photo-activity than DC deposited films. The combination of the progressive increase of nucleation in the gas phase with increasing concentration and the retarding effect induced to the precursor would have produced favourable changes in morphology and film thickness.

Substrate temperature

Substrate temperatures below 450 °C caused detrimental effects on the photo-activity of deposited films. AC and DC deposited films showed similar photo-activity with half-life values of 25.9 – 26 min for AC and 25.7 – 23.1 min for DC. Films produced at 300 °C showed poor crystallinity, which would have influenced the photo-activity. At higher temperatures, films showed higher crystallinity. In addition, the increase of the substrate temperature produced a progressive reduction of the particle size in DC deposited films, which would have positively affected the photo-activity. Furthermore, condition 21(with a substrate temperature of 400 °C) was found the most photoactive of all DC deposited films.

Gas flow rate

Gas flow rate values below 1 $L.min^{-1}$ but above 2 $L.min^{-1}$ produced detrimental effects on titania photocatalytic performance for AC deposited films with half-life values of 22 min and 23.2 min, respectively. The morphological changes induced by AC electric fields under these conditions (discussed in section 3.4.3) would have hindered the photo-activity of deposited films.

3.4. Conclusions

The application of electric fields during the EACVD reaction of TTIP in toluene at fixed conditions induced changes in the particle size and shape, film thickness and crystal orientation. These induced changes in the microstructure influenced the photo-activity of the material, which was favoured by the application of AC electric fields. In any case, it was observed that an optimum photocatalytic performance can be obtained by tailoring the experimental conditions, which differ depending on the electric field applied. Titania thin films produced under AC electric fields showed an

optimum photo-activity at a deposition time of 17 minutes, TTIP concentration of 0.17, substrate temperature of 450 °C, M and gas flow rate of 2 $L.min^{-1}$. DC deposited films showed better photo-activity for deposition time of 20 minutes, TTIP concentration of 0.17, substrate temperature of 400 °C and gas flow rate of 2 $L.min^{-1}$

Chapter 4:

Titanium Dioxide Thin Films Produced from the Electric Field Assisted Aerosol Chemical Vapour Deposition of Titanium (IV) Chloride in Toluene

4.1. Introduction

Titanium dioxide has been extensively produced from aerosol assisted chemical vapour deposition (AACVD) processes typically using Titanium Isopropoxide (TTIP) as a precursor. To the best of our knowledge no AACVD process to produce (TiO_2) has been reported using Titanium (IV) chloride ($TiCl_4$) as a source. This can be partially due to the high volatility of this metal halide which in presence of humid air reacts forming opaque clouds of TiO_2 and hydrogen chloride (HCl). This chapter presents the results on the experimental study of the TiO_2 thin films growth from Electric Field Assisted AACVD using $TiCl_4$ as a precursor.

4.2. Results

4.2.1. Film synthesis and characterisation of AC deposited films

This section presents the results obtained for the AC EACVD deposited films at 450 °C and 1 $L.min^{-1}$ (Table 2.3) and at 600 °C and 5 $L.min^{-1}$ (Table 2.4). All deposited films tested presented good adherence passing the scratch test using Scotch tape test and a piece of towel. XRD was conducted to identify titania crystal phases but the lack of crystallinity of the films made it difficult. Raman spectroscopy techniques were used to quantify the relative ratio of anatase and rutile phases which are shown in Table 4.1.

Table 4.1: Experimental conditions and material phases of deposited films from the AC EACVD reaction of 1M titanium (IV) chloride solution in toluene. Samples A - G were produced at 600 °C and 5 $L.min^{-1}$ .Samples H – L produced at 450 °C and 1 $L.min^{-1}$.

Sample	Applied Voltage (V)	Field Strength (Vm^{-1})	Material Phase	
			Unannealed	Annealed
A	0	0	Rutile	Rutile
B	1	1×10^2	Rutile/Anatase	Anatase/Rutile
C	5	5×10^2	Rutile/Anatase	Rutile
D	10	10×10^2	Rutile/Anatase	Rutile
E	15	15×10^2	Anatase/Rutile	Anatase/Rutile
F	20	20×10^2	Anatase/Rutile	Anatase/Rutile
G	30	30×10^2	Anatase/Rutile	Rutile/Anatase
H	0	0	Anatase	--
I	10	10×10^2	Anatase	--
J	15	15×10^2	Anatase	--
K	20	20×10^2	Anatase	--
L	30	30×10^2	Anatase	--

Scanning electron microscopy

Scanning electron microscopy (SEM) images of the deposited titanium dioxide films at 600 °C and 5 $L.min^{-1}$ are shown in Figure 4.1. It was observed that films presented a different morphology, particle size and thickness depending on the field strength applied (Table 4.2). Films deposited in the absence of an applied electric field revealed angular agglomerations of 150 ± 5 nm in length with a secondary growth of rod-like nanoparticles of 83 ± 17 nm length. The thickness for sample A was found to be 82 ± 9 nm (Figure 4.1 A). Applying an electric field and increasing the field strength ($1 \times 10^2 - 5 \times 10^2$ Vm^{-1}) caused the microstructure to change to that of spherical nanoparticles 5 – 8 nm in diameter forming larger aggregates of 95 ± 7 nm – 92 ± 12 nm diameter (Figure 4.1 B and 1C). The thickness in this range of field strength was found to decrease to 4 ± 1 nm – 17 ± 6 nm. Increasing the field strength to $10 \times 10^2 - 20 \times 10^2$ Vm^{-1} led to further systematic changes in the microstructure of the deposited films. Between $10 \times 10^2 - 15 \times 10^2$ Vm^{-1} the shape changes from angular 86 ± 6 nm particles (Figure 4.1 D) to spherical nanoparticles 70 ± 6 nm in diameter

(Figure 4.1 E) and the film thickness increases to 116 ±10 nm – 93 ± 13 nm, respectively. Increasing the field strength to 20 x 10^2 – 30 x 10^2 Vm^{-1}) produced elongated nanoparticles of 112 ± 24 nm length (Figure 4.1 F) and rod-like nanoparticles 135 ± 70 nm length (Figure 4.1 G). The film thickness decreased to 11 ± 10 nm and 2 ± 0.8 nm, respectively.

In order to improve the crystallinity, deposited films were annealed in air at 600 °C for 2 h. Figure 4.2 shows the SEM images of the annealed films. The annealing process resulted agglomeration of particles increasing the particle size to 248 ± 17 nm for films deposited with no electric field (Figure 4.2 A). The annealing of deposited films B and C (1 x 10^2 – 5 x 10^2 Vm^{-1}) produced agglomeration of particles forming clusters of 170 ± 12 nm (Figure 4.2 B) and 150 ± 16 nm (Figure 4.2 C). For samples D & E the annealing process not only produced an increase of particle size to 160 ± 8 nm (Figure 4.2 D) and 280 ± 8 nm (Figure 4.2 E) but also better defined particles. The annealing produced an agglomeration of the elongated nanoparticles in samples F & G forming clusters of 330 ± 33 nm in length (Figure 4.2 F) and angular independent particles of the same size (Figure 4.2 G).

SEM was also conducted for thin films produced at substrate temperature 450 °C and gas flow rate 1 $L.min^{-1}$ for comparison purposes. In absence of electric fields the film produced showed a porous microstructure in which no individual particles could be distinguished (Figure 4.3 H). The film thickness was very low and found to be 2 ± 0.6 nm. The introduction of the field strength of 10 x 10^2 Vm^{-1} produced a differentiation of spherical particles of 170 ± 5 nm in length (Figure 4.3 I) but no change in film thickness. At 15 x 10^2 Vm^{-1}, deposited films showed a decrease in particle size and a different morphology with well-defined particles of 130 ± 4 nm in length and film thickness of 60 ± 20 nm. At higher field strength (20 x 10^2 – 30 x 10^2 Vm^{-1}) deposited films exhibited agglomerated spherical particles of 120 ± 15 nm – 200 ± 26 nm in diameter and the film thickness dramatically increased to 300 ± 10 nm (Figure 4.3 K – L)..

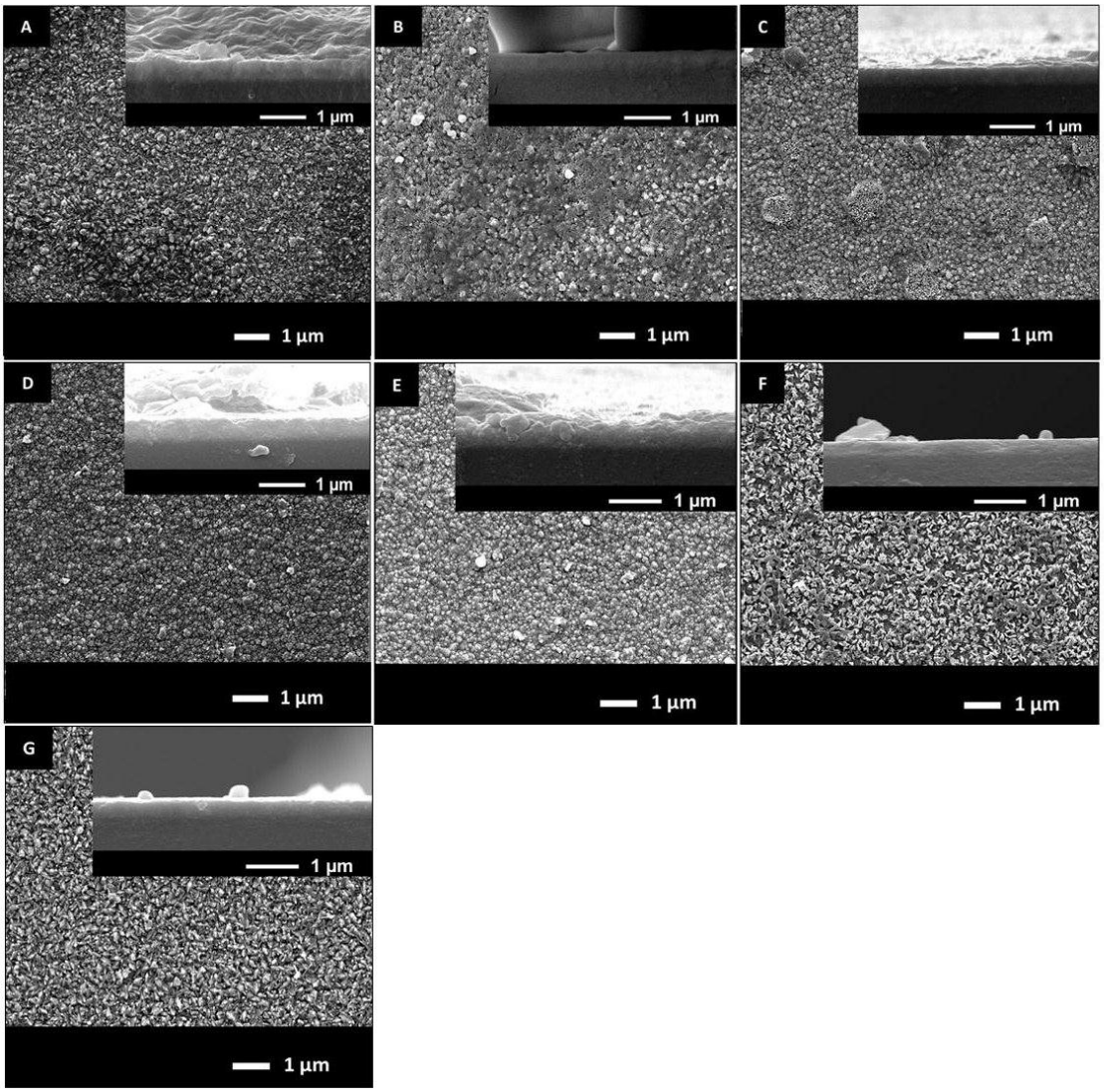

Figure 4.1: Scanning Electron Microscope images of samples prepared the AC EAACVD reaction of 1M$TiCl_4$ solution in toluene at 600 °C and 5 L.min^{-1} before annealing with representative cross section images. A) 0 Vm^{-1}, B) 1 x 10^2 Vm^{-1}, C) 5 x 10^2 Vm^{-1}, D) 10 x 10^2 Vm^{-1}, E) 15 x 10^2 Vm^{-1}, F) 20 x 10^2 Vm^{-1}, G) 30 x 10^{2}Vm^{-1}. Side-on images were captured at 30,000 magnification and cross-section images at 40,000 magnification.

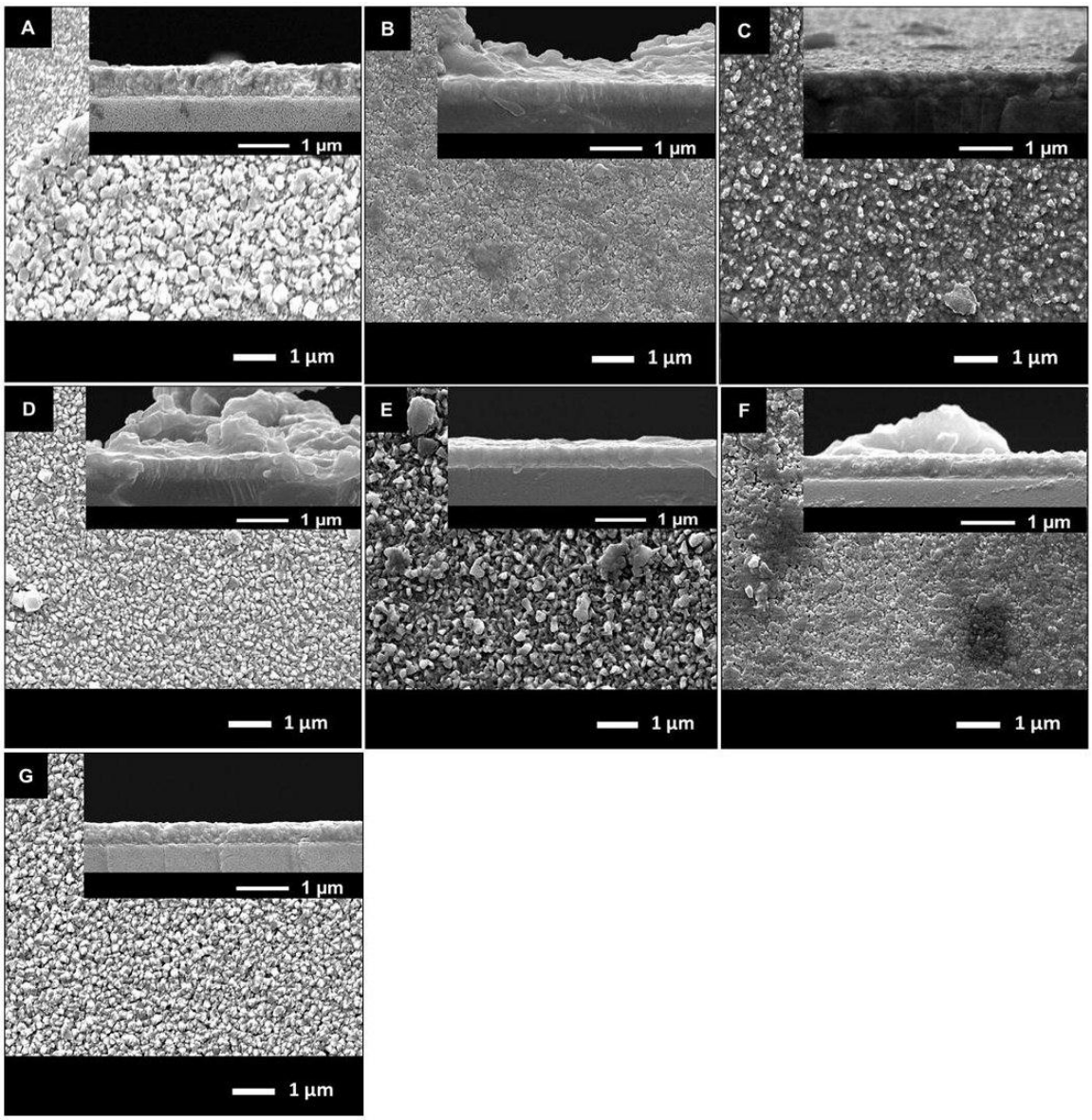

Figure 4.2: Scanning Electron Microscope images of deposited films at 600 °C and 5 $L.min^{-1}$ annealed in atmospheric air at 600 °C for 2 h with representative images of cross section. A) 0 Vm^{-1} , B) 1 x 10^2 Vm^{-1}, C) 5 x 10^2 Vm^{-1}, D) 10 x 10^2 Vm^{-1}, E) 15 x 10^2 Vm^{-1}, F) 20 x 10^2 Vm^{-1}, G) 30 x 10^2 Vm^{-1}. All images were captured at 40,000 magnification.

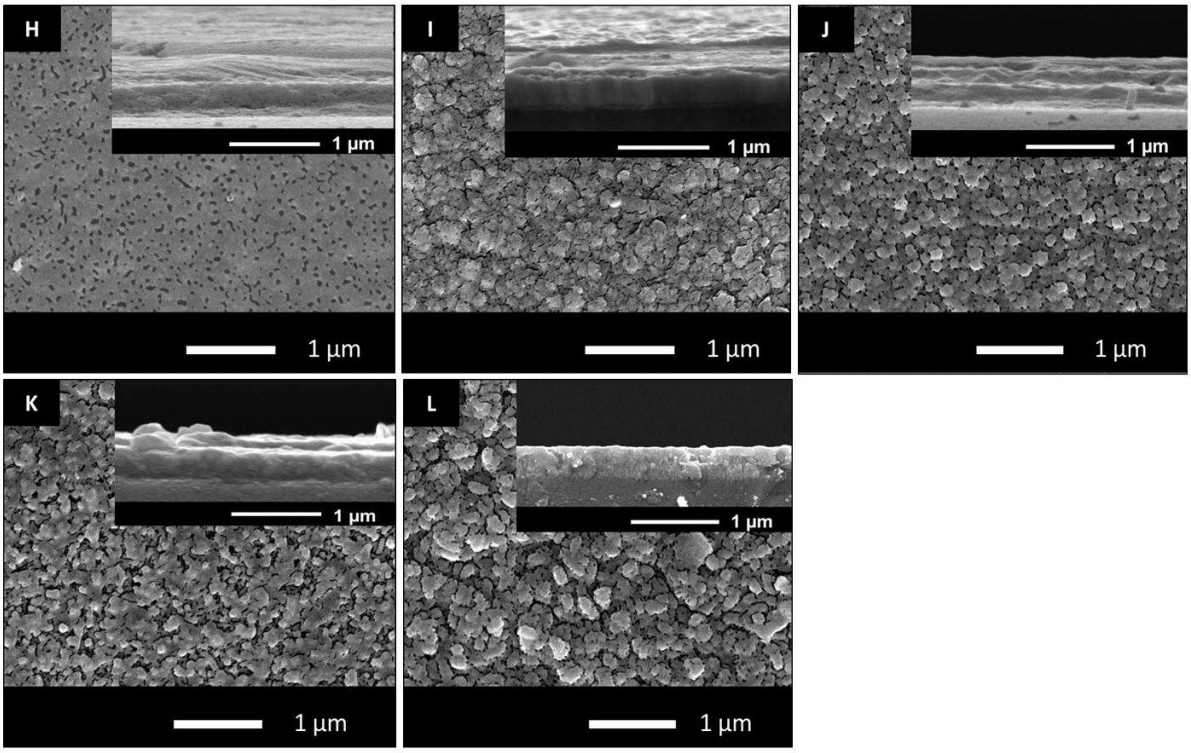

Figure 4.3: Scanning Electron Microscope images of films produced from the AC EAACVD reaction of 1 M $TiCl_4$ solution in toluene at 450 °C and gas flow rate of 1 $L.min^{-1}$ with representative cross-section images. H) 0 Vm^{-1} , I) 10 x 10^2 Vm^{-1}, J) 15 x 10^2 Vm^{-1}, K) 20 x 10^2 Vm^{-1}, L) 30 x 10^2 Vm^{-1}. Side-on images were captured at 80,000 magnification and cross-section images at 60,000 magnification.

Different particle morphologies, particle size and film thickness values were found for different substrate temperature and gas flow rate conditions. In particular, it was observed that films produced with lower substrate temperature (450 °C) and gas flow rate (1 $L.min^{-1}$) tended to produce bigger agglomerations for the same field strength tested. However, a different behaviour for film thickness was observed. Films deposited at lower substrate temperature and gas flow rate showed increasing thickness with the field strength whereas films produced at 600 °C and 5 $L.min^{-1}$ showed the opposite trend. Furthermore, for the last, it was found that the annealing process increased film thickness for Samples A, B and G, as well as particle size in all films tested and (Figure 4.4).

Table 4.2: Agglomerate size (nm) and film thickness (nm) with standard error (SE) (nm) for deposited films from AC EACCVD at 600 °C and 5 L.min^{-1} (A to G) and at 450 °C and 1 L.min^{-1} (H to L).

Sample	Applied Voltage (V)	Field Strength (Vm^{-1})	Agglomerate size ± SE (nm)		Thickness ± SE (nm)	
			Unannealed	Annealed	Unannealed	Annealed
A	0	0	150±5 83±17	248±17	82±9	128±16
B	1	1 x 10^2	95±7	170±12	4±1	32±10
C	5	5 x 10^2	92±12	155±16	17±6	12±7
D	10	10 x 10^2	86±6	163±8	116±10	32±8
E	15	15 x 10^2	70±6	277±8	93±13	2±1
F	20	20 x 10^2	112±24	326±46	11±10	3±1
G	30	30 x 10^2	135±70	333±33	2±0.8	5±2
H	0	0	--	--	2±0.6	--
I	10	10 x 10^2	166±5	--	2±0.7	--
J	15	15 x 10^2	134±4	--	63±19	--
K	20	20 x 10^2	124±15	--	12±3	--
L	30	30 x 10^2	202±24	--	305±9	--

X-ray diffraction

X-ray diffraction (XRD) analysis was conducted and compared to previous investigations (JCPDS database file 021-1272) to examine the phases present in the samples. As indicated above, XRD examination was hindered by strong peaks from the cassiterite (SnO_2) substrate and it appeared that the TiO_2 films showed low crystallinity (Fig. 4.5 A). However, for samples D and G peaks from anatase and rutile can be clearly discerned in the pattern. The annealing process appeared to have little effect on the crystallinity of most of the deposited films (Fig. 4.5 B). Sample B exhibits a peak due to the (101) reflection of anatase. In the case of Sample D, the anatase peaks disappear but a new (040) rutile peak is observed. The annealed Sample G showed lower anatase content than the unannealed sample and more rutile peaks. That result is confirmed by the Raman spectroscopic analysis (below).

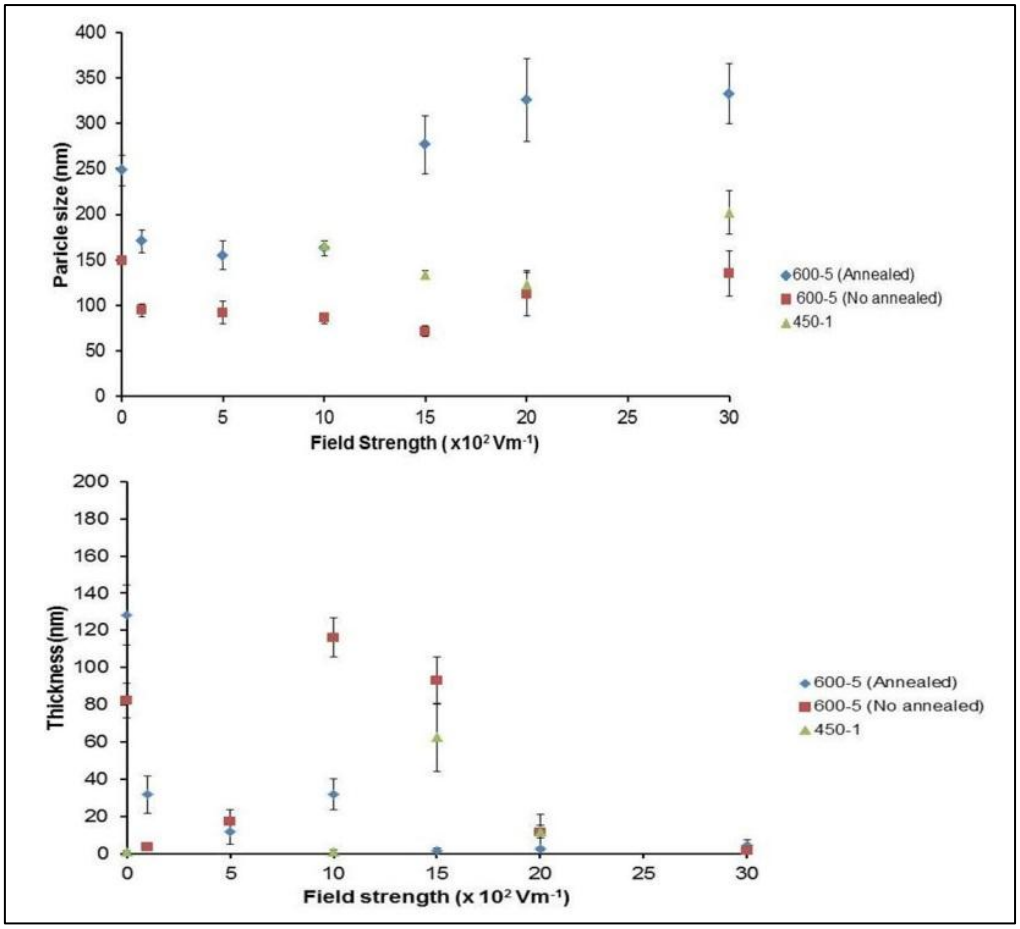

Figure 4.4: Particle size (up) and thickness (below) with corresponding standard error of TiO_2 thin films deposited films from the AC EAACVD reaction of 1 M $TiCl_4$ solution in toluene at 600 °C and 5 $L.min^{-1}$ (labelled as 600-5) before and after annealing and deposited films at 450 ºC and 1 $L.min^{-1}$ (labelled as 450-1).

Figure 4.6 shows the XRD pattern for deposited films at 450 °C and 1 $L.min^{-1}$ (Samples H to L). An improvement in the deposited films crystallinity as the applied field strength was increased was observed. The samples deposited with electric fields showed the characteristic peaks of anatase in the (004) plane (2 Theta = 37.8°) and rutile in the (211) plane (2 Theta = 54.3°). Samples I and L presented higher quality in terms of crystallinity showing also (101) and (200) anatase peaks, with a higher intensity recorded for sample L.

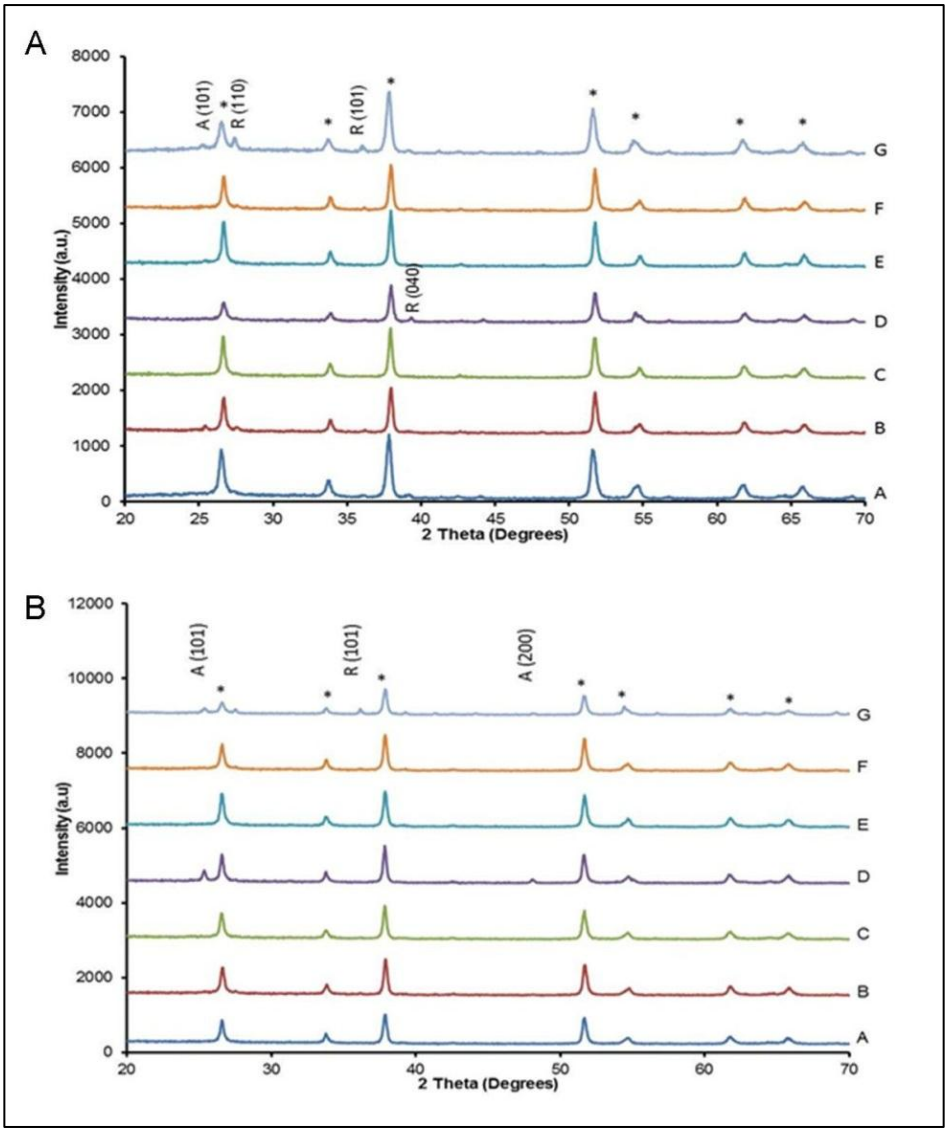

Figure 4.5: XRD patterns for samples prepared without an applied electric field and from the EAACVD reaction of 1M $TiCl_4$ solution in toluene at 600 °C and a gas flow rate of 5 $L.min^{-1}$ before (A) and after annealing (B). A) 0 Vm^{-1}, B) 1 x $10^2 Vm^{-1}$, C) 5 x 10^2 Vm^{-1}, D) 10 x 10^2 Vm^{-1}, E) 15 x 10^2 Vm^{-1}, F) 20 x 10^2 Vm^{-1}, G) 30 x 10^2 Vm^{-1}. **A** stands for anatase crystal phase and **R** for rutile. The peaks marked with dots denote the casserite peaks specific of SnO_2 crystalline phase, material used for the glass substrate coating.

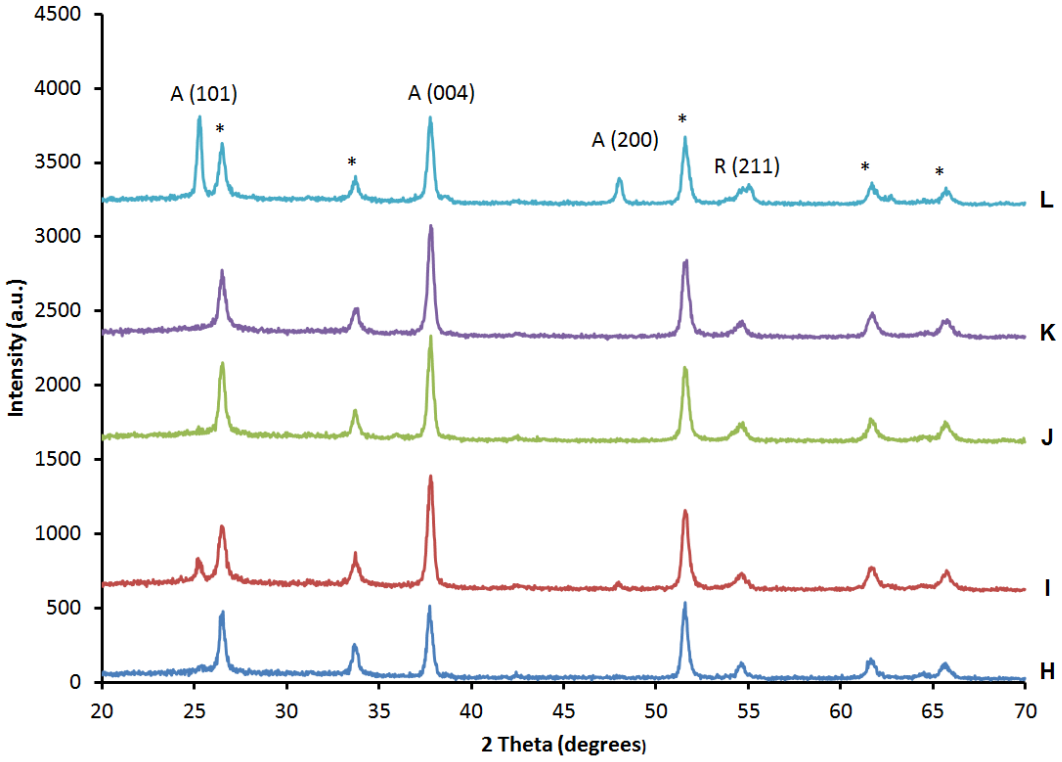

Figure 4.6: XRD pattern for deposited films at 450 °C and 1 L.min^{-1} H) 0 Vm^{-1}, I) 10 x 10^{2} Vm^{-1}, J) 15 x 10^{2} Vm^{-1}, K) 20 x 10^{2} Vm^{-1}, L) 30 x 10^{2} Vm^{-1}. The peaks marked with * denote cassiterite peaks of SnO_2 used for the glass substrate coating. A stands for anatase and R for rutile crystal phase.

Raman spectroscopy

Microbeam Raman spectroscopy was conducted to identify the TiO_2 phases present in deposited films and estimate their relative proportion for films deposited at 600 °C and 5 L.min^{-1} (samples A – G). Anatase was identified by its characteristic Raman peaks at 147 cm^{-1}, 198 cm^{-1}, 395 cm^{-1}, 513 cm^{-1}, 519 cm^{-1} and 642 cm^{-1} [134] for all deposited films (Figure 4.7). Rutile gave rise to Raman peaks at 446 cm^{-1} and 610 cm^{-1} [38] before and after annealing (Figure 4.7 A and B). Quantifiable values of the content of anatase and rutile in deposited films A – G were obtained by deconvoluting the overlapping rutile A_{1g} (612 cm^{-1}) and anatase E_g (639 cm^{-1}) contributions and inserting the % area of contribution of rutile component (x) into a predetermined equation derived from powder standards as previously reported [63]. The percentages of anatase and rutile for deposited films at 600 °C and 5 L.min^{-1} before and after annealing are shown in Table III. It was found that for the same experimental

conditions the phase assemblage was different depending on the field strength applied. Pure rutile was found for the film produced with no field strength. As the field strength is applied and increased (Samples B to D), anatase peaks start to appear with percentages varying from 40 to 49%. At higher field strength (Samples E to G) the percentage of anatase increased in comparison to the rutile crystal phase. Noteworthy, at 15 x 10^2 Vm^{-1} (Sample E) an important increase of percentage of anatase is produced (98%). The annealing process was found to give different results. For the film deposited with no electric field (Sample A) and film produced at 15 x 10^2 Vm^{-1} (Samples E) no changes in crystal phase were found. In some other cases, the annealing process produced an increase in percentage of anatase to values greater than 90% (Samples B and F). In the rest of cases, the annealing process gave as a result a decrease in anatase in the crystal phase showing 100% rutile for Samples C and D.

Raman spectroscopy for films produced at 450 °C and 1 $L.min^{-1}$ (Sample H to L) showed different crystal phase depending on the field strength (Figure 3 C). The film produced with no electric field (sample H) was amorphous and showed only the peak at 147 and 642 cm^{-1} corresponding to anatase. Raman quantification confirmed that this sample showed 100% anatase crystal phase (Table 4.3) The introduction and increase of electric fields improved the crystallinity of deposited films and, except for Sample J, all exhibited Raman peaks at 147 cm^{-1}, 395 cm^{-1}, 513 cm^{-1} and 642 cm^{-1}, corresponding to anatase [134]. Sample J showed peaks centred at 446 and 610 cm^{-1} [38], corresponding to rutile. Raman quantification confirmed an increase of the rutile content from 33% to 100% when applying and increasing the field strength (sample I –J). As the field strength was increased, the anatase content increased from 74% to 100% (samples K –L).

Atomic force microscopy

AFM was performed scanning over a 2 µm x 2 µm region in order to obtain Root Mean Square (RMS) roughness values as a proxy of surface roughness (Figure 4.8). As it can be observed, the application of AC electric fields slightly increased the surface roughness from 16 ± 6 nm to 31 ± 15 nm (Sample A and B). The increase of field strength produced a decrease in surface roughness to 11 ± 6 nm (Sample C). For the rest of field strength tested the surface roughness remained between 9 ± 2 nm and

8 ± 4 nm (Samples D to G). Deposited films at 450 °C and 1 L.min^{-1} (Figure 4.9) in absence of electric fields showed roughness values of 19 ± 11 nm. The induction of electric fields decreased the surface roughness to values close to 0.5 nm. The annealing produced a decrease in the surface roughness except from Samples A, D and G (Figure 4.10). Surface roughness values (RMS) can be seen in Table 4.4.

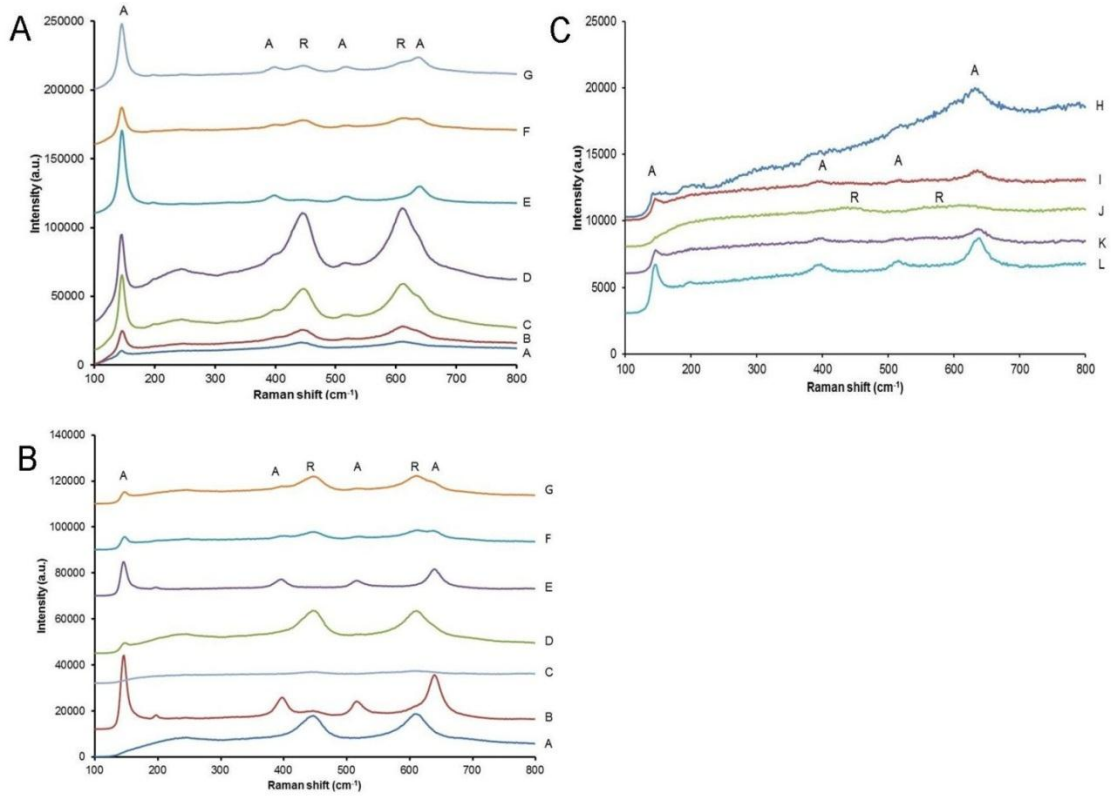

Figure 4.7: Raman spectra for unannealed films deposited from the AC EAACVD reaction of 1 M $TiCl_4$ in toluene at 600 °C and 5 L.min^{-1} (A) annealed deposited films at 600 °C for 2 h (B) and films deposited at 450 ºC and 1 L.min^{-1} (C). **A** stands for anatase and **R** for rutile.

UV-vis spectroscopy

UV-vis spectroscopy showed differences in transmission values in the visible region before and after the annealing for films deposited at 600 °C and 5 L.min^{-1}. As Figure 4.11 shows all deposited films except from Sample D presented higher maximum transmission values than those produced without electric field (Sample A), being Sample G (produced at 30 x 10^2 Vm^{-1}) the deposited film with the highest transmission value (77%). Maximum transmission values in the visible are listed in

Table 4.4. The annealing process seemed to have a favourable effect on the optical transparency of some deposited films but was detrimental to others. Thus, deposited films B to F showed maximum transmission values greater than 70%. Sample C showed the largest increase in transmission in the visible region (83%).

Table 4.3: Percentage of anatase and rutile calculated from Raman spectroscopy for AC deposited films at 600 °C and 5 L.min^{-1} before and after annealing at 600 °C for 2 h.

			Material Phase Raman			
			Unannealed		Annealed	
Sample	Applied Voltage (V)	Field Strength (Vm^{-1})	Rutile %	Anatase %	Rutile %	Anatase %
A	0	0	100	0	100	0
B	1	1 x 10^2	60	40	2	98
C	5	5 x 10^2	53	47	100	0
D	10	10 x 10^2	51	49	100	0
E	15	15 x 10^2	2	98	2	98
F	20	20 x 10^2	48	52	10	90
G	30	30 x 10^2	47	53	67	33
H	0	0	0	100	--	--
I	10	10 x 10^2	33	67	--	--
J	15	15 x 10^2	100	0	--	--
K	20	20 x 10^2	26	74	--	--
L	30	30 x 10^2	0	100	--	--

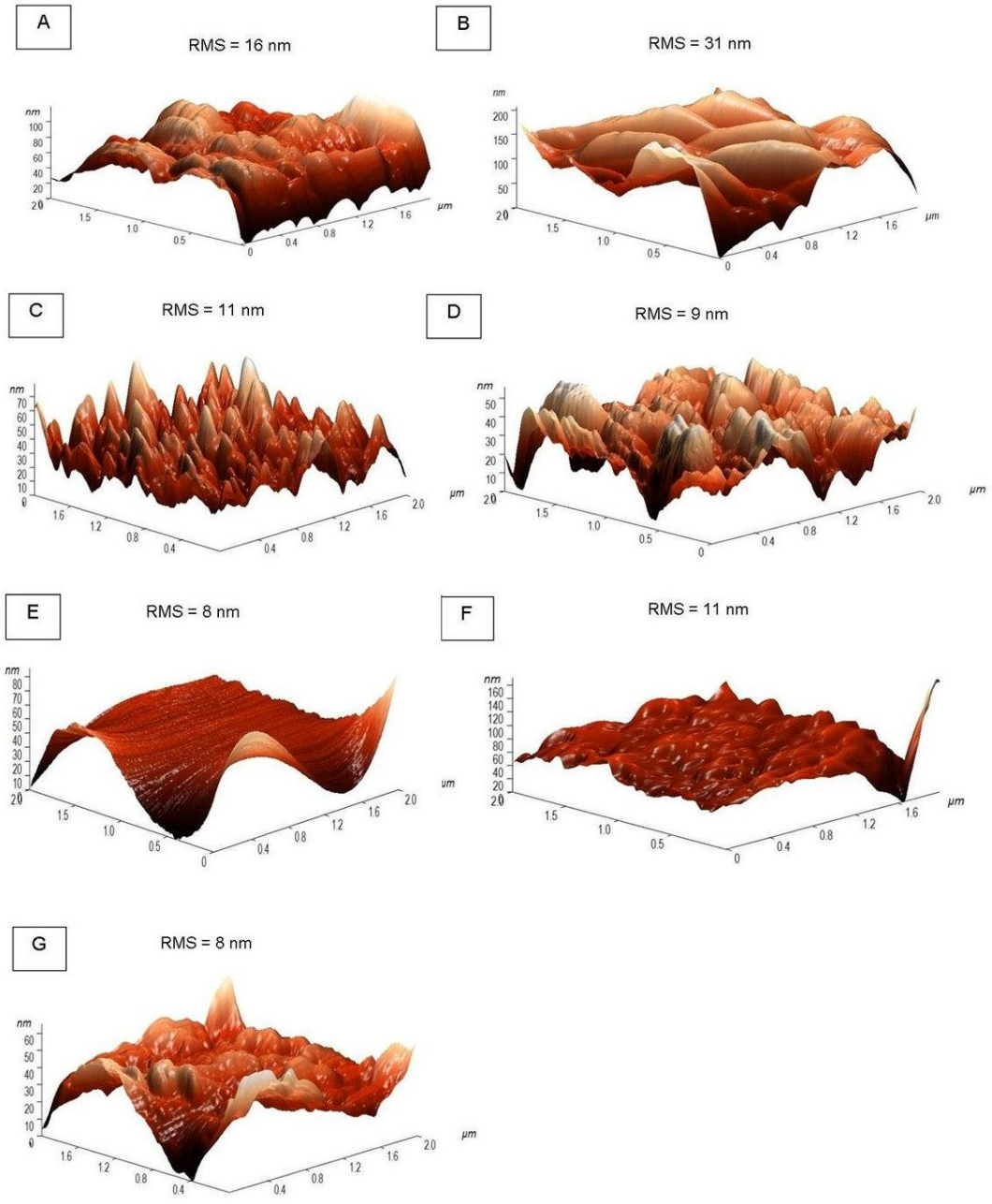

Figure 4.8: AFM images with corresponding Root Mean Square (RMS) values (nm) for films deposited from the AC EAACVD reaction of 1 M $TiCl_4$ in toluene at 600 °C and 5 $L.min^{-1}$ (samples A – G).

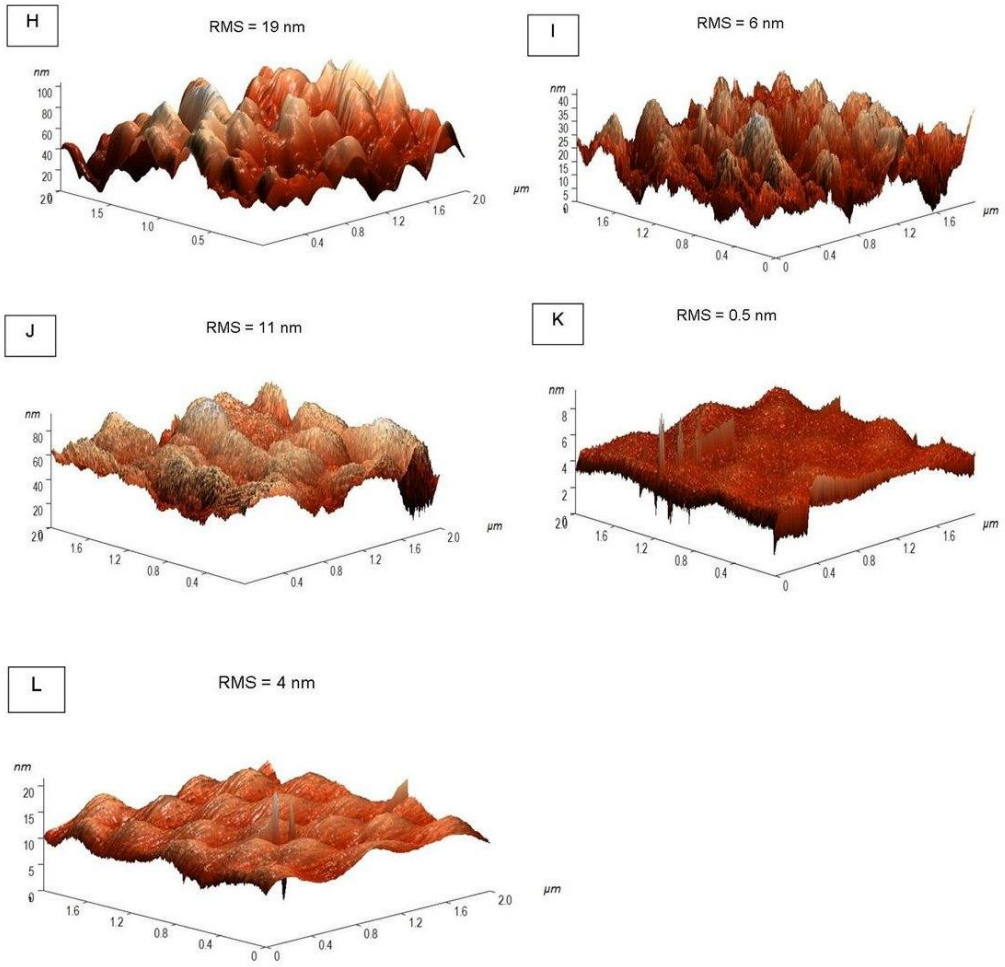

Figure 4.9: AFM images with corresponding Root Mean Square (RMS) values (nm) for films deposited from the AC EAACVD reaction of 1 M $TiCl_4$ in toluene at 450 ºC and 1 $L.min^{-1}$ (samples H – I).

Generally speaking, deposited films at 450 °C and 1 $L.min^{-1}$ showed higher transmission values in the visible (Figure 4.12). Film deposited in absence of electric fields (Sample H) showed transmission values of 75%. The application and increase of field strength from 10 x 10^2 – 15 x10^2 Vm^{-1} (samples I and J) decreased the transmission up to 59%. However, it was observed that at higher field strength (samples K and L) the transmission values increased up to 75%.

Direct band gap (DBG) analysis was performed using the Tauc method [154]. As presented in Raman analysis, field strength influenced the anatase/rutile composition of deposited films at 600 °C and 5 $L.min^{-1}$ and as a consequence, the direct band. It was found that different combination of anatase/rutile content resulted in different

direct band gaps. Thus, standard anatase band gap values between 3.1 to 3.3 eV were found for films which showed percentage of anatase from 39 to 53 % (sample B and samples E - G). The film which showed the lowest direct band gap were sample D (2.85 eV) and sample F (2.7 eV) which showed a percentage of anatase of 49 and 52 %, respectively. Deposited films which showed pure rutile after annealing (sample A, C and D) presented a band gap from 2.85 eV (sample D) to 3.1 (sample A and C). Likewise, deposited films which increased their content in anatase to 98% after annealing (sample B and E) showed a direct band gap of 3.2 eV, typically of this polymorph. Although sample G showed a decrease in anatase after annealing (33%) the direct band gap value remained 3.2 eV. Surprisingly, the film which showed the lowest direct band gap after annealing was sample F (2.7 eV) which had increased the content in anatase to 90%. Films deposited at 450 °C and 1 L.min^{-1} (samples H to L) showed standard direct band gap values for anatase crystal phase. The sample which showed the lowest band gap value was sample K (2.8 eV).

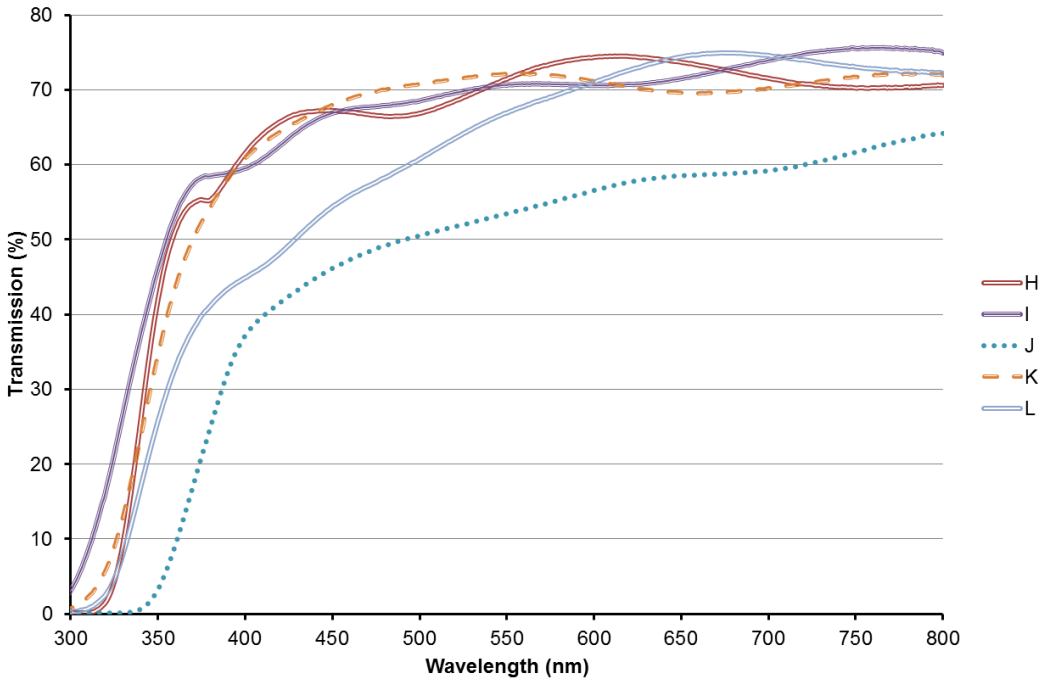

Figure 4.12: UV-vis spectroscopy for films deposited from the AC AACVD reaction of 1 M $TiCl_4$ in toluene at 450 °C and 1 L.min^{-1} (Samples H to L).

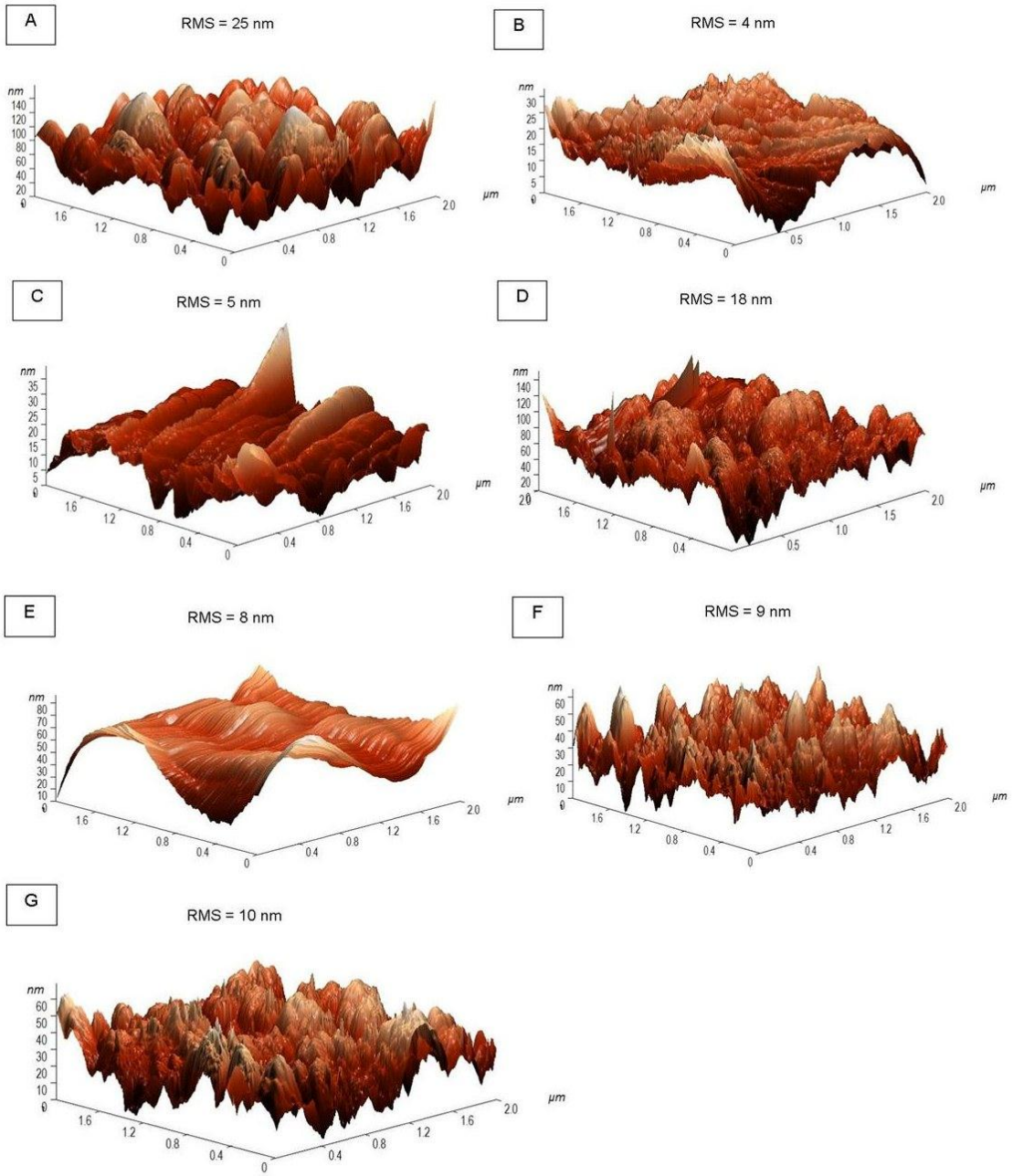

Figure 4.10: AFM images with corresponding Root Mean Square (RMS) values (nm) for films deposited from the AC AACVD reaction of 1 M $TiCl_4$ in toluene at 600 °C and 5 $L.min^{-1}$ after annealing at 600 °C for 2 hours.

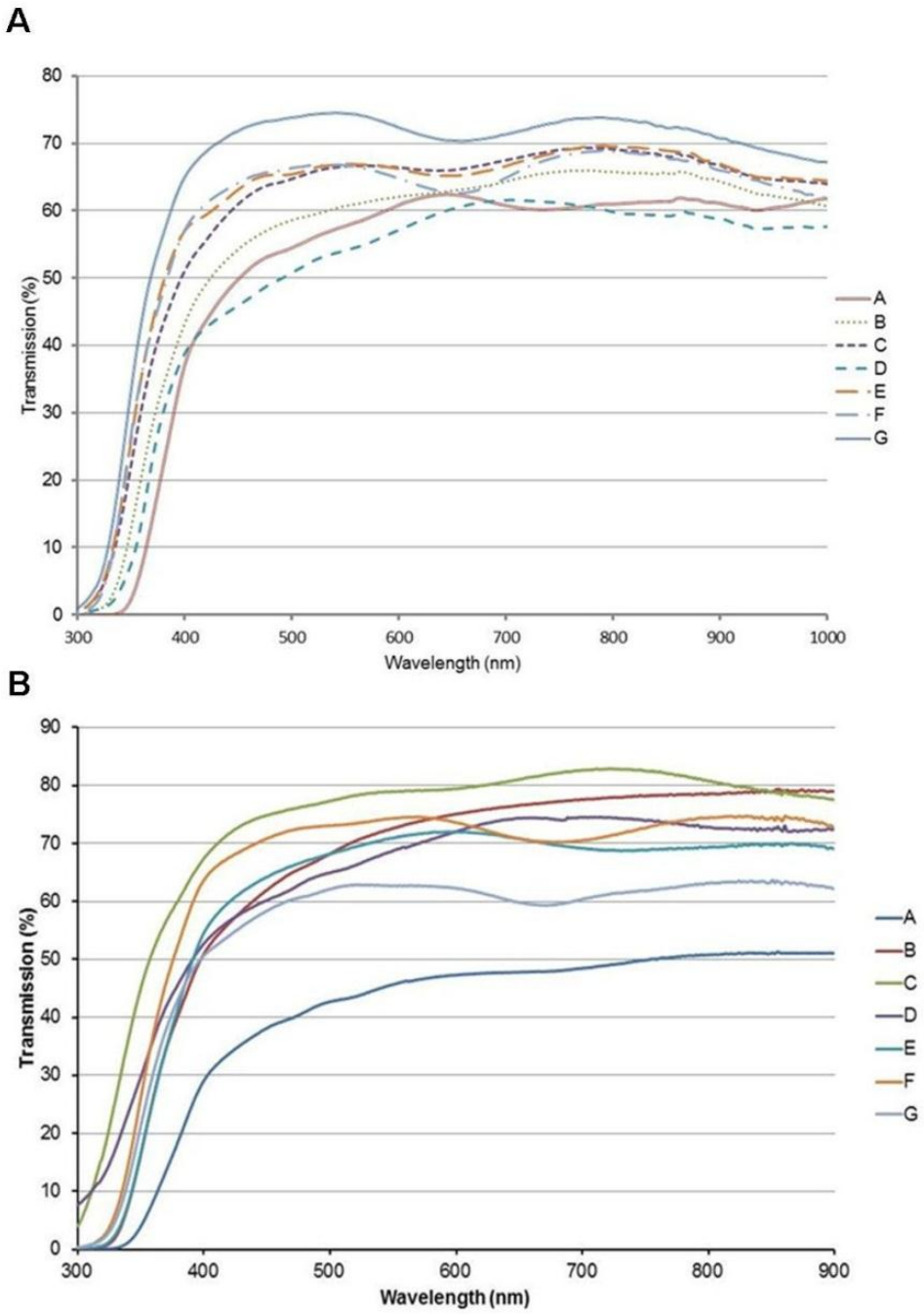

Figure 4.11: UV-vis spectroscopy for films deposited from the AC AACVD reaction of 1 M $TiCl_4$ in toluene at 600 °C and 5 $L.min^{-1}$ (Samples A to G) before annealing (A) and after annealing at 600 °C for 2 h.

Table 4.4: Root Mean Square (RMS, nm), Transmission values in the visible range, Direct band gap (B.G, eV) for unanneaed and annealed samples produced at 600 °C and 5 L.min^{-1} (Samples A to G) and films produced at 450 °C and 1 L.min^{-1} (Samples H to L).

			Unannealed			Annealed		
Sample	Applied Voltage (V)	Field Strength (Vm^{-1})	RMS (nm)	T%	B.G (eV)	RMS (nm)	T%	B.G (eV)
A	0	0	16±6	62	3.1	25±6	51	3.1
B	1	1 x 10^2	31±15	66	3.2	4±3	79	3.2
C	5	5 x 10^2	11±6	69	3.1	5±4	83	3.2
D	10	10 x 10^2	9±2	74	2.85	18±4	75	2.6
E	15	15 x 10^2	8±3	62	3.1	8±1	72	3.2
F	20	20 x 10^2	11±6	70	2.7	9±5	75	2.7
G	30	30 x 10^2	8±4	78	3.2	10±3	63	3.2
H	0	0	19±11	75	3.2	--	--	--
I	10	10 x 10^2	6±2	72	3.2	--	--	--
J	15	15 x 10^2	11±7	59	3.1	--	--	--
K	20	20 x 10^2	0.5±0.1	72	2.8	--	--	--
L	30	30 x 10^2	4±1	75	3.2	--	--	--

4.2.2. Functional properties of deposited films from AC electric fields

4.2.2.1. Photo-activity of TiO_2 thin films

Before annealing, all films produced under the influence of AC electric fields presented higher photocatalytic activity in comparison to the film produced with no electric field (Figure 4.13 A). The quantification of the photo-activity was calculated by the time needed for the thin films to degrade half of the ink initial concentration (Table 4.5). The results indicated that samples C and G showed the highest photocatalytic activity with a half-life of 3.5 min. The second –more active sample was sample F with a half-life of 4.5 min. The samples with the lowest photo-activity were sample A (no electric field) and sample E (15 x 10^2 Vm^{-1}), with half-life values of 21.5 min and 21 min, respectively. The annealing produced a detrimental effect on

AC deposited films except for sample E, which showed a half-life value of 19.5 min after the annealing (Figure 4.13 B). The most important increase of the half-life was observed for sample C (22.5 min), D (19.5 min) and F (22 min).

The films produced at 450 °C and 1 $L.min^{-1}$ exhibited worse photocatalytic activity (Figure 4.14) than films produced at 600 °C and 5 $L.min^{-1}$. The films produced with AC electric fields gave half-life values in the range of 21 – 26.1 min (Table 4.5) which slightly differed to the half-life found for the film produced with no electric fields (29 min).

Table 4.5: Table showing water-contact angles of deposited TiO_2 thin films on glass substrate from the AACVD reaction of $TiCl_4$ solution in toluene before and after UV irradiation (60 min) with SE; half-life photocatalytic testing or time needed to degrade 50% of the ink initial concentration, $t_{1/2}$ (min).

		No annealed			Annealed		
Sample	Field Strength (Vm^{-1})	Contact Angle (degrees)		Half-life	Contact Angle (degrees)		Half-life
		0 min	60 min	$t_{1/2}$ (min)	0 min	60 min	$t_{1/2}$ (min)
A	0	75±2	62±0.7	21.5	52±1	48±3	24.5
B	1×10^2	77±4	58±4	11.5	57±3	23±6	16.9
C	5×10^2	64±8	50±6	3.5	48±2	44±6	22.5
D	10×10^2	50±3	50±3	9	50±3	50±6	19.5
E	15×10^2	72±5	69±6	21	49±1	45±4	19.5
F	20×10^2	76±5	55±6	4.5	51±6	38±4	22
G	30×10^2	72±10	23±6	3.5	23±5	21±3	8
H	0	69±2	8±0.4	29	--	--	--
I	10×10^2	67±5	19±4	21	--	--	--
J	15×10^2	75±2	65±3	25.5	--	--	--
K	20×10^2	56±2	49±10	26.1	--	--	--
L	30×10^2	76±3	49±4	24	--	--	--

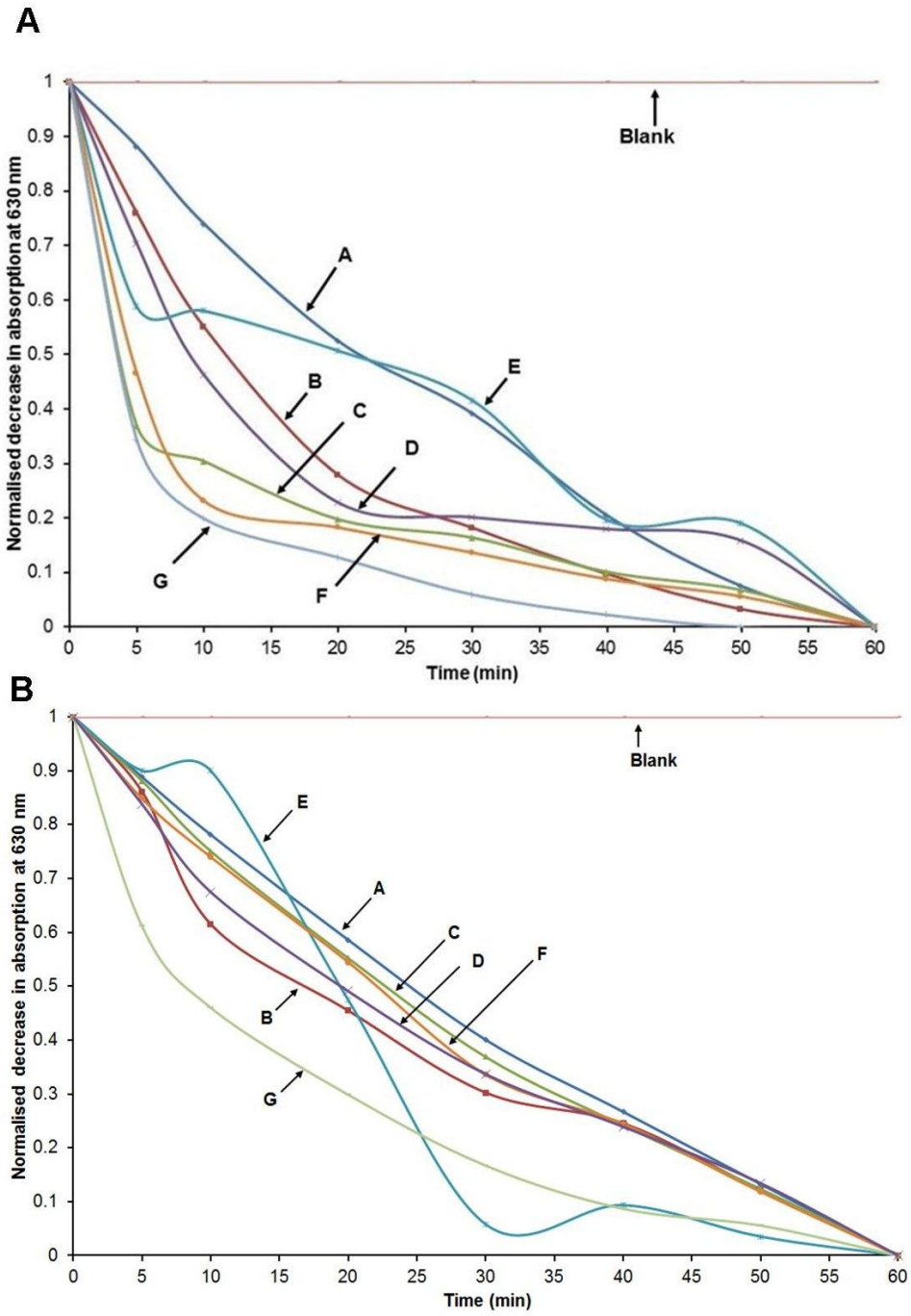

Figure 4.13: Normalised decrease in absorption of Resazurin intelligent ink at 630 nm with UVA irradiation (365 nm) against time (min) for deposited films from the AC AACVD reaction of 1 M $TiCl_4$ in toluene at at 600 °C and 5 $L.min^{-1}$ before annealing (A) and after annealing (B)

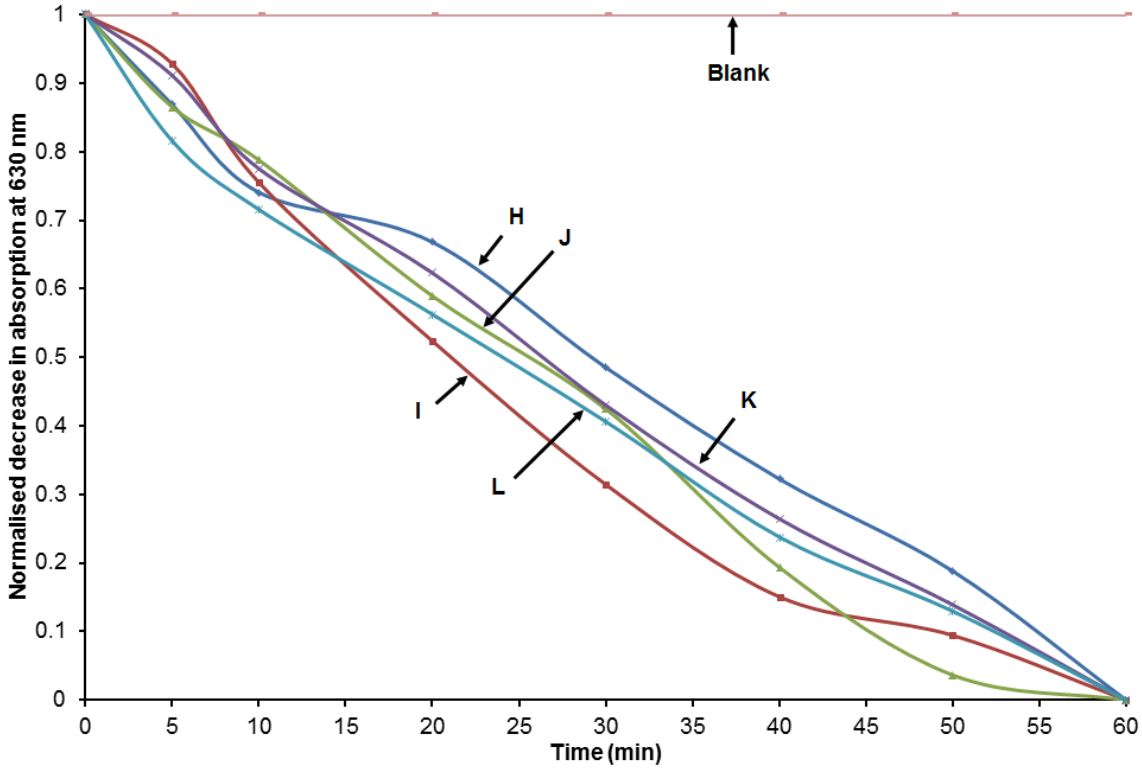

Figure 4.14: Normalised decrease in absorption of Resazurin intelligent ink at 630 nm with UVA irradiation (365 nm) against time (min) for deposited films at 450 °C and 1 $L.min^{-1}$. H) 0 Vm^{-1}, I) 10 x 10^2 Vm^{-1}, J) 15 x 10^2 Vm^{-1}, K) 20 x 10^2 Vm^{-1}, L) 30 x 10^2 Vm^{-1}.

4.2.2.2. Water-contact angles

TiO_2 thin films deposited at 600 °C and 5 $L.min^{-1}$ before annealing showed hydrophilicity with water-contact angles in the range of 47.4 - 77.3° (Table 4.5). Figure 4.15 shows representative water contact angle images for deposited films at 600 °C and 5 $L.min^{-1}$ before and after annealing. After 60 min UV irradiation (254 nm) all films decreased their water-contact angles. In particular, films produced with electric fields (Sample B, F and G) showed the highest water-contact angle reduction. After 60 min UV irradiation the film deposited with no electric field showed a dramatic decrease in water contact angle (8°) whereas films deposited under the influence of electric fields showed a more modest decrease (49°to 65°). However, the film deposited at 1000 Vm^{-1} (D) showed a decrease to 19°.

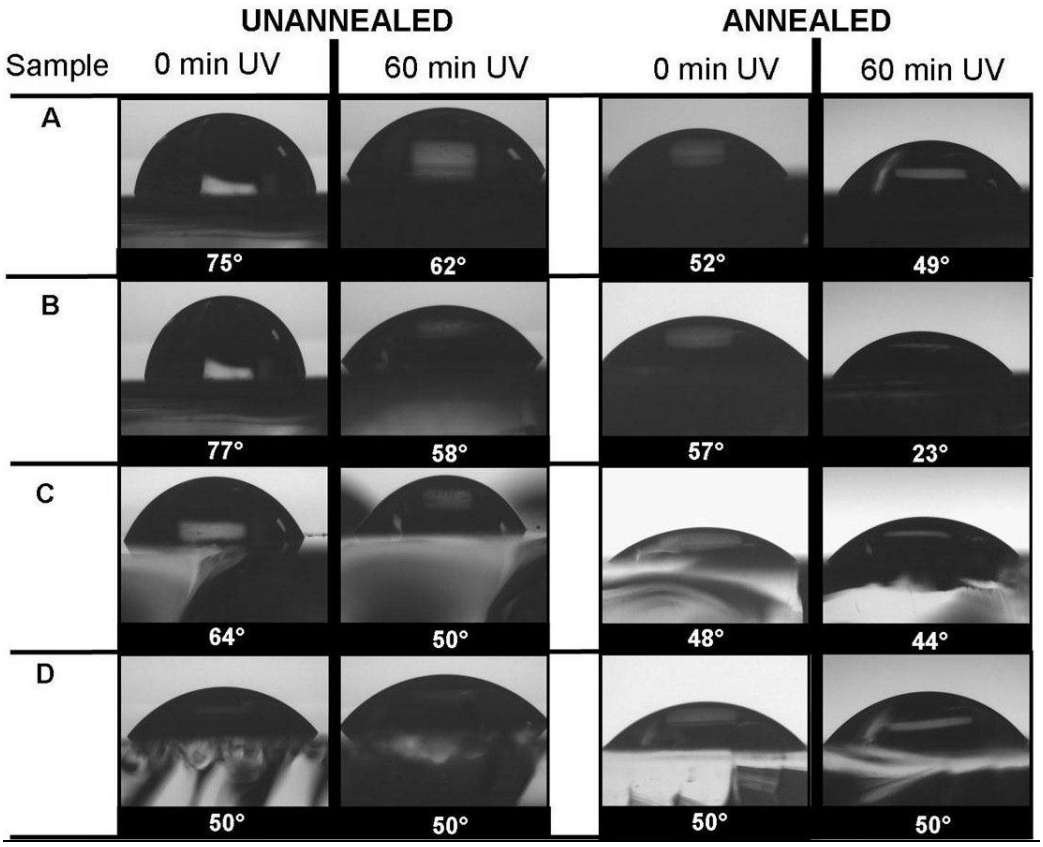

Figure 4.15: Representative average water contact angle images for deposited films (samples A to D) at 600 °C and 5 L.min^{-1} (no annealed and annealed samples) before and after 60 min UVA irradiation 254 nm.

Deposited films at 450 °C and 1 L.min^{-1} also showed hydrophilic surfaces before and after 60 min UVA irradiation with water contact angles ranging from 55.5° to 76° (Table 4.5). Figure 4.16 shows representative water contact angle images for deposited films at 450 °C and 1 L.min^{-1}. After 60 minutes irradiation the water contact angle decreased for all samples produced from AC electric fields with water contact angles ranging from 64.8 to 19.4°. However, the lowest water contact angle was found for the sample produced in absence of an electric field (8.2°).

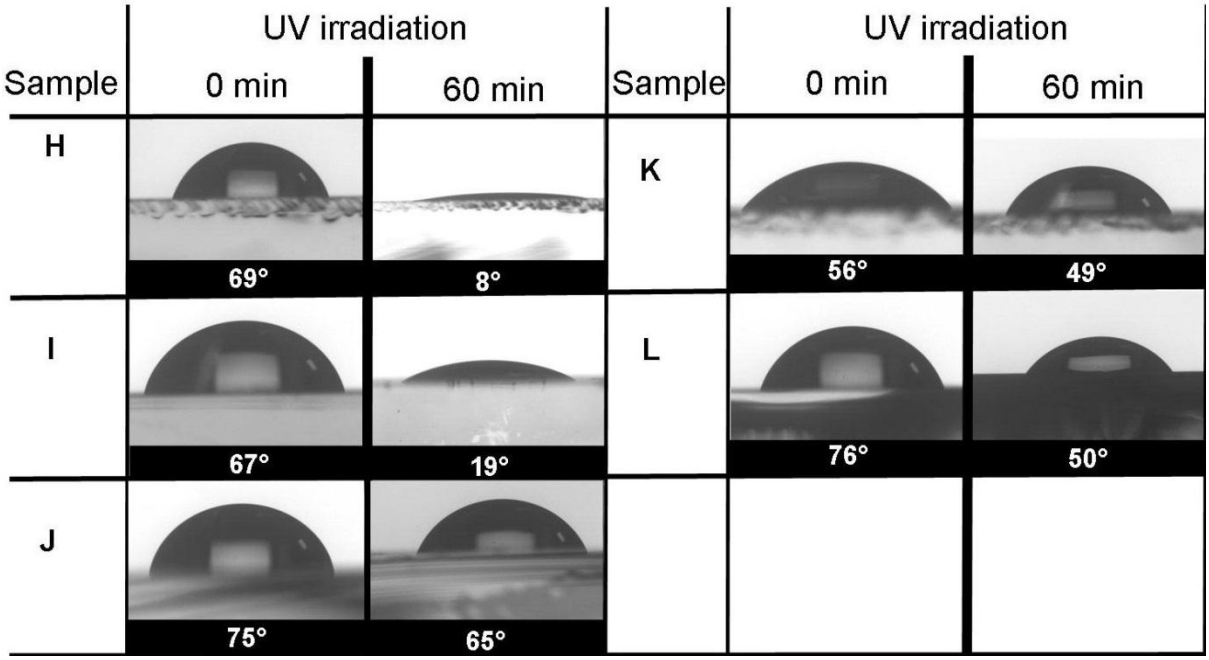

Figure 4.16: Average water contact angle images for deposited films at 450 °C and 1 L.min^{-1}before and after 60 min UVA irradiation 254 nm.

4.2.3. Film synthesis and characterisation of DC deposited films

This section presents the results of titania thin films produced from the DC EAC reaction of 1 M titanium (IV) chloride solution in toluene at 600 °C and 5 L.min^{-1} before and after annealing at 600 °C for 2 h. Deposited films presented good adherence passing the scratch test using Scotch tape test and a piece of towel. Characterisation analysis was carried out to investigate the material phase using XRD and Raman spectroscopy was used to quantify the relative ratio of anatase and rutile phases (Table 4.6).

Scanning electron microscopy

Scanning electron microscopy (SEM) images of the deposited titanium dioxide films from positive bias DC electric fields are shown in Figure 4.17. Measurements of the agglomerate size and thickness are tabulated in Table 4.7. Films deposited in the absence of an applied electric field revealed angular agglomerations of 150 ± 5 nm in length with a secondary growth of rod-like nanoparticles of 83 ± 17 nm in length. The application of positive biased

field strength (1 x 10^2 Vm^{-1}, Figure 4.17 M) induced changes in the morphology to a porous orthogonal microstructure of 93 ± 6 nm length and film thickness of 40 ± 10 nm. The increase of the field strength produced rod-like nanoparticles of 170 nm ± 18 –120 ± 12 length, 40 ± 7 nm diameter (5 x 10^2 –10 x 10^2 Vm^{-1}; Figure 4.17 N –O), forming angular agglomerations of 320 ± 10 nm (Figure 4.17 O). Film thickness in this range decreased to 36 ± 15 nm. The increase of field strength to 15 x 10^2 Vm^{-1}induced changes in the morphology to spherical nanoparticles of 112 ± 10 nm diameter (Figure 4.17 P) and an increase of film thickness to 66 ± 15 nm. The increase of field strength to 20 x 10^2 Vm^{-1} produced rod-like nanoparticles of 175 ± 14 nm in length with angular agglomerations of 200 ± 13 nm (Figure 4.17 Q). The film thickness decreased to 20 ± 10 nm. At 30 x 10^2 Vm^{-1}(Figure 4.17 R) the morphology changed to spherical of 135 ± 10 nm diameter and the film thickness increased to 75 ± 22 nm.

Table 4.6: Experimental conditions and material phase of deposited films from the DC EAACVD reaction of 1 M titanium (IV) chloride solution in toluene at 600 °C and 5 $L.min^{-1}$before and after annealing at 600 °C for 2 h.

Sample	**Applied Voltage (V)**	**Field Strength (Vm^{-1})**	**Substrate Bias**	**Material Phase**	
				Pre-annealing	Post-annealing
A	0	0		Rutile	Rutile
M	1	1 x 10^2	Positive	Anatase-Rutile	Anatase-Rutile
N	5	5 x 10^2	Positive	Anatase-Rutile	Rutile-Anatase
O	10	10 x 10^2	Positive	Rutile-Anatase	Rutile-Anatase
P	15	15 x 10^2	Positive	Anatase-Rutile	Rutile
Q	20	20 x 10^2	Positive	Anatase-Rutile	Rutile
R	30	30 x 10^2	Positive	Anatase-Rutile	Anatase-Rutile
S	1	1 x 10^2	Negative	Anatase-Rutile	Anatase-Rutile
T	5	5 x 10^2	Negative	Rutile	Rutile-Anatase
U	10	10 x 10^2	Negative	Anatase-Rutile	Anatase-Rutile
V	15	15 x 10^2	Negative	Rutile-Anatase	Rutile-Anatase
W	20	20 x 10^2	Negative	Anatase-Rutile	Anatase-Rutile
X	30	30 x 10^2	Negative	Anatase-Rutile	Anatase-Rutile

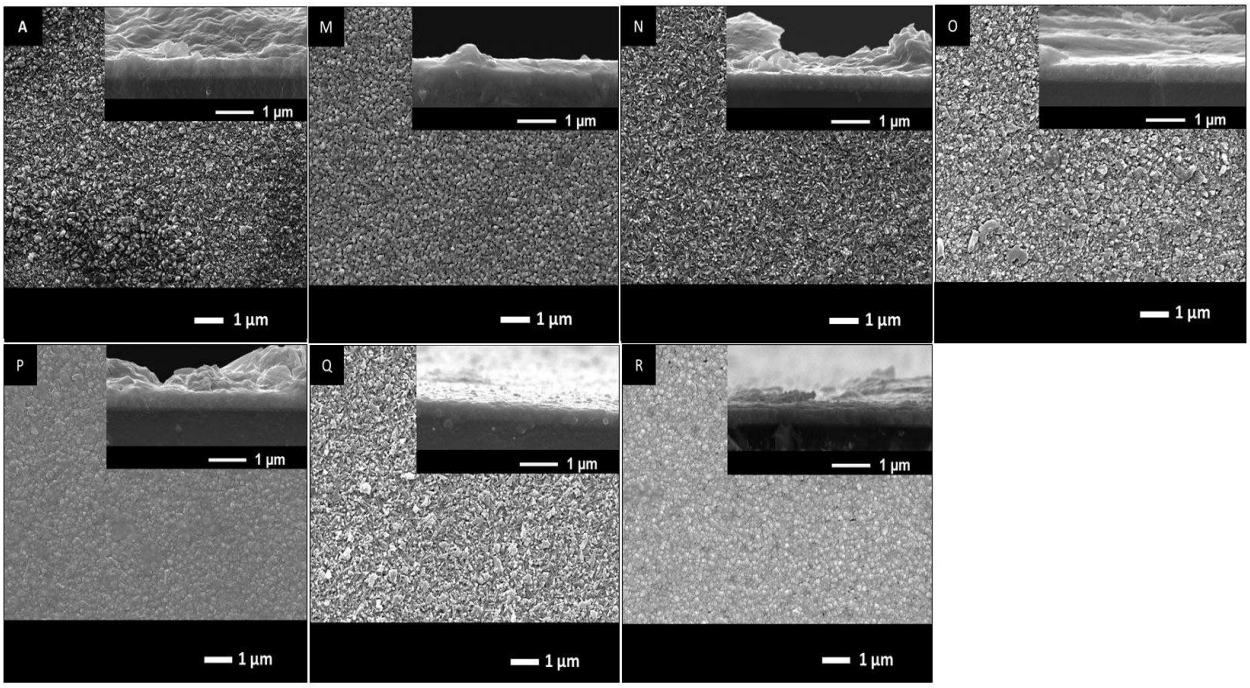

Figure 4.17: Scanning Electron Microscope images of samples prepared without electric field and from the positive biased DC EAACVD reaction of 1M $TiCl_4$ solution in toluene at 600 °C with a flow rate of 5 $L.min^{-1}$. A) 0 Vm^{-1}, M) 1 x $10^2 Vm^{-1}$, N) 5 x $10^2 Vm^{-1}$, O) 10 x 10^2 Vm^{-1}, P) 15 x 10^2 Vm^{-1}, Q) 20 x 10^2 Vm^{-1}, R) 30 x 10^2 Vm^{-1}. Side on images were captured at 30,000 magnification and cross-section images at 40,000 magnification.

When applying and increasing negative biased electric fields (1 x 10^2 –5 x 10^2 Vm^{-1}, Figure 4.18 S –T) the microstructure showed angular agglomerations of 83 ± 12 nm – 86 ±7 nm in length and a film thickness of 43 ± 24 nm –100 ± 23nm. The increase of field strength (10 x 10^2 – 15 x 10^2 Vm^{-1}) produced spherical agglomerations of 112 ± 9 nm– 100 ± 6 nm in diameter forming clusters in the range of 540 ± 55 nm – 430 ± 23 (Figure 4.18 U –V). Film thickness values in this range dramatically increased to 225 ± 20 nm. The increase of field strength up to 30 x 10^2 Vm^{-1} produced angular nanoparticles of 110 ± 8 nm in length (Figure 4.18 W) and spherical nanoparticles 110 ± 7 nm in diameter (Figure 4.18 X). The film thickness in this range decreased to 30 ± 5nm.

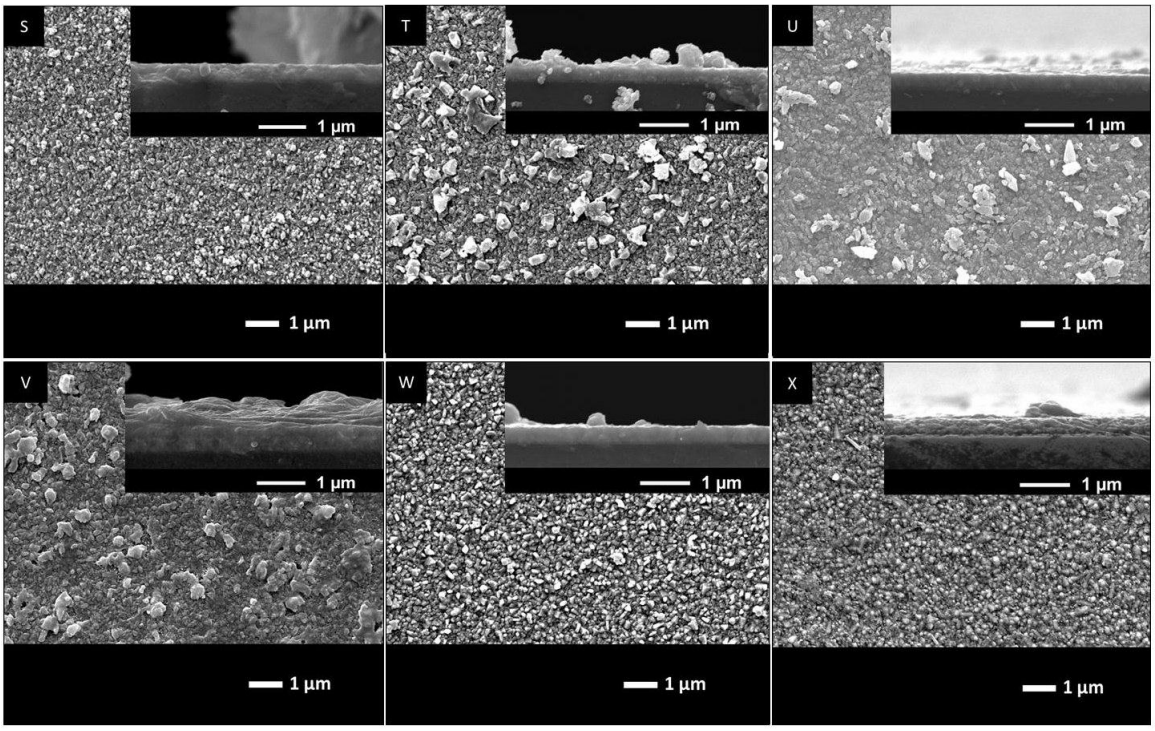

Figure 4.18: Scanning Electron Microscope images of samples prepared from the negative biased DC EAACVD reaction of 1 M $TiCl_4$ solution in toluene at 600 °C with a flow rate of 5 $L.min^{-1}$. Sample S) 1 x 10^2 Vm^{-1}, T) 5 x 10^2 Vm^{-1}, U) 10 x 10^2 Vm^{-1}, V) 15 x 10^2 Vm^{-1}, W) 20 x 10^2 Vm^{-1}, X) 30 x 10^2 Vm^{-1} Side on images were captured at 30,000 magnification and cross-section images at 40,000 magnification.

SEM was also conducted for annealed samples (Figure 4.19). The annealing process resulted agglomeration of particles increasing the particle size to 250 ± 17 nm and thickness to 130 ± 16 nm for films deposited with no electric field (Figure 4.19 A). The annealing of positive bias deposited films (samples M –R) produced agglomeration of particles and increase of film thickness for samples M – Q. Some samples showed changes of morphology in their microstructure. Samples M and N changed their morphology to spherical and angular with a particle size of 150 ± 15 nm (Figure 4.19 M –N). The film thickness for these samples increased in a range of 40 ± 15 nm. The annealing process reduced the particle size for Sample O to 70 ± 9 nm but increased the film thickness up to 30 ± 10 nm. The annealing produced agglomeration of spherical (Figure 4.19 P –R) and angular particles (Figure 4.19 Q) forming clusters of 200 ± 17 nm – 220 ± 25 nm. Samples Q and R showed a significant decrease in film thickness to 2 ± 1 nm. Likewise, the annealing also increased the agglomeration of particles for all negative bias deposited films but an increase of film thickness only

for Samples U and X. The annealing produced the coalition of angular agglomerates to form spherical particles of 160 ± 18 nm (Figure 4.19 S – T) and film thickness of 6 – 10 ± 2 nm. For Samples U – W the annealing formed clusters of 220 ± 52 nm – 130 ± 10 nm (Figure 4.19 U –W). Film thickness increased for Sample U (110 ± 40 nm) but decreased for Sample V and W (150 – 30 ± 6 nm). For sample X the annealing produced a change in the morphology from rod-like to spherical particles 170 ± 13 nm and an increase in film thickness to 90 ± 35 nm. Agglomerate size and film thickness values after annealing can be seen in Table 4.7. Figure 4.20 shows the different patterns for the agglomerate size and film thickness before and after annealing for positive and negative bias deposited films.

X-ray diffraction

X-ray diffraction (XRD) analysis was conducted and compared (JCPDS database file 021-1272) to investigate the materials phase. As in the case of films produced from AC electric fields, XRD pattern did not show clear evidence of the materials phase. As Figure 4.21 shows only cassiterite SnO_2 peaks from the substrate appear for most of the deposited films indicating poor crystallinity of TiO_2 thin films. However, all deposited films showed peaks at 2 Theta = 54.3° corresponding to rutile (211). Deposited films M and Q showed a peak of anatase (101) but the last one showed particularly poor crystallinity. Negative biased deposited films were more amorphous than positive biased films as shown in XRD pattern. Samples S – W showed a peak at 2 theta = 29.6° which corresponds to SiO_2 from the substrate [162]. However, when these samples were annealed at 600 °C for 2 hours, the crystallinity of these films improved and the peak at 2 Theta = 29.6° disappeared (Figure 4.22). Furthermore, samples U and V showed characteristic peaks of anatase (101) and anatase (200) after annealing. However, it was observed that the annealing process showed no apparent effect on the positive bias deposited films crystallinity.

Table 4.7: Table showing agglomerate size (nm) from SEM with standard error (SE), film thickness (nm) from SEM cross section with SE, for DC EAACVD deposited films from the reaction of 1 M $TiCl_4$ solution in toluene 600 °C and 5 $L.min^{-1}$.

Sample	Field Strength (Vm^{-1})	Substrate bias	Agglomerate size (nm)				Film Thickness (nm)	
			Unannealed		Annealed		Unannealed	Annealed
A	0		150±5		250±17		82±9	130±16
M	1 x 10^2	Positive	93±6		150±9		40±10	19±5
N	5 x 10^2	Positive	170±18 40±6		71±5	150±15	40±15	47±9
O	10 x 10^2	Positive	120±12 40±7	320±10	70±9		22±8	30±10
P	15 x 10^2	Positive	112±10		200±17		66±15	67±20
Q	20 x 10^2	Positive	175±14 46±3	200±13	190±20		20±10	2±1
R	30 x 10^2	Positive	135±10		36±2	220±25	75±22	2±1
S	1 x 10^2	Negative	83±12		160±15		43±24	6±2
T	5 x 10^2	Negative	86±7	412±58	160±18		100±23	10±2
U	10 x 10^2	Negative	112±9	540±55	220±52		80±26	110±40
V	15 x 10^2	Negative	100±6	430±23	120±18		225±20	150±6
W	20 x 10^2	Negative	110±8		64±6	130±10	40±6	30±6
X	30 x 10^2	Negative	110±7		170±13		30±5	90±35

Raman spectroscopy

Raman analysis was conducted to investigate the materials phase as no reliable information was obtained from XRD . Anatase crystal phase was identified at Raman shifts 147 cm^{-1}, 197 cm^{-1}, 399 cm^{-1}, 513 cm^{-1}, 519 cm^{-1} and 639 cm^{-1} [134] (Figure 4.23). Likewise, rutile crystal phase was identified at Raman shifts 446 cm^{-1} and 610 cm^{-1} [38]. As conducted for deposited films from AC electric fields, quantifiable values of the content of anatase and rutile in deposited films were obtained by de-convoluting the overlapping rutile A_{1g} (612 cm^{-1}) and anatase E_g (639 cm^{-1}) contributions and inserting the % area of contribution of rutile component (x) into a predetermined equation derived from powder standards [163].The percentage of anatase and rutile for all deposited film before and after annealing is shown in Table 4.8. It was found that

for the same experimental conditions the material phase was different depending on the field strength applied. Pure rutile was found for the film produced with no field strength (sample A). When applying electric fields the percentage of anatase dramatically increased to 98 % in all cases except for samples N, O, T and V. In particular, samples O and V showed mostly rutile crystal phase with a percentage greater than 60% and sample T showed purely rutile.

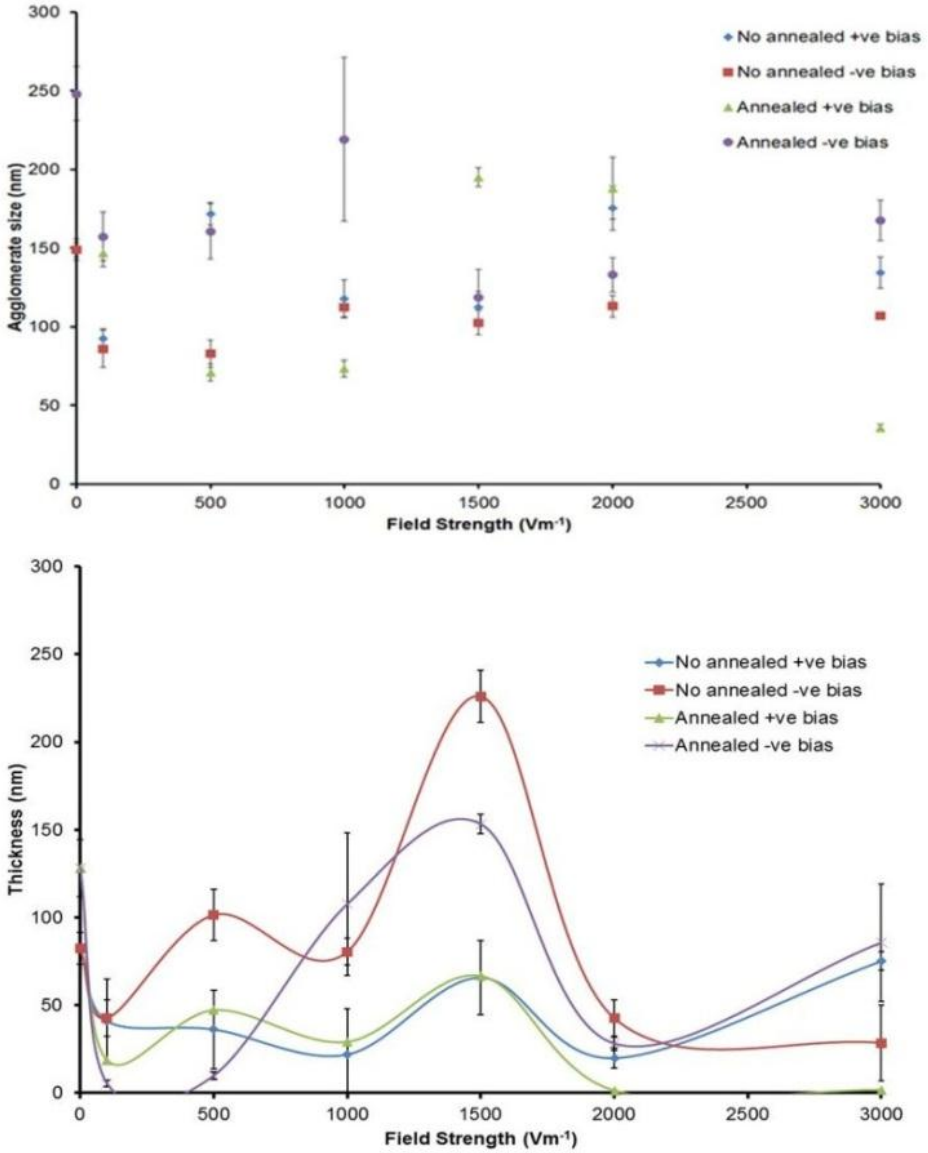

Figure 4.20: Primary agglomeration size (up) and thickness (below) with corresponding standard error of deposited films from the DC EACVD 1 M $TiCl_4$ solution in toluene at 600 °C and 5 $L.min^{-1}$ from positive bias (labelled as +ve bias) and from negative bias(labelled as –ve bias) before and after annealing.

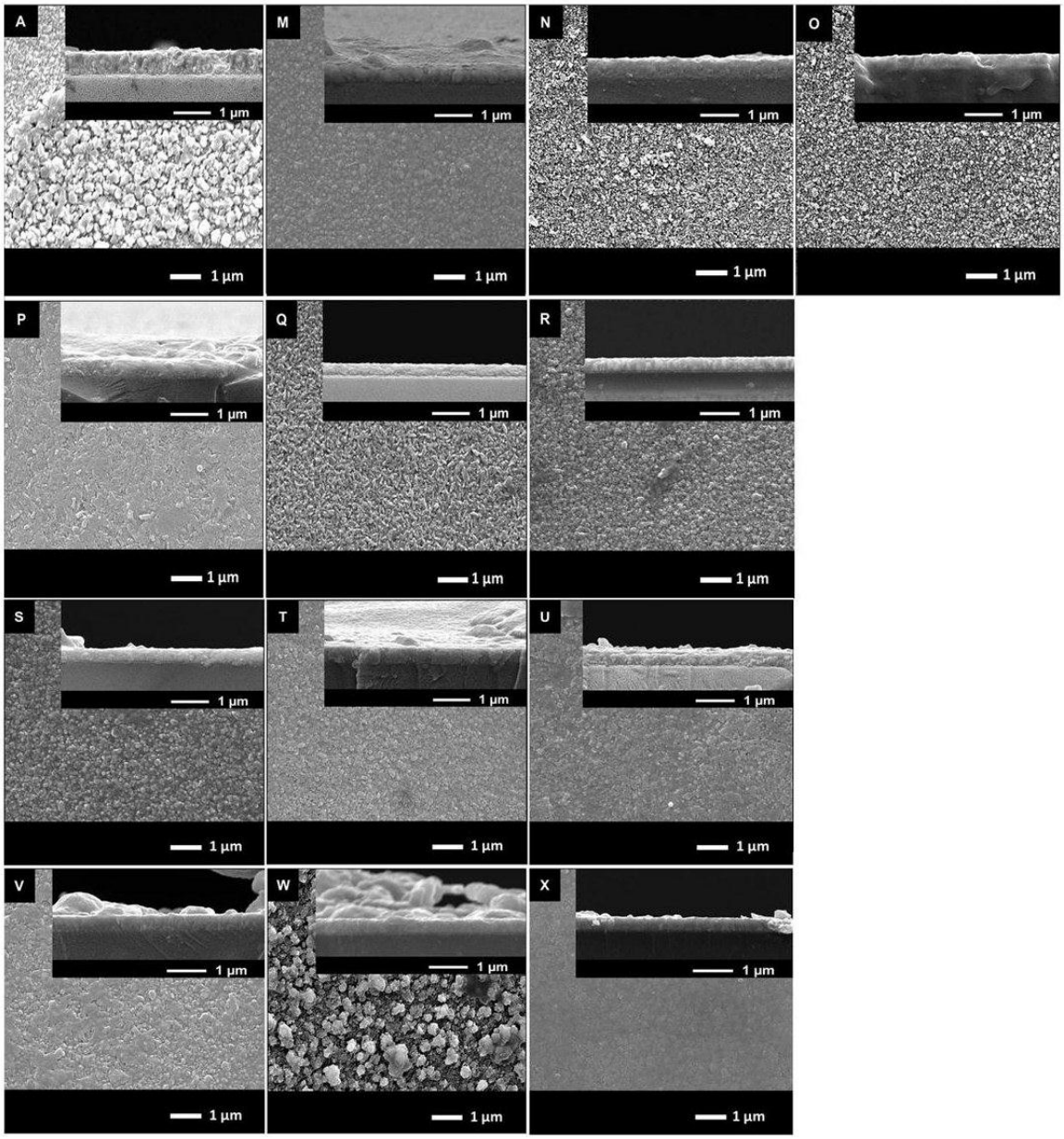

Figure 4.19: Scanning Electron Microscope images of samples prepared the DC EAACVD reaction of 1 M $TiCl_4$ solution in toluene at 600 °C and 5 $L.min^{-1}$ after annealing at 600 °C for 2 h. A) 0 Vm^{-1}, M) 1 x $10^2 Vm^{-1}$, N) 5 x $10^2 Vm^{-1}$, O) 10 x 10^2 Vm^{-1}, P) 15 x 10^2 Vm^{-1}, Q) 20 x 10^2 Vm^{-1}, R) 30 x 10^2 Vm^{-1}, S) 1 x 10^2 Vm^{-1}, T) 5 x $10^2 Vm^{-1}$, U) 10 x 10^2 Vm^{-1}, V) 15 x 10^2 Vm^{-1}, W) 20 x 10^2 Vm^{-1}, X) 30 x 10^2 Vm^{-1}. Side on images were captured at 30,000 magnification and cross-section images at 40,000 magnification.

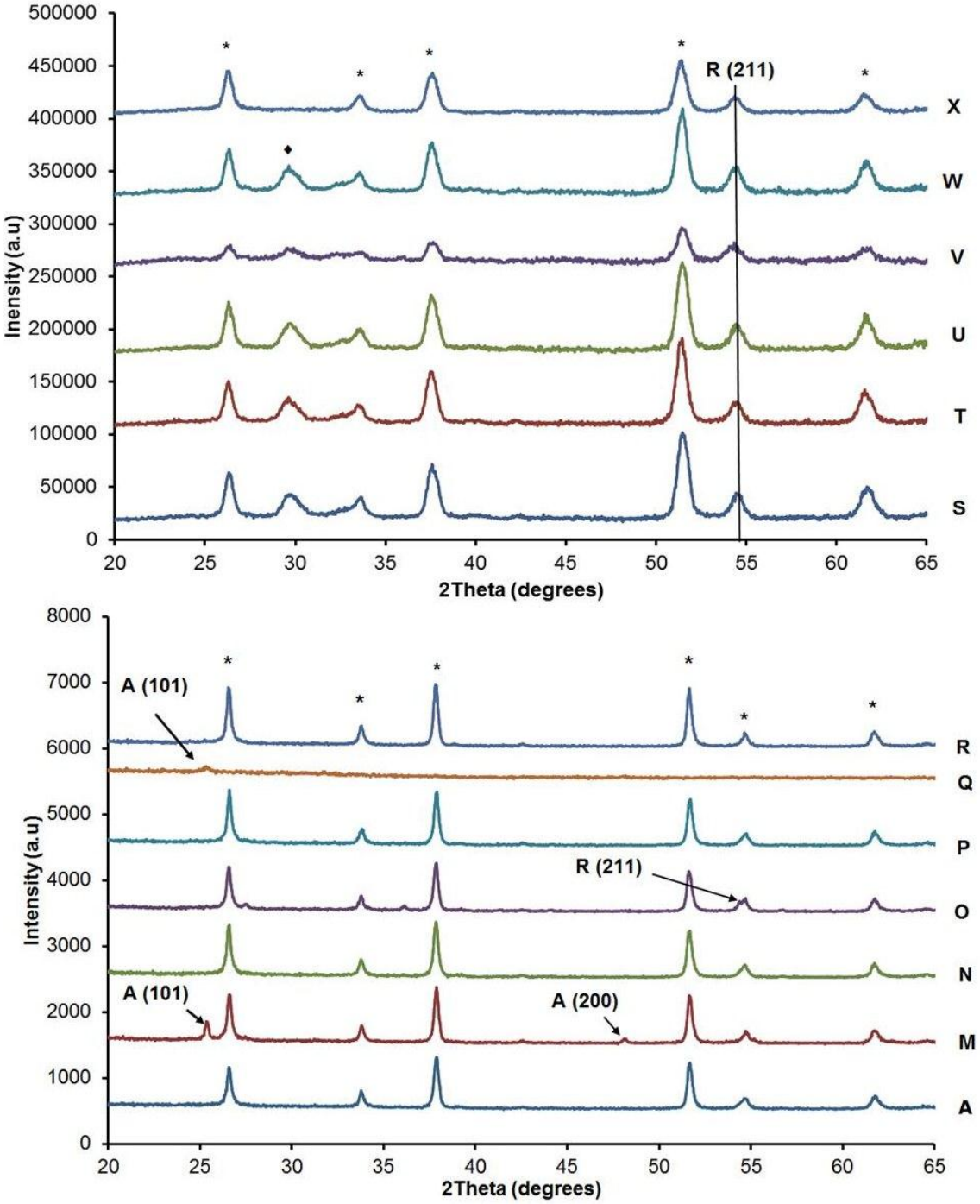

Figure 4.21: XRD pattern for samples prepared from EAACVD reaction of 1 M $TiCl_4$ solution in toluene at 600 °C and a gas flow rate of 5 $L.min^{-1}$, films deposited in absence of electric fields (A), positive biased (M-R) and negative biased electric fields (S-X) . **A** stands for anatase and **R** for rutile crystal phase. The peaks marked with asterisks denote the cassiterite peaks specific of SnO_2 crystalline phase and peaks marked with rhomboid denote SiO_2, materials used for the glass substrate coating.

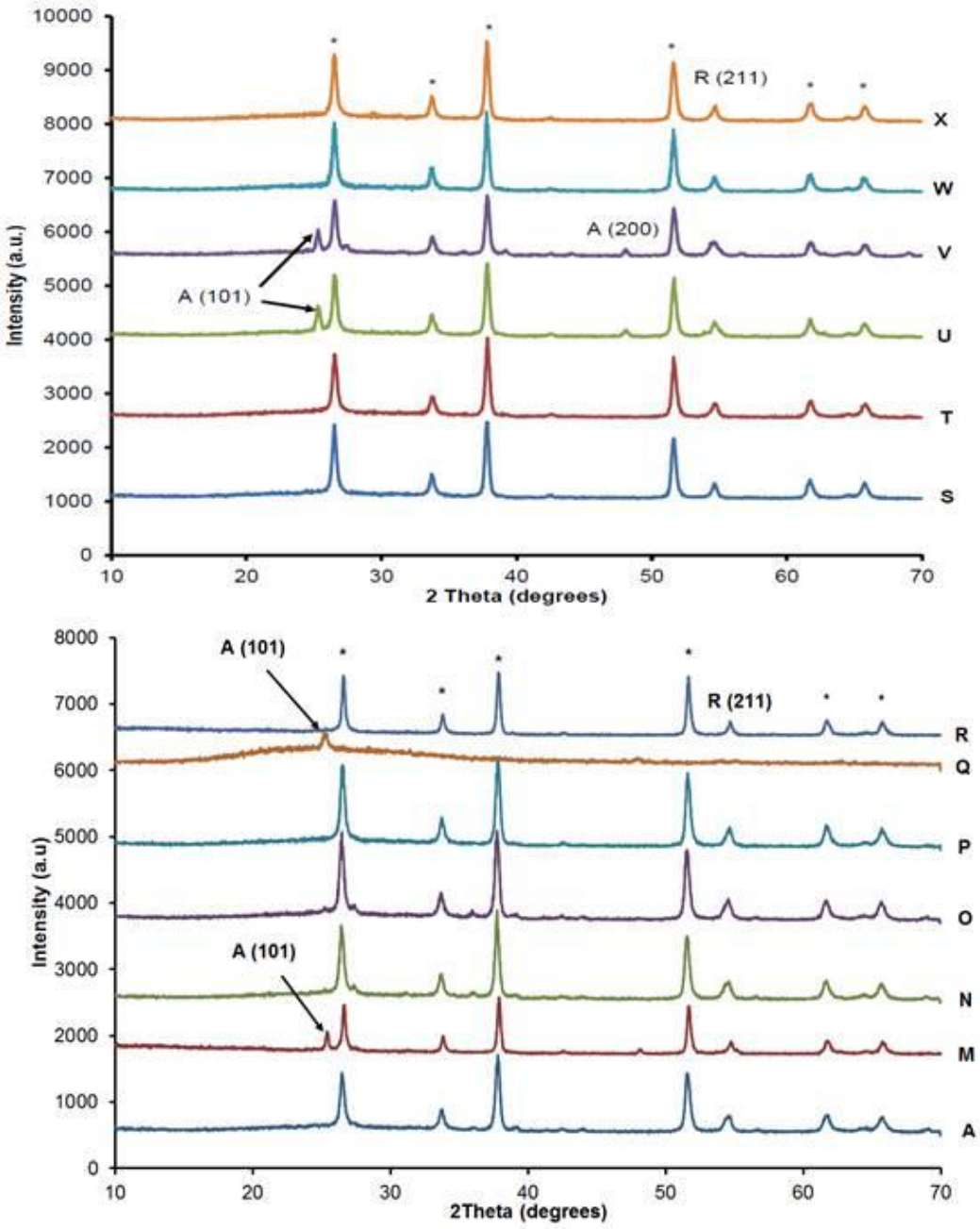

Figure 4.22: XRD pattern for samples prepared from EAACVD reaction of 5 ml $TiCl_4$ solution in toluene at 600 °C and a gas flow rate of 5 $L.min^{-1}$ after annealing at 600 °C for 2 h, films deposited in absence of electric fields (A), positive biased (M-R) and negative biased electric fields (S-X) . **A** stands for anatase and **R** for rutile crystal phase. The peaks marked with asterisks denote the cassiterite peaks specific of SnO_2 crystalline phase and peaks marked with rhomboid denote SiO_2, materials used for the glass substrate coating.

Raman spectroscopy of the annealed samples revealed transformation in polymorphs for deposited films (Figure 4.24). Quantifying analysis revealed that the annealing process had no effect on the content of polymorphs for some deposited films (samples R, U, W and X). However, it was observed that for most of deposited films the content in anatase decreased in a range of 13 – 57% (samples M – O, S) and in some cases only pure rutile was shown (sample P and Q).

Atomic force microscopy

AFM was performed scanning over a 2 μm x 2 μm region in order to obtain Root Mean Square (RMS) roughness values as a proxy of surface roughness. Figure 4.25 and 4.26 show representative AFM images with corresponding RMS values of positive bias and negative deposited films, respectively. Generally, positive bias deposited films showed lower surface roughness values (range of 5 –20 nm) than sample A (16 ± 6 nm). RMS values can be seen listed in Table 4.9. A rend for rougher surfaces at low field strengths (samples M –O) was observed. As the field strength was increased (samples P-R), surface roughness gradually decreased to 5 ± 4 nm (sample R). The highest surface roughness values were found for samples N and O with 20 ± 4 nm and 15 ± 2 nm, respectively. Negative bias deposited films showed higher surface roughness values than positive bias deposited films with RMS values in the range of 9 – 22 nm (Figure 4.26, Table 4.9). It was observed that the surface roughness increased with the field strength. The highest surface roughness values were found for samples U (17 ± 10 nm), W (22 ± 12 nm) and X (16 ± 4 nm).

Figure 4.27 shows representative AFM images of DC deposited films after annealing with corresponding mean RMS values. Generally, the annealing process produced either no changes or an increase in surface roughness (Table 4.9). However, in some cases the annealing produced a decrease in surface roughness. In particular, an important decrease of surface roughness after annealing was observed for samples R (from 5 to 10 ± 4 nm), W (from 22 ± 12 nm to 4 ± 2 nm) and sample X (from 16 ± 4 nm to 4 ± 3 nm).

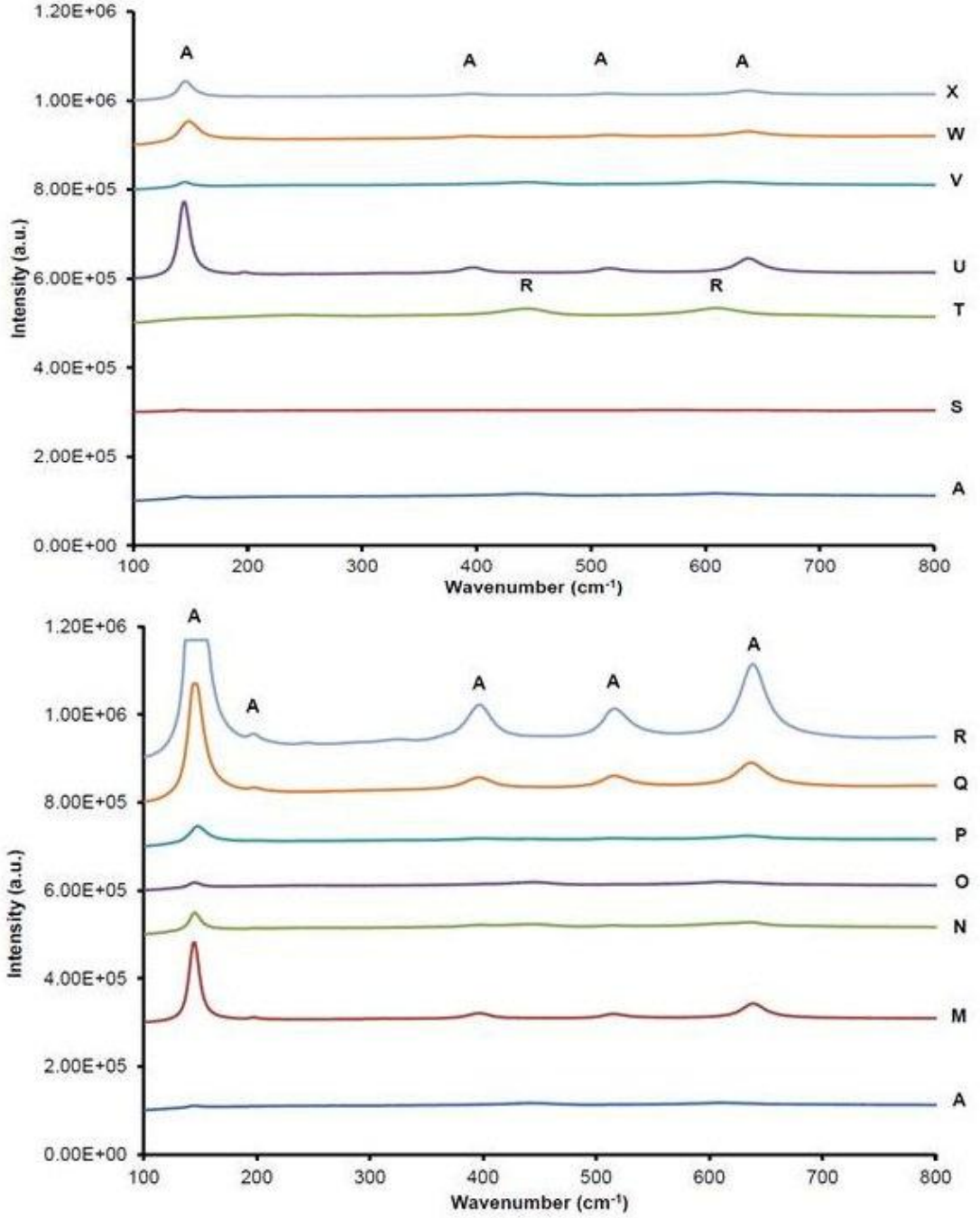

Figure 4.23: Raman spectra for deposited films from the DC EAACVD reaction of 1 M $TiCl_4$ solution in toluene at 600 °C and 5 $L.min^{-1}$, in absence of electric fields (A) and from positive (M-R) and negative biased field strength (H-X) . A stands for anatase and R for rutile.

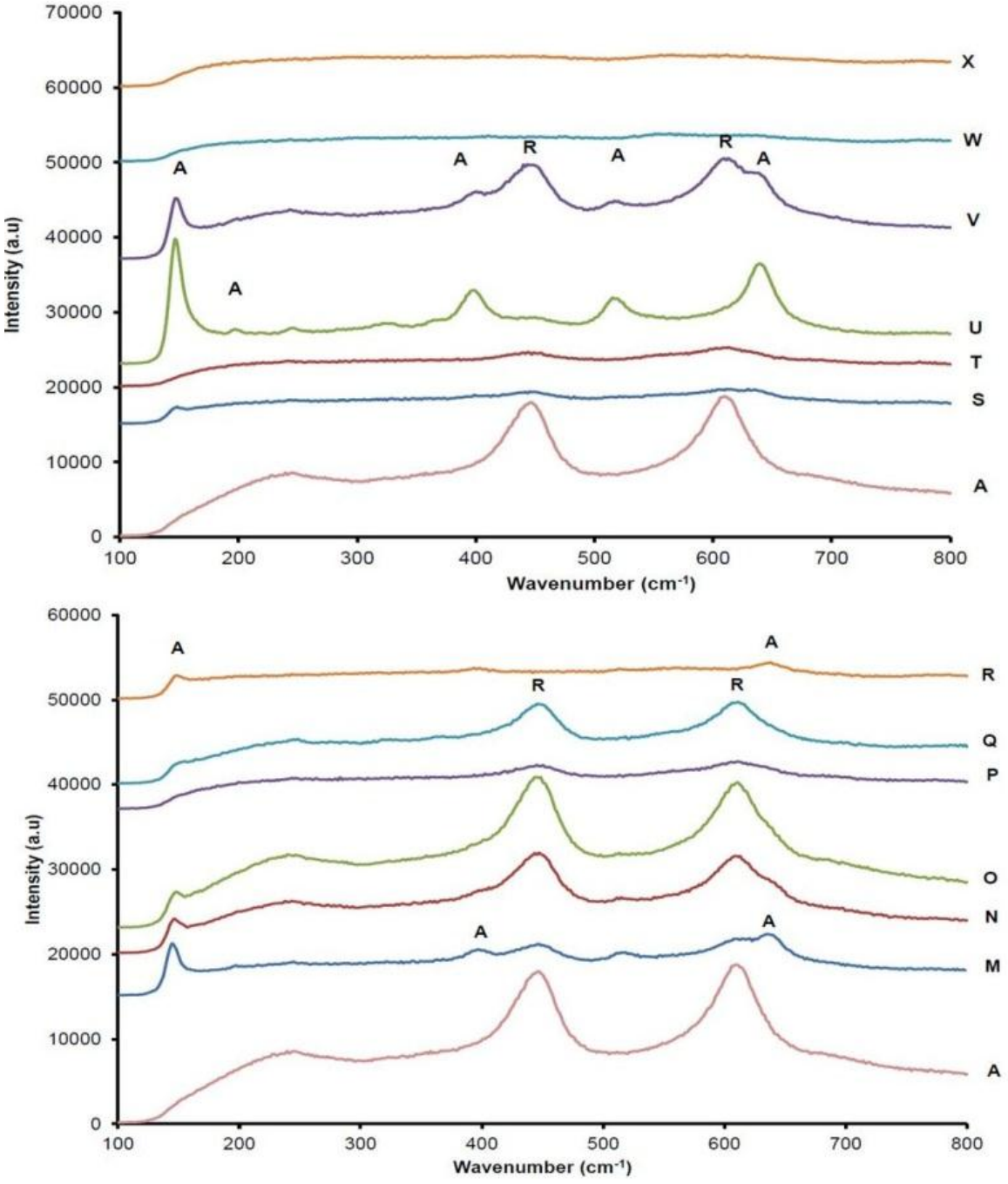

Figure 4.24: Raman spectra for films from the DC EAACVD reaction of 1 M $TiCl_4$ solution in toluene at 600 °C and 5 $L.min^{-1}$ after annealing at 600 °C for 2 h, in absence of electric fields (A) and from positive (M-R) and negative biased field strength (H-X) . A stands for anatase and R for rutile.

UV-vis spectroscopy

UV/VIS spectroscopy showed differences in the maximum transmission values in the visible region. The film deposited in absence of electric fields (sample A) showed transmission values in the visible region up to 62% (Figure 4.28, Table 4.9). All deposited films from positive biased electric films showed higher transmission (64 – 76%) than sample A except for sample R (58%) (Figure 4.28, Table 4.9). Films deposited from negative biased electric fields showed even higher maximum transmission values in the visible (65% – 82%) except for samples W and X with 62 % and 6 %, respectively (Figure 4.28, Table 4.9).

Table 4.8: Content in anatase (% A) and rutile (% R) crystal phase calculated from Raman spectroscopy for titania thin films deposited from the DC EAACVD reaction of 1 M

			Crystal Phase			
			Unannealed		Annealed	
Sample	Field Strength (Vm^{-1})	Substrate bias	% A	% R	% A	% R
A	0		0	100	0	100
M	1×10^2	Positive	98	2	84	16
N	5×10^2	Positive	79	21	22	78
O	10×10^2	Positive	37	63	24	76
P	15×10^2	Positive	98	2	0	100
Q	20×10^2	Positive	98	2	0	100
R	30×10^2	Positive	98	2	98	2
S	1×10^2	Negative	98	2	56	44
T	5×10^2	Negative	0	100	22	78
U	10×10^2	Negative	98	2	98	2
V	15×10^2	Negative	37	63	43	57
W	20×10^2	Negative	98	2	98	2
X	30×10^2	Negative	98	2	98	2

For positive bias deposited films the annealing process increased the transmission values in the range of 76 – 80% with the exception of Samples P (49%) and R (32%) (Figure 4.29, Table 4.9). Likewise, the transmission values increased in the range of

69% – 88% for negative bias deposited films with the exception of Samples S (79%) and T (68%).

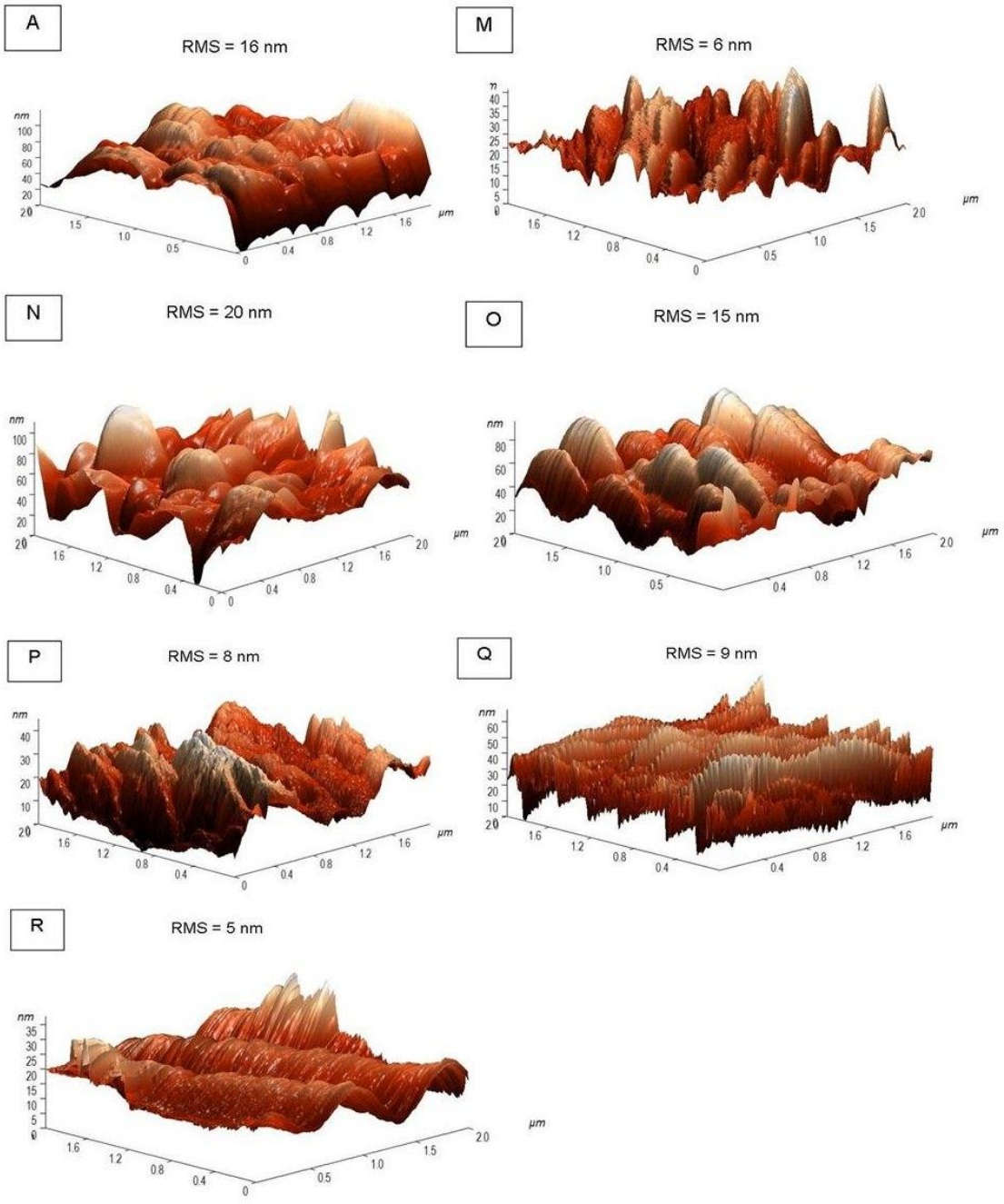

Figure 4.25: AFM images with corresponding Root Mean Square (RMS) values (nm) for films deposited from the positive bias DC EAACVD reaction of 1 M $TiCl_4$ solution in toluene at 600 °C and 5 $L.min^{-1}$.

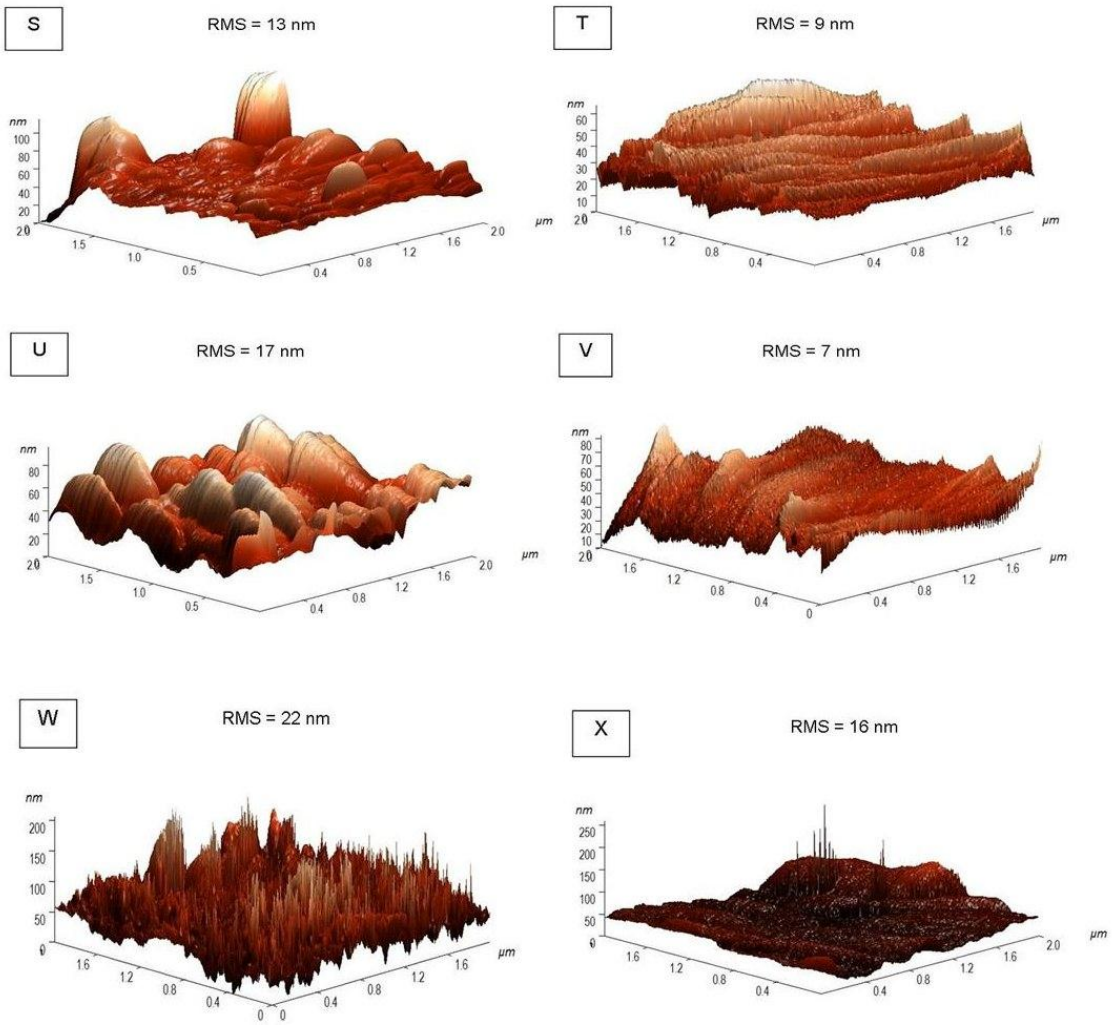

Figure 4.26: AFM images with corresponding Root Mean Square (RMS) values (nm) for films deposited from the negative bias DC EAACVD reaction of 1 M $TiCl_4$ solution in toluene at 600 °C and 5 $L.min^{-1}$.

Direct band gap (DBG) analysis was performed using the Tauc method [154]. As presented in Raman analysis, field strength influenced the anatase/rutile composition of deposited films and as a consequence, the direct band. It was found that different combination of anatase/rutile content resulted in different direct band gaps (Table 4.9). Thus, standard anatase band gap values between 3.05 to 3.2 eV were found for films which showed a percentage of anatase greater than 70% (samples M, N, P – V, X). The film which showed the lowest DBG were samples D (2.80 eV) and sample I (3.0 eV) which showed a percentage of rutile of 63% and 100%, respectively. Sample

W showed a low DBG (2.9 eV) with an anatase percentage of 98%. Generally speaking, the annealing process produced an increase of the direct band gap of all deposited films in the range of 3.0 – 3.2 eV. Deposited which showed the lowest direct band gap were those which showed high content of rutile after annealing (samples O – Q) with a direct band gap value of 3.0 – 3.1 eV.

4.2.4. Functional properties of DC deposited films

4.2.4.1. Photo-activity of TiO_2 thin films

The photocatalytic activity of deposited films was investigated from the UV/Vis absorption of Resazurin intelligent ink under UV irradiation (365 nm). Figure 4.30 shows the normalised absorption at 630 nm for films produced under the influence of DC electric fields. The quantification of the photo-activity was calculated by the time needed for the thin films to degrade half of the ink initial concentration or half-life (min) (Table 4.10). The results indicated that most of the films produced under the influence of DC electric fields showed higher photocatalytic performance than the film produced in absence of electric fields (sample A; half-life = 21.5 min). In particular, positive bias deposited films showed greater photo-activity with half -life values in the range of 5 –17.2 min (samples N – R). As an exception, sample M showed worse photo-activity than sample A with a half-life value of 24.3 min. Samples Q and R showed the highest photo-activity with half-life values of 3.3 and 5 min, respectively. Negative biased deposited films showed lower photocatalytic activity. Samples T, U and W still showed higher photo-activity than the film deposited in absence of electric fields (sample A) with half-life values between 6 – 17 min. The worst photocatalytic performance was observed for samples V and X with a half-life values of 40 and 30 min, respectively.

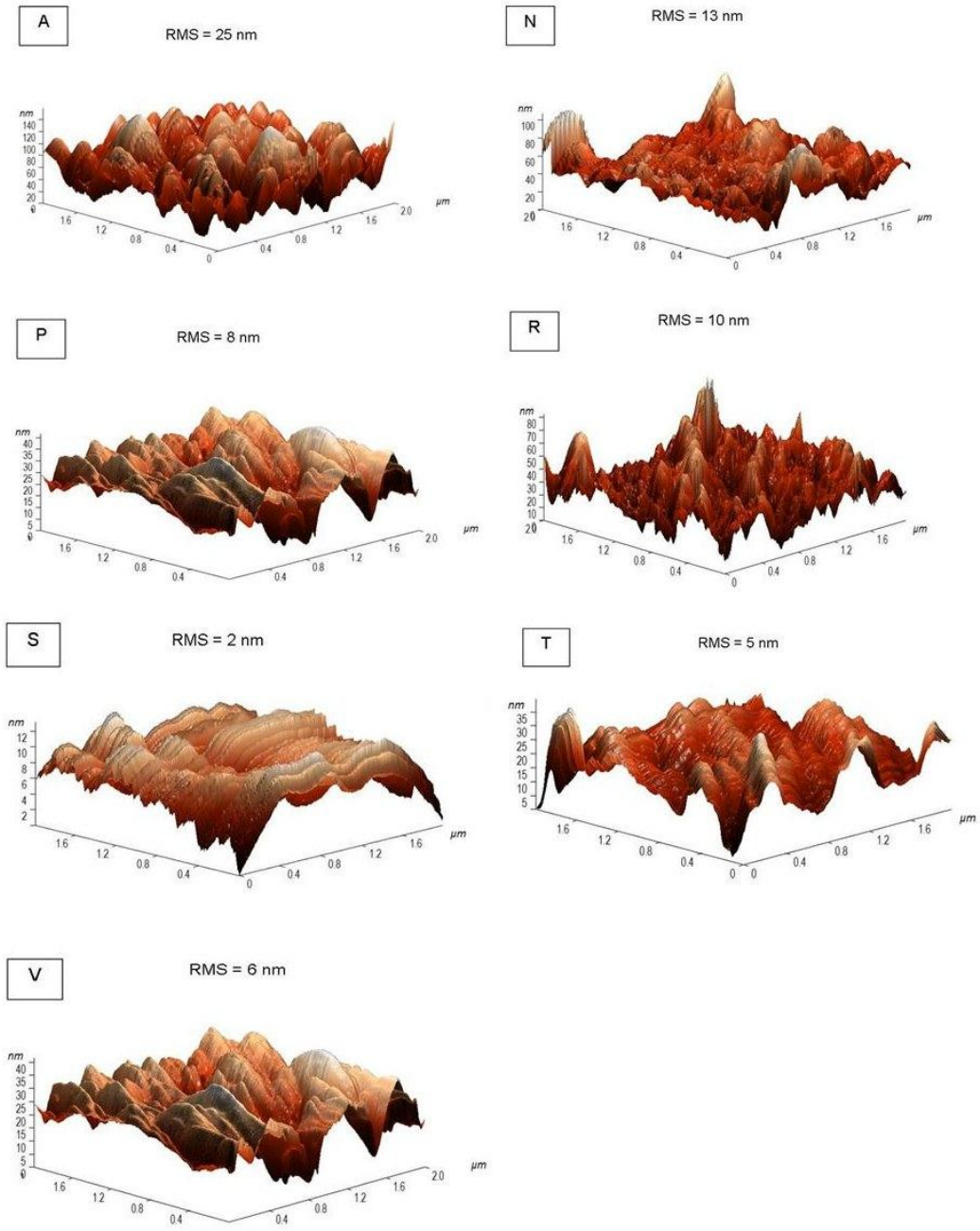

Figure 4.27: Representative AFM images with corresponding Root Mean Square (RMS) values (nm) for films deposited from the positive bias DC EAACVD reaction of 1 M $TiCl_4$ solution in toluene at 600 °C and 5 $L.min^{-1}$ after annealing at 600 °C for 2 hours.

Table 4.9: Root Mean Square (RMS, nm), maximum transmission values in the visible (T%), direct band gap (DBG, eV) for unanneaed and annealed samples produced from the DC EACVD reaction of 1 M $TiCl_4$ solution in toluene at 600 °C and 5 $L.min^{-1}$ in absence of electric fields (sample A) and from positive (samples M to R) and negative bias (samples S to X) field strength.

				Unannealed			Annealed		
Sample	Applied Voltage (V)	Field Strength (Vm^{-1})	Substrate bias	RMS (nm)	T%	B.G (eV)	RMS (nm)	T%	B.G (eV)
A	0	0	--	16±6	63	3.1	25±6	51	3.2
M	1	1×10^2	Positive	6±3	76	3.25	24±12	77	3.2
N	5	5×10^2	Positive	20±4	64	3.2	13±6	76	3.2
O	10	10×10^2	Positive	15±2	69	2.9	25±13	77	3.0
P	15	15×10^2	Positive	8±2	59	3.0	8±4	49	3.1
Q	20	20×10^2	Positive	9±5	72	3.1	6±2	80	3.0
R	30	30×10^2	Positive	5±4	58	3.0	10±4	32	3.19
S	1	1×10^2	Negative	13±6	82	3.2	2±1	79	3.19
T	5	5×10^2	Negative	9±2	78	3.1	5±3	68	3.2
U	10	10×10^2	Negative	17±10	71	3.15	12±8	79	3.2
V	15	15×10^2	Negative	7±3	65	3.0	6±4	69	3.2
W	20	20×10^2	Negative	22±12	62	2.9	4±2	88	3.15
X	30	30×10^2	Negative	16±4	60	3.2	4±3	81	3.2

Resazuring photocatalytic testing was also conducted for annealed samples (Figure 4.29). It was found that the annealing process had a beneficial effect on negative bias deposited films with the exception of sample W (increased half-value from 6 to 13.5 min) and a detrimental effect on the majority of positive deposited films with the exception of samples M (decreased half-life value from 24.3 to 23.4 min) (Table 4.10). In particular, the annealing significantly improved the photo-activity of negative bias deposited films to half-life values lower than 7 min (samples T and U).

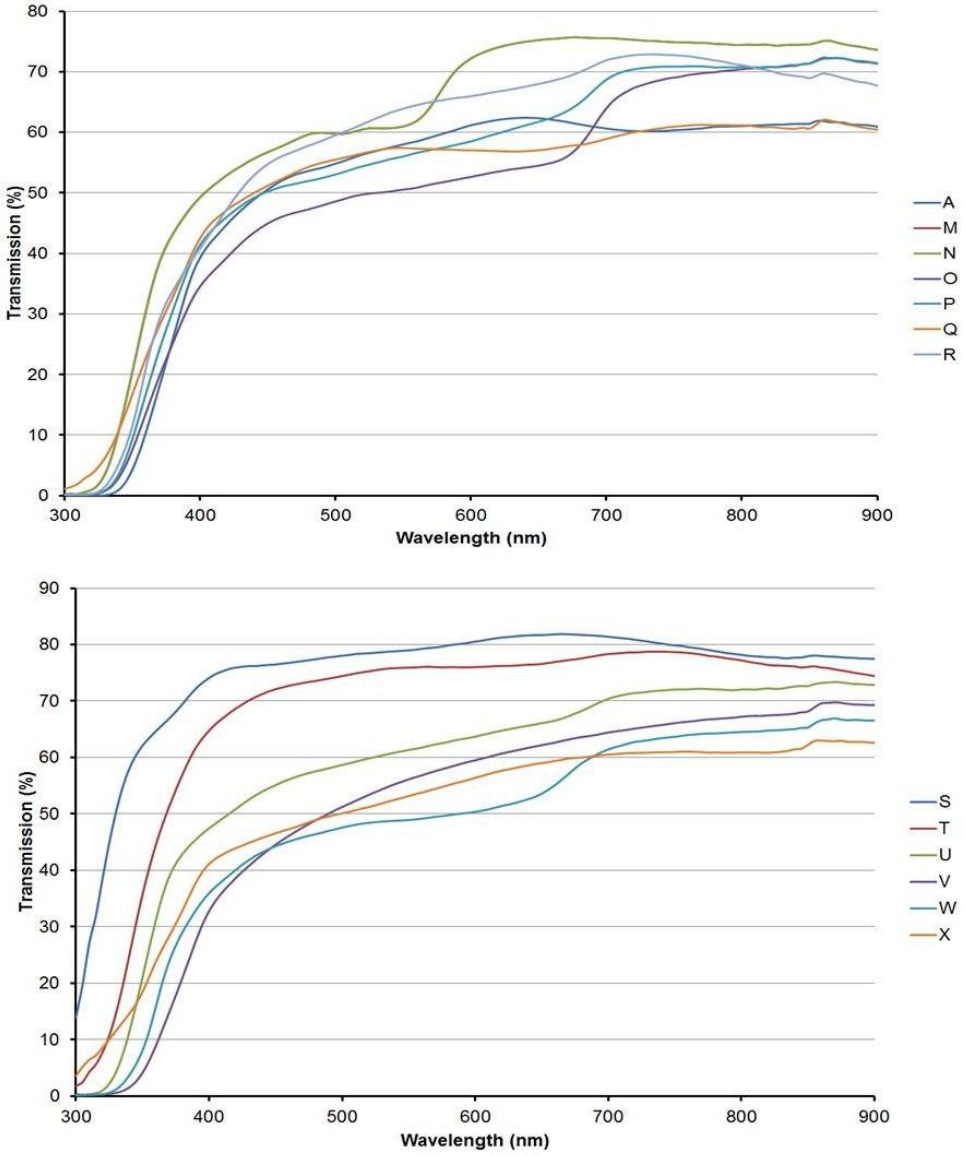

Figure 4.28: UV-vis spectroscopy for deposited films from the DC EAACVD reaction of 1 M $TiCl_4$ solution in toluene at 600 °C and 5 $L.min^{-1}$ in absence of electric fields (sample A) and from the positive (samples M – R) and negative bias (samples S – X) field strength.

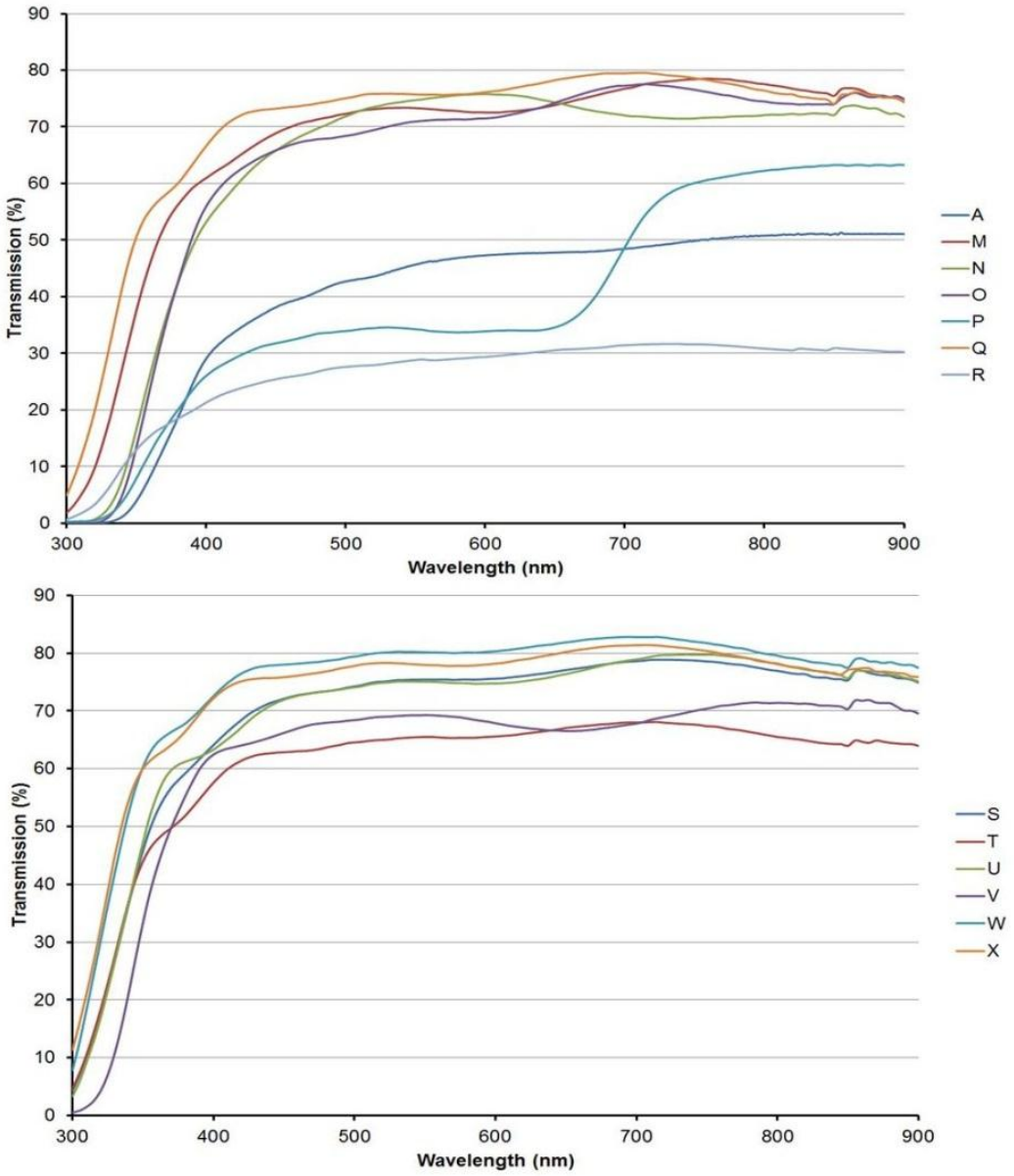

Figure 4.29: UV-vis spectroscopy deposited films from the DC EAACVD reaction of 1 M $TiCl_4$ solution in toluene at 600 °C and 5 $L.min^{-1}$ in absence of electric fields (A) and from the positive (M – R) and negative bias (S – X) field strength, after annealing at 600 °C for 2 h.

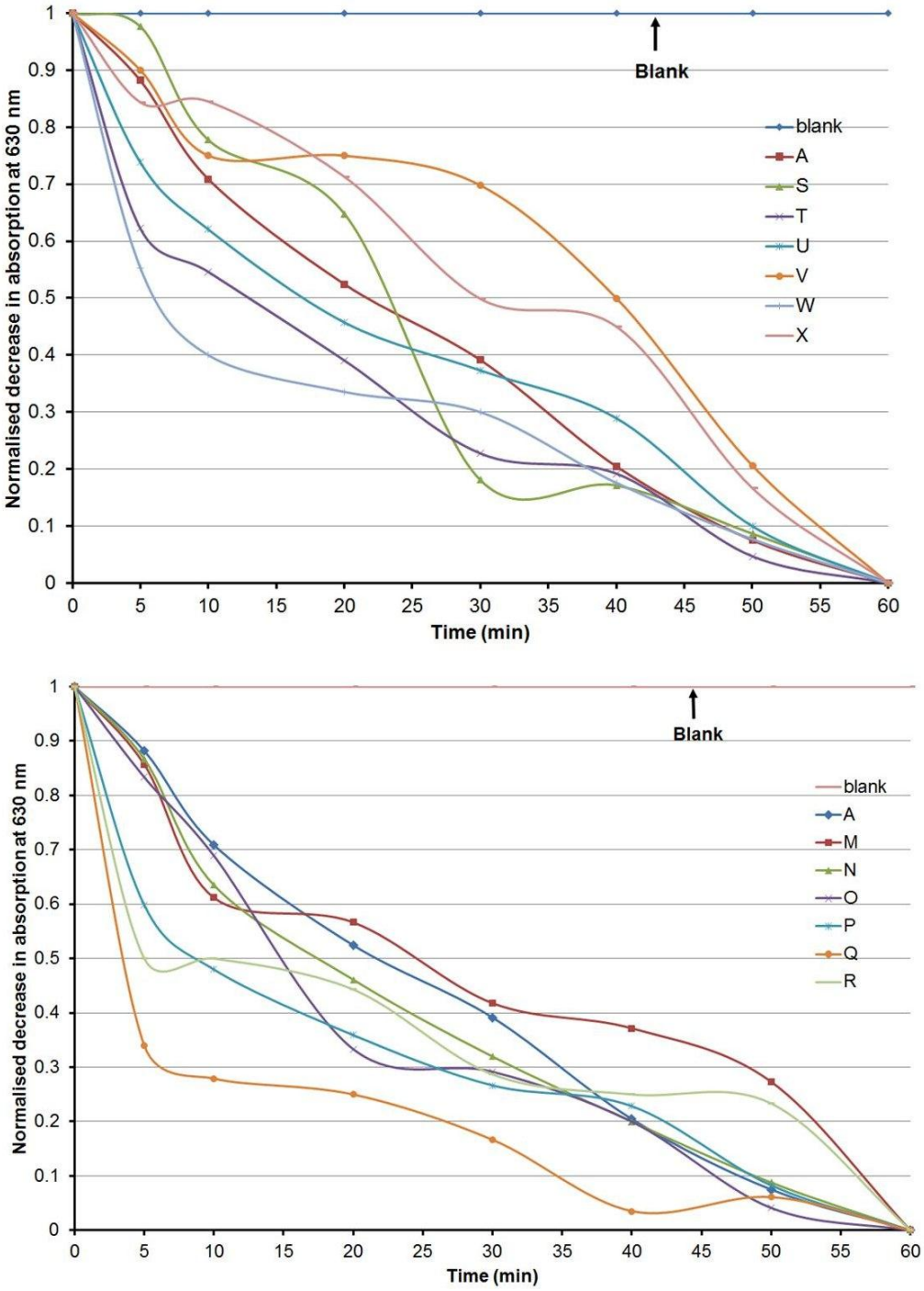

Figure 4.30: Normalised decrease in absorption of Resazurin intelligent ink at 630 nm with UVA irradiation (365 nm) against time (min) for deposited films from the DC EAACVD reaction of 1 M $TiCl_4$ solution in toluene at 600 °C and 5 $L.min^{-1}$ in absence of electric fields (sample A), from the positive bias (M-R) and the negative bias (S-X).

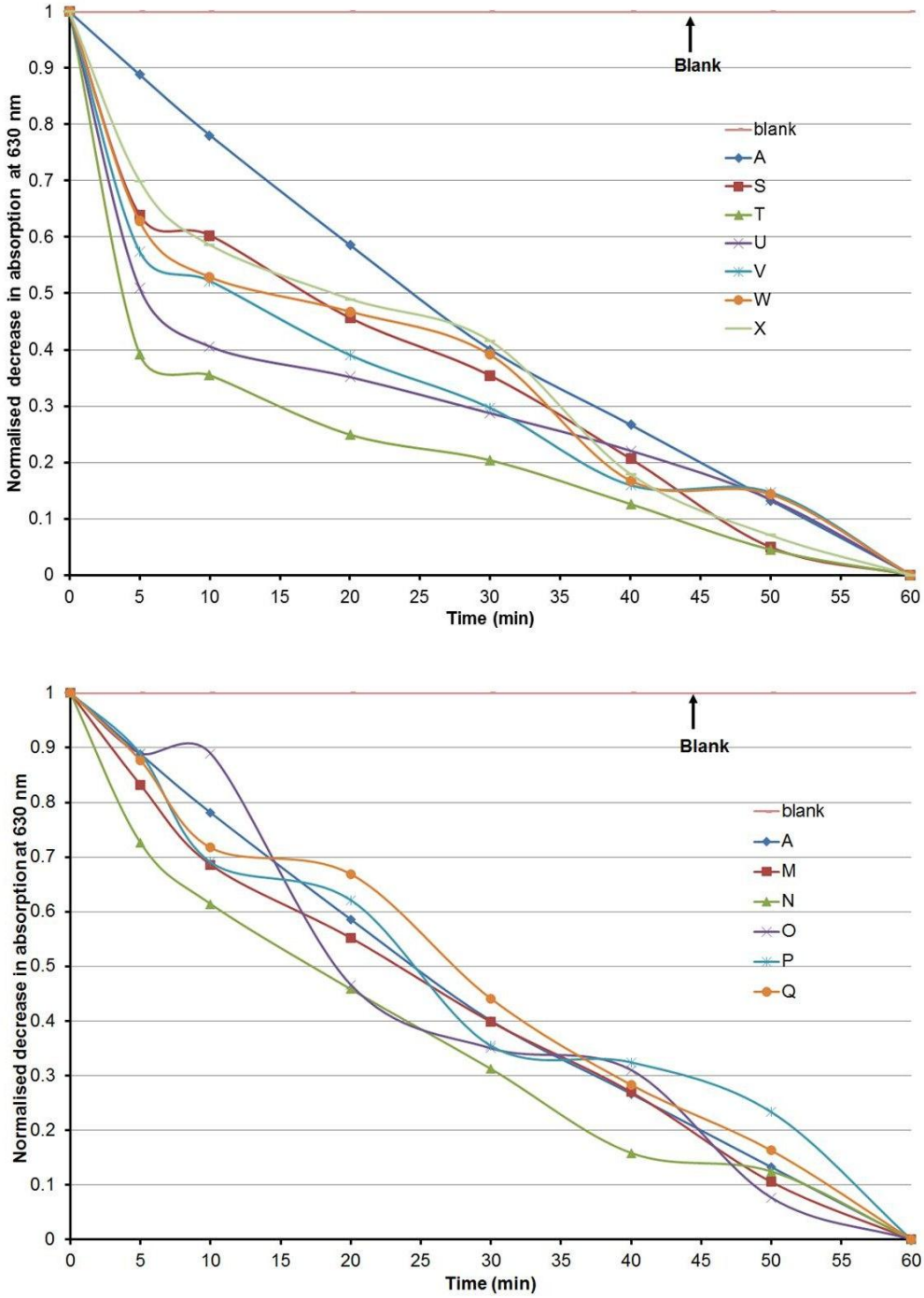

Figure 4.31: Normalised decrease in absorption of Resazurin intelligent ink at 630 nm with UVA irradiation (365 nm) against time (min) for deposited films from the DC EAACVD reaction of 1 M $TiCl_4$ solution in toluene at 600 °C and 5 $L.min^{-1}$ after annealing; in absence of electric fields (A), from the positive bias (M-R) and the negative bias (S-X) deposited films.

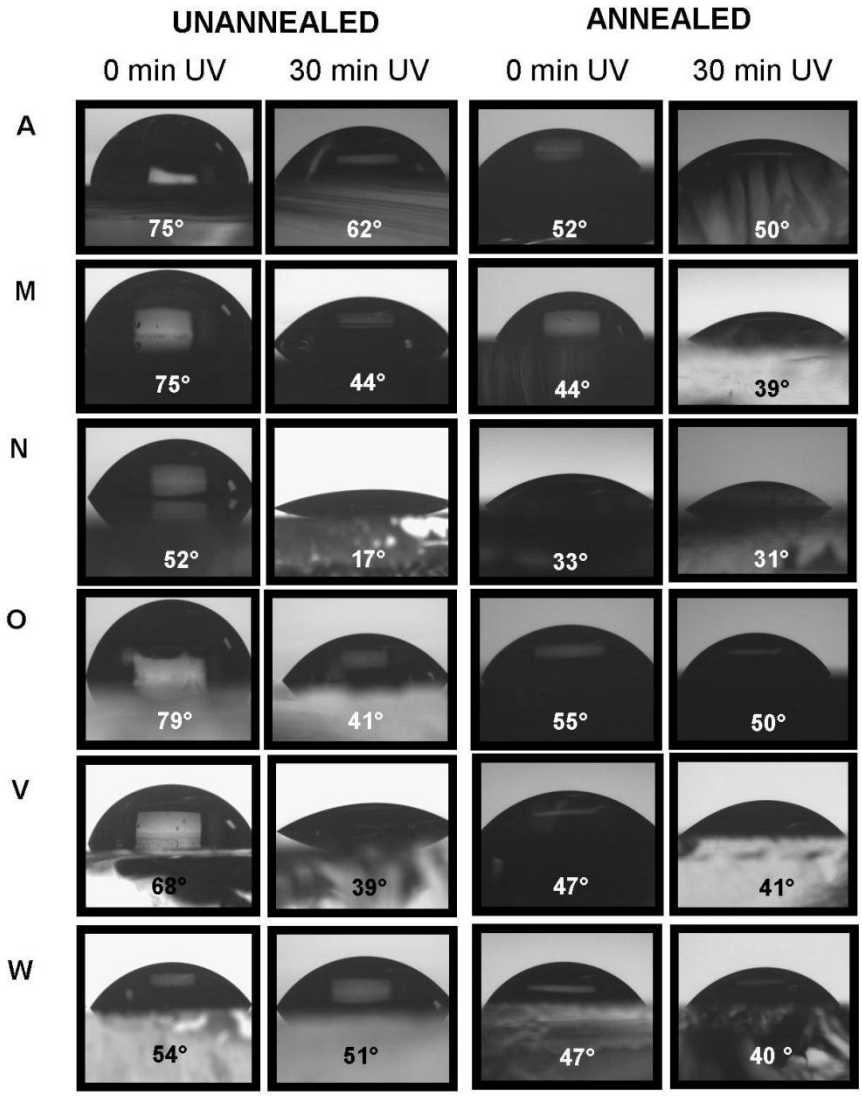

Figure 4.32: Representative mean-water contact angle images for deposited films from the DC EAACVD reaction of 1M $TiCl_4$ solution in toluene at 600 °C and 5 $L.min^{-1}$.

4.2.4.2. Water contact angles

TiO_2 thin films deposited from the DC EAACVD reaction of 1 M $TiCl_4$ solution in toluene at 600 °C and 5 $L.min^{-1}$ showed hydrophilicity with water-contact angles in the range of 52– 89° (Table 4.10). Figure 4.32 shows representative images for mean water-contact angle values measurements of DC deposited films before and after annealing. After 30 min UV irradiation (254 nm) all films decreased their water-contact angles. In particular, Samples Q, T and U showed the highest water-contact

angle reduction (41 – 47°). The lowest water contact angle reduction was observed for samples P, W and X (3 – 12°).The annealing process produced a decrease in water contact angles for all deposited films. The most important decrease was observed for samples A, M and O (23 – 26°). After 30 minutes UV irradiation (254 nm) all films decreased their water-contact angles. The most important water-contact angle decrease was observed for Sample U (73 – 52°).

Table 4.10: Average water-contact angles with SE of deposited films from the DC EACVD reaction of 1 M $TiCl_4$ solution in toluene before and after 30 min UV irradiation (254 nm); half-life photocatalytic testing or time needed to degrade 50% of the ink initial concentration, $t_{1/2}$ (min).

			Unannealed			Annealed		
Sample	Field Strength (Vm^{-1})	Substrate bias	Contact Angle (degrees) ± SE		Half-life	Contact Angle (degrees) ± SE		Half-life
			0 min	30 min	$t_{1/2}$ (min)	0 min	30 min	$t_{1/2}$ (min)
A	0	--	75±2	62±1	21.5	52±1	48±3	24.5
M	1 x 10^2	Positive	75±5	44±8	24.3	49±1	39±2	23.4
N	5 x 10^2	Positive	52±4	17±2	17.2	33±2	31±2	19
O	10 x 10^2	Positive	79±2	41±8	14.9	55±3	50±3	18.8
P	15 x 10^2	Positive	52±3	46±2	8.5	41±3	38±5	24.5
Q	20 x 10^2	Positive	71±4	24±3	3.3	50±1	51±2	27.3
R	30 x 10^2	Positive	64±5	42±10	5	54±3	44±3	--
S	1 x 10^2	Negative	74±2	56±4	23.5	60±0.5	60±2	17
T	5 x 10^2	Negative	59±2	17±2	13	39±7	34±3	4
U	10 x 10^2	Negative	89±5	46±3	17	73±4	52±5	5.1
V	15 x 10^2	Negative	68±2	40±7	40	47±5	41±3	11.9
W	20 x 10^2	Negative	54±2	51±2	6	47±5	40±2	13.5
X	30 x 10^2	Negative	58±5	46±7	30	40±4	34±4	19

4.3. Discussion

4.3.1. Modifications in microstructure

The AC EAACVD growth of TiO_2 from the reaction of 1 M $TiCl_4$ in toluene influenced the morphology and particle size of deposited films. The application and increase of the field strength (from 1 x 10^2 to 15 x 10^2 Vm^{-1}) produced an important decrease of particle size from 150 nm to 70 nm. At higher field strength (20 x 10^2 – 30 x 10^2 Vm^{-1}) films showed a change in morphology from spherical to elongated shape and an increase in particle size to 110 – 130 nm. This can be explained by the thermal decomposition of $TiCl_4$ on the substrate. Pratsinis *et al* [164] proposed a mechanism in which $TiCl_4$ decomposed to $TiCl_z$ radicals ($z < 4$) via thermal decomposition and abstraction reactions. Subsequently, those radicals would oxidise to yield various TiO_yCl_z oxychlorides ($y \leq 2$, $z < 4$) which would go through a dimerization process to finally yield TiO_2. Effusion beam mass spectroscopy studies in the decomposition of Ti-Al-Cl systems at elevated temperatures (up to 1400 K) showed that $TiCl_3^+$ species predominated at 900 K [165], suggesting Equation 4.1 as the most probable starting reaction in $TiCl_4$ thermal decomposition. Likewise, it was found that $TiClO_2$ and ClO were the most predominating intermediate species (Equation 4.2) which was later corroborated by other thermodynamics studies on $TiCl_4$ thermal decomposition [166,167].

$$TiCl_4 + M \rightarrow TiCl_3^+ + Cl + M \qquad \text{(Equation 4.1)}$$

$$TiCl_3 + O_2 \rightarrow TiOCl_2^+ + OCl^- \qquad \text{(Equation 4.2)}$$

Electric fields may interact with the intermediate species produced during the thermal decomposition of $TiCl_4$, either in the gas phase or during the nucleation on the substrate. Films produced at 600 °C and 5 $L.min^{-1}$ showed a gradual decrease of the particle size from 150 nm to 70 nm as the electric field was introduced and increased. This can be explained by a retarding effect of the diffusion process of the precursor towards the substrate as a consequence of the interaction of lower field strength and the intermediate species. Likewise, at higher field strength (20 x 10^2 – 30 x 10^2 Vm^{-1}) the particle size is increased to 135 nm and the morphology changes from spherical to elongated shape. Thus, as the field strength is increased, the kinetic energy of precursors is also increased inducing the acceleration of intermediate species towards

the surface. Likewise, intermediate species could undergo a stretching effect similar to that observed in previous section (Figure 3.34). Furthermore, Furthermore, such an effect could cover nucleation sites for incoming species to the substrate which could explain why for sample F particle agglomeration is lower and film thickness decreased from 90 nm to 10 nm. However, this could be due to a rebound effect consequence of the high kinetic energy induced to the intermediate species. It would appear that the application of electric fields reduces the number of active precursors reaching the surface which produced a reduction of film thickness (Sample A and B). As the field strength is increased (samples C and D) the active species also increased favouring film thickness until reaching an optimum (sample D). Similar effects can be observed for deposited films produced at 450 °C and 1 L.min^{-1}. In absence of electric fields the microstructure showed big clusters with no particle differentiation. The thermal decomposition of the precursor happens almost immediately on the substrate. However, as the field strength is applied and increased a differentiation of orthogonal particles is produced and thus, the same retard effect on particles nucleation is observed under these experimental conditions. However, contradictorily to the results observed at 600 °C and 5 L.min^{-1}, the film thickness progressively increased with the field strength and the microstructure showed bigger agglomerate size. This can be explained in terms of residence time, which can be calculated using equation 3.4.

Considering that samples B to G were produced at 5 L.min^{-1} and samples I to L were produced at 1 L.min^{-1}, the volumetric flow results in 83.33 cm^3 s^{-1} and 16.66 cm^{3}s^{-1}, respectively, substituting in equation 3.5;

$$t_{res}\ (samples\ B\ to\ G) = \frac{67.5}{83.33} = 0.76\ \text{s}$$

$$t_{res}\ (samples\ I\ to\ L) = \frac{67.5}{83.33} = 4.05\ \text{s}$$

Knowing the residence time of the precursor and the frequency of the electric field, it is possible to know the number of changes in bias using equation 3.5.

$$N_{bias}\ (samples\ B\ to\ G) = 0.76 \times 50 = 38.2 \approx 38\ changes$$

$$N_{bias}\ (samples\ I\ to\ L) = 4.05 \times 50 = 202.73 \approx 203\ changes$$

According to this, during a residence time of 4.05 s, the precursor can be influenced by a maximum of 203 changes throughout deposition. This, combined with the acceleration induced by higher field strength, would have encouraged the agglomeration of particles as well as the film thickness.

On the other hand, the annealing process for studied deposited films at 600 °C and 5 $L.min^{-1}$ produced higher agglomeration (especially, samples B, C and F) and an increase of particle size in accordance with literature [35,168]. Likewise, changes in morphology were observed for samples D and E (from spherical to angular), sample F (from acicular to spherical) and sample G (from acicular to angular) which can be explained in terms of anatase to rutile transformation.

Different composition of polymorphs anatase and rutile was found for titania thin films deposited at 600 °C and 450 °C. For films produced at 600 °C , the sample deposited with no electric field showed pure rutile before and after the annealing which indicates that the transformation from an individual anatase crystallite proceeds rapidly to the entire crystallite [169]. However, deposited films under the influence of electric fields showed a mix of polymorphs anatase-rutile. We have found that the application of electric fields during titania thin films growth alter the particle size and shape of deposited films which along the experimental temperature (600 °C) might have influenced their content in anatase and rutile. Wang *et al.* [170] found that the transformation of anatase to rutile responded an interface and surface nucleation when producing titania by hydrothermal methods at 600 – 700 ºC. According to this argument rutile crystals are initialized at the interface of small sized anatase nanoparticles which also serve as nucleation sites for rutile growth. Although in this work the particle size is greater, it was observed that deposited films with particle size from 100 – 90 nm (Samples B – D) showed the highest content in rutile (60 to 54 %). Moreover, except from Sample B, these deposited films showed the same behaviour after annealing by increasing the content in rutile to 100%. Anatase has a greater transformation rate for smaller particles. However, the stability crossover in the transformation depends on a critical size mechanism which Zhang *et al.*[36] identified at 14 nm. Thus, according to this study when the particle decreased below 14 nm, anatase became more stable than rutile. This argument corresponds to the results shown in this work as deposited films with the smallest particle size (Sample E)

presented the highest anatase content (98%) before and after annealing which would set our critical size at 70 nm. However, the energies of different titania polymorphs are close that phase could be changed by small differences in surface energies [36]. This would explain the disparity of polymorph contents for films produced at 450 °C regardless the particle size.

After annealing some samples dramatically increased their content in anatase (sample B and F) having similar or greater particle size than those which increased their content in rutile (sample C and D). This can be explained by the crystal structure. Both polymorphs consist of tetragonal structures of TiO_6^{2-} octahedra in which each Ti^{4+} ion is surrounded by an irregular octahedron of oxide ions. However, the type of linkage differs in rutile and anatase. TiO_2 crystals are formed by two types of linkages, edge sharing and corner sharing. In rutile crystal phase two opposite edges of each octahedron are edge shared forming a linear chain and the chains are linked together via corner oxygen atoms [29]. Anatase has four edges shared per octahedron and thus, more collision among molecules favours the formation of this crystal phase as more edges are available to form a bond [37]. Therefore, the annealing process produced a coalescence of particles in form of clusters in samples B and F which would have enhanced the content in anatase.

The induction of DC electric fields during the AACVD growth of TiO_2 thin films from the reaction of 1 M $TiCl_4$ solution in toluene at 600 °C and 5 $L.min^{-1}$ also influenced the shape and morphology of deposited films. However, no predominance of certain morphology was observed depending on the substrate bias. It was observed that the application of DC electric fields produced mostly angular and spherical morphology of 100 – 170 nm except for sample N and O which showed rod-like morphology. Considering the thermal decomposition pathways of $TiCl_4$ it would have been expected a different behaviour in the shape of nanostructure for negative biased electric fields. However, the application of AC and DC electric fields indistinctly produced predominantly angular nanostructures. It can be due to the high reactivity of the precursor in the experimental conditions tested (600 °C, 5 $L.min^{-1}$) which produced reactions in the gas phase. Thus, the decomposition and nucleation of intermediate species might happen too quickly for the morphology to be influenced by

the pulling or repelling forces (depending on the substrate bias) of the field strength applied.

Nonetheless, the interaction of the electric fields with the charge intermediate species result of the thermal decomposition of $TiCl_4$ can be observed by the difference in film thickness depending on the substrate bias. Negative biased produced thicker films as the field strength increased until reaching a maximum at 15 x 10^2 Vm^{-1} (225 nm) and then dramatically decreased to 30 nm. The intermediate species produced during the thermal decomposition are positively charged and would be pulled towards the substrate as the field strength is increased. The decrease of film thickness at high field strength (15 x 10^2 – 20 x 10^2 Vm^{-1}) has been already reported [22] and explained by a rebound of species due to a high acceleration towards the surface at high field strength.

As in AC deposited films, the application and increase of DC electric fields increase the content of anatase crystal phase. Furthermore, most of deposited films showed primarily anatase in a range of 79% – 98%. As an exception, samples O and V showed a percentage of anatase under 40% and sample T showed purely rutile. Thus, there is no evidence that the substrate bias produced a particular effect in the crystal phase as such. For positive bias deposited films, the difficulty of establishing a cross-over particle size in which the transformation from anatase to rutile occurs can be attributed to the heterogeneity in shape and size of the microstructures as well as the lack of crystallinity. It was observed 21% of rutile content at a particle size of 170 nm (sample N) which gradually increased to 63% with a decrease of the particle size to 120 nm. However, sample R showed high content in anatase (98%) with a particle size of 130 nm. It was observed that samples N and O showed rod-like nanoparticles whereas the rest of deposited films showed either angular or spherical morphology. Agglomerate morphology is known to be one of the numerous parameters that control the anatase to rutile transformation [33]. In this case, it seems that rod-like structure (samples N and O) favoured edge share bonding to promote rutile crystal phase.

On the other hand, negative biased deposited films showed higher rutile content (63%) at particle size of 100 nm (sample V) and increased to 100 % as the particle size decreased to 85 nm (sample T) in accordance with results found for AC deposited films. Lower particle size produced the stability of anatase crystal phase which set the

cross-over particle size in 80 nm (sample S). Contradictory to AC deposited films, most of DC deposited films showed a decrease in anatase content after annealing with the exception of samples T and V. These films showed flatter clusters in their microstructure after annealing which, as suggested above, could have favoured the anatase transformation by the coalescence of nanoparticles.

The application of electric fields during the reaction influenced the surface roughness of as-deposited films probably as a result of the induced changes in the grain size and film thickness. The deposition rate is considered one of the most important parameters influencing the structure and morphology of deposited thin films [171]. However, it was observed that in some cases, the increase of grain size resulted in thinner films (samples F and G) with no changes in surface roughness in comparison to other of deposited films (samples D and E). In other cases, films with high thickness showed lower surface roughness (samples L, V) as previously reported [172]. This can be due to a decrease of nucleation sites with increasing thickness which could significantly decrease the surface roughness of deposited films. Grain growth can be limited by the grain boundary energy rather than by the film thickness [173]. The grain morphology plays an important role in the growth kinetics process and therefore, the surface roughness [174]. This would explain why different RMS values were found for different the agglomerates morphology. For instance, deposited films with elongated nanoparticles in their morphologies such as samples F and G showed low surface roughness whereas deposited films with spherical morphology (samples U and X) showed higher surface roughness. Generally, the annealing produced an increase in surface roughness of deposited films. The annealing process is related to a secondary growth in the film which is believed to be driven by the reduction of the total boundary energy. According to this, the secondary grain growth increases when the film thickness decreases [173].

4.3.2. Photocatalytic properties

As observed in films produced from TTIP (chapter 3), the most photocatalytically active titania thin films produced from $TiCl_4$ were those which showed small particle size and elongated shape. Thus, samples C and D with spherical particles of 90 nm

length showed half-life values of 3.5 min and 9 min, respectively. Although Samples F and G showed slightly bigger particle size (110 – 130 nm) their microstructure showed elongated particles which would explain why these deposited films also showed the highest photo-activity with half-life values of 4.5 and 3.5 min, respectively. Thinner films gave better photocatalytic performance. In this work, the optimum film thickness was in the range of 2 – 10 nm. Nevertheless, film thickness does not seem to be as determining as the particles morphology and size as thin films such as sample B with similar thickness (~ 4 nm) but slightly bigger particle size (~110 nm) gave worse half-life values (11.5 min). Furthermore, it was observed that the most photo-active films (samples C, D, F, and G) showed an anatase to rutile ratio close to 1:1 which agreed with previous works [41,65]. Hence, it seems clear that an optimum in titania photocatalytic performance can be reached when having equal amount of anatase and rutile and that, increasing or decreasing the content of anatase in the microstructure has detrimental effects on the photo-activity as it was observed in samples A, B and E. Thus, it seems plausible that rutile nanoparticles growing on the surface of anatase aggregates produced an effective charge separation by providing channels for rapid transfer of photo-generated electrons to the conductive substrate, similarly to the observations found by Song *et al*. (Song et al., 2008) when studying the photo-electrochemical response of titania thin films composed of rutile nanorods in anatase aggregates.

Surprisingly, the annealing process had a detrimental effect on the most photoactive thin films (samples C, D and F). Although this has been attributed to contaminated species acting as recombination centres at annealing temperatures above 400 °C [168], the decrease in the photocatalytic performance can be due to an unbalance content of both polymorphs as either the rutile (samples C and D) or the anatase (sample F) content increased to values close to 100%.

Generally, the application of DC electric fields produced more photoactive films comparing to the film produced in absence of electric fields (sample A, half-life = 21.5 min). The best photocatalytic performance was observed for films which showed high content in anatase crystal phase (98%) with half-life values from 3.3 to 8.5 min (samples P –R and W). The superiority of anatase photocatalytic performance over rutile independently of film thickness has been already reported [63,175] and attributed to a more efficient bulk transport of excitons to the surface comparing to rutile crystal

phase [175]. With the same content in anatase samples M, S U and X showed comparably worse photocatalytic performance with half-life values in the range of 17 – 30 min. SEM images showed a porous microstructure for sample M. The lack of agglomeration of the particles could have created grain boundaries which could have acted as recombination sites. In the case of samples S, U and X, the decrease in films photo-activity can be attributed to the poor crystallinity observed in negative biased deposited films.

It has been reported that elongated nanoparticles are more favourable for photocatalysis [176]. As stated in section 4.3.1., samples O and N showed rod-like nanoparticles in its microstructure. However, their half-life values were not among the optimum (14.9 – 17.2 min). Nevertheless, the anatase content in these samples were lower (79 – 37%) which might have been detrimental for its photocatalytic performance. In some cases, samples with pure rutile content (sample T, half-life = 13 min) showed better photo-activity than films with high content in anatase (samples S and U). The lower photo-activity of rutile is often related to its larger particle size and lower specific surface areas [177]. However, sample T showed in comparison small particle size (86 ± 7 nm) which could have been favourable for photocatalysis.

The worst photocatalytic performance was observed for Sample V (40 min). This sample presented high film thickness (225 nm) which has been previously reported to impede charge carrier transfer from the bulk of the material to the surface and thus, hinder photocatalysis [52,55].

Generally, the annealing process had a detrimental effect on positive bias deposited films which can be attributed to a decrease in anatase content. The most significant decrease in photo-activity was observed for Samples P and Q, which showed an increase in half- life values from 8.5 min and 3.3 min to 24.5 min and 27.3 min, respectively. These samples showed an important decrease in anatase (98%) to form pure rutile after annealing. A slightly lower decrease in photo-activity was observed for sample M, which increased the half-value from 24.3 min to 23.4 min. However, the decrease in anatase in this sample was only from 98% to 84%. For negative bias deposited films, the annealing process significantly improved the photo-activity of deposited films. The beneficial effect can be attributed to an increase in anatase content as well as a significant improvement of crystallinity after annealing. Sample

T, which had shown pure rutile after annealing, decreased its half-life value from 13 min to 4 min with an increase in anatase to 22%. Sample V showed an important decrease of its half-life value from 40 min to 11.9 min. This sample increased its anatase content to 43% after annealing which reaffirms previous observations on increase of photo-activity for anatase to rutile ratio close to 1:1 [178]. Other deposited films showed better photo-activity with equal content in anatase after annealing (samples U and W), thus the decrease in half-values can be attributed to an improvement in films crystallinity.

Finally, the application of electric fields did not seem to have significantly influenced the wettability of deposited films, which showed hydrophylicity in all cases.

4.4. Conclusions

TiO_2 thin films were successfully produced applying AC electric fields during the aerosol assisted-CVD films from the reaction of 1 M $TiCl_4$ solution in toluene at different substrate temperatures and gas flow rates. It was found that the field strengths induced changes in the morphology and size of particles. Consequently, this affected the content in anatase and rutile in the microstructure and thus, the photocatalytic performance of deposited films. The most photoactive films (half-life values of 3.5 min) showed an anatase to rutile ratio close to 1:1. It was also found that values above or below this ratio produced detrimental effects on titania photocatalytic activity.

Likewise, the application and increase of DC field strength induced changes in the microstructure as well as in the crystal phase improving the photocatalytic properties in most of the samples tested. Nevertheless, films deposited from DC electric fields showed lower photo-activity than films deposited from AC electric fields. The best photocatalytic performance was observed for samples which showed high content in anatase (98%) with half-life values of 3.3 min. The annealing process significantly improved the crystallinity of negative bias deposited films improving their photo-activity by up to ten times in some cases.

Chapter 5:

Titanium Dioxide Thin Films Produced from the Electric Field Assisted Atomospheric Pressure Chemical Vapour Deposition of Titanium (IV) Isopropoxide in Ethanol

5.1. Introduction

This chapter presents the results on the experimental study of the TiO_2 thin films growth from Electric Field Assisted APCVD (EAAPCVD) using Titanium Tetraisopropoxide (TTIP) as a precursor and ethanol as an oxygen source.

5.2. Results

5.2.1. Film synthesis and characterisation of AC deposited films

The EAAPCVD reaction of TTIP and ethanol at 550 °C and plain flow rate of 2 $L.min^{-1}$ produced thin films with good adherence to the substrate, the films passed the Scotch tape test and could not be wiped off with a piece of towelling. The experimental conditions and films appearance are described in section 2.2.2.1. The deposited films were clear and transparent with the exception of the films produced with an applied electric field of 1 x 10^2 Vm^{-1} and 10 x 10^2 Vm^{-1}, which had a brown colour suggesting the incorporation of carbon throughout the film. XRD analysis confirmed anatase in all deposited films. Further analysis on Raman spectroscopy also confirmed the presence of rutile crystal phase for Samples A – C (Table 5.1).

Table 5.1: Field strength and material phase for titania thin films produced from the AC EAAPCVD reaction of TTIP and ethanol at 550 °C and 2 L.min^{-1}.

Sample	Applied Voltage (V)	Field Strength (Vm^{-1})	Material Phase (XRD /Raman)
A	0	0	Anatase-Rutile
B	1	1×10^2	Anatase-Rutile
C	5	5×10^2	Anatase-Rutile
D	10	10×10^2	Anatase
E	15	15×10^2	Anatase
F	20	20×10^2	Anatase
G	30	30×10^2	Anatase

Scanning electron microscopy

Scanning electron microscopy images of the titanium dioxide depositions are shown in Figure 5.1. Deposition carried out in absence of an electric field (Figure 5.1 A) revealed a thin film comprised of agglomerated acicular nanoparticles of 150 ± 8 nm in length and spherical agglomerations of 90 ± 5 nm in diameter with a film thickness of 48 ± 10 nm. The introduction of an electric field of 1×10^2 Vm^{-1} (sample B) across the electrodes of the glass substrate during the deposition produced similar morphology and particle size. However, an increase in the diameter of the spherical nanoparticles (100 ± 10 nm) and film thickness (80 ± 9 nm) was observed. As the field strength was increased to 5×10^2 Vm^{-1} (sample C), the morphology changed to spherical agglomerations of 110 ± 7 nm in diameter and the film thickness significantly increased to 170 ± 14 nm. The increase of the field strength to 10×10^2 Vm^{-1} (sample D) produced a change in morphology to acicular agglomerations of reduced particle size (80 ± 15 nm) forming clusters of 230 ± 16 nm. The film thickness decreased to 120 ± 5 nm. Further increase of the field strength (up to 30×10^2 Vm^{-1}) slightly increased the size of elongated nanoparticles (120 ± 17 – 150 ± 14 nm). Likewise, particle agglomeration increased with the field strength forming clusters of 180 ± 22 – 210 ± 12 nm for Samples E and F and 590 ± 105 nm for sample G. The film thickness in this range fluctuated between 150 ± 19 nm to 290 ± 10 nm. Agglomerate size and film thickness values are listed in Table 5.2.

Table 5.2: Agglomerate size (nm), film thickness (nm) with standard error (SE) obtained from SEM and mean crystallite size (nm) obtained from the Scherrer equation, for deposited films from AC EAAPCVD reaction of TTIP and ethanol at 550 °C and 2 $L.min^{-1}$.

Sample	Applied Voltage (V)	Field strength (Vm^{-1})	Agglomerate size (nm)±SE		Thickness (nm)±SE	Mean crystallite size (nm)
			acicular	spherical		
A	0	0	150±8	90±5	48±10	18±0.5
B	1	1 x 10^2	150±18	100±10	80±9	14±2
C	5	5 x 10^2	--	110±7	170±14	--
D	10	10 x 10^2	80±15	230±16	120±5	--
E	15	15 x 10^2	120±17	180±22	150±19	19±1
F	20	20 x 10^2	150±4	210±12	290±10	22±2
G	30	30 x 10^2	110±9	590±105	150±9	18±1

X-ray diffraction

X-ray diffraction was carried out and compared to the JCPDS database (JCPDS file number: 00-021-1272) to investigate the materials phase (Figure 5.2). All deposited films showed anatase TiO_2. Characteristic peaks for anatase (101) plane (2 Theta = 25.28°) and anatase (004) plane (2 Theta = 37.8°) were found for all deposited films. Likewise, characteristic peaks for the anatase (200) plane was observed for all films except for samples C and D. Peaks for the anatase (211) (2 Theta = 48.05°) plane were only observed for films deposited with higher field strength (sample E – G). Casserite SnO_2, from the underlying FTO coated glass substrate was also observed. The relative intensity of the Bragg peaks associated with TiO_2 changed with the field strength revealing a preferred orientation. Texture coefficient analysis was conducted to investigate the preferred crystal orientation [151,152]. As Table 5.3 shows, all films presented high preferential orientation in the (004) plane with texture coefficient greater than 3. Lower values were found for Samples F and G (2.6 – 3).

The crystallite size of the deposited films was calculated from the full width at half maximum (FWHM) of different peaks using the Scherrer equation[155] (Table 5.2). Characteristic peaks of 2θ = 25.28° (101), 2θ = 37.8° (004), 2θ = 48.05° (200) were used. Likewise, shape factor of 0.9 [153] was chosen. However, no crystallite size value could have been obtained for samples C and D as their XRD pattern only showed two peaks. The application of electric

fields produced a decrease in the mean crystallite size from 18 ± 0.5 nm to 14 ± 2 nm (sample B). As the electric field is increased the crystallite size also increases (19 ± 1 – 22 ± 2 nm for samples E and F). At 30 x 10^2 Vm^{-1} (sample G) the crystallite size decreased to 18 ± 1 nm.

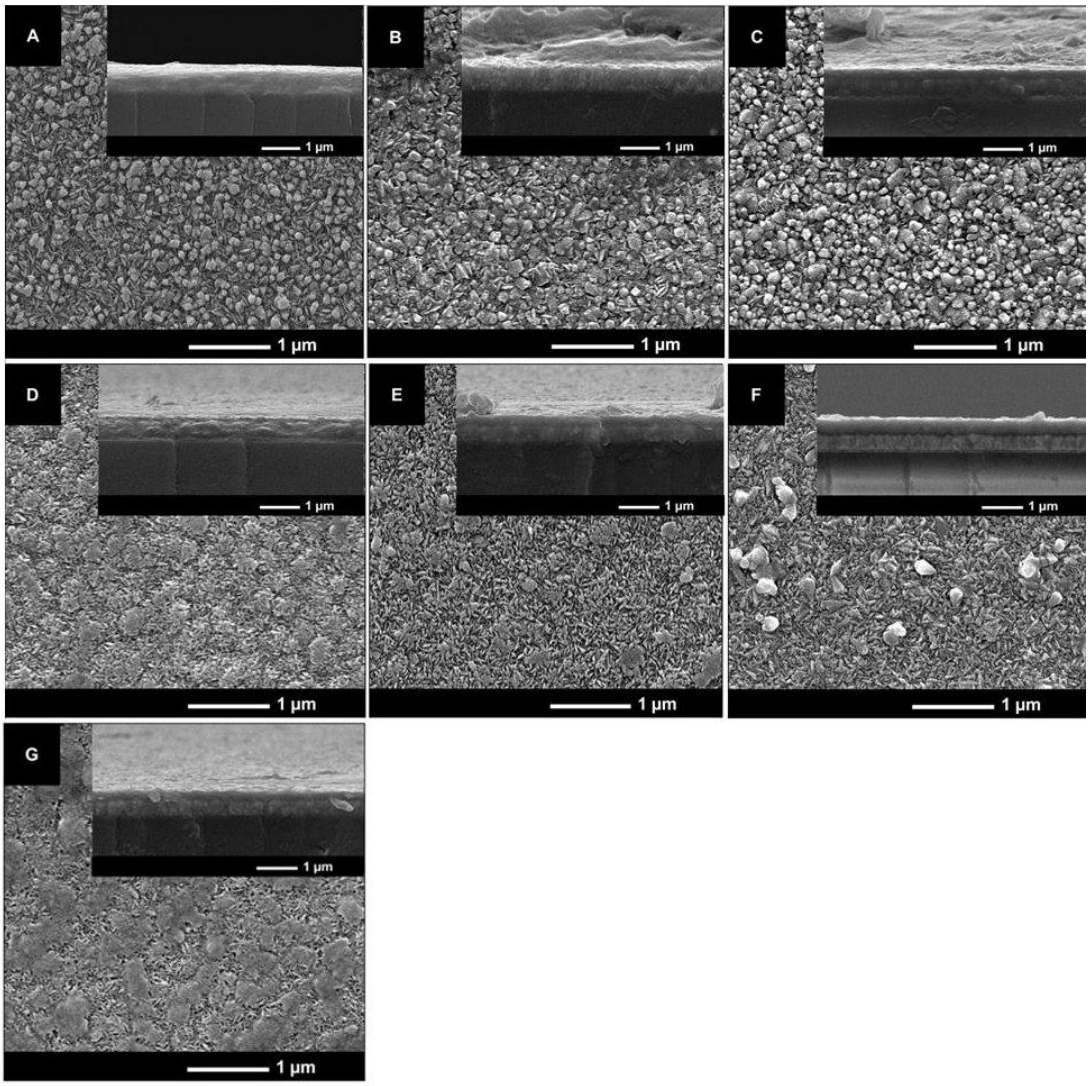

Figure 5.1: Scanning Electron Microscope images of samples prepared without electric field and from the AC EAAPCVD reaction of TTIP solution and ethanol at 550 °C with a flow rate of 2 $L.min^{-1}$. A) 0 Vm^{-1}, B) 1 x 10^2 Vm^{-1}, C) 5 x 10^2 Vm^{-1}, D) 10 x 10^2 Vm^{-1}, E) 15 x 10^2 Vm^{-1}, F) 20 x 10^2 Vm^{-1}, G) 30 x 10^2 Vm^{-1}. Side-on images were captured at 60,000 magnification and cross-section images at 40,000 magnification.

Raman spectroscopy

Raman spectroscopy was carried out in order to complement XRD analysis for phase identification. Figure 5.3 shows Raman spectra for all the deposited films. Generally, samples gave strong Raman peaks centred at 147 cm^{-1} and 642 cm^{-1} and weaker peaks centred at 198 cm^{-1}, 395 cm^{-1}, 513 cm^{-1}, revealing characterizing bands of anatase TiO_2 [134]. Furthermore, strong Raman peaks for rutile 447 cm^{-1} and 612 cm^{-1} [38] was observed for samples B and C. Quantification analysis from Raman spectra (see section 2.3.3) confirmed the presence of rutile in all deposited films but the percentage varied depending on the field strength (Table 5.3). Sample A (no electric field) showed mostly anatase (90%). As the field strength was applied and increased (1 – 5 x 10^2 Vm^{-1}) the content in anatase decreased to 58% – 56% (sample B and C). As the field strength was increased (to 30 x 10^2 Vm^{-1}) the content in anatase increased to 98% (samples D to G).

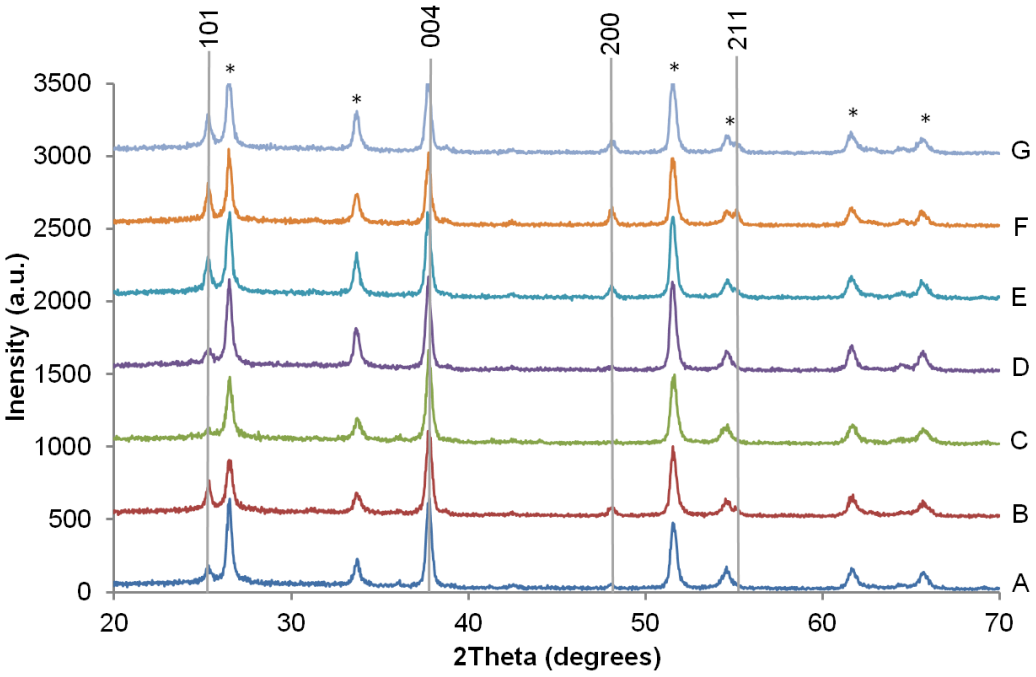

Figure 5.2: XRD patterns for samples prepared from the EAAPCVD reaction of TTIP and ethanol at 550 °C and a gas flow rate of 2 $L.min^{-1}$. A) 0 Vm^{-1}, B) 1 x 10^2 Vm^{-1}, C) 5 x 10^2 Vm^{-1}, D) 10 x 10^2 Vm^{-1}, E) 15 x 10^2 Vm^{-1}, F) 20 x 10^2 Vm^{-1}, G) 30 x 10^2 Vm^{-1}. The peaks marked with dots denote the cassiterite peaks specific of SnO_2 crystalline phase, from the underlying FTO glass substrate.

Atomic force microscopy

AFM was performed scanning over a 2 µm x 2 µm region in order to obtain Root Mean Square (RMS) roughness values as a proxy of surface roughness (Figure 5.4). As it can be observed, the application of AC electric fields slightly decreased the surface roughness from 6 ± 4 nm to 2 ± 1 nm (Sample A and B). The increase of field strength produced an increase in surface roughness to 10 ± 4 nm (Sample C). For the remainder of the field strengths a gradual decrease in surface roughness to 1 ± 0.2 nm (Sample G) was observed. RMS values are listed in Table 5.5.

Table 5.3: Texture Coefficient of TiO_2 thin films produced from the EAAPCVD reaction of TTIP and ethanol at 550 °C and 2 $L.min^{-1}$.

Sample	Field Strength (Vm^{-1})	Texture Coefficient ($TC_{(hkl)}$)			
		(101)	(004)	(200)	(211)
A	0	0.2	3.54	0.15	0.11
B	1×10^2	0.28	3.15	0.17	0.42
C	5×10^2	0.1	3.55	0.1	0.24
D	10×10^2	0.17	3.41	0.14	0.27
E	15×10^2	0.3	3.05	0.32	0.34
F	20×10^2	0.31	2.6	0.42	0.72
G	30×10^2	0.32	3	0.34	0.38

UV-vis spectroscopy

UV/VIS spectroscopy revealed that the application of field strength during the EAAPCVD deposition had a detrimental effect on the transmission values of the thin films (Figure 5.5). Hence, maximum transmission values in the visible gradually decreased when applying and increasing the field strength. Sample A showed the highest transmission values in the visible (70%). As the field strength was applied and increased up to 10×10^2 Vm^{-1} the transmission in the visible gradually decreased to 55%, likely due to the incorporation of carbon into the films. At higher field strength (samples E – F) the maximum transmission values in the visible gradually increased up to 66 % but were still lower than Sample A.

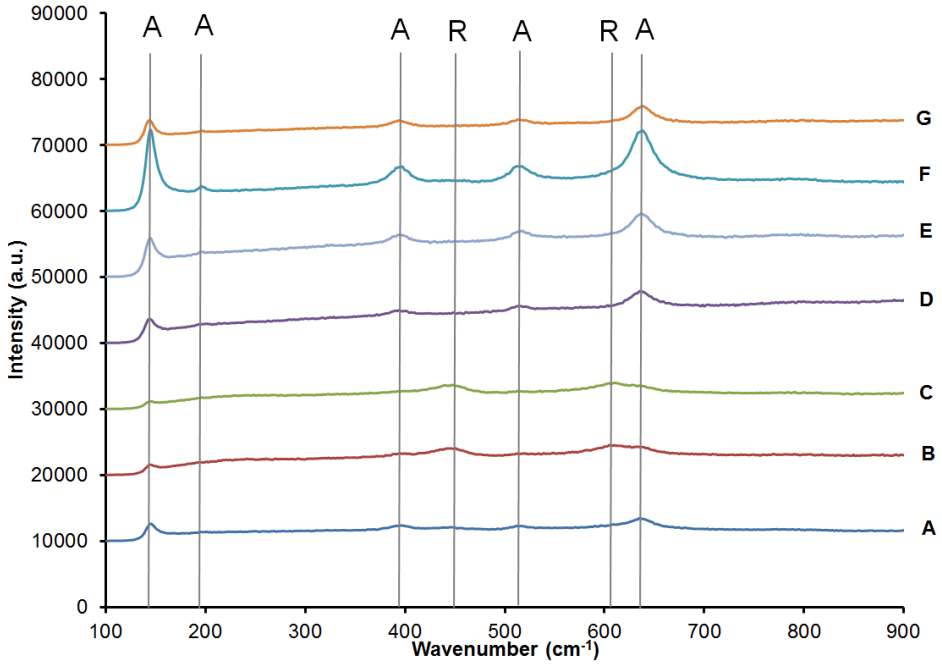

Figure 5.3: Raman spectra for samples prepared without an applied electric field (Sample A) and from the AC EAAPCVD (samples B to G) reaction of TTIP and ethanol at 550 °C and a gas flow rate of 2 L.min^{-1}.

Table 5.4: Percentage of anatase and rutile crystal phase for tiania thin films produced from the EAAPCVD reaction of TTIP and ethanol at 550 °C and 2 L.min^{-1}.

Sample	Applied Voltage (V)	Field strength (Vm^{-1})	Material phase	
			Rutile (%)	Anatase (%)
A	0	0	10	90
B	1	1 x 10^2	42	58
C	5	5 x 10^2	44	56
D	10	10 x 10^2	2	98
E	15	15 x 10^2	2	98
F	20	20 x 10^2	2	98
G	30	30 x 10^2	2	98

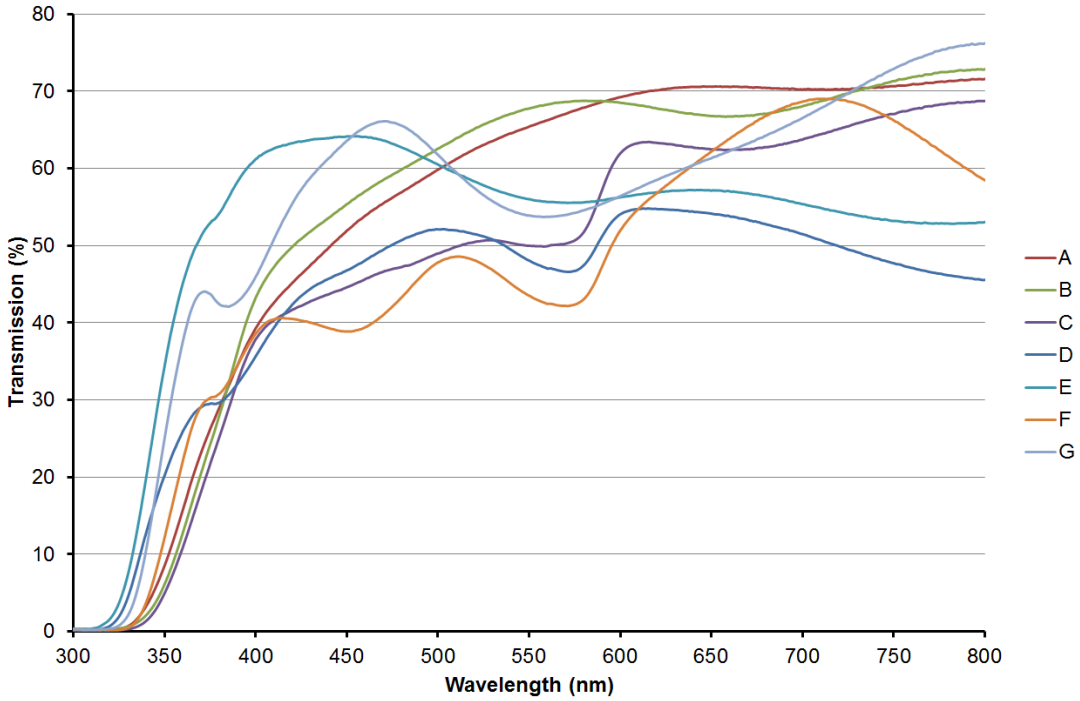

Figure 5.5: UV-vis spectroscopy for samples prepared without an applied electric field (A) and from the AC EAAPCVD (B to G) reaction of TTIP and ethanol at 550 °C and a gas flow rate of 2 L.min^{-1}.

Direct band gap (DBG) values were calculated using the Tauc method [154]. The film produced in absence of electric fields showed a direct band gap of 3.1 eV due to the mix of the crystal phase. Samples B and C showed even lower band gap values (3.0 eV) due to the increase in rutile content. The rest of deposited films showed typical direct band gap values for anatase (3.2 – 3.3 eV).

5.2.2. Functional properties of deposited films from AC electric fields

5.2.2.1. Photo-activity of TiO_2 thin films

UV/Vis investigation of the films photocatalytic abilities (Figure 5.6) indicated that all the films grown with applied electric fields (Figure 5.6, B – G) showed similar photo-activity but slightly lower than film produced with no electric field (Figure 5.6, A). Half-life ($t_{1/2}$) values as a quantification of the photocatalytic performance of as-deposited films are listed in Table 5.6. It can be observed that sample C was the most active ($t_{1/2}$ = 17 minutes) closely followed

by Samples D, F and G ($t_{1/2}$ = 17.5 minutes). The highest $t_{1/2}$ value was obtained for the film grown with no electric field (Sample A, $t_{1/2}$ = 22.2 minutes).

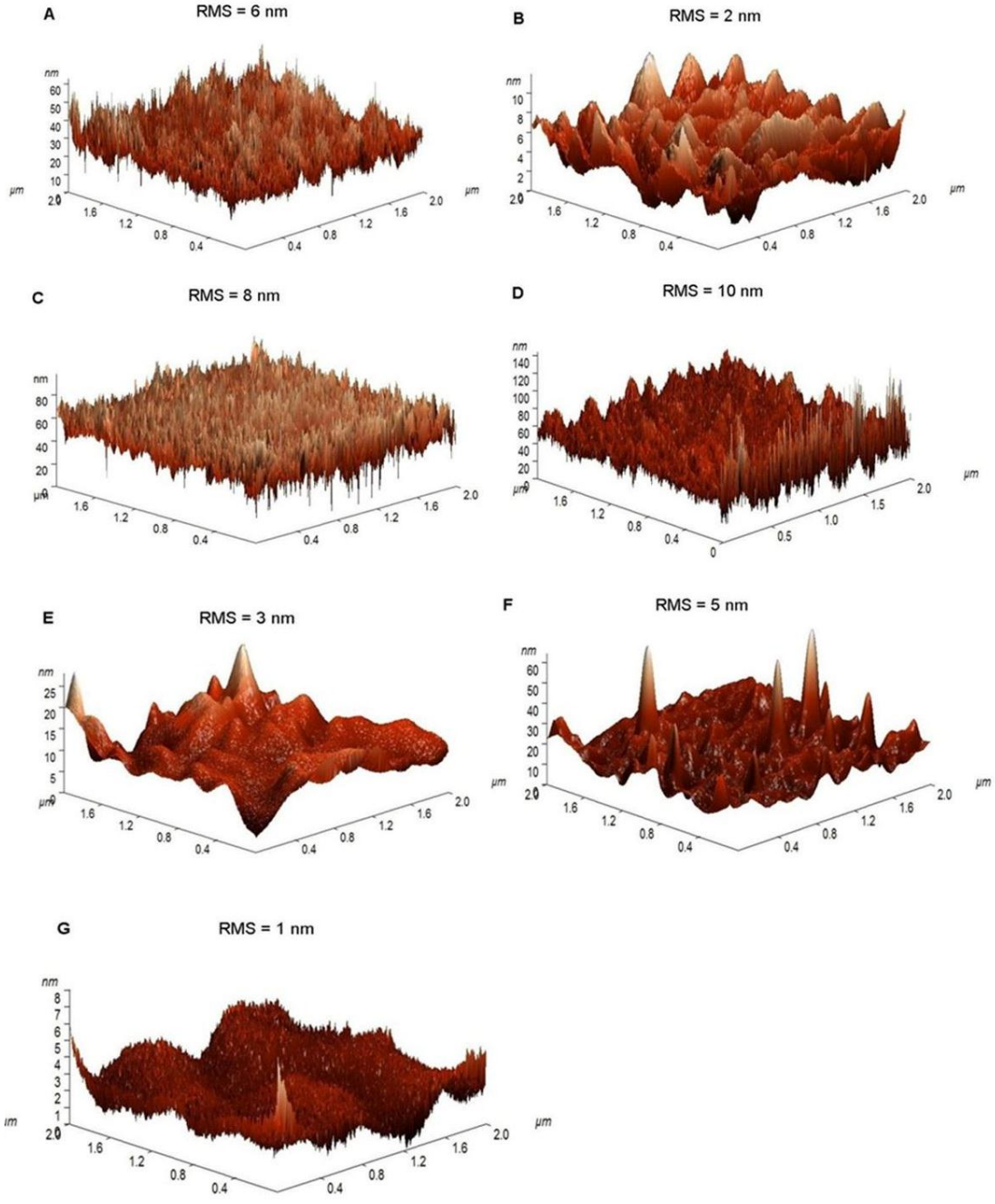

Figure 5.4: AFM images with corresponding Root Mean Square (RMS) values (nm) for films deposited from the EAAPCVD reaction of TTIP and ethanol at 550 °C and 2 $L.min^{-1}$ in absence of electric fields (sample A) and from applied AC electric fields (samples B to G).

Table 5.5: Root Mean Square (RMS) values (nm) from AFM, maximum transmission in the visible (T%) from UV-vis spectroscopy and direct band gap (DBG) values (e.V) calculated from the Tauc method for films produced from the AC EAAPCVD reaction of TTIP and ethanol.

Sample	Applied Voltage (V)	Field Strength (Vm^{-1})	RMS (nm)	T%	D.B.G (eV)
A	0	0	6 ±4	70	3.1
B	1	1×10^2	2±1	69	3.0
C	5	5×10^2	8±3	64	3.1
D	10	10×10^2	10±4	55	3.3
E	15	15×10^2	3±2	64	3.3
F	20	20×10^2	5±2	68	3.2
G	30	30×10^2	1±0.2	66	3.3

5.2.2.2. Water-contact angles

Mean water-contact angle measurements were carried out to study the wettability of surfaces (Figure 5.7). The film produced with no electric field showed the highest mean water contact angle (75°) (Table 5.5). It can be observed that as the introduction and increase of AC field strength slightly decreased the water contact angles of deposited films (64 – 73°). After 30 minutes of 254 nm UV irradiation, all electric fields deposited films showed hydrophilicity with contact-angles between 17°- 5 °. The lowest water contact angles were found for samples A, D and G.

5.2.3. Film synthesis and characterisation of DC deposited films

The EAAPCVD deposition from the reaction of TTIP and ethanol in toluene at 550 °C under the influence of DC electric fields produced anatase TiO_2 thin films as confirmed by XRD and Raman spectroscopy (Table 5.7). Deposited films presented good adherence to the substrate passing the Scotch tape test and a scratch test using a piece of towel. The deposited films were clear and transparent with the exception of the films produced with positive bias 1×10^2 Vm^{-1} – 10×10^2 Vm^{-1}, which had brown colour indicating the incorporation of carbon throughout the film. In some cases (samples I, J and L) deposited films showed a white

opaque colour which indicated nucleation in the gas phase. The experimental conditions and films appearance are described in section 2.2.2.1.

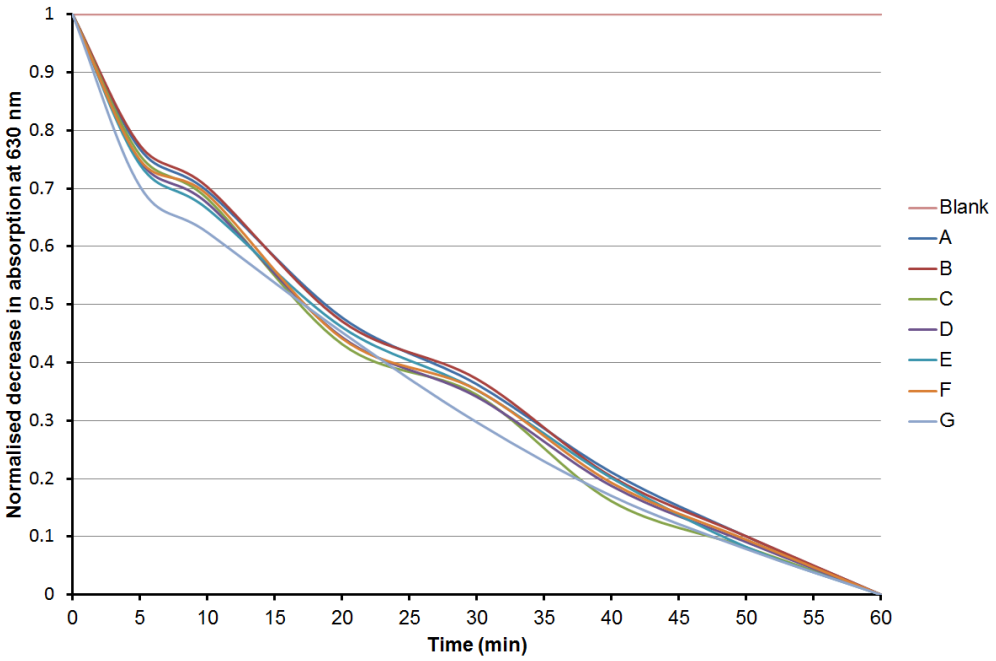

Figure 5.6: Normalised decrease in absorption of Resazurin intelligent ink at 630 nm with UVA irradiation (365 nm) against time (min) for deposited films from AC EAAPCVD reaction of TTIP and ethanol at 550 °C and 2 $L.min^{-1}$.

Table 5.6: Mean water-contact angles of deposited TiO_2 thin films from the EAAPCVD reaction of TTIP and ethanol before and after UV irradiation (30 min) with SE; half-life photocatalytic testing or time needed to degrade 50% of the ink initial concentration, $t_{1/2}$ (min).

Sample	Field Strength (Vm^{-1})	Mean Contact Angle (degrees) ± SE		Half-life
		0 min	30 min	$t_{1/2}$ (min)
A	0	75 ± 1	8 ± 2	22.2
B	1 x 10^2	67 ± 2	16 ± 2	18.5
C	5 x 10^2	63± 4	17 ± 5	17
D	10 x 10^2	67 ± 3	5 ± 1	17.5
E	15 x 10^2	64 ± 2	10 ± 1	18
F	20 x 10^2	74 ± 4	10 ± 2	17.5
G	30 x 10^2	73 ± 6	5 ± 1	17.5

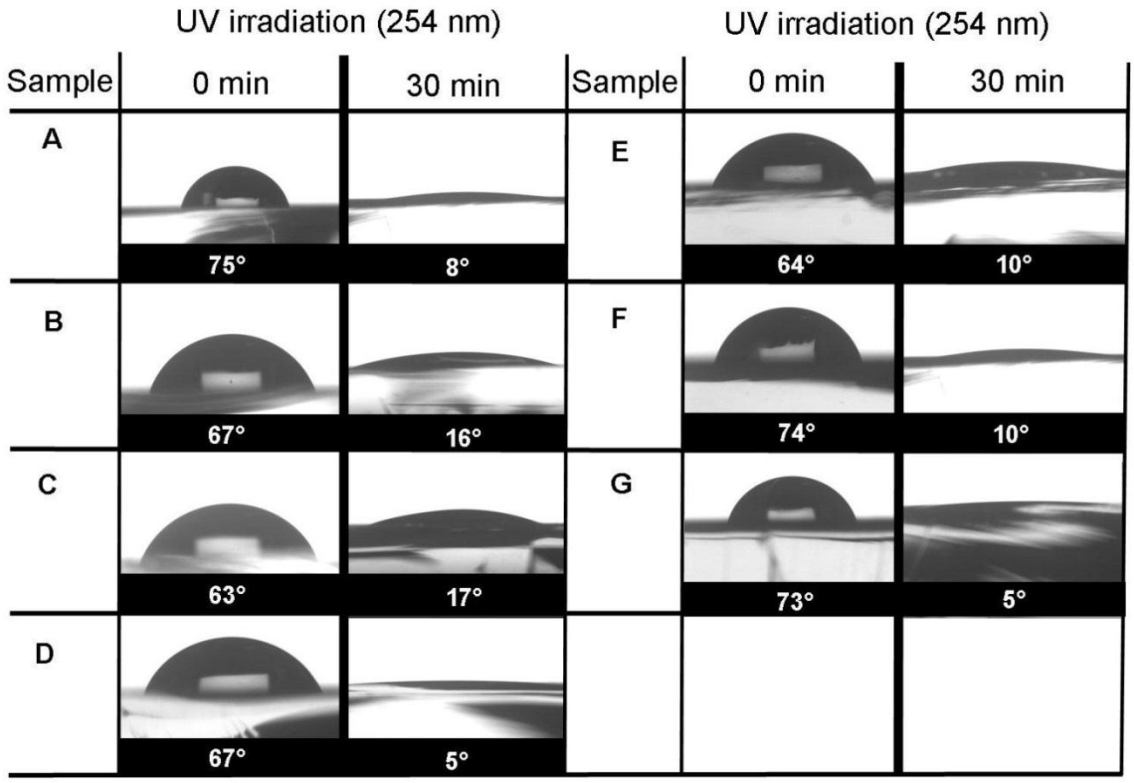

Figure 5.7: Mean water contact angle images for AC EAAPCVD (A to G) deposited films at 450 °C and 2 $L.min^{-1}$ before and after 30 min UVA irradiation 254 nm.

Scanning electron microscopy

Scanning electron microscopy images of the titanium dioxide depositions are shown in Figure 5.8. Deposition carried out in absence of an electric field (Figure 5.8 A) revealed a thin film comprised of agglomerated acicular nanoparticles of 150 ± 8 nm in length and spherical agglomerations of 90 ± 5 nm in diameter with a film thickness of 48 ± 10 nm. The introduction of an electric field (1 x 10^2 Vm^{-1}, sample B) across the electrodes of the glass substrate during the deposition produced elongated particles of 150 ± 8 nm length forming spherical agglomerations of 300 ± 9 nm diameter. The film thickness for this sample increased to 150 ± 35 nm. As the field strength was increased to 5 x 10^2 Vm^{-1} (sample C), similar morphology was observed. However, a decrease in the elongated particles (90 ± 14 nm) and an important increase in film thickness (490 ± 24 nm) were observed. The increase of the field strength to 10 x 10^2 Vm^{-1} (sample D) produced elongated nanoparticles of 85 ± 14 nm in length and a decrease in film thickness to 250 ± 16 nm. For this sample, angular particles (380 ± 33 nm in length), likely the result of a gas phase reaction, were observed.

Further increase of the field strength (up to 30 x 10^2 Vm^{-1}) produced a gradual agglomeration of acicular nanoparticles (190 ± 11 – 90 ± 7 nm) forming clusters of 275 ± 33 – 255 ± 21 nm. The film thickness in this range was 300 ± 9 – 150 ± 20 nm.

Table 5.7: Experimental conditions of deposited films from the EAAPCVD reaction of TTIP and ethanol at 550 °C and gas flow rate of 2 $L.min^{-1}$ with an applied DC electric field.

Sample	Applied Voltage (V)	Field Strength (Vm^{-1})	Substrate bias	Material Phase (XRD/Raman)
A	0	0	---	Anatase -Rutile
H	1	1 x 10^2	Positive	Anatase
I	5	5 x 10^2	Positive	Anatase
J	10	10 x 10^2	Positive	Anatase
K	15	15 x 10^2	Positive	Anatase
L	30	30 x 10^2	Positive	Anatase
M	1	1 x 10^2	Positive	Anatase
N	5	5 x 10^2	Negative	Anatase
O	10	10 x 10^2	Negative	Anatase
P	15	15 x 10^2	Negative	Anatase
Q	30	30 x 10^2	Negative	Anatase

Changing the film bias to a negative bias (Figure 5.9) led to further microstructural and thickness changes. The introduction of biased electric fields (1 x 10^2 Vm^{-1}) led to a slight increase of particle size to 190 ± 17 nm length (sample M). The film thickness decreased to 27 ± 9 nm. At 5 x 10^2 Vm^{-1} (sample N) the size of elongated nanoparticles and clusters decreased to 150 ± 9 nm and 180 ± 20 nm, respectively. The film thickness slightly increased to 40 ± 15 nm. An increase of field strength (10 x 10^2 Vm^{-1}) also produced a further decrease in the elongated nanoparticles (85 ± 12 nm) forming spherical agglomerations of 320 ± 35 nm (sample O). The film thickness dramatically increased to 300 ± 35 nm. The increase of field strength (15 x 10^2 Vm^{-1}) produced spherical nanoparticles of 180 ± 17 nm in diameter and a decrease in film thickness to 270 ± 84 nm (sample P). At 30 x 10^2 Vm^{-1}, the shape of nanoparticles changed back to elongated (100 ± 8 nm) forming spherical clusters of 200 ± 28 nm. The film thickness dramatically decreased to 8 ± 5 nm.

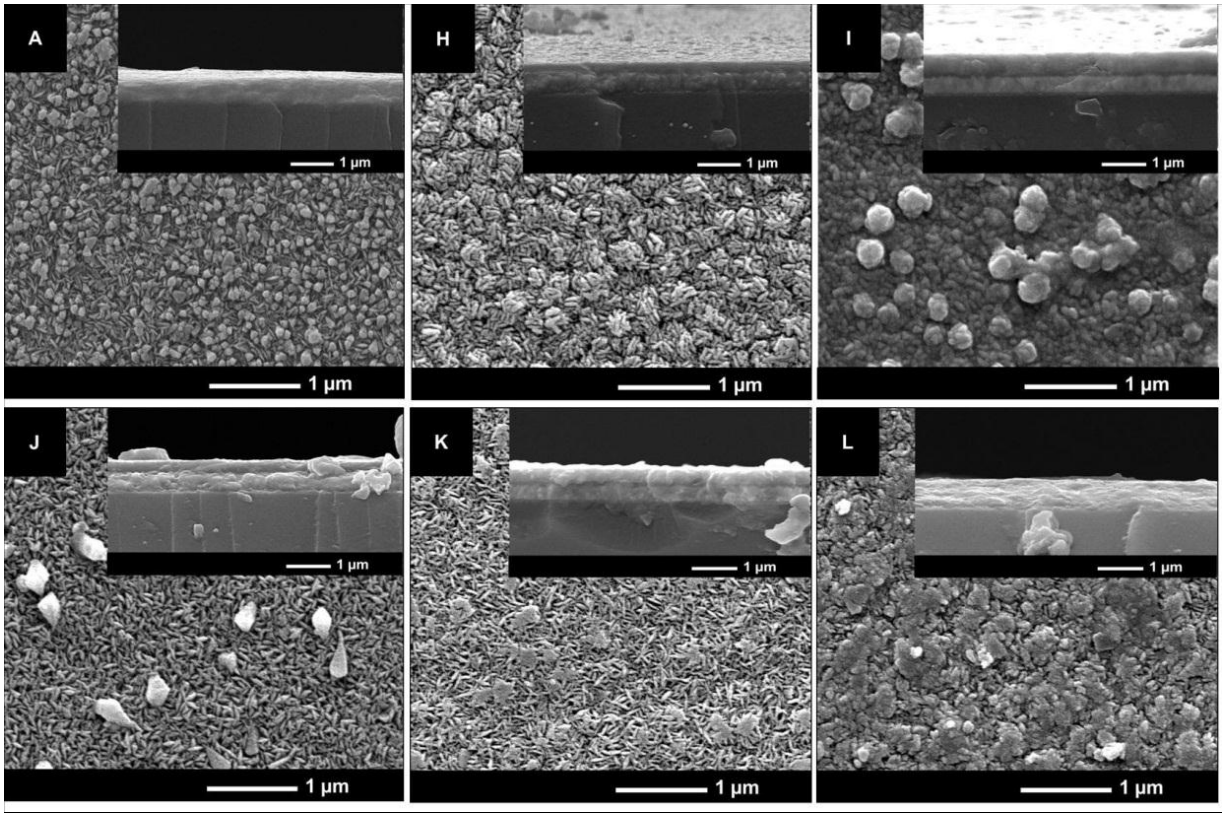

Figure 5.8: Scanning Electron Microscope images of samples prepared from the positive biased DC EAAPCVD reaction of TTIP and ethanol in toluene at 550 °C with a flow rate of 2 L.min^{-1}. A) 0 Vm^{-1}, H) 1 x 10^{2} Vm^{-1}, I) 5 x 10^{2} Vm^{-1}, J) 10 x 10^{2} Vm^{-1}, K) 15 x 10^{2} Vm^{-1}, L) 30 x 10^{2} Vm^{-1}. Side-on images were captured at 60,000 magnification and cross-section images at 40,000 magnification.

Different trends in film thickness were observed for different substrate bias. As Figure 5.10 shows, an increase in film thickness with field strength was observed for positive bias deposited films whereas a decrease was seen for negatively bias deposited films.

X-ray diffraction

X-ray diffraction (XRD) analysis was carried out and compared to previous investigations (JCPDS database file (021-1272)) to study the materials phase. All deposited films under the influence of electric fields showed anatase TiO_2 crystalline phase and also cassiterite SnO_2 from the FTO glass substrate. The relative intensity of the Bragg peaks associated with TiO_2 changed depending on the field strength applied, revealing a preferred orientation (Figure 5.11). Thus, deposited films prepared with no electric field showed higher intensity peaks in the (004) plane. The application of a positive bias field strength gave strong intensity peaks in

the (101) plane except for samples N and Q. Likewise, the application of negative bias electric fields gave strong peaks in the (101) plane except for sample J. Furthermore, all samples prepared with DC electric fields showed weak peaks in the (112) plane except for sample Q which did not show such a peak.

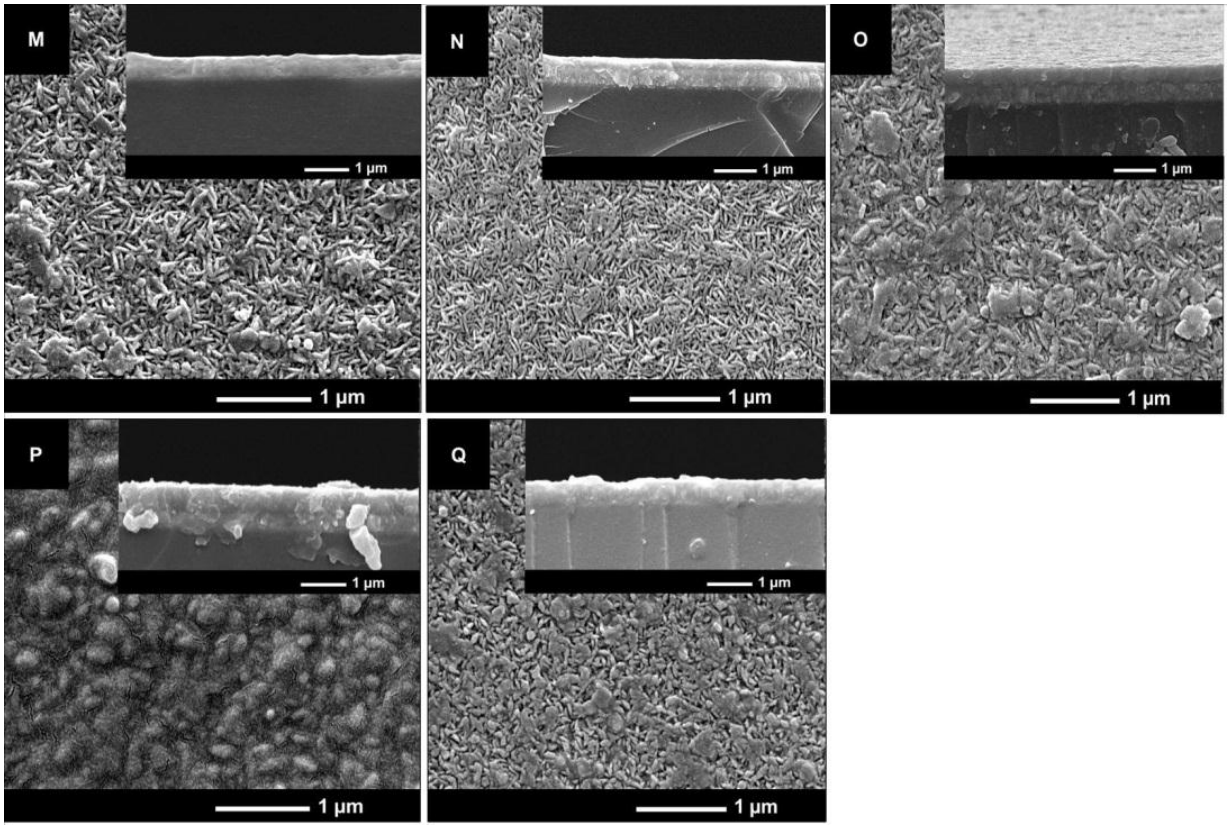

Figure 5.9: Scanning Electron Microscope images of samples prepared from the negative biased DC EAAPCVD reaction of TTIP and ethanol at 550 °C and 2 L.min^{-1}. M) 1 x 10^{2} Vm^{-1}, N) 5 x 10^{2} Vm^{-1}, O) 10 x 10^{2} Vm^{-1}, P) 15 x 10^{2} Vm^{-1}, Q) 30 x 10^{2} Vm^{-1}. Side-on images were captured at 60,000 magnification and cross-section images at 40,000 magnification.

Texture coefficient calculations were carried out to confirm the preferred crystal orientation found in XRD analysis [151,152]. The results (shown in Table 5.9) revealed that all deposited films were strongly oriented in the (004) plane. The highest texture coefficient values in the anatase (004) plane were found for samples L, N and Q (2.88 – 3.5).

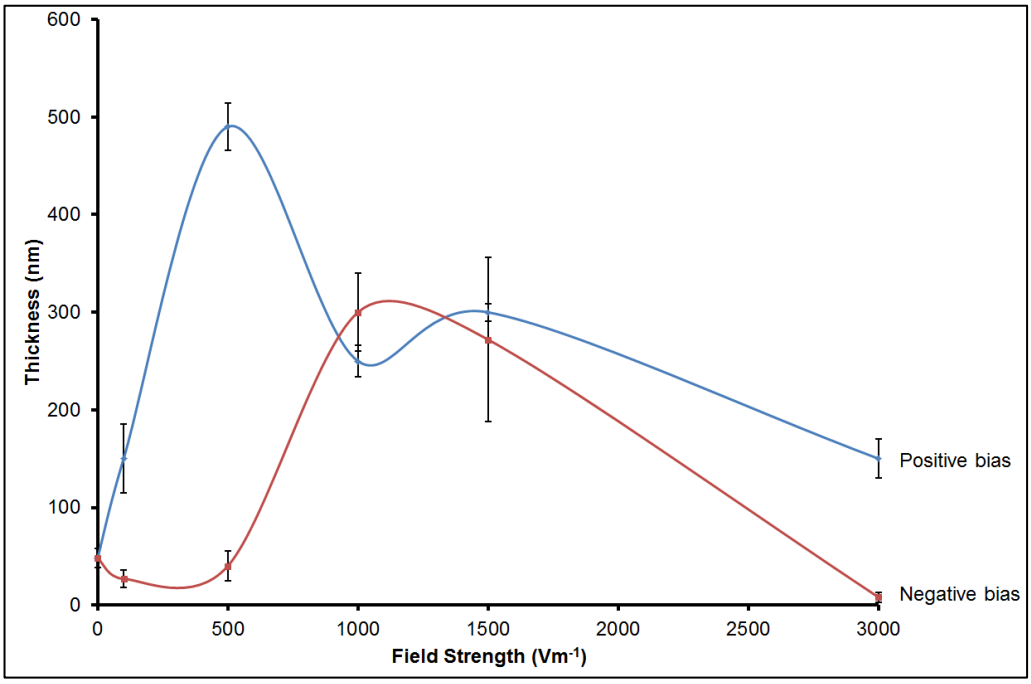

Figure 5.10: Film thickness trend with SE for positive and negative bias deposited films from the EAAPCVD reaction of TTIP and ethanol at 550 °C and 2 L.min^{-1}.

Raman spectroscopy

Raman spectroscopy was carried out in order to complement XRD analysis for phase identification. Figure 5.12 shows Raman spectra for all the deposited films. The sample prepared in absence of electric fields (Sample A) showed a Raman shift centred at 147 cm^{-1}, 395 cm^{-1}, 513 cm^{-1}, 642 cm^{-1} which correspond to anatase crystal phase [134]. This sample also showed a Raman shift at 447 cm^{-1} which corresponds to rutile crystal phase [38]. Positive bias (Samples H – L) and negative bias (samples M – Q) deposited films showed strong anatase Raman peaks centred at 147 cm^{-1}, 198 cm^{-1}, 395 cm^{-1}, 513 cm^{-1}, 642 cm^{-1} [134]. Although Sample Q presented an amorphous structure, weak anatase Raman peaks at 147 cm^{-1} and 642 cm^{-1} were observed.

Atomic force microscopy

Deposited films surfaces were scanned using AFM over a 10 µm x 10 µm region in order to obtain Root Mean Square (RMS) roughness values as a proxy of surface roughness. Figure 5.13 shows the representative AFM images with corresponding RMS values for sample A

and positive bias deposited films (samples H to L). The application of positive bias electric fields produced a decrease in surface roughness from 25 ± 5 nm (sample A) to 23 ± 3 nm (sample H). The increase of the field strength to 5 x 10^2 Vm^{-1} (sample I) increased the surface roughness to 27 ± 5 nm. Further increase of the field strength produced a gradual decrease of the surface roughness to 17 ± 7 nm (sample L). Figure 5.14 shows the representative AFM images of negative bias deposited films (samples M to Q). Generally, the application of negative bias electric fields produced lower surface roughness comparing to positive bias deposited films. The application of the field strength decreased the surface roughness to 11 ± 4 nm (sample M). As the field strength increased, the surface roughness also increased up to 29 ± 3 nm (sample O). Further increase of the field strength produced a gradual decrease of the surface roughness to 11 ± 4 nm (Sample Q). The RMS values are listed in Table 5.10.

Table 5.8: Agglomerate size (nm) from SEM with standard error (SE), film thickness (nm) from SEM cross section with SE and mean crystallite size (nm) obtained from the Scherrer equation.

Sample	Field Strength (Vm^{-1})	Substrate bias	Agglomerate size (nm)		Film Thickness (nm)	Mean crystallite size (nm)
			acicular	spherical		
A	0	--	150±8	90±5	48±10	18±0.5
H	1 x 10^2	Positive	150±8	300±9	150±35	21±2
I	5 x 10^2	Positive	90±14	310±27	490±24	19±2
J	10 x 10^2	Positive	85±14	380±33	250±16	16±1
K	15 x 10^2	Positive	190±11	275±33	300±9	18±1
L	30 x 10^2	Positive	90±7	255±21	150±20	19±2
M	1 x 10^2	Negative	190±17	340±20	27±9	18±1
N	5 x 10^2	Negative	150±9	180±20	40±15	16±1
O	10 x 10^2	Negative	85±12	320±35	300±40	18±2
P	15 x 10^2	Negative	--	180±17	270±84	19±1
Q	30 x 10^2	Negative	100±8	200±28	8±5	17±1

Furthermore, XRD analysis of full width at half maximum (FWHM) was carried out using the Scherrer equation [155] in order to investigate the crystallite size of deposited films. Characteristic peaks of 2 Theta = 25.28° (101), 2 Theta = 37.8° (004), 2 Theta = 48.05° (200)

were selected and the generally used shape factor of 0.9 [153] was chosen. As Table 5.8 shows, the application of DC electric fields produced changes in the mean crystallite size. The application of positive bias electric fields produced an increase in the mean crystallite size from 18 ± 0.5 to 21 ± 2 nm. As the field strength increased, the crystallite size remained in 18 – 19 nm except for samples J which showed the smallest crystallite size (16 ± 1 nm). The application of negative bias electric fields showed no influence in the crystallite size which remained in 18 – 19 nm. The smallest crystallite size was found for samples N and Q.

Table 5.9: Texture Coefficient of TiO_2 thin films produced from the positive bias (H – L) and negative bias (M – Q) EAAPCVD reaction of TTIP and ethanol at 550 °C and 2 $L.min^{-1}$.

	Texture Coefficient (TC_{hkl})			
Sample	(101)	(004)	(200)	(211)
A	0.2	3.54	0.15	0.11
H	0.48	2.78	0.36	0.36
I	0.35	2.32	0.53	0.8
J	0.25	2.48	0.46	0.8
K	0.41	2.14	0.54	0.9
L	0.44	2.88	0.39	0.29
M	0.53	2.36	0.59	0.51
N	0.27	3.24	0.23	0.25
O	0.59	2.37	0.52	0.51
P	0.6	2.22	0.6	0.56
Q	0.14	3.5	0.12	0.21

UV-vis spectroscopy

UV/VIS spectroscopy showed different maximum transmission values in the visible depending on the substrate bias (Figure 5.15). The application and increase of positive bias electric fields decreased the transmission values from 71% (sample A) to 64% – 68% (samples H to L). However, the application and increase of negative bias electric fields increased the transmission values to 73% (samples M and N). Further increase of the field strength decreased the transmission in the visible to 65% (samples O and P). At 15 x 10^2 Vm^{-1}, the transmission in the visible increased to 70% (sample Q). Direct band gap (DBG) analysis was performed using the Tauc method [154]. Field strength seems to have certain influence in the direct band gap of deposited films. Sample A showed a typical direct band gap value for rutile (3.1 eV). Furthermore, standard anatase DBG values between 3.2 to 3.3 eV were found for most of positive and negative biased deposited films (samples I – O and

sample Q). Although, samples H and P showed only anatase crystal phase in their Raman spectra and XRD pattern, these films showed lower DBG values (3.05 – 3.15 eV) than that of the standard anatase.

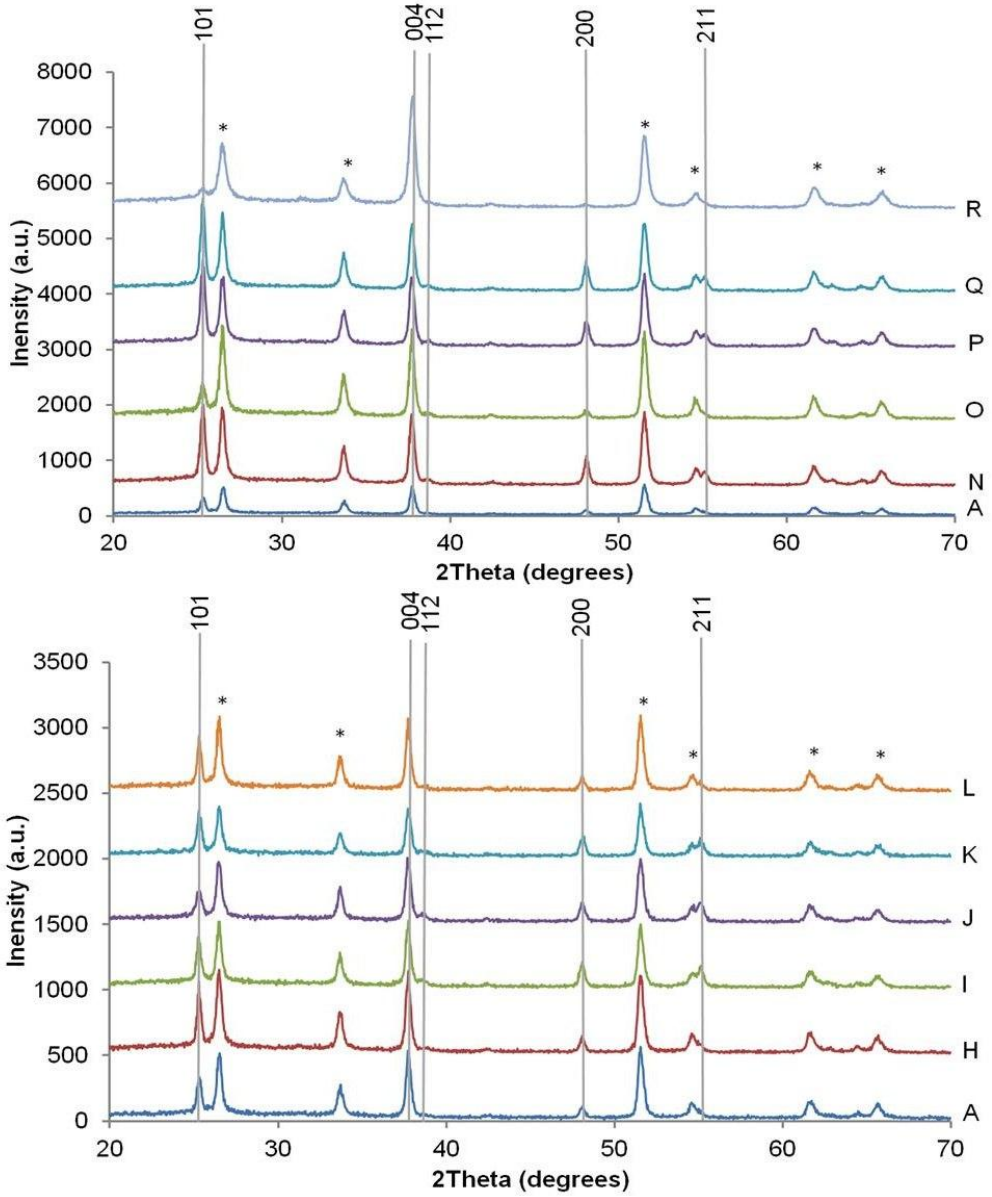

Figure 5.11: XRD pattern for samples prepared from EAAPCVD reaction of TTIP and ethanol at 550 °C and 2 $L.min^{-1}$, films deposited in absence of electric fields (A), positive biased (H-L) and negative biased electric fields (M-Q). The peaks marked with asterisks denote the cassiterite peaks specific of SnO_2 crystalline phase, from the underlying FTO glass substrate.

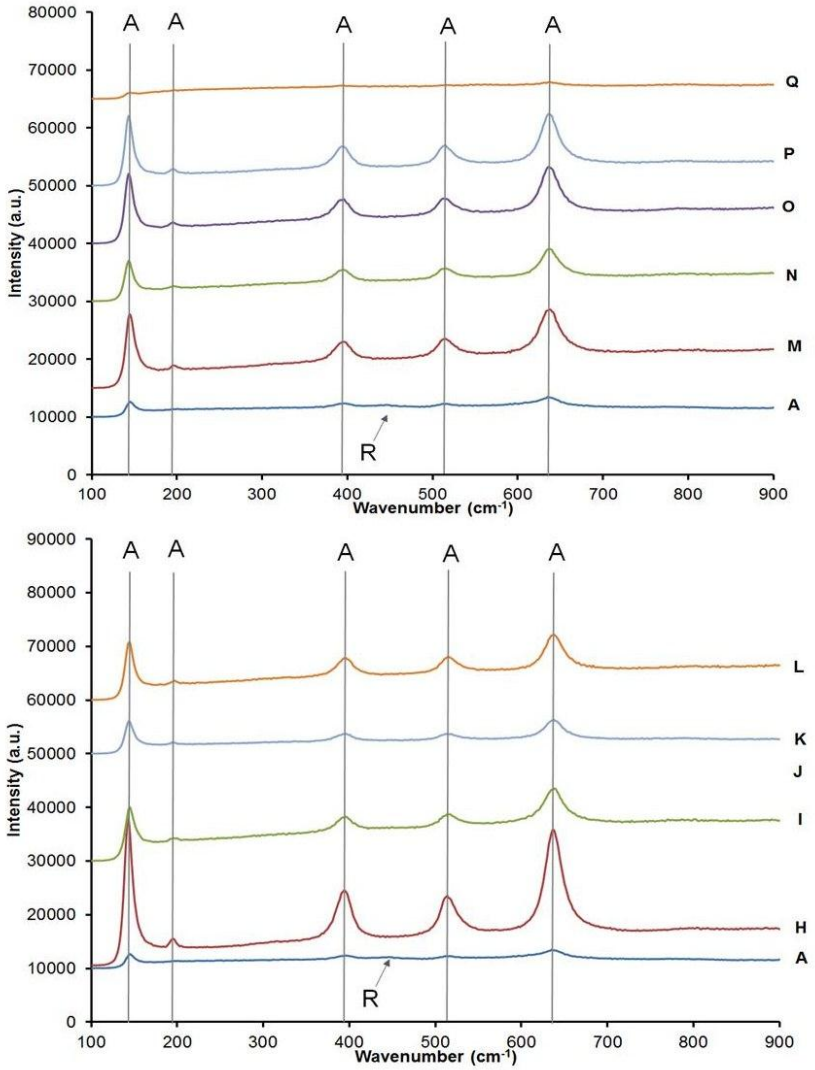

Figure 5.12: Raman spectra for films deposited in absence of electric fields (sample A) and from the positive bias (H – L) and negative bias (M – Q) EAAPCVD reaction of TTIP and ethanol at 550 °C and 2 $L.min^{-1}$. A stands for anatase and R for rutile crystal phase.

5.2.4. Functional properties of DC deposited films

5.2.4.1. Photo-activity of TiO_2 thin films

The photocatalytic activity of the titania thin films deposited from EAAPCVD was investigated from the UV/Vis absorption of Resazurin (Rz) intelligent ink under UV irradiation (365 nm). Figure 5.16 shows the normalised decrease in absorption of Rz at 630 nm. When analysing the half-life values of deposited films (Table 5.11), it was observed that all DC deposited films showed higher photoactive than sample A (22.2 min) except for

sample O (28.2 min). Positive bias electric fields produced poor photoactive films (18.1 –22) in comparison to negative bias (5.1 – 15.6 min). The most photoactive films were sample Q (5.1 min) followed by sample P (11 min).

5.2.4.2. Water contact angles

The films produced from DC electric fields showed hydrophilicity with mean water contact angles in the range of 17 – 79° (samples K – M and O – Q) and hydrophobicity with mean water contact angles greater than 90° (samples H – J and N) (Table 5.11). After 30 minutes UV irradiation (254 nm) all films showed hydrophilicity with mean water contact angles in the range 8 – 61°. Samples K, L and N – P showed the lowest mean water contact angles after UV irradiation (6 – 9°). Figure 5.17 shows representative images of water-contact angles for films deposited from the DC EAAPCVD reaction of TTIP in ethanol.

Table 5.10: Root Mean Square (RMS) values (nm) from AFM, maximum transmission in the visible values (T%) from UV-vis spectroscopy and DBG values (e.V) calculated from the Tauc method, for films deposited from the DC EAAPCVD reaction of TTIP and ethanol.

Sample	Applied Voltage (V)	Field Strength (Vm^{-1})	Substrate bias	RMS (nm)	T%	D.B.G (eV)
A	0	0	--	25±5	70	3.1
H	1	1×10^2	Positive	23±3	64	3.05
I	5	5×10^2	Positive	27±5	68	3.2
J	10	10×10^2	Positive	23±1	62	3.2
K	15	15×10^2	Positive	22±2	68	3.2
L	30	30×10^2	Positive	17±7	65	3.2
M	1	1×10^2	Negative	11±4	72	3.25
N	5	5×10^2	Negative	16±2	73	3.3
O	10	10×10^2	Negative	29±3	69	3.2
P	15	15×10^2	Negative	21±2	65	3.15
Q	30	30×10^2	Negative	11±4	70	3.2

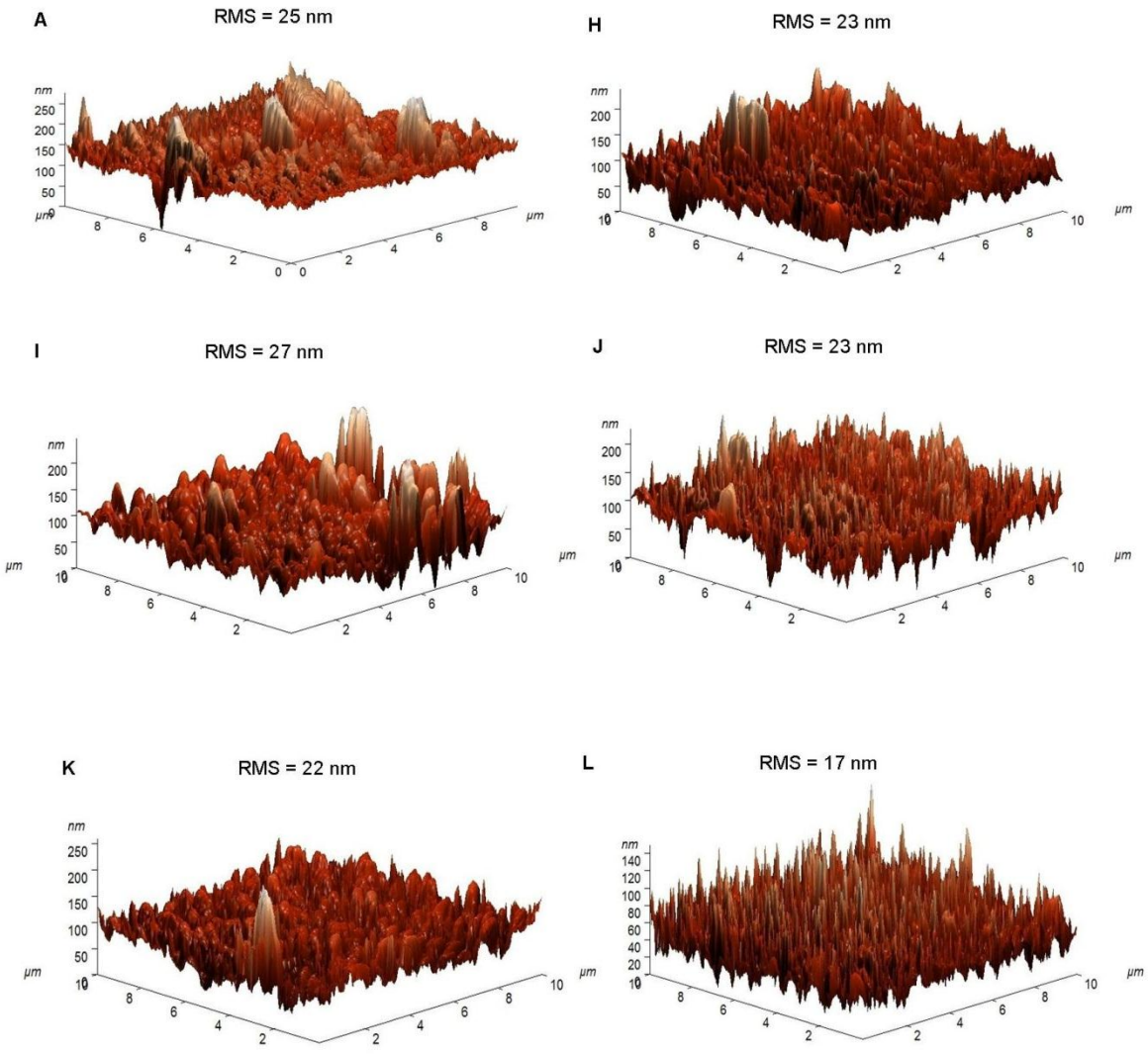

Figure 5.13: Representative AFM images with corresponding Root Mean Square (RMS) values (nm) for films deposited from the EAAPCVD reaction of TTIP and ethanol at 550 °C and 2 $L.min^{-1}$ in absence of electric fields (A) and positive bias DC electric fields (H – L).

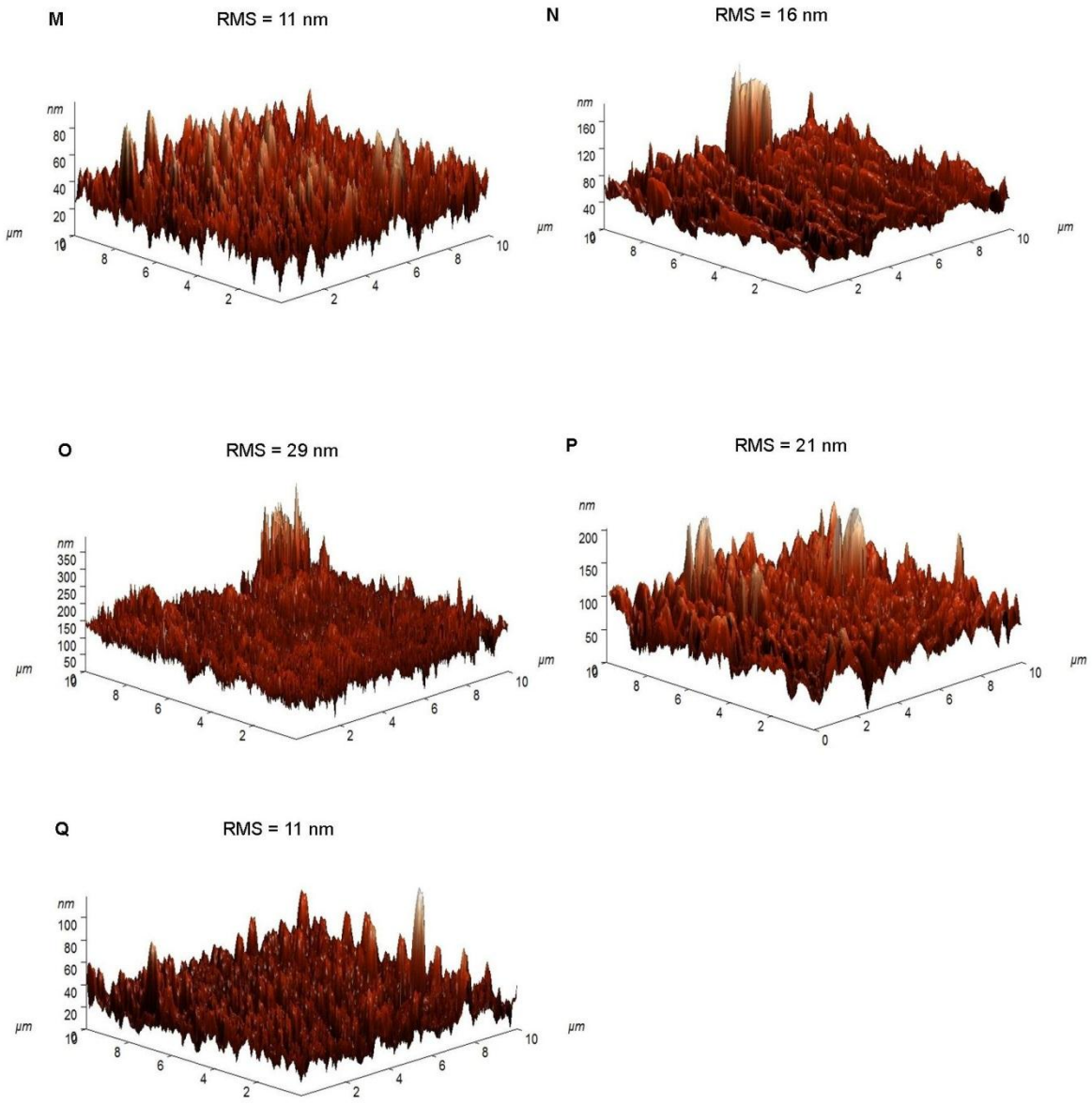

Figure 5.14: Representative AFM images with corresponding Root Mean Square (RMS) values (nm) for films deposited from the negative bias EAAPCVD reaction of TTIP and ethanol at 550 °C and 2 L.min^{-1}.

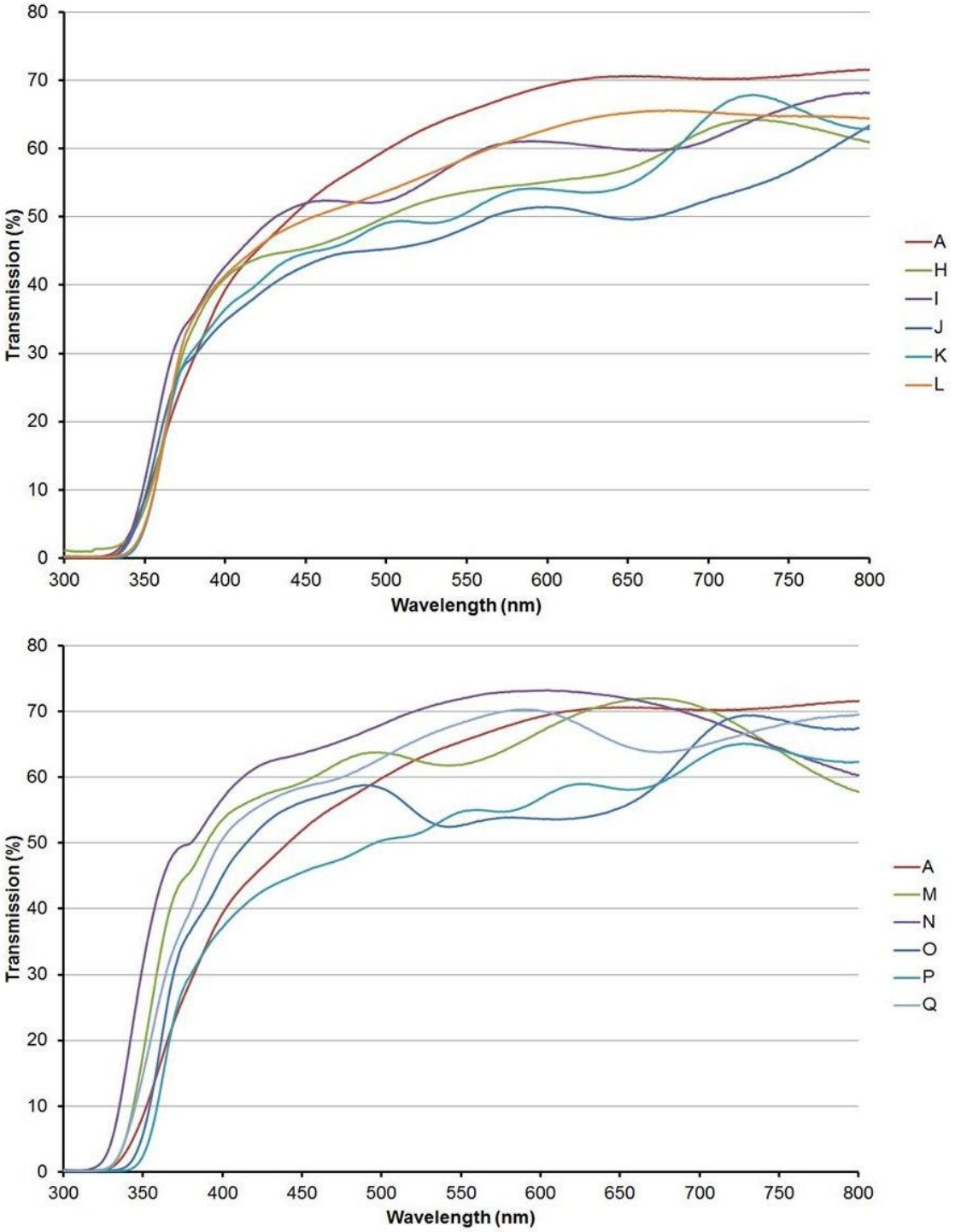

Figure 5.15: UV-vis spectroscopy for films deposited from the EAAPCVD reaction of TTIP and ethanol at 550 °C and 2 L.min^{-1} in absence of electric fields (sample A) and positive bias (samples H – L) and negative bias (M – Q) DC electric fields.

5.3. Discussion

5.3.1. Modifications in microstructure

The application of AC and DC electric fields induced changes in the microstructure in different ways. The application of lower field strength (1 x 10^2 Vm^{-1} – 10 x 10^2 Vm^{-1}) produced a gradual increase of granular nanoparticles (90 to 110 nm) in AC deposited films. However, the morphology drastically changed to acicular nanoparticles when increasing the field strength (10 x 10^2 Vm^{-1} – 30 x 10^2 Vm^{-1}). The deposited film at 10 x 10^2 Vm^{-1} (sample D) showed the smallest particle size (80 nm). Further increase of the field strength not only increased the size of the elongated nanoparticles but also the size of the agglomerations or clusters formed by those particles. Granular microstructures in aerosol assisted CVD processes are produced when the residence time of the precursor is greater than its reaction time [114]. Although in APCVD the delivery of the precursor to the reactor chamber is different, that same principle can be applied. In absence of electric fields (sample A) elongated particles are produced but there is also a predominance of angular particles on the surface. The application and increase of the field strength to 10 x 10^2 Vm^{-1} seemed to induce a retarding effect on the diffusion of the precursor to the substrate surface. This would explain why a gradual increase of granular nanoparticles of increasing size was observed for samples B and C. However, the increase of the field strength to 30 x 10^2 Vm^{-1} seemed to have induced a higher kinetic energy to the precursor that would have enhanced the diffusion of the precursor towards the substrate and thus, the morphology of the microstructure. Therefore, further increase of the field strength and higher acceleration of the precursor, would have increased the particle size forming gradually bigger clusters. This behaviour in the film growth was also observed in deposited films from the EACVD reaction of TTIP in toluene (Chapter 3). In that case, granular microstructure was observed for lower field strength but also for the highest field strength applied. Thus, as has been discussed, the method, solvent and deposition time have an important influence in the morphology of the microstructure. As for the films produced from EACVD, fluctuations in film thickness regardless of the field strength were observed for TTIP EAAPCVD deposited films.

Different behaviour in titania thin films microstructure was observed with applied DC electric fields. All deposited films showed elongated nanoparticles of 85 – 190 nm length forming bigger agglomerates except for Sample P (-ve 20 x 10^2 Vm^{-1}) which showed spherical

nanoparticles of 180 nm diameter. As observed in DC EACVD deposited films (Chapter 3), the film thickness of negative bias deposited films was lower and showed a decreasing trend with field strength. Thus, it can be assumed that the thermal decomposition pathway is the same and the morphology of deposited films was influenced by the deposition method and experimental parameters. According to the discussion in Chapter 3, the repelling forces induced by negative bias electric would have been responsible for the spherical morphology. Aerosol delivery of precursors provides a high mass transport rate [125] but the solvent has to evaporate as the precursor reaches the substrate for the reaction to occur. This means that the interaction of the electric field with the precursor is higher before the reaction (Figure 5.18 A). In APCVD the precursor is readily available in vapour phase and the interaction of the electric fields with the precursor is direct (Figure 5.18 B). This would explain why for the same residence time, AC electric fields induced more changes in the morphology and crystal orientation in AACVD than APCVD processes. This would also explain why all deposited films showed preferred orientation in the (004) plane. The reaction occurs more quickly and therefore, the crystal growth is led by the preferred orientation of the substrate. Likewise, in the case of DC electric fields, the attracting (positive bias) and repelling forces (negative bias) produced the similar elongated morphology due to a higher reaction rate.

Previous studies on the APCVD growth of TiO_2 thin films from TTIP have shown a mix of titania polymorphs for deposition temperatures between 500 and 600 °C [160]. In absence of electric fields an anatase to rutile ratio of 9:1 was found. As the field strength was increased up to 5 x 10^2 Vm^{-1} (sample B – C) the content of the mix phase reached values close to 1:1 ratio. However, at higher field strength deposited films showed mainly anatase (98%). As discussed in Chapter 4, the anatase to rutile transformation highly depends on the particle size and morphology. In this case, angular nanoparticles seemed to favour the crystal phase transformation as the rutile content increased with the gradual increase of angular depositions on the substrate. Thus, it seemed that angular morphology enhanced corner sharing bonding which favoured the rutile transformation. This can explain why mostly anatase was observed for the rest of deposited films (samples D to G) which showed elongated nanoparticles forming agglomerations of bigger size. As discussed in Chapter 4, the agglomeration of particles favoured the formation of anatase as more edges are available to form a bond. This argument is supported by XRD and Raman analysis of DC deposited films which only showed anatase crystal phase. As it was observed in SEM analysis, all deposited films

showed a high agglomeration forming clusters, which would have promoted the formation of anatase instead of rutile.

Generally speaking, the application of AC and DC electric had a detrimental effect on the transmission values in the visible. For AC deposited films the incorporation of carbon gradually increased with the field strength (up to 10 x 10^2 Vm^{-1}). Further increase of the field strength produced transparent thin films but still the transmission values were lower than the film produced in absence of electric fields (sample A). However, when analysing the transmission in the wavelength range from 300 – 400 nm samples B, E and G showed higher transmission than sample A. Furthermore, negative bias deposited films showed slightly higher transmission in the visible than positive bias deposited films. This supports the argument of Chapter 3 that the films produced with a strong electric field and negative substrate bias would effectively deflect any radicals, negatively charged species or centres of negative charge away from the substrate surface, accounting for why less carbon was found in the deposited films.

Direct band gap analysis gave standard values of 3.2 – 3.3 eV for films showing purely anatase (sample I – O and Q) or high percentage of anatase (sample D – G). Likewise, typical band gap values close to 3.0 eV were found for films which showed rutile phase in their microstructure (samples A – C). Unexpectedly, samples H and P showed direct band gap values of 3.0 – 3.1 eV with anatase content of 98% in their microstructure. Nevertheless, it has been reported values from 2.86 to 3.34 eV for the anatase phase which has been attributed to variations in the stoichiometry of the synthesis, impurities content, crystallite size and type electronic transition [144].

5.3.2. Photocatalytic properties

Sample C exhibited the highest photo-activity with a half-life value of 17 min. This film showed a content of anatase and rutile close to 1:1 ratio which, as discussed in Chapter 4, has been reported to favour titania photocatalytic activity. However, the half-life value obtained did not significantly differ to the others. Furthermore, sample B (with an anatase to rutile ratio close to 1:1) showed a higher half-life value (18.5 min) than samples D – G (17.5 – 18 min) which showed mostly anatase. In Chapter 4, the results showed that the most photoactive films were those with an anatase to rutile ratio close to 1:1 regardless film

thickness. However, due to the lack of crystallinity, some data could not be collected and thus, information about other factors that could have improved the photo-activity was missing. In EAACVD $TiCl_4$ deposited films (Chapter 4), the most photoactive films showed homogeneous angular and spherical microstructure. In this case, it was observed that deposited films with a 1:1 anatase to rutile ratio showed a heterogeneous microstructure in which an underlying elongated microstructure was covered by angular depositions. This could have created recombination sites which could explain lower half-life values comparing to the results of Chapter 4. Nevertheless, sample C showed the highest coefficient value in the (004) plane which, as discussed in Chapter 3, favours the photocatalytic activity.

Table 5.11: Mean water-contact angles before and after UV irradiation (30 min) with SE; half-life photocatalytic testing or time needed to degrade 50% of the ink initial concentration, $t_{1/2}$ (min), for deposited films from the EAAPCVD reaction of TTIP and ethanol.

			Contact Angle (degrees) ± SE		Half-life
Sample	Field Strength (Vm^{-1})	Substrate bias	0 min	30 min	$t_{1/2}$ (min)
A	0	--	75 ± 1	8 ± 2	22.2
H	1×10^2	Positive	96 ± 4	11 ± 1	18.8
I	5×10^2	Positive	105 ± 1	19 ± 4	22
J	10×10^2	Positive	104 ± 1	11 ± 2	20.9
K	15×10^2	Positive	61 ± 5	8 ± 1	20.5
L	30×10^2	Positive	55 ± 9	9 ± 1	18.1
M	1×10^2	Negative	79 ± 2	61 ± 7	15.6
N	5×10^2	Negative	94 ± 5	9 ± 2	14
O	10×10^2	Negative	40 ± 6	6 ± 2	28.2
P	15×10^2	Negative	17 ± 4	8 ± 2	11
Q	30×10^2	Negative	51 ± 1	11 ± 1	5.1

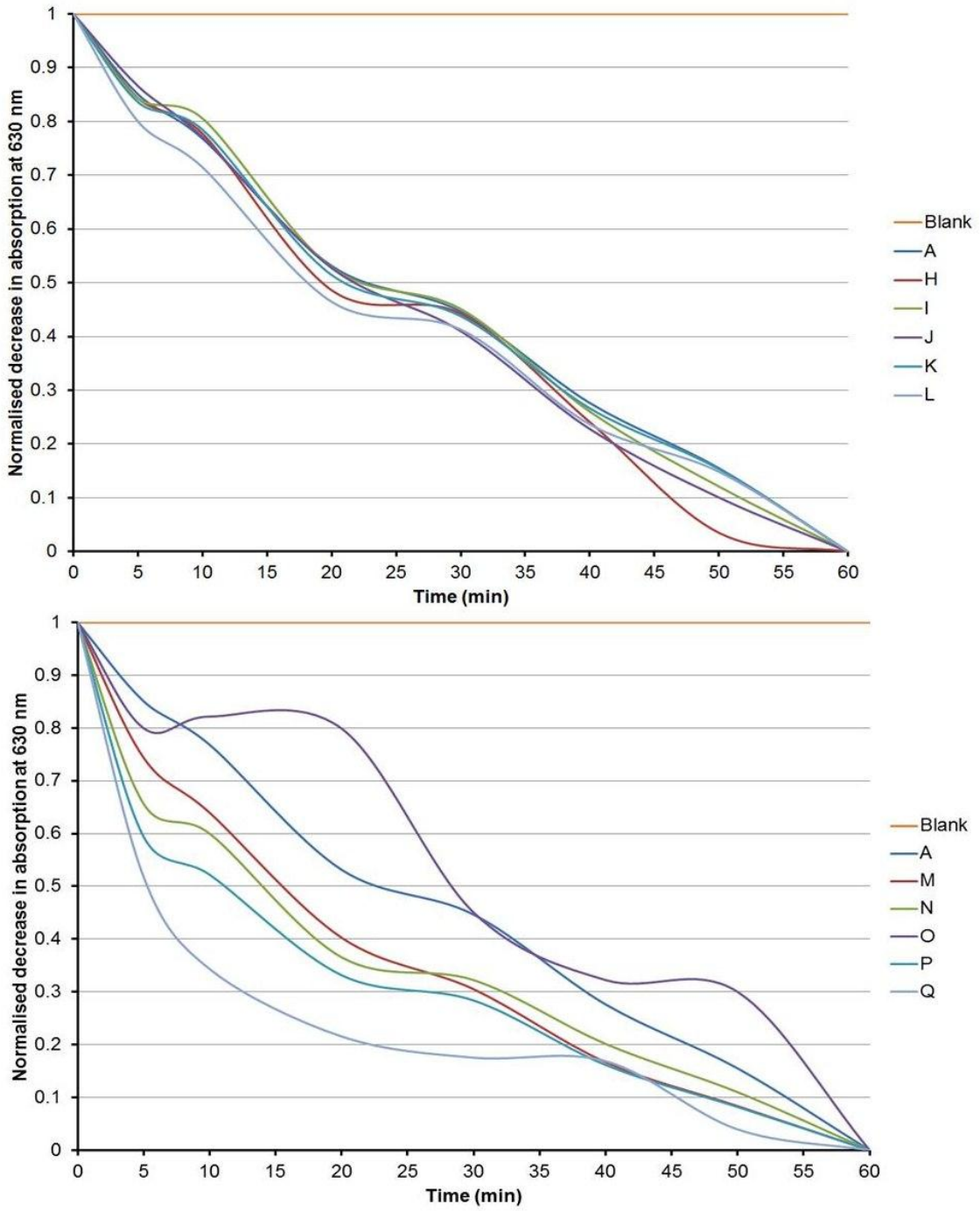

Figure 5.16: Normalised decrease in absorption of Resazurin intelligent ink at 630 nm with UVA irradiation (365 nm) against time (min) for film deposited in absence of electric fields (sample A), from the positive bias (H – L) and the negative bias (M – Q) EAAPCVD reaction of TTIP and ethanol.

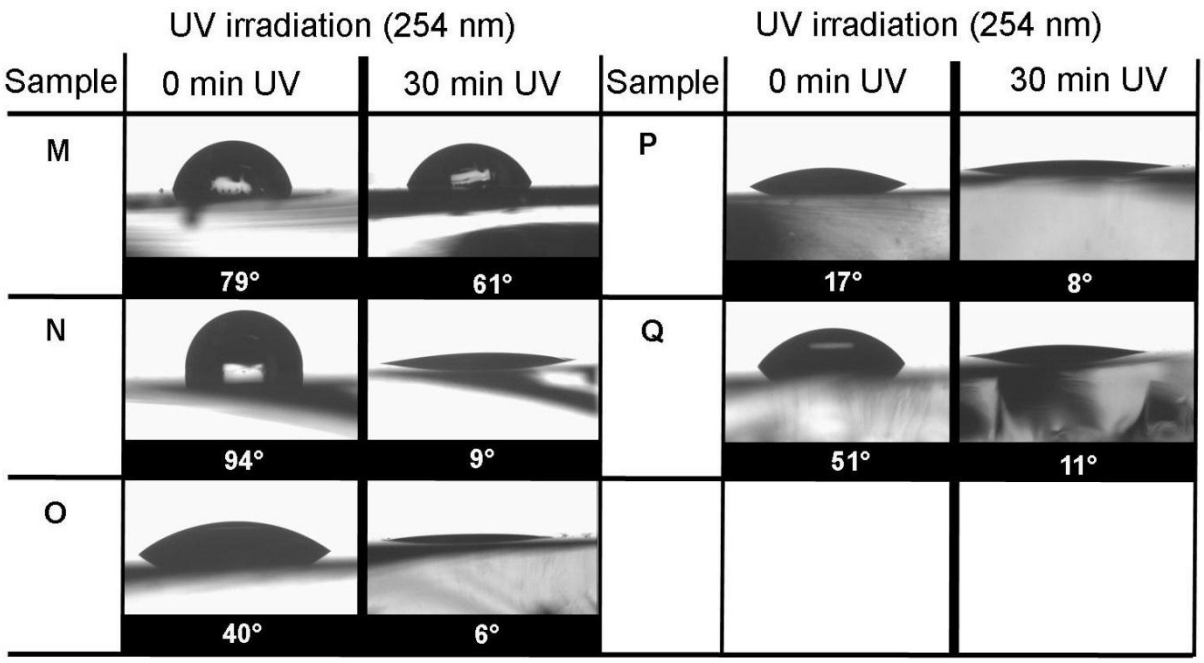

Figure 5.17: Representative water contact angle images for negative bias deposited films (Sample M – Q) at 550 °C and 2 L.min^{-1} before and after 30 min UVA irradiation 254 nm.

Contradictory to the results obtained from EAACVD TTIP deposited films the application of AC electric field did not significantly improve the photo-activity of titania thin films. According to the results observed in Chapter 3, deposited films with reduced elongated particle size, small crystallite size and highly oriented in the (004) such as sample G, should have given better photocatalytic performance. However, this sample showed a half-life value of 17.5 min. The source of oxygen used for the EAACVD TiO_2 growth from TTIP (Chapter 3, section 3.2.3) was toluene. It has been reported that the coarsening rate is favoured with longer solvent chain length due to the influence of the viscosity and surface energy in other metaloxides [179]. Deposited films from the EAACVD reaction of TTIP in toluene showed higher surface roughness which would have favoured the photocatalytic performance. In some cases deposited films the EAAPCVD of TTIP and ethanol such as sample D showed lower half-life values (17.5 min) with similar surface roughness (10 nm). However, this sample showed high agglomeration of clusters which would have had a detrimental effect on the photo-activity by reducing the surface area.

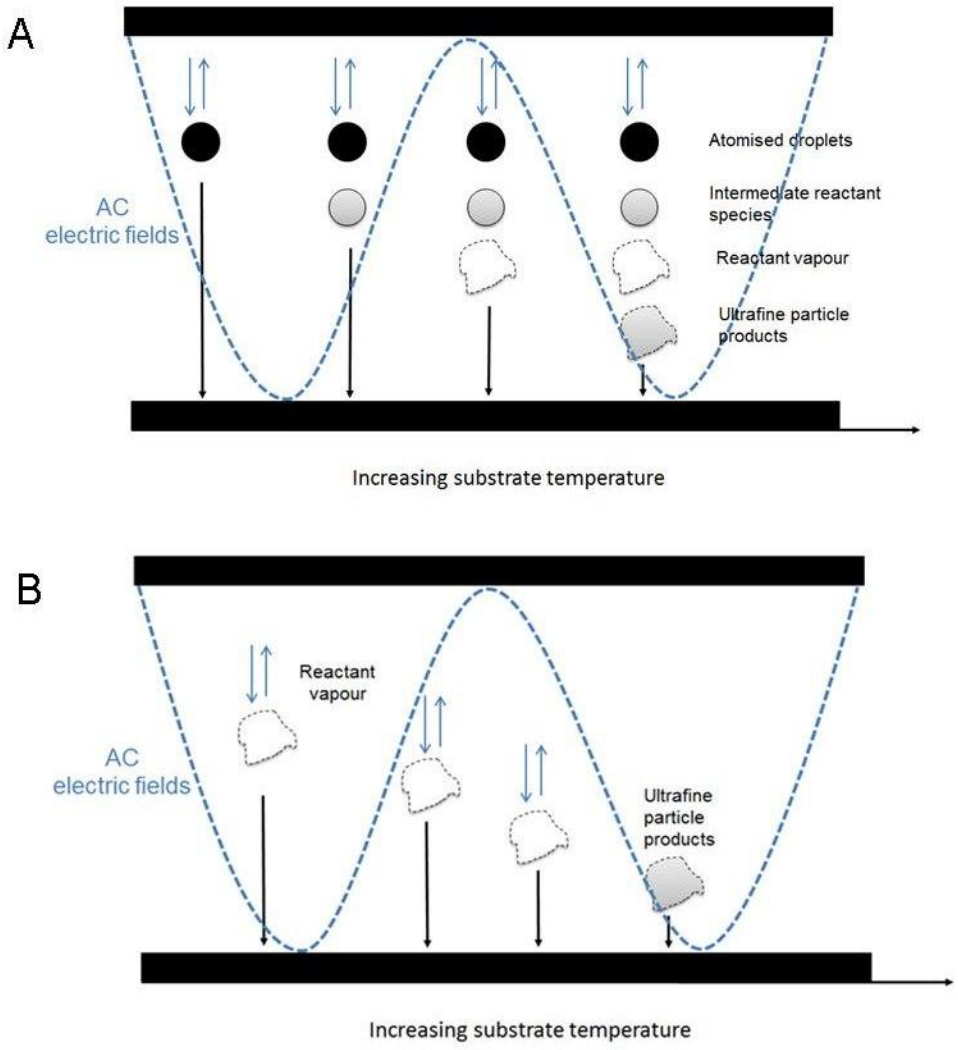

Figure 5.18: Diagrams showing the interactions of AC electric fields with the precursor in AACVD (A) and APCVD systems.

As observed for EAACVD TTIP, the application of DC electric fields did not significantly improve the photocatalytic activity of deposited films. Deposited films showed better photo-activity than sample A except for sample O (28.2 min). However, as observed in Chapter 3 the half-life values among them were very similar. Negative bias deposited films exhibited better photo-activity. All DC deposited films showed anatase, but negative bias deposited films showed lower film thickness that, as discussed in Chapter 3, would have favoured charge carrier transfer from the bulk of the material to the surface. The most photoactive film (sample Q, 5.1 min) also showed the lowest film thickness (8 nm). This sample also showed a small particle and crystallite size which would have improved the photo-activity by increasing the surface area.

5.4. Conclusions

Titanium dioxide thin films were successfully produced from the electric field assisted APCVD reaction of TTIP and ethanol at 550 °C and main gas flow rate of 2 $L.min^{-1}$. It was observed that for AC electric fields, lower field strength gave a mix of titania polymorphs as well as angular morphology in their microstructure. Higher field strength gave elongated morphology and mostly anatase. DC electric fields deposited films produced similar elongated morphology and pure anatase independently of the substrate bias and field strength applied. Contradictory to the results obtained from EAACVD (Chapter 3), negative bias deposited films gave more photoactive titania thin films than AC deposited films. This has been attributed to a combination of factors such as film thickness, crystal orientation and crystal phase which were more favoured under negative bias DC electric fields.

Chapter 6:

Titanium Dioxide Thin Films Produced from the Electric Field Assisted Atmospheric Pressure Chemical Vapour Deposition of Titanium (IV) Chloride and Ethyl Acetate

6.1. Introduction

This chapter presents the results on the experimental study of the TiO_2 thin films growth from Electric Field Assisted APCVD (EAPCVD) using Titanium Tetrachloride ($TiCl_4$) as a precursor and ethyl acetate as an oxygen source. Different experimental conditions have been tested in order to investigate the conditions for the optimum photocatalytic performance of deposited films.

6.2. Results

6.2.1. Film synthesis and characterisation of AC deposited films

Titanium dioxide thin films were deposited from the AC electric field assisted APCVD reaction of $TiCl_4$ and ethyl acetate at fixed conditions (see section 2.2.2.2). Thin films showed good adherence to the substrate, passed the Scotch tape test and could not be wiped off with a piece of towelling. XRD and Raman spectroscopy analysis confirmed the presence of anatase TiO_2 in all deposited films (Table 6.1).

Table 6.1: Field strength and material phase for titania thin films produced from the AC EAAPCVD reaction of $TiCl_4$ and ethyl acetate at fixed conditions.

Sample	Applied Voltage (V)	Field Strength (Vm^{-1})	Material Phase (XRD /Raman)
A	0	0	Anatase
B	1	1×10^2	Anatase
C	5	5×10^2	Anatase
D	10	10×10^2	Anatase
E	15	15×10^2	Anatase
F	20	20×10^2	Anatase
G	30	30×10^2	Anatase

Scanning electron microscopy

Scanning electron microscopy images of the titanium dioxide depositions are shown in Figure 6.1. Deposition carried out in absence of an electric field (sample A) revealed a thin film comprised of agglomerated spherical nanoparticles of 130 ± 4 nm in length with a film thickness of 700 ± 14 nm. The application of AC electric fields (sample B) produced thin films with elongated (175 ± 15 nm) and spherical (215 ± 14 nm) nanoparticles as well as a decrease in film thickness to 130 ± 8 nm. The increase of field strength to 10×10^2 Vm^{-1} produced spherical nanoparticles of 130 ± 5 nm (Sample C) – 85 ± 11 nm (Sample D). However, Sample C showed a higher film thickness (315 ± 13 nm) than Sample D (9 ± 2 nm). The increase of field strength up to 30×10^2 Vm^{-1} (Sample F and G) produced elongated nanoparticles of 210 ± 11 nm. At a field strength of 20×10^2 Vm^{-1} the film thickness was higher (Sample F, 120 ± 23 nm) than at 30×10^2 Vm^{-1} (Sample G, 35 ± 5 nm).

X-ray diffraction

X-ray diffraction was carried out and compared to the JCPDS database (JCPDS file number: 00-021-1272) to investigate the materials phase (Figure 6.2). All deposited films showed anatase TiO_2. Characteristic peaks for the anatase (101) plane ($2\theta = 25.28°$) and the anatase (004) plane ($2\theta = 37.8°$) were found for all deposited films. Likewise, characteristic peaks for

the anatase (200) plane was observed for all films except for samples D and F. Peaks from cassiterite SnO_2 from the underlying FTO coated glass substrate was also observed. The relative intensity of the Bragg peaks associated with TiO_2 changed with the field strength revealing a preferred orientation. Texture coefficient analysis was conducted to investigate the preferred crystal orientation [151]. As Table 6.3 shows, all films presented high preferential orientation in the (004). Generally, the application and increase of AC electric fields increased the texture coefficient in the (004) plane comparing to sample A (2.79). The films which showed the highest texture coefficient were sample D (3.62) and F (3.43).

Table 6.2: Agglomerate size (nm), film thickness (nm) with standard error (SE) obtained from SEM and mean crystallite size (nm) obtained from the Scherrer equation, for deposited films from the AC EAPCVD reaction of $TiCl_4$ and ethyl acetate at fixed conditions.

Sample	Applied Voltage (V)	Field strength (Vm^{-1})	Agglomerate size (nm)±SE		Thickness (nm)±SE	Mean crystallite size (nm)
			elongated	spherical/ angular		
A	0	0	--	130±4	700±14	19±2
B	1	1 x 10^2	175±15	215±14	130±8	17±4
C	5	5 x 10^2	--	130±5	315±13	19±1
D	10	10 x 10^2	--	85±11	9±2	--
E	15	15 x 10^2	--	220±12	56±10	17±0.7
F	20	20 x 10^2	210±7	--	12±23	--
G	30	30 x 10^2	210±11	--	35±5	17±0.5

The crystallite size of the deposited films was calculated from the full width at half maximum (FWHM) of different peaks using the Scherrer equation [155] (Table 6.2). Characteristic peaks of $2\theta = 25.28°$ (101), $2\theta = 37.8°$ (004), $2\theta = 48.05°$ (200) were used. However, no crystallite size value could have been obtained for samples D and F as their XRD pattern only showed two peaks. The application of electric fields produced a decrease in the mean crystallite size from 19 ± 2 nm to 17 ± 4 nm (sample B). Further increase of the electric fields produced an increase in the crystallite size to 19 ± 1 nm (sample C). However, for the rest of deposited films the crystallite size remained in 17 ± 0.5 nm.

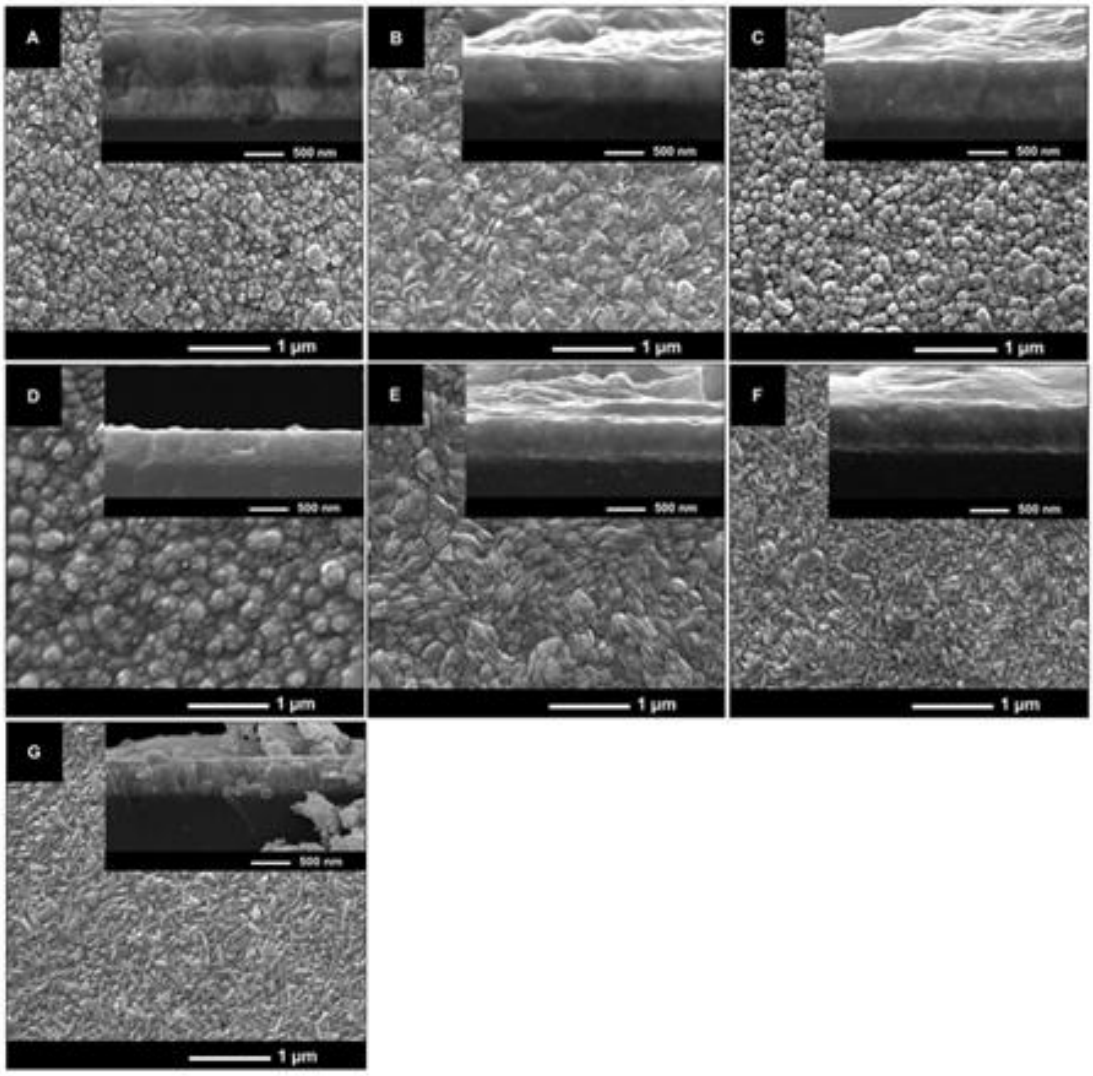

Figure 6.1: Scanning Electron Microscope images of samples prepared without electric field (A) and from the AC EAAPCVD reaction (S B to G) of $TiCl_4$ and ethyl acetate at fixed conditions (460 °C with a flow rate of 5 $L.min^{-1}$). A) 0 Vm^{-1}, B) 1 x 10^2 Vm^{-1}, C) 5 x 10^2 Vm^{-1}, D) 10 x 10^2 Vm^{-1}, E) 15 x 10^2 Vm^{-1}, F) 20 x 10^2 Vm^{-1}, G) 30 x 10^2 Vm^{-1}. Side on images were collected at x 60,000 magnification and cross section images at x 80,000.

Raman spectroscopy

Raman spectroscopy was carried out in order to complement XRD analysis for phase identification. As Figure 6.3 shows, no Raman peaks corresponding to rutile were found. Generally, samples gave strong Raman peaks centred at 147 cm^{-1}, 395 cm^{-1}, 513 cm^{-1} and 642 cm^{-1} [134] corresponding to anatase, except for sample D, which showed an amorphous spectra.

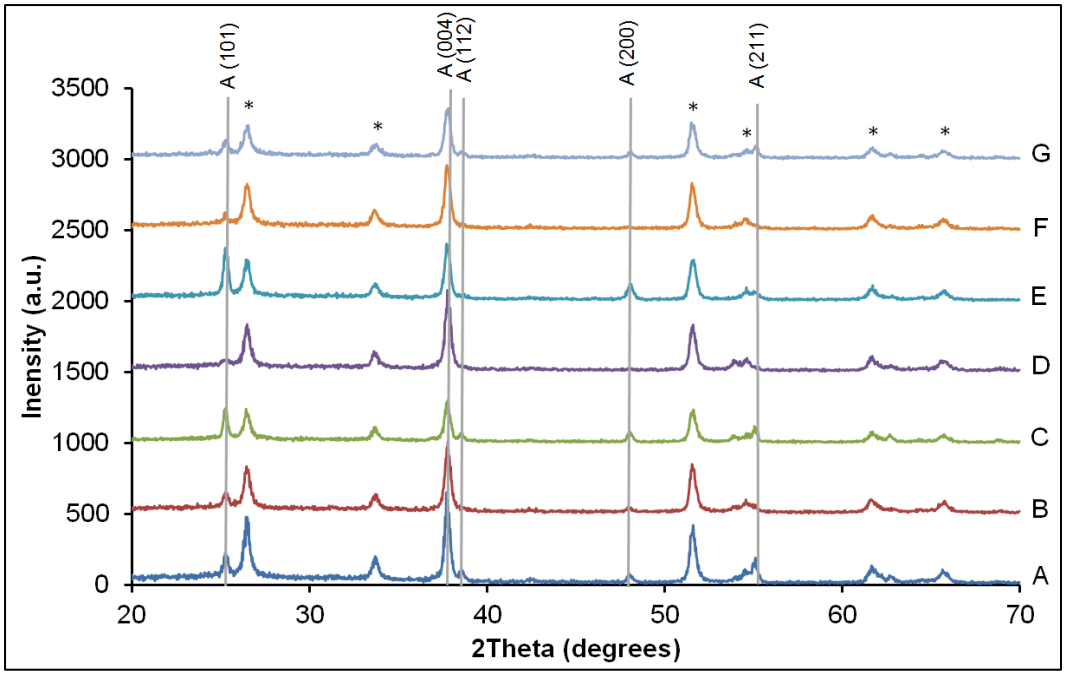

Figure 6.2: XRD patterns for samples prepared without an applied electric field (sample A) and from the EAAPCVD (samples B to G) reaction of $TiCl_4$ and ethyl acetate at fixed conditions. A stands for anatase. The peaks marked with dots denote the cassiterite peaks specific of SnO_2 crystalline phase (substrate).

Atomic force microscopy

AFM was performed scanning over a 10 µm x 10 µm region in order to obtain Root Mean Square (RMS) roughness values as a proxy of surface roughness (Figure 6.4). As it can be observed, the application and increase of AC electric fields decreased the surface roughness from 25 ± 8 nm to 15 ± 9 nm (sample A – D). Further increase of electric fields increased the surface roughness except for sample F (15 ± 2 nm). The highest RMS values were found for samples E (50 ± 10 nm) and G (43 ± 12 nm). The RMS values are listed in Table 6.4.

UV-vis spectroscopy

Generally, the application of field strength during the EAPCVD deposition increased the transmission in the visible (Figure 6.5, Table 6.4). Increasing field strength produced an increase in the transmission in the visible range comparing to sample A (72%). The highest transmission values were found for Samples E (80%), D (77%) and F (75%). However, higher field strength to 30 x 10^2 Vm^{-1} (Sample G) had a detrimental effect on the

transmission (68%). DBG values were calculated using the Tauc method [154]. All deposited films showed standard DBG for anatase (3.2 – 3.3 eV). The lowest direct band gap was found for sample C (3.15 eV).

Table 6.3: Texture Coefficient of TiO_2 thin films produced from the AC EAAPCVD reaction of $TiCl_4$ and ethyl acetate at fixed conditions.

Sample	Field Strength (Vm^{-1})	Texture Coefficient ($TC_{(hkl)}$)			
		(101)	(004)	(200)	(211)
A	0	0.2	2.79	0.19	0.85
B	1×10^2	0.18	3.04	0.16	0.64
C	5×10^2	0.38	2.33	0.35	1.02
D	10×10^2	0.11	3.62	0.07	0.2
E	15×10^2	0.48	2.6	0.45	0.52
F	20×10^2	0.19	3.43	0.1	0.29
G	30×10^2	0.21	2.8	0.23	0.79

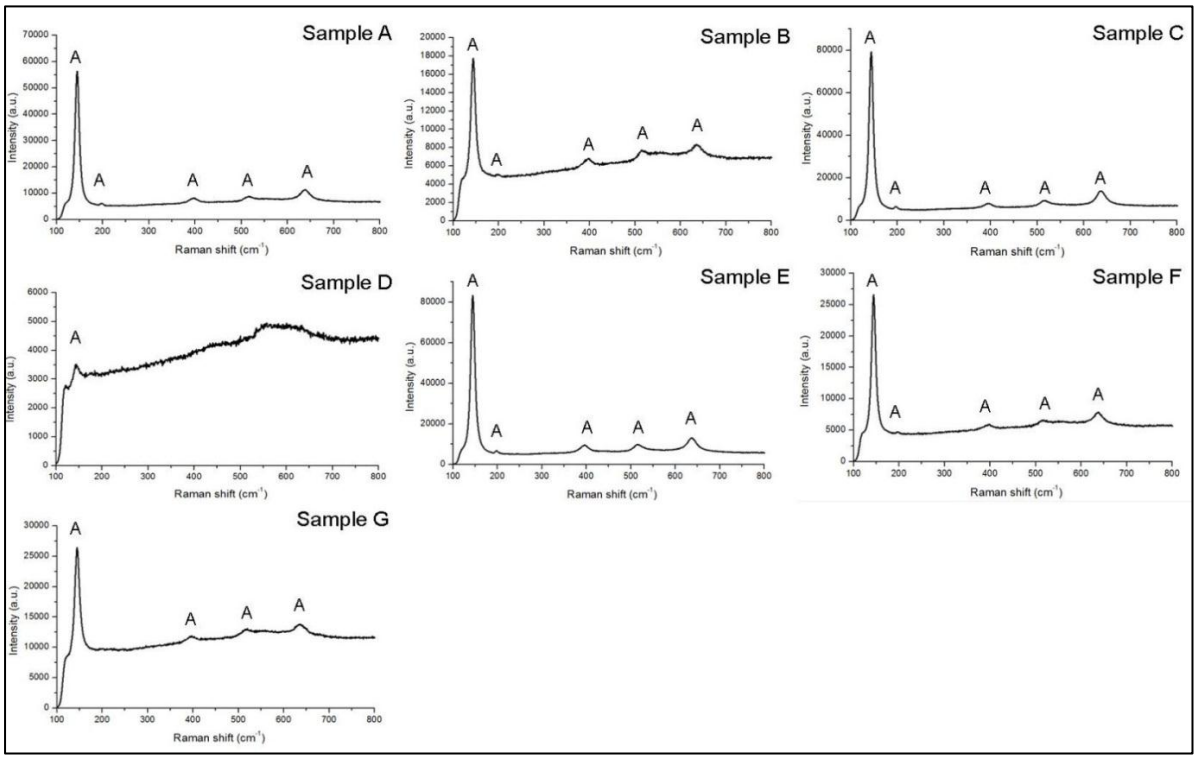

Figure 6.3: Raman spectra for samples prepared without an applied electric field (sample A) and from the AC EAAPCVD (samples B to G) reaction of $TiCl_4$ and ethyl acetate at fixed conditions.

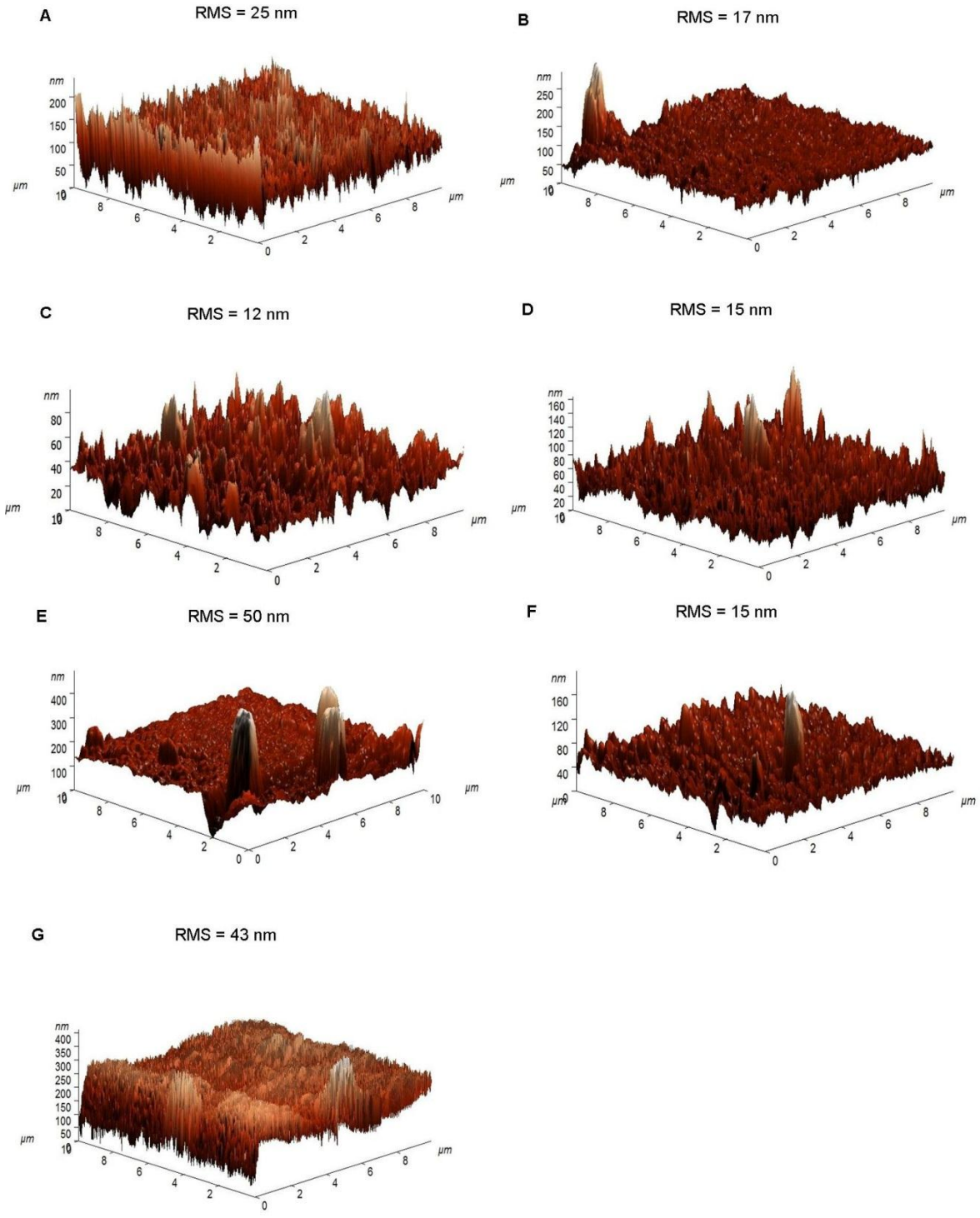

Figure 6.4: AFM images with corresponding Root Mean Square (RMS) values (nm) for films deposited from EAAPCVD reaction of $TiCl_4$ and ethyl acetate at 460 °C and 5 $L.min^{-1}$ in absence of electric fields (sample A) and with applied AC electric fields (samples B to G).

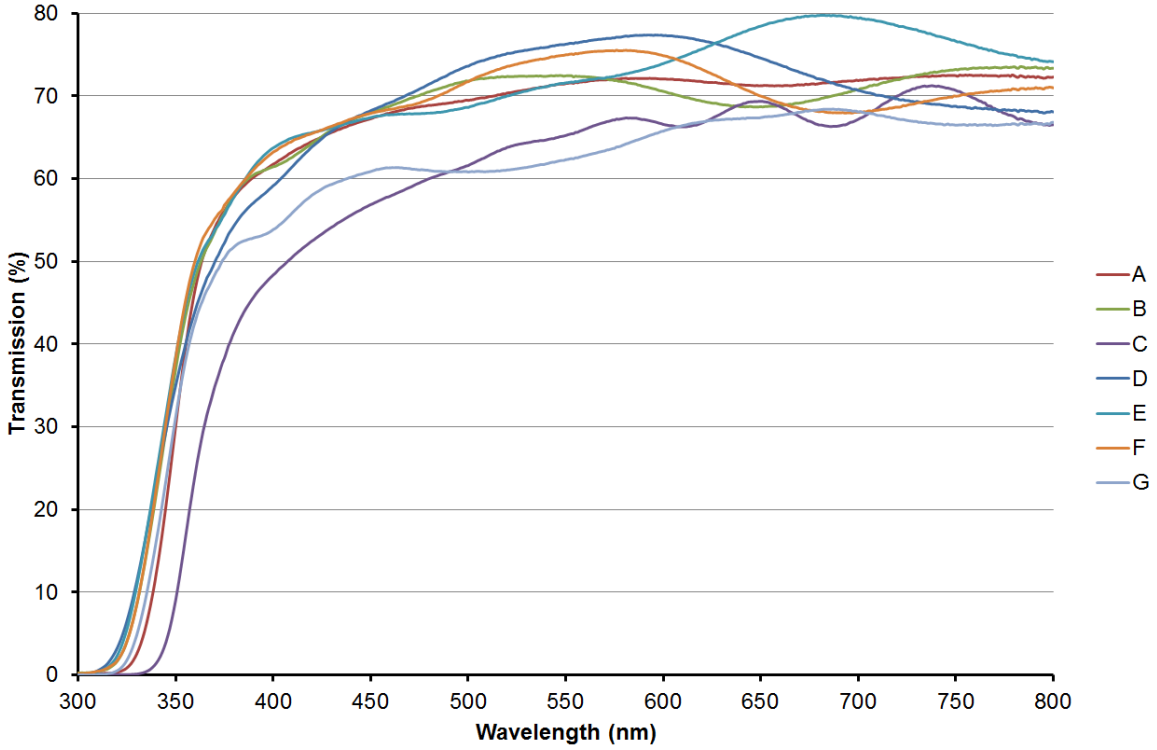

Figure 6.5: UV-vis spectroscopy for samples prepared without an applied electric field (sample A) and from the AC EAAPCVD (samples B to G) reaction of $TiCl_4$ and ethyl acetate at fixed conditions.

6.2.2. Functional properties of deposited films from AC electric fields

6.2.2.1. Photo-activity of TiO_2 thin films

UV/Vis investigation of the films photocatalytic abilities (Figure 6.6) indicated that the application of AC electric fields improved the photo-activity only for three deposited films (samples B, C and E). As Table 6.5 shows, the application of electric fields decreased the half-life from 29 min (sample A) to 17 min (sample B). The increase of field strength to 5 x 10^2 Vm^{-1} produced a further decrease of the half-life to 13.8 min (sample C). However, higher field strength to 30 x 10^2 Vm^{-1} (sample D – G) significantly decreased the photo-activity with half-life values in the range of 30.5 – 32.6 min. As an exception, sample E showed a half-life value of 27 min, which was slightly lower than sample A.

Table 6.4: Root Mean Square (RMS) (nm) from AFM, maximum transmission in the visible (%) from UV-vis spectroscopy and DBG (e.V) calculated by the Tauc method for films produced from the AC EAAPCVD reaction of $TiCl_4$ and ethyl acetate at fixed conditions.

Sample	Applied Voltage (V)	Field Strength (Vm^{-1})	RMS (nm)	T vis (%)	B.G (eV)
A	0	0	25±8	72	3.2
B	1	1×10^2	17±5	72	3.3
C	5	5×10^2	12±4	69	3.15
D	10	10×10^2	15±9	77	3.3
E	15	15×10^2	50±10	80	3.3
F	20	20×10^2	15±2	75	3.3
G	30	30×10^2	43±12	68	3.3

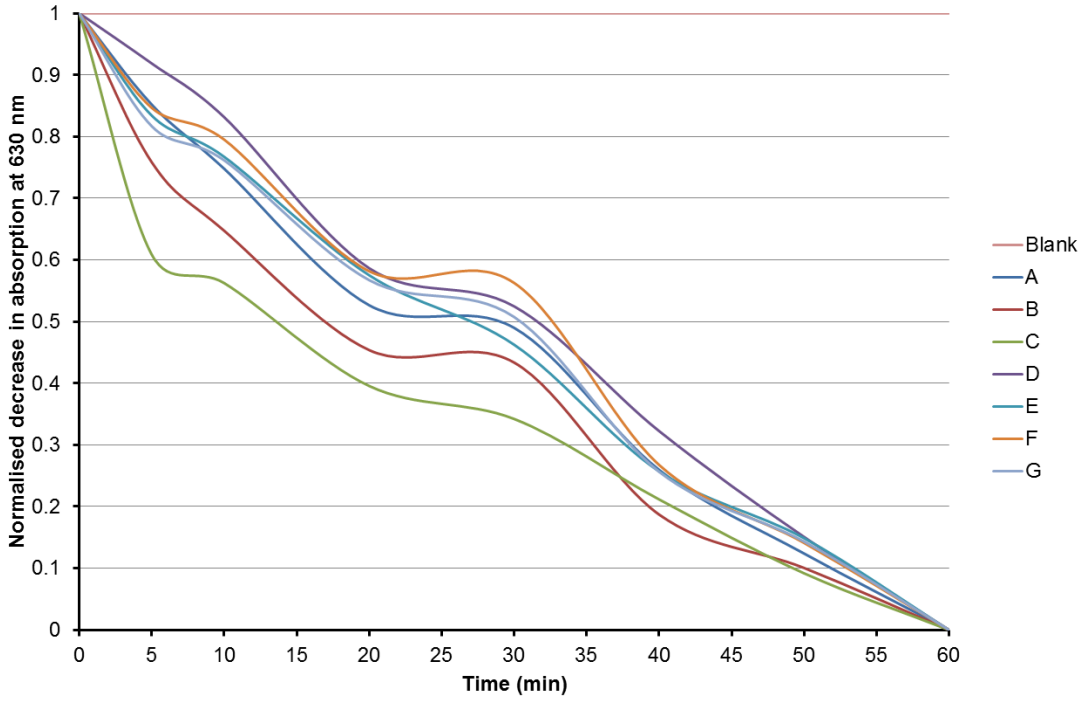

Figure 6.6: Normalised decrease in absorption of Resazurin intelligent ink at 630 nm with UVA irradiation (365 nm) against time (min) for deposited films from AC EAAPCVD reaction of $TiCl_4$ and ethyl acetate at 460 °C and 5 $L.min^{-1}$. A) 0 Vm^{-1}, B) 1×10^2 Vm^{-1}, C) 5×10^2 Vm^{-1}, D) 10×10^2 Vm^{-1}, E) 15×10^2 Vm^{-1}, F) 20×10^2 Vm^{-1}, G) 30×10^2 Vm^{-1}.

6.2.2.2. Water-contact angles

Mean water-contact angles measurements were carried out to study the wettability of surfaces (Figure 6.7). All deposited films showed hydrophilicity with water contact angles in the range of 42 – 77° (Table 6.5). The lowest water contact angle before UV irradiation was found for sample D (42°) followed by the film deposited in absence of electric fields (sample A, 46°). After 30 minutes of 254 nm UV irradiation, all electric fields deposited films showed hydrophilicity with contact-angles between 30° - 8 ° and superhydrophilicity for samples A and B.

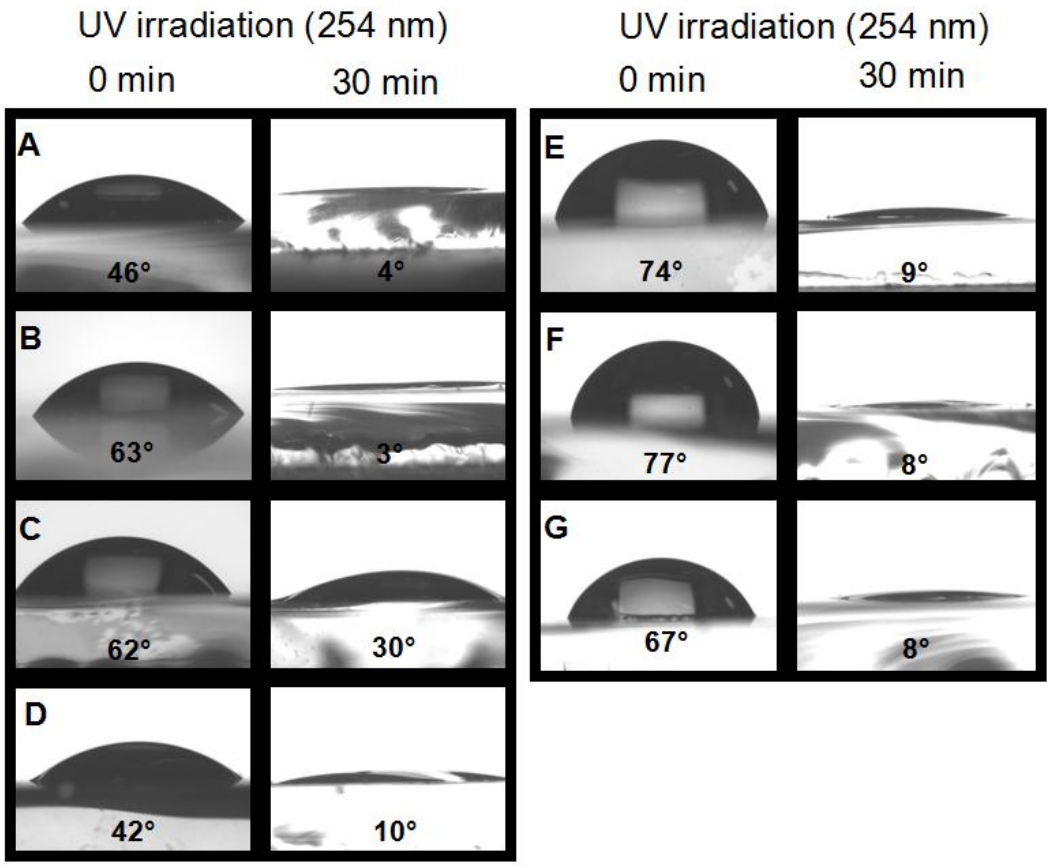

Figure 6.7: Representative mean water-contact angle images for deposited films from the AC EAAPCVD reaction of $TiCl_4$ and ethyl acetate at 460 °C and 5 $L.min^{-1}$ before and after 30 min UVA irradiation (254 nm).

6.2.3. Film synthesis and characterisation of DC deposited films

TiO_2 thin films were deposited from the EAAPCVD reaction of $TiCl_4$ and ethyl acetate at fixed conditions (see section 6.2.2) under the influence of DC electric field. Deposited films presented good adherence to the substrate passing the Scotch tape test and a scratch test using a piece of towel. Films appearance and experimental conditions are described in Chapter 2, section 2.2.2.1. XRD analysis confirmed TiO_2 anatase in all deposited films. Further Raman spectroscopy analysis also confirmed the presence of rutile crystal phase for samples H and M (Table 6.6).

Scanning electron microscopy

Scanning electron microscopy images of the titanium dioxide depositions are shown in Figure 6.8. Deposition carried out in absence of an electric field (Figure 6.8 A) revealed a thin film comprised of agglomerated angular nanoparticles of 130 ± 4 nm in length and a film thickness of 700 ± 14 nm. The application of positive bias electric fields (sample H) produced a change in morphology to worm-like nanoparticles of 230 ± 39 nm in length and an increase in film thickness to 170±15 nm. Increasing field strength up to 10 x 10^2 Vm^{-1} produced a change in morphology to spherical nanoparticles of 220 ± 10 – 170 ± 15 nm (samples I and J). Film thickness in this range gradually increased to 500 ± 9 nm. Further increase of the field strength to 15 x 10^2 Vm^{-1} (sample K) produced a significant decrease in particle size and film thickness to 140 ± 7 nm and 7 ± 1 nm, respectively. At 20 x 10^2 Vm^{-1}, films showed angular nanoparticles of 160± 11 nm in length and important increase in film thickness to 380 ± 10 nm (sample L). The increase of the field strength to 30 x 10^2 Vm^{-1}, produced an agglomeration of angular nanoparticles of 365 ± 26 nm in length forming a rose-like morphology (sample M). The film thickness registered at this field strength was 250 ± 27 nm.

Changing the film bias to a negative bias (Figure 6.9) led to further microstructural and thickness changes. The introduction of negatively biased electric fields (1 x 10^2 Vm^{-1}, sample N) produced a morphology similar to the one observed for sample M. However, the particle size and film thickness was higher for this sample (515 ± 20 nm and 270 ± 9 nm, respectively).

Table 6.5: Mean water-contact angles of deposited TiO_2 thin films from the AC EAAPCVD reaction of $TiCl_4$ and ethyl acetate at fixed conditions, before and after UV irradiation (30 min); half-life values, $t_{1/2}$ (min).

Sample	Field Strength (Vm^{-1})	Mean Contact Angle (degrees) ± SE		Half-life
		0 min	30 min	$t_{1/2}$ (min)
A	0	46±5	3.9±4	29
B	1×10^2	63±11	3±2	17
C	5×10^2	62±6	30±8	13.8
D	10×10^2	42±1	10±5	31.6
E	15×10^2	74±4	9±2	27
F	20×10^2	77±6	8±1	32.6
G	30×10^2	67±1	8±1	30.5

Table 6.6: Experimental conditions of deposited films from the EAPCVD reaction of $TiCl_4$ and ethyl acetate at fixed conditions with an applied DC electric field.

Sample	Applied Voltage (V)	Field Strength (Vm^{-1})	Substrate bias	Material Phase (XRD/Raman)
A	0	0	---	Anatase
H	1	1×10^2	Positive	Anatase/Anatase-Rutile
I	5	5×10^2	Positive	Anatase
J	10	10×10^2	Positive	Anatase
K	15	15×10^2	Positive	Anatase
L	20	20×10^2	Positive	Anatase
M	30	30×10^2	Positive	Anatase/Anatase-Rutile
N	1	1×10^2	Negative	Anatase
O	5	5×10^2	Negative	Anatase
P	10	10×10^2	Negative	Anatase
Q	15	15×10^2	Negative	Anatase
R	20	20×10^2	Negative	Anatase
S	30	30×10^2	Negative	Anatase

The increase of field strength to 5 x 10^2 Vm^{-1} (Sample O) produced spherical nanoparticles forming clusters of 190 ± 13 nm and an increase in film thickness to 290 ± 57 nm. At 5 x 10^2 Vm^{-1} (Sample P), films showed angular nanoparticles of 360 ± 32 nm and an important increase in film thickness to 600 ± 20 nm. Further increase of the field strength (samples Q – S) produced a change to elongated nanoparticles of 240 ± 23 – 500 ± 45 nm in length. Film thickness gradually increased to 850 ± 26 nm in this range of field strength.
Agglomerate size and thickness for all deposited films are listed in Table 6.7.

Different trends in film thickness were observed for different substrate bias. As Figure 6.10 shows, an increase in film thickness with field strength was observed for negative bias deposited films whereas a decrease trend was shown for positively bias deposited films.

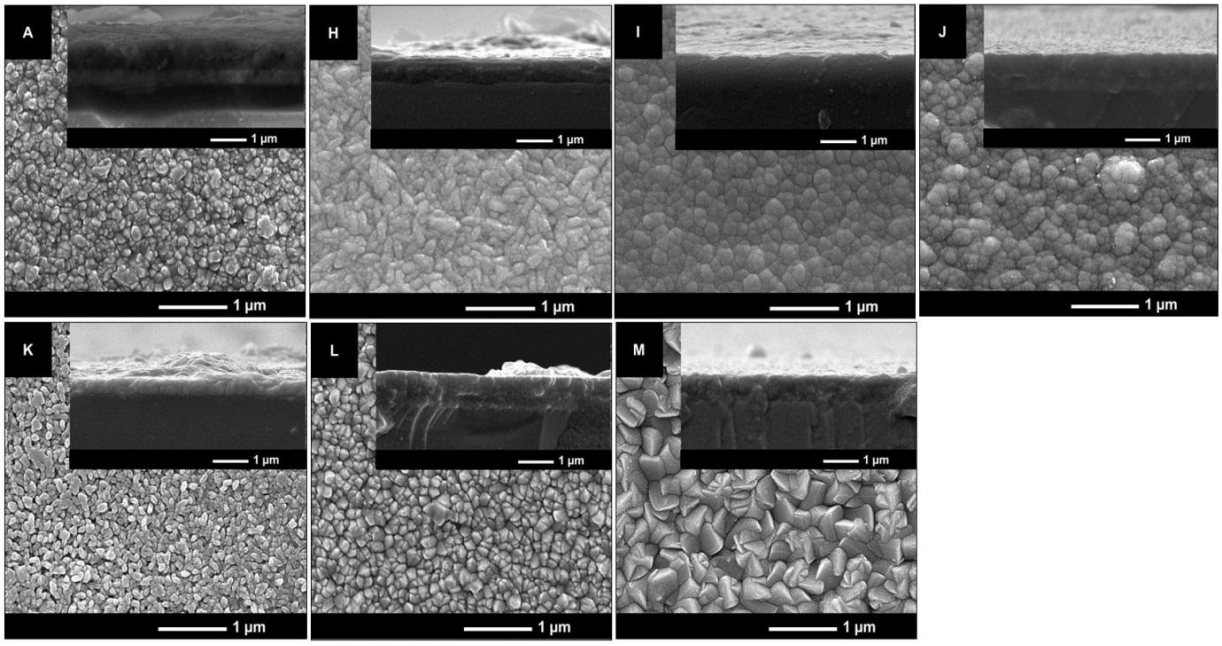

Figure 6.8: Scanning Electron Microscope images of samples prepared from the positive biased DC EAPCVD reaction of $TiCl_4$ and ethyl acetate at fixed conditions. The images above correspond to A) 0 Vm^{-1}, H) +ve 1 x 10^2 Vm^{-1}, I) +ve 5 x 10^2 Vm^{-1}, J) +ve 10 x 10^2 Vm^{-1}, K) +ve 15 x 10^2 Vm^{-1}, L) +ve 30 x 10^2 Vm^{-1}. Side on images were collected at x 60,000 magnification and cross section images at x 40,000.

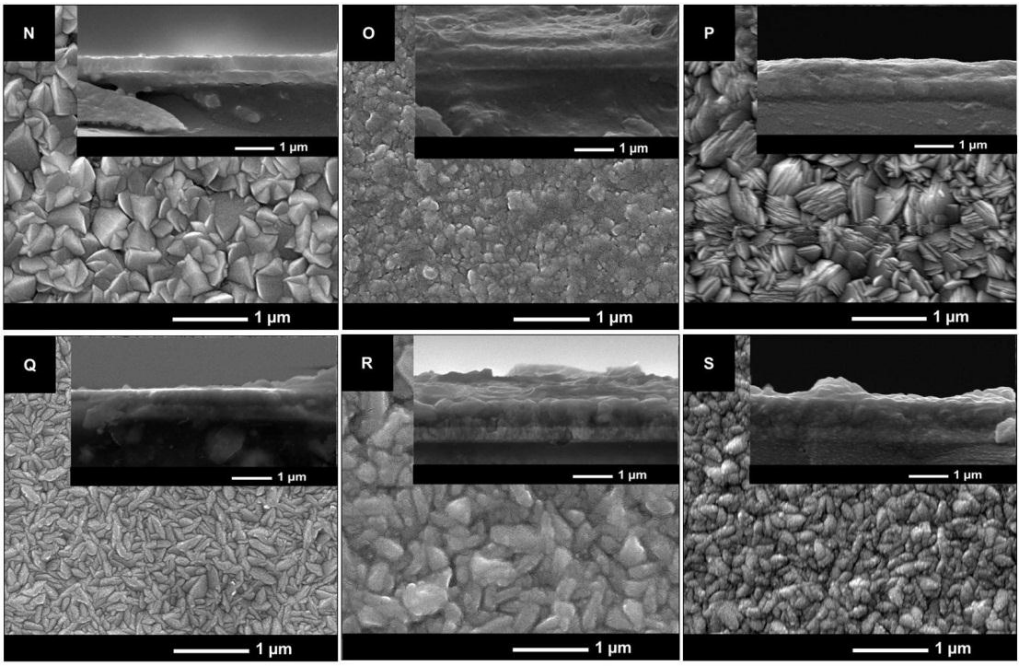

Figure 6.9: Scanning Electron Microscope images of samples prepared from the negative biased DC EAPCVD reaction of $TiCl_4$ and ethyl acetate at fixed conditions. The images above correspond to M) –ve 1 x 10^2 Vm^{-1}, N) –ve 5 x 10^2 Vm^{-1}, O) –ve 10 x 10^2 Vm^{-1}, P) –ve 15 x 10^2 Vm^{-1}, Q) –ve 30 x 10^2 Vm^{-1}. Side on images were collected at x 60,000 magnification and cross section images at x 40,000.

X-ray diffraction

X-ray diffraction (XRD) analysis was carried out and compared to previous investigations (JCPDS database file (021-1272)) to study the materials phase. All deposited films showed the presence of anatase TiO_2 and cassiterite SnO_2 from the FTO glass substrate except for sample S which showed amorphous pattern (Figure 6.11). As mentioned in section 6.2.2, the film produced in absence of electric fields (sample A) showed characteristics peaks for anatase (101) (2 Theta = 25.28°), (004) (2 Theta = 37.8°), (200) (2 Theta = 48.05°) and (211) (2 Theta = 55.06°). This sample also showed characteristic peak for rutile (211) (2 Theta = 54.3°). Positive bias deposited films showed anatase crystal phase. Generally, all positive bias deposited films showed weak characteristic peaks for anatase (101) and anatase (211). Samples I, K – M also showed peaks for anatase (112) (2 Theta = 38.5°). No rutile peaks were observed for positive bias deposited films. Generally, the application of negative bias electric fields showed characteristic peaks of anatase (101), (112), (200) and (211). Furthermore, samples N and O showed a peak at 2 Theta = 54.3° corresponding to rutile (211).

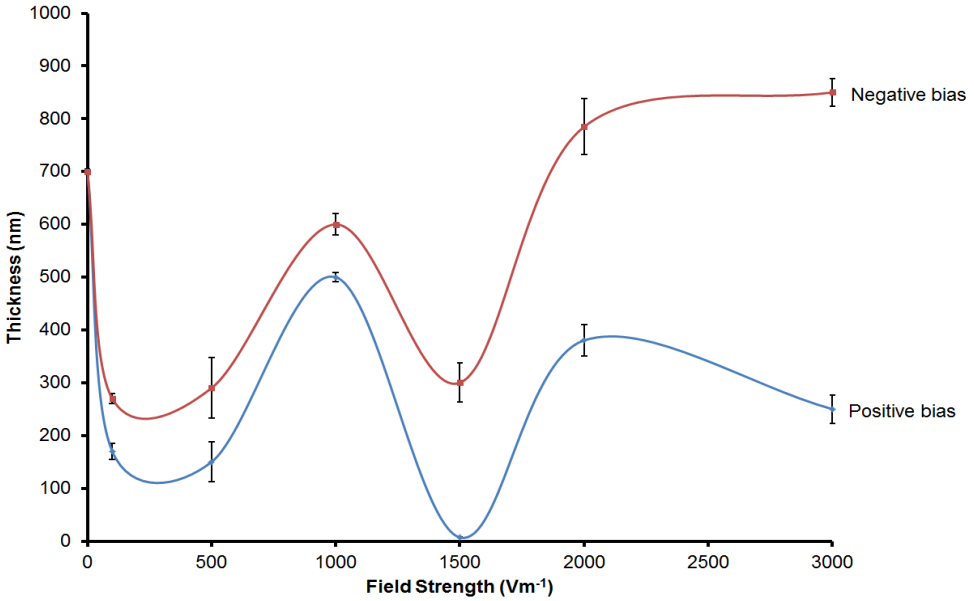

Figure 6.10: Film thickness trend with SE for positive and negative bias deposited films from the DC EAAPCVD reaction of $TiCl_4$ and ethyl acetate at fixed conditions.

Table 6.7: Agglomerate size (nm) from SEM with standard error (SE), film thickness (nm) from SEM cross section with SE and mean crystallite size (nm) obtained from the Scherrer equation for films produced from the DC EAPCVD reaction of $TiCl_4$ and ethyl acetate at fixed conditions.

Sample	Field Strength (Vm^{-1})	Substrate bias	Agglomerate size (nm)±SE		Film Thickness (nm)±SE	Mean crystallite size (nm)±SE
			Elongated	Spherical/ angular		
A	0	--	--	130±4	14±4	19±2
H	1 x 10^2	Positive	230±39	--	170±15	--
I	5 x 10^2	Positive	--	220±10	150±38	20±6
J	10 x 10^2	Positive	--	170±15	500±9	16±3
K	15 x 10^2	Positive	--	140±7	7±1	17±0.6
L	20 x 10^2	Positive	--	160±11	380±30	30±8
M	30 x 10^2	Positive	--	365±26	250±27	--
N	1 x 10^2	Negative	--	515±20	270±9	24±3
O	5 x 10^2	Negative	--	190±13	290±57	17±3
P	10 x 10^2	Negative	--	360±32	600±20	24±5
Q	15 x 10^2	Negative	240±23	--	300±37	33±7
R	20 x 10^2	Negative	500±45	--	785±53	21±2
S	30 x 10^2	Negative	270±13	--	850±26	--

Texture coefficient calculations were carried out to confirm the preferred crystal orientation found in XRD analysis [151]. The results (shown in Table 6.8) revealed that all deposited films were strongly oriented in the anatase (004) with texture coefficient in the range of 1.85 – 3.32. As an exception, sample R showed preferred orientation in the anatase (211) plane with a texture coefficient of 1.95.The highest texture coefficient values in the anatase (004) plane were found for samples J, M and O (3.15 – 3.32).

Furthermore, XRD analysis of full width at half maximum (FWHM) was carried out using the Scherrer equation [155] in order to investigate the crystallite size of deposited films. Characteristic peaks of 2 Theta = 25.28° (101), 2 Theta = 37.8° (004), 2 Theta = 48.05° (200) were selected and the generally used shape factor of 0.9 [152] was chosen. As Table 6.7 shows, the application of DC electric fields generally produced an increase in the mean crystallite size. However, the application of negative bias electric fields produced a higher increase in the mean crystallite size with values in the range of 17 – 33 (± 3 – 7) nm.

Table 6.8: Texture Coefficient of TiO_2 thin films produced from the APCVD from the positive bias (H – M) and negative bias (N – S) reaction of $TiCl_4$ and ethyl acetate at 460 °C and 5 $L.min^{-1}$.

	Texture Coefficient (TC_{hkl})			
Sample	(101)	(004)	(200)	(211)
A	0.2	2.79	0.19	0.85
H	0.17	2.84	0.2	0.78
I	0.16	1.85	0.27	1.72
J	0.25	3.22	0.25	0.27
K	0.26	2.3	0.38	1.06
L	0.28	2.22	0.37	1.13
M	0.2	3.15	0.16	0.48
N	0.27	2.63	0.34	0.76
O	0.24	3.32	0.23	0.2
P	0.44	2.48	0.41	0.67
Q	0.32	2.7	0.25	0.73
R	0.28	0.9	0.87	1.95

Raman spectroscopy

Raman spectroscopy was carried out in order to complement XRD analysis for phase identification. All DC deposited films gave strong Raman shifts centred at 147 cm^{-1}, 395 cm^{-1}, 513 cm^{-1} and 642 cm^{-1} which correspond to anatase crystal phase [134]. As an exception Sample O showed an amorphous spectra. Samples H and M showed a Raman peak centred at 447 cm^{-1} which correspond to the rutile crystal phase [38]. Sample N showed purely rutile with Raman peaks centred at 143 cm^{-1}, 447 cm^{-1} and 642 cm^{-1} [38]. Quantifiable values of the content of anatase and rutile in deposited films H, M and N were calculated from Raman spectra. As the rest of deposited films showed purely anatase in both XRD and Raman spectroscopy such calculation was not considered necessary. Anatase and rutile contents were obtained by de-convoluting the overlapping rutile A_{1g} (612 cm^{-1}) and anatase E_g (639 cm^{-1}) contributions and inserting the % area of contribution of rutile component (x) into a predetermined equation derived from powder standards as previously reported [63]. As Table 6.9 shows, samples H and M showed mostly anatase (72%) whereas Sample N showed a lower content of anatase crystal phase (57%).

Atomic force microscopy

Deposited films surfaces were scanned using AFM over a 10 µm x 10 µm region in order to obtain Root Mean Square (RMS) roughness values as a proxy of surface roughness. Table 6.10 shows the RMS values of deposited films from the DC EAPCVD reaction of $TiCl_4$ and ethyl acetate at fixed conditions. The increasing field strength progressively increased the surface roughness regardless of the substrate bias. However, it was observed higher a surface roughness for negative bias deposited films with RMS values in the range of 9 –20 nm vs 3 – 15 nm of positive bias deposited films. Figure 6.13 shows representative AFM images of deposited films from the DC EAPCVD reaction of $TiCl_4$ and ethyl acetate at fixed conditions.

UV-vis spectroscopy

UV/VIS spectroscopy showed different transmission values in the visible depending on the substrate bias. Generally, the application of negative bias electric fields produced lower transmission values in the visible than positive bias (Figure 6.14). The application and

increase of positive bias electric fields produced a gradual increase in the transmission in the visible from 65 – 79% (samples H – M), Table 6.10. The application of negative bias electric fields produced a decrease in the transmission in the visible from 55 – 68% (samples N, P, R, S). However, samples O and Q showed higher transmission in the visible (79 – 73%) than Sample A (72%). Direct band gap analysis was performed using the Tauc method [154]. Generally, the application of electric fields seemed to have little influence in the direct band gap of deposited films. All deposited films showed typical direct band gap values of anatase crystal phase (3.2 –3.3 eV). However, Samples H and N showed lower direct band gaps (3.15 –3.0 eV).

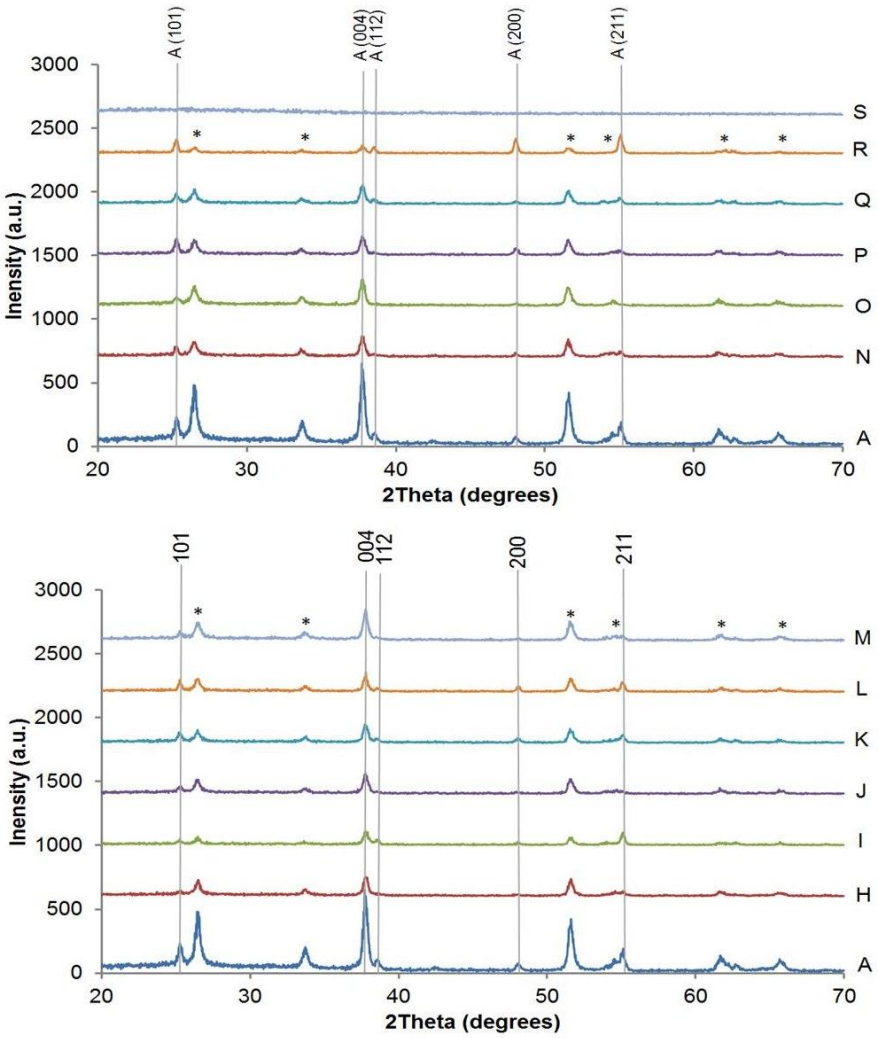

Figure 6.11: XRD pattern for samples prepared from EAAPCVD reaction of $TiCl_4$ and ethyl acetate at 460 °C and 5 $L.min^{-1}$, films deposited in absence of electric fields (A), positive biased (H-M) and negative biased electric fields (N-S). The peaks marked with asterisks denote the cassiterite peaks specific of SnO_2 crystalline phase from the glass substrate.

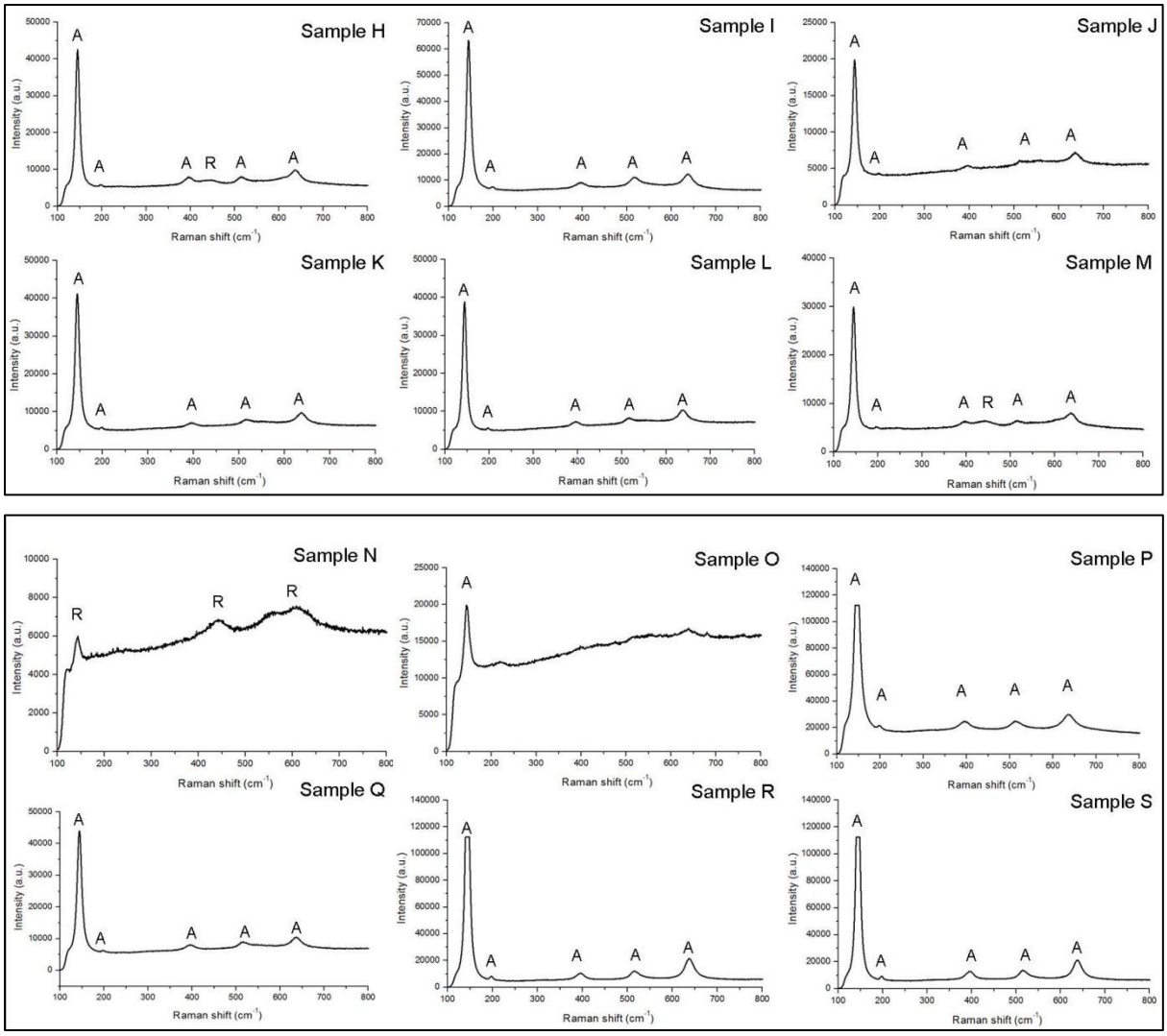

Figure 6.12: Raman spectra for films deposited from the EAPCVD reaction of TiCl4 and ethyl acetate at fixed conditions in absence of electric fields (A) and from the positive (H-M) and negative biased field strength (N-S). A stands for anatase and R for rutile crystal phase.

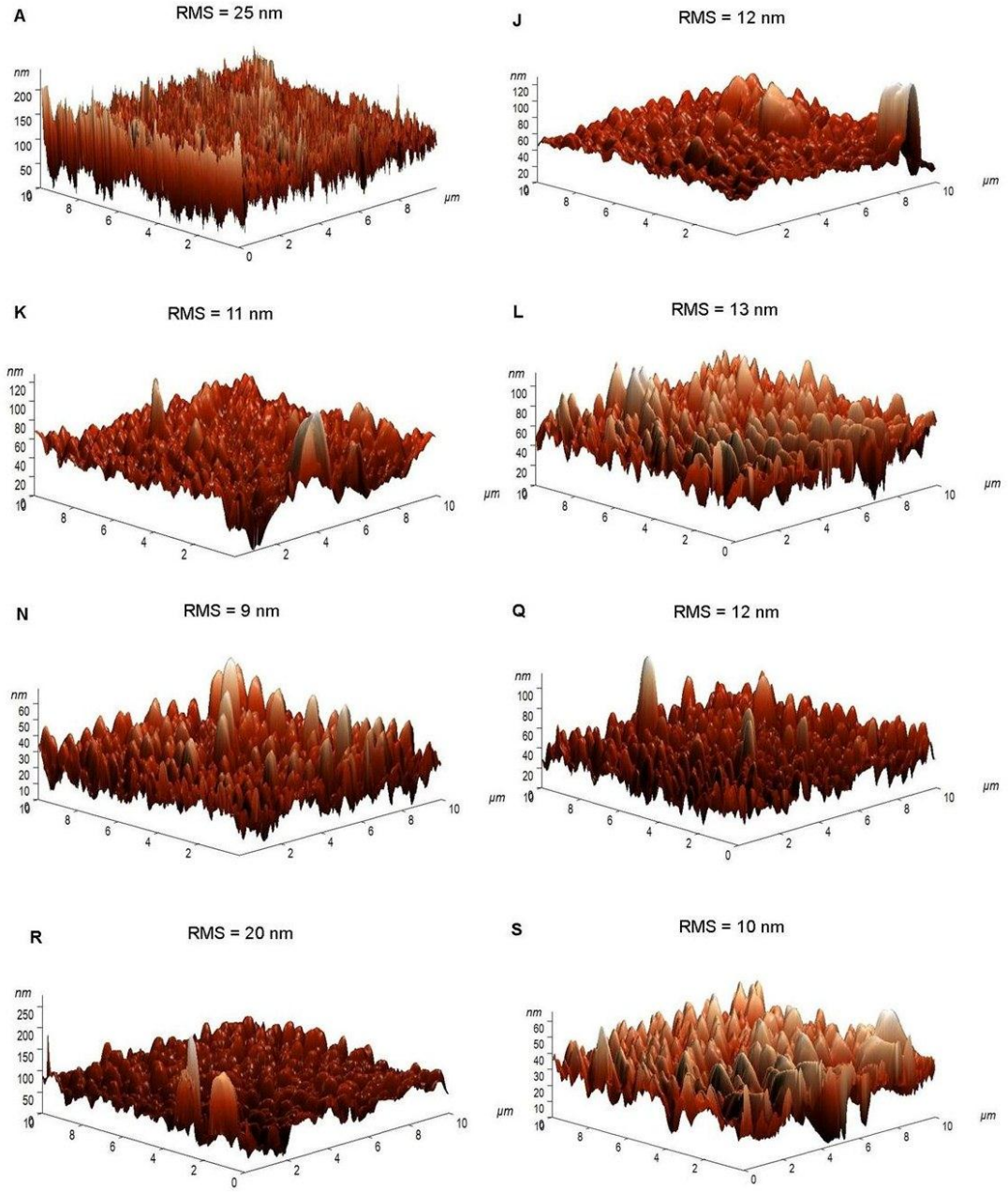

Figure 6.13: Representative AFM images with corresponding Root Mean Square (RMS) values (nm) for films deposited from the EAPCVD reaction of $TiCl_4$ and ethyl acetate at fixed conditions. A) 0 Vm^{-1}, J) +ve 10 x 10^2 Vm^{-1}, K) +ve 15 x 10^2 Vm^{-1}, L) +ve 20 x 10^2 Vm^{-1}, N) –ve 1 x 10^2 Vm^{-1}, Q) – ve 15 x 10^2 Vm^{-1}, R) – ve 20x 10^2 Vm^{-1}, Q) – ve 30 x 10^2 Vm^{-1}.

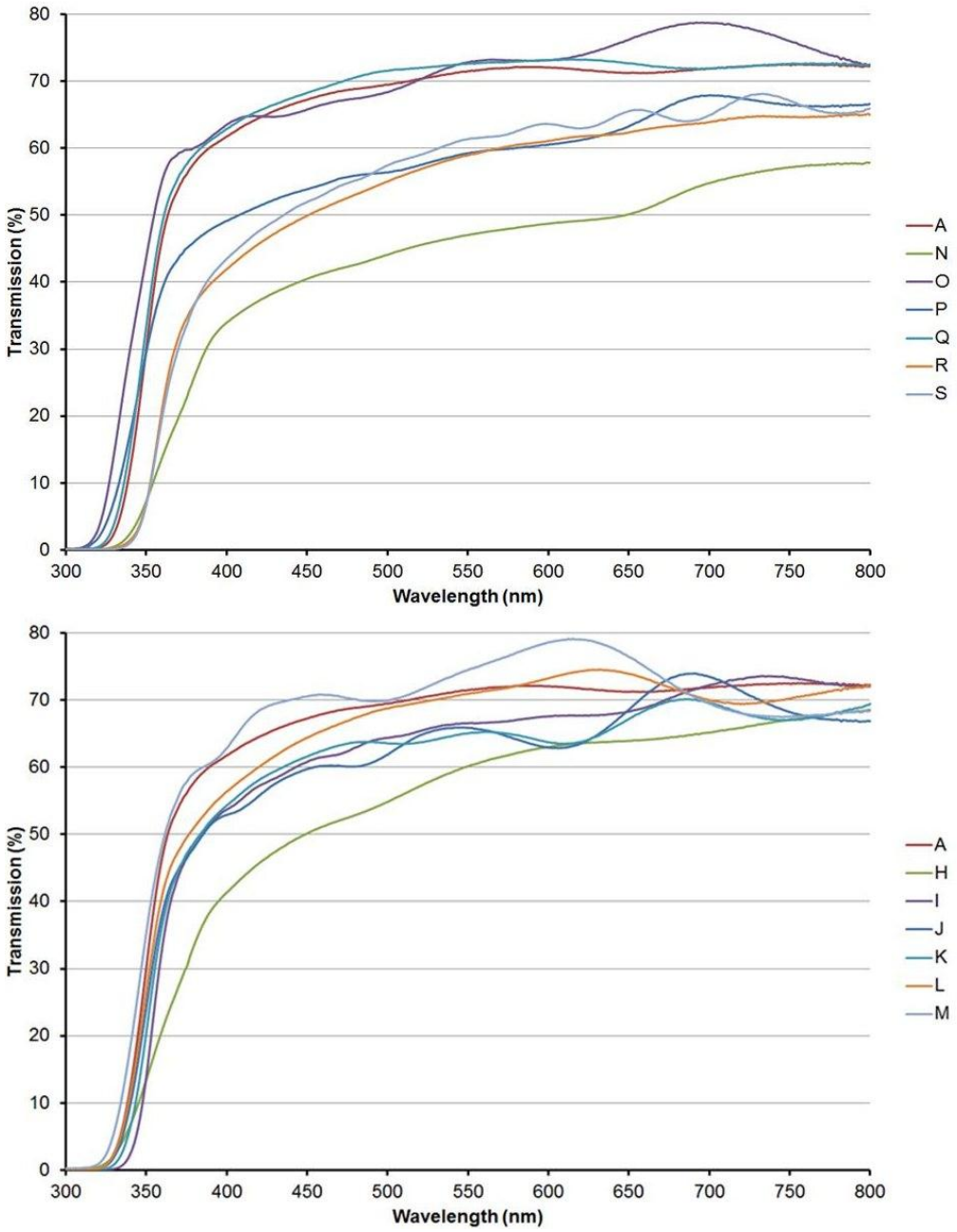

Figure 6.14: UV-vis spectroscopy for samples prepared without an applied electric field (Sample A) and from the positive bias electric field (Samples H to L) and the negative bias electric field (Samples M to Q) EAAPCVD reaction of $TiCl_4$ and ethyl acetate at fixed conditions.

Table 6.9: Content in anatase crystal phase (%) obtained from Raman spectroscopy, Root Mean Square (RMS) (nm) from AFM, maximum transmission in the visible (T%) from UV-vis spectroscopy and DBG (e.V) calculated by the Tauc method, for films deposited from the EAAPCVD reaction of $TiCl_4$ and ethyl acetate at fixed conditions.

Sample	Applied Voltage (V)	Field Strength (Vm^{-1})	Substrate bias	Anatase (%)	RMS (nm)	T%	D.B.G (eV)
A	0	0	--	100	25±8	72	3.2
H	1	1×10^2	Positive	70	3±2	65	3.15
I	5	5×10^2	Positive	100	4±1	72	3.3
J	10	10×10^2	Positive	100	12±5	74	3.3
K	15	15×10^2	Positive	100	11±3	70	3.3
L	20	20×10^2	Positive	100	13±4	74	3.3
M	30	30×10^2	Positive	65	15±6	79	3.3
N	1	1×10^2	Negative	59	9±1	55	3.05
O	5	5×10^2	Negative	100	16±4	79	3.3
P	10	10×10^2	Negative	100	17±5	68	3.3
Q	15	15×10^2	Negative	100	12±2	73	3.25
R	20	20×10^2	Negative	100	20±7	64	3.2
S	30	30×10^2	Negative	100	10±2	66	3.2

6.2.4. Functional properties of DC deposited films

6.2.4.1. Photo-activity of TiO_2 thin films

All films deposited under the influence of DC electric fields showed higher photo-activity than the film produced in absence of electric fields (Figure 6.15). Positive bias deposited films showed slightly higher photo-activity than sample A (29 min) with half-life values in the range of 19.8 – 26.8 min (Table 6.10). Sample I, the sole exception, showed the poorest photo-activity with a half-life value of 42 min. Negative bias deposited films showed higher photo-activity than positive bias deposited films with half-life values in the range of 3.9 –27.1 min. The highest photo-activity was shown for Sample N (3.9 min) followed by sample P (19.1 min).

6.2.4.2. Water contact angles

The films produced from DC electric fields showed hydrophilicity with mean water contact angles in the range of 58 – 88° (Figure 6.16, Table 6.10). However, sample A still showed a lower mean water contact angle (46°). After 30 minutes UV irradiation (254 nm) all films showed hydrophilicity with mean water contact angles in the range 7 – 38°. Sample S showed superhydrophilicity with a mean contact angle of 3°. Sample L showed the lowest wettability with a mean water contact angle of 38°.

Table 6.10: Mean water-contact angles for deposited films from the DC EAAPCVD reaction of $TiCl_4$ and ethyl acetate at fixed conditions, before and after UV irradiation (30 min) with SE; half-life photocatalytic testing or time needed to degrade 50% of the ink initial concentration, $t_{1/2}$ (min).

Sample	Field Strength (Vm^{-1})	Substrate bias	Contact Angle (degrees) ± SE		Half-life
			0 min	30 min	$t_{1/2}$ (min)
A	0	--	46±5	4±4	29
H	1×10^2	Positive	79±5	7±1	24
I	5×10^2	Positive	81±3	12±2	42
J	10×10^2	Positive	88±6	8±4	26.8
K	15×10^2	Positive	74±1	12±3	26
L	20×10^2	Positive	64±5	38±9	25.5
M	30×10^2	Positive	68±3	14±6	19.8
N	1×10^2	Negative	79±7	21±3	3.9
O	5×10^2	Negative	58±8	4±2	22
P	10×10^2	Negative	61±6	15±5	19.1
Q	15×10^2	Negative	53±8	35±1	27.1
R	20×10^2	Negative	64±4	24±8	26.2
S	30×10^2	Negative	78±1	3±2	20.5

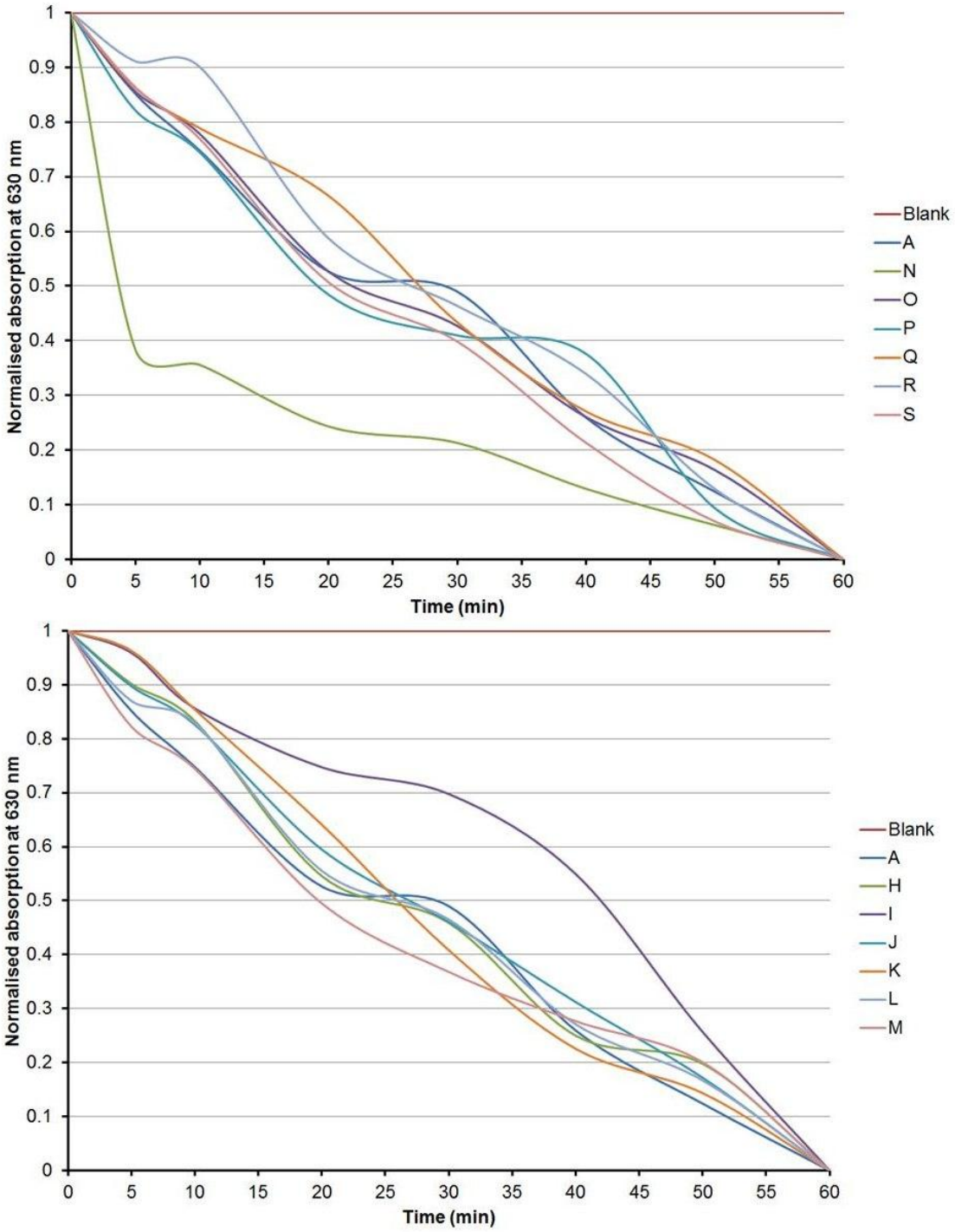

Figure 6.15: Normalised absorption of Resazurin intelligent ink at 630 nm with UVA irradiation (365 nm) against time (min) for film deposited in absence of electric fields (Sample A), from the positive bias (H – M) and the negative bias (N – S) deposited films.

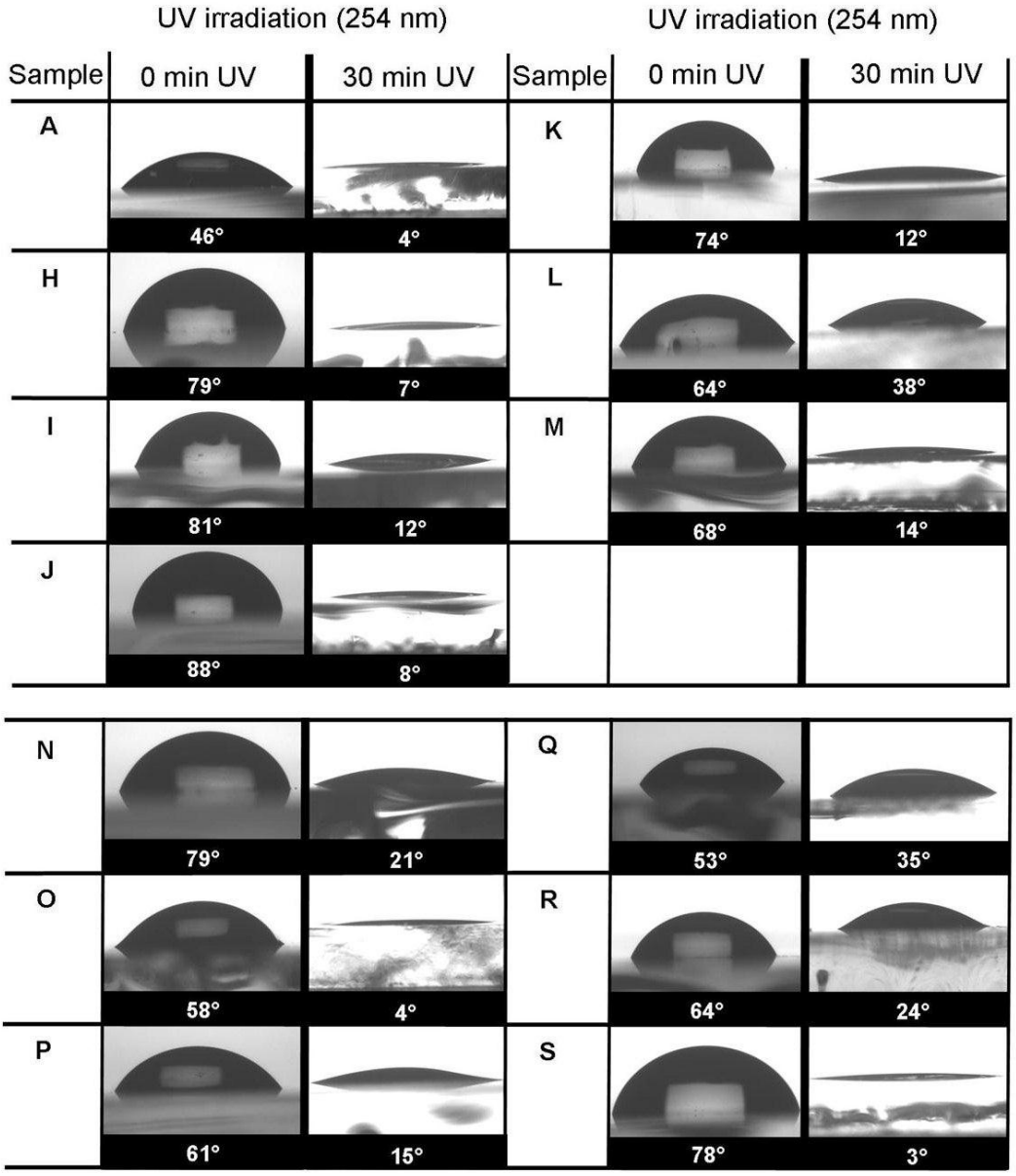

Figure 6.16: Mean water contact angle images for deposited films in absence of electric fields (A), from positive bias (H – M) and negative bias deposited films from the EAAPCVD reaction of $TiCl_4$ and ethyl acetate before and after 30 min UVA irradiation (254 nm).

6.2.5. Film synthesis and characterisation at different conditions

Titanium dioxide thin films were deposited from the EAPCVD reaction of $TiCl_4$ and ethyl acetate at different experimental conditions (Chapter 2, section 2.2.2.2). A total of 18 conditions were tested with applied AC field strength of 1 x 10^2 Vm^{-1} and DC- 5 x 10^2 Vm^{-1}

(labelled as 5 –ve DC). Furthermore, a sample in absence of electric fields was produced for every condition tested. Films produced at different conditions were compared to those films produced at fixed conditions labelled in previous sections as sample A (0 V), Sample B (1 V) and Sample O (5 –ve DC). For the ease of labelling, this section will refer to applied voltage (V) or electric potential. Thin films produced at different conditions showed good adherence to the substrate. They all passed the Scotch tape test and could not be wiped off with a piece of towelling. Deposited films appearance can be seen in Chapter 2, section 2.2.2.2.

Scanning electron microscopy

Scanning electron microscopy images of the titanium dioxide depositions for conditions at different conditions are shown in Figure 6.17 – 6.22. Table 6.11 shows the agglomerate size and film thickness values for conditions 1 – 9. Table 6.12 shows the agglomerate size and film thickness values for conditions 10 – 18. Figure 6.17 shows SEM images for conditions 1 –3 where the experimental variable was the substrate temperature. At a substrate temperature of 350 °C (condition 1 or C1), films produced in absence of electric fields (C1 (0 V)) showed angular nanoparticles of 140 ± 10 nm in length and a film thickness of 90 ± 10 nm. The application of AC and DC electric fields produced a change in morphology to spherical particles of similar film thickness. C1 (1V AC) showed spherical nanoparticles of 130 ± 5 nm in diameter and a decrease in film thickness to 32 ± 6 nm. The application of DC- field strength of 5 x 10^2 Vm^{-1} (C1 (5 –ve DC)) produced spherical nanoparticles of 120 ± 10 nm in diameter and a decrease in film thickness of 23 ± 5 nm. Increasing the substrate temperature to 400 °C (condition 2 or C2) produced a change in particle morphology to elongated shape with an important increase in particle size (430 ± 14 nm) and film thickness (1,400 ± 12 nm) for the film produced at 0 V (C 2 (0 V)). The application of an applied voltage of 1 V (C2 (1 V AC)) revealed spherical particles 130 ± 13 nm and film thickness of 130 ± 23 nm. At 5 V DC - (C2 (–ve DC)) angular nanoparticles of 250 ± 14 nm in length and a decrease in film thickness of 80 ± 8 nm was observed. Increasing the substrate temperature to 500 °C (condition 3 or C3) produced further changes in the shape and size of the microstructure. In the absence of electric fields (C3 (0V)), films showed spherical nanoparticles of reduced particle size (130 ± 9 nm) and a film thickness of 40 ± 9 nm. The application of a field strength of 1 x 10^2 Vm^{-1} (C3 (1 V AC)) produced a change in morphology to elongated shape and an important increase in particle size (370 ± 44 nm) as well as an increase in film

thickness to 470 ± 50 nm. At 5 V DC - (Cond 3 (5 –ve DC), spherical particles of reduced particle size (110 ± 3 nm) was observed and film thickness of 400 ± 40 nm.

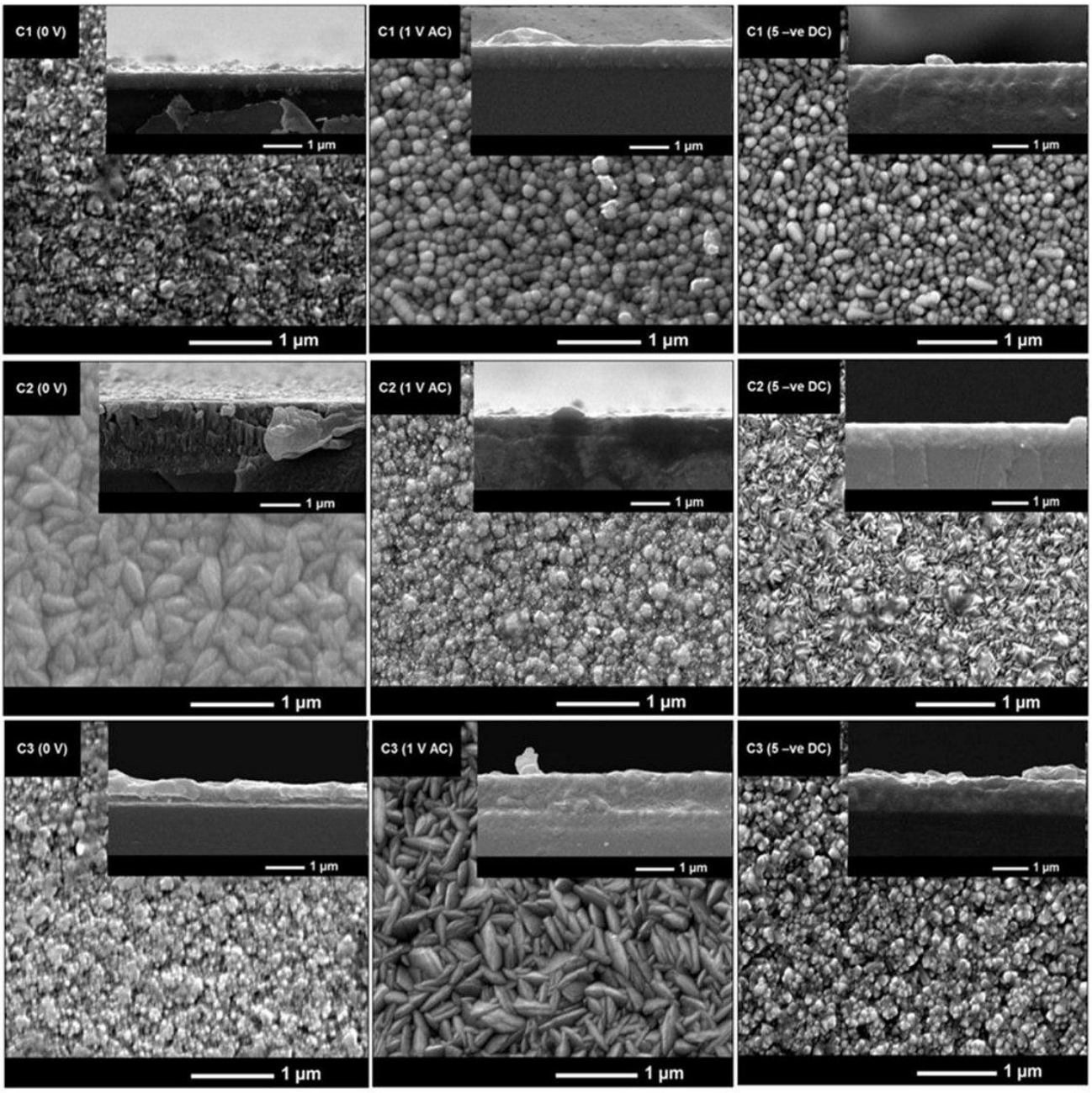

Figure 6.17: Scanning Electron Microscope images of experimental condition 1 – 3 with 0V, 1 V AC and 5 -ve DC (5 –ve DC) applied voltage.

Figure 6.18 shows SEM images for conditions 4 – 6 where the experimental variable was the precursor bubbler temperature. It was observed that increasing the temperature from 50 – 85 ºC produced a gradual change from angular to spherical particles regardless the field strength

applied. However, the film thickness gradually decreased with increasing the temperature for films deposited in the absence of electric fields and with applied DC electric fields whereas the opposite effect was observed for DC- deposited films. In the absence of electric fields, the decrease of $TiCl_4$ temperature to 50 °C (C4 (0V)) produced angular nanoparticles of 270 ± 11 nm in length and film thickness of 500 ± 15 nm. At an applied voltage of 1 V (C4 (1 V AC)) a decrease in particle size was found (140 ± 10 nm) and an important increase in film thickness to 400 ± 13 nm.

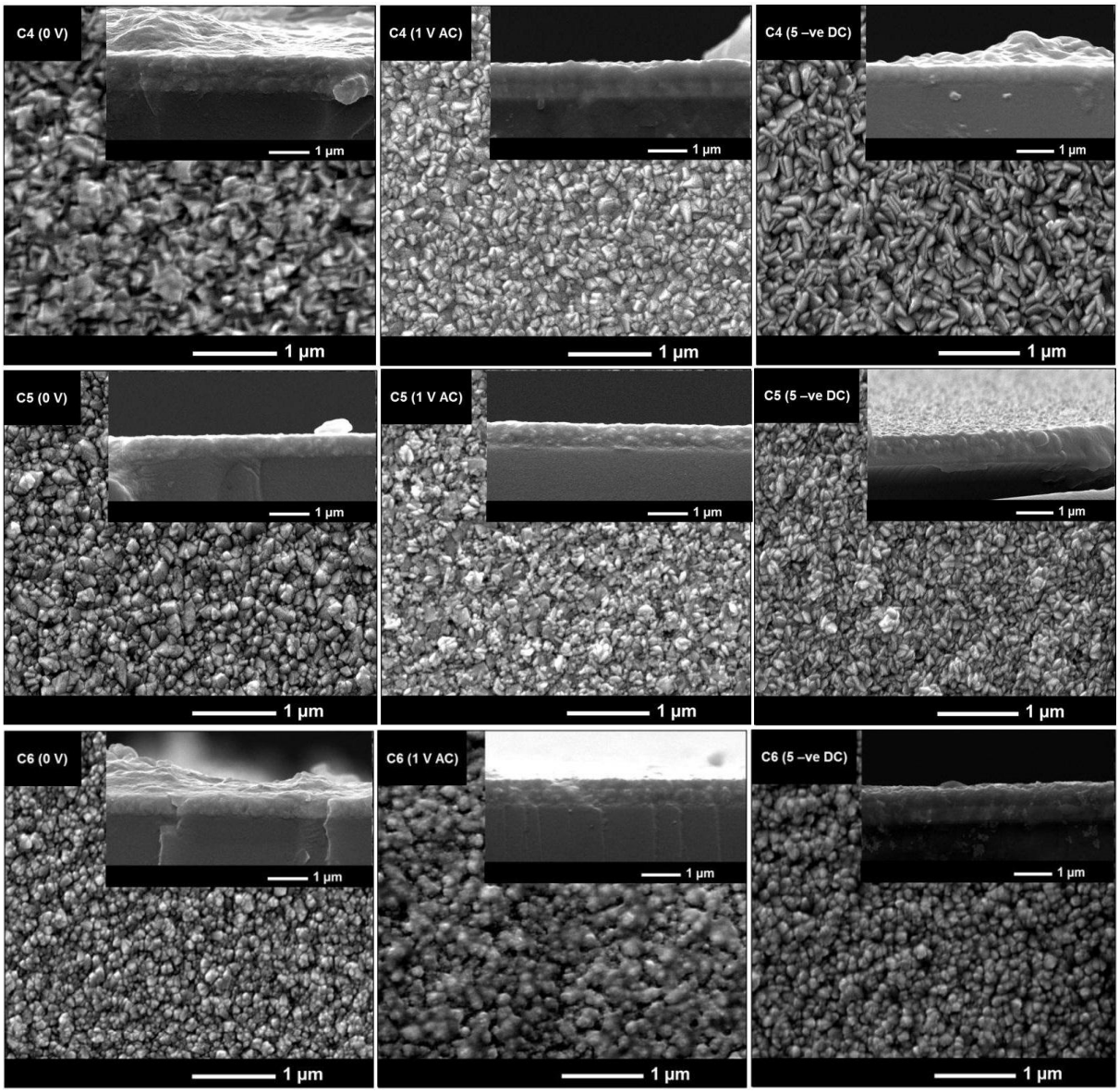

Figure 6.18: Scanning Electron Microscope images of experimental condition 4 – 6 with 0V, 1 V AC and 5 -ve DC (5 –ve DC) applied voltage.

At DC- 5 V applied voltage (C4 (5 –ve DC)), elongated nanoparticles of 230 ± 9 nm in length and a significant decrease in film thickness to 20 ± 5 nm was observed. When $TiCl_4$ temperature was set to 60°C (condition 5 or C5) produced angular nanoparticles of reduced particle size. C5 (0V) showed angular nanoparticles 75 ± 9 nm in length and film thickness of 50 ± 8 nm. C5 (1 V AC) showed spherical agglomerations that have a similar particle size (170 ± 14 nm) but lower film thickness (40 ± 8 nm). The application of DC- 5 V under condition 5 (C5 (5 –ve DC)) produced a decrease in particle size (120 ± 5 nm) and film thickness (120 ± 20 nm). Generally, increasing $TiCl_4$ temperature to 85°C produced a decrease in particle size and an increase in film thickness regardless the field strength. In the absence of electric fields, condition 6 (C6 (0V)) showed spherical particles of reduced size (80 ± 5 nm in diameter) and a film thickness of 20 ± 3. C6 (1 V AC) showed spherical particles of 170 ± 15 nm in diameter and an increase in film thickness to 180 ± 10 nm. C6 (5 –ve DC) showed spherical particles of 110 ± 6 nm and a film thickness of 490 ± 20 nm.

Figure 6.19 shows SEM images for conditions 7 – 9 where the variable condition was the solvent temperature. Increasing ethyl acetate temperature from 30 – 60 °C had a different influence of deposited films depending on the field strength. Generally, in absence of electric fields the increasing temperature produced a gradual decrease of the rice-like particles. For electric fields deposited films, a change in morphology from angular (AC), rice-like (DC-) to spherical particles were observed. For AC deposited films an important decrease of particle size with increasing solvent temperature was observed. For DC- deposited films, a gradual decrease in film thickness was observed with increasing solvent temperature.

Decreasing the ethyl acetate bubbler temperature to 30°C (condition 7 or C7) produced elongated nanoparticles of 250 ± 16 nm in length and an important increase in film thickness (830 ± 15 nm) for the film produced in absence of electric fields (C7 (0V)). An applied voltage of 1 V (C7 (1 V AC)) produced angular nanoparticles of reduced particle size (130 ± 8 nm) and a film thickness of 300 ± 15 nm. Similarly to C7 (0V), the application of 5 -ve DC applied voltage under condition 7 (Cond 7 (5 –ve DC) produced elongated nanoparticles of 200 ± 13 nm in length and a film thickness of 330 ± 10 nm. The increase of ethyl acetate temperature to 50°C (condition 8 or C8) produced angular nanostructures and an increase in film thickness regardlessof the voltage applied.

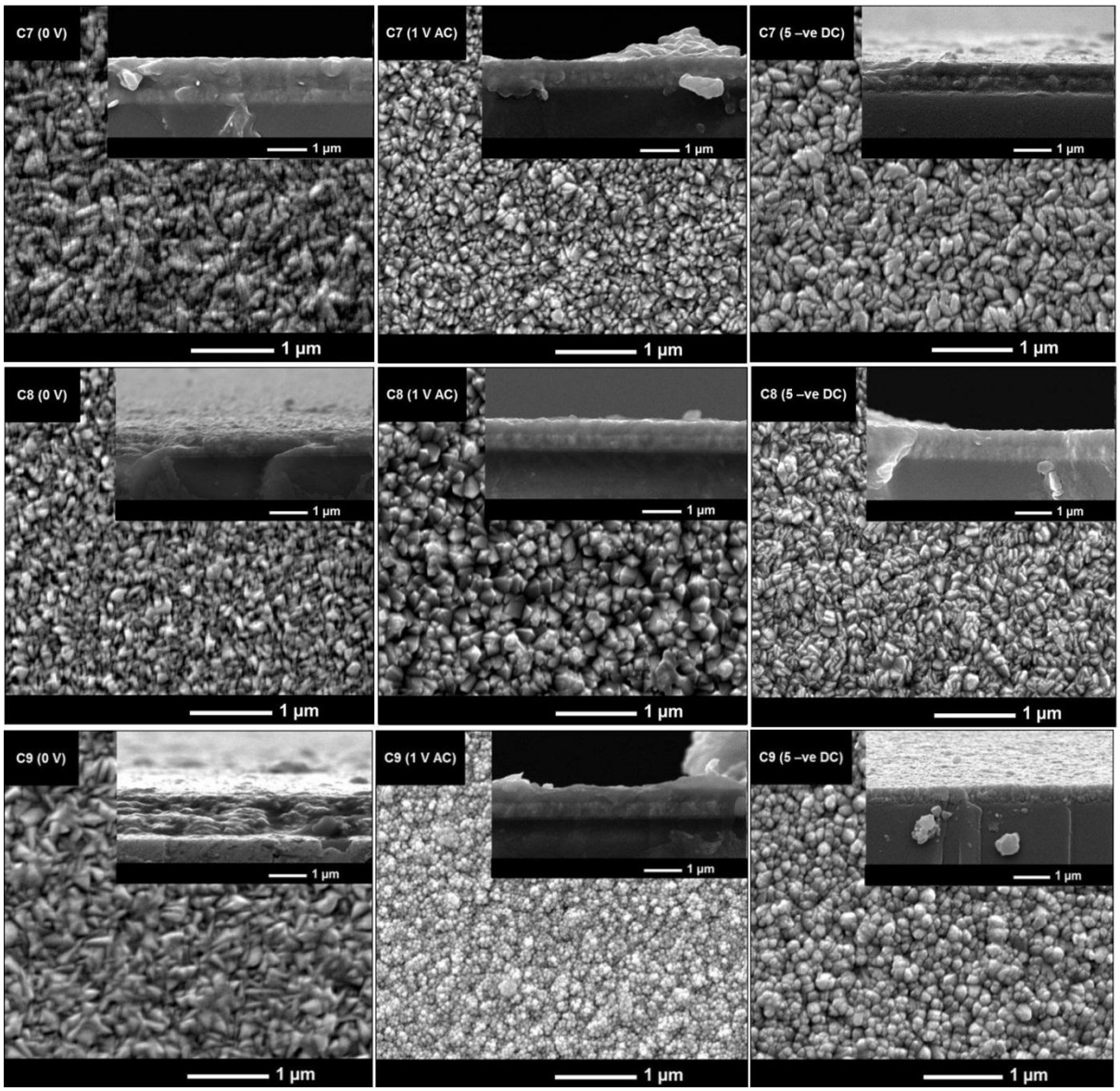

Figure 6.19: Scanning Electron Microscope images of experimental condition 7 – 9 with 0V, 1 V AC 5 -ve DC (5 –ve DC) applied voltage.

C8 (0V) showed angular particles of 140 ± 13 nm in length and an important decrease in film thickness to 40 ± 15 nm. At an applied voltage of 1 V (C8 (1 V AC)), films showed angular particles of 190 ± 16 nm in length and higher film thickness (300 ± 7 nm). The application 5 -ve DC under condition 8 (C8 (5 –ve DC)) showed elongated nanoparticles of 120 ± 4 nm in length and a film thickness of 330 ± 20 nm. The increase of ethyl acetate temperature to 60°C (condition 9 or C9) showed significant changes in morphology and decreasing film thickness depending on the field strength applied. In the absence of electric fields, increasing the solvent temperature to 60°C (C9 (0V)) produced angular particles with increasing particle

size (220 ± 17 nm) and film thickness (550 ± 30 nm). The application of an applied voltage of 1 V (Cond 9 (1V)) produced spherical nanoparticles of reduced particle size (40 ± 3 nm) and film thickness (330 ± 20 nm). The application 5 -ve DC applied voltage under condition 9 (C9 (5 –ve DC)) produced spherical nanoparticles of 140 ± 10 in diameter and an important decrease in film thickness to 40 ± 5 nm.

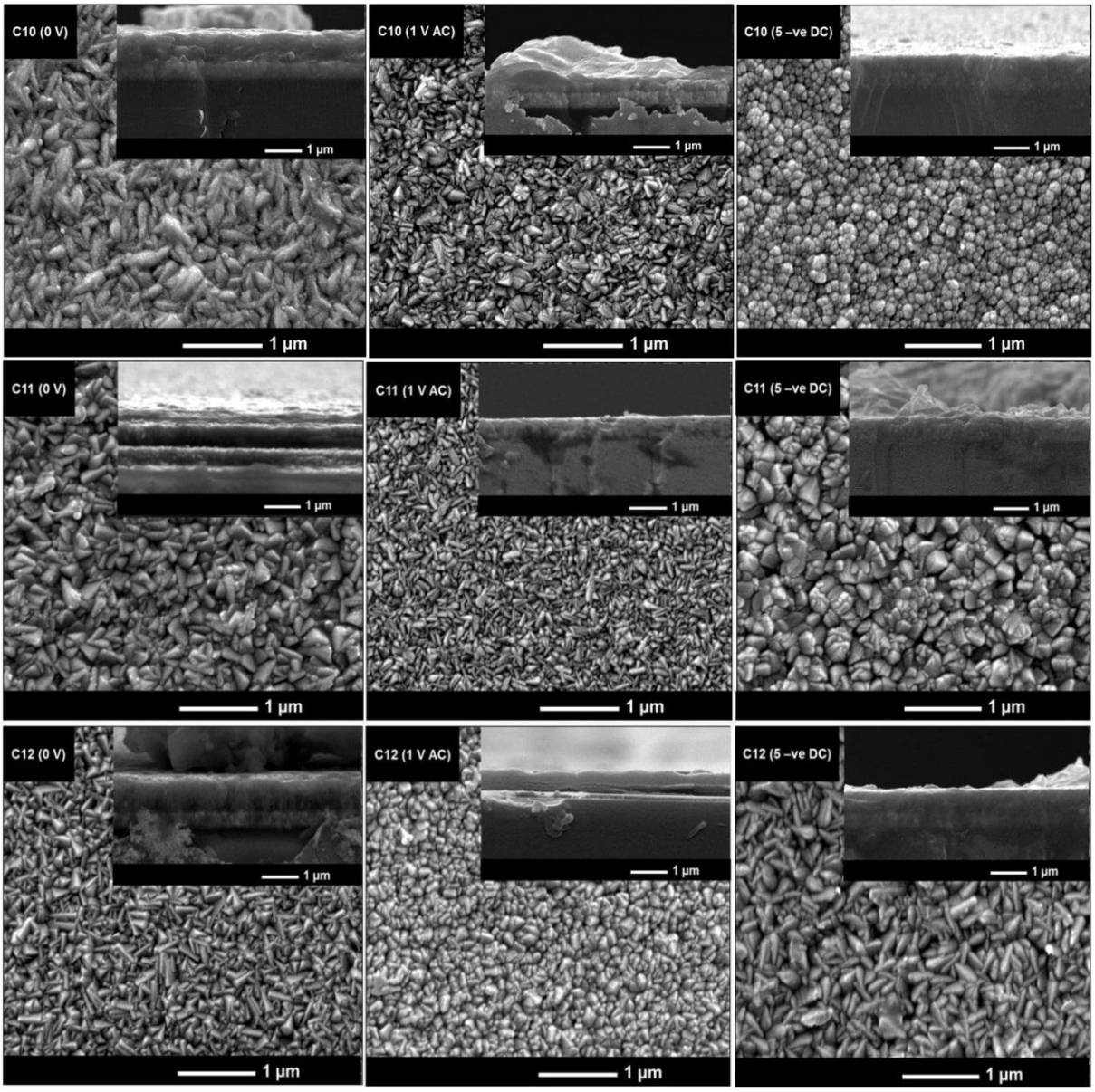

Figure 6.20: Scanning Electron Microscope images of experimental condition 10 – 12 with 0V, 1 V AC and 5 -ve DC (5 –ve DC) applied voltage.

Figure 6.20 shows SEM images for conditions 10 – 12 where the variable condition was the gas flow rate of the plain line. Decreasing the plain gas flow rate from 4 – 2 L.min^{-1} produced a gradual decrease in the particle size of deposited films in absence of electric fields (0 V) and applied AC electric fields (1 V AC). Significant changes were observed for films deposited films from DC- electric fields (5 -ve DC). As the plain gas flow rate was decreased the morphology changed from spherical to angular and finally elongated shaped particles of increased size.

In absence of electric fields, condition 10 or C10 (plain gas flow rate of 4 L.min^{-1}) showed elongated nanoparticles of 300 ± 30 nm in length and film thickness of 650 ± 35 nm. C10 (1 V AC) showed similar morphology but smaller particle size (150 ± 11 nm) and film thickness (250 ± 27 nm). C10 (5 –ve DC) showed an important change to spherical particles of 100 ± 6 nm in diameter and a film thickness of 430 ± 19 nm. Decreasing the plain gas flow rate to 3 L.min^{-1} (condition 11 or C11) produced similar morphology and particle size to condition 10 for samples produced in absence of electric fields (C11 (0 V)) and with an applied voltage of 1 V (C11 (1 V AC)). In particular, C11 (0 V) showed angular particles of 230 ± 13 nm in length and a film thickness of 160 ± 23 nm. C11 (1 V AC)) showed an important decrease in particle size (180 ± 6 nm) and film thickness (100 ± 10 nm). The application of 5 -ve DC applied voltage (C11 (5 -ve DC)) produced angular particles of 200 ± 13 in length and a decrease in film thickness to 120 ± 13 nm. Decreasing the plain gas flow rate to 2 L.min^{-1} (condition 12 or C12) produced a similar morphology to that of condition 11 (except for 5 -ve DC) but an important increase in film thickness. C12 (0 V) showed angular particles of similar particle size 230 ± 16 nm but higher film thickness (760 ± 20 nm). C12 (1 V AC) showed a decrease in the particle size (150 ± 8 nm) and film thickness (240 ± 9 nm). C12 (5 – ve DC) showed angular particles of increased size (280 ± 14 nm) and increased film thickness (470 ± 12 nm).

Figure 6.21 shows SEM images for conditions 13 – 15 where the variable condition was the gas flow rate of the reactants. It was observed that the increase of the reactants gas flow rate influenced the microstructure and film thickness depending on the field strength. For films produced in absence of electric fields (0 V) the increase of the reactants gas flow rate produced a gradual change in morphology from cubic (condition 13 or C13) to angular facets of increased size (condition 14 or C14) and finally spherical shaped particles (condition 15 or C15). Likewise, a gradual increase in film thickness was observed. For films produced with

applied AC electric fields the increase of the reactants gas flow rate produced a change of the morphology from angular to spherical with a gradual decrease in the particle size. In all cases, the increase of the reactants gas flow rate from 1 – 1.5 L.min^{-1} produced a significant increase in the particle size (0 V and DC- films) and/or film thickness (AC films).

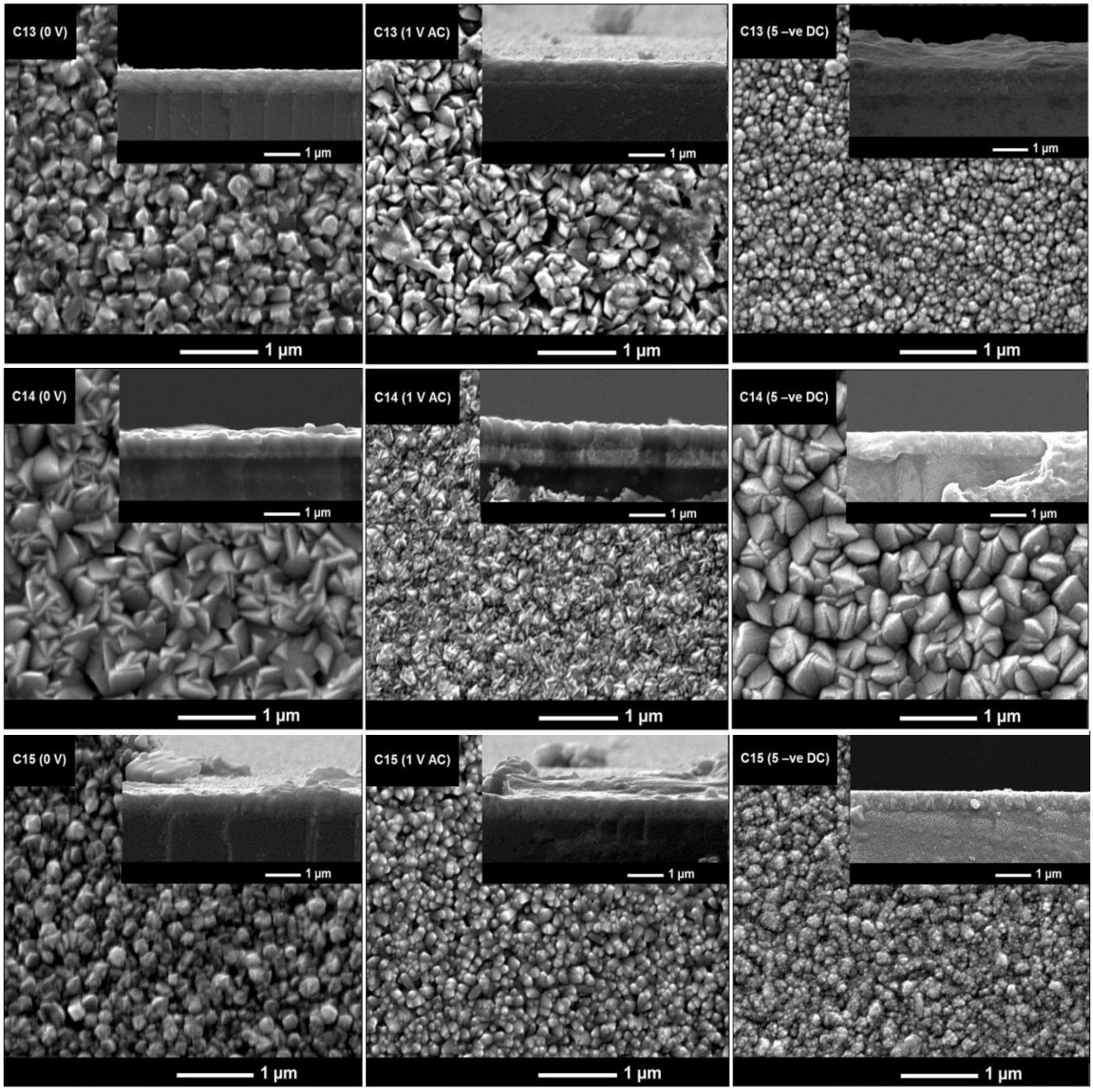

Figure 6.21: Scanning Electron Microscope images of experimental condition 13 – 15 with 0V, 1 V AC and 5 -ve DC (5 –ve DC) applied voltage.

In absence of electric fields, condition 13 (reactant gas flow rate of 1 $L.min^{-1}$) showed cubic particles of 200 ± 11 nm (side length) and a film thickness of 20 ± 4 nm (C13 (0 V)). C13 (1 V AC) showed angular particles of the same size and a slight increase in film thickness to 90 ± 15 nm. C13 (5 -ve DC) produced a drastic change in morphology to spherical particles of 100 ± 5 nm in diameter and a significant increase in film thickness to 350 ± 37 nm. In absence of electric fields, increasing the reactants gas flow rate to 1.5 $L.min^{-1}$ (condition 14) produced angular particles of increased size (400 ± 24 nm) and a film thickness of 70 ± 10 nm (C14 (0 V)). C14 (1 V AC) showed an important decrease of particle size with spherical agglomerations of 120 ± 8 nm and a significant increase in film thickness to 570 ± 18 nm. C14 (5 -ve DC) showed a similar morphology to that of C14 (0 V) with angular particles of 350 ± 22 nm and a film thickness of 110 ± 18 nm. Increasing the reactants gas flow rate to 2 $L.min^{-1}$ (condition 15) showed a drastic change in morphology comparing to that of conditions 13 and 14. Regardless the field strength applied, deposited films under condition 15 showed spherical particles of decreasing size and film thickness. C15 (0 V) showed a particle size of 180 ± 9 nm and a film thickness of 100 ± 9 nm. C15 (1 V AC) showed a particle size of 100 ± 6 nm and a film thickness of 125 ± 14 nm. C15 (5 -ve DC) showed a particle size of 80 ± 16 nm and a film thickness of 45 ± 13 nm.

Figure 6.22 shows SEM images for conditions 16 – 18 where the variable condition was the deposition time, 15 seconds (condition 16 or C16), 30 seconds (condition 17 or C17) and 45 seconds (condition 18 or C18). In absence of electric fields (0 V), increasing the deposition time led to a gradual change of the morphology from angular to elongated-shaped particles as well as an increasing film thickness (from 25 ± 12 to 680 ± 10 nm). Generally, electric field deposited films showed a decreasing film thickness with deposition time. Thus, at a deposition time of 15 seconds films produced at an applied 1 V (C16 (1 V AC)) showed a film thickness of 140 ± 8 nm. As the deposition was increased to 30 – 45 seconds (C17 – 18 (1 V AC)) the film thickness was 120 ± 13. The application of negative bias 5 V for conditions 16 and 17 (C16 –17 (5 -ve DC)) produced film thickness of 70 ± 13 nm and 50 ± 8 nm, respectively. Contradictorily to films produced at 1 V AC, increasing the deposition time to 45 seconds at 5 -ve DC (C18 (5 -ve DC)) produced thicker films (280 ± 46 nm).

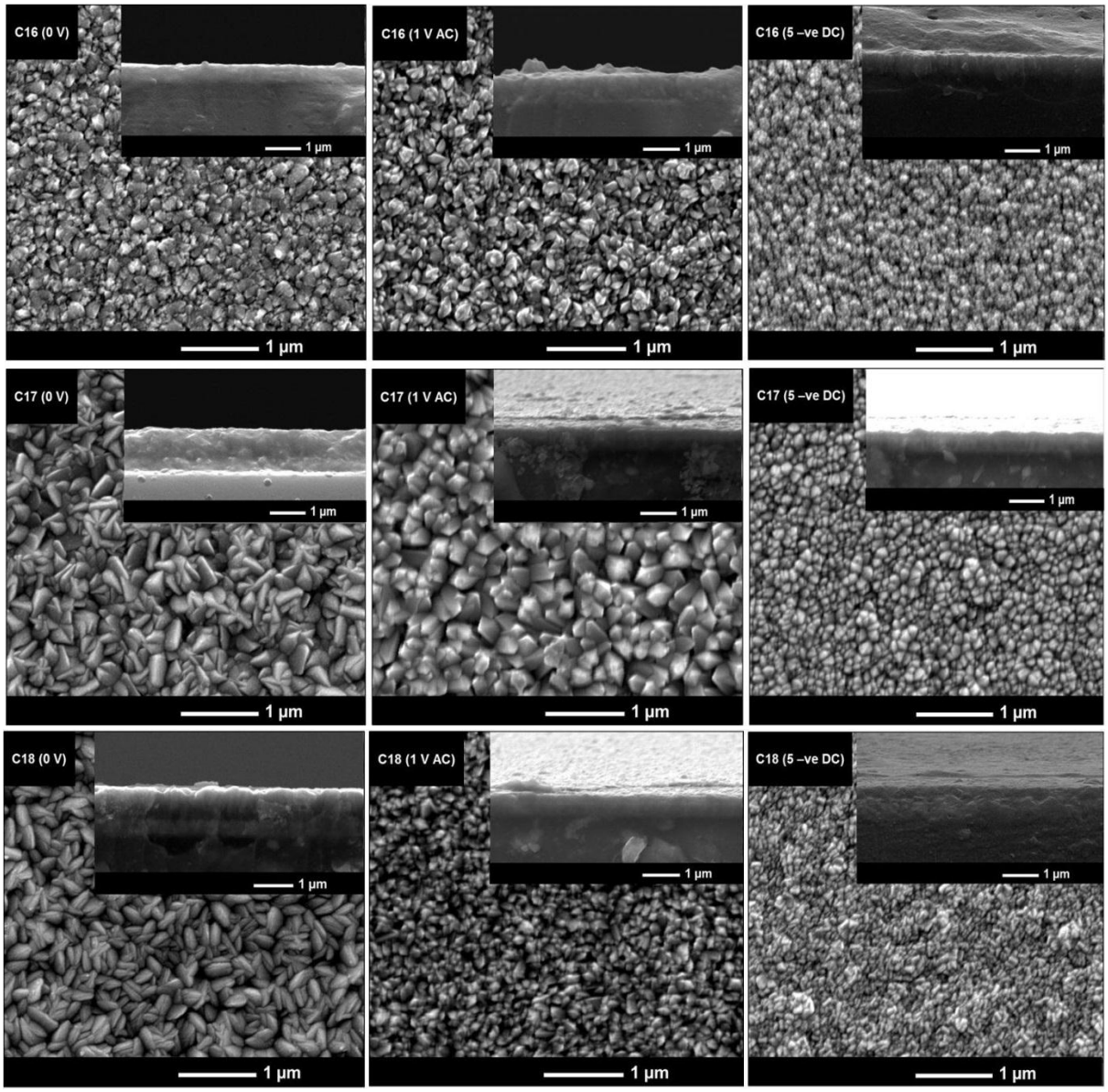

Figure 6.22: Scanning Electron Microscope images of experimental condition 16 – 18 with 0V, 1 V AC and 5 -ve DC (5 –ve DC) applied voltage.

X-ray diffraction

X-ray diffraction was carried out and compared to the JCPDS database (JCPDS file number: 00-021-1272) to investigate the materials phase. Figure 6.23 shows the XRD pattern for conditions 1 - 9 and Figure 6.24 the XRD pattern for conditions 10 –18. It was observed that all deposited films showed anatase TiO_2 independently of the conditions tested, but the intensity of the Braggs peaks changed depending on the conditions. Cassiterite SnO_2 from the underlying FTO coated glass substrate was also observed. Texture coefficient analysis was

conducted also to investigate the preferred crystal orientation. Generally, all deposited films showed crystal preferential orientation in the anatase (004) plane. Table 6.11 shows the texture coefficient in the (004) plane for conditions 1 –9. Table 6.12 shows the texture coefficient in the (004) plane for conditions 10 –18.

Conditions 1 – 3 tested the effect of substrate temperature with the field strength. It was observed that the crystallinity was not only improved by the increase of temperature but also by the application of the field strength. In absence of electric fields, a substrate temperature of 350 ºC (Condition 1 (0 V)) produced characteristic peaks for anatase (101) plane (2 Theta = 25.28°) and anatase (004) plane (2 Theta = 37.8°). Nevertheless, the application of electric fields (C1 (1 V AC), (5 -ve DC)) caused detrimental effects in the crystallinity and XRD patterns mostly showed peaks from the substrate. Increasing the substrate temperature to 400 °C (condition 2) improved the crystallinity of deposited films. C2 (0 V) showed peaks for anatase (101) and (004) plane but also for (112) (2 Theta = 38.5°) and (211) plane (2 Theta = 54.3°). C2 (1 V AC) and (5 -ve DC) did not show peaks for (112) and (211) planes. However, films showed higher preferred orientation in the (004) with texture coefficient of 3.8 (1 V AC) and 3.64 (5 -ve DC). Increasing the substrate temperature to 500 °C (condition 3) showed a detrimental effect on the film crystallinity produced in the absence of electric fields (C3 (0V)) but a significant improvement for electric field deposited films. Films produced with an applied voltage of 1 V (C3 (1 V AC)) and DC- 5 V (C3 (5 -ve DC)) showed peaks corresponding to anatase (112) and (211). However, C3 (5 -ve DC) showed a higher preferential orientation in the (004) plane with a texture coefficient of 2.76.

Conditions 4 – 6 tested the effect the precursor blubbler temperature with the field strength. In absence of electric fields, a $TiCl_4$ temperature of 50 °C (condition 4) produced good crystallinity and all films showed anatase peaks in the (101), (004), (112), (200) and (211) planes regardless of the field strength applied. However, it was observed that the texture coefficient in the (004) plane was higher for electric fields deposited films. C4 (1 V AC) showed a texture coefficient of 2.58 and C4 (5 -ve DC) a texture coefficient of 3.39. Increasing the $TiCl_4$ bubbler temperature to 60 °C (condition 5) produced a detrimental effect on the crystallinity of electric fields deposited films. C5 (1 V AC) and (5 -ve DC) showed anatase peaks in the (101) and (004) planes. However, under these conditions, all films showed high orientation in the (004) plane with texture coefficient values in the range of 3.78 – 3.84. Increasing the $TiCl_4$ bubbler temperature to 85 °C (condition 6) led to an increase in the crystallinity of the deposited films. However, the film produced in absence of electric

fields showed higher texture coefficient in the (004) plane (at 0 V, 3.84) than films deposited from AC (1 V, 2.6) and DC- (5 V, 2.48) electric fields.

Conditions 7 – 9 tested the effect of the solvent bubbler temperature with the field strength. At a solvent bubbler temperature of 30 ºC (condition 7), all deposited films showed good crystallinity showing anatase peaks in the (101), (004), (112), (200) and (211) planes regardless the field strength applied. However, it was observed that electric field deposited films showed higher texture coefficient in the (004) plane than that of the films deposited in absence of electric fields (C7 (0 V), 1.55). In particular, C7 (1 V AC) showed the higher preferential orientation in the (004) plane with a texture coefficient of 2.61. Increasing the solvent bubbler temperature to 50 ºC (condition 8) produced a detrimental effect on the crystallinity only for the film deposited in absence of electric fields, which showed mostly peaks from the substrate. However, electric fields deposited films showed good crystallinity with texture coefficient values in the (004) plane (C8 (1 V AC) with 2.18 and C8 (5 -ve DC) with 2.59). When increasing the solvent bubbler temperature to 60 ºC (condition 9) the opposite effect was observed. The crystallinity improved for the field deposited in absence of electric fields but decreased for electric fields deposited films. C9 (1 V AC) showed an amorphous pattern whereas C9 (5 -ve DC) showed mostly peaks from the substrate.

Conditions 10 – 12 tested the effect of the plain gas flow rate with the field strength. Condition 10 (plain gas flow rate of 4 $L.min^{-1}$) showed peaks in the anatase (101), (004), (112), (200) and (211) for films produced in absence of electric fields (C10 (0 V)) and with applied AC electric fields (C10 (1 V AC)). C10 (5 -ve DC) did not show peaks in the (200) and (211) plane, but the XRD pattern revealed a peak at 2 Theta = 53.89º, characteristic of anatase (105). It was observed that electric fields deposited films showed higher preferential orientation in the (004) plane. In particular, Furthermore, C10 (5 -ve DC) showed a higher preferential orientation in the (004) plane with a texture coefficient of 3.52. Decreasing the plain gas flow rate to 3 $L.min^{-1}$ (condition 11) improved the crystallinity of the film produced in absence of electric fields (C10 (0 V)) and with applied AC electric fields (C11 (1 V AC)). Thus, characteristic peaks of the (101), (004), (105) and (211) planes were observed. C11 (5 –ve DC) showed mostly peaks from the substrate but a higher preferential orientation in the (004) plane with a texture coefficient of 3.8. Decreasing the plain gas flow rate to 2 $L.min^{-1}$ (condition 12) increased the crystallinity of DC deposited film, but C12 (1 V AC) showed higher preferential orientation in the (004) plane with a texture coefficient of 2.32.

Conditions 13 – 15 tested the effect of the reactants gas flow rate with the field strength. Condition 13 (reactants gas flow rate of 1 $L.min^{-1}$) produced films with anatase peaks in the (101), (004), (200) and (211). However, it was observed that the application of AC and DC electric fields decreased the texture coefficient in the (004) plane comparing to the film deposited in absence of electric fields (3.32). Films produced at reactants gas flow rate of 1.5 $L.min^{-1}$ (condition 14) also showed the anatase peak in the (112) plane. Similar texture coefficient values (2.4) were found for C14 (0 V) and (1 V AC). C14 (5 -ve DC) showed a lower texture coefficient value (2.2). Condition 15 (reactants gas flow rate of 2 $L.min^{-1}$) produced significant detrimental effects on the crystallinity of electric fields deposited films, but higher preferential orientation in the (004) plane (3.8 – 3.75).

Conditions 16 – 18 tested the effect of the deposition time with the field strength. Increasing the deposition time enhanced the crystallinity of deposited films. At a deposition time of 15 seconds (condition 16) films showed mostly peaks from the substrate. However, AC and DC electric fields films showed peaks in the anatase (101) and (004) planes. Increasing the deposition time to 30 seconds (condition 17) produced an improvement of the crystallinity of all deposited films. The texture coefficient calculations revealed that the application of AC electric fields (C17 (1 V AC)) favoured the crystal preferential orientation in the (004 plane (3.1). At a deposition time of 45 seconds (condition 18), films showed similar XRD pattern to that for condition 17, but a peak for the (112) was not identified. The texture coefficient calculations revealed higher preferential orientation in the (004) plane for AC electric fields deposited films (C18 (1 V AC), 3.01).

The crystallite size of the deposited films was calculated from the full width at half maximum (FWHM) of different peaks using the Scherrer equation [155]. Characteristic peaks of 2θ = 25.28° (101), 2θ = 37.8° (004), 2θ = 48.05° (200) were used. Likewise, shape factor of 0.9 [152] was chosen. However, no crystallite size value could have been obtained for films which showed only showed two peaks in their XRD pattern (denoted in Tables 6.12 -6.13 as --). Table 6.11 shows the crystallite size for conditions 1 – 9. It was observed that the increase of the substrate temperature from 350 to 500 ºC (conditions 1 –3) produced an increase in the crystallite size. In particular DC electric fields deposited film showed an increase in the crystallite size to 43 ± 23 nm under condition 3 (C 3 (5 -ve DC)). No significant effects were observed when varying the precursor bubbler temperature from 50 – 85 ºC (conditions 4 – 6). However, it was observed that for condition 4 (50 ºC) and important decrease in the

crystallite size from 27 ± 8 nm to 13 ± 3 nm was produced when applying AC electric fields (C4 (1 V AC)). Similarly, the application of AC electric fields produced an important decrease in crystallite size from 25 ± 8 nm to 14 ± 1 nm at a solvent bubbler temperature of 30 ºC (condition 7). Table 6.12 shows the crystallite size for conditions 10 – 18. Condition 10 (plain gas flow rate of 4 $L.min^{-1}$) also showed a decrease in the crystallite size with applying AC electric fields (20 ± 6 nm to 17 ± 2 nm). However, it was observed that decreasing the plain gas flow rate to 2 $L.min^{-1}$ produced similar crystallite size (14 – 19 nm) regardless the electric field applied. The reactants gas flow rate (conditions 13 – 15) had an important effect on the crystallite size of deposited films. At a reactants gas flow rate of 1 $L.min^{-1}$ (condition 13), the application of AC electric fields increased the crystallite size from 17 to 20 nm (C13 (1 V AC)), whereas the application of DC electric fields led to a decrease in the crystallite size to 14 ± 3 nm (C13 (5 -ve DC)). When the reactants gas flow rate was increased to 1.5 $L.min^{-1}$ (condition 14), the application of AC electric fields decreased the crystallite size from 19 to 16 nm (C14 (1 V AC)), whereas the application of DC electric fields led to an important increase in the crystallite size to 33 ± 9 nm (C14 (5 -ve DC)). Deposition time (conditions 16 – 18) also revealed changes in the crystallite size that were more accentuated for condition 17 (deposition time of 30 seconds) as the application of AC electric fields produced a decrease in the crystallite size from 20 ± 3 nm to 14 ± 2 nm (C17 (1 V AC)).

Raman spectroscopy

Raman spectroscopy conducted in random films under conditions 1 – 18 confirmed the presence of pure anatase in the films tested (not shown).

UV-vis spectroscopy

Figure 6.25 shows the transmission spectra for films deposited under conditions 1 – 9. The maximum value of the transmission in the visible for conditions 1 – 9 can be seen in Table 6.11. Increasing the substrate temperature from 350 – 400 ºC (condition 1 and 2) produced beneficial effects on the transmission values when applying AC and DC electric fields. Thus, condition 1 showed an increase in the maximum transmission in the visible from 70% (C 1 (0 V)) to 76% and 78% corresponding to C1 (1 V AC) and C1 (5 -ve DC), respectively. Likewise, condition 2 showed an increased in the maximum transmission in the visible from

56% to 66% (AC electric fields) and 76% (DC electric fields). However, at a substrate temperature 500 ºC (condition 3), the application of AC and DC electric fields decreased the maximum transmission in the visible from 79% to 66% and 56%, respectively. As Table 6.11 shows, the gradual increase of the precursor bubbler temperature from 50 – 85 ºC (conditions 4 – 6) enhanced the maximum transmission values in the visible. In particular, condition 6 showed a significant increase in the maximum transmission from 66% (C6 (0 V)) to 78% (C6 (1 V AC)). Generally, increasing the solvent bubbler temperature from 30 – 60 ºC (conditions 7 – 9) decreased the maximum transmission in the visible. However, the increase of the solvent bubbler temperature to 60 º (condition 9) produced an important increase in the maximum transmission in the visible from 65% (C9 (0 V)) to 81% (C9 (5 -ve DC) when applying DC electric fields.

Figure 6.26 shows the transmission spectra for films deposited under conditions 10 – 18. The maximum value of the transmission in the visible for conditions 10 – 18 can be seen in Table 6.12. Conditions 1 – 10 showed different results depending on the plain gas flow rate. At plain gas flow rate of 4 $L.min^{-1}$ (condition 10), the application of AC and DC electric fields increased the maximum transmission in the visible from 56% to 76% and 70%, respectively. No important effect was observed when the gas flow rate was decreased to 3 $L.min^{-1}$ (condition 11) and 2 $L.min^{-1}$ (condition 12). The application of AC and DC electric fields with the increased reactants gas flow rate from 1 to 2 $L.min^{-1}$ (conditions 13 – 15) enhanced the maximum transmission in the visible comparing to the films produced in absence of electric fields. A significant increase in the maximum transmission in the visible was observed for condition 14. Thus, C14 (0 V) showed very low maximum transmission in the visible (37%) which were importantly increased with the application of AC electric fields (C14 (1 V AC), 72%) and DC electric fields (C14 (5 -ve DC), 63%). It was observed that the increase of the reactants gas flow rate decreased the maximum transmission in the visible. Deposition time (condition 16 – 18) was also found to be an influencing factor for the transmission values in the visible. It was found that increasing the deposition time from 15 to 45 seconds gradually increased the maximum transmission in the visible regardless the field strength. However, it was also observed that the application of AC and DC electric fields increased the transmission in the visible. In particular, at a deposition time of 30 and 45 seconds (conditions 17 – 18), the application of AC electric fields gave higher maximum transmission values in the visible with an increase from 67% to 71% for condition 17 and from 69% to 77% for condition 18.

DBG values were calculated using the Tauc method [154]. DBG values for conditions 1 – 9 are listed in Table 6.11 and for conditions 10 – 18 in Table 6.12. All deposited films showed standard direct band gaps for anatase (3.2 – 3.3 eV). Lower direct band gap values between 3.0 – 3.15 eV were found for films deposited in absence of electric fields (conditions 12, 14, 15, 17 and 18), with applied AC electric fields (condition 13) and with applied DC electric fields (condition 3, 14 and 15).

6.2.6. Functional properties of deposited films at variable conditions

6.2.6.1. Photo-activity of TiO_2 thin films

Figure 6.27 showed the normalised decrease in absorption of the resazurin ink at 630 nm for conditions 1 – 9 and Figure 6.28 for conditions 10 – 18. Generally, the application of electric fields improved the photo-activity of deposited films under all conditions. Table 6.11 shows the half-life values for deposited films under conditions 1 – 9. The application of AC electric fields with increasing substrate temperature (conditions 1 – 3) favoured photo-activity of deposited films. A significant decrease in the half-life value was observed for condition 2 (substrate temperature of 400 ºC) from 37.1 min (C2 (0 V)) to 17.6 min (C2 (1 V AC)). However, the application of DC electric fields with increasing substrate temperature led to a decrease in the photo-activity. In particular, for condition 3 the application of DC electric fields increased the half-life from 33.3 min (0 V) to 38.3 min (5 -ve DC). The application of AC electric fields was also favoured by the increase of the precursor bubbler temperature (conditions 4 – 6). The most photoactive films was that produced a pre-heating temperature of 60 ºC, C5 (1 V AC), with a decrease in the half-life from 30 min (0 V) to 14.2 min. Generally, the application of DC electric fields caused a detrimental effect on the photocatalysis which was accentuated for condition 4 (50 ºC) with an increase of the half-life to 40.2 min. Increasing the solvent bubbler temperature (condition 7 – 9) produced significant improvements in the photo-activity of the deposited films with half-life values in the range of 3.1 – 12.9 min, comparing to the half-life values obtained for films produced in absence of electric fields (17.2 – 33.5 min). The most photo-active film was C9 (5 -ve DC) with a half-life value of 3.1 min.

Table 6.12 shows the half-life values for deposited films under conditions 10 – 18. The photo-activity was favoured with decreasing plain gas flow rate (conditions 10 – 12) when

applying DC electric fields. Although under conditions 10 – 12 the application of AC electric fields improved the photo-activity, more significant results were found for DC electric fields. In particular, at a plain gas flow rate of 2 $L.min^{-1}$ (condition 12) applying negative bias DC electric fields decreased the half-life values from 20.9 min (C12 (0 V)) to 9 min (C12 (5 -ve DC)). Generally, the application of electric fields produced a detrimental effect on deposited films photo-activity when testing the influence of the reactants gas flow rate (conditions 13 – 15). However, C14 (1 V AC) showed slightly higher photo-activity than C14 (0 V) with a decrease in the half-life value from 24.2 min to 23.5 min. Likewise, the application of DC electric fields increased the photo-activity under condition 15, decreasing the half-life value from 17.9 min (C15 (0 V) to 13.9 min (C15 (5 -ve DC)). Generally speaking, AC electric fields showed worse photo-activity regardless the deposition time (conditions 16 – 18). As an exception, C17 (1 V AC) showed a slightly higher photo-activity decreasing the half-life value from 27.7 min (0 V) to 21.5 min. Nevertheless, DC deposited films improved the photo-activity of deposited films regardless the deposition time. In particular, at a deposition time of 30 seconds (condition 16) the application of negative bias DC electric fields decreased the half-life from 19.3 min (C16 (0 V)) to 9.9 min (C16 (5 -ve DC).

6.2.6.2. Water-contact angles

Mean water-contact angles measurements were carried out to study the wettability of surfaces Table 6.11 shows the mean water-contact angles before and after UV irradiation (254 nm) for conditions 1 – 9 and Table 6.12 for conditions 10 – 18. All deposited films showed hydrophilicity with water contact angles in the range of 11 – 85°. The lowest water contact angle before UV irradiation was found for C5 (1 V AC) (11 ± 7°) followed by C9 (5-ve DC)). (15 ± 3°). After 30 minutes of UV irradiation (254 nm), all electric fields deposited films showed hydrophilicity with contact-angles between 5°- 40 ° and superhydrophilicity for AC electric fields (condition 8, 12, 15and 18) and DC electric fields (condition 14 and 16).

Table 6.11: Agglomerate size (nm) from SEM, film thickness (nm) from SEM cross section, mean crystallite size (nm) obtained from the Scherrer equation, texture coefficient, crystal phase from XRD, maximum transmission in the visible (%), direct band gap (DBG, eV), mean water-contact angles and half-life (min), for films produced from the EAPCVD reaction of $TiCl_4$ and ethyl acetate at variable conditions 1 – 9.

Condition (C)	Sample	Agglomerate size (nm)	Thickness (nm)	Mean crystallite size (nm)	Texture Coefficient (004)	Crystal Phase (XRD)	T (%)	DBG (eV)	Mean water-contact angle		Half-life
									0 min	30 min	$t_{1/2}$ (min)
1	0	140±10	90±10	15±3	3.25	Anatase	70	3.3	81±1	31±5	32.1
	1 V AC	130±5	32±6	--	--	Anatase	76	3.3	80±3	39±3.5	17.7
	-ve 5 DC	120±10	23±5	--	--	Anatase	78	3.3	78±4	8±2	24.9
2	0	430±14	1400±12	13±4	1.63	Anatase	56	3.2	62±0.4	13±4	37.1
	1 V AC	130±13	130±23	--	3.8	Anatase	68	3.2	63±7	8±0.8	17.6
	-ve 5 DC	250±14	80±8	16±0.5	3.64	Anatase	76	3.3	73±6	6±2	37.2
3	0	130±9	40±9	--	--	Anatase	79	3.2	66±11	18±1	33.3
	1 V AC	370±44	470±50	19±0.7	1.15	Anatase	66	3.2	66±0.5	5±2	20
	-ve 5 DC	110±3	400±40	43±23	2.76	Anatase	56	3.1	70±10	29±15	38.3
4	0	270±11	500±15	27±8	2.22	Anatase	74	3.2	85±4	8±2	35
	1 V AC	140±10	400±13	13±3	2.58	Anatase	67	3.3	69±7	4±1	27.6
	-ve 5 DC	230±9	20±5	17±2	3.39	Anatase	74	3.3	69±11	8±1	40.2
5	0	75±9	50±8	13±3	3.38	Anatase	64	3.25	50±8	8±2	30
	1 V AC	170±14	40±8	--	3.78	Anatase	70	3.2	11±7	6±0.5	14.2
	-ve 5 DC	120±5	120±20	--	3.68	Anatase	77	3.3	76±4	14±5	33.6
6	0	80±5	20±3	--	3.84	Anatase	66	3.2	39±12	10±1.5	33.5
	1 V AC	170±15	180±10	14±3	2.6	Anatase	78	3.3	54±8	5±1	19.2
	-ve 5 DC	110±6	490±20	13±3	2.48	Anatase	76	3.2	56±10	8±1	32
7	0	250±16	830±15	25±8	1.55	Anatase	72	3.2	59±9	16±15	33.5
	1 V AC	130±8	300±15	14±1	2.61	Anatase	74	3.3	80±1.7	16±7	18
	-ve 5 DC	200±13	330±10	18±2	1.99	Anatase	70	3.25	63±6	8±3	4.3
8	0	140±13	40±15	--	--	Anatase	80	3.3	41±23	8±4	17.2
	1 V AC	190±16	300±7	20±8	2.18	Anatase	75	3.25	53±6.5	4±1	19.6
	-ve 5 DC	120±4	370±7	12±3	2.59	Anatase	70	3.25	50±2	14±3	12.9
9	0	220±17	550±30	23±2	1.7	Anatase	65	3.2	85±3.6	13±1	24
	1 V AC	40±3	330±20	--	--	Anatase	69	3.3	50±3	11±3	22
	-ve 5 DC	140±10	40±5	--	--	Anatase	81	3.4	15±3	11±5	3.1

Table 6.12: Agglomerate size (nm) from SEM, film thickness (nm) from SEM cross section, mean crystallite size (nm) obtained from the Scherrer equation, texture coefficient, crystal phase from XRD, maximum transmission in the visible (%), direct band gap (DBG, eV), mean water-contact angles and half-life (min), for films produced from the EAPCVD reaction of $TiCl_4$ and ethyl acetate at variable conditions 1 0– 18.

Condition (C)	Field Strength (Vm^{-1})	Aggl. size (nm)	Thickness (nm)	Mean crystallite size (nm)	Texture Coefficient (004)	Crystal phase	T (%)	DBG (eV)	Mean water-contact angle		Half-life
									0 min	30 min	$t_{1/2}$ (min)
10	0	300±30	650±35	20±6	1.79	Anatase	56	3.2	66±11	20±5	22.6
	1 V AC	150±11	250±27	17±2	2.67	Anatase	76	3.3	56±2	7±0.3	19
	-ve 5 DC	100±6	430±19	22±2	3.52	Anatase	70	3.3	18±5	17±5	12.4
11	0	230±13	160±23	21±4	2.45	Anatase	67	3.2	74±9	14±5	20
	1 V AC	180±6	100±10	--	2.95	Anatase	63	3.3	62±12	9±3	18.7
	-ve 5 DC	200±13	120±13	--	3.8	Anatase	65	3.3	35±1	14±3	25
12	0	230±16	760±20	14±1	2.09	Anatase	77	3.15	58±22	7±2	20.9
	1 V AC	150±8	240±9	15±3	2.32	Anatase	74	3.2	75±1.5	4±0.6	19.4
	-ve 5 DC	280±14	470±12	19±3	2.03	Anatase	74	3.2	26±3	6±1	9
13	0	200±11	20±4	17±5	2.9	Anatase	69	3.2	92±8	6±1	21.4
	1 V AC	200±12	90±15	20±2	2.95	Anatase	75	3.15	70±10	6±0.4	35
	-ve 5 DC	100±5	350±37	14±3	2.47	Anatase	72	3.2	41±3	10±2	30.2
14	0	400±24	70±10	19±4	2.4	Anatase	37	3.0	85±9	12±2	24.2
	1 V AC	120±8	570±18	16±4	2.46	Anatase	72	3.25	43±2	8±1	23.5
	-ve 5 DC	350±22	110±18	33±9	2.2	Anatase	63	3.1	32±2	4±2	33.4
15	0	180±9	100±9	17±3	2.52	Anatase	59	3.0	78±5	40±11	17.9
	1 V AC	100±6	125±14	--	3.8	Anatase	67	3.3	33±2	4±1	31.6
	-ve 5 DC	80±16	45±13	--	3.75	Anatase	63	3.1	59±11	17±5	13.9
16	0	150±11	25±12	--	--	Anatase	62	3.2	56±12	15±2	19.3
	1 V AC	130±5	140±8	--	3.85	Anatase	66	3.2	73±1	17±4	21.1
	-ve 5 DC	90±15	70±13	--	3.76	Anatase	67	3.2	59±3	4±1	9.9
17	0	300±20	450±9	20±3	1.86	Anatase	67	3.15	78±8	11±6	27.7
	1 V AC	260±9	120±13	14±2	3.1	Anatase	71	3.3	50±5	10±1	21.5
	-ve 5 DC	120±5	50±8	24±5	2.17	Anatase	65	3.2	61±8	23±8	15.3
18	0	270±8	680±10	22±3	1.72	Anatase	69	3.15	65±9	12±2	31.2
	1 V AC	160±8	125±13	23±4	3.01	Anatase	77	3.3	39±5	4±1	36.9
	-ve 5 DC	120±4	280±46	25±4	2.19	Anatase	71	3.2	80±4	23±2	23

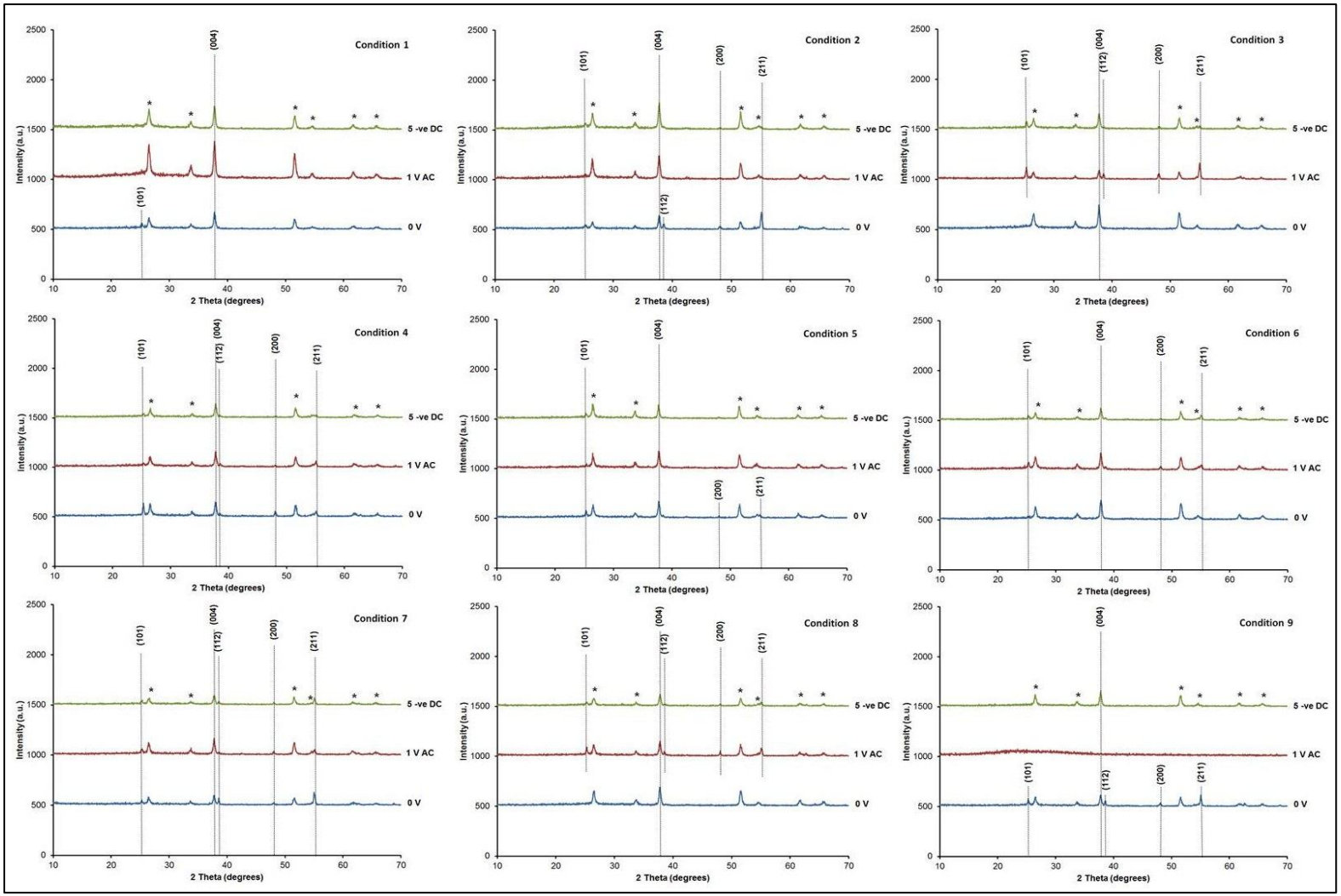

Figure 6.23: XRD patters for films produced from the EAPCVD reaction of $TiCl_4$ and ethyl acetate at variable conditions 1 – 9**.** All peaks correspond to anatase crystal phase. The asterisks denote cassiterite from the underlying substrate.

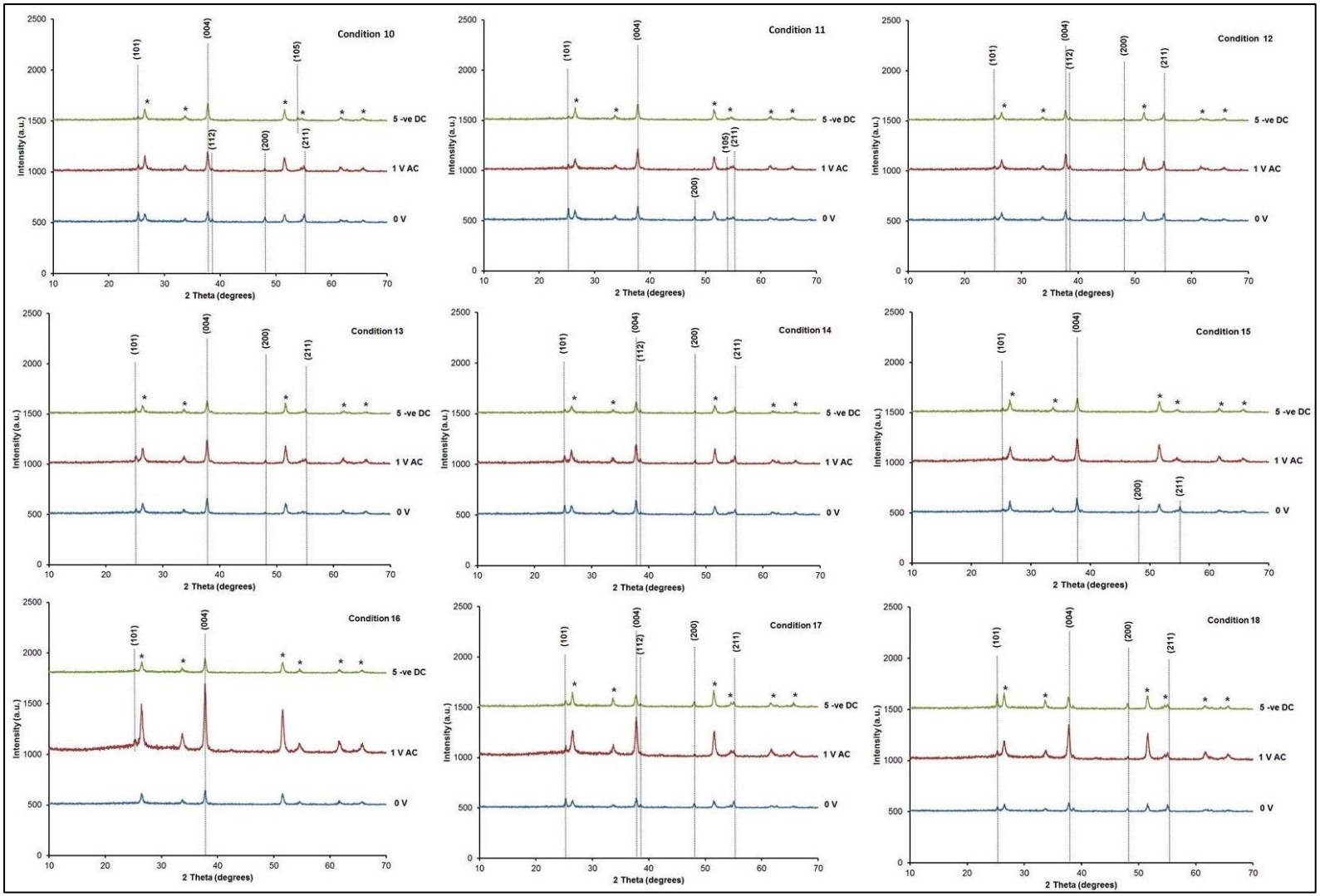

Figure 6.24: XRD patters for films produced from the EAPCVD reaction of $TiCl_4$ and ethyl acetate at variable conditions 10 – 18**.** All peaks correspond to anatase crystal phase. The asterisks denote cassiterite from the underlying substrate.

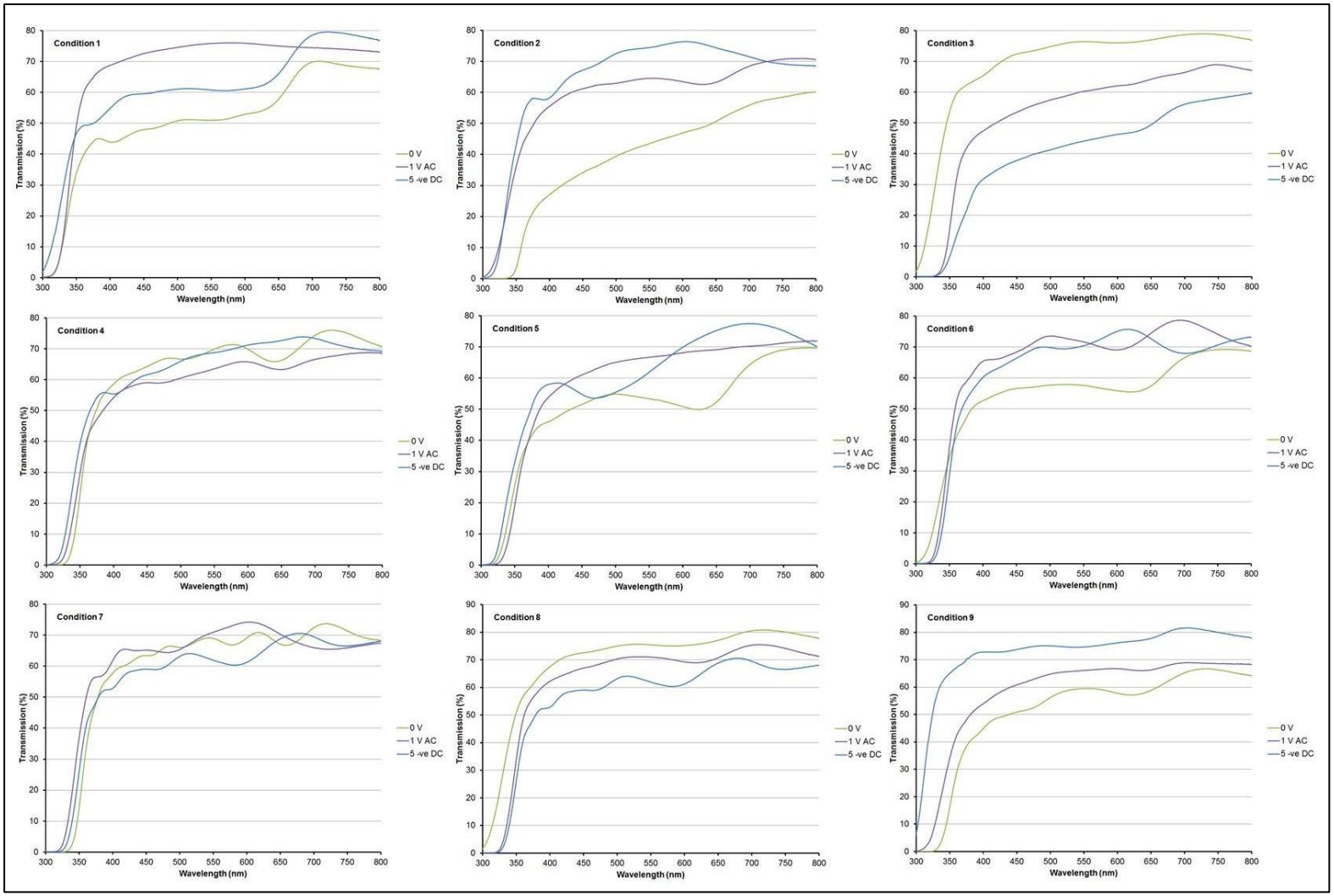

Figure 6.25: Transmission (%) obtained from UV-vis spectroscopy for films produced from the EAPCVD reaction of $TiCl_4$ and ethyl acetate at variable conditions 1 – 9**.**

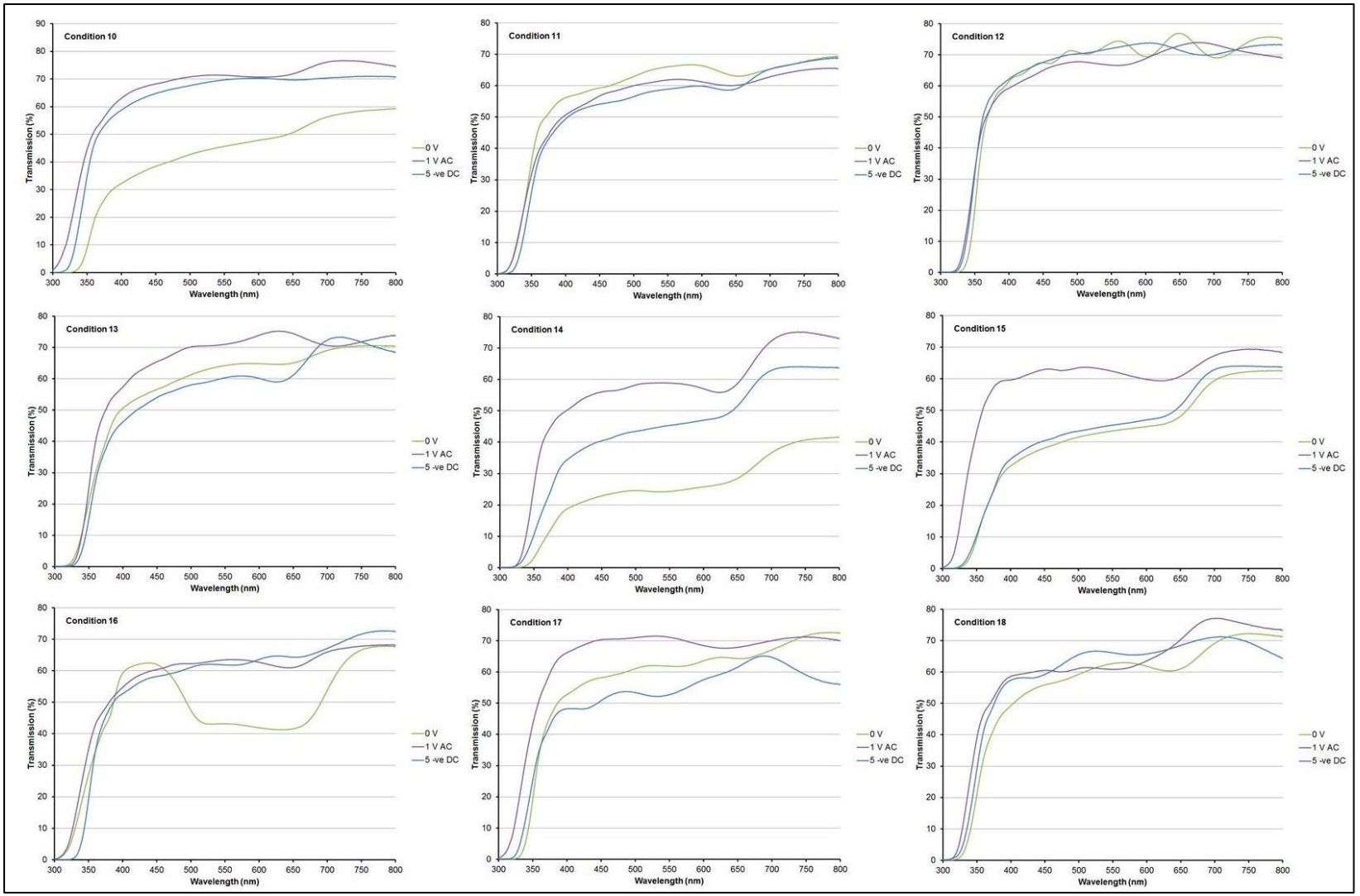

Figure 6.26: Transmission (%) obtained from UV-vis spectroscopy for films produced from the EAPCVD reaction of $TiCl_4$ and ethyl acetate at variable conditions 10 – 18**.**

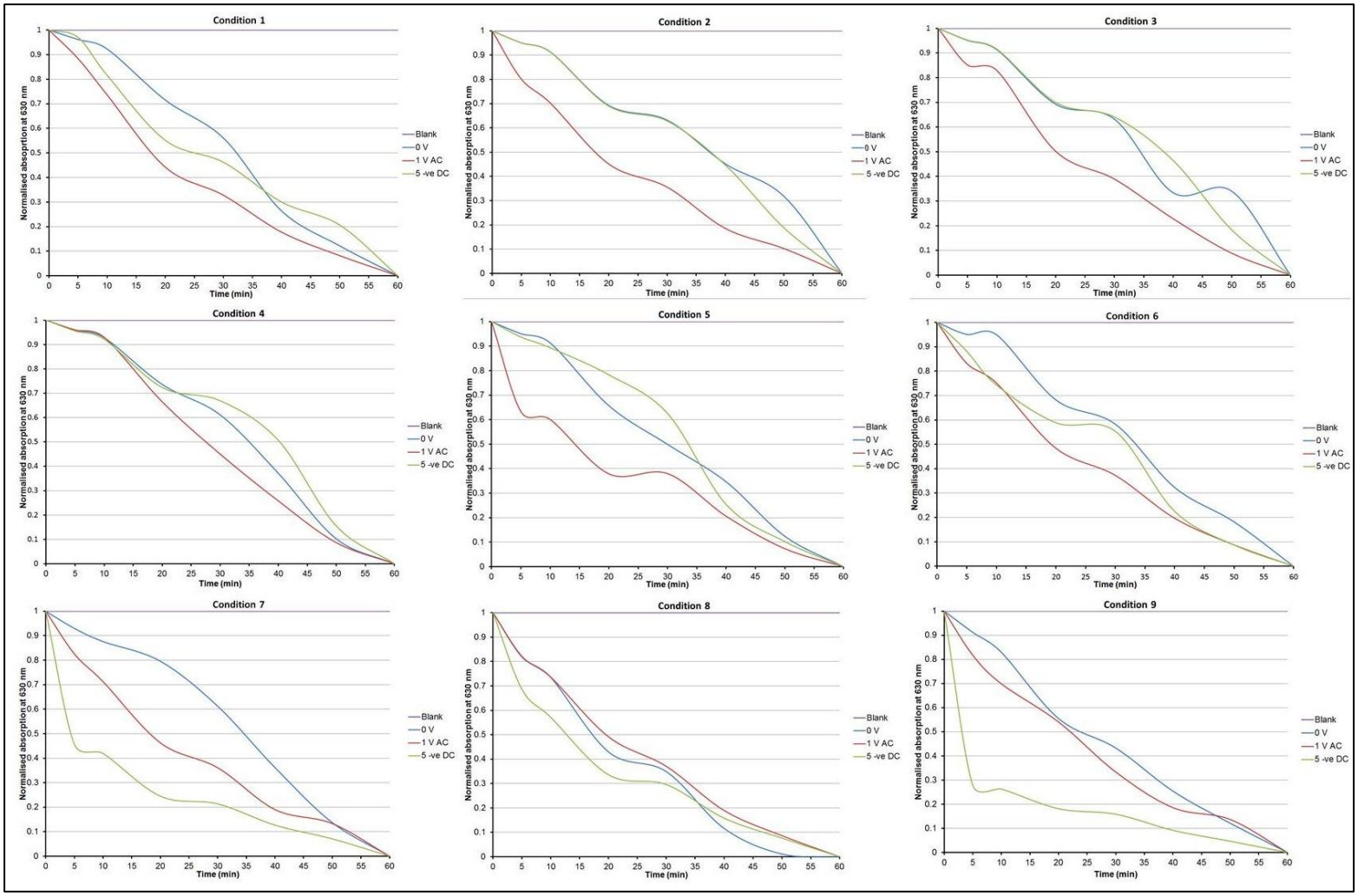

Figure 6.27: Normalised decrease in absorption at 630 nm vs UV irradiation time for films produced from the EAPCVD reaction of $TiCl_4$ and ethyl acetate at variable conditions 1 – 9**.**

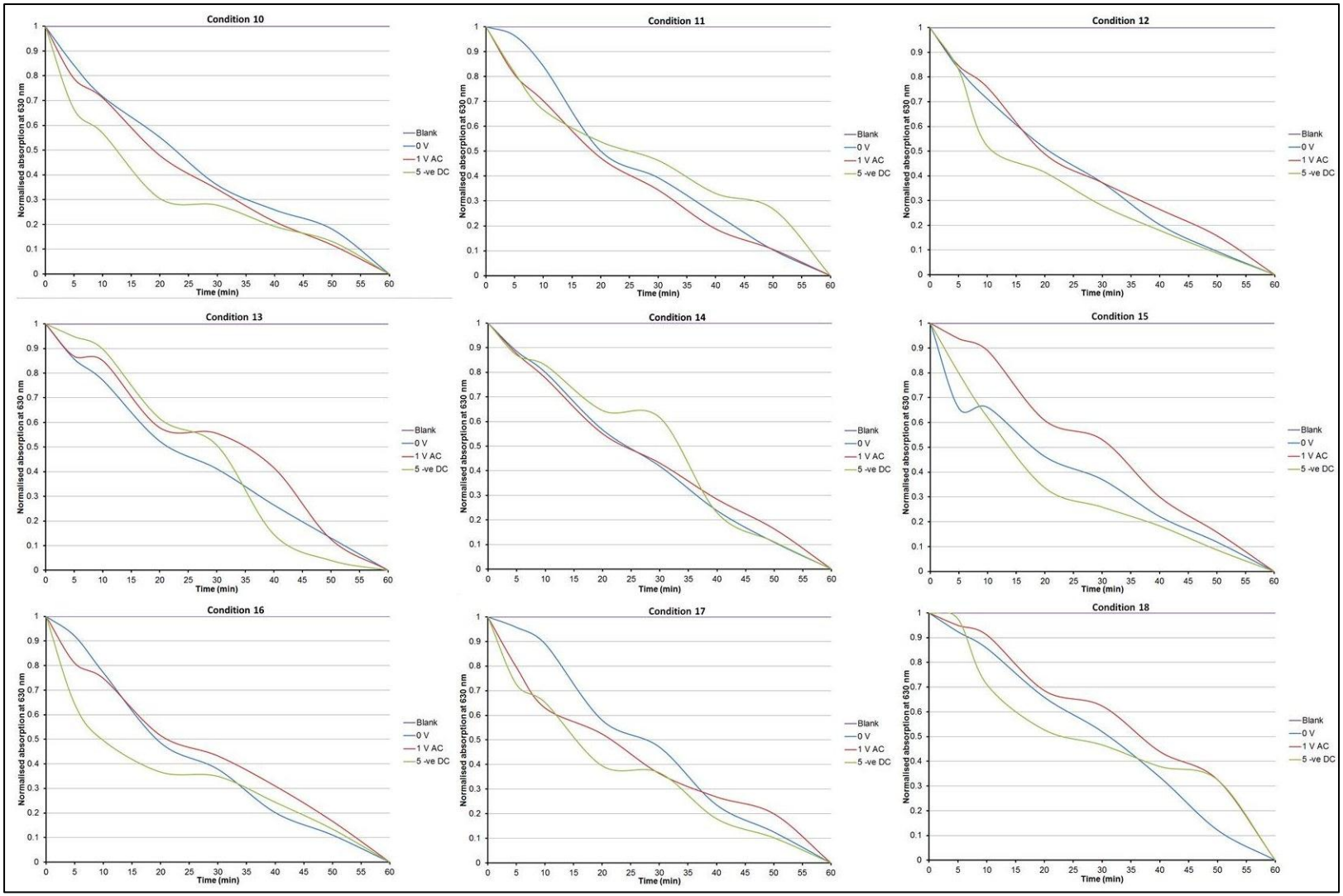

Figure 6.28: Normalised decrease in absorption at 630 nm vs UV irradiation time for films produced from the EAPCVD reaction of $TiCl_4$ and ethyl acetate at variable conditions 10 – 18.

6.3. Discussion

6.3.1. Modifications in microstructure at fixed conditions

As observed for films produced from the AC EAAPCVD reaction of TTIP and ethanol (Chapter 5, section 5.2.1), the application of lower field strength (1 x 10^2 Vm^{-1} – 10 x 10^2 Vm^{-1}) produced spherical particles and the application of higher field (20 x 10^2 Vm^{-1} – 30 x 10^2 Vm^{-1}) long-shaped particles for films deposited from the EAAPCVD reaction of $TiCl_4$ and ethyl acetate. However, the application and increase of the field strength produced a gradual decrease in the particle size until reaching a minimum at 10 x 10^2 Vm^{-1} (Sample D, 85 nm). Surprisingly, this growth pattern was similar for two different precursors and substrate temperatures, which can be attributed to a change in the dominating interaction mechanism between the electric field and the precursor species. Section 1.5.4 describes three main mechanisms in which we anticipate the electric field might interact with the precursor species: gas phase interaction, bond activation and surface mediated growth. It seems that the interaction mechanism of the electric fields with the precursor species change when applying field strength higher than 10 x 10^2 Vm^{-1}. As the film thickness for films B to C were higher (Figure 6.1), the growth mechanism in this range could be determined by a combination of a gas phase interaction or a surface mediated growth and a bond activation mechanism. Sample D (10 x 10^2 Vm^{-1}) showed spherical particles but an important decrease in film thickness (9 nm) (Figure 6.1), indicating that the field strength produced a detrimental effect on the bond activation mechanism and only the gas phase interaction or surface mediated growth prevailed. Although films produced from the AC EAACPVD reaction of TTIP and ethanol showed fluctuating film thickness regardless the field strength, the changes in morphology with increasing the field strength revealed a change in the interaction mechanisms and thus, growth mechanisms of titania thin films.

The particle size for films produced from the AC EAPCVD reaction of $TiCl_4$ and ethyl acetate were comparably bigger than that for films produced from the AC EAACVD reaction of $TiCl_4$ in toluene (see Table 4.2). This can be explained in terms of the residence time and influence of the solvent. EAAPCVD deposited films from $TiCl_4$ and ethyl acetate, were produced with a plain gas flow rate of 5 $L.min^{-1}$ and reactants gas flow rate of 0.8 $L.min^{-1}$. In total, the reactants enter the chamber at a gas flow rate of 6.6 $L.min^{-1}$ or, in terms of volumetric flow, at 110 cm^3s^{-1}. Substituting in equation 3.4;

$$t_{res} = \frac{67.5}{110} = 0.61\ \text{s}$$

Knowing the residence time of the precursor and the frequency of the electric field, it is possible to know the number of changes in bias using equation 3.5.

$$N_{bias} = 0.61 \times 50 = 30.5 \approx 36\ changes$$

According to this, during a residence time of 0.61 s the precursor can be influenced by a maximum of 36 changes throughout deposition. The number of changes with residence time was very similar to those of films produced from EAACVD processes (see section 4.3.1). Thus, the increasing particle size and film thickness of films produced from the EAPCVD reaction of $TiCl_4$ and ethyl acetate can be attributed to the CVD technique used (as discussed in section 5.4.1) and the influence of the solvent (as discussed in section 5.4.2).

Films produced from the DC EAPCVD reaction of $TiCl_4$ and ethyl acetate showed different morphology and film thickness depending on the substrate bias applied. Thus, a predominance of spherical particles of variable size (140 – 365 nm) was observed for DC+ deposited films whereas a predominance of long-shaped particles (240 – 500 nm in length) was observed for DC- at higher field strength. Likewise, a comparably higher film thickness was observed for DC- deposited films. This supports the argument which defends the interaction of the electric fields with the electrically charge precursor species result of its thermal decomposition (see section 3.3.1). According to this, positively charge precursors species (equation 4.1 – 4.2) would be attracted to a negatively charged surface, explaining the increase in film thickness and the long-shaped morphology result of the pulling forces at higher field strength. The repelling forces exerted by DC+ would have produced a predominance of spherical particles, similarly to films produced from the DC EAACVD reaction of TTIP in toluene. The effect of the DC- electric fields were also observed with a slightly increase of the crystallite size for this substrate bias.

DC deposited films also showed possible changes in the interaction mechanisms between the electric fields and the precursor species. Interestingly, at DC+ and DC- field strength of 15 x 10^2 Vm^{-1}, a change in the growth mechanism was produced. For DC+ deposited films a decrease in film thickness from 500 to 7 nm (Table 6.8, samples J – K) was observed as well as a change in particles morphology from spherical to angular. For DC- deposited films the decrease in thickness from 600 to 300 nm (Table 6.8, samples P – Q) was not as significant as for DC+, probably due to the strong attracting forces exerted by this substrate bias as

described above. However, it was observed that the morphology changed to better-defined long-shaped particles at DC- 15 x 10^2 Vm^{-1} (Figure 6.9 Q). This suggests that at least two growth mechanisms might interact simultaneously at lower field strength (up to 15 x 10^2 Vm^{-1}) that enhanced the growth of deposited films. At higher field strength one of the mechanisms would stop interacting and thus, decreasing the deposition rate and enhancing the interactions of the electric fields with the precursors species.

The texture coefficient analysis confirmed that all AC deposited films showed a high preferential orientation in the anatase (004) plane (Table 6.3). Similarly, DC deposited films showed high orientation in the anatase (004) plane regardless the substrate bias applied (Table 6.9). However, it was observed that the film prepared from a DC- 30 x 10^2 Vm^{-1} showed a preferential orientation in the (211) plane (Table 6.9, sample S). This phenomenon was already observed for films deposited from the AC EAACVD reaction of TTIP in toluene (Figure 3.36)., which was attributed to an increase of the kinetic energy to the intermediate species at higher field strength, either in the gas phase or during nucleation.

Raman spectroscopy revealed pure anatase for AC deposited films but a mix of anatase and rutile for DC+ films produced at 1 x 10^2 Vm^{-1} and 30 x 10^2 Vm^{-1} (samples H and M, 72% anatase content) and DC- film produced at 1 x 10^2 Vm^{-1} (sample N, 57% anatase content). As described in section 4.3.1, long-shaped particles would enhance edge-sharing bonding promoting the formation of anatase. Furthermore, sample H showed smaller particle size comparing to other deposited films with similar morphology (samples Q – S), which would have act as nucleation sites for the formation of rutile. Interestingly, samples M and N showed a similar rose-like microstructure formed by angular blocks of increased size, which would have favoured the transformation to the rutile crystal phase as described in previous (chapter 4, section 4.3.1).

AFM analysis showed that, generally, films with higher thickness showed lower surface roughness as previously discussed (chapter 4, section 4.3.1). This was more significant in AC deposited films at higher field strength. Thus, samples E to G (thickness 12 – 56 nm) showed RMS values between 15 – 50 nm, significantly higher than that for samples A to C (Figure 6.4).

The application of AC and DC+ electric fields during the EAAPCVD reaction of $TiCl_4$ and ethyl acetate produced films with high maximum transmission values in the visible. However, some DC- films showed lower maximum transmission values in the visible. Thus, sample N

showed a maximum transmission in the visible value of 55% (Table 6.10). Slightly higher values were found for samples R and S with 64% and 66%, respectively. This can be attributed to the incorporation of carbon from ethyl acetate ($C_4H_8O_2$) into the films. Positively charged species from the oxygen source thermal decomposition would be attracted to the negative bias substrate surface. At field strength of 5 x 10^2 Vm^{-1} - 15 x 10^2 Vm^{-1} the maximum transmission in the visible significantly increased, accounting for a combination of two or more interaction mechanisms Thus, at that range of field strength the reaction happens very quickly and no much carbon is incorporated into the films. At higher field strength, one mechanism prevails (either gas phase interaction or surface mediated growth) over the bond activation mechanism, hindering the retarding effect on the diffusion of reactants and therefore, more carbon is incorporated into the films.

All deposited films showed standard direct band gap (DBG) values for anatase (3.2 – 3.3 eV). Samples H and N showed typical rutile DBG values with 3.15 and 3.0 eV, respectively. Sample C showed a DBG of 3.15 eV. Although no rutile was identified in the XRD patterns and/or Raman spectroscopy, reduced DBG values for pure anatase were observed (chapter 5, section 5.4.1).

All AC and DC deposited films showed hydrophylicity and even superhydrophilicity after 30 min UV irradiation (254 nm). The films, which showed the lowest decrease in the water-contact angles after UV irradiation were samples C and L, which showed similar morphology (spherical – angular), particle size (130 – 160), film thickness (315 – 380 nm) and surface roughness (12 – 13 nm).

6.3.2. Photocatalytic properties at fixed conditions

The application and increase of AC field strength during the EAAPCVD reaction of $TiCl_4$ and ethyl acetate produced beneficial effects on the photo-activity for some cases and detrimental in others. Generally, films produced at lower field strength (samples B and C) showed higher photo-activity than sample A (29 min). The most photo-activity film was sample C with a half-life value of 13.8 min (Figure 6.6). This film showed spherical morphology, the lowest texture coefficient value in the (004) plane and the worst wettability of deposited films produced under those conditions. Considering the arguments presented in previous chapters, these conditions would not have favoured the photo-activity. However,

this film showed the lowest DBG (3.15 eV) that would have favoured increased photo-activity by increasing the photo-response in the visible. The least photoactive film was sample F with a half-life of 32.6 min (Figure 6.6). This sample showed long-shaped particles highly orientated in the (004) plane and good wettability. However, the film thickness was very low (12 nm) which would have hindered the creation of active sites. Similarly, sample D showed a half-life value of 31.6 min with a film thickness of 9 nm.

Generally, all DC deposited films showed a higher photo-activity than the film produced in absence of electric fields (sample A). DC- deposited films shower a higher photo-activity (half-life values of 3.9 – 26.2 min) than DC+ deposited films (half-life values of 19.8 – 42 min). The most photo-active film was sample N with a half-life value of 3.9 min (Figure 6.15). This film showed a rose-like morphology and a texture coefficient in the (004) plane of 2.63, which was not the highest. However, as observed in sample C, sample N showed the lowest DBG 3.0 eV. The increase of the photo-activity could have been produced by an enhancement of the photo-response in the visible, but it could have been also produced by a synergistic effect of anatase and rutile, as observed in chapter 4, due to its content in anatase close to the 1:1 ratio. The worst photo-activity was found for sample I, which showed a half-life value of 42 min. This film showed spherical particles and the lowest texture coefficient in the (004) plane (1.85), which as described previously (chapter 3, section 3.4.2) could have caused a detrimental effect on the photo-activity. Samples J, Q and R showed half-life values in the range of 26.2 – 27.1 min. Sample R showed preferential orientation in the anatase (211), which, as discussed in previous sections (1.4.1.1.2.), is less reactive than the (001) plane. Sample Q showed long-shaped particles and a texture coefficient in the (004) plane of 2.7. However, this sample showed one of the highest half-life values (27.1 min). This sample showed similar particle size as sample H, but this last one showed a lower DBG (3.15 eV), which would explain a decrease in the half-life value (24 min).

6.3.3. Modifications in microstructure at different conditions

Crystal growth

The effect of electric fields with substrate temperature was revealed by the changes observed in the microstructure and growth rate. At substrate temperature of 350 – 400 ºC, the application of AC and DC electric fields indistinctively produced a change to spherical

morphology and a decrease in film thickness comparing to the films produced in absence of electric fields (0 V). The retarding effect induced by AC and DC electric fields was shown by an important change in morphology from long-shaped to spherical for condition 2. As discussed (Figure 1.15), the increase of substrate temperature enhances film thickness until the system becomes mass - transport limited. This might be the case of the film produced in absence of electric fields (0 V) at condition 3 (500 ºC), which showed an important decrease in film thickness (Table 6.11). The application of electric fields would have enhanced the feed rate by the retarding effect induced to the precursor species. The morphology was influenced by the type of electric fields applied. Thus, the fluctuating nature of AC electric fields would have favoured the interaction of electric fields with precursor species resulting in a change to long-shaped particles. DC electric fields would have produced comparably a rapid diffusion of precursor species towards the substrate, which could have explained why similar morphology to the sample produced in absence of electric fields (0 V) (Figure 6.18, C3).

Interesting changes in the microstructure and growth rate were observed when testing the influence of the $TiCl_4$ and ethyl acetate bubbler temperature with electric fields. At condition 4 (50 ºC), the application of electric fields produced a decrease in the particle size and, for DC- deposited film, an important decrease in film thickness. However, for conditions 5 – 6 (50 – 85 ºC) the opposite effect was observed. The application of AC and DC electric fields produced not only an increase in the particle size but also an increase in film thickness, which can be attributed to an increase in the precursor feed rate.

Previous investigations on TiO_2 thin films growth from the APCVD reaction of $TiCl_4$ and ethyl acetate at temperatures below 550 °C have reported an increase of particle size and a decrease in film thickness with decreasing reactants mass flow rate [132]. The results shown for conditions 10 – 12 suggest a slight decrease in particle size with decreasing flow rate and a decrease in film thickness when reducing the gas flow rate from 4 to 3 $L.min^{-1}$. Likewise, the results shown for conditions 13 – 15 suggest that a progressive reduction in particle size and increase in film thickness are produced when increasing $TiCl_4$ and ethyl acetate gas flow rate (in absence of electric fields). This can be attributed to a decrease in the boundary layer with increasing gas flow rate as described in section 3.4.4.

As expected, the increase in deposition time led to a gradual increase in particle size and film thickness for the films produced in absence of electric fields. Similar behaviour was observed

for DC- deposited films. However, films deposited from AC electric fields showed a significant increase in particle size from 15 to 30 seconds deposition time, but a decrease in particle size after 45 seconds deposition time. This shows that the higher the interaction between the electric field and the precursor species, the more induced changes are produced in the microstructure.

Crystal orientation

Increasing the substrate temperature favoured the crystal growth in the (004) plane as observed for conditions 1 – 3. Crystal growth is thermodynamically favoured along the facets with the lowest surface energy. In the case of titanium dioxide, that facet corresponds to the anatase (101) plane. However, all films produced in the absence of electrics showed a preferential orientation in the anatase (004) plane. As the substrate used (FTO glass substrate) has a preferential orientation in the (004) plane, the crystal growth along that plane can be attributed to the preferential orientation of the glass substrate. When applying AC and DC electric fields (see condition 2), the crystal preferred orientation in the anatase (004) is enhanced as the increasing texture coefficient values showed. Thus, although the crystal preferential orientation can be attributed to that of the substrate, the interaction between the electric fields and the precursor species also influenced the crystal growth in that plane. Similarly, the increase of $TiCl_4$ and ethyl acetate bubbler temperature favoured the crystal growth in the (004) plane by increasing the feed rate of titanium precursor and oxygen source. However, it was observed that the application of AC and DC electric fields at a $TiCl_4$ bubbler temperature of 85 ºC (condition 6) produced a decrease in the texture coefficient in the (004) plane values (see Table 6.11). At this temperature the precursor feed rate is so high that the most of the reaction occurs in the gas phase. The resulting particles of the gas phase reaction could "snow" down to the substrate interfering in the growth along that plane as previously observed (section 3.4.3).

The effect on the crystal growth for conditions 10 – 15 can be explained by the kinetics of the system. Decreasing the plain gas flow rate from 4 to 3 $L.min^{-1}$ (condition 10 to 11) produced an increase in the crystal preferential orientation in the (004) plane. The application of AC and DC electric fields increased the texture coefficient in the (004) plane. However, at lower gas flow rate (condition 12) the texture coefficient decreased for all deposited films. Decreasing the gas flow rate would have encouraged the interaction of the electric fields with the precursor species and subsequently favouring the crystal growth along that plane. At

lower gas flow rate (condition 12) the texture coefficient values in the (004) plane decreased even for the film produced in absence of electric fields. Thus, the decrease in the preferential orientation along that plane can be attributed to an increase of the boundary layer thickness, which would have hindered the diffusion of reactants towards the surface substrate.

Increasing the reactants gas flow rate (conditions 13 – 15) also influenced the crystal preferential orientation. The application of AC and DC electric fields significantly increased the crystal preferential orientation in the (004) plane at higher gas flow rate (condition 15), accounting the retarding effect induced to precursor species during the deposition.

Films produced in absence of electric fields with deposition times between 30 to 45 seconds (conditions 16 – 18) showed low texture coefficient values which were increased with the induction of AC and DC electric fields, supporting the effect induced in the microstructure with a higher interaction between the electric fields and the precursor species.

Optical properties

Generally, all conditions produced thin films with maximum transmission in the visible greater than 65%. Films produced in absence of electric fields under conditions 5, 10, 11, 15 and 16 showed slightly lower maximum transmission in the visible (62 – 64%). Likewise, C14 (0 V) showed the lowest maximum transmission in the visible (37%). In all cases, the application of AC and DC electric fields increased the maximum transmission in the visible most probably by hindering the deposition of carbon as a result of the interaction mechanisms described above. The application of AC and DC electric fields decreased the maximum transmission in the visible for condition 11 (plain gas flow rate of 3 $L.min^{-1}$). Films showed a decrease in the maximum transmission in the visible from 67% to 63% and 65% when applying AC and DC electric fields, respectively (Table 6.12). However, considering the increase of the maximum transmission in the visible from condition 10 to 12, the slight decrease for condition 11 was not significant.

All deposited films showed standard DBG values of anatase (3.2 – 3.3 eV). Lower DBG values (3.0 – 3.15 eV) were found for film produced in absence of electric fields (conditions 12, 14, 17 and 18), at an applied AC field strength of 100 Vm^{-1} (condition 13) and at an applied DC- field strength of 500 Vm^{-1} (conditions 3, 14 and 15). However, the impossibility to conduct Raman spectroscopy on those samples makes uncertain whether those values correspond to a presence of rutile crystal phase or to a variation of stoichiometry.

Wettability

All conditions produced hydrophilic surfaces after 30 min UV irradiation (254 nm) with water-contact angles in the range of 40 – 5º. In addition, films AC electric fields produced superhydrophilic surfaces under condition 4, 8, 12, 15, 18 with water-contact angles <5º. These samples showed similar angular morphology with reduced particle size which would have favoured a heterogeneous structure for the Wenzel and Cassie-Baxter model (section 1.4.2.1).

6.3.4. Photocatalytic properties at different conditions

Most of the conditions tested produced either a detrimental effect or did not significantly improve the photo-activity of deposited films. The application of AC electric fields produced an improvement in the photo-activity of deposited films except for conditions 13, 15, 16 and 18. These films showed similar angular particles in their microstructure which, as discussed, are less favourable for photocatalysis than long-shaped morphology. However, the poor photo-activity of these films can be also attributed to a poor crystallinity as observed in Figure 6.24, conditions 15 and 16).

The application of AC electric fields improved the photo-activity of deposited films when increasing the substrate temperature, obtaining half-life values in the range of 17. 6 – 20 min. However, a better photo-activity was found for the film produced at 460 ºC (sample B), which showed a half-life value of 17 min.

Generally, the application of DC- electric fields produced a detrimental effect on deposited films photo-activity. However, the most photoactive films were found for DC- deposited films under conditions 7 (solvent bubbler temperature of 30 ºC), 9 (solvent bubbler temperature of 60 ºC), 12 (plain gas flow rate of 2 $L.min^{-1}$) and 16 (deposition time of 15 seconds), with half-life values in the range of 3.1 – 9.9 min. The most photo-active film was condition 9 (3.1 min) which showed reduced particle size (140 nm) which would have favour photocatalysis by increasing the surface area. The second best photo-activity was found for condition 7 (4.3 min) and 12 (9 min) which showed long-shaped particles in their microstructure. The third best photo-activity was found for condition 16 (9.9 min) which showed reduced particle (90 nm) and high orientation in the (004) plane.

The application of DC- electric fields (5 x 10^2 Vm^{-1}) increased the photo-activity for ethyl acetate bubbler temperature in the range of 30 – 60 ºC, plain gas flow rate of 4 $L.min^{-1}$ and 2 $L.min^{-1}$ and a deposition time in the range of 15 – 30 seconds.

The only condition that produced a detrimental effect on the photo-activity when applying electric fields was at $TiCl_4$ and ethyl acetate gas flow rate of 1 $L.min^{-1}$.

6.4. Conclusions

Titanium dioxide thin films were successfully produced from the electric field assisted APCVD reaction of $TiCl_4$ and ethyl acetate at fixed and variable experimental conditions. As observed for films produced from the AC EAPCVD reaction of TTIP and ethanol (Chapter 5, section 5.2.1), the application of lower field strength (1 x 10^2 Vm^{-1} – 10 x 10^2 Vm^{-1}) produced a switch in the microstructure and growth rate, accounting for a simultaneous interaction of various mechanisms between the electric field and the precursor species. DC deposited films showed similar thickness patterns as those deposited from EAACVD reaction of $TiCl_4$ (in toluene chapter 4, section 4.3.1). Furthermore, the induced changes in morphology depending on the substrate bias, shows an interaction of the electric field and the intermediate species of the thermal decomposition of the precursor.

The application and increase of AC field strength during the EAPCVD reaction of $TiCl_4$ and ethyl acetate produced beneficial effects on the photo-activity for some cases and detrimental in others. The most photoactive film (sample C, 13.8 min) showed the lowest DBG (3.15 eV), which would have favoured the photo-activity by increasing the photo-response in the visible.

Generally, all DC deposited film showed a higher photo-activity than the film produced in absence of electric fields (sample A). DC- deposited films shower a higher photo-activity (half-life values of 3.9 – 26.2 min) than DC+ deposited films (half-life values of 19.8 – 42 min). The most photoactive film was sample N with a half-life value of 3.9 min, which showed the lowest DBG (3.0 eV). The increase of the photo-activity could have been produced by an enhancement of the photo-response in the visible, but it could have been also produced by a synergistic effect of anatase and rutile, as observed in chapter 4, due to its content in anatase close to the 1:1 ratio

The retarding effect induced by the electric fields during the deposition was revealed by changes in the morphology, particle size, crystal orientation and growth rate at different experimental conditions. Generally, such retarding effect induced by AC and DC electric fields would have influenced thin films growth differently, favouring the formation of long-shaped particles with decreasing particle size, an increase in film thickness and even a higher crystal orientation in the (004) plane.

Most of the conditions tested produced either a detrimental effect or did not significantly improve the photo-activity of deposited films. However, the most photoactive films were found for DC – deposited films at a solvent bubbler temperature of 30 ºC and 60 ºC (conditions 7 and 9), plain gas flow rate of 2 $L.min^{-1}$ (condition 12) and deposition time of 15 seconds (condition 16), with half-life values in the range of 3.1 – 9.9 min. Previous chapters of this work have pointed out optimum photo-activity for films with reduced long-shaped particles highly orientated in the anatase (004) plane. The deposited films from the DC- 5 V under conditions 7 and 12 showed long-shaped particles. The highest photo-activity was found for the film produced under condition 9 (3.1 min) which showed spherical morphology. However, this film showed comparably smaller particles that would have favoured the photocatalytic activity. Furthermore, no texture coefficient values and therefore, no data about the preferential orientation could have obtained for that sample.

Chapter 7:

Overall Conclusions and Future Work

7.1. Overall conclusions

This work has investigated the effect of electric fields on the production of titanium dioxide thin films from aerosol assisted and atmospheric pressure chemical vapour deposition reactions of titanium isopropoxide and titanium tetrachloride with different solvents (toluene, ethanol and ethyl acetate). The application of electric fields during the reaction was thought to produce modifications in the morphology, particle size and growth rate which could influence the functional properties of the material. This work has looked at the interaction mechanisms between the electric fields and the precursor species and how these induced changes influenced the photocatalytic performance of the titanium dioxide thin films. In order to investigate the optimal conditions to increase the photo-activity, variable conditions were tested using both EAACVD and EAPCVD processes.

Chapter 3 investigated the effect of electric fields on the aerosol assisted chemical vapour deposition of titanium dioxide thin films from the reaction of titanium isopropoxide in toluene. The application and increase of AC electric fields in films produced at fixed conditions (substrate temperature of 450 ºC and gas flow rate of 2 $L.min^{-1}$) showed a gradual change in morphology from spherical to long-shaped particles with similar particle size and increasing film thickness. At higher field strength (3000 Vm^{-1}) an increase in surface roughness was observed (Table 3.4). All films showed anatase crystal phase as shown in the XRD analysis. At field strength in the range of 0 – 15000 Vm^{-1} films showed a crystal preferential orientation in the anatase (004), but at higher field strength (2000 – 3000 Vm^{-1}) a drastic change in the crystal orientation to the (211) plane was produced. This was attributed to a rotation result of a higher kinetic energy induced to the precursor species (in the gas

phase or during nucleation) at higher field strength. The photocatalytic testing showed that the most photoactive film was sample E (Table 3.6) with a half-life of 3.9 min. This sample showed long-shaped morphology with high preferential orientation in the anatase (004) plane, which is believed to increase the photo-activity and wettability due to its low atom packing density and oxygen reactivity.

The application of DC electric fields produced changes in the microstructure depending on the substrate bias. The application of DC+ produced a predominance of long-shaped particles and an increase in film thickness with field strength. The application of DC- produced a predominance of spherical particles and a decrease in film thickness with the field strength. This was explained by the thermal decomposition of the precursor during the CVD reaction. According to this, negatively charge hydroxyl groups ($Ti - OH^-$) would be attracted to the positive bias substrate, accounting for the increase in film thickness. This also explained the predominance of long-shaped particles result of the pulling forces exerted on the precursor species by DC+ and the predominance of spherical particles result of the repelling forces exerted by DC- electric fields. The application of DC electric fields produced a decrease in the photo-activity of deposited films comparing to the films deposited from AC electric fields. This was attributed to an increase in the particle and crystallite size as well as an increase in film thickness, which would have caused a detrimental effect on the photocatalysis by decreasing the surface area and by hindering the electron transfer to the surface of the material, respectively.

Films deposited at variable conditions and field strengths showed differences in the microstructure, growth rate and crystal orientation which influenced the photocatalytic performance. It was observed that for AC deposited films the optimum deposition time was that for the depletion of the precursor (18 min). For DC deposited films, the most photoactive film was produced at a deposition time of 15 min (condition 15) with a half-life value of 22.5 min. Better half-life results were found as the deposition time was decreased, mostly due to a decrease in film thickness. The photo-activity was also improved with the increase of the precursor concentration for AC deposited films. However, no significant improvements were observed for DC electric fields. This was attributed to a combination of the progressive increase of nucleation in the gas phase with increasing concentration and the retarding effect induced to the precursor by AC electric fields, which would have produced favourable changes in morphology and film thickness. Substrate temperatures below 450 °C caused detrimental effects on the photo-activity of deposited films. AC and DC deposited films

showed similar photo-activity with half-life values. The increase of the substrate temperature produced a progressive reduction of the particle size in DC deposited films, which would have positively affected the photo-activity. Furthermore, condition 21 was found the most photoactive of all DC deposited films. Different gas flow rates produced morphological changes. It was observed that gas flow rate values below 1 $L.min^{-1}$ but above 2 $L.min^{-1}$ produced detrimental effects on titania photocatalytic performance for AC deposited films with half-life values of 22 min and 23.2 min, respectively.

Chapter 4 investigated the effect of electric fields on the aerosol assisted chemical vapour deposition of titanium dioxide thin films from the reaction of 1 M titanium tetrachloride solution in toluene. Films were deposited at substrate temperature of 600 ºC and a gas flow rate of 5 $L.min^{-1}$. Subsequently, films were annealed at 600 ºC in atmospheric air for 2 h in order to improve their crystallinity. The application and increase of AC field strength produced a gradual decrease in the particle size and film thickness as well as changes in the morphology. This was attributed to a retarding effect in the diffusion of the precursor as a result of the interaction between the electric fields and the products of the precursor thermal decomposition. As the field strength is increased, the kinetic energy of precursors is also increased inducing this way the acceleration of $TiCl_3^+$ and $TiOCl_2^+$ towards the surface which could undergo a stretching effect at higher field strength. Furthermore, such an effect could cover nucleation sites for incoming species to the substrate, which could explain why for Sample F particles agglomeration is lower and film thickness decreased from 90 nm to 10 nm.

Raman spectroscopy showed a mix of polymorphs contents depending on the field strength applied. It was observed that the gradual decrease in the particle size was accompanied by a progressive increase in the anatase (98%) content until reaching a maximum for the sample with the smallest particle size (sample E). This was explained by a cross-over particle size which promoted the formation of anatase instead of rutile. The annealing process produced the coarsening of particles, which also influenced the content in anatase by the enhancement of edge sharing bonds.

As observed for films deposited from the EAACVD reaction of TTIP in toluene (chapter 3), the most photocatalytic active titania thin films were those which showed small particle size and elongated shape. Samples F and G showed long-shaped particles and half-life values of 4.5 and 3.5 min, respectively. Film thickness was not found as determining as the particles

morphology and size. Furthermore, it was observed that the most photoactive films (Samples C, D, F, and G) showed an anatase to rutile ratio close to 1:1, accounting for a possible photocatalytic synergy between anatase and rutile. The annealing process had a detrimental effect on the most photoactive thin films (Samples C, D and F), which was attributed to an unbalance content of both polymorphs.

The induction of DC electric fields also influenced the shape and morphology of deposited films. However, no predominance of certain morphology was observed depending on the substrate bias. This was attributed to a rapid decomposition of the precursor which would have hindered the interaction between the electric fields and the intermediate species. However, different film thickness depending on the substrate bias was observed. Thus, negative biased produced thicker films as the field strength increased until reaching a maximum at 15 x 10^2 Vm^{-1} (225 nm) and then dramatically decreased to 30 nm. As in AC deposited films, the application and increase of DC electric fields increased the content of anatase crystal phase. However, there was no evidence that the substrate bias produced a particular effect on the crystal phase as such. Contradictory to AC deposited films, most of DC deposited films showed a decrease in anatase content after annealing with the exception of Samples T and V. These films showed flatter clusters in their microstructure after annealing, which could have favoured the anatase transformation by the coalescence of nanoparticles.

The application of electric fields during the reaction influenced the surface roughness of as-deposited films likely as a result of the induced changes in the grain size and film thickness. However, it was observed that in some cases, the increase of grain size resulted in thinner films (samples F and G) with no changes in surface roughness in comparison to other deposited films (samples D and E). This was attributed to the variable morphology of particles, which would have influenced the surface roughness.

Generally, the application of DC electric fields produced more photoactive films comparing to the film produced in absence of electric fields (sample A, half-life = 21.5 min). The best photocatalytic performance was observed for films which showed a content in anatase crystal of 98% with half-life values from 3.3 to 8.5 min (samples P –R and W). Other films (M, S U and X) showed worse photo-activity with similar content in anatase, which was attributed to the recombination sites consequence of a lack of agglomeration of the particles Sample T showed better photo-activity (half-life of 13 min) than films with high content in anatase

(samples S and U), which was attributed to an enhancement of the surface area. Generally, the annealing process had a detrimental effect on positive bias deposited films, which was attributed to a decrease in anatase content.

Chapter 5 investigated the effect of electric fields on the atmospheric pressure chemical vapour deposition of titanium dioxide thin films from the reaction of titanium isopropoxide and ethanol at a substrate temperature 550 ºC, TTIP pre-heating temperature of 150 ºC, ethanol pre-heating temperature of 65 ºC and gas flow rate of 4 $L.min^{-1}$.

The application of lower field strength (1 x 10^2 Vm^{-1} – 10 x 10^2 Vm^{-1}) produced a gradual increase of granular nanoparticles (90 to 110 nm) in AC deposited films. Further increase of the field strength (10 x 10^2 Vm^{-1} – 30 x 10^2 Vm^{-1}) produced long-shaped nanoparticles of forming
clusters of increased size. This was attributed to the induced retarding effect on the diffusion of the precursor to the substrate surface at lower field strength as observed in EAACVD processes (chapter 3). As illustrated in Figure 5.18 B, in APCVD the precursor is readily available in vapour phase and the interaction of the electric fields with the precursor is direct. Since the reaction occurs more quickly than that in AACVD systems, the interaction of electric fields and the precursor species are lower and as a consequence, the induced changes in the microstructure are also lower.

Raman spectroscopy showed a mix content of anatase and rutile crystal phase. The film produced in absence of electric fields showed an anatase to rutile ratio of 9:1. As the field strength was increased up to 5 x 10^2 Vm^{-1} (Sample B – C) the content of the mix phase reached values close to 1:1 ratio. However, at higher field strength deposited films showed mainly anatase (98 %), which was attributed to an increase of particle coarsening as observed in chapter 4.

The application of DC electric fields produced long-shaped nanoparticles of 85 – 190 nm in length. As observed for DC EACVD deposited films (chapter 3), the film thickness of negative bias deposited films was lower and showed a decreasing trend with field strength. Thus, it can be assumed that the thermal decomposition pathway is the same and the morphology of deposited films was influenced by the deposition method and experimental parameters.

Generally, the application of AC and DC electric fields did not significantly improve the photo-activity of deposited films. Sample C exhibited the highest photo-activity with a half-life value of 17 min. This film showed a content of anatase and rutile close to 1:1 ratio, which, as discussed in Chapter 4, has been reported to favour titania photocatalytic activity. Contradictory to the results obtained from the EAACVD reaction of TTIP in toluene, the application of AC electric fields did not significantly improve the photo-activity of titania thin films. This was attributed to an enhancement of the particles coarsening and surface roughness with toluene.

As observed for EAACVD TTIP, the application of DC electric fields did not significantly improve the photocatalytic activity of deposited films. However, the application of DC- high field strength (30 x 10^2 Vm^{-1}, Sample Q) showed an important decrease in the half-life to 5.
1 min. This film presented reduced long-shaped particles with high crystal preferential orientation in the (004) plane, which, as discussed, could have enhanced the photo-activity.

Chapter 6 investigated the effect of electric fields on the atmospheric pressure chemical vapour deposition of titanium dioxide thin films from the reaction of titanium tetrachloride and ethyl acetate at fixed and variable conditions. Films at fixed conditions were produced with a substrate temperature of 460 ºC, $TiCl_4$ pre-heating temperature of 70ºC, ethyl acetate pre-heating temperature of 40 ºC and gas flow rate of 6.6 $L.min^{-1}$. As observed for films produced from the AC EAPCVD reaction of TTIP and ethanol (Chapter 5, section 5.2.1), the application of lower field strength (1 x 10^2 Vm^{-1} – 10 x 10^2 Vm^{-1}) produced a switch in the microstructure and growth rate, accounting for a simultaneous interaction of various mechanisms between the electric field and the precursor species. Although films produced from the AC EACPVD reaction of TTIP and ethanol (chapter 5) showed fluctuating film thickness regardless of the field strength, the changes in morphology with increasing the field strength revealed a change in the interaction mechanisms and thus, growth mechanisms of titania thin films.

Films produced from the DC EAPCVD reaction of $TiCl_4$ and ethyl acetate showed different morphology and film thickness depending on the substrate bias applied. Thus, a predominance of spherical particles of variable size (140 – 365 nm) was observed for DC+ deposited films whereas a predominance of long-shaped particles (240 – 500 nm length) was observed for DC- at higher field strength. Likewise, a comparably higher film thickness was

observed for DC- deposited films, supporting the interaction of the electric fields with the electrically charge precursor species result of its thermal decomposition.

DC deposited films also showed possible changes in the interaction mechanisms between the electric fields and the precursor species. Interestingly, at DC+ and DC- field strength of 15 x 10^2 Vm^{-1}, a change in the morphology and growth rate was produced, accounting for a switch of the interaction mechanisms already described.

The texture coefficient analysis confirmed that all AC deposited films showed a high preferential orientation in the anatase (004) plane (Table 6.3). Similarly, DC deposited films showed high orientation in the anatase (004) plane regardless the substrate bias applied (Table 6.9). However, it was observed that the film prepared from a DC- 30 x 10^2 Vm^{-1} showed a preferential orientation in the (211) plane (Table 6.9, sample S). This phenomenon was already observed for films deposited from the AC EAACVD reaction of TTIP in toluene (Figure 3.36), which was attributed to an increase of the kinetic energy to the intermediate species at higher field strength, either in the gas phase or during nucleation.

Raman spectroscopy revealed pure anatase for AC deposited films but a mix of anatase and rutile for DC+ films produced at 1 x 10^2 Vm^{-1} and 30 x 10^2 Vm^{-1} (samples H and M, 72% content in anatase) and DC- film produced at 1 x 10^2 Vm^{-1} (sample N, 57% content in anatase). As described in section 4.3.1, long-shaped particles would enhance edge-sharing bonding promoting the formation of anatase.

AFM analysis showed that, generally, films with higher thickness showed lower surface roughness as previously discussed (chapter 4, section 4.3.1). This was more significant in AC deposited films at higher field strength.

The application of AC and DC+ electric fields during the EAAPCVD reaction of $TiCl_4$ and ethyl acetate produced films with high maximum transmission values in the visible. However, some DC- films showed lower maximum transmission values in the visible. This was attributed to the incorporation of carbon from ethyl acetate ($C_4H_8O_2$) into the films. Positively charged species from the oxygen source thermal decomposition would be attracted to the negative bias substrate surface. At field strength of 5 x 10^2 Vm^{-1} - 15 x 10^2 Vm^{-1} the maximum transmission in the visible significantly increased, accounting for a combination of two or more interaction mechanisms. Thus, at that range of field strength the reaction happens very quickly and not much carbon is incorporated into the films. At higher field

strength, one mechanism prevails over the others hindering the retarding effect on the diffusion of reactants and therefore, more carbon is incorporated into the films.

All deposited films showed standard direct band gap (DBG) values for anatase (3.2 – 3.3 eV). Samples H and N showed typical rutile DBG values with 3.15 and 3.0 eV, respectively. Sample C showed a DBG of 3.15 eV. Although no rutile was identified in its XRD patter and/or Raman spectroscopy, it was already observed low DBG values for pure anatase (chapter 5, section 5.4.1).

All AC and DC deposited films showed hydrophylicity and even superhydrophilicity after 30 min UV irradiation (254 nm). The films, which showed the lowest decrease in the water-contact angles after UV irradiation were samples C and L, which showed similar morphology (spherical -angular), particle size (130 – 160), film thickness (315 – 380 nm) and surface roughness (12 – 13 nm).

Generally, all DC deposited film showed a higher photo-activity than the film produced in absence of electric fields (sample A). DC- deposited films shower a higher photo-activity (half-life values of 3.9 – 26.2 min) than DC+ deposited films (half-life values of 19.8 – 42 min). The most photoactive film was sample N with a half-life value of 3.9 min, which showed the lowest DBG (3.0 eV). The increase of the photo-activity could have been produced by an enhancement of the photo-response in the visible, but it could have also been produced by a synergistic effect of anatase and rutile, as observed in chapter 4, due to its content in anatase close to the 1:1 ratio

The retarding effect induced by the electric fields during the deposition was revealed by changes in the morphology, particle size, crystal orientation and growth rate at different experimental conditions. Generally, such retarding effect induced by AC and DC electric fields would have influenced thin films growth differently, favouring the formation of long-shaped particles with decreasing particle size, an increase in film thickness and even a higher crystal orientation in the (004) plane.

Most of the conditions tested produced either a detrimental effect or did not significantly improve the photo-activity of deposited films. However, the most photoactive films were found for DC – deposited films under conditions 7, 9, 12 and 16, with half-life values in the range of 3.1 – 9.9 min. These films showed either long-shaped particles highly orientated in

the anatase (004) plane (conditions 7 and 12) or reduced particle size (conditions 9 and 16), accounting for the higher photo-activity.

7.2. Future work

This work has looked at the interactions of the electric fields with the precursor species during the aerosol assisted and atmospheric pressure chemical vapour deposition. This was achieved by a systematic group of depositions using different experimental conditions, titanium precursors (titanium isopropoxide and titanium tetrachloride) and solvents (toluene, ethanol and ethyl acetate).This study has analysed such interactions by providing supporting information from analytical techniques (SEM, XRD, Raman spectroscopy, among others). Further investigations about these mechanisms would be highly beneficial. In particular, computational simulation studies would be beneficial to understand the nature of the switch of mechanisms which has been observed to happen at certain field strength and that have revealed important changes in the microstructure and growth rate.

This study has shown that electric field assisted chemical vapour deposition processes produced an important improvement of the photocatalytic performance, which has an important potential in industrial processes. Numerous companies use CVD processes for the mass production of coated surfaces. Companies such as NSG Group use on-line and off-line APCVD processes for the production of a varied range of self-cleaning glazing products. Considering the photocatlytic and wettability results obtained in this study, this technique has a great a potential for industrial processes. This study has shown the ease for the adaptability of the electric field to the APCVD system, which could be scaled up to be used in industry. Bearing in mind that the substrate is in continuous movement during the on-line production of these products, scaling up this technique for industrial processes would imply the application of electric fields similarly to sputtering systems such as DC magnetron sputtering. Further design studies would be required to include a top plate, especially when inducing DC electric fields. Electric field assisted CVD processes would importantly provide benefits not only from the business, but also from the environmental point of view by increasing the efficiency of the photocatalytic processes of commercial products.

Further investigations on the electric field assisted CVD reaction of titanium dioxide thin films would be desirable. This could include testing the changes produced at different electric field frequencies, different field strength ranges (smaller and bigger potential differences), using different precursors and substrates. Finally, it would be interesting to investigate the changes in the microstructure when stopping and starting the electric fields during the deposition, especially to get a better understanding of the interaction mechanisms.

8. References

(1) Fujishima, A., Honda, K. *Nature* **1972**, *238*, 37.

(2) Mills, A.; Hill, G.; Bhopal, S.; Parkin, I. P.; O'Neill, S. A. *J. Photochem. Photobiol. A Chem.* **2003**, *160*, 185.

(3) CARP, O. *Prog. Solid State Chem.* **2004**, *32*, 33.

(4) Jitputti, J., Pavasupree, S., Suzuki, Y. & Yoshikawa, S. *J. Solid State Chem.* **2007**, *180*, 1743.

(5) Khan, M. A., Yang, O. B. *Catal. Today* **2009**, *146*, 177.

(6) Liao, Y.-H., Chou, J.-C. *Mater. Chem. Phys.* **2009**, *114*, 542.

(7) Yu, Y.-Y., Chien, W.-C., Tsai, T.-W., Yu, H.-H. *Mater. Chem. Phys.* **2011**, *126*, 962.

(8) Parkin, I. P.; Palgrave, R. G. *J. Mater. Chem.* **2005**, *15*, 1689.

(9) Quagliarini, E., Bondioli, F., Goffredo, G. B., Cordoni, C. & M. *Constr. Build. Mater.* **2012**, *37*, 51.

(10) Colmenares, J. C., Aramendia, M. A., Marinas, A., Marinas, J. M., Urbano, F. J. *J. Mol. Catal. A Chem.* **2010**, *331*.

(11) MacFarlane, J. W., Jenkinson, H. F., Scott, T. B. *Appl. Catal. B Environ.* **2011**, *106*, 181.

(12) Oh, S., Brammer, K.-S., Moon, K.-S., Bae, J.-M, Jin, S. *Mater. Sci. Eng. C* **2011**, *31*, 873.

(13) Liang, Jia; Zhu, Gang-Qiang; Liu, Peng; Xu, C. *J. Nanosci. Nanotechnol.* **2014**, *14*, 4185.

(14) Wang, Z.; Huang, B.; Dai, Y.; Qin, X.; Zhang, X.; Wang, P.; Liu, H.; Yu, J. *J. Phys. Chem. C* **2009**, *113*, 4612.

(15) He, C.; Gu, M. *Scr. Mater.* **2006**, *54*, 1221.

(16) Yin, J.; Zou, Z.; Ye, J. *J. Phys. Chem. B* **2004**, *108*, 8888.

(17) Parkin, I. P.; Palgrave, R. G. *J. Mater. Chem.* **2005**, *15*, 1689.

(18) Chen, X., Mao, S. S. *Chem. Rev.* **2007**, *107*, 2891.

(19) Kumar, S. G.; Devi, L. G. *J. Phys. Chem. A* **2011**, *115*, 13211.

(20) Duminica, F.D., Maury, F., Hausbrand, R. *Surf. Coatings Technol.* **2007**, *201*, 9349.

(21) Mungkalasiri, J., Bedel, L., Emieux, F., Dore´, J., Renaud, F.N.R., Sarantopoulos, C.; Maury, F. *Chem. Vap. Depos.* **2010**, *16*, 35.

(22) Crane, J., Warwick, M., Smith, R., Furlan, N., Binions, B. *J. Electrochem. Soc.* **2011**, *158*, D62.

(23) Shaw, G., Parkin, I.P., Pratt, K.F.E., Williams, D. E. *J. Mater. Chem.* **2005**, *15*, 149.

(24) Panjawi, N., Naik, A., Warwick, M.E.A., Hyett, G., Binions, R. *Chem. Vap. Depos.* **2012**, *18*, 102.

(25) Bickley, R. I., Gonzalez-Carreno, T., Lees, J. S., Palmisano, L., Tilley, R. J. D. *J. Solid State Chem.* **1991**, *92*, 178.

(26) Hurum, D. C., Agrios, A. G., Gray, K. A., Rajh, T., Thurnauer, M. C. *J. Phys. Chem. B* **2003**, *107*, 4545.

(27) Scanlon, D.O., Dunnill, C.W., Buckeridge, J., Shevlin, S.A., Longsdail, A.J., Woddley. S.M., Catlow, C.R.A., Powell, M.J.m Palgrave, R.G., Parkin, I.P., Watson, G.W., Keal, T.W., Sherwood, P., Walsh, A., Sokola, A. A. *Nat. Mater.* **2013**, *12*, 798.

(28) Kohtani, S.; Yoshioka, E.; Miyabe, H. In *Hydrogenation*.

(29) Watson, S. S.; Beydoun, D.; Scott, J. A.; Amal, R. *Chem. Eng. J.* **2003**, *95*, 213.

(30) Li, G., Jin, Y., Zhang, Y., Lide, Z. *J. Phys. D. Appl. Phys.* **2002**, *35*, L37.

(31) Linsebigler, A. L., Lu, G., Yates, J. T. *Chem. Rev.* **1995**, *95*, 735.

(32) Nguyen-Manh, N. H. V. and H. V. L. and T. M. C. and V. V. P. and H. M. L. and D. *J. Phys. Condens. Matter* **2012**, *24*, 405501.

(33) Hanaor, D. H.; Sorrell, C. *J. Mater. Sci.* **2011**, *46*, 855.

(34) Duminica, F.; D., Maury, Senocq, F. *Surf. Coatings Technol.* **2004**, 255.

(35) Mathpal, M.C., Tripathi, A.K., Singh, M.K., Gairola, S.P., Pandey, S.N., Agarwal, A. *Chem. Phys. Lett.* **2013**, *555*, 182.

(36) Zhang, H.; F. Banfield, J. *J. Mater. Chem.* **1998**, *8*, 2073.

(37) Kwon, C. H.; Shin, H.; Kim, J. H.; Choi, W. S.; Yoon, K. H. *Mater. Chem. Phys.* **2004**, *86*, 78.

(38) Evans, P.; English, T.; Hammond, D.; Pemble, M. E.; Sheel, D. W. *Appl. Catal. A Gen.* **2007**, *321*, 140.

(39) O'Neill, S.A., Parkin, I.P., Clark, R.J.H., Mills, A., Elliott, N. *J. Mater. Chem.* **2003**, *13*, 56.

(40) Guo, Y., Zhang, X.-W., Han, G.-R. *Mater. Sci. Eng. B* **2006**, *135*, 83.

(41) Edusi, C.; Sankar, G.; Parkin, I. P. *Chem. Vap. Depos.* **2012**, *18*, 126.

(42) Testino, A., Bellobono, I.R., Buscaglia, V., Canevali, C., D'Arienzo, M., Polizzi, S., Scotti, R., Morrazoni, F. *J. Am. Chem. Soc.* **2007**, 3564.

(43) Cheng, H., Wang, J., Zhao, Y., Han, X. *RSC Adv.* **2014**, *4*, 47301.

(44) Lin, H., Huang, C. P., Li, W., Ni, C., Shah, S. I., Tseng, Y.-H. *Appl. Catal. B Environ.* **2006**, *68*, 1.

(45) Sun, C., Liu, L.-M., Selloni, A., Lu, G. Q. & Smith, S. C. *J. Mater. Chem.* **2010**, *20*, 10319.

(46) Lyandres, O., Finkelstein-Shapiro, D., Chackthranont, P., Graham, M., Gray, K. A. *Chem. Mater.* **2012**, *24*, 3355.

(47) Gerbasi, R., El Habra, N., Rossetto, G., Schiavi, L., Strini, A., Barison, S. *J. Electrochem. Soc.* **2009**, *156*, K223.

(48) Shen, J., Zhu, Y., Yang, X., Li., C. *J. Mater. Chem.* **2012**, *22*, 13341.

(49) Tung, H.-T., Song, J.-M., Feng, S.-W., Kuo, C., Chen, I.-G. *Phys. Chem. Chem. Phys.* **2010**, *12*, 740.

(50) Selloni, A. *Nat. Mater.* **2008**, *7*, 613.

(51) Sun, C., Liu, L.-M., Selloni, A., Lu, G.Q, Smit, S. C. *J. Mater. Chem.* **2010**, *20*.

(52) Aziz, R. A. *Indian J. Chem.* **2009**, *48A*, 951.

(53) Sheng, J., Karasawa, J., Fukami, T. *J. Mater. Sci. Lett.* **1997**, *16*, 1709.

(54) Wu, C.-Y., Lee, Y.-L., Lo, Y.-S., Lin, C.-J., Wu, C.-H. *Appl. Surf. Sci.* **2013**, *280*, 737.

(55) Hyett, G., Darr, J.A., Mills, A., Parkin, I. P. *Chem. – A Eur. J.* **2010**, *16*, 10546.

(56) Ozawa, K., Emori, M., Yamamoto, S., Yukawa, R. Yamamoto, S., Hobara, R., Fujikawa, K., Samaka, H., Matsuda, I. *J. Phys. Chem. Lett.* **2014**, *5*, 1953.

(57) Liu, H., Yang, W., Ma, Y., Ye, X., Yao, J. *New J. Chem.* **2003**, *27*, 529.

(58) Yam, T., Yuan, R., Li, W., You, J. *Appl. Catal. A Gen.* **2014**, *478*, 204.

(59) Habibi, M.H., Vosooghian, H. *J. Photochem. Photobiol. A Chem.* **2005**, *174*, 45.

(60) Ohno, T., Sarukawa, K., Matsumura, M. *New J. Chem.* **2002**, *26*, 1167.

(61) Kho, Y.K., Iwase, A., Teoh, W.Y., Mädler, L., Kudo, A., Amal, R. *J. Phys. Chem. C* **2010**, *114*, 2821.

(62) Bakardjieva, S., Šubrt, J., Štengl, V., Dianez, M. J., Sayagues, M. J. *Appl. Catal. B Environ.* **2005**, *58*, 193.

(63) Kafizas, A., Carmalt, C.J., Parking, I. P. *Chem. Eur. J.* **2012**, *18*, 13048.

(64) Kääriäinen, M.-L.; Kääriäinen, T. O.; Cameron, D. C. *Thin Solid Films* **2009**, *517*, 6666.

(65) Su, R.; Bechstein, R.; Sø, L.; Vang, R. T.; Sillassen, M.; Esbjörnsson, B.; Palmqvist, A.; Besenbacher, F. *J. Phys. Chem. C* **2011**, *115*, 24287.

(66) Serpone, N.; Salinaro, A.; Horikoshi, S.; Hidaka, H. *J. Photochem. Photobiol. A Chem.* **2006**, *179*, 200.

(67) Mao, L.; Wang, Y.; Zhong, Y.; Ning, J.; Hu, Y. *J. Mater. Chem. A* **2013**, *1*, 8101.

(68) Andersson, M.; Birkedal, H.; Franklin, N. R.; Ostomel, T.; Boettcher, S.; Palmqvist, A. E. C.; Stucky, G. D. *Chem. Mater.* **2005**, *17*, 1409.

(69) Sonawane, R. S.; Dongare, M. K. *J. Mol. Catal. A Chem.* **2006**, *243*, 68.

(70) Zhang, N.; Liu, S.; Fu, X.; Xu, Y.-J. *J. Phys. Chem. C* **2011**, *115*, 9136.

(71) Tian, G.; Chen, Y.; Zhai, R.; Zhou, J.; Zhou, W.; Wang, R.; Pan, K.; Tian, C.; Fu, H. *J. Mater. Chem. A* **2013**, *1*, 6961.

(72) Zhong, H. Y. and J. H. and H. Z. and Q. Z. and X. *Nanotechnology* **2014**, *25*, 215702.

(73) Zhong, H. Y. and J. H. and H. Z. and Q. Z. and X. *Nanotechnology* **2014**, *25*, 215702.

(74) Zhu, Y. W. and K. Y. and H. Y. and C. S. and Z. Z. and S. L. and H. S. and Q. Z. and B. Z. and Y. Z. and Z. *J. Phys. D. Appl. Phys.* **2013**, *46*, 175303.

(75) Andronic, L.; Enesca, A.; Vladuta, C.; Duta, A. *Chem. Eng. J.* **2009**, *152*, 64.

(76) Gutiérrez, D. J. R.; Mathews, N. R.; Martínez, S. S. *J. Photochem. Photobiol. A Chem.* **2013**, *262*, 57.

(77) Rosario, A. V.; Pereira, E. C. *Appl. Catal. B Environ.* **2014**, *144*, 840.

(78) Gohin, M.; Allain, E.; Chemin, N.; Maurin, I.; Gacoin, T.; Boilot, J.-P. *J. Photochem. Photobiol. A Chem.* **2010**, *216*, 142.

(79) Tachikawa, T.; Takai, Y.; Tojo, S.; Fujitsuka, M.; Irie, H.; Hashimoto, K.; Majima, T. *J. Phys. Chem. B* **2006**, *110*, 13158.

(80) Xu, Q.; Wellia, D. V.; Sk, M. A.; Lim, K. H.; Loo, J. S. C.; Liao, D. W.; Amal, R.; Tan, T. T. Y. *J. Photochem. Photobiol. A Chem.* **2010**, *210*, 181.

(81) Li, D.; Haneda, H.; Hishita, S.; Ohashi, N. *Chem. Mater.* **2005**, *17*, 2596.

(82) Wenzel, R. N. *Ind. Eng. Chem.* **1936**, *28*, 988.

(83) Cassie, A. B. D.; Baxter, S. *Trans. Faraday Soc.* **1944**, *40*, 546.

(84) Faustini, M.; Nicole, L.; Boissière, C.; Innocenzi, P.; Sanchez, C.; Grosso, D. *Chem. Mater.* **2010**, *22*, 4406.

(85) Mu, Q.; Li, Y.; Wang, H.; Zhang, Q. *J. Colloid Interface Sci.* **2012**, *365*, 308.

(86) Midtdal, K.; Jelle, B. P. *Sol. Energy Mater. Sol. Cells* **2013**, *109*, 126.

(87) Marmur, A. *Langmuir* **2003**, *19*, 8343.

(88) Neinhuis, C.; Barthlott, W. *Ann. Bot.* **1997**, *79* , 667.

(89) Extrand, C. W. *Langmuir* **2002**, *18*, 7991.

(90) Cannavale, A.; Fiorito, F.; Manca, M.; Tortorici, G.; Cingolani, R.; Gigli, G. *Build. Environ.* **2010**, *45*, 1233.

(91) Ding, X.; Zhou, S.; Wu, L.; Gu, G.; Yang, J. *Surf. Coatings Technol.* **2010**, *205*, 2554.

(92) Kapridaki, C.; Maravelaki-Kalaitzaki, P. *Prog. Org. Coatings* **2013**, *76*, 400.

(93) Kapridaki, C.; Pinho, L.; Mosquera, M. J.; Maravelaki-Kalaitzaki, P. *Appl. Catal. B Environ.* **2014**, *156-157*, 416.

(94) Faustini, M.; Nicole, L.; Boissière, C.; Innocenzi, P.; Sanchez, C.; Grosso, D. *Chem. Mater.* **2010**, *22*, 4406.

(95) Mills, A.; Hill, G.; Bhopal, S.; Parkin, I. P.; O'Neill, S. A. *J. Photochem. Photobiol. A Chem.* **2003**, *160*, 185.

(96) Zhao, X.; Zhao, Q.; Yu, J.; Liu, B. *J. Non. Cryst. Solids* **2008**, *354*, 1424.

(97) Kesmez, Ö.; Erdem Çamurlu, H.; Burunkaya, E.; Arpaç, E. *Sol. Energy Mater. Sol. Cells* **2009**, *93*, 1833.

(98) Askar, K.; Phillips, B. M.; Fang, Y.; Choi, B.; Gozubenli, N.; Jiang, P.; Jiang, B. *Colloids Surfaces A Physicochem. Eng. Asp.* **2013**, *439*, 84.

(99) Verma, L. K.; Sakhuja, M.; Son, J.; Danner, A. J.; Yang, H.; Zeng, H. C.; Bhatia, C. S. *Renew. Energy* **2011**, *36*, 2489.

(100) Deubener, J.; Helsch, G.; Moiseev, A.; Bornhöft, H. *J. Eur. Ceram. Soc.* **2009**, *29*, 1203.

(101) Liao, Y.-T.; Huang, C.-W.; Liao, C.-H.; Wu, J. C.-S.; Wu, K. C.-W. *Appl. Energy* **2012**, *100*, 75.

(102) Kubacka, A.; Diez, M. S.; Rojo, D.; Bargiela, R.; Ciordia, S.; Zapico, I.; Albar, J. P.; Barbas, C.; Martins dos Santos, V. A. P.; Fernandez-Garcia, M.; Ferrer, M. *Sci. Rep.* **2014**, *4*.

(103) Sunada, K.; Watanabe, T.; Hashimoto, K. *Environ. Sci. Technol.* **2003**, *37*, 4785.

(104) Fukuda, T., Imamura, Y., Maeda, M., Satou, T., Oonaka, M., Morita, H. *Jourrnal Environ. Biotechnol.* **2009**, *9*, 37.

(105) Gupta, K., Singh, R.P., Pandey, A., Pandey, A. *Beilstein J. Nanotechnol.* **2013**, 345.

(106) Yadav, H. M.; Otari, S. V.; Bohara, R. A.; Mali, S. S.; Pawar, S. H.; Delekar, S. D. *J. Photochem. Photobiol. A Chem.* **2014**, *294*, 130.

(107) Zhao, Q.; Liu, C.; Su, X.; Zhang, S.; Song, W.; Wang, S.; Ning, G.; Ye, J.; Lin, Y.; Gong, W. *Appl. Surf. Sci.* **2013**, *274*, 101.

(108) Kong, H., Song, J., Jang, J. *Environ. Sci. Technol.* **2010**, 5672.

(109) Visai, L., De Nardo, L., Punta, C., Melone, L., Cigada, A., Imbriani, M., Arciola, C. R. *Int. J. Artif. Organs* **2011**, *9*, 929.

(110) Romero, L., Piccirillo, C., Castro, P.M.L., Bowman, C., Warwick, M.E.A., Binions, R. *Chem. Vap. Dep. Press.* **2014**.

(111) Choy, K. *Prog. Mater. Sci.* **2003**, *48*, 57.

(112) Krumdieck, S. P. In *Chemical Vapour Deposition: Precursors and Processes:*; A.C. Jones and M.L. Hitchman (Ed.), . Cambridge, UK: Royal Society of Chemistry Publishing. (Chapters in Books), 2009; pp. 37 – 92.

(113) Pierson, H. O. In *Handbook of Chemical Vapor Deposition (CVD) (Second Edition)*; Norwich, NY: William Andrew Publishing, 1999.

(114) An, W.-J.; Jiang, D. D.; Matthews, J. R.; Borrelli, N. F.; Biswas, P. *J. Mater. Chem.* **2011**, *21*, 7913.

(115) Jung, S.-C.; Kim, S.-J.; Imaishi, N.; Cho, Y.-I. *Appl. Catal. B Environ.* **2005**, *55*, 253.

(116) Zeng, Jie, Wang, Xiaoping, and Hou, J. G. In *Nanocrystal*; Masuda, D. Y., Ed.; 2011; pp. 85–110.

(117) Hitchman, M.L., Jensen, K. F. *Chemical Vapour Deposition: Principles and Applications*; 1993.

(118) Eden, J. G. *Thin Film Processes II*; Vossen, J.L., Kern, W., Ed.; Academic Press, New York, 1991.

(119) Dobkin, D.M., Zuraw, M. K. *Principles of Chemical Vapor Deposition*; Kluwer Academic Publishers, 2003.

(120) Waugh, M., Hyett, G., Parkin, I. P. *Chem. Vap. Depos.* **2008**, *14*, 366.

(121) Qureshi, U.; Dunnill, C. W.; Parkin, I. P. *Appl. Surf. Sci.* **2009**, *256*, 852.

(122) Chua, C. S.; Tan, O. K.; Tse, M. S.; Ding, X. *Thin Solid Films* **2013**, *544*, 571.

(123) Lim, S. P.; Pandikumar, A.; Huang, N. M.; Lim, H. N. *Int. J. Hydrogen Energy* **2014**, *39*, 14720.

(124) Lim, S. P.; Huang, N. M.; Lim, H. N.; Mazhar, M. *Ceram. Int.* **2014**, *40*, 8045.

(125) Marchand, P.; Hassan, I. A.; Parkin, I. P.; Carmalt, C. J. *Dalt. Trans.* **2013**, *42*, 9406.

(126) Conde-Gallardo, A.; Castillo, N.; Guerrero, M. *J. Appl. Phys.* **2005**, *98*, 054908.

(127) Duminica, F.D., Maury, F., Abisset, S. *Thin Solid Films* **2007**, *515*, 7732.

(128) Sun, H.; Wang, C.; Pang, S.; Li, X.; Tao, Y.; Tang, H.; Liu, M. *J. Non. Cryst. Solids* **2008**, *354*, 1440.

(129) Vallejo, B.; Gonzalez-Mañas, M.; Martínez-López, J.; Morales, F.; Caballero, M. A. *Sol. Energy Mater. Sol. Cells* **2005**, *86*, 299.

(130) Gauthier, V.; Bourgeois, S.; Sibillot, P.; Maglione, M.; Sacilotti, M. *Thin Solid Films* **1999**, *340*, 175.

(131) Arvan, B.; Khakifirooz, A.; Tarighat, R.; Mohajerzadeh, S.; Goodarzi, A.; Soleimani, E. A.; Arzi, E. *Mater. Sci. Eng. B* **2004**, *109*, 17.

(132) Cross, A. J.; Dunnill, C. W.; Parkin, I. P. *Chem. Vap. Depos.* **2012**, *18*, 133.

(133) Naik, A. J. T.; Bowman, C.; Panjwani, N.; Warwick, M. E. A.; Binions, R. *Thin Solid Films* **2013**, *544*, 452.

(134) Warwick, M.E.A., Dunnill, J. Goodall, C.W., Darr, J.A., Binions, R. *Thin Solid Films* **2011**, 5942.

(135) Gordillo Delgado, F.; Villa Gómez, K.; Mejía Morales, C. *Microelectronics J.* **2008**, *39*, 1333.

(136) Su, C.; Hong, B.-Y.; Tseng, C.-M. *Catal. Today* **2004**, *96*, 119.

(137) Li, Y.; Hagen, J.; Schaffrath, W.; Otschik, P.; Haarer, D. *Sol. Energy Mater. Sol. Cells* **1999**, *56*, 167.

(138) Alekhin, A. P.; Gudkova, S. A.; Markeev, A. M.; Mitiaev, A. S.; Sigarev, A. A.; Toknova, V. F. *Appl. Surf. Sci.* **2010**, *257*, 186.

(139) Avril, L.; Reymond-Laruinaz, S.; Decams, J. M.; Bruyère, S.; Potin, V.; de Lucas, M. C. M.; Imhoff, L. *Appl. Surf. Sci.* **2014**, *288*, 201.

(140) Grigal, I. P.; Markeev, A. M.; Gudkova, S. A.; Chernikova, A. G.; Mityaev, A. S.; Alekhin, A. P. *Appl. Surf. Sci.* **2012**, *258*, 3415.

(141) Lüdecke, C.; Bossert, J.; Roth, M.; Jandt, K. D. *Appl. Surf. Sci.* **2013**, *280*, 578.

(142) Vijayalakshmy, S.; Subramanian, B. *Electrochim. Acta* **2014**, *116*, 334.

(143) Valencia, S.; Vargas, X.; Rios, L.; Restrepo, G.; Marín, J. M. *J. Photochem. Photobiol. A Chem.* **2013**, *251*, 175.

(144) Valencia, S., Marin, J.M., Restrepo, G. *Open Mater. Sci. J.* **2010**, *4*, 9.

(145) Johnson, R. W.; Hultqvist, A.; Bent, S. F. *Mater. Today* **2014**, *17*, 236.

(146) Moser, E. M.; Chappuis, S.; Olleros, J. *Surf. Coatings Technol.* **2013**, *227*, 2.

(147) Tavares, C. J.; Marques, S. M.; Viseu, T.; Teixeira, V.; Carneiro, J. O.; Alves, E.; Barradas, N. P.; Munnik, F.; Girardeau, T.; Rivière, J.-P. *J. Appl. Phys.* **2009**, *106*, 113535.

(148) Warwick, M. E. A. New CVD Methods for Energy Efficient Glazing, University College of London (UCL), 2014, pp. 1–284.

(149) Kafizas, A.; Mills, A.; Parkin, I. P. *Anal. Chim. Acta* **2010**, *663*, 69.

(150) Kafizas, A.; Adriaens, D.; Mills, A.; Parkin, I. P. *Phys. Chem. Chem. Phys.* **2009**, *11*, 8367.

(151) Tsay, C.-Y., Fan, K,-S., Lei, C.-M. *J. Alloys Compd.* **2012**, *512*, 216.

(152) Saleem, M., Ruan, H.B., Wu, F., Huang, Q.L., Xu, C.L., Kong, C. Y. *J. Phys. Sci.* **2012**, *7*, 2971.

(153) Tayade, R.J., Kulkarni, R.G., Jasra, R. V. *Sci. Technol. Adv. Mater.* **2007**, *8*, 455.

(154) Tauc, J. *Res. Bull.* **1968**, *3*, 37.

(155) Patterson, A. L. *Phys. Rev.* **1939**, *56*, 978.

(156) Warwick, M.E.A., Binions, R. *J. Nanosci. Nanotechnol.* **2011**, *11*, 8158.

(157) Choa, S.-I., Chan-Hwa Chung, C.-H., Sang Heup Moona, S.-H. *J. Electrochem. Soc.* **2001**, *148*, C599.

(158) Narayan, H., Alemu, H., Macheli, L., Sekota, M. Thakurdesai, M., Gundu Rao, T. K. *Bull. Mater. Sci.* **2009**, *32*, 499.

(159) Dahl , M., Dang, S., Bong, J. Joo, Zhang, Q., Yin, Y. *CrystEngComm* **2012**, *14*, 7680.

(160) Yates, H.M., Evans, P., Sheel, D. W. *ECS Trans.* **2009**, *8*, 781.

(161) An, W.J., Wang, W.N., Ramalingam, B., Mukherjee, S., Daubayev, B., Gangopadhyay, S., Biswas, P. *Langmuir* **2012**, *28*, 7528.

(162) A.V., C. *Mater. Sci. Forum* **1994**, *166*, 193.

(163) Dunnill, C. W.; Kafizas, A.; Parkin, I. P. *Chem. Vap. Depos.* **2012**, *18*, 89.

(164) Pratsinis, S.E., Bai, H., Biswas, P., Frenklach, M., Mastrangelo, S. V. R. *J. Am. Ceram. Soc.* **1990**, *73*, 2158.

(165) Hildenbrand, D.L., Lau, K.H., Mastrangelo, S. V. R. *J. Phys. Chem.* **1991**, *95*, 3435.

(166) Kalermo, B., Koukkari, P., Paloniemi, J. *Plasma Chem. Plasma Process.* **1996**, *16*, 59.

(167) Herzler, J., Roth, P. *Proc. Combust. Inst.* **2002**, *29*, 1353.

(168) Lin, C.P., Chen, H., Nakaruk, A., Koshy, P., Sorell, C. C. *Energy Procedia* **2013**, *34*, 627.

(169) Gribb, A.A., Banfield, J. F. *Am. Mineral.* **1997**, *82*, 717.

(170) Wang, J., Mishra, A.K., Zhao, Q., Huang, L. *J. Phys. D. Appl. Phys.* **2013**, *46*, 255303.

(171) Bordo, K., Rubahn, H.-G. *Mater. Sci.* **2012**, *18*, 1392.

(172) Qiu, H.; Wang, F.; Wu, P.; Pan, L.; Li, L.; Xiong, L.; Tian, Y. *Thin Solid Films* **2002**, *414*, 150.

(173) Zhang, X., Song, X-H., Zhang, D.-L. *Chin. Phys. B* **2010**, *19*, 086802.

(174) Melo, L.L., Vaz, A.R., Salvadori, M.C., Cattani, M. *J. Metastable Nanocrystalline Mater.* **2004**, *20-21*, 623.

(175) Luttrell, T.; Halpegamage, S.; Sutter, E.; Batzill, M. *Thin Solid Films* **2014**, *564*, 146.

(176) Romero, L.; Binions, R. *Surf. Coatings Technol.* **2013**, *230*, 196.

(177) Zhang, J.; Zhou, P.; Liu, J.; Yu, J. *Phys. Chem. Chem. Phys.* **2014**, *16*, 20382.

(178) Romero, L., Jorge, A.B., McMillan, P.F., Binions, R. *J. Solid State Sci. Technol.* **2014**, *3*, N107.

(179) Hu, Z.; Oskam, G.; Searson, P. C. *J. Colloid Interface Sci.* **2003**, *263*, 454.